Optimising catalyst and membrane performance and performing a fundamental analysis on the dehydrogenation of ethanol and 2-butanol in a catalytic membrane reactor

by

JOHAN NICO KEULER

B.Eng (Chemical)

M. Eng (Chemical)

Dissertation presented for the Degree

of

DOCTOR OF PHILOSOPHY IN ENGINEERING

(Chemical Engineering)

In the Department of Chemical Engineering

at the University of Stellenbosch

Promoters:

PROF. L LORENZEN

PROF. RD SANDERSON

STELLENBOSCH

September 2000

DECLARATION

I hereby certify that this dissertation is my own original work, except where specifically acknowledged in the text. Neither the present dissertation, nor any part thereof, has previously been submitted for a degree at any University

JN KEULER

September 2000

SUMMARY

Stricter government regulations and higher energy costs have forced the chemical industry to focus more on environmentally friendly processes and to reduce energy consumption. The main goals of chemical companies are to obtain a high product yield and selectivity, and to reduce unwanted side products. Furthermore, if reactions can be performed at lower temperature, while maintaining the reaction conversion, it will result in large energy savings.

Low temperature dehydrogenation reactions (below 300 °C) are very selective and do not produce many by-products, but conversion is limited by the reaction equilibrium. The conversion limitations have resulted in the development of alternative processes in recent years for producing alkenes from alkanes and aldehydes or ketones from alcohols. Advances in membrane technology have created the possibility of using a new type of reactor, called a catalytic membrane reactor, in which separation and reaction occurs simultaneously. A catalytic membrane reactor, of the palladium composite type, can selectively remove hydrogen and manipulate the reaction equilibrium in dehydrogenation reactions. The possibility exists to save energy, obtain high conversions and perform very selective reactions in the catalytic membrane reactor.

This dissertation describes a thorough investigation carried out into the design, optimisation, operation and modelling of a catalytic membrane reactor. The two components of the membrane reactor, i.e. the catalyst packing and the membrane structure, were optimised individually for the dehydrogenation of ethanol and 2-butanol. The optimised catalyst and optimised membrane were combined and their combined performance compared to a conventional plug flow reactor. A fundamental model was developed for the catalytic membrane reactor and a full sensitivity analysis was conducted to test the effects of membrane parameters, reaction rate parameters and process variables on reaction conversion.

Copper-based catalysts were prepared by impregnation of alumina, silica and magnesium oxide supports. The low surface area of MgO yielded poor conversions, while the Al_2O_3 support favoured dehydration and not dehydrogenation. Silica supports yielded good

dehydrogenation results and an optimum copper loading of 15% gave the highest dehydrogenation conversion for both the ethanol and the 2-butanol reactions. The copper-silica catalyst was stable at 280 °C and below for ethanol dehydrogenation, and at 250 °C and below for 2-butanol dehydrogenation. At higher temperatures in ethanol dehydrogenation, the catalyst deactivated due to both sintering and coking. Kinetic data from 200 °C to 300 °C for ethanol dehydrogenation, and from 190 °C to 280 °C for 2-butanol dehydrogenation, indicated that both reactions could be well described by the dual site, surface reaction, controlling mechanism.

Significant advances were made in the production of very thin Pd films (1.0 to 1.5 μm) on the inside of 200 nm α-alumina membrane tubes (from Societé des Céramiques Techniques). A modified electroless plating technique was used for producing the Pd films. Hydrogen permeances through the films varied between about 8 and 15 $\mu mol/m^2.Pa.s$ for temperatures from 330 °C to 450 °C and palladium films from 1.0 to 1.5 μm. Hydrogen to nitrogen selectivity was greater than 100 for all membranes tested and greater than 400 for all but two membranes (thickness 1.0 to 1.5 μm). These values are a significant improvement over other published results. Pd membranes can only be used above 300 °C and since the catalyst was unstable in that temperature region, Pd-Ag membranes had to be prepared. Pd-Ag films of thickness less than 2.2 μm were successfully synthesised and tested. Good high temperature (500 °C) and low temperature (below 300 °C) stability was obtained for the Pd-Ag membranes.

The performance of an optimised Pd-Ag membrane, packed with an optimised 14.4 wt % copper on silica catalyst (the catalytic membrane reactor), was compared to that of a plug flow reactor. The best results for ethanol dehydrogenation in a membrane reactor were obtained at 275 °C. At this temperature, the membrane reactor improved the total exit ethanol conversion from 45% (plug flow reactor) to 60% at low feed flow rates and from 36% to 46% at high feed flow rates. The maximum 2-butanol conversion in a plug flow reactor at 240 °C was 80% and that was increased to above 90% for the membrane reactor.

OPSOMMING

Strenger wetgewing en hoër energiekoste dwing die chemiese industrie om te kyk na meer omgewingsvriendelike prosesse en om energieverbruik te minimeer. Die belangrikste doelwitte van chemiese maatskappye is om hoë opbrengste en hoë selektiwiteite te verkry van hul verlangde produkte. Ongewenste byprodukte moet so ver as moontlik uitgeskakel word. Reaksies wat hoë omsettings gee by laer temperature sal lei tot groot energie besparings.

Lae temperatuur dehidrogeneringsreaksies (onder 300 °C) is baie selektief met min newe produkte, maar omsetting word beperk deur die reaksie ewewig. Ewewigsbeperkings in konvensionele prosesse het gelei tot die ontwikkeling van nuwe prosesse in die laaste dekade vir die produksie van alkene vanaf alkane en vir aldehiede en ketone vanaf alkohole. Membraanontwikkeling het die moontlikheid geskep vir 'n nuwe generasie reaktore, die katalitiese membraanreaktore, waarin skeiding en reaksie gelyktydig plaasvind. 'n Palladium-tipe reaktor kan selektief waterstof skei en die ewewig verskuif in dehidrogeneringsreaksies. Die moontlikheid bestaan om energie te bespaar en om hoë omsetting sowel as hoë selektiwiteit te verkry in die katalitiese membraanreaktor.

Hierdie proefskrif beskryf 'n omvattende ondersoek van die ontwerp, bedryf, optimering en modellering van 'n katalitiese membraanreaktor. Die twee komponente van die membraanreaktor, nl. die katalis pakking en die membraanstruktuur, is individueel geoptimeer vir die dehidrogenering van etanol en 2-butanol. Die optimum katalis en die optimum membraan is gekombineer en hul gekombineerde werking is vergelyk met die werking van 'n propvloeireaktor. 'n Fundamentele model is geformuleer vir die membraanreaktor en 'n volledige sensitiwiteitsanalise is uitgevoer op die model. Die effek van die reaksietempo parameters, membraan parameters en die proses veranderlikes op die reaksie omsetting is ondersoek.

Koper kataliste is berei deur die impregnasie van alumina, silika en magnesium oksied partikels. Die lae oppervlak area van MgO het gelei tot lae omsettings terwyl alumina meer dehidrasieprodukte as dehidrogeneringsprdukte opgelewer het. Koper op silika het die beste

dehidrogeneringsresultate getoon met 'n optimum koperkonsentrasie van 15 massa % op silika. Vir laasgenoemde koperkonsentrasie is die hoogste dehidrogeneringsomsettings verkry vir beide die etanol en 2-butanol reaksies. Die koper-silika katalis was stabiel by 280 °C en laer vir etanol dehidrogenering en by 250 °C en laer vir 2-butanol dehidrogenering. By hoër temperature (etanol dehidrogenering) het die katalis begin deaktiveer weens sintering en koolstofvorming. Kinetiese data vanaf 200 °C tot 300 °C vir etanol dehidrogenering en vanaf 190 °C tot 280 °C vir 2-butanol dehidrogenering het daarop gedui dat die reaksies goed beskryf kan word deur die dubbel posisie, oppervlak reaksie, beherende meganisme.

Goeie vordering is gemaak met die vervaardiging van baie dun Pd films (1.0 tot 1.5 μm) op die binnekant van 200 nm α-alumina membraanbuise (verskaf deur Societé des Céramiques Techniques). 'n Gemodifiseerde elektrodelose plateringstegniek is gebruik vir die vervaardiging van die films. Waterstof permeasies deur die films het gewissel van 8 tot 15 μmol/m^2.Pa.s vir temperature vanaf 330 °C tot 450 °C en palladium filmdiktes vanaf 1.0 tot 1.5 μm. Waterstof tot stikstof selektiwiteit was meer as 100 vir al die getoetste membrane en meer as 400 vir almal behalwe twee membrane (dikte 1.0 tot 1.5 μm). Hierdie waardes is beduidend beter as ander gepubliseerde resultate. Pd membrane kan slegs gebruik word bo 300 °C en aangesien die kataliste onstabiel was in daardie temperatuurgebied, is Pd-Ag membrane berei. Pd-Ag membrane met totale filmdikte kleiner as 2.2 μm is suksesvol berei en getoets. Die Pd-Ag membrane was stabiel tussen 200 °C en 500 °C.

Die werking van 'n geoptimeerde membraan, gepak met 'n geoptimeerde 14.4 massa % koper-silika katalis (die katalitiese membraanreaktor), is vergelyk met 'n propvloeireaktor. Die beste resultate verkry vir etanol dehidrogenering was by 275 °C. By daardie temperatuur is die etanol omsetting verhoog vanaf 45% vir die propvloeireaktor tot 60% vir die membraanreaktor by lae etanol vloeitempo's en vanaf 36% tot 46% by hoë etanol vloeitempo's. Die maksimum 2-butanol omsetting vir die propvloeireaktor was 80% by 240 °C en dit is verhoog tot bo 90% vir die membraanreaktor.

TABLE OF CONTENTS

CHAPTER 1: INTRODUCTION 1

CHAPTER 2: BACKGROUND AND LITERATURE SURVEY 6

2.1. MEMBRANE SEPARATION PROCESSES 6

2.2. INORGANIC MEMBRANES 6

2.2.1. Dense inorganic membranes 7

2.2.1.1. Dense metal membranes 7

2.2.1.2. Nonporous electrolyte membranes 7

2.2.1.3. Dense inorganic polymer membranes 8

2.2.1.4. Dense metal composite membranes 8

2.2.2. Porous inorganic membranes 9

2.2.2.1. Porous glass 10

2.2.2.2. Porous metal 10

2.2.2.3. Molecular sieving membranes 10

2.2.2.4. Porous ceramic and composite membranes 11

2.2.2.5. Zeolite membranes 11

2.2.3. Membrane modification 12

2.3. MEMBRANE PREPARATION AND CHARACTERISATION 13

2.4. SEPARATION MECHANISMS 14

2.4.1. Knudsen diffusion 15

2.4.2. Surface diffusion 16

2.4.3. Capillary condensation 16

2.4.4. Molecular sieve separation 16

2.4.5. Flow through non-porous membranes 17

2.5. PALLADIUM AND PALLADIUM ALLOYS 20

2.5.1. Palladium-hydrogen system 20

2.5.2. Palladium-silver systems 21

2.5.3. Palladium and copper or gold 22

2.5.4. Palladium and rare earth elements, nickel or others 22
2.6. PREPARING PALLADIUM MEMBRANES 23
2.6.1. Wet impregnation 24
2.6.2. Sol gel process 24
2.6.3. Vapour deposition techniques 25
2.6.3.1. Physical vapour deposition 25
2.6.3.2. Spray pyrolysis 26
2.6.3.3. Chemical vapour deposition 26
2.6.4. Electroplating 27
2.6.5. Electroless plating 27
2.6.5.1. Substrate pretreatment 28
2.6.5.2. Electroless plating solution composition 29
2.6.5.3. Recent advances in electroless palladium plating 30
2.6.5.4. Electroless palladium-silver coatings 32
2.6.6. Palladium membrane temperature stability 33
2.6.7. Palladium-silver alloying 33
2.6.8. Deactivation of palladium membranes 34
2.7. APPLICATIONS OF INORGANIC MEMBRANES 35
2.8. CATALYTIC MEMBRANE REACTORS 36
2.8.1. General advantages of catalytic membrane reactors 37
2.8.2. Catalytic membrane applications 37
2.8.2.1. Membranes as distributors 38
2.8.2.2. Membranes for dehydrogenation reactions 38
2.8.2.3. Other applications 39
2.8.3. Problems with catalytic membrane reactors 39
2.9. DEHYDROGENATION OF ALKANES 40
2.9.1. General principles 41
2.9.2. Alkane dehydrogenation catalysts 41
2.9.3. Commercial dehydrogenation processes 42
2.9.3.1. FBD Process (Snamprogetti-Yarsintez) 43
2.9.3.2. UOP Oleflex process 44

2.9.3.3. Lummus Catofin process 44
2.9.3.4. STAR process (Phillips steam active reforming) 45
2.9.3.5. Linde-BASF process 45
2.9.4. Alternative dehydrogenation processes 45
2.9.4.1. Coupled dehydrogenation and hydrogen oxidation 46
2.9.4.2. Oxidative dehydrogenation 46
2.9.4.3. Dehydrogenation in a membrane reactor 46
2.9.5. Methane steam reforming reaction 46
2.9.6. Water gas shift reaction 48
2.9.7. Ethane dehydrogenation 49
2.9.8. Dehydrogenation of propane 50
2.9.9. Dehydrogenation of butanes and butenes 52
2.9.9.1. Iso-butane dehydrogenation 52
2.9.9.2. n-Butane and butene dehydrogenation 53
2.9.10. Dehydrogenation of ethylbenzene to styrene 55
2.10. ALCOHOL DEHYDROGENATION CATALYSTS 56
2.10.1. Effect of copper percentage on catalyst performance 57
2.10.2. Catalyst preparation techniques 58
2.10.2.1. Precipitation 59
2.10.2.2. Urea hydrolysis 59
2.10.2.3. Electroless plating 60
2.10.2.4. Impregnation 60
2.10.3. Catalyst reduction 60
2.10.4. Catalyst deactivation 62
2.10.4.1. Sintering 62
2.10.4.2. Coking and poisoning 63
2.11. DEHYDROGENATION KINETICS 64
2.12. DEHYDROGENATION OF ALCOHOLS 65
2.12.1. Dehydrogenation of methanol to yield formaldehyde 65
2.12.2. Dehydrogenation of iso-propanol to acetone 66
2.12.3. Dehydrogenation of cyclohexanol to cyclohexanone 67

2.12.4. Dehydrogenation of C4 alcohols 69
2.12.5. Dehydrogenation of ethanol 69
2.12.5.1. Catalyst selectivity 70
2.12.5.2. Catalyst activity 72
2.12.5.3. Ethanol dehydrogenation kinetics 74
2.12.5.4. Oxidative dehydrogenation of ethanol 76
2.12.5.5. Dehydrogenation of ethanol in a membrane reactor 77
2.13. ALCOHOL DEHYDRATION REACTIONS 77
2.14. SUMMARY 78

3. EXPERIMENTAL PROCEDURES 80

3.1. OPTIMISING CATALYST COMPOSITION 80
3.1.1. Support types 80
3.1.2. Catalyst preparation 81
3.1.3. Summary of catalysts investigated 82
3.1.4. Catalyst testing for determining the optimum catalyst composition 83
3.1.4.1. Ethanol reaction 85
3.1.4.2. 2-Butanol reaction 86
3.1.5. Product analysis 86
3.1.6. Catalyst characterisation 87
3.2. KINETIC TESTING 88
3.2.1. Ethanol dehydrogenation 88
3.2.1.1. Catalyst deactivation testing 88
3.2.1.2. Characterising deactivated catalysts 90
3.2.1.3. Determining the mass transfer limited regime 90
3.2.1.4. Determining kinetic parameters 91
3.2.2. 2-Butanol reaction 92
3.3. MEMBRANE PREPARATION AND TESTING 93
3.3.1. Membrane support 93
3.3.2. Composite membrane preparation 95
3.3.2.1. Electroless plating pre-treatment 95

3.3.2.2. Electroless Pd plating 97
3.3.2.3. Membrane cleaning 100
3.3.2.4. Electroless silver plating 101
3.3.3. Determining palladium film thickness 102
3.3.4. Membrane testing 102
3.3.4.1. Reactor temperature profiles 107
3.3.5. Membrane heat treatment and reduction 108
3.3.6. Palladium-silver alloying 109
3.3.7. Membrane characterisation 110
3.4. CATALYTIC MEMBRANE REACTOR EXPERIMENTS 111
3.4.1. Ethanol dehydrogenation 112
3.4.2. 2-Butanol dehydrogenation 112
3.5. SUMMARY 113
4. OPTIMISING CATALYST COMPOSITION 114
4.1. DEHYDROGENATION OF ETHANOL 114
4.1.1. MgO catalysts 114
4.1.2. Al_2O_3 catalysts 117
4.1.2.1. BET and copper surface areas for Cu on Al_2O_3 catalysts 120
4.1.2.2. Literature data on surface areas of copper catalysts 122
4.1.2.2.1. N_2O titration 123
4.1.2.2.2. Chemisorption 123
4.1.2.2.3. Effect of preparation method on catalyst characteristics 123
4.1.2.3. The effect of additives on ethanol conversion and product distribution 125
4.1.2.4. Summary for using Cu on alumina catalysts 127
4.1.3. Silica catalysts 127
4.1.3.1. The effects of copper loading and temperature on acetaldehyde yield 127
4.1.3.2. The effect of additives on product distribution and yields 129
4.1.3.3. Effect of particle size on acetaldehyde yield 131

4.1.3.4. Surface area data for silica-based catalysts 132
4.1.3.4.1. TEM and XRD data for copper on silica catalysts *134*
4.2. DEHYDROGENATION OF 2-BUTANOL **136**
4.2.1. MgO catalysts **136**
4.2.2. Silica catalysts **139**
4.2.2.1. Effect of particle size on 2-butanol conversion 141
4.3. SUMMARY **142**
4.3.1. Ethanol reaction **142**
4.3.2. 2-Butanol reaction **143**
5. REACTION KINETICS **145**
5.1. CATALYST DEACTIVATION TESTING **146**
5.1.1. Effect of reduction temperature on ethanol reaction **146**
5.1.2. Effect of reaction temperature and additives on catalyst stability **147**
5.1.3. Further deactivation testing **149**
5.1.3.1. Deactivation mechanism 153
5.1.4. Catalyst stability for dehydrogenation of 2-butanol **153**
5.2. REACTION MASS TRANSFER RESISTANCE **154**
5.2.1. Determining the mass transfer limiting regime for ethanol dehydrogenation **154**
5.2.2. Determining the mass transfer limiting regime for 2-butanol dehydrogenation **155**
5.3. KINETICS FOR ALCOHOL DEHYDROGENATION **156**
5.3.1. Ethanol dehydrogenation **158**
5.3.1.1. Equation optimisation 162
5.3.2. 2-Butanol dehydrogenation **167**
5.3.2.1. Equation optimisation 170
5.4. SUMMARY **172**
6. Pd MEMBRANE PREPARATION AND CHARACTERISATION **174**
6.1. MEMBRANE STRUCTURE **174**
6.2. SURFACE PRETREATMENT **175**

6.3. THE ELECTROLESS Pd PLATING PROCESS 176
6.3.1. Solution feeding to membrane tube 177
6.3.2. Effect of plating rate on membrane performance 179
6.3.3. Pd membrane thickness measurement 181
6.3.4. Membrane post plating treatment 181
6.4. THE EFFECT OF SUPPORT STRUCTURE ON Pd FILMS 183
6.5. STRUCTURAL CHARACTERISATION OF Pd MEMBRANES 184
6.6. PERMEANCE TESTING OF Pd MEMBRANES 186
6.6.1. The effect of ΔP on H_2 and N_2 permeance 187
6.6.1.1. Nitrogen experiments 187
6.6.1.2. Hydrogen experiments 188
6.6.2. The effect of temperature on H_2 and N_2 permeance 190
6.6.3. The effect of film thickness on permeance 192
6.6.3.1. Hydrogen permeance 192
6.6.3.2. Nitrogen permeance 193
6.6.3.3. Membrane selectivity 194
6.6.3.4. Arrhenius parameters for hydrogen permeance 194
6.6.4. Comparison with literature data 195
6.6.4.1. Hydrogen permeances in the present study 196
6.6.5. H_2 permeance employing a sweep gas 197
6.7. SUMMARY 204
7. Pd-Ag MEMBRANE ALLOYING AND STABILITY TESTING 206
7.1. Pd-Ag MEMBRANE PREPARATION 206
7.2. UNALLOYED Pd-Ag MEMBRANES 207
7.2.1. Characterising unalloyed Pd-Ag membranes 209
7.2.1.1. Unalloyed Pd-Ag membranes tested with a sweep gas 211
7.3. LITERATURE DATA ON ALLOYING Pd-Ag MEMBRANES 214
7.3.1. Alloying co-deposited Pd-Ag films 214
7.3.2. Alloying successive Pd-Ag films 214
7.3.3. Diffusion kinetics 215
7.4. ALLOYING RESULTS FOR Pd-Ag MEMBRANES 216

7.4.1. Alloying in a tube furnace 217
7.4.1.1. Alloying at a temperature of 545 °C 217
7.4.1.2. Alloying at a temperature of 530 °C 219
7.4.1.3. Alloying at a temperature of 590 °C 220
7.4.2. Temperature stability of Pd-Ag membranes 220
7.4.2.1. Literature data on Pd membrane stability 220
7.4.2.2. Pd-Ag membrane stability 221
7.4.2.3. Structural changes of Pd-Ag membranes during heating 224
7.4.3. Alloying in situ in the reactor 227
7.4.3.1. Alloying in a hydrogen environment 227
7.4.3.2. Alloying in nitrogen and argon environments 229
7.4.3.3. Further treatment of Pd-Ag films 231
7.4.3.4. Suggested heat treatment procedure for Pd-Ag films 232
7.5. FULL CHARACTERISATION OF MEMBRANES N4x AND N8x 233
7.6. SUMMARY 234
8. CATALYTIC MEMBRANE REACTOR MODELLING 236
8.1. REACTANT FEED RATES 236
8.2. ALCOHOL PERMEANCE DATA 237
8.3. DEVELOPING A PROCESS MODEL 239
8.3.1. Model assumptions 239
8.3.2. Design equation 240
8.3.3. Modelling of mass transfer effects 242
8.3.3.1. Interphase mass transfer resistance modelling 242
8.3.3.1.1. The effectiveness factor *246*
8.3.3.2. Intraparticle mass transfer resistance modelling 247
8.3.3.2.1. Effective diffusion coefficient (De_i) *249*
8.3.3.3. Summary of modelling mass transfer 249
8.3.4. Mass transfer coefficients from experimental data 250
8.3.4.1. Ethanol dehydrogenation 250
8.3.4.2. 2-Butanol dehydrogenation 253

8.4. EXPERIMENTAL DATA FOR A PLUG FLOW REACTOR 253
8.4.1. Ethanol dehydrogenation in a plug flow reactor 253
8.4.2. 2-butanol dehydrogenation in a plug flow reactor 256
8.4.3. Summary of model for ethanol dehydrogenation 257
8.4.4. Summary of model for 2-butanol dehydrogenation 262
8.5. SELECTIVITY ANALYSIS OF THE PROCESS MODEL 266
8.5.1. The effect of k'-values on model performance 267
8.5.1.1. Back diffusion 268
8.5.2. The effect of K_{acet} on model performance 268
8.5.3. The effect of the membrane selectivity on model performance 269
8.5.4. The effect of the reaction effectiveness factor on model performance 270
8.5.5. The effect of the ethanol feed rate on model performance 270
8.5.6. The effect of the sweep gas on model performance 271
8.5.7. The effect of the H_2 permeance at constant selectivity on model performance 272
8.5.8. The effect of the H_2 permeance at varying selectivity on model performance 272
8.5.9. Model performance under non-standard conditions 273
8.5.10. Optimising membrane performance on model performance 274
8.6. SUMMARY 275
9. CATALYTIC MEMBRANE REACTOR DATA 278
9.1. ETHANOL DEHYDROGENATION 279
9.1.1. Membrane reactor experiments at 250 °C 279
9.1.2. Membrane reactor experiments at 275 °C 283
9.1.3. Membrane reactor experiments at 300 °C 286
9.1.4. Further discussion of ethanol dehydrogenation 288
9.2. 2-BUTANOL DEHYDROGENATION 291
9.2.1. Membrane reactor experiments at 190 °C 291
9.2.2. Membrane reactor experiments at 215 °C 294
9.2.3. Membrane reactor experiments at 240 °C 297

9.2.4. Further discussion of 2-butanol dehydrogenation 300
9.3. SUMMARY 302

10. CONCLUSIONS 304

10.1. CATALYST OPTIMISATION 304
10.2. REACTION MODELLING FOR ETHANOL AND 2-BUTANOL DEHYDROGENATION 305
10.3. MEMBRANE OPTIMISATION 306
10.4. MEMBRANE MODELLING 307
10.5. MEMBRANE REACTOR VS. PLUG FLOW REACTOR 307
10.6. MEMBRANE REACTOR MODELLING 308

11. FUTURE WORK 310

12. REFERENCES 311

LIST OF SYMBOLS 336
LIST OF ABBREVIATIONS 340

APPENDIX A: List of chemicals used 341

APPENDIX B1: Ethanol and 2-butanol response factors as determined with a HP G1800A GC 343
APPENDIX B2: Ethanol and 2-butanol response factors as determined with a HP 5850 GC 348

APPENDIX C1: Equations for determining ethanol dehydrogenation kinetics 351
APPENDIX C2: Equations for determining 2-butanol dehydrogenation kinetics 355

APPENDIX D1: Hydrogen and nitrogen permeance data for Pd films 358
APPENDIX D2: Hydrogen and nitrogen permeance data for Pd-Ag films 378

APPENDIX E: Literature data on Pd and Pd-alloy thin films 394

APPENDIX F1:	Plug flow reactor data and membrane reactor data for ethanol dehydrogenation	402
APPENDIX F2:	Plug flow reactor data and membrane reactor data for 2-butanol dehydrogenation	410
APPENDIX G:	Sensitivity analysis for the catalytic membrane reactor model	420

LIST OF FIGURES

CHAPTER 1:

Figure 1.1: Project flow diagram 5

CHAPTER 2:

Figure 2.1: Separation by a semi-permeable membrane 6

Figure 2.2: Knudsen diffusion 15

Figure 2.3: Surface diffusion 15

Figure 2.4: Capillary condensation 15

Figure 2.5: Molecular sieve separation 15

Figure 2.6: Hydrogen and oxygen flow through a non-porous membrane 17

Figure 2.7: Equilibrium solubility isotherms of PdH_n for bulk Pd (Shu et al., 1991) 20

Figure 2.8: Permeability of H_2 through Pd alloy membranes at 350 °C and 2.2 Mpa 23

Figure 2.9: Pore blocking by deposited copper 58

Figure 2.10: The effect of temperature on copper surface structure 61

CHAPTER 3:

Figure 3.1: Set-up used for testing the kinetics of the catalyst at the CNRS, France 84

Figure 3.2: SCT membrane structure 94

Figure 3.3: Curing process for enamelled membranes 94

Figure 3.4: Pre-treatment set-up 96

Figure 3.5: Electroless Pd plating set-up 99

Figure 3.6: Membrane reactor used to test the membrane permeance 103

Figure 3.7: Set-up used for membrane testing at room temperature 103

Figure 3.8: Set-up used for high temperature (> 300 °C) hydrogen and nitrogen permeance testing 105

Figure 3.9: Set-up used for testing ethanol permeance 106

Figure 3.10: Reactor temperature profiles at different oven temperatures 108

Figure 3.11: Membrane packed with catalyst 111

CHAPTER 4:

Figure 4.1:	Total ethanol conversion for Cu on MgO catalysts	115
Figure 4.2:	Ethanol to acetaldehyde yield (Cu on MgO catalysts)	115
Figure 4.3:	Acetaldehyde selectivity for Cu on MgO catalysts	115
Figure 4.4:	Total ethanol conversion (Cu on alumina catalysts)	118
Figure 4.5:	Ethanol to ethene yield (Cu on alumina catalysts)	118
Figure 4.6:	Ethanol to di-ethyl ether yield (Cu on alumina catalysts)	118
Figure 4.7:	Ethanol conversion to di-ethyl ether (0% Cu on alumina) at different W/F ratios	118
Figure 4.8:	Acetaldehyde yields for Cu on alumina catalysts (W/F = 393 kg.s/mol)	119
Figure 4.9:	Butene yields for Cu on alumina catalysts (average W/F)	119
Figure 4.10:	Effect of Cu% on catalyst surface area for Cu on alumina catalysts	120
Figure 4.11:	Effect of Cu% on Cu surface area for alumina-based catalysts	120
Figure 4.12:	Pore size distribution for Cu on alumina catalysts	121
Figure 4.13:	Effect of Cr, Ni and Co (on alumina) on total ethanol conversion	125
Figure 4.14:	Effect of Cr, Ni and Co (on alumina) on ether yield	125
Figure 4.15:	Effect of Cr, Ni and Co (on alumina) on ethene yield	126
Figure 4.16:	Total ethanol conversion (Cu on silica catalysts)	128
Figure 4.17:	Ethanol to acetaldehyde yield (Cu on silica catalysts)	128
Figure 4.18:	Ethanol to acetaldehyde selectivity (Cu on silica catalysts)	128
Figure 4.19:	Total ethanol conversion (15 wt % Cu on silica catalyst)	129
Figure 4.20:	Ethanol converted to acetaldehyde (15 wt % Cu on silica)	129
Figure 4.21:	Effect of Co, Cr or Ni additives on total ethanol conversion (Cu on silica)	130
Figure 4.22:	Effect of Co, Cr or Ni additives on acetaldehyde yield (Cu on silica)	130
Figure 4.23:	Effect of Co, Cr or Ni additives on total ethanol conversion (Cu on silica)	131
Figure 4.24:	Effect of Co, Cr or Ni additives on acetaldehyde yield (Cu on silica)	131
Figure 4.25:	Effect of catalyst particle size on total ethanol conversion	131
Figure 4.26:	Effect of catalyst particle size on acetaldehyde yield percentage	131
Figure 4.27:	Effect of Cu% on catalyst surface area for Cu on silica catalysts	133
Figure 4.28:	Effect of Cu% on Cu surface area for silica-based catalysts	133
Figure 4.29:	Pore size distribution for copper on silica catalysts	133

Figure 4.30: TEM images of the unused 14.4 wt % copper on silica catalyst 135
Fig 4.30a: TEM (20 nm) 135
Fig 4.30b: TEM (20 nm) 135
Fig 4.30c: TEM (20 nm) 135
Fig 4.30d: TEM (20 nm) 135
Fig 4.30e: TEM (20 nm) 135
Fig 4.30f: TEM (20 nm) 135
Fig 4.30g: TEM (50 nm) 135
Fig 4.30h: TEM (200 nm) 135
Fig 4.30i: TEM (200 nm) 135
Figure 4.31: Total 2-butanol conversion for Cu on MgO catalysts 137
Figure 4.32: Total butene yield for Cu on MgO catalysts 137
Figure 4.33: MEK yield for Cu on MgO catalysts 138
Figure 4.34: MEK yield for a 16.9 wt % Cu on MgO catalyst 138
Figure 4.35: MEK selectivity for a 16.9 wt % Cu on MgO catalyst 138
Figure 4.36: Total 2-butanol conversion for Cu on silica catalysts 139
Figure 4.37: MEK yield for Cu on silica catalysts 139
Figure 4.38: Butene yields for Cu on silica catalysts 140
Figure 4.39: MEK yield for a 15 wt % Cu on silica catalyst 141
Figure 4.40: MEK selectivity for a 15 wt % Cu on silica catalyst 141
Figure 4.41: Effect of catalyst particle size on total 2-butanol conversion 141
Figure 4.42: Effect of catalyst particle size on MEK yield percentage 141
Figure 4.43: Equilibrium ethanol conversion vs. measured values for a 15 wt % Cu on silica catalyst 143
Figure 4.44: Equilibrium 2-butanol conversion vs. measured values for a 15 wt % Cu on silica catalyst 144

CHAPTER 5:

Figure 5.1: Effect of reduction T on acetaldehyde production rate over time (14.4 wt % Cu on silica) 147

Figure 5.2: Effect of reduction T on acetaldehyde production rate over time (14.4 wt % Cu on silica) 147
Figure 5.3: Acetaldehyde production rate as a function of time and temperature (14.4 wt % Cu on silica) 148
Figure 5.4: Effect of additives (Cr and Co) on acetaldehyde production rate 149
Figure 5.5: Effect of additives (Cr and Co) on acetaldehyde production rate at 280 °C 149
Figure 5.6: TEM images of a 14.4 wt % copper on silica catalyst after being in use 400 °C 151
Figure 5.6a: TEM (20 nm) 150
Figure 5.6b: TEM (20 nm) 150
Figure 5.6c: TEM (50 nm) 150
Figure 5.6d: TEM (50 nm) 150
Figure 5.6e: TEM (100 nm) 150
Figure 5.6f: TEM (100 nm) 150
Figure 5.6g: TEM (100 nm) 151
Figure 5.6h: TEM (200 nm) 151
Figure 5.6i: TEM (1 μm) 151
Figure 5.7: Catalyst activity (14.4 wt % Cu on silica) after re-oxidation 152
Figure 5.8: MEK production rate as a function of time for a 14.4 wt % Cu on silica catalyst 154
Figure 5.9: The effect of feed flow rate on acetaldehyde production rate 155
Figure 5.10: The effect of 2-butanol feed flow rate on the MEK production rate 156
Figure 5.11: Linear fits of reaction rate data at 1 atm. total pressure and 225 °C 158
Figure 5.12: Linear fits of reaction rate data at 1 atm. total pressure and 300 °C 158
Figure 5.13: % Catalyst deactivation after 24 hours of operation 160
Figure 5.14: Parameters for ethanol reaction equation as a function of temperature 161
Figure 5.15: Difference between model 1 rates and actual rates at different temperatures 164
Figure 5.16: Difference between model 2 rates and actual rates at different temperatures 164
Figure 5.17: Percentage deviation between model 1 rates and measured rates 165

Figure 5.18: Percentage deviation between model 2 rates and measured rates 165
Figure 5.19: Model 1 rates vs. actual rates at different rate values 165
Figure 5.20: Model 2 rates vs. actual rates at different rate values 165
Figure 5.21: Percentage deviation between model values and measured values at 573 K 166
Figure 5.22: Linear fits of reaction rate data at 1 atm. total pressure and 220 °C 168
Figure 5.23: Linear fits of reaction rate data at 1 atm. total pressure and 280 °C 168
Figure 5.24: Parameters for 2-butanol reaction equation as a function of temperature 170
Figure 5.25 Comparison between measured reaction rates and model reaction rates 172

CHAPTER 6:

Figure 6.1: Cross section view of a three layer SCT membrane 175
Figure 6.2: Top view (20 000x) of a three layer SCT membrane 175
Figure 6.3: Top view (5 000x) of a three layer SCT membrane 175
Figure 6.4: Pd concentration in solution after repeated plating sessions 178
Figure 6.5: Cross section of membrane (a) (10 000x) 179
Figure 6.6: Top view of membrane (a) (25 000x) 179
Figure 6.7: Top view of membrane (a) (50 000x) 180
Figure 6.8: Cross section of membrane (b) (10 000x) 180
Figure 6.9: Top view of membrane (b) (25 000x) 180
Figure 6.10: Top view of membrane (b) (5000x) 181
Figure 6.11: Top view of membrane (b) (25000x) 181
Figure 6.12: Effect of oxidation post treatment on H_2 permeance (membrane 2, 1.43 μm Pd) 182
Figure 6.13: Effect of oxidation post treatment on selectivity (membrane 2, 1.43 μm Pd) 182
Figure 6.14: Cross section of membrane (3b) (10 000x) 184
Figure 6.15: Top view of membrane (3b) (5000 x) 185
Figure 6.16: Top view of membrane (3b) (25 000x) 185
Figure 6.17: Cross section of membrane (11) (10 000x) 185
Figure 6.18: Top view of membrane (11) (5000 x) 186

Figure 6.19: Top view of membrane (11) (25 000x) 186
Figure 6.20: Effect of pressure on N_2 permeance for a 1.47 micron Pd film (6) 188
Figure 6.21: Effect of pressure on N_2 permeance for a 2.4 micron Pd film (3a) 188
Figure 6.22: Effect of pressure on N_2 permeance for a 3.08 micron Pd film (1a) 188
Figure 6.23: Effect of pressure on N_2 permeance for a 4.43 micron Pd film (3b) 188
Figure 6.24: Effect of pressure on H_2 permeance for a 1.47 micron Pd film (6) 189
Figure 6.25: Effect of pressure on H_2 permeance for a 2.4 micron Pd film (3a) 189
Figure 6.26: Effect of pressure on H_2 permeance for a 3.08 micron Pd film (1a) 189
Figure 6.27: Effect of pressure on H_2 permeance for a 4.43 micron Pd film (3b) 189
Figure 6.28: Selectivity data for membrane (3a) 190
Figure 6.29: Selectivity data for membrane (N8) 190
Figure 6.30: Selectivity data for membrane (N2) 191
Figure 6.31: Hydrogen permeance in $\mu mol/m^2.Pa.s$ (membrane 2a) 191
Figure 6.32: Hydrogen permeance in $\mu mol/m^2.Pa.s$ (membrane N7) 191
Figure 6.33: Hydrogen permeance for Pd films from 1 to 6.5 micron thickness 192
Figure 6.34: Hydrogen permeance for Pd films from 1 to 1.5 micron thickness 193
Figure 6.35: Nitrogen permeance for Pd films from 1 to 6.5 micron thickness 193
Figure 6.36: Nitrogen permeance for Pd films from 1 to 1.5 micron thickness 193
Figure 6.37: H_2 to N_2 selectivity for Pd films from 1 to 6.5 micron thickness 194
Figure 6.38: H_2 to N_2 selectivity for Pd films from 1 to 1.5 micron thickness 194
Figure 6.39: Arrhenius parameters for hydrogen permeance (1 to 6.5 micron Pd films) 195
Figure 6.40: Arrhenius parameters for hydrogen permeance (1 to 1.5 micron Pd films) 195
Figure 6.41: % H_2 permeated with N_2 sweep gas and space time = 2.37 s 201
Figure 6.42: % H_2 permeated with N_2 sweep gas and space time = 1.19 s 201
Figure 6.43: Hydrogen flow in tube (cm^3/min) as predicted by model for N7 (τ = 2.37 s) 202
Figure 6.44: Hydrogen flow in tube (cm^3/min) as predicted by model for N7 (τ = 2.37 s) 202
Figure 6.45: Hydrogen flow in tube (cm^3/min) as predicted by model for N7 (τ = 1.19 s) 202

Figure 6.46: Hydrogen flow in tube (cm^3/min) as predicted by model for N7 (τ = 1.19 s) 202
Figure 6.47: % H_2 permeated with N_2 sweep gas and space time = 2.37 s 203
Figure 6.48: % H_2 permeated with N_2 sweep gas and space time = 1.19 s 203
Figure 6.49: Hydrogen flow in tube (cm^3/min) as predicted by model for N4 (τ = 2.37 s) 203
Figure 6.50: Hydrogen flow in tube (cm^3/min) as predicted by model for N4 (τ = 2.37 s) 203
Figure 6.51: Hydrogen flow in tube (cm^3/min) as predicted by model for N4 (τ = 1.19 s) 204
Figure 6.52: Hydrogen flow in tube (cm^3/min) as predicted by model for N4 (τ = 1.19 s) 204

CHAPTER 7:

Figure 7.1: Hydrogen permeances for Pd and Pd-Ag membranes (8, N1, 8b, N1b) 209
Figure 7.2: Hydrogen permeances for Pd and Pd-Ag membranes (N3, N4, N3b, N4b) 210
Figure 7.3: Measured vs. calculated % H_2 permeance for 8b 212
Figure 7.4: Measured vs. calculated % H_2 permeance for N1b 212
Figure 7.5: Measured vs. calculated % H_2 permeance for N3b 212
Figure 7.6: Measured vs. calculated % H_2 permeance for N4b 212
Figure 7.7: % H_2 permeated with N_2 sweep gas and space time = 2.37 s 213
Figure 7.8: % H_2 permeated with N_2 sweep gas and space time = 1.19 s 213
Figure 7.9: Hydrogen flow in tube (cm^3/min) as predicted by model for N3b (τ = 2.37 s) 213
Figure 7.10: Hydrogen flow in tube (cm^3/min) as predicted by model for N3b (τ = 2.37 s) 213
Figure 7.11: Hydrogen flow in tube (cm^3/min) as predicted by model for N3b (τ = 1.19 s) 213
Figure 7.12: Hydrogen flow in tube (cm^3/min) as predicted by model for N3b (τ = 1.19 s) 213

Figure 7.13: Heating times required to obtain similar Pd-Ag diffusion at different temperatures 216
Figure 7.14: Effect of heating time in argon on hydrogen permeance through a Pd-Ag film (membranes N3b to N3e) 208
Figure 7.15: Effect of heating in argon on H_2 permeance for N4 220
Figure 7.16: Effect of heating in argon on N_2 permeance for N4 222
Figure 7.17: Effect of heating in argon on nitrogen permeance (N3) 223
Figure 7.18: Effect of heating in argon on selectivity (N3) 223
Figure 7.19: Membrane d1 (25 000x) 225
Figure 7.20: Membrane d2 (25 000x) 225
Figure 7.21: Membrane d3 (25 000x) 225
Figure 7.22: Membrane d1 (50 000x) 225
Figure 7.23: Membrane d2 (50 000x) 225
Figure 7.24: Membrane d3 (50 000x) 225
Figure 7.25: Membrane d1 (5 000x) 226
Figure 7.26: Membrane d2 (5 000x) 226
Figure 7.27: Membrane d3 (5 000x) 226
Figure 7.28: Membrane d3 (2000x) 226
Figure 7.29: Side view of d2 226
Figure 7.30: Side view of d3 226
Figure 7.31: Effect of heating time in H_2 on H_2 and N_2 permeance for N4x 228
Figure 7.32: Effect of heating time in H_2 at 590 °C on H_2 permeance for N1x 228
Figure 7.33: Effect of heating time in H_2 at 590 °C on N_2 permeance for N1x 228
Figure 7.34: Effect of temperature on H_2 and N_2 permeance for N1x 229
Figure 7.35: Effect of heating time in N_2 and Ar at 500 and 550 °C on H_2 permeance for N2x 230
Figure 7.36: Effect of heating time in N_2 at 500 °C on N_2 permeance for N2x 230
Figure 7.37: Effect of heating time in Ar at 500 and 550 °C on Ar permeance for N2x 231
Figure 7.38: Effect of temperature on H_2 permeance for N2x 231
Figure 7.39: H_2 and N_2 permeances for N4x 233
Figure 7.40: H_2 and N_2 permeances for N8x 233

Figure 7.41: Measured vs. calculated % H_2 permeance for N4x 234

Figure 7.42: Measured vs. calculated % H_2 permeance for N8x 234

CHAPTER 8:

Figure 8.1: Theoretical effect of feed rate on equilibrium conversion 236

Figure 8.2: Comparison between H_2 to N_2 and H_2 to ethanol selectivities for a 1.5 μm Pd film 238

Figure 8.3: Ethanol to nitrogen permeance ratio for a 1.5 μm Pd film 238

Figure 8.4: Description of catalytic membrane reactor process 241

Figure 8.5: Effect of Reynolds number on effectiveness factor 251

Figure 8.6: C_1 vs. inverse Re at different temperatures 252

Figure 8.7: C_1 vs. inverse $Re^{0.81}$ at different temperatures 252

Figure 8.8: Plug flow reactor data for ethanol dehydrogenation at 250 °C 254

Figure 8.9: Plug flow reactor data for ethanol dehydrogenation at 275 °C 254

Figure 8.10: Plug flow reactor data for ethanol dehydrogenation at 300 °C 254

Figure 8.11: Selectivity towards acetaldehyde production for a plug flow reactor 254

Figure 8.12: Re as a function of temperature and conversion (feed rate = $4.77*10^{-5}$ mol/s) 255

Figure 8.13: Re as a function of temperature and conversion (feed rate = $9.54*10^{-5}$ mol/s) 255

Figure 8.14: Re as a function of temperature and conversion (feed rate = $1.43*10^{-4}$ mol/s) 255

Figure 8.15: Plug flow reactor data for 2-butanol dehydrogenation at 190 °C 256

Figure 8.16: Plug flow reactor data for 2-butanol dehydrogenation at 215 °C 256

Figure 8.17: Plug flow reactor data for 2-butanol dehydrogenation at 240 °C 256

Figure 8.18: Selectivity towards MEK production for a plug flow reactor 256

Figure 8.19: Effect of sweep gas to standard feed molar ratio on ethanol conversion and ethanol losses 275

CHAPTER 9:

Figure 9.1: Ethanol conversion at 250 °C vs. sweep gas flow rate ($F_{et} = 2.39*10^{-5}$ mol/s) 280

Figure 9.2: Ethanol conversion at 250 °C vs. sweep gas flow rate ($F_{et} = 4.77*10^{-5}$ mol/s) 280

Figure 9.3: Measured acetaldehyde selectivity (250 °C) 282

Figure 9.4: Ethanol conversion at 275 °C vs. sweep gas flow rate ($F_{et} = 4.77*10^{-5}$ mol/s) 283

Figure 9.5: Ethanol conversion at 275 °C vs. sweep gas flow rate ($F_{et} = 9.54*10^{-5}$ mol/s) 283

Figure 9.6: Ethanol conversion at 275 °C vs. sweep gas flow rate ($F_{et} = 1.43*10^{-4}$ mol/s) 284

Figure 9.7: Acetaldehyde yield at 275 °C for a membrane reactor 284

Figure 9.8: Measured acetaldehyde selectivity (275 °C) 286

Figure 9.9: Ethanol conversion at 300 °C vs. sweep gas flow rate ($F_{et} = 4.77*10^{-5}$ mol/s) 287

Figure 9.10: Ethanol conversion at 300 °C vs. sweep gas flow rate ($F_{et} = 9.54*10^{-5}$ mol/s) 287

Figure 9.11: Measured acetaldehyde selectivity (300 °C) 288

Figure 9.12: Measured acetaldehyde selectivity at a constant feed rate ($F_{et} = 9.54*10^{-5}$ mol/s) 290

Figure 9.13: 2-Butanol conversion at 190 °C vs. sweep gas flow rate ($F_{2But} = 1.52*10^{-5}$ mol/s) 292

Figure 9.14: 2-Butanol conversion at 190 °C vs. sweep gas flow rate ($F_{2But} = 3.04*10^{-5}$ mol/s) 292

Figure 9.15: 2-Butanol conversion at 190 °C vs. sweep gas flow rate ($F_{2But} = 4.56*10^{-5}$ mol/s) 292

Figure 9.16: MEK yield at 190 °C 292

Figure 9.17: Measured MEK selectivity at 190 °C 294

Figure 9.18: 2-Butanol conversion at 215 °C vs. sweep gas flow rate ($F_{2But} = 1.52*10^{-5}$ mol/s) 295

Figure 9.19: 2-Butanol conversion at 215 °C vs. sweep gas flow rate ($F_{2But} = 3.04*10^{-5}$ mol/s) 295
Figure 9.20: 2-Butanol conversion at 215 °C vs. sweep gas flow rate ($F_{2But} = 6.08*10^{-5}$ mol/s) 296
Figure 9.21: MEK yield at 215 °C 296
Figure 9.22: Measured MEK selectivity at 215 °C 297
Figure 9.23: 2-Butanol conversion at 240 °C vs. sweep gas flow rate ($F_{2But} = 1.52*10^{-5}$ mol/s) 298
Figure 9.24: 2-Butanol conversion at 240 °C vs. sweep gas flow rate ($F_{2But} = 3.04*10^{-5}$ mol/s) 298
Figure 9.25: 2-Butanol conversion at 240 °C vs. sweep gas flow rate ($F_{2But} = 6.08*10^{-5}$ mol/s) 299
Figure 9.26: MEK yield at 240 °C 299
Figure 9.27: Measured MEK selectivity at 240 °C 300
Figure 9.28: MEK yield % vs. flow rate and temperature 301
Figure 9.29: Effect of sweep ratio on MEK yield % 301

LIST OF TABLES

CHAPTER 2:

Table 2.1:	The effect of repairing of electroless Pd plated coatings (Li et al., 1999)	31
Table 2.2:	Operating conditions for various dehydrogenation processes	42
Table 2.3:	Process efficiency for propane and iso-butane dehydrogenation	43
Table 2.4:	Catalyst supports (Carrizosa and Munuera, 1977; Rosynek et al., 1990)	57
Table 2.5:	Possible rate equations for solid catalysed dehydrogenation reactions	64
Table 2.6:	Common supports for copper catalysts	67
Table 2.7:	Selectivities for ethanol dehydrogenation (Iwasa and Takezawa, 1991)	71
Table 2.8:	Effect of Cr and Co addition to Cu on ethanol dehydrogenation (Church et al., 1951)	71
Table 2.9:	Reaction rate parameters for ethanol dehydrogenation (Tu et al., 1994b)	72
Table 2.10:	Activities and TOFs for ethanol dehydrogenation at 190 °C Kanoun et al. (1991, 1993)	73

CHAPTER 3:

Table 3.1:	Characteristics of alumina and silica supports used	81
Table 3.2:	Different copper loadings investigated for copper-supported catalysts	83
Table 3.3:	Other copper supported catalysts	83
Table 3.4:	Reactor conditions used to test Cu on SiO_2 and MgO supports in the ethanol dehydrogenation reaction	85
Table 3.5:	Reactor conditions used to test Cu on Al_2O_3 supports in the ethanol dehydrogenation reaction	86
Table 3.6:	Reactor conditions used to test Cu on SiO_2 and MgO supports in the ethanol dehydrogenation reaction	86
Table 3.7:	Different combinations of reduction and reaction temperatures studied	89
Table 3.8:	Summary of catalyst deactivation tests for ethanol dehydrogenation	89
Table 3.9:	Determining the region free of interphase mass transfer resistance	91
Table 3.10:	Conditions investigated for determining interphase mass transfer limited regime for 2-butanol dehydrogenation	93

Table 3.11: Membrane layer characteristics of a SCT membrane 94
Table 3.12: Compositions of pre-treatment solutions 96
Table 3.13: Stirring sequence and times used in pre-treatment 97
Table 3.14: Composition of the Pd plating solution per litre (for 2.00 g/litre Pd in solution) 98
Table 3.15: Plating procedure used for producing Pd films 100
Table 3.16: Composition of silver plating bath per litre of plating solution 101
Table 3.17: Plating procedure used for producing Ag films 102

CHAPTER 4:

Table 4.1: BET surface areas for Cu on MgO catalysts in m^2/g 116
Table 4.2: Yield matrix indicating main products and by-products for Cu/MgO 117
Table 4.3: Surface areas of unsupported copper catalysts 123
Table 4.4: Surface areas of supported copper catalysts 124
Table 4.5: BET and copper surface areas for Cu/alumina catalysts with additives 126

CHAPTER 5:

Table 5.1: Summary of catalyst deactivation at different reaction temperatures 148
Table 5.2: Performance of Cu/Cr/Co on silica catalyst 149
Table 5.3: XRD and TOC results of tested catalysts 150
Table 5.4: Copper surface areas for 14.4 wt % Cu on silica catalysts 152
Table 5.5: Reaction rate parameters for ethanol dehydrogenation 159
Table 5.6: Kinetic model parameters for ethanol dehydrogenation 164
Table 5.7: Reaction rate parameters for 2-butanol dehydrogenation 168
Table 5.8: Kinetic model parameters for 2-butanol dehydrogenation 171

CHAPTER 6:

Table 6.1: Composition (per litre) of plating solutions for membrane plating 177
Table 6.2: Experimental H_2 permeances vs. calculated values for membrane (N7) 199
Table 6.3: Experimental H_2 permeances vs. calculated values for membrane (N4) 200

CHAPTER 7:

Table 7.1:	Alloying procedures used for Pd-Ag membranes	208
Table 7.2:	N_2 permeance and selectivity data for 8b, N1b, N3b and N4b	211
Table 7.3:	Ag-Pd diffusion coefficients	215
Table 7.4:	Effect of heating on hydrogen permeances for membrane N3	219
Table 7.5:	Nitrogen permeances of membranes (8c) and (N6) after heating at 600 °C	223
Table 7.6:	Description of different membrane stages (d1-d3)	224
Table 7.7:	Hydrogen permeances at 410 °C	231
Table 7.8:	Hydrogen and nitrogen permeances at 410 °C after oxidation	232

CHAPTER 8:

Table 8.1:	Different liquid hourly space volumes (LHSV) used for dehydrogenation reactions in a membrane reactor	237
Table 8.2:	Surface reaction rates at different temperatures	251
Table 8.3:	Ethanol reaction rate parameters	261
Table 8.4:	Permeance data for N8x at 250, 275 and 300 °C	261
Table 8.5:	Parameters for solving ethanol dehydrogenation model	261
Table 8.6:	Reaction rate coefficients for 2-butanol dehydrogenation	265
Table 8.7:	Permeance data for N8x at 190, 215 and 240 °C	265
Table 8.8:	Parameters for solving 2-butanol dehydrogenation model	265
Table 8.9:	Parameters for ethanol dehydrogenation at 275 °C	266

CHAPTER 9:

Table 9.1:	Model differences for ethanol conversion at 250 °C	281
Table 9.2:	Improvements in total X_{et} for the membrane reactor at 250 °C	282
Table 9.3:	Model differences for ethanol conversion at 275 °C	285
Table 9.4:	Improvements in total X_{et} for the membrane reactor at 275 °C	285
Table 9.5:	Model differences for ethanol conversion at 300 °C	287
Table 9.6:	Improvements in total X_{et} for the membrane reactor at 300 °C	288
Table 9.7:	Improvements in total X_{2But} for the membrane reactor at 190 °C	293
Table 9.8:	Model differences for 2-butanol conversion at 190 °C	293

Table 9.9: Improvements in total X_{2But} for the membrane reactor at 215 °C 296

Table 9.10: Model differences for 2-butanol conversion at 215 °C 296

Table 9.11: Improvements in total X_{2But} for the membrane reactor at 240 °C 299

Table 9.12: Model differences for 2-butanol conversion at 240 °C 299

ACKNOWLEDGEMENTS

I want to give special thanks to the following people:

JG Keuler and SCJ Keuler (my parents),

C Nel (my grandmother),

All the other members of my family,

C Brown and her family,

DW Mouton for hours of assistance, and

For every friend that listened and/or gave advice.

For technical support I want to thank:

Prof. L Lorenzen,

Prof. R Sanderson,

Prof. J Dalmon,

Dr. S Miachon, and

Dr. B Jager.

I want to thank those who assisted me with analyses:

H Botha and

M Waldron

For financial support I want to thank:

Sasol,

FRD, and

CNRS

And most of all, I want to thank the LORD for the gift of life.

1. INTRODUCTION

In this study the possibility of dehydrogenating alcohols in a palladium-based membrane reactor was investigated. Recent developments in membrane technology have opened the way for performing conventional reactions in a new type of reactor called a catalytic membrane reactor. This type of reactor offers the possibility of doing separation and reaction simultaneously in a single process unit. The Pd membrane reactor offers several theoretical advantages over the conventional plug flow reactor.

- In equilibrium restricted reactions, the equilibrium can be shifted, resulting in higher conversions at the same operation temperatures.
- Selectivity is usually better for the membrane reactor than for the plug flow reactor.
- The reactions can be performed at lower temperatures, which will increase catalyst life by reducing catalyst deactivation.
- Lower operating temperatures will reduce energy consumption, and finally,
- For selective Pd-based membranes, high purity hydrogen can be separated through the membrane. Hydrogen is an important commodity on chemical plants.

Traditional dehydrogenation reactions have become less favourable due to high energy costs and have been replaced by alkene oxidation processes to yield the same products. An example is the oxidation of ethylene (Wacker process) to produce acetaldehyde. By exploiting advantages offered by membranes, dehydrogenation in a catalytic membrane reactor becomes a very competitive alternative to alkene oxidation. This process is more selective and provides high purity separated hydrogen as a by-product.

The six main goals of this dissertation were:

- To optimise the performance of an alcohol dehydrogenation catalyst,
- To model the kinetics of an alcohol dehydrogenation reaction,
- To optimise the composition and thickness of Pd and Pd-alloy films for hydrogen separation,

- To model the membrane separation process with a sweep gas and a pressure differential,
- To compare the performance of a membrane reactor consisting of the optimised catalyst and optimised membrane with a plug flow reactor, and
- To model the membrane reactor.

The dehydrogenation of ethanol to yield acetaldehyde was chosen as model reaction. A model was developed for this reaction and the validity of the model was tested with the dehydrogenation of 2-butanol to give 2-butanone, also known as methyl ethyl ketone (MEK). Acetaldehyde is an important intermediate for producing other chemicals. The dehydrogenation of 2-butanol is a well known industrial process and the main process used for producing the solvent MEK. The latter is of great industrial importance.

A flow diagram for the project is shown in **Figure 1.1**. The project can be divided into three sections: firstly, membrane development and modelling; secondly, some catalyst development and modelling and thirdly, a final section in which catalysis and separation are combined in the membrane reactor. For Pd plating (block 1), the composition of the plating solution, the plating conditions and the solution feeding mechanism to the inside of the membrane tube were investigated. The thickness of the Pd film was minimised to obtain films with very high hydrogen permeances, while retaining good hydrogen to nitrogen selectivities. Films were tested from 330 °C to 450 °C (block 2) under positive pressure and by using a sweep gas. Palladium thin films were used as supports for depositing silver (block 3). Pd-Ag films were heat treated in different gas environments and at different temperatures. The stability of the films was determined as a function of time.

Catalysts were prepared (blocks 7 and 8) using the impregnation technique. The effects of support type, copper loading, added stabilisers and catalyst particle size were studied for the dehydrogenation of ethanol and 2-butanol. For each catalyst, experiments were performed over a wide range of operating conditions and both the conversion and selectivity towards the desired product were optimised. The optimised catalyst was then

used for determining the reaction kinetics of the dehydrogenation of ethanol and the dehydrogenation of 2-butanol.

The optimised catalyst and optimised membrane were combined to form a catalytic membrane reactor. Experiments in the membrane reactor were performed at different temperatures, feed flow rates and sweep gas to feed molar ratios. The results were compared to those obtained in a conventional plug flow reactor.

In this dissertation, the following contributions were made to existing work from other researchers:

Catalyst development: The contribution made in this area was not large. The deactivation of a copper-based catalyst during ethanol dehydrogenation was studied in depth and a more accurate deactivation mechanism was developed. Reaction rate mechanisms and kinetic parameters were determined for ethanol and 2-butanol dehydrogenation with the optimised catalyst. Kinetic data was used for modelling purposes.

Membrane development: Significant advances were made in this field. Much thinner, yet very selective, Pd films were prepared on the inside of alumina membrane tubes with a modified electroless plating technique. The Pd film tickness in this study was less than half of the lowest thickness previously reported (see **Appendix E**) for the same membrane configuration. Thin Pd-Ag films were successfully prepared on the inside of membrane tubes with thickness less than 2.2 microns. The stability and alloying of Pd-Ag membranes were investigated thoroughly, something that has not been done previously. A method was developed for improving the hydrogen permeance through Pd-Ag films.

Membrane reactor work: Significant advances were made in the dehydrogenation of alcohols in a membrane reactor. Previously, ethanol dehydrogenation was studied by a few groups in a membrane reactor under very limited conditions (see **9.1.4**). The high quality membranes prepared in this dissertation, made it possible to study the ethanol

dehydrogenation reaction at higher ethanol feed flow rates, yielding very good results. A thorough investigation was conducted into 2-butanol dehydrogenation in a membrane reactor. This, to our knowledge, has not been investigated previously. A full sensitivity analysis on the membrane reactor model gave more insight into the effects of different parameters on the dehydrogenation process.

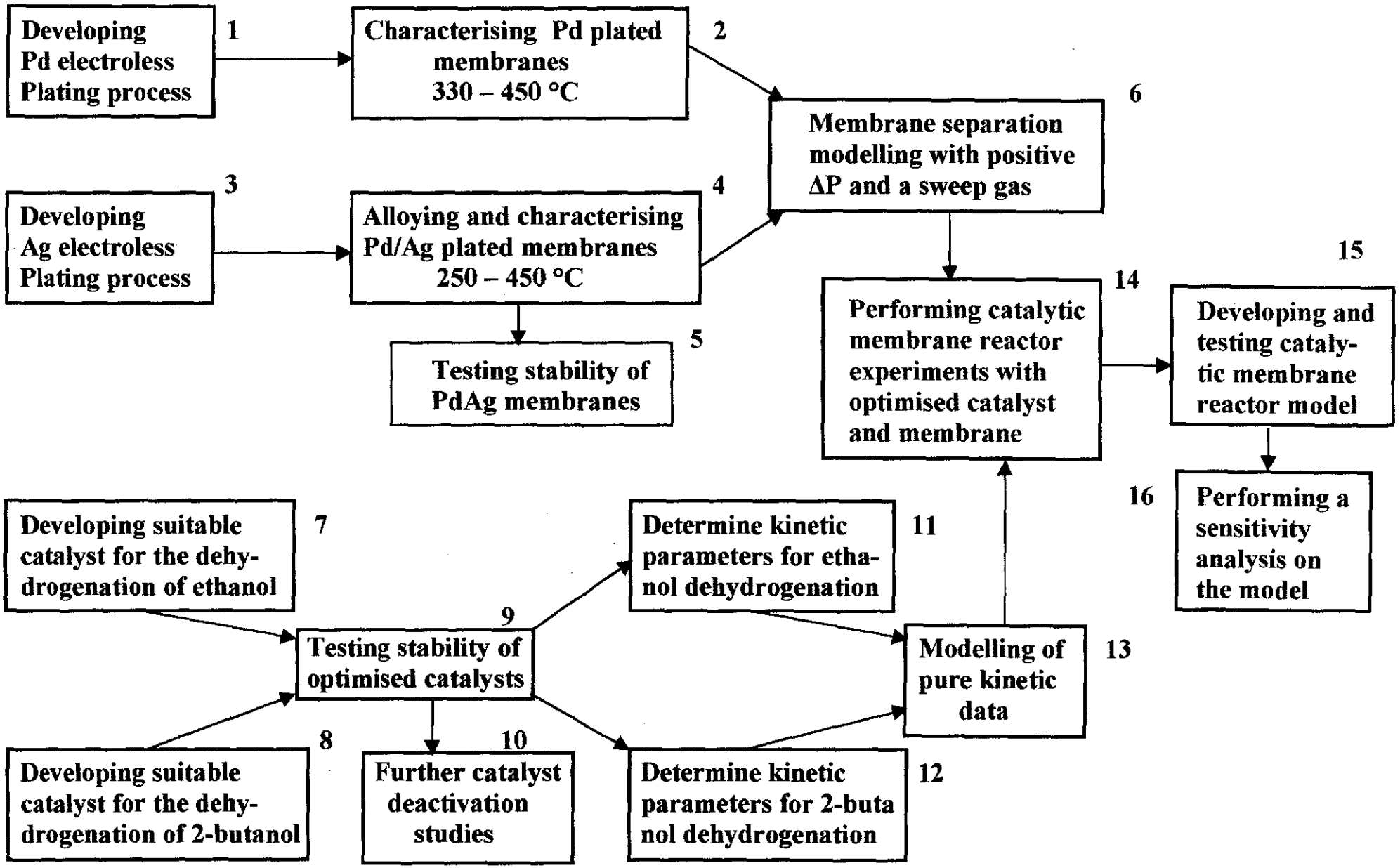

Figure 1.1: Project flow diagram

2. BACKGROUND AND LITERATURE SURVEY

2.1. MEMBRANE SEPARATION PROCESSES

A membrane is any semi-permeable active or passive barrier, which separates particles, molecules or any other species in a gaseous and/or liquid mixture (see **Figure 2.1**) when certain driving forces are applied. The driven force that causes preferential movement of species through the membrane may be a pressure difference, concentration difference or voltage difference across the membrane.

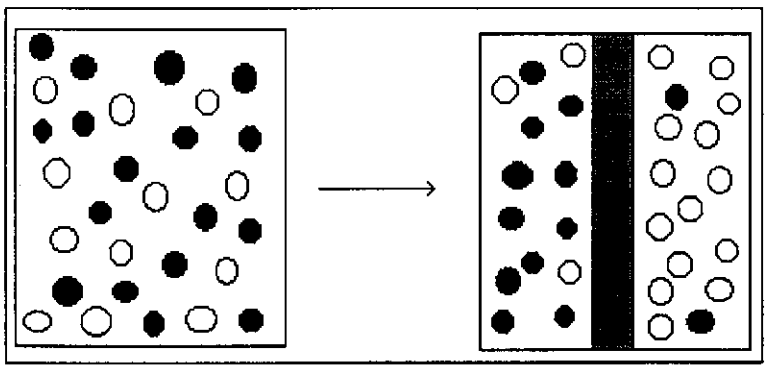

Figure 2.1: Separation by a semi-permeable membrane (right)

Membrane processes are classified according to the separation method and the size of the separated species. Basic processes are microfiltration, ultrafiltration, reverse osmosis, dialysis, electrodialysis and gas separation.

2.2. INORGANIC MEMBRANES

All membranes are either organic (polymeric) or inorganic. There are two types of inorganic membranes: dense and porous. Dense membranes can further be classified into either metal membranes or solid electrolyte membranes. They are prepared by different methods and from different materials. The preparation method has a definite effect on the pore structure. Membranes with a uniform pore structure across the thickness of the membrane and made in a single step are called symmetric membranes. Single step membranes with a changing structure throughout the thickness are asymmetric. When a

membrane consists of two or more layers, prepared in consecutive steps, it is called a composite membrane. For composite membranes, the initial layer usually provides mechanical strength and acts as a support on which further layers are deposited on. The second layer and subsequent layers, determine the membrane's separation properties.

2.2.1. DENSE INORGANIC MEMBRANES

There are several classes of dense inorganic membranes. They are either oxide based, metal based or a combination of the two. A new class of inorganic polymers has also been studied in recent years.

2.2.1.1. Dense metal membranes

Dense metal membranes are mostly made from palladium and its alloys. Pd can be alloyed with Ag, Ru, Rh, Ni or Au. Ag is, however, most frequently added to Pd to prevent hydrogen embrittlement of pure Pd that occurs below 300 °C. Johnson Matthey has used palladium-silver (77 wt %, 23 wt %) alloy membranes for hydrogen purification since the early 1960s (Hsieh, 1996). Unit production is about 56 m^3/h (Hsieh, 1996). Union Carbide installed a Pd alloy membrane plant in the 1960s to separate hydrogen from refinery off gas (McBride and McKinley, 1965). Membrane cost, durability and poisoning by carbon and sulphur compounds have restricted large scale progress (Armor, 1989). Membrane permeance tends to be low due to thick alloy layers. Alternative metals like niobium, tantalum and vanadium have been investigated for hydrogen separation (Buxbaum and Kinney, 1996). Silver membranes have been used on a much smaller scale to selectively separate oxygen from other gases.

2.2.1.2. Nonporous electrolyte membranes

Solid electrolytes are impervious to gases and liquids, but allow some ions to pass through their lattices under an applied voltage difference or a chemical potential difference. Calcium-stabilised zirconia allows for oxygen transport, while other gases (Itoh, 1990) cannot pass through. PbO selectively separates oxygen from other gases. Other electrolytes under investigation (Hsieh, 1996) include simple or complex halides

($RbAg_4I_5$), simple or complex oxides (β-aluminas) and oxide solid solutions (ZrO_2-Y_2O_3, ZrO_2-CaO, ThO_2-Y_2O_3).

Silica deposited on porous Vycor glass gives high hydrogen separation factors. Hydrogen passes through defects in the silica network. Gavalas et al. (1989) obtained Knudsen separation values for hydrogen and nitrogen at room temperature, but the value increased to over 2000 at 450 °C. The main problem with silica deposited membranes is that they have a very poor stability.

2.2.1.3. Dense inorganic polymer membranes

These types of membranes have been developed for separation and reaction at intermediate temperatures (up to 200 °C for long periods of time). Organic membranes cannot withstand such high temperatures. Polyphosphazenes (Hsieh, 1996) are amorphous rubbery polymers which exhibit higher permeances but lower selectivities than glassy polymer membranes. They are very selective in separating acidic (carbon dioxide and hydrogen sulphide) and non-acidic gases (e.g. methane). They consist of alternating phosphorous and nitrogen double and single bonds in a polymer network. Polysilazanes, containing silicon and nitrogen bonds, is another class of organometallic polymers that can be employed as membranes.

2.2.1.4. Dense metal composite membranes

This category of membranes has a dense metal substrate as support with some sort of palladium modification. Dense Pd-porous stainless steel membranes thus fall outside this group and are discussed separately. Refractory metals like vanadium, tantalum and niobium have very high hydrogen permeances, they are cheap compared to palladium, easy to fabricate into tubes and they are stronger than palladium. They are, however, much more prone to hydrogen embrittlement. Niobium must operate above 420 °C and tantalum above 350 °C in hydrogen. Buxbaum et al. (1993, 1996) have done extensive research on refractory metals coated with palladium for hydrogen separation. A palladium coating is necessary to reduce surface poisoning. They used commercial

niobium (150 μm thickness) and tantalum (75 μm thickness) tubes coated with palladium by electroless plating. The membranes were very stable over time.

Peachey et al. (1996) tested composite palladium-tantalum membranes. Tantalum foils of 7.5, 10 and 12.5 μm were used with 1 μm Pd deposited on both sides by electron beam evaporation. They found that by cleaning the tantalum foils prior to Pd deposition they could obtain much higher hydrogen fluxes through the composite membranes. Cleaning consisted of bombarding the Ta foil with argon ions (ion milling). Edlund (1993a, 1995a) made many multi-layered membranes based on vanadium as substrate. A typical example was Pd-SiO_2-V-SiO_2-Pd (25-25-30-25-25 μm). The SiO_2 was compared to many other oxides in the 5-layer membrane, but gave the best hydrogen permeance results.

2.2.2. POROUS INORGANIC MEMBRANES

Advances and research in the field of porous inorganic membranes have been dramatic in recent years (Hsieh, 1989; Soria, 1995). Industrial application of inorganic membranes started during the post World War II period in the field of nuclear power. The uranium isotope, ^{235}U, was enriched from 1% to between 3 and 5% for fuel in nuclear reactors or up to 90% for nuclear weapons. Since the 1940s, membranes have played an important role in gaseous diffusion, with France, the United States and the Soviet Union leading the way. More than 100 million porous membrane tubes have been made employing French technology (Hsieh, 1996). Composite membranes have been in very high demand. Thin separation layers allow for high fluxes, while the support gives mechanical strength. The pores in porous membranes can be divided into three classes:

- Macroporous > 50 nm,
- Mesoporous 2 nm < pore size < 50 nm, and
- Microporous < 2 nm.

Some general membrane applications will be mentioned later (see **Section 2.7**).

2.2.2.1. Porous glass

Macroporous Vycor glass membranes became available in the 1940s. They are made by acid leaching one of the phases in the glass. Currently these membranes can be prepared with pores as small as 4 nm. Kameyama et al. (1981) claimed to produce porous Vycor glass membranes with 86% of their pore diameters within 1 nm of the 4.5 nm average pore diameter. The brittleness and loss of microstructure upon heating for long periods at elevated temperatures (> 300 °C), limit their application.

2.2.2.2. Porous metal

Porous silver membranes were commercialised in the 1960s, but their use has been limited. Porous stainless steel membranes have been employed as high quality filters for many years. Porous stainless steel membranes can be used as supports for preparing composite membranes. The large pore size of these membranes and the possibility of inter metal diffusion at higher temperatures require some substrate modification. This is discussed in **Section 2.2.3**. Many researchers have used porous stainless steel as substrate to prepare high selectivity composite membranes (Edlund, 1996; Shu et al., 1996a; Nam et al., 1999).

2.2.2.3. Molecular sieving membranes

Molecular sieving membranes have pore sizes ranging from 0.2 to 1 nm. Carbon molecular sieves, silica molecular sieves and zeolites are the most widely known. Carbon molecular sieves can separate molecules differing by as little as 0.02 nm in critical dimensions (Hsieh, 1996). They are prepared by pyrolysis of the membrane material between 500 °C and 750 °C. The pyrolysis temperature and conditions determine the pore size. These membranes are usually formed as hollow fibres (outer diameter between 5 microns and 1mm). Haag and Tsikoyiannis (1991) prepared aluminophosphate molecular sieve membranes and Raman and Brinker (1995) prepared molecular sieving silica membranes.

2.2.2.4. Porous ceramic and composite membranes

Ceramics have several properties that make them the superior choice for inorganic membranes. Al_2O_3 remains stable up to 800 °C without degradation of the pore structure, (Kameyama et al., 1983), it is resistant to corrosive environments, it is mechanically stable and can withstand pressure drops of up to 1.5 MPa. Metals and oxides can easily be dispersed on the membrane surface and into the pores to add catalytic properties. The acidity of the support must be taken into account and modified if it catalyses undesirable reactions.

Ceramics are mainly used as composite membranes, where several layers with decreasing pore sizes are deposited on one another. The final or permselective layer is typically a few microns thick and allows for high fluxes. A common example is one or more α-alumina support layers with a final γ-alumina separation layer, yielding a membrane with 4 to 5 nm pores. The top layer determines the characteristics (permeance and selectivity) and the pore size of the membrane. Top layers that have been deposited and studied include γ-alumina, zirconia, titania, oxide mixtures, zeolites, silica, metals and metal alloys. Each of these top layers will result in different pore sizes, with the aim being to make the membrane very selective (very small pore sizes in the Angstrom range) and allowing for a high flux to pass through the membrane (very thin selective layers in the nanometer range).

2.2.2.5. Zeolite membranes

Zeolite membranes are composite membranes, where a thin zeolite layer is deposited on a support (usually α-alumina with or without γ-alumina modification). Jansen et al. (1998) prepared a specific zeolite structure (called a MFI-type zeolites) on steel, silicon and quartz. This type of membrane has received much attention in the last decade, because zeolites can separate molecules in the Angstrom range. Possible applications are for use in isomerisation processes, hydrogen separation, water-alcohol separation and separation of organic compounds.

Crystals can be grown parallel or perpendicular to the support. Ishikawa et al. (1989) deposited zeolite coatings on porous Vycor glass and obtained water to butanol separation factors of 2700. Suzuki (1987) prepared A, X, Y, L, FU-1, ZSM5 and silicalite zeolites on porous Vycor glass, stainless steel, nickel and alumina. Jia et al. (1993) prepared silicalite zeolite membranes in situ on a porous ceramic support, while Sano et al. (1994) prepared a similar zeolite on stainless steel.

2.2.3. MEMBRANE MODIFICATION

Porous ceramic membranes are often multi-layered, with two or more α-alumina support layers, as mentioned earlier. A γ-alumina layer can be deposited on the α-alumina layers to reduce the final pore size. With a smaller pore size, the final Pd layer can be made thinner, but metal to ceramic adhesion can become poor.

In recent years, special attention has been given to porous stainless steel membranes. Their larger pore size (0.2-0.5 μm), compared to ceramic membranes, and the wider pore size distribution are, however, some drawbacks for depositing thin films on them. A further problem is the diffusion of palladium or its alloy into the stainless steel and a gradual decline in hydrogen flux upon use. Nam et al. (1999) modified a porous stainless steel support with a nickel deposit to reduce pore size. Jemaa et al. (1996) used a shot peening technique to reduce the pore size of stainless steel membranes. During shot peening, iron particles of less than 125 μm were fired onto the support. Jemaa et al. (1996) obtained favourable results and observed a reduction in pore size.

To reduce inter metal diffusion, Gryaznov et al. (1993) introduced a diffusion barrier between the stainless steel and the palladium layer. It was mainly iron that diffused into the palladium. They achieved a constant hydrogen permeability for 1000h at 800 °C with an intermediate layer of tungsten (0.8 μm), tantalum oxide (0.1 μm), magnesia (0.5 μm) and zirconia (1.0 μm), each applied individually. Shu et al. (1996a) applied a 0.1 μm titanium nitride layer onto porous stainless steel. Their Pd-Ag/TiN/stainless steel membrane was thermally stable up to 700 °C.

Edlund and McCarthy (1995b) observed a very rapid hydrogen flux decline in their palladium-vanadium composite metal membranes at 700 °C. Vanadium diffused into palladium and the process was accelerated in a hydrogen atmosphere. They introduced a 250 μm thick porous alumina diffusion barrier between palladium and vanadium. Thereafter, the hydrogen flux remained constant at 700 °C for the duration of the testing time (76h).

2.3. MEMBRANE PREPARATION AND CHARACTERISATION

Several techniques for preparing dense and porous membranes are discussed by Hsieh (1989), Hsieh (1996) and Keuler (1997a). These include:

- Conventional powder metallurgy methods such as pressing, extrusion and slip casting followed by sintering,
- Anodic oxidation (Hsieh, 1989; Nourbakhsh et al., 1989),
- Pyrolysis (Linkov, 1994; Soria, 1995),
- Phase separation and leaching (Soria, 1995), and
- Cold rolling and annealing.

When composite membranes are prepared, additional thin film formation techniques are required to modify the membrane support. Thin film formation techniques will be discussed in greater detail later.

Several structural characterisation techniques are discussed by Mulder (1991), Hsieh (1996) and Keuler (1997a, 1999a). They include:

- Scanning electron microscopy (Hearle et al., 1974),
- Transmission electron and atomic force microscopy,
- X-ray diffractometry (Cullity, 1978),
- Pore size measurement techniques, and
- Particle induced X-ray emission (Johansson et al., 1988).

Membranes can also be characterised by the transport mechanism through the membrane pores. In the next section, separation mechanisms, which are determined by pore size and pore structure, will be discussed.

2.4. SEPARATION MECHANISMS

There is only one basic separation mechanism for flow through dense membranes and this method is restricted to hydrogen and oxygen permeance. For porous membranes, the flow mechanism can be viscous flow, Knudsen diffusion, capillary condensation, surface diffusion or molecular sieving (see **Figures 2.2** to **2.5**, Noble and Stern, 1995). Viscous flow does not yield any separation and thus is not relevant for membrane separation processes. In most cases Knudsen diffusion dominates, but more than one flow mechanism can occur simultaneously.

In the literature the following terms are used for flow through a membrane.

- Permeability, in mol.m/(m^2.s.Pa),
- Permeance, in mol/(m^2.s.Pa),
- Flux, permeation flux or permeation rate, in mol/(m^2.s), and
- Flow rate, in mol/s.

The selectivity of two components is the ratio between their permeation rate. The separation factor (α) is a similar parameter and defined as:

$$\alpha_{ij}=(F_{ix}/F_{iy})/(F_{jx}/F_{jy}) \qquad (2.1)$$

with F the flow rate, x the high pressure side, y the low pressure side and i and j are the components being separated. When the pressure drop across the membrane is small, back diffusion will take place and it will reduce the separation factor. The separation factor further depends on pore size distribution, temperature, and interaction between the gases being separated and the membrane surfaces.

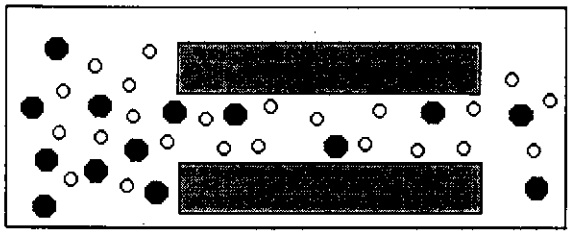

Figure 2.2: Knudsen diffusion

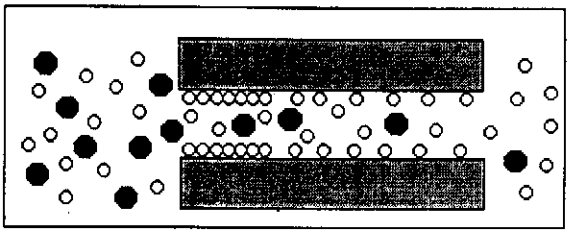

Figure 2.3: Surface diffusion

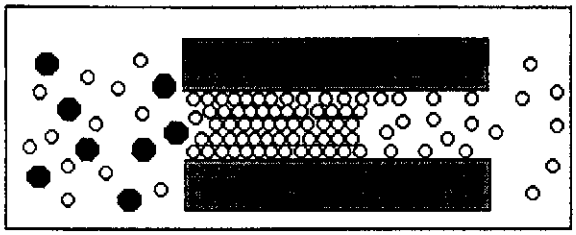

Figure 2.4: Capillary condensation

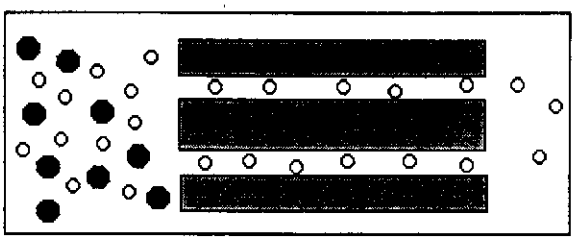

Figure 2.5: Molecular sieve separation

2.4.1. KNUDSEN DIFFUSION

When viscous flow dominates, molecules collide more with one another than with the pore walls of the membrane (see **Figure 2.2**). The pore diameter is large compared to the mean free path of the molecule and no separation can take place. By decreasing the pore size, separation can occur when molecules collide more with the pore walls than with one another. The flux (J) through a membrane of thickness *l* is (Noble and Stern, 1995):

$$J_i = \frac{G_f S_c}{\sqrt{2\pi M_i R_0 T}} \frac{\Delta P_i}{l} \qquad (2.2)$$

with G_f the geometric factor accounting for porosity and tortuosity, ΔP the pressure difference across the membrane, M the molecular weight and S_c the Sievert's constant. The separation factor for an equimolar gas mixture diffusing by Knudsen diffusion is the square root of the ratio of the molar masses:

$$\alpha_{ij} = \sqrt{\frac{M_i}{M_j}} \qquad (2.3)$$

Separation by Knudsen diffusion is limited in membrane reactors, since a lot of the feed is lost through the membrane's pores, which reduces the product yield. The best separation is obtained for light components like hydrogen.

2.4.2. SURFACE DIFFUSION

Surface diffusion is more important at low temperatures. Surface diffusion is an adsorption-dependant process (see **Figure 2.3**). It can occur in parallel with Knudsen diffusion but at higher temperatures Knudsen diffusion dominates, as molecules desorb from the surface. Molecules adsorb onto the pore wall and migrate along the surface of the membrane pore. The permeability of the more strongly adsorbed molecule is increased. Many examples of this phenomenon are documented in literature (Hwang and Kammermeyer, 1966; Kameyama et al., 1979; Weaver and Metzner, 1966). Reported permeability ratios increase between a factor of 1 to 2.5, compared to Knudsen diffusion ratios, for examples encountered in the literature. Surface flow has been expressed mathematically (Uhlhorn et al., 1989), but parameters must be determined experimentally.

2.4.3. CAPILLARY CONDENSATION

Condensable vapour components in a mixture can condense in pores and block gas-phase diffusion through it if the pores are small enough (see **Figure 2.4**). The condensate will evaporate on the low pressure side of the membrane. The result is that the permeance of other components will be slow and limited by their solubility in the condensable component. In studies involving capillary condensation, separation factors of 80 for C_3H_6 and N_2 (Uhlhorn et al., 1990), 460 for water and air, 1000 for SO_2 and H_2 (Keizer et al., 1982) and 120 for methanol and water (Hsieh et al., 1988), have been reported.

2.4.4. MOLECULAR SIEVE SEPARATION

Molecular sieve membranes allow for molecular sieve separation (see **Figure 2.5**). Pore sizes are less than 1 nm and allow for diffusion of only very small molecules. Uhlhorn et al. (1990) used SiO_2-modified alumina membranes with pores of less than 1 nm to separate hydrogen and propylene. Separation factors exceeding 100 were obtained at

200 °C. In another study by Suzuki (1987), an equimolar ratio of methane, ethane and propane at 15 bar yielded a mixture of 73.5% methane, 26% ethane and 0.5% propane as the permeate in a porous stainless steel membrane with a zeolite layer.

2.4.5. FLOW THROUGH NON-PORous MEMBRANES

Hydrogen and oxygen transport through a non-porous membrane is illustrated in **Figure 2.6.** For hydrogen permeance there are several transport steps (Ward and Dao, 1999). A mathematical description of each process has been described by Ward and Dao (1999). These processes include:

1. Molecular transport from the bulk to the surface film layer.
2. Dissociative adsorption on the membrane surface.
3. Atomic hydrogen dissolves in the membrane.
4. Diffusion of hydrogen through the bulk membrane.
5. Transition from the bulk to the surface on the low pressure side.
6. Hydrogen atoms recombine to form molecules and desorb on the other side of the membrane.
7. Gas transport from the membrane surface into the bulk gas.

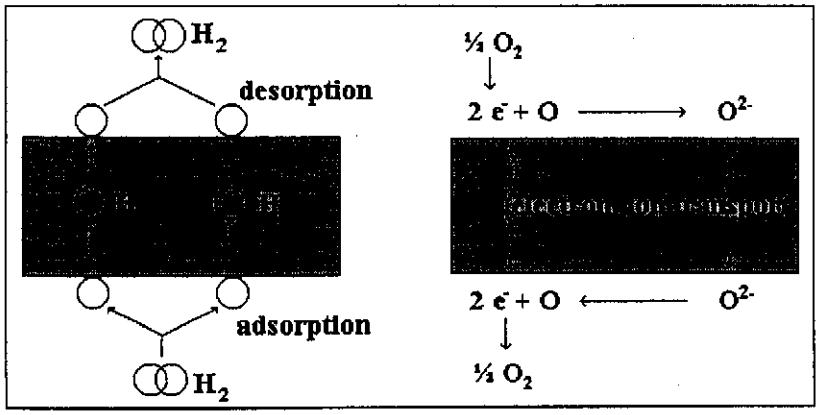

Figure 2.6: Hydrogen and oxygen flow through a non-porous membrane

The permeation flux (J) can be expressed using Fick's law (Buxbaum and Kinney, 1996):

$$J = \frac{D\ (C_{i,1} - C_{i,2})}{l} \tag{2.4}$$

The diffusivity (D) is an Arrhenius function:

$$D = D_0 e^{-E_D / R_0 T} \tag{2.5}$$

The hydrogen surface concentration (C) is the product of the Sievert's constant (S_c) and the hydrogen pressure (P_{H_2}):

$$C = S_c P_{H_2}^n \tag{2.6}$$

When Sievert's law applies, n = ½. The conditions for Sievert's law have been discussed by Shu et al. (1991) and Ward and Dao (1999). In general, as films get thicker (above 10 μm) they approach Sievert's law and n = ½. Diffusion becomes the rate limiting step in hydrogen permeation. For very thin films, in the order of a few microns, the value of n approaches one. Hydrogen chemisorption on the palladium surface becomes the rate limiting step (Nam et al., 1999; Yan et al., 1994). Surface poisoning, grain boundaries and external mass transfer will cause further deviations from Sievert's law. The limiting transport mechanism is very temperature dependent. Ward and Dao (1999) concluded the following after an intensive investigation into hydrogen transport:

- Diffusion is likely to be rate limiting above 300 °C, even for thin membranes (approaching 1 μm).
- Desorption is likely to be rate limiting at lower temperatures.
- Adsorption is likely to be rate limiting for low hydrogen partial pressure and high surface contamination.
- For thin films (much less than 10 μm), external mass transfer becomes important, especially on the low pressure side.
- The membrane fabrication technique plays a significant role in permeation, which is probably related to the microstructure.

Furthermore, the permeability (P_{er}) expressed in mol.m/(m^2.Pa.s) is defined as:

$$P_{er} = S_c D_0 e^{-E_D/R_0T} = P_0 e^{-E_D/R_0T} \qquad (2.7)$$

The flux equation can now be expressed in terms of pressure difference and permeability. Substituting equations (**2.5**) and (**2.6**) into (**2.4**), and then (**2.7**) into the result gives:

$$J = \frac{S_c D_0 e^{-E_D/R_0T}}{l}\left(P_{H_{2x}}^n - P_{H_{2y}}^n\right) = \frac{P_{er}}{l}\left(P_{H_{2x}}^n - P_{H_{2y}}^n\right) \qquad (2.8)$$

And the permeance (P_m) in mol/(m^2.Pa.s) is:

$$P_m = \frac{P_{er}}{l} \qquad (2.9)$$

The hydrogen flux is very high through palladium and palladium alloys, mainly because palladium has a high hydrogen solubility. D_o and E_D values for the different palladium phases and at different temperatures have been given by Shu et al. (1991).

Oxygen permeance through silver is similar to that of hydrogen through palladium. The value of n can be taken as ½ (Gryaznov et al., 1986a). Competitive adsorption by other gases in a gas mixture on silver, reduces the oxygen permeability. For nonporous silica glass, the activation energy for hydrogen permeance is significantly higher than for palladium. For palladium it is in the order of 20-25 kJ/mol (Shu et al., 1991) and for silica about 35 kJ/mol (Gavalas et al., 1989). The flux of oxygen through solid electrolytes has been reported to be proportional to $P^{1/4}$ (Itoh, 1990).

2.5. PALLADIUM AND PALLADIUM ALLOYS

Palladium and certain palladium alloys have a high hydrogen permeance. The characteristics and performance of palladium and palladium alloys have been studied for many years.

2.5.1. PALLADIUM-HYDROGEN SYSTEM

An in-depth study on the palladium-hydrogen system was conducted by Lewis (1994). The solubility characteristics of hydrogen in small palladium crystallites (nm range) are different to those in bulk palladium (Boudart and Hwang, 1975). Structural changes for palladium in hydrogen presented in this study is for bulk palladium or palladium films and not palladium crystallites. At temperatures below 298 °C and pressures below 2.0 MPa, the β phase of palladium will co-exist with the α phase in a hydrogen atmosphere (see **Figure 2.7** from Shu et al., 1991). There is a considerable difference in lattice expansion of the two phases, for example a hydrogen to palladium ratio of 0.5 results in an expansion of about 10% in volume (Knapton, 1977). Severe strains are induced by the nucleation and growth of the β phase in the α phase matrix.

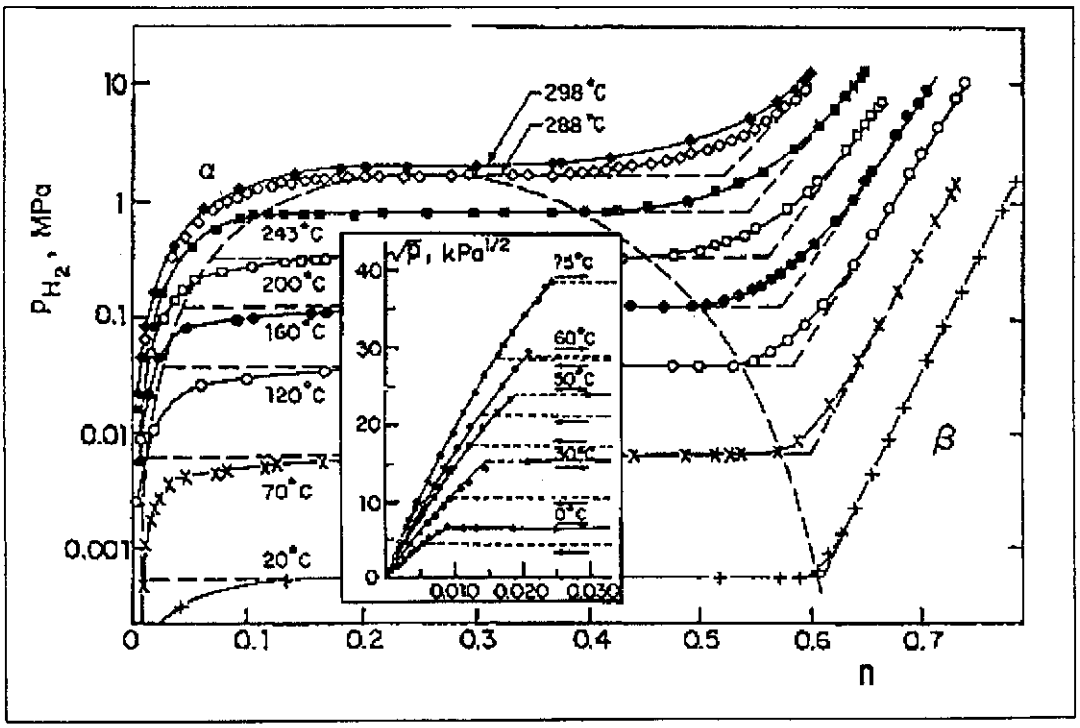

Figure 2.7: Equilibrium solubility isotherms of PdH_n for bulk Pd (Shu et al., 1991)

De Ninno et al. (1997) discussed the stress fields that are created when hydrogen dissolves in palladium. The results were hardening, embrittlement and distortion of the film, which led to cracks in the membrane after a few hydrogenation-dehydrogenation cycles. To avoid these negative effects, the palladium must be kept in the α phase above 300 °C at all time. Lewis (1994) studied the irreversible effects that took place near the phase transition in a hydrogen atmosphere.

Alternatively, the palladium can be alloyed to suppress α to β phase transitions and avoid distortion. The permeability of the alloy should be comparable to or better than that of the pure palladium, have high mechanical strength and be resistant to poisoning.

Yan et al. (1994) and Aoki et al. (1996), performed temperature cycling tests on palladium. Thin Pd films (< 1 μm) prepared by chemical vapour deposition remained stable for many temperature cycles between 100 °C and 300 °C.

2.5.2. PALLADIUM-SILVER SYSTEMS

Hunter (1956, 1960) discovered that silver addition to palladium improved dimensional stability. The addition of about 20% silver depressed the α to β phase transition to below room temperature. Further studies (Makrides, 1964; Jewett and Makrides, 1965; Holleck, 1970; Knapton, 1977) determined hydrogen diffusion coefficients and hydrogen solubility coefficients in Pd-Ag systems. The addition of silver reduces the diffusion coefficient. There is, however, a very sharp optimum in hydrogen solubility when the silver content increases. The net result is an optimum hydrogen permeability ($P_{er}=SD_H$) at a Ag percentage of 23 wt %. This permeability value is about 1.7 times higher than that of pure palladium. The Pd-Ag (77 wt %, 23 wt %) alloy was used for commercial hydrogen separation by Johnson Matthey. Several researchers have used Pd-Ag films to study the performance of catalytic membrane reactors (Sathe et al., 1994; Clayson and Howard, 1987; Shu et al., 1994, Uemiya et al., 1991a). Ali et al. (1994a) investigated the deactivation and regeneration of palladium-silver membranes.

The morphological changes of the Pd-Ag system upon hydrogen permeation was described by Shu et al., 1997a. They used SEM images to study changes in a 50 μm Pd-Ag (75:25 wt %) foil before and after hydrogen permeation. Several defects such as transgranular cracks, intergranular cracks and hydrogen blisters were identified under different conditions. Lattice strains caused minor cracks, which later developed into large transgranular cracks.

2.5.3. PALLADIUM AND COPPER OR GOLD

Knapton (1977) reported that gold-containing alloys show higher resistance to sulphur poisoning that silver-containing alloys do. Weyten et al. (1997) reported that Pd-Ag membranes have a low chemical resistance for H_2S. H_2S gradually destroys the Pd-Ag alloy film. The problem can be solved to an extent, by covering the Pd-Ag film with a thin layer of gold to improve their resistance to sulphur. Maestas and Flanagan (1973) studied hydrogen diffusion rates in palladium-gold alloys. Up to 20 wt % gold, the diffusion rate was relatively unchanged from that of pure palladium. For a higher gold content, the diffusion rate decreased logarithmically with gold increase.

For copper-containing alloys, there is an optimum copper concentration for maximum hydrogen permeance. This maximum permeance occurs at 40% copper, which is associated with the formation of an ordered β-CuPd phase. This alloy has a higher hydrogen diffusivity than pure palladium, but the low hydrogen solubility results in weaker permeances than for pure palladium. Uemiya et al., (1991b) compared a Pd-Cu (94:6 wt %) and Pd-Ag (94:6 wt %) membrane and found that the first one had a much lower hydrogen permeance.

2.5.4. PALLADIUM AND RARE EARTH ELEMENTS, NICKEL OR OTHERS

Knapton (1977) also studied palladium-cerium and palladium-yttrium systems. Both showed high permeance values. Cerium is prone to poisoning by oxidation, but not yttrium. **Figure 2.8** (Shu et al., 1991) show permeance data for various palladium alloy systems. Binary alloys of Pd with B (McKinley, 1967), Ni (McKinley, 1967, Roshan et al., 1983), Rh (Rodina et al., 1968), Ru (Armor, 1995), Cr, V and Fe (see Shu et al.,

1991) have been investigated as well as ternary alloys of Pd-Ag with Ni, Rh, Pt and Au (Knapton, 1977).

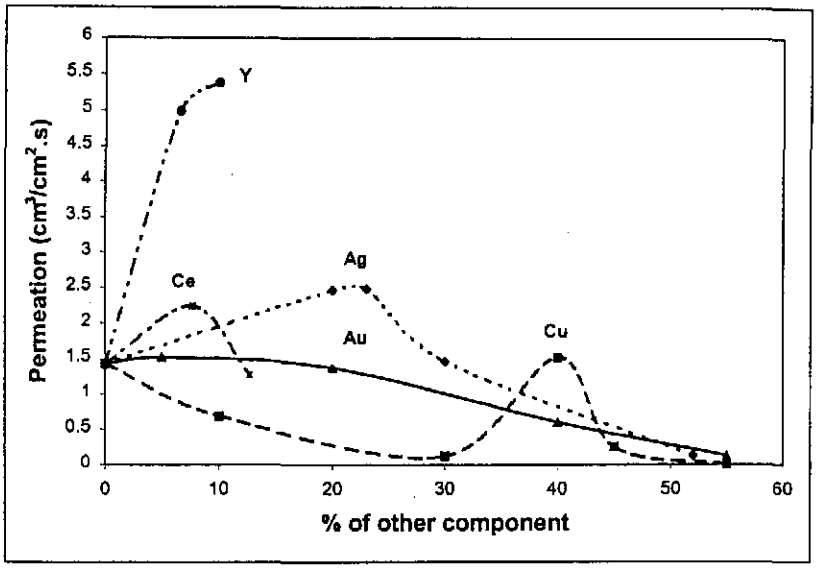

Figure 2.8: Permeability of H_2 through Pd alloy membranes at 350 °C and 2.2 Mpa

The addition of elements to palladium not only suppresses the phase transition, but can also improve strength. Rodina et al. (1968) tested the strength implications of the addition of Ni and Au to palladium and found Ni to be very effective. The improvements in catalytic properties of palladium with Ni (Smirnov et al., 1978; Bulenkova et al., 1978), Ru (Gryaznov, 1986b; Skakunova et al., 1988), Rh (Parfenova et al., 1983; Gryaznov et al., 1986c), Sn, Sb, Cu and Mo have been studied.

2.6. PREPARING PALLADIUM MEMBRANES

Initial work on palladium membranes used foils, typically 50 μm or thicker. The advances made in preparing inorganic membranes have shifted research away from foils towards composite membranes with much thinner palladium layers. Not only is this cheaper, but it also allows for a large increase in hydrogen flux through the film. Composite palladium membranes are prepared by depositing palladium or palladium alloys on a multi-layer inorganic membrane support. Several thin film deposition techniques have been developed to deposit thin palladium layers with minimum defects.

Prior to any deposition, the membrane support needs to be thoroughly cleaned. Keuler (1997a) discussed substrate cleaning. Different cleaning methods for porous glass, porous stainless steel and porous alumina were presented. Different thin film deposition techniques will be discussed briefly in the next few paragraphs. More detail on preparing thin films can be found in Keuler (1997a).

2.6.1. WET IMPREGNATION

This technique is not suitable for preparing dense metal layers on inorganic supports. The metal is deposited in the pores of the membrane and often these membranes are used as contactors. Champagnie et al. (1992) prepared Pt-impregnated membranes and Cannon et al. (1992) prepared Pd-impregnated porous Vycor glass membranes. The change in membrane pore size was minimal. Porosity control and uniform impregnation were some problems encountered. The metal served as a catalyst and not as a separator. Uzio et al. (1993) found that the membrane permeability was not changed after depositing Pt through ion exchange on an alumina membrane (Societé des Céramiques Techniques or SCT multi-layer membrane with a 4 nm γ-alumina toplayer). For the membranes tested by Uzio et al. (1993), the diffusion mechanism remained Knudsen diffusion after depositing Pt on an alumina membrane. Jun and Lee (1999) used a $Pd(C_3H_3)(C_5H_5)$ organometallic precursor to impregnate a porous stainless steel membrane modified with sintered nickel. They claim to have obtained a hydrogen to nitrogen selectivity of 1600 after annealing the Pd composite membrane. Kizling et al. (1997) used a similar pore plugging technique to prepare Pd-Ag (77:23 wt %) on alumina membranes, but found it difficult to remove the surfactants after deposition.

2.6.2. SOL GEL PROCESS

Livage et al. (1988), Brinker and Scherer (1990) and Julbe and Guizard (1993) described sol gel chemistry. Particles of a few nanometer in size can be made and deposited on a support membrane. The gel is applied onto the membrane by slip casting. The organic components in the gel are burned off during the firing stage, and the result is an inorganic membrane support with a metal or oxide layer deposited on it.

Several attempts have been made to prepare Pd or Pt composite membranes by the sol gel method. Hongbin et al. (1995) prepared Pd/γ-alimuna membranes of which the pore size varied between 5.5 and 6.5 nm for the different Pd concentrations employed, indicating that there was little success in reducing the pore size. Vitulli et al. (1995) prepared a Pt/SiO_2 layer by the sol gel process on a SCT multi-layer alumina support. The resultant membrane showed Knudsen diffusion properties with a hydrogen to nitrogen selectivity of less than 3. Zhao (1997) was able to obtain a hydrogen to nitrogen selectivity of 23 for his composite membrane. He used an AlOOH sol to prepare Pd/γ-alumina membranes.

2.6.3. VAPOUR DEPOSITION TECHNIQUES

There are two basic types of vapour deposition techniques for preparing thin films: chemical and physical vapour deposition. Physical vapour deposition can be either through evaporation or sputtering.

2.6.3.1. Physical vapour deposition

With physical vapour deposition, complex alloys can be prepared, the deposition rate can be accurately controlled and very thin films (< 1 μm) can be prepared, but deposition on non-flat surfaces poses problems. Chemical vapour deposition can be performed inside tubes, but there is a large loss of vapour through the membrane in the initial stages (Morooka et al., 1995).

Evaporation can be performed with resistive heating, but it is far less common than sputtering. During sputtering, atoms from the target are dislodged through ion bombardment by an inert gas and deposited on the substrate. Argon is most frequently used. A magnetron sputtering setup is depicted in Xomeritakis and Lin (1997) and sputtering conditions for palladium (Xomeritakis and Lin, 1997) and palladium-silver (Gobina and Hughes, 1996) have been reported. Key parameters during sputtering are the sputtering time, plasma power, substrate temperature and target to substrate distance. Jayaraman et al. (1995a, b) investigated the effects of some of those parameters on the quality and permeance of the sputtered film. Gryaznov et al. (1993) prepared complex

alloys of palladium and one or more of Ru, Co, Pb, Mn and In on porous metal discs. All examples encountered in literature for palladium sputtering on porous supports used discs as the substrate.

2.6.3.2. Spray pyrolysis

Spray pyrolysis is similar to sputtering. Li ZY et al. (1993) rotated capillary membranes in a high temperature flame to deposit palladium and silver on the outer surface of the membrane. Palladium and silver nitrate were atomised and the aerosol fed with oxygen to a hydrogen-oxygen flame. The metal condensed on the membrane to form a metal layer.

2.6.3.3. Chemical vapour deposition

For chemical vapour deposition (CVD), a metal salt is heated and deposited on the substrate. Palladium acetate is commonly used (Morooka et al., 1995; Yan et al., 1994) as the metal salt. CVD reactors are described by Aoki et al. (1996) and Xomeritakis and Lin (1996). Typical sublimation conditions for palladium acetate are temperatures between 400 °C and 500 °C and a reduced pressure in an argon atmosphere. Palladium chloride can also be used for CVD. The detailed experimental conditions have been given by Xomeritakis and Lin (1996). $PdCl_2$ was reduced with hydrogen. The reduced pressure was applied on the one side of the tube and the layer deposited on the other side of the tube. There was some deposition of palladium inside the pores. Layers prepared by CVD are typically thicker than those prepared by sputtering. Some examples are:

- 4 μm Pd on porous α-alumina, with 150 nm pores (Huang et al., 1997; Yan et al., 1994),
- 4.4 μm Pd on porous α-alumina ,with 150 nm pores (Morooka et al., 1995; Aoki et al., 1996), and
- 1 μm Pd on porous α-alumina/γ-alumina, with 5 nm pores (Xomeritakis and Lin, 1996).

2.6.4. ELECTROPLATING

Metals and alloys can be plated on a conducting substrate that acts as a cathode. Ceramics and plastics need to be treated before they can be electroplated. The metal cations are suspended in solution and reduced by an external current passing through the electrolyte. The cation concentration, bath temperature and current density determine the deposition rate. Even deposition on large surfaces is difficult due to a variance in current density and a declining metal ion concentration in the plating bath. Kikuchi (1988) electroplated Pd-Cu alloys on a porous support. The Pd content was varied between 71 and 94 wt % and the Cu content between 6 and 29 wt %. A method for plating Pd and its alloys on porous supports was also described by Itoh and Govind (1989a).

In a more recent study, Nam et al. (1999) used a vacuum electroplating technique to deposit palladium on a modified porous stainless steel support. A submicron Ni layer was dispersed on the surface of the porous stainless steel support (0.5 μm pore size) under low vacuum and then sintered at 800 °C for 5h under high vacuum. A thin copper layer was deposited on the Ni and finally a Pd layer was electroplated on the copper under vacuum. The resultant film was about 1 μm thick with 78 wt % Pd and 22 wt % Ni. Hydrogen to nitrogen selectivities varied between 500 and 5000 at temperatures over 350 °C.

2.6.5. ELECTROLESS PLATING

Electroless plating is an autocatalytic oxidation-reduction reaction in which metal ions are reduced and deposited as metal atoms. It is similar to electroplating, but no external current is supplied. A detailed discussion can be found in Keuler (1997a). It can be applied onto any material that has been properly pretreated. Some materials that have been electroless plated are porous Vycor glass (Yeung et al., 1995a; Uemiya et al., 1991b), porous stainless steel (Shu et al., 1993) and porous alumina (Collins and Way, 1993a; Yeung and Varma 1995b). The main advantages and disadvantages of electroless plating are listed in Keuler (1997a). The advantages of this process can be summarised as:

- The technique is quick, simple and inexpensive.

- Dense, non-porous films of even thickness can be prepared on any shape.
- There is good metal to ceramic adhesion.

The main disadvantages are:

- Impurities might form in the metal layer when using certain reducing agents. Using sodium hypophosphite as reducing agent causes some phosphor deposition (Loweheim, 1974, reported a 1.5% phosphor deposition) and using boronhydride results in a 3-8% boron deposit (Shipley, 1984). Hydrazine gives very pure deposits, but the deposition rates tend to be slow (Athavale and Totlani, 1989).
- Thickness control is difficult and costly losses might occur due to the decomposition of the plating solution (Shu et al., 1991).
- Today, co-deposition with other metals to form alloys has not been very successful. Deposition of separate metal layers and subsequent alloying has also proven to be very difficult.

2.6.5.1. Substrate pretreatment

As mentioned earlier (see **Section 2.6**) the substrate needs to be thoroughly cleaned before any thin film deposition technique can be successfully applied. For electroless plating on non-conducting surfaces (ceramics and plastics), the surface needs to be activated prior to plating. There are two procedures for catalysing the surface to be plated (Feldstein N, 1974). Both processes employ palladium and tin salts. In the older process the substrate is first placed in a tin chloride solution (sensitising step) and then in a palladium salt solution (activation step). For the exchange process, a colloidal solution containing both palladium and tin salts is required. The substrate is placed in this solution and then in an acid solution containing HCl or H_2SO_4 (Cohen and Meek, 1976).

Palladium ions are reduced and Pd nuclei are deposited on the substrate. Models for nuclei growth on the substrate have been developed by Cohen et al. (1971, 1973). Several pretreatment solutions are listed (Osaka and Takematsu, 1980) in literature and have been tested and evaluated (Horkans, 1983). The two step process deposits more

metal than the exchange process does and there is a higher Pd content (Horkans, 1983) in the deposit. This is favourable for preparing high purity deposits.

2.6.5.2. Electroless plating solution composition

An electroless plating solution has a few basic components:

- a metal salt of the required metal than needs to be deposited,
- a reducing agent,
- a pH regulator, and
- a stabiliser that forms a complex with the metal ions and allows for a slower metal release from the solution.

Not all metals can be electroless plated, but metals that form good hydrogenation-dehydrogenation catalysts can be plated. A universal plating mechanism is described by Van den Meerakker (1981). Ethylene di-amine tetra acetate (EDTA) is most commonly used as stabiliser with hydrazine or sodium hypophosphite as the reducing agent. Ohno et al. (1985) lists five reducing agents that can be used for various metal depositions. The amine complex of palladium is used for electroless plating: $(NH_3)_4PdX$, with X = Cl_2 or NO_3.

Rhoda (1959) and Athavale and Totlani (1989) reported the chemical reactions involved in electroless palladium plating based on hydrazine and sodium hypophosphite as reducing agents, respectively. Various factors need to be taken into consideration to ensure a stable plating bath, an even thickness coating and an adequate plating rate. These are:

- bath temperature,
- solution pH,
- Pd ion concentration,
- reducing agent concentration and stabiliser concentration, and
- solution volume to plated area ratio.

Furthermore, different plating characteristics are observed when plating the inside and the outside of porous tubes. Pearlstein and Weightman (1969) studied some of the plating variables. Keuler et al. (1997b) investigated the interaction between various plating variables and their effect on solution stability.

2.6.5.3. Recent advances in electroless palladium plating

With the conventional electroless plating technique, membrane selectivity drops fast when palladium films are thinner than 5 μm. The deposit tends to be columnlike and defects are present in the thinner films. Research has focussed on trying to make films thinner, yet maintaining high selectivity.

Yeung et al. (1995a,b) studied the application of osmotic pressure during electroless plating. They used porous Vycor membranes as well as α/γ-alumina membranes as supports. They found that modifying the plating solution with between 1 and 2 ml formaldehyde per litre made the films denser, with smaller grain sizes and higher scratch resistance. A higher formaldehyde concentration inhibited plating, while a lower one showed no improvement. The plating solution was pumped through the membrane tube with air, distilled water, sucrose solution or $CaCl_2$ solution on the other side of the membrane. By having plating solution on the inside of the tube and either sucrose solution or $CaCl_2$ solution on the other side, an osmotic pressure was created from the inside to the outside. The pressure strength was dependent on the solute concentration. Yeung and co-workers found that the osmotic pressure made the Pd coatings more dense, nonporous, thinner and with a smoother surface morphology.

Li et al. (1997, 1999) used a similar approach to repair defects in their electroless plated Pd films. Porous stainless steel (0.1 μm pore size) and α-alumina (0.16 μm pore size) membranes were used as supports. An initial Pd coating was applied and then one or more coatings were added under osmotic pressure with NaCl as solute. This resulted in film densification and defect minimisation. **Table 2.1** (Li et al., 1999) shows how the selectivity of the Pd film improved after it was repaired.

Zhao et al. (1998) used a different pretreatment process to the traditional Pd/Sn activation and sensitisation process. The porous alumina substrate was activated by a Pd(II) modified boehmite sol. The gel-coated substrate was dried, calcinated at 600 °C and then reduced in hydrogen at 500 °C. Electroless plating was performed on those activated substrates which they claimed had a smoother surface and more uniform distribution than those prepared by conventional pretreatment. After using very high hydrazine concentrations, they observed that the electroless Pd coating consisted of much finer particles and this resulted in a more compact film.

Table 2.1: The effect of repairing of electroless Pd plated coatings (Li et al., 1999)

Plating	Film thickness (μm)	Total H_2 permeance μmol/m^2.s.Pa	H_2/N_2 ratio
Original	7.6	6.24	10.3
1st Repair	9.2	3.24	96.5
2nd Repair	10.3	2.68	970

Paglieri et al. (1999) investigated the effects of pretreatment on hydrogen permeance for coatings prepared by electroless plating. They tested tin sensitisers of different concentration as well as a new approach based of palladium acetate without any tin. They found that high tin concentrations deposited in the pretreatment step led to poor membrane stability at temperatures exceeding 500 °C. Hydrogen to nitrogen selectivity declined quite rapidly with time. One possible explanation is that tin, with its low melting point (232 °C), could be enhancing metal diffusion along the grain boundaries. This creates wider channels for diffusion of gases. A pretreatment method based on palladium acetate gave a better high temperature stability. Pretreatment consisted of dipping the membrane in a Pd acetate, chloroform solution, drying the membrane by heating it up to 500 °C and reducing it in hydrogen at 500 °C before cooling it down to room temperature.

2.6.5.4. Electroless palladium-silver coatings

Palladium-silver coatings can either be made by consecutive palladium and silver coating steps or by a single co-deposition technique. Some attempts have been made on Pd-Ag co-deposition (Shu et al., 1993; Yeung and Varma, 1995b). The co-deposition process is very complex and the success has been limited. Silver is much less stable than palladium in solution, thus very dilute solutions have to be used. Furthermore, silver passivates palladium deposition, but not vice versa. During the plating process, more and more silver will be deposited with the net result that the final coating composition varies significantly from the initial plating solution composition (Pd to Ag ratio). Shu et al. (1993) investigated the electrochemistry of palladium-silver co-deposition, but many questions remained unanswered.

An easier approach is to deposit palladium and silver separately. Keuler (1997a) has given the composition of a typical silver plating bath. The textural differences after changing the deposition order (Pd on Ag or Ag on Pd) were discussed by Keuler et al. (1999a, b). Results indicated that better metal to ceramic adhesion could be obtained by depositing silver on palladium rather that palladium on silver. Concentration profiles across the thickness of the Pd-Ag films, after initial alloying attempts, were also discussed.

Cheng and Yeung (1999) attempted to model palladium, silver and palladium-silver electroless plating on porous Vycor tubes (5 nm pores). Separate palladium and silver plating was well modelled by their equations. Only the metal ion concentration and hydrazine concentration were, however, treated as variables. Ammonia and EDTA concentrations and the temperature were fixed. They were unable to properly describe palladium-silver co-deposition. In general, higher temperatures, lower ammonia concentrations and higher hydrazine concentrations favoured palladium deposition from a palladium-silver plating bath. These conditions may result in poor bath stability. Silver inhibited palladium plating and influenced the film microstructure.

2.6.6. PALLADIUM MEMBRANE TEMPERATURE STABILITY

There has been some work done on the long term stability of metal composite membranes (Buxbaum and Kinney, 1996), where palladium is coated onto other refractory metals. Very little has been published on the long term stability of palladium or palladium alloys deposited on porous supports and on alloying procedures.

Paglieri et al. (1999) recently studied the high temperature stability of Pd composite films prepared by electroless plating. Plating was performed on the inside of a 200 nm α-alumina support. At temperatures of 550 °C and above, the membranes failed after a few days and the separation factors dropped to the Knudsen level. Removing tin from the pretreatment procedure in electroless plating reduced the problem of membrane failure, but substantial selectivity decline still occurred above 550 °C. At 450 °C and 500 °C, the membranes remained fairly stable for a number of weeks, and the time of stability depended on the Pd film thickness. It was found that the amount of time to fail was proportional to the Pd film thickness and that the same failing mechanism prevailed for all thicknesses. Possible reasons for failing were:

- Impurities might be trapped at the Pd-alumina interface during pretreatment and plating, which later result in pore formation.
- Differences in thermal expansion of Pd and alumina can cause cracking.
- Residual porosity in the Pd film can transform into pores.

2.6.7. PALLADIUM-SILVER ALLOYING

Both Keuler (1997a) and Shu et al. (1996a) annealed their silver on palladium coatings in hydrogen, for 5h at 650 °C and above 500 °C, respectively. Keuler (1999a, b) used alumina-zirconia supports and Shu et al. (1996a) used porous stainless steel supports with a diffusion barrier. In both cases, silver diffused into the palladium matrix. When silver was deposited on palladium, an annealing time of 5h did not produce a constant Pd:Ag ratio across the thickness of the film. The film was asymmetric with a high silver content at the film's outer edge and a low silver content near the support. The alloy composition was not uniform. Unfortunately, neither Keuler (1997a) nor Shu et al. (1996a) included any permeance data comparing coatings before and after annealing.

Uemiya et al., (1991a) coated the outside of a 200 nm porous α-alumina membrane with palladium and silver. They heat treated it at 900 °C in argon for 12h and observed the formation of a Pd-Ag alloy. Hydrogen permeance was 2.7 times higher after heat treatment than before heat treatment. They reported no tearing or loosening of the alloy film from the support. Kikuchi (1995) used the same process for heat treating their Pd-Ag coating on the outside of a porous alumina tube. In both instances the heating process was only vaguely described; no heating and cooling rates were supplied and no long term stability test results were reported.

No data could be found on alloying processes for coatings on the inside of porous ceramic tubes.

2.6.8. DEACTIVATION OF PALLADIUM MEMBRANES

Palladium and palladium alloy membranes perform well when exposed to only pure hydrogen. The presence of other gases may severely impair hydrogen transport through the membrane. Although this field has not been extensively studied, some investigators have reported important findings. McBride and McKinley (1965) studied the effects of about 50% CO, H_2S, CH_4 and C_2H_4 in hydrogen. They reported that all gases showed some decrease in hydrogen permeance, with H_2S giving the worst result. They concluded that at lower temperatures, molecules adsorb on palladium to decrease the sites available for hydrogen adsorption. At high temperatures a thin contaminant layer (coking) may form on the palladium. Antoniazzi et al. (1989) studied membrane deactivation caused by H_2S. They concluded that H_2S poisoning was irreversible and that the reduction in hydrogen permeance through the Pd foil fell by about 1% for every ppm H_2S present in the feed.

A number of studies have focussed on the effects of carbon monoxide on hydrogen permeance (Yoshida et al. 1983; Chabot et al. 1988; Sakamoto et al. 1996) through palladium and palladium alloys. The general conclusion was that the operating temperature of the membrane in the presence of CO should be above 350 °C, to prevent

CO adsorption and loss of hydrogen flux. Jorgensen et al. (1997) reported that CO adsorption could be used favourably during Pd membrane start-up and shutdown. By covering the Pd surface with CO at low temperatures (during Pd membrane start-up and shutdown), the solution of hydrogen in Pd was substantially reduced and the risk of hydrogen embrittlement restricted.

Jung et al. (2000) studied hydrogen permeance through palladium in the presence of steam, methane, propane and propylene. Propane and methane had a negligible effect on the hydrogen flux through the palladium film. Propylene caused severe flux decline, which dropped further with time. A carbonaceous layer was formed on the Pd due to the dehydrogenation of propylene. Steam had both a positive and a negative effect. Steam adsorbed strongly on palladium to decrease the available surface for hydrogen adsorption and thus the hydrogen flux through the film. On the other hand, steam volatilised carbon species on the palladium surface to reduce coking and improve the hydrogen flux. The findings by Li et al. (2000) on palladium deactivation by steam and CO were in line with those of other studies. Steam adsorbed more strongly on palladium than CO did and caused greater reduction in hydrogen permeance than CO did.

2.7. APPLICATIONS OF INORGANIC MEMBRANES

There are many advantages and disadvantage of using inorganic membranes for separation and reaction. Keuler (1997a) gave an extensive list of these advantages and disadvantages. More advantages and disadvantage were given by Armor (1995).

Inorganic membrane technology has been fully commercialised and is used in many different industries. These include food processing, processing of beverages, drinking water, biotechnology, pharmaceuticals, waste oil treatment and petrochemical processing. Hsieh (1989) and Hsieh (1996) discussed these and many other specialised applications. Pd alloy metal membranes are commercially used as hydrogen purifiers (Hsiung et al., 1999). The present study will concentrate on a class of modified inorganic membrane

called catalytic membranes, and more specifically on palladium-based catalytic membranes.

2.8. CATALYTIC MEMBRANE REACTORS

A catalytic membrane reactor combines the functions of a membrane and a catalyst in a single unit. Reaction and separation can thus be performed in one step. Commercial applications are still limited and most of the work in this field is of a fundamental nature. Membrane tubes with an inside diameter of larger than 6 mm are mostly used. Capillary membranes (outer diameter = 1 to 3 mm) and hollow fibres (outer diameter < 1 mm) have been successfully produced, but not widely studied in catalytic membrane reactors due to mechanical problems.

The catalyst can either be deposited into the membrane pores (Cannon et al., 1992) or the membrane can be packed (Tsotsis et al., 1992; Yeung et al., 1994) with a catalyst. A third alternative is to deposit the catalyst only on the inner or outer membrane surface next to, or as part of, the separation layer. In the latter case the catalytic surface area is very small and not effective unless the catalyst is on the inside of a membrane with a very small inner diameter (hollow fibre). Membrane tubes need to be packed to provide sufficient catalyst surface area. There are two flow possibilities. One or more reactants can enter the membrane reactor on the same side (either both shell side or both tube side) and one or more of the products are separated by the membrane. The second alternative is to feed reactants into both the shell side and the tube side of the reactor. One of the reactants moves through the membrane, which acts as a distributor, to react with the other one(s) on the opposite side of the membrane. This is often used in hydrogenation and oxidation reactions and in such a case the catalyst is usually in the membrane pores.

To create a driving force for the components being separated by the membrane, either a sweep gas or a pressure difference is used. The sweep gas enters the shell and tube reactor on the opposite side of the membrane than the reactant(s), and the sweep gas can be inert or active. In the case of an active sweep gas, the sweep gas will react with the

component permeating through the membrane, for example a oxygen sweep (Itoh and Govind, 1989b) in dehydrogenation reactions. Furthermore, the sweep gas can be co- or counter current. The reactor can be adiabatic or isothermal. The effects of different flow patterns and reactor configurations on reaction conversions have been well documented (Shu et al., 1991; Itoh, 1995a; Ross and Xue, 1995).

2.8.1. GENERAL ADVANTAGES OF CATALYTIC MEMBRANE REACTORS

Noble and Stern (1995) have proposed several applications in which catalytic membranes have a potential edge over other processes.

- The equilibrium conversion of an equilibrium-restricted reaction can be exceeded by removing one of the reaction products. This allows for higher conversions at the same operating temperature. By performing the reaction at slightly lower temperatures, the reaction selectivity and catalyst life can be increased and the energy input reduced.
- In consecutive reactions the selectivity towards intermediate products can be increased (Agarwalla and Lund, 1992). Undesirable products can be removed or decomposed before they poison the catalyst.
- When one of the reactants is fed through the membrane in a controlled way, the concentration can be manipulated to limit side reactions. Thermal runaway can be eliminated in highly exothermic reactions.
- Feeding a reactant through the membrane can yield a higher concentration of that reactant on the catalyst surface and improve mass transfer.
- Separation and catalysis can be performed in a single unit, which might be cheaper than two separate units.
- Exothermic and endothermic reactions can take place at the same time on opposite sides of the membrane. This is favourable from an energy point of view and only requires one reactor instead of two.

2.8.2. CATALYTIC MEMBRANE APPLICATIONS

There are two main areas of catalytic membrane applications. They can either be used for equilibrium-restricted reactions, to shift the equilibrium, or as contactors for better

feeding control. The latter is mainly used for oxidation and hydrogenation reactions, while the first application is for dehydrogenation reactions.

2.8.2.1. Membranes as distributors

When feeding oxygen or hydrogen through the membrane to react on the other side, separation of unreacted H_2 or O_2 can be eliminated. Hydrogenation or oxidation reaction rates are higher and the reactions are more selective. An impure H_2 or O_2 feed can be used on the one side of the membrane if the membrane is very selective for H_2 or O_2 permeance. A uniform concentration of H_2 or O_2 can be obtained along the length of the membrane. Nagamoto and Inoue (1981, 1985) compared the reaction rates of olefin hydrogenation when separated feeds and mixed feeds were used. Separated feeds gave better yields of the desired products in the olefin hydrogenation reactions. Ciavarella et al. (1997) used a SCT membrane (α-alumina with γ-alumina toplayer impregnated with Pt) as contactor for hydrogenation reactions. The membrane reactor had a higher kinetic activity, due to higher hydrogen coverage of active Pt sites, compared to the conventional reactor. Shirai et al. (1998) used a Pd membrane reactor as a hydrogen distributor for the hydrosulphurisation of thiophene. They found that hydrogen atoms permeating through the palladium film gave higher desulphurisation activity as compared to a system where thiophene and hydrogen co-adsorb on the active sites. Itoh and Sathe (1997) tested the validity of the bubble model and the solution model for the gas to liquid phase transport of hydrogen through a palladium membrane during liquid phase hydrogenation reactions.

Gryaznov et al. (1986a) studied the oxidation of alcohols with oxygen fed through a 100 μm silver film. Zaspalis et al. (1989) used microporous membranes for feeding oxygen and observed an improved catalyst life in some cases. Many more oxygen reactions are given by Noble and Stern (1995).

2.8.2.2. Membranes for dehydrogenation reactions

A membrane with a high separation factor is necessary to be effective in enhancing conversion in an equilibrium-restricted reaction. For effective operation, the membrane type must be non-porous. Palladium alloy, composite membranes are mostly used where

a thin layer of palladium is deposited on an inorganic support. Most reversible dehydrogenation reactions are either alkane or alcohol dehydrogenations. The literature contains many examples of reactions that have been studied (Shu et al. 1991; Agarwalla and Lund, 1992; Noble and Stern, 1995). A more detailed discussion on alkane and alcohol dehydrogenation reactions will follow (**Sections 2.9** and **2.10**). The membrane reactor can also be operated in such a way that simultaneous reactions take place on opposite sides of the membrane. For example, a dehydrogenation reaction may take place in the membrane tube and the hydrogen that passes through the membrane may be used for a hydrogenation reaction on the other side.

2.8.2.3. Other applications

Another class of equilibrium-restricted reactions that can benefit from a membrane reactor is decomposition reactions, to remove impurities that can poison catalysts downstream. These include the decomposition of water (Compagnie des Métaux Précieux, 1976), ammonia (Collins, 1993b) and hydrogen sulphide (Edlund and Pledger, 1993b; Ohashi et al., 1998).

Some niche applications of palladium membranes that have been investigated include: the production of hydrogen from methanol for fuel cell powered vehicles (Jorgensen et al., 1997) and for low CO_2 power generation (Weyton et al., 1997).

2.8.3. PROBLEMS WITH CATALYTIC MEMBRANE REACTORS

There are many problems associated with catalytic membrane reactors, both from a mechanical and a membrane structural point of view. Some mechanical problems are (Armor, 1995):

- For catalytic membrane operation, membrane tubes need to be packed with catalyst, which can damage the alloy film. Replacing catalyst after a long operating time is often very difficult.
- To obtain a large membrane surface area, capillary membranes or hollow fibres need to be used. These membranes suffer from poor mechanical strength, and coating a uniform dense Pd layer on the inside of these tubes will be very difficult.

- Methods have been developed for sealing ceramic tubes (10 mm outer diameter) at high temperatures. Sealing capillaries or hollow fibres at temperatures above 400 °C will pose problems and replacing broken membranes will be time consuming.
- High temperature operation of Pd composite, ceramic membranes might require special reactor construction materials. The difference in thermal expansion of the ceramic membranes and, for instance, a steel reactor will cause damage to the palladium film deposited on the ceramic supports.
- Films are sensitive to start-up and shutdown procedures. It should be performed slowly and proper purging procedures must be followed.

Besides these mechanical problems, there are numerous other membrane structural and related problems that still need to be addressed.

- The membrane cost is very high and needs to be reduced by making the supports cheaper, as well as producing thin very selective Pd alloy films.
- Membrane poisoning and competitive adsorption on palladium sites reduce hydrogen permeance.
- Pd alloying and the long term performance of palladium alloy membranes, need to be studied further.
- Migration of elements in the palladium alloy matrix takes place, resulting in loss of uniformity.
- Membrane regeneration procedures need to be improved.

2.9. DEHYDROGENATION OF ALKANES

Ethylene and propylene have traditionally been produced by mainly steam cracking, while gasoline production utilises the fluid catalytic cracking process. The disadvantage of both processes is the simultaneous production of a range of other products, which reduces the yield of the desired product. Alkanes have become an alternative feedstock for alkenes due to their good availability from wet natural gas. Typical commodity chemicals produced by dehydrogenation include butadiene, styrene and alkylbenzene

derivatives. Dehydrogenation not only exploits the cheap and abundant natural gas liquids, but it also offers improved selectivity towards the desired products.

2.9.1. GENERAL PRINCIPLES

Dehydrogenation reactions are endothermic and require large amounts of energy to remove hydrogen molecules. To obtain conversions in the region of 50% for C2 to C5 paraffins, reaction temperatures of between 530 °C and 730 °C must be employed (Ertl et al., 1997). For lighter paraffins even higher temperatures are required. High temperatures cause thermal cracking, lowering selectivity. A compromise between selectivity and conversion must be found when choosing the operating temperatures.

Unwanted side reactions produce heavy aromatics and coke during dehydrogenation. These compounds are irreversibly adsorbed on the catalyst and can cause very significant catalyst deactivation, even though they make up only a fraction of the reaction products (1% or less). Catalysts are frequently exposed to an air atmosphere to burn off coke.

According to stoichiometry, a pressure increase has a negative effect on reaction conversion. Processes often operate at lower pressures to increase conversion. The hydrocarbon partial pressure is reduced by co-feeding it with a diluent such as steam or hydrogen, and thereby shifting the equilibrium. Alternatively the process is operated in a vacuum.

2.9.2. ALKANE DEHYDROGENATION CATALYSTS

Ertl et al. (1997) cited three basic catalyst classes for paraffin dehydrogenation, with further differentiation between each class depending on the support type. Catalysts contain a support, doped with alkali metals to reduce acidity, and one or more different active sites.

1. Chromium oxides on zirconia and alumina supports with promoters,
   - The Snamprogetti-Yarsintez FBD (fluidized bed dehydrogenation) process and the Lummus Catofin processes use a catalyst consisting of an alumina support doped with an alkali metal and chromium oxide as the active sites.

- The higher thermal stability and lower acidity of ZrO_2 compared to alumina has resulted in further investigation into this possibility (Ertl et al., 1997).

2. Supported noble metal catalysts (usually platinum) with additional promoters, or
   - The UOP Oleflex process (James and Castor, 1994) employs an alumina support with alkali metals and Pt/Sn active sites.
   - The Phillips STAR (steam active reforming) process uses $ZnAl_2O_4$ or $MgAl_2O_4$ supports doped with alkali elements and Pt/Sn active sites.

3. Miscellaneous catalysts such as supported nickel sulphides and vanadium or molybdenum oxides supported on alumina. The alumina is doped with alkaline metals. The addition of sulphur to nickel improves selectivity significantly (Lundin et al., 1993). Without sulphur, nickel becomes non-selective for dehydrogenation reactions.

2.9.3. COMMERCIAL DEHYDROGENATION PROCESSES

Low alkanes (propane, butane, iso-butane and isopentane) are currently dehydrogenated in chemical plants all over the world. **Table 2.2** and **2.3** (from Ertl et al., 1997) indicate the process conditions and efficiency for propane and iso-butane dehydrogenation.

Table 2.2: Operating conditions for various dehydrogenation processes

Process	Operating pressure (kPa)	Operating temperature (°C)	Feed rate LHSV (h^{-1})
FBD	110-150	547-597	0.4-2.0
Oleflex	200-500	547-597	4
Catofin	33-50	587-647	0.4-2
Star	300-800	477-597	0.5-10

LHSV is the liquid hourly space volume, i.e. the time it takes to process one reactor volume of feed liquid

Table 2.3: Process efficiency for propane and iso-butane dehydrogenation

Process	Feed	Conversion (%)	Selectivity (mol%)
FBD	Propane	40	89
	Iso-butane	50	91
Oleflex	Propane	25	89-91
	Iso-butane	35	91-93
Catofin	Propane	48-65	82-87
	Iso-butane	60-65	93
Star	Propane	30-40	80-90
	Iso-butane	40-55	92-98
Linde	Propane	30	90

2.9.3.1. FBD Process (Snamprogetti-Yarsintez)

The reaction is carried out in a bubbling fluidised bed reactor (multi-stage) without steam addition and at atmospheric pressure. A chromia/alumina catalyst is continuously cycled to a regenerator unit and back (Sanfilippo et al., 1992). The catalyst has the following properties:

- microspheroidal (average particle < 0.1 mm),
- high attrition resistance, and
- the support is a mixture of aluminas containg Cr_2O_3 (12-20 wt %), K_2O (1-2 wt %) and SiO_2 (1-2 wt %).

The catalyst recycle rate is 5-15 kg catalyst per kg iso-butane. The process is quite safe, since the catalyst regeneration zone (oxidation) and reaction zone are separated. The absence of fired heaters and the presence of highly effective dust filters make the process environmentally friendly. The well controlled temperature profile allows for the highest temperature and maximum conversion at the reactor outlet.

2.9.3.2. UOP Oleflex process

This process uses separate units for reaction and regeneration to dehydrogenate mainly C3 and C4 paraffins. The reaction is performed in moving bed reactors (stacked and adiabatic) with external heating between stages (Pujado and Vora, 1990). Hydrogen is used as a diluent. The catalyst properties are:

- spherical pellets,
- a γ-alumina support with platinum (0.1-1 wt %), tin (0.1-4.0 wt %) and alkali metals (0.1-4.0 wt %), with a surface area of between 50 and 120 m^2/g, and
- the operational lifespan for the catalyst is between 1 and 3 years.

The hydrogen to hydrocarbon ratio is between 1 and 10. The dehydrogenation process is continuous and the catalyst retains its activity for a long time period, giving a constant yield. The positive reaction pressure improves safety by reducing air leakage and allows for smaller equipment to be used. The separated reaction and regeneration units also ensure safe operation.

2.9.3.3. Lummus Catofin process

A cyclic multi-reactor is used to dehydrogenate C3 and C4 paraffins at sub-atmospheric pressure. Reaction and catalyst regeneration are performed in the same vessel. During reaction the temperature is gradually raised towards the end of the cycle, which lowers the selectivity. The catalyst has the following characteristics:

- cylindrical pellets,
- γ-alumina support (120 m^2/g) with Cr_2O_3 (17-20 wt %) and alkaline metals (1-2 wt %), and
- a catalyst life of 1 to 2 years.

Due to the low operating pressure, this process gives a high selectivity and a high yield per pass of the required dehydrogenated product. Heat is supplied by the exothermic regeneration reactions as well as by external heating. The catalyst is not only thermally very stable, but has a high resistance to breaking and good tolerance to poisons.

2.9.3.4. STAR process (Phillips steam active reforming)

This process is suitable for both the dehydrocyclization of C6 and C7 alkanes and the dehydrogenation of shorter alkanes. A multitude of fixed beds operate in fired furnaces with steam added as a diluent. The catalyst properties can be summarised as:

- a support of zinc or magnesium aluminate with a calcium aluminate binder,
- platinum (0.01-5 wt %) as active component with tin (0.1-5 wt %) as promoter (alkali metals are optional), and
- the catalyst is very stable in a steam atmosphere and its life is between 1 and 2 years (Dunn et al., 1992).

The steam to hydrocarbon ratio is 4 to 5. Steam reduces the hydrogen and hydrocarbon partial pressures, which shifts the reaction equilibrium towards the product side. Furthermore, it supplies heat to the reaction zone and reduces coking through the steam reforming reaction. Coke formation is also limited by the use of fired reactors and the absence of high temperature pre-heating sections. The positive pressure reduces leakage risks.

2.9.3.5. Linde-BASF process

An iso-thermal fixed bed reactor is used without a diluent to dehydrogenate light alkanes at pressures exceeding atmospheric pressure. The catalyst is a chromia/alumina catalyst (Bölt and Zimmermann, 1991).

Cracking is minimised by isothermal conditions, giving maximum selectivity. Positive pressures improve safety and the absence of a diluent reduces equipment size.

2.9.4. ALTERNATIVE DEHYDROGENATION PROCESSES

Dehydrogenation processes other than those described in **Section 2.9.3** are discussed here.

2.9.4.1. Coupled dehydrogenation and hydrogen oxidation

The oxidation of hydrogen is an exothermic reaction, which can be used to supply heat to the endothermic dehydrogenation reaction. This process can take place in two separate steps or in a single step. The latter is referred to as oxidative dehydrogenation (see **Section 2.9.4.2.**). Hydrogen must first be removed in the dehydrogenation step and then oxidised in the oxidation step. The catalyst must be selective towards hydrogen oxidation without oxidising the hydrocarbon. The catalyst must also be very stable in steam and air or molecular oxygen.

Single multi-functional (Imai and Schmidt, 1989) and dual catalysts (Imai and Schmidt, 1989; Imai, 1983) have been proposed, but without commercial application.

2.9.4.2. Oxidative dehydrogenation

This is similar to coupled dehydrogenation and hydrogen oxidation, but takes place in a single step. Oxygen removes the hydrogen from the hydrocarbon molecule to form water. Thermodynamic equilibrium restrictions are avoided and the exothermic reaction supplies heat to the reaction zone. Catalysts generally suffer from low selectivity, since carbon oxides and other oxygenates are formed in significant amounts.

2.9.4.3. Dehydrogenation in a membrane reactor

Dehydrogenation in a membrane reactor has several theoretical advantages over performing the reaction in a conventional reactor. In theory, simultaneous reaction and separation can occur, shifting the equilibrium towards the product side and giving higher conversion at the same operating temperature. Some dehydrogenation reactions that have been studied will be discussed.

2.9.5. METHANE STEAM REFORMING REACTION

In the 1980s, refineries were net producers of hydrogen (Courty and Chauvel, 1996). However, in the 1990s they became net consumers as the world demand grew. Large hydrogen plants were, and still are being, built to meet this ever growing need. Hydrogen

is the number one choice for desulphurising fuels and as environmental considerations increase, more hydrogen is required (Armor, 1998).

Methane steam reforming is one of the most widely applied commercial processes for the production of hydrogen from synthesis gas. The reactions (**2.10** and **2.11**) are very endothermic and require operating temperatures up to 850 °C.

$$CH_4 + H_2O\,(g) \leftrightarrow CO + 3H_2 \qquad \Delta H^0_{298} = -206\ kJ/mol \qquad \textbf{(2.10)}$$

$$CH_4 + 2H_2O\,(g) \leftrightarrow CO_2 + 3H_2 \qquad \Delta H^0_{298} = -165\ kJ/mol \qquad \textbf{(2.11)}$$

The reaction requires a nickel supported catalyst operating at 800-850 °C under pressures ranging from 1.6 to 4.1 MPa and with steam to methane ratios of between 2 and 4 (Shu et al., 1995). Under these conditions conversion is around 78%. Methane steam reforming kinetics and carbon deposition reactions for methane steam reforming are discussed extensively by Shu et al. (1994).

Oertel et al. (1987) obtained 90% methane conversion below 850 °C in a palladium membrane reactor (Pd thickness was 50 μm). Shu et al. (1995) indicated, through mathematical modelling, that hydrogen removal through the membrane could best be exploited at temperatures between 500 and 600 °C. Using porous stainless steel supported Pd and Pd-Ag membranes, packed with Ni/Al_2O_3 catalyst, significant improvements with the membrane reactor were obtained by Shu's group. Methane conversion was 1.4 times higher in the membrane reactor at 500 °C, 136 kPa and a steam to methane ratio of 3. Uemiya and co-workers (1991c) achieved 80% conversion at 500 °C and 100 kPa with a Ni/Al_2O_3 catalyst and a steam to methane ratio of 3 compared to an equilibrium value of 42%. They used a membrane consisting of a 80 μm Pd_{77}-Ag_{23} alloy, coated on a porous glass tube. In similar work a team from Haldor Topsoe (Jorgensen et al., 1995; Armor JN, 1998) achieved 51% conversion (equilibrium = 21%) at 500 °C and 6 atm pressure with a 100 μm Pd-Ag alloy tube and commercial Ni/MgO catalyst.

The group from Haldor Topsoe performed an economic analysis of this process and indicated that the membrane process was not yet competitive with the conventional process. This was due to a low hydrogen flux through the membrane, poor membrane selectivity, membrane sealing problems and the absence of data regarding carbon formation on the membrane during reaction.

Oxidation of methane can be considered as an oxidative dehydrogenation process. Total oxidation must be avoided to prevent the formation of useless carbon dioxide. Membranes can be used for achieving partial oxidation and yielding C2s (Cheng and Shuai, 1995) or formaldehyde (Yang et al., 1998). Methane and oxygen enter the reactor at different sides of the membrane tube i.e. shell and tube side. Oxygen is added to methane by permeating it through the porous membrane. The trans-membrane pressure controls the permeance. This process is called dosing. Alternatively, dense oxygen conducting membranes can be used.

2.9.6. WATER GAS SHIFT REACTION

This reaction is also important for hydrogen production or CO removal. Natural gas, oil, coal and, more recently, biomass are hydrogen sources. These sources can produce a CO/hydrogen mixture (syn gas) and the water gas shift reaction can be used to adjust the gas composition for downstream processing or increase the hydrogen concentration. Kinetic expressions for the exothermic water gas shift reaction can be found in Shu et al. (1994).

$$CO + H_2O\,(g) \leftrightarrow CO_2 + H_2 \qquad \Delta H^0_{298} = +41\ kJ/mol \qquad (2.12)$$

Increasing temperature decreases CO conversion. Higher hydrogen yields can be obtained using intercooling between multiple reactors, cooling with inert gas addition, increasing the steam to CO ratio and shifting the equilibrium to the product side (Burggraaf and Cot, 1996). The catalyst employed needs to be active and selective at low steam to CO ratios as well as resistant to catalyst poisons. Three types of catalysts that

have received attention are Fe-Cr catalysts (high temperature), Cu-Zn (low temperature) and the more expensive Pt on ZnO catalysts (Bracht et al., 1997). The latter one shows higher sulphur resistance, higher activity and very good selectivity compared to the commercially available Fe-Cr catalyst, which is inactive below 300 °C. A newly developed Co-Mo catalyst looks promising (Burggraaf and Cot, 1996).

Basile et al. (1996) reported conversions below equilibrium values with their Pd coated alumina membranes. The 0.2 μm Pd coating was too thin and resulted in poor membrane selectivity and low reaction yield. With a 20 μm Pd coating on porous glass, Uemiya and co-workers (1991d) achieved a conversion of 88%, compared to a 78% equilibrium value. They used a Fe-Cr catalyst at 400 °C, 1 bar and a steam to CO ratio of 2:1. The catalyst unit and membrane separation unit can be separated to simplify catalyst and membrane regeneration (Ross and Xue, 1995). The units can then be operated at different temperatures and membrane sealing is simplified. The additional cost of a separate unit and the smaller driving force in the reaction are some disadvantages to be considered.

Van Veen and co-workers (Burggraaf and Cot, 1996) calculated that the optimum H_2 to CO_2 membrane selectivity required for this process, is about 40. The high pressure, high temperature membrane sealing and the large membrane surface areas required (1500 m^2 for a 300 MW_e power plant), remain problematic.

2.9.7. ETHANE DEHYDROGENATION

The dehydrogenation of ethane is an important industrial reaction for ethylene production, which is a valuable commodity especially in the plastics industry. High temperature, homogeneous thermal cracking of ethane is the predominant ethylene production process. The production of methane, acetylene and higher hydrocarbons as by-products, reduces selectivity to about 80% with recycle. At 730 °C the equilibrium conversion for the ethane dehydrogenation reaction is still only about 50% (Ertl et al., 1997).

$$C_2H_6 \leftrightarrow C_2H_4 + H_2 \qquad \Delta H^0_{298} = +137 \text{ kJ/mol} \qquad (2.13)$$

Platinum (Champagnie et al., 1992) and palladium (Gobina and Hughes, 1994) supported on alumina catalysts can be used for ethane dehydrogenation. Champagnie and co-workers performed ethane dehydrogenation experiments in a multi-layer alumina membrane (MEMBRALOX) impregnated with Pt. At 550 °C, a trans-membrane pressure of 1 bar and a sweep gas to feed ratio of 2, they obtained about 19% conversion compared to the equilibrium value of just under 10%. A good fit was obtained with a model developed by them. Gobina and co-workers (1994, 1995a, 1995b) used a 6 μm Pd_{77}-Ag_{23} deposited on a porous Vycour glass membrane, for studying ethane dehydrogenation. The membrane was housed inside a stainless steel reactor and packed with a 0.5 wt % Pd on γ-alumina catalyst. They studied different parameters including the type of sweep gas used, sweep gas to feed flow ratio and feed contact time, to draw up a mathematical model for the process.

2.9.8. DEHYDROGENATION OF PROPANE

Most propylene in Europe and the Far East is produced from gasoil and/or naphtha in steam cracker plants. About 90% of the propylene in the United States originates from refinery operations or steam crackers. Catalytic dehydrogenation plants account for the balance. Propylene consumption is estimated to grow annually at 3-4% world-wide (Burggraaf and Cot, 1996). Additional demand cannot be met with traditional methods, and dehydrogenation will become increasingly important.

Dehydrogenation can be performed in adiabatic reactors using the Snamprogetti-Yarsintez FBD process, Lummus Catofin or the UOP Oleflex process. Alternatively it can be performed in isothermal reactors using the Phillips STAR process or the Linde-BASF process. Two endothermic reactions are of importance, i.e.:

$$C_3H_8 \leftrightarrow C_3H_6 + H_2 \qquad \Delta H^0_{298} = +124 \text{ kJ/mol} \qquad (2.14)$$

$$C_3H_8 \leftrightarrow C_2H_4 + CH_4 \qquad \Delta H^0_{298} = +81 \text{ kJ/mol} \qquad (2.15)$$

The latter is favoured from a thermodynamic point of view, but should be suppressed by using a very selective catalyst. Thermal cracking at high temperature should also be avoided. Different types of catalysts can be used depending on the desired result. For the oxidative dehydrogenation of propane to propene in a conventional reactor a V-Mg-O catalyst gave 65% selectivity and 10% conversion at 540 °C (Chaar et al., 1987). Cadus et al. (1996) studied Mg-Mo-O catalysts for the same reaction, obtaining very good selectivity, but poor conversion. Saracco et al. (1996) applied the process of dosing to the oxidative dehydrogenation of propane. Air was fed in a controlled manner through a Pt-impregnated tubular alumina membrane to react with propane on the opposite side of the membrane.

Aromatisation of propane can be performed at 500-600 °C with a gallium-silicate catalyst (Kusakabe et al., 1996) yielding mainly benzene, toluene and xylene. For this, a membrane reactor consisting of a 4.4 μm Pd layer deposited on an α-alumina membrane support was used. Benzene, toluene and xylene yields increased by about 10% (compared to a conventional reactor) to 47% at 500 °C in the membrane reactor. Sheintuch and Dessau (1996) used a 254 μm thick (2% Ru/Pd) tube and a 76 μm thick (25% Ag-Pd) tube packed with 0.52 wt % Pt supported catalyst to study propane dehydrogenation. At 550 °C, 70% propane conversion was obtained compared to 23%, which is the equilibrium value. The flow rates used were very low to ensure equilibrium conversion for the plug flow reactor (see discussion in **section 8.1**). Increasing the flow rate reduced the conversion to values below the equilibrium value. The thick tubes resulted in very low hydrogen fluxes and the low hydrogen partial pressure in the product stream accelerated membrane coking and bed deactivation. Ziaka et al. (1993) obtained 48% conversion at 580 °C compared to an equilibrium value of 31% with a ceramic membrane.

Burggraaf and Cot (1996) performed modeling calculations and did an economic analysis on the use of membranes for the dehydrogenation of propane. Membrane selectivity should be significantly greater than Knudsen diffusion selective membranes to prevent

reactant and product loss through the membrane pores. High hydrogen diffusion rates must be obtained to reduce the membrane surface area. The use of Knudsen diffusion membranes improve the return on investment for both the Catofin and Oleflex processes by about 3% and 1%, respectively. However, the process seems to be uneconomical with a price difference of less than $250-300 between a ton of propylene and a ton of propane.

2.9.9. DEHYDROGENATION OF BUTANES AND BUTENES

Commercially produced butenes are predominantly obtained as by-products of thermal or catalytic cracking reactions. Catalytic dehydrogenation of n-butane yields a mixture of 1- and 2-butenes. This process is still used to some extent in Eastern Europe where butenes serve as intermediates in the Phillips two-step process for obtaining butadiene from butane (Ullmann, 1987). In the 1970s this process was frequently used in the USA, but in recent years it has been replaced by butadiene from steam cracking. 1-Butene and 2-butene are either purified and separated or fed to the second stage in the Phillips process for butadiene production.

Iso-butene demand is increasing due to changes in the Clean Air Act passed by the US Congress in 1990 (Udomsak and Anthony, 1996). Iso-butene is one of the reactants for producing the octane booster, methyl tert-butyl ether (MTBE).

2.9.9.1. Iso-butane dehydrogenation

The endothermic iso-butane dehydrogenation reaction is performed between 500 and 600 °C and yields a variety of products. The purpose of the catalyst is to maximise both conversion and selectivity towards iso-butene production. Isomerisation products, coking products and other butenes must be minimised. Chromia type catalysts supported on alumina, titania or silica (Udomsak and Anthony, 1996) and supported noble metal catalyst with or without alkali metal promoters are generally used (Loc et al., 1995).

The dehydrogenation of iso-butane in a membrane reactor has been studied by several research teams. Sheintuch and Dessau (1996) used a 254 μm thick (2% Ru/Pd) tube and a 76 μm thick (25% Ag-Pd) tube packed with 0.52 wt % Pt-supported catalyst to study

the reaction. The best yield obtained was 76% at 500 °C towards total butenes (68% iso-butene) with a reaction conversion of 81%. Increasing the flowrate reduced the conversion to that of the equilibrium value (32.4%), due to poor hydrogen permeance through the relatively thick Pd membrane. A hydrogen feed concentration of about 2% gave better results due to less catalyst deactivation. Matsuda et al. (1993) obtained iso-butane conversions exceeding the equilibrium value at temperatures between 350 °C and 450 °C with a Pd (deposited by electroless plating) on alumina membrane. Membrane deactivation was reduced by co-feeding iso-butane with a small percentage of hydrogen. Shu et al. (1997b) improved iso-butane conversion from 12% to 32.7% and iso-butene yield from 8.8% to 30.8% at 450 °C with a membrane reactor. Their membrane consisted of a 2 μm Pd coating on a multi-layer (α-alumina support and γ-alumina toplayer) SCT membrane.

Zhu et al. (1993) impregnated a 4 nm γ-alumina membrane with Cr_2O_3 and used it to test iso-butane dehydrogenation, while Ioannides and Gavalas (1993) used a membrane consisting of a CVD deposited SiO_2 layer on porous Vycor glass for the same reaction. Zeolite-coated membranes, for iso-butane dehydrogenation, have also been studied (Casanave et al., 1995).

2.9.9.2. n-Butane and butene dehydrogenation

Prior to the 1940s many catalytic processes were already known for preparing butadiene from butenes and butane (Egloff and Hulla, 1942). During World War II the single step Houdry Catadiene process (Forster, 1973; Craig and Dufallo, 1979) and the two step Phillips process (Reidel, 1957; Husen et al., 1971; Hutson et al., 1974) were commercially introduced for producing butadiene from butane. Later the Lummus Catofin process was derived from the Houdry process (Craig and White, 1980). The Phillips process uses oxidative dehydrogenation for butadiene production. Similar oxidative dehydrogenation processes were developed in latter years by BP Chemicals (Newman, 1970) and Petro-Tex (Welch et al., 1978).

Dehydrogenation has been studied widely and modelled in fixed bed reactors (Acharya and Hughes, 1990). Chromia/alumina is the most common catalyst used for butane dehydrogenation (Happel et al., 1966; Hakuli et al., 1996) and the kinetics of the reaction have been documented (Noda et al., 1967). Since catalyst coking is such an important phenomenon, many researchers have investigated chromia/alumina coking during butene dehydrogenation (Hughes and Koon, 1994; Brito et al., 1995, 1996). Coking kinetics has been formulated (Romero et al., 1996; Peña et al., 1993). Other types of catalysts that have also received attention include iron oxides supported on titania (Boot et al., 1994, 1996), calcium-nickel-phosphate catalysts (Arnold, 1961; Swift et al., 1976) and platinum on alumina catalysts (Loc LC et al., 1993, 1996).

Oxidative dehydrogenation of butenes takes place mainly on ferrites (Xu et al., 1992; Yang et al., 1984) or magnesium ferrites (Gibson and Hightower, 1976; Yang et al., 1991). Iron-zinc oxides (Armendáriz et al., 1992) and vanadium-magnesium oxides (Bhattacharyya et al., 1992) are just some of the other catalysts that have also been studied for this reaction.

Gobina and Hughes (1996) studied butane dehydrogenation in a membrane reactor packed with a 0.5 wt % Pd/alumina catalyst. The membrane had a 6 μm Pd-Ag coating on porous Vycor glass. Using reactive sweep gases, the equilibrium conversion of 5% at 400 °C was surpassed. A 21% oxygen sweep gas gave a reaction conversion of 39% and a 11% carbon monoxide sweep gas gave 26% conversion. Rezac and co-workers (1994, 1995) used a thermally stable polymer-ceramic membrane for hydrogen extraction from the product mixture. They improved conversions from 22% to 33% for reaction temperatures between 480 and 540 °C. Zaspalis et al. (1991) used an α-alumina membrane with a γ-alumina top layer (4-5 nm pore size) and a Pt/SiO_2 catalyst for performing butane dehydrogenation reactions. At 500 °C, they achieved a 15% conversion, exceeding the calculated equilibrium conversion by 6%.

2.9.10. DEHYDROGENATION OF ETHYLBENZENE TO STYRENE

The worldwide demand for styrene reached 18.2 million tons in 1992. This figure is estimated to grow at 3-5% per annum, to reach 23.9 million tons in 2000 (Burggraaf and Cot, 1996). Styrene is converted to polystyrene (> 65%) and co-polymerised with butadiene (13%) for rubber elastomer production. A fraction is used for styrene-acrylonitrile production (9%) and mixed with unsaturated polyester resins (James and Castor, 1994). The endothermic reaction is usually performed at temperatures between 550 °C and 650 °C, 0.5-1.0 atm pressure and with steam as a diluent. Ertl et al. (1997) lists many reasons for adding steam. The main by-products of the dehydrogenation reaction are toluene and benzene, with smaller amounts of ethylene, methane and coking products.

Potassium-promoted iron oxide catalysts are mostly used for this reaction and have been studied extensively (Muhler et al., 1990, 1992; Addiego et al., 1994). Catalyst activity decays due to changes in the surface concentration of the potassium promoter (Matsui et al., 1989, 1991). The kinetics of the dehydrogenation reaction (Abdalla et al., 1994a, 1995; Coulter et al., 1995) and modelling of commercial fixed bed reactors (Abdalla and Elnashaie, 1995; Elnashaie et al., 1993) have received significant attention. Oxidative dehydrogenation allows for lower reaction temperatures (around 450 °C), to be used but catalysts usually suffer from poor selectivity. Magnesium vanadates (Chang et al., 1995), Zn-Fe-Cr catalysts (Jebarathinam et al., 1996) and carbonaceous catalysts (Drago et al., 1994) are some that have been investigated for use in oxidative dehydrogenation.

Most membrane studies regarding ethylbenzene dehydrogenation have used Knudsen separation membranes (40-50 Å pore size) made of α-alumina with a γ–alumina toplayer (MEMBRALOX). Yang et al. (1995) obtained 4% and 11% yield improvements over a conventional reactor at 620 °C with different membrane reactor configurations. Gallaher et al. (1993) also observed a 4% yield increase at 600 °C with a MEMBRALOX membrane. Both his group and Tiscareno-Lechuga et al. (1993) observed significant carbon deposition on the membrane during operation. Jiang and Wang (1998) obtained a 10% increase in yield between 560 and 600 °C using a similar Knudsen separation

membrane. Becker et al. (1993) reported improvements as high as 20%. Wu and Liu (1992) as well as Abdalla and Elnashaie (1994b) have modelled the membrane reactor for ethylbenzene dehydrogenation. Gobina et al. (1995c) compared the effects of the separation factor of different microporous membranes and dense Pd-Ag membranes on styrene yield. There seems to be an optimum membrane thickness for microporous membranes, which depends on the porosity of the separation layer. Pd-Ag membranes of less than 50 μm thickness outperform microporous membranes.

In a feasibility study on the dehydrogenation of ethylbenzene in a membrane reactor, performed by Burggraaf and Cot (1996), they concluded that the process was not feasible. With the exception of palladium-based membranes, other inorganic membranes caused high ethylbenzene permeation through the membrane resulting in large reactant losses. Higher reaction rates, higher hydrogen permeances and good selectivity needed to be achieved to make this process profitable. The high steam to ethylbenzene ratio in the feed, resulted in a low hydrogen partial pressure on the product side. This reduced the driving force for hydrogen permeance through the membrane.

2.10. ALCOHOL DEHYDROGENATION CATALYSTS

The industrially used alcohol dehydrogenation catalysts are copper and/or zinc-based. Some oxidative dehydrogenation processes employ silver as a catalyst. Copper-based catalysts can either be unsupported or supported. Most are of the supported type, where the support provides a large surface for the copper to be deposited on. Unsupported copper catalysts have a much smaller surface area. Catalyst supports can be basic, acidic or both. The acidity of the support, determines whether the dehydration or the dehydrogenation reaction will be favoured. Basic supports (high pH) favour the dehydrogenation reaction, while acidic supports (low pH) favour the dehydration reactions. **Table 2.4** lists some of the metal oxides which are often used as catalyst supports.

Table 2.4: Catalyst supports (Carrizosa and Munuera, 1977; Rosynek et al., 1990)

Basic oxides	Acidic oxides
Pure silica	Alumina
MgO	Silica-alumina (zeolites)
ZnO	TiO_2
ZrO_2	
Alkiline earth oxides	

It is not only the acidity of the support that is important. Other factors which are also very important are:

- surface area,
- abrasion resistance and crushing strength,
- temperature stability and resistance to fouling, and
- toxicity.

Silica and alumina have very high surface areas compared to the other oxides (typically in the hundreds of m^2/g area). High copper surface areas can be obtained by depositing copper on these supports. The activity of the catalyst is usually proportional to the surface area of the active sites and thus a large copper surface area will yield a more active catalyst.

2.10.1. EFFECT OF COPPER PERCENTAGE ON CATALYST PERFORMANCE

The percentage copper on the support has an effect on both reaction conversion and selectivity. **Figure 2.9** indicates what happens when the copper concentration on the support is increased. There is a decrease in the number of exposed surface sites of the support as the copper concentration increases, and the total surface area of the catalyst declines. For the copper, there is an optimum concentration, which yields a maximum copper surface area. In the second image (**b**) of **Figure 2.9** the copper concentration and the copper surface area is higher than in the first image (**a**). When the copper concentration is increased further, some of the pores in the support becomes blocked

(image (c)). The total copper surface area available for reaction declines as no reactant can enter the blocked pores to react.

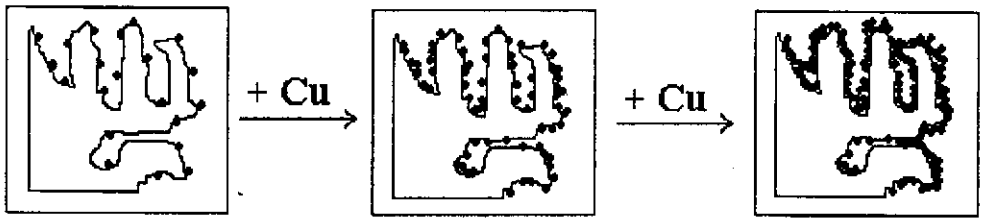

(a) (b) (c)

Figure 2.9: Pore blocking by deposited copper

Sivaraj and Kantarao (1988a) prepared copper-supported on γ-alumina catalysts by a precipitation technique. For the 240 m^2/g γ-alumina support, a copper loading of 20 to 25 wt % gave an optimum copper surface area of about 40 m^2/g catalyst. Chang and Saleque (1993) determined cyclohexanol conversion on copper/α-alumina catalysts. Maximum conversions were obtained with copper loadings of about 12-17 wt % prepared by electroless plating, 12-17 wt % (prepared by precipitation) and about 10 wt % (prepared by impregnation). Chang and Saleque (1994) obtained a maximum cyclohexanol conversion on copper/γ-alumina with 18-20 wt % copper loadings. For alumina-based catalysts, the selectivity towards aldehyde or ketone formation increases with increasing copper loading (Sivaraj et al., 1990; Chang and Saleque, 1994). The reason is that the acidic sites, which reduce dehydrogenation selectivity, become covered and thus neutralised. Jeon and Chung (1994) observed a continuous decrease in cyclohexanol conversion with an increase in copper loading on copper/silica catalysts. The selectivity remained constant (very high) over a wide range of copper values.

2.10.2. CATALYST PREPARATION TECHNIQUES

The are a few basic methods by which to prepare copper catalysts. Unsupported catalysts are usually prepared via a co-precipitation technique, while several methods can be used for preparing supported catalysts viz. precipitation, impregnation, urea hydrolysis, electroless plating or ion exchange.

2.10.2.1. Precipitation

This technique is suitable for preparing copper-supported or unsupported catalysts (Opitz and Urbanski, 1958). A copper salt (usually copper nitrate) is dissolved in distilled water in a stirring vessel. The support is added to the vessel while stirring and sodium carbonate is added as a precipitant. The rate of addition is controlled to keep the solution at a constant pH, usually pH=8.0. The precipitation temperature and precipitation time both have an effect on catalyst performance. Increasing the precipitation temperature from 20 °C to 90 °C (Jeon and Chung, 1994) resulted in a catalyst that gave a much higher cyclohexanol conversion at the higher precipitation temperature. From TEM measurements, Jeon and Chung (1994) observed that copper particles precipitated at 20 °C were about 7 nm to 15 nm in size, while those precipitated at 90 °C were about 1.7 nm to 7 nm in size. Conversion was a weak function of precipitation time, with about 4 hours precipitation time giving the best conversion.

Unsupported copper catalysts are prepared in a similar way, with other metals (for example chromium and/or cobalt) added in the correct mass ratio. The precipitate is filtered, washed with ample amounts of water and then dried overnight at about 100 °C. Thereafter, it is calcinated at temperatures exceeding 450 °C. Kanoun et al. (1991, 1993) described methods for preparing vanadium-copper-zinc and copper-chromium-aluminum catalysts via precipitation. Ammonia was added to precipitate the hydroxides. Further ammonia was added to redissolve the hydroxides as amine complexes. Ammonia was then removed by heat to yield the precipitate with the desired structure.

2.10.2.2. Urea hydrolysis

This method is a precipitation technique in which urea is used as the precipitant (Chang and Saleque, 1994). An aqueous solution of copper nitrate, urea and the support are added together in a stirring vessel. The solution is then heated to between 90 and 95 °C (Sivaraj et al., 1988a, 1990). The pH stabilises at about 7 to 7.5 after the deposition is complete. The precipitate is then filtered, washed and dried.

2.10.2.3. Electroless plating

Electroless copper plating has been used on occasion to deposit copper on the support (Chang and Saleque, 1993, 1994). The support is first pretreated with palladium and tin chloride solutions before copper plating. Palladium seeds on the support provide catalytic centres for copper to plate on. Copper plating requires an alkaline solution and is performed at high temperatures (typically > 70 °C). Either formaldehyde or hydrazine is used as reducing agent and EDTA as a stabiliser. The concentration of the plating solution or the volume of the plating solution can be altered to give different copper loadings on the support. After plating the catalyst is filtered, washed, dried and calcinated.

2.10.2.4. Impregnation

This is a quick and easy way to prepare copper-supported catalysts with or without additional elements like chromium, cobalt or rhodium. The support particles are dried at about 200 °C overnight to remove water vapour from the pores. The particles are then cooled in a desiccator. Either a copper solution or copper mixed with additives in the desired mass ratio are added to the support particles. The mixture is well stirred while adding the solution. The paste is then dried at 90 °C to 110 °C for several hours and later calcinated at above 400 °C in air for at least 5 hours. Iwasa and Takezawa (1991) used this technique to impregnate Al_2O_3, SiO_2, MgO, ZrO_2 and ZnO with copper. Shiau and Liaw (1992) prepared Ba-copper/SiO_2 catalysts and Mendes and Schmal (1997) prepared Rh-copper/γ-alumina catalysts by impregnation for alcohol dehydrogenation.

2.10.3. CATALYST REDUCTION

The reduction of copper oxide by hydrogen is a necessary step for copper activation. It is now readily accepted that it is Cu^0 that is the active species on the catalyst, and not Cu^{2+} and Cu^{1+}. The reduction reaction is highly exothermic.

$$CuO\,(s) + H_2 \rightarrow Cu\,(s) + H_2O\,(g) \qquad \Delta H^0_{420K} = -85\ kJ/mol \qquad (2.16)$$

The temperature inside the catalyst particle can rise considerably, causing sintering and reducing the surface area of the copper. On the other hand, poor reduction will occur if the reduction temperature is not high enough. From literature (Bart and Sneeden, 1987), it appears as if standard prescribed reduction methods for Cu/ZnO catalysts result in poor reduction. Reduction temperatures in excess of 300 °C give a better reduction percentage from Cu^{2+} to Cu^{0}, but give rise to more sintering of copper clusters. Lower temperatures cause less sintering, but also poor reduction.

Furthermore, the copper concentration on the support influences the reduction ability. At low Cu concentrations, the Cu-ion to support bond is very strong. Bart and Sneeden (1987) reported that for 5-10 wt % CuO on ZnO, the surface content of copper was not altered by hydrogen reduction for 2h at 250 °C. Cu^{2+} was converted to both Cu^{1+} and Cu^{0}. For copper concentrations up to 35 wt % CuO, Cu^{1+} was still detected.

Tohji et al. (1985) developed a structural model for copper particles in hydrogen during reduction (**Figure 2.10**). In the first step, below 127 °C, a two dimensional copper layer develops over the ZnO support. Between 127 °C and 277 °C copper metal clusters are formed reversibly on the support. Above 327 °C, large copper clusters are formed irreversibly due to sintering.

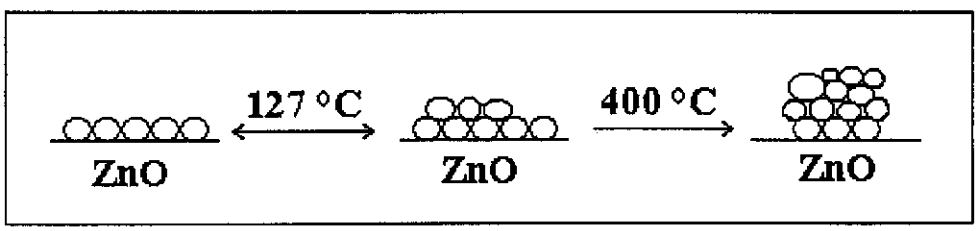

Figure 2.10: The effect of temperature on copper surface structure

Mendes and Schmal (1997) reported that there is a strong interaction between alumina and CuO, for low CuO percentages (0.5 wt % in his study). They could only obtain 57% CuO reduction even if the reduction temperature was increased up to 500 °C. Tu et al. (1994a) reduced their unsupported Cr/Cu catalysts at 200 °C for 6 hours in a hydrogen/argon mixture. Some sintering occurred during the reduction process. A

proper dispersion of Cr_2O_3 promoter slowed down sintering during reduction. At high Cr to Cu ratios (20:40), the reducibility of the catalyst at 200 °C was very poor. Kanoun et al. (1991) reduced their vanadium-copper-zinc catalyst for 3 hours at 300 °C. Chung et al. (1994) reduced their silica-supported copper catalyst for 4 hours at 250 °C with reduction percentages of 65% and higher. Iwasa and Takezawa (1991) reduced their copper-supported catalyst for 18 hours at 250 °C.

2.10.4. CATALYST DEACTIVATION

There are three processes which cause catalyst deactivation, namely, sintering, coking or fouling and poisoning. Sintering is dependent on the reaction temperature, while coking depends on the reaction process and poisoning is determined by the composition of the feed. In most high temperature, solid-catalysed reactions, more than one deactivation process will take place simultaneously.

2.10.4.1. Sintering

Irreversible sintering of copper catalysts at temperatures exceeding 250 °C is a major cause of catalyst deactivation. Sintering will increase gradually as the temperature is raised (see **Section 2.10.3**) and the degree of sintering depends on the metal to support physical and chemical bond as well as the copper crystallite size. Bart and Sneeden (1987) reported that copper sintering for $Cu/ZnO/Al_2O_3$ catalysts is less than expected on the basis of Tamman temperatures, due to strong bonding between Cu and ZnO, which reduces copper mobility.

Church et al. (1951) found that Cr and Co addition improve long term copper catalyst stability. After 100 hours of ethanol dehydrogenation, the activity of a Cu-asbestos catalyst was 60% of the original activity, for a Cu(95%)-Co(5%)-asbestos catalyst the activity was 70% of the original and for a Cu(93%)-Co(5%)-Cr(2%)-asbestos catalysts the activity was 83% of the original. The support also proved to have a large effect on catalyst life. Under identical conditions a Cu-Cr-Co/asbestos catalyst retained 80% activity and a Cu-Cr-Co-pumice catalyst retained only 32% of initial activity after reaction at 275 °C for 48 hours.

Tu et al. (1994a, 1994b) determined copper surface areas of unsupported Cr/Cu catalysts before and after eight hours of use at 310 °C (ethanol dehydrogenation reaction). For catalysts both before and after use, the Cu surface area passed through a maximum at a Cr to Cu ratio of 4:40. There was a significant decline in surface area after use. For pure copper, the decline was from 9 to 6 m^2/g copper and for Cr:Cu = 4:40, the decline was from 19 to 17 m^2/g copper. They found the deactivation kinetics to be second order and concentration independent, which is similar to common sintering kinetics (Fogler, 1992). Chinchen et al. (1988) concluded that in the absence of catalyst poisoning, sintering is the major deactivation process for copper-based methanol synthesis catalysts.

2.10.4.2. Coking and poisoning

Coking is a common phenomenon in hydrocarbon reactions, where a carbonaceous layer is deposited on the catalyst. Coking increases with time and is related to the feed composition and the selectivity of the reaction. Polymerisation of reaction products may result in the formation of heavy molecules, which adsorb on the catalyst and reduce catalyst activity. Franckaerts and Froment (1964) reported that polymerisation of acetaldehyde on the catalyst surface during the dehydrogenation of ethanol causes gradual deactivation. Uemichi et al. (1995) stated that the deposition of cyclohexanone oligomers on active copper sites during cyclohexanol dehydrogenation cause deactivation of copper catalysts. Coking is a much more serious problem for oxidative dehydrogenation reactions. The selectivity towards the desired product is usually lower for oxidative dehydrogenation and CO, CO_2 and other carbonaceous product are formed which results in coking.

Poisoning is similar to coking. The poisoning molecules become irreversibly chemisorbed onto active sites, reducing the number of sites available for reaction and thus lowering activity. The poison may be a reactant, a product or an impurity in the feedstream. Poisoning is usually associated with impurities, while reaction products cause coking. Chinchen et al. (1988) reported that the rate of sulphur adsorption on copper-based, methanol synthesis catalysts is proportional to the copper surface area.

Copper-zinc-alumina was very resistant to sulphur poisoning, with 2% sulphur in the feed only causing a 20% decline in catalyst activity. For copper-alumina catalysts, 0.2% sulphur in the feed caused total deactivation of the catalyst.

2.11. DEHYDROGENATION KINETICS

Perry and Chilton (1973) listed six possible rate equations for solid-catalysed dehydrogenation reactions (**Table 2.5**).

Table 2.5: Possible rate equations for solid-catalysed dehydrogenation reactions

Chemical equation	Catalytic steps	Rate equation	
$A \leftrightarrow R + S$	$A + s \leftrightarrow As$	$r = \frac{k(C_A - C_R C_S / K_{eq})}{1 + K_{RS} C_R C_S + K_R C_R + K_S C_S}$	**(2.17)**
	$As + s \leftrightarrow Rs + Ss$	$r = \frac{k(C_A - C_R C_S / K_{eq})}{(1 + K_A C_A + K_R C_R + K_S C_S)^2}$	**(2.18)**
	$Rs \leftrightarrow R + s$ $Ss \leftrightarrow S + s$	$r = \frac{k(C_A - C_R C_S / K_{eq})}{C_R[1 + K_A C_A + (K_{AR} C_A / C_R) + K_R C_R]}$	**(2.19)**
$A \leftrightarrow R + S$	$A + s \leftrightarrow As$	$r = \frac{k(C_A - C_R C_S / K_{eq})}{1 + K_R C_R + K_{RS} C_R C_S}$	**(2.20)**
	$As \leftrightarrow Rs + S$	$r = \frac{k(C_A - C_R C_S / K_{eq})}{1 + K_A C_A + K_R C_R}$	**(2.21)**
	$Rs \leftrightarrow R + s$	$r = \frac{k(C_A - C_R C_S / K_{eq})}{C_S[1 + K_A C_A + (K_{AS} C_A / C_S)]}$	**(2.22)**

For solid-catalysed reactions there are five basic steps:

1. diffusion of the reactants from the bulk fluid to the external catalyst surface and into the catalyst pores,
2. adsorption of the reactant onto the catalyst surface (exterior and in pores),
3. reaction of the adsorbed reactants to form product molecules,
4. desorption of the product molecules from the surface, and

5. diffusion of the products from inside the pores and close to the external surface into the bulk fluid.

2.12. DEHYDROGENATION OF ALCOHOLS

The catalytic dehydrogenation of primary and secondary alcohols yields aldehydes and ketones and is an industrial process. The corresponding reaction is:

$$R^1\text{-CHOH-}R^2 \leftrightarrow R^1\text{-CO-}R^2 + H_2 \qquad (2.23)$$

with R^2 = H for primary alcohols and R^2 = alkyl or aryl for secondary alcohols. Alcohol dehydrogenation reactions are endothermic and are usually performed at temperatures between 250 °C and 450 °C. Reactants are fed in the gas phase with conversion being favoured by low operating pressures. The principal side reaction is dehydration of the alcohol to yield the alkene and the di-ether. Oxidative dehydrogenation is an exothermic reaction and requires strict temperature control to prevent total combustion and the formation of carbon oxides.

Very few studies have dealt with membrane assisted dehydrogenation of alcohols. Most membrane reactor experiments have thus far focussed on alkane dehydrogenation.

2.12.1. DEHYDROGENATION OF METHANOL TO YIELD FORMALDEHYDE

The older process combines dehydrogenation and oxidative dehydrogenation, using a silver catalyst in the presence of water. The result is a 40% formaldehyde solution. The more recent process employs an iron-molybdenum catalyst for methanol dehydrogenation, yielding formaldehyde gas, which is dissolved in water. The catalyst consists of about 19 wt % Fe_2O_3 and 81 wt % MoO_3 with cobalt and chromium oxide promoters (Ertl et al., 1997). Vanadium supported on silica catalysts have also been investigated (Sorensen and Weber, 1993) for this reaction. The two reactions are:

$$CH_3\text{-}OH\ (g) \leftrightarrow HCHO + H_2 \qquad \Delta H^0_{298} = +84\ kJ/mol \qquad (2.24)$$

$$CH_3\text{-}OH\ (g) + O_2 \rightarrow HCHO + H_2O\ (g) \qquad \Delta H^0_{298} = -159\ kJ/mol \qquad (2.25)$$

Reaction temperatures vary between 647 °C and 717 °C, giving a formaldehyde yield of about 87% (Ertl et al., 1997) for the older process. For the newer process, reaction temperatures vary between 350 °C and 450 °C, with a formaldehyde yield of about 90%.

Zaspalis et al. (1991) used an α-alumina membrane with a γ-alumina toplayer (4-5 nm pore size) and a commercial ZnO catalyst for methanol dehydrogenation. At 500 °C, the membrane reactor gave a 19% formaldehyde yield compared to the 14.4% yield of the conventional reactor. The disadvantage of this Knudsen separation membrane is, however, the loss of reactant through the pores due to poor separation characteristics.

The decomposition of methanol in a Pd/Ru/In membrane reactor to yield CO and hydrogen has been studied recently (Hara et al., 1999).

2.12.2. DEHYDROGENATION OF ISO-PROPANOL TO ACETONE

The dehydrogenation of iso-propanol to acetone is endothermic, yielding acetone as the main product. The main side reaction is the dehydration reaction, yielding propene.

$$CH_3CH(OH)CH_3\ (g) \leftrightarrow CH_3COCH_3\ (g) + H_2 \qquad \Delta H^0_{298} = +84\ kJ/mol \qquad (2.26)$$

The equilibrium constant K_p (in bar) is as follows (with T in K):

$$\log K_p = -2764/T + 1.526*\log T + 1.765 \qquad (2.27)$$

Many different catalysts have been tested for use in this reaction, the most common being copper and/or zinc-based. For ZnO the reaction is performed at 300-400 °C with a selectivity of 90% and a conversion of 98%. Cunningham et al. (1986) studied unsupported CuO, Cu_2O and Cu metal, while Szabó et al. (1975) determined activation

energies and Arrhenius parameters for MgO, CaO and SrO. Yashima et al. (1974) studied iso-propanol dehydration and dehydrogenation on alkali exchanged zeolites and found the dehydration behaviour to be proportional to the acidity of the catalyst. Other catalysts tested include lead, manganese oxide, tin-iridium complexes (Matsubara et al., 1991) and supported platinum and rhodium catalysts. Oxidative dehydrogenation of iso-propanol uses similar catalysts (Gil et al., 1996a, 1996b).

2.12.3. DEHYDROGENATION OF CYCLOHEXANOL TO CYCLOHEXANONE

The dehydrogenation of cyclohexanol to cyclohexanone is an important industrial reaction for the production of caprolactam, which in turn is used for producing nylon.

$$C_6H_{11}OH\ (g) \leftrightarrow C_6H_{10}\ (g) + H_2 \qquad \Delta H^0_{298} = +80\ kJ/mol \qquad \textbf{(2.28)}$$

The reaction becomes pseudo first order when surface adsorption is weak. The use of several catalysts has been studied, usually in the temperature range between 200 °C and 400 °C. The most common catalysts are copper-supported or unsupported catalysts, as indicated in **Table 2.6**.

Table 2.6: Common supports for copper catalysts

Support	Additives	Reference
Al_2O_3	ZnO	Sivaraj et al., 1988b
ZnO	-	Lin et al., 1988
γ-Al_2O_3	Rh	Mendes and Schmal, 1997
MgO, ZnO, Fe_3O_4, SiO_2	-	Jeon and Chung, 1994
α-Al_2O_3	-	Chang and Saleque, 1993
α-Al_2O_3	-	Sivaraj et al., 1990
α-Al_2O_3, γ-Al_2O_3	-	Chang and Saleque, 1994

Other catalysts that have also been studied for cyclohexanol dehydrogenation include alumina-supported Pt-Co catalysts (Reddy et al., 1997), carbon-supported cobalt catalysts

(Uemichi et al., 1995), tin oxides (Hino and Arata, 1990) and zinc phosphate complexes (Aramendia et al., 1995).

The activity and selectivity of copper-based catalysts depends on several factors. The more important ones are:

- acidity of the support,
- preparation technique,
- copper loading,
- calcination temperature, and
- reduction temperature.

Jeon and Chung (1994) prepared copper-supported catalysts using a deposition precipitation method. They studied the effects of precipitation time, precipitation temperature and copper loading on cyclohexanone yield. Cyclohexanol conversion increased with catalysts prepared at higher precipitation temperatures. There was an optimum precipitation time, while conversion decreased with increasing copper content. Selectivities and conversions of MgO, ZnO, Fe_3O_4 and SiO_2 were compared after catalyst deactivation.

Chang and Saleque (1993) studied three preparation methods viz. electroless plating, impregnation and deposition precipitation to determine the effects of the preparation method on cyclohexanol conversion. Each method showed an optimum copper percentage for maximum cyclohexanol conversion. Chang and Saleque (1993) listed activation energies and Arrhenius frequency factors for various catalysts. Catalysts prepared by electroless plating gave the highest BET surface area and the best conversion. Chang and Saleque (1994) also compared the activities of electroless plated Cu on α-Al_2O_3, and γ-Al_2O_3 supports, while Sivaraj et al. (1990) determined the relationship between dehydrogenation selectivity and catalyst acidity.

2.12.4. DEHYDROGENATION OF C4 ALCOHOLS

The dehydrogenation of butanol yields butyraldehyde, an important intermediate in the manufacture of solvents, plasticisers, synthetic resins and rubber vulcanisation accelerators. This process is not performed on an industrial scale, but several researchers have investigated the reaction. Copper, copper-chromium and zinc-based catalysts have been studied (Rao et al., 1969; Purohit and Gandhi, 1975).

Shiau and Liaw (1992) used copper-barium supported on silica to investigate the kinetics of the oxidative dehydrogenation of n-butanol between 230 °C and 290 °C. Sintering occurred and the addition of oxygen increased catalyst coking. Raizada et al. (1993) determined reaction rate parameters for the dehydrogenation of n-butanol over a zinc oxide catalyst at temperatures between 350 °C and 450 °C. Copper, zinc or copper-zinc catalysts were most widely used.

The dehydrogenation of sec-butyl alcohol (iso-butanol) to yield methyl ethyl ketone (MEK) is an important industrial process. MEK is a widely used industrial solvent. Perona and Thodos (1957) determined the kinetics of iso-butanol dehydrogenation between 340 °C and 400 °C and 1 atm, using a brass catalyst (65 wt % Cu, 35 wt % Zn). Using a similar catalyst, Thaller and Thodos (1960) studied the reaction between 290 °C and 370 °C at pressures up to 15 atm. Ford and Perlmutter (1964) observed a change in reaction mechanism with temperature. Below about 320 °C and above about 425 °C, the single site surface reaction was rate limiting. In the temperature range in between, especially from 350 °C to 400 °C, the adsorption of the alcohol was the controlling mechanism.

2.12.5. DEHYDROGENATION OF ETHANOL

Prior to the 1970s the dehydrogenation of ethanol to produce acetaldehyde was a very widely practised commercial process, but it has become less attractive due to high energy costs. In 1989 more than 98% of the world's 2.5 million ton acetaldehyde production was from the oxidation of ethylene (Raich and Foley, 1998). This is the so-called Wacker process. It, however, produces some chlorinated wastes, which are undesirable.

Combining membrane technology with ethanol dehydrogenation results in advantages that could not be exploited previously. The added value of separated hydrogen as a co-product and a dehydrogenation processes that operates at a lower temperatures, give more credibility to ethanol dehydrogenation.

There are two main catalyst classes for ethanol dehydrogenation; zinc or zinc oxides and copper-based catalysts. With ZnO and Cu catalysts, the ethanol dehydrogenation reaction proceeds via different mechanisms on the catalyst surface (Chung et al., 1993). Copper is more active and reaction temperatures are usually in the region of 250 °C to 300 °C. Higher temperatures cause catalyst deactivation and promoters like cobalt and chromium are often added to copper to improve catalyst stability. The lower activity of zinc-based catalysts lead to higher operating temperatures, typically 350 °C to 450 °C. Although zinc-based catalysts are thermally more stable, they have other disadvantages. Higher temperatures decrease reaction selectivity and cause thermal cracking of reactants and reaction products.

The dehydrogenation reaction is:

$$CH_3CH_2OH\,(g) \leftrightarrow CH_3CHO\,(g) + H_2 \qquad \Delta H^{0}_{298} = +52\ kJ/mol \qquad \textbf{(2.29)}$$

The ethanol dehydrogenation capabilities of some materials, including pure magnesium oxide (Takezawa et al., 1975), silica pillared rectorite (Hao et al., 1994), highly dehydrated silica (Matsumura et al., 1989) and silicalite-1 (Matsumura et al., 1990, 1991), but excluding copper and zinc, have been tested. All the materials tested, suffer from low activity and the selectivity towards acetaldehyde production is generally poor as well.

2.12.5.1. Catalyst selectivity

Iwasa and Takezawa (1991) found the dehydrogenation of ethanol to acetaldehyde to be most selective on SiO_2 and MgO supports (see **Table 2.7**), but MgO has a much smaller surface area than SiO_2. ZnO and ZrO_2 gave a high selectivity towards ethyl acetate

formation, while Al_2O_3 supports resulted in C4 and di-ethyl ether formation at 220 °C. Furthermore, they found that high copper percentages suppress ethyl acetate formation.

Table 2.7: Selectivities for ethanol dehydrogenation (Iwasa and Takezawa, 1991)

Support	Active Materials	T (°C)	P (kPa)	Conver-sion	Selecti-vity
Al_2O_3	30% Cu	220	20.5	50*	54.1
SiO_2	30% Cu	220	20.5	50*	77.9
MgO	30% Cu	220	20.5	50*	74.2
ZrO_2	30% Cu	220	20.5	50*	57.3
ZnO	30% Cu	220	20.5	50*	67.3
-	Cu	220	20.5	50*	70.6

*Conversion was fixed at 50% to test selectivities.

Church et al. (1951) found an improvement in both conversion and selectivity when Co and Cr were added to Cu supported on asbestos (see **Table 2.8**).

Table 2.8: Effect of Cr and Co addition to Cu on ethanol dehydrogenation (Church et al., 1951)

Support	Active Materials	T (°C)	P (kPa)	Conver-sion	Selecti-vity
-	Cu, 7% ZnO	335	-	80	78
-	Cu, 5% MgO	332	-	78	78
Asbestos	Cu	328	-	79	90
Asbestos	Cu, 5% Co	337	-	94	89
Asbestos	Cu, 5% Co, 2% Cr	330	-	93	83

2.12.5.2. Catalyst activity

To test catalyst activity, the reaction is usually performed under differential reactor conditions, i.e. very low reactant conversion. Under such conditions, the selectivity towards acetaldehyde production is high and usually not considered.

Tu et al. (1994b) tested the effects of chromium addition to unsupported copper catalysts for reaction temperatures ranging from 250 °C to 310 °C. There appeared to be an optimum Cr to Cu ratio of 4 to 40. That composition gave the highest activity over time with the smallest deactivation rate. The high activity was related to the highest copper surface area at that Cr to Cu ratio. **Table 2.9** (Tu et al., 1994b) gives the reaction rate parameters for the first order dehydrogenation reaction of ethanol over Cr:Cu = 0:40 and Cr:Cu = 4:40 catalysts. There was a significant improvement in the reaction rate for the optimum Cr to Cu ratio compared to that for pure copper.

Table 2.9: Reaction rate parameters for ethanol dehydrogenation (Tu et al., 1994b)

Catalyst	T (°C)	k ($dm^3gcat^{-1}.h^{-1}$)	A ($dm^3gcat^{-1}.h^{-1}$)	E_a (cal/mol)
Cr:Cu = 0:40	250	14.39	$1.12*10^6$	12100
	280	23.36	''	''
	310	51.97	''	''
Cr:Cu = 4:40	250	47.58	$8.39*10^5$	11510
	280	70.12	''	''
	310	131.60	''	''

'' The same as above value

The catalyst activity for dehydrogenation is also strongly dependent on the copper loading. Sivaraj and Kantarao (1988a) investigated the effects of the copper percentage on γ-alumina for 4 to 34 wt % Cu. They found an optimum copper surface area in the region of 20-25 wt % Cu. The overall reaction rate dropped sharply, to about 16 wt % copper for temperatures from 250 °C to 300 °C, thereafter it dropped only marginally and became almost constant above 27 wt % Cu. Below 20 wt % copper, the acidic

γ-alumina support caused a sharp shift in product distribution at 275 °C. Dehydration products increased sharply and dehydrogenation products decreased sharply when the copper content dropped below 20 wt %.

Kanoun et al. (1991, 1993) determined the activities of V-Cu-Zn and Cu-Cr-Al catalysts for the dehydrogenation of ethanol at 190 °C. Changes in total catalysts surface area and copper surface area, with an increase in Cu percentage, were discussed. They also calculated the molecules of acetaldehyde produced per surface copper atom per second (turnover frequency or TOF) as indicated in **Table 2.10**. For the Cu-Cr-Al systems the activation energy varied between 20 and 22 kcal/mol, which was much higher than values of 11 to 12 kcal/mol obtained by Tu et al. (1994a).

Table 2.10: Activities and TOFs for ethanol dehydrogenation at 190 °C Kanoun et al. (1991, 1993)

Catalysts	A (mol.kg $cat^{-1}.h^{-1}$)	TOF x 10^3	Catalysts	A (mol.kg $cat^{-1}.h^{-1}$)	TOF x 10^3
Cu	5.2	45	Cu-Cr	4.34	1.8
V-Cu	2.89	2.8	Cu-Cr0.9Al0.1	4.32	1.9
Zn-Cu	1.59	6.5	Cu-Cr0.7Al0.3	4.16	1.9
V-Zn	0	-	Cu-Cr0.5Al0.54.34	4.07	1.6
V-Cu0.9Zn0.1	3.93	2.4	Cu4.25-Cr0.3Al0.7	4.34	1.9
V-Cu0.8Zn0.2	3.84	2.1	Cu-Cr0.1Al0.9	4.25	1.5
V-Cu0.6Zn0.4	3.98	2.1	Cu-Al	4.43	4.9
V-Cu0.5Zn0.5	4	2.1			
V-Cu0.4Zn0.6	3.84	2.2			
V-Cu0.2Zn0.8	2.84	2.1			
V-Cu0.1Zn0.9	2.43	1.8			

For the catalysts in mentioned in**Table 2.10** the following two criteria apply:

- Cu/(Cr+Al) = 1
- V/(Cu+Zn) = 1

Cu-Al and Cu-Cr were the best performing binary systems where the ratio of Cu to other metal is 1 to 1. 'Varying the Cr to Al ratio did not have a significant effect on catalyst activity. For V-Cu-Zn catalysts, an equal amount of copper and zinc combined with vanadium gave the highest dehydrogenation activity.

2.12.5.3. Ethanol dehydrogenation kinetics

Franckaerts and Froment (1964) performed a kinetic study on the dehydrogenation of ethanol between 225 °C and 285 °C, with a CuO(94%)-CoO(5%)-Cr_2O_3(1%) on asbestos catalyst. Only the main reaction was considered and the formation of ethylacetate or other products were not taken into account, since the selectivity towards acetaldehyde production was very high. They constructed initial reaction rate vs. flowrate curves and used numerical differentiation to determine the kinetic mechanism. They found that the following equation best fitted the data, which is similar to **equation 2.19** but uses partial pressure instead of concentration:

$$r_A = \frac{kK_A\left(P_A - P_R P_S / K_{eq}\right)}{\left(1 + K_A P_A + K_R P_R + K_S P_S + K_W P_W\right)^2} \qquad \textbf{(2.30)}$$

with A, R, S, W = ethanol, acetaldehyde, hydrogen and water.

The water term was added for when water might be present in the feed, but for modelling purposes it was excluded. The calculated values for the constants (**equations 2.31** to **2.34**) between 225 °C and 285 °C were:

$$\ln k = -\frac{16310}{R_0 T} + 16.25 \qquad \textbf{(2.31)}$$

$$\ln K_A = \frac{5890}{R_0 T} - 6.40 \qquad \textbf{(2.32)}$$

$$\ln K_R = \frac{11070}{R_0 T} - 9.40 \qquad \textbf{(2.33)}$$

$$\ln K_S = \frac{6850}{R_0 T} - 7.18 \qquad (2.34)$$

For equations (**2.31**) to (**2.34**) the units are:

k [mol/g cat.h.atm]

K [atm^{-1}]

T [K]

Peloso et al. (1979) also studied dehydrogenation kinetics between 225 °C and 280 °C with the following catalyst: 41.2% CuO, 33.4% Cr_2O_3, 9.3% SiO_2, 3.3% Na_2O and 12.8% binder. Of the mechanisms investigated the dual site reaction mechanism was once again rate controlling (see **equation 2.19**).

$$r_A = \frac{kK_A\left(P_A - P_R P_S / K_{eq}\right)}{\left(1 + K_A P_A + K_R P_R + K_S P_S + K_W P_W\right)^2} \qquad (2.35)$$

with A, R, S, W = ethanol, acetaldehyde, hydrogen and water.

The constants were:

$$\ln k = -\frac{5810.5}{T} + 17.90 \qquad (2.36)$$

$$\ln K_A = \frac{1166.6}{T} - 1.175 \qquad (2.37)$$

$$\ln K_{RS} = \frac{690.2}{T} + 1.057 \qquad (2.38)$$

$$\ln K_{eq} = -\frac{6189.1}{T} + 11.82 \qquad (2.39)$$

with,

k [mol/kg cat.h.atm]

K [atm^{-1}]

T [K]

Tu et al. (1994b) found the dehydrogenation reaction to be pseudo first order and of the form:

$$-r_A = kC_A \qquad (mmol.gcat^{-1}h^{-1}) \qquad \textbf{(2.40)}$$

with $k = 1.12 \times 10^6 \exp(-12100/RT)$ for pure copper **(2.41)**

and $k = 0.84 \times 10^6 \exp(-11510/RT)$ for Cu:Cr = 4:40 **(2.42)**

($k = dm^3.gcat^{-1}.h^{-1}$)

2.12.5.4. Oxidative dehydrogenation of ethanol

The oxidation of ethanol is usually carried out in the vapour phase, over silver (Faith et al., 1957; Sanford, 1963) or copper-based catalysts. Commercial operating temperatures range from 400 °C to 500 °C with about 80% conversion per pass. Some studies have been done on the oxidative dehydrogenation of ethanol in the liquid phase over Pt-graphite catalysts at temperatures between 30 °C and 50 °C (Van den Tillaart et al., 1994, 1996).

Cullis and Newitt (1956) investigated ethanol oxidation between 270 °C and 370 °C. Initially acetaldehyde was formed, but then further oxidation occurred, yielding methanol, formaldehyde, methane and carbon oxides. Rao et al. (1991) tested a medium pore, titanium silicate molecular sieve catalyst for the oxidative dehydrogenation of ethanol. At 300 °C the selectivity towards acetaldehyde production was over 90%, but the conversion was only about 20%. At 400 °C the conversion increased to above 90%, but the selectivity dropped to below 70%. Quaranta et al. (1994) investigated the possibility of using vanadium complexes for oxidative dehydrogenation.

2.12.5.5. Dehydrogenation of ethanol in a membrane reactor

Deng et al. (1995) modified alumina membranes (500 nm pore size) with a γ-alumina layer containing Pd, Pt, Cu or Ni. The net pore diameter varied between 3 nm and 9 nm. Hydrogen-argon selectivities for the Pt and Pd-based membranes were higher than the Knudsen values and for the others lower than the Knudsen selectivities. Ethanol dehydrogenation was studied in the temperature range from 250 °C to 310 °C, employing a Cu-P/SiO_2 catalyst. The acetaldehyde yield for the conventional reactor was slightly below the equilibrium value, while the values for the alumina membrane were higher than the equilibrium value. Cu and Ni-modified alumina yielded results similar to alumina membranes. The best results were obtained with the Pd and the Pt-modified alumina membranes. Acetaldehyde yields were further improved by increasing the space time and/or the sweep gas flow rate.

Raich and Foley (1998) studied ethanol dehydrogenation in a Pd tube with a wall thickness of 76 μm. The operating temperature varied between 175 °C and 225 °C and the tube was packed with Cu or Pt on silica catalysts. The best results were obtained with a copper on silica catalyst prepared by ion exchange followed by copper on silica prepared by impregnation. The latter catalyst gave higher selectivity, but lower activity and lower overall yield. Ethyl acetate was the main by-product at lower temperatures. They compared a palladium reactor packed with copper on silica catalyst (prepared by ion exchange) with a conventional reactor and obtained the following results: conversion increased from 60% to 90% and selectivity from 35% to 70%.

2.13. ALCOHOL DEHYDRATION REACTIONS

Alcohol dehydration is an important side reaction of dehydrogenation reactions. The acidity of the catalyst determines whether, and to what extent, dehydration of the alcohol will occur and the reaction temperature dictates which dehydration reaction will take place. It can either be uni-molecular dehydration to form olefins or bi-molecular dehydration to form ethers. For primary alcohols, the di-ether is easily formed at lower

temperatures, while for secondary and tertiary alcohols, olefin formation dominates also at the lower temperatures.

De Boer and Visseren (1971) observed that the rate constant for ethanol dehydration is proportional to the amount of aluminium (acidic sites) on the catalyst's surface. For ethanol the following was found:

$$CH_3CH_2OH \rightarrow CH_2CH_2 + H_2O \quad \text{at temp.} > 300\ ^\circ C \qquad (2.43)$$

$$2CH_3CH_2OH \rightarrow CH_3CH_2OCH_2CH_3 + H_2O \quad \text{at temp.} < 260\ ^\circ C \qquad (2.44)$$

Several papers describe the dehydration of ethanol over zeolitic and non-zeolitic molecular sieves (De las Pozas et al., 1993; Teo and Ti, 1990). For n-butanol dehydration, the alumina percentage in silica-alumina catalysts has a significant effect on the dehydration products, with a higher alumina percentage favouring di-butyl ether formation (Berteau et al., 1991). C4 dehydration has been studied over various types of zeolites (Makarova et al., 1994; Williams et al., 1991) and over γ-alumina (Lu et al., 1995).

2.14. SUMMARY

This chapter has described the various types of inorganic membranes that are currently available. The main advantages and disadvantages of using inorganic membranes as well as the areas of application have been mentioned. Inorganic membranes were separated into three classes i.e. dense, porous and composite membranes. The different separation mechanisms through porous membranes were discussed. Palladium and palladium alloy membranes were discussed in more detail, with specific attention being given to the palladium-hydrogen system and the effects of alloying on palladium stability in hydrogen. Different methods by which to prepare composite palladium membranes were described. The more important methods were listed and compared. Electroless plating was discussed in detail, covering substrate cleaning, pretreatment and the actual plating process. Recent advances in electroless plating were mentioned. Techniques available

for alloying palladium-silver membranes and what deactivation processes occur during operation have also been described.

The main advantages of using catalytic membranes are for manipulating the reaction rate in dehydrogenation reactions and as gas distributors to improve mass transfer. The various dehydrogenation reactions that have been studied in membrane reactors, including both alkane and alcohol dehydrogenation, have been discussed. For alcohol dehydrogenation, catalyst preparation techniques, catalyst reduction and catalyst deactivation due to sintering and coking, were discussed. Dehydrogenation kinetics was listed and the kinetic parameters for ethanol dehydrogenation, obtained by previous researchers, were also summarised.

3. EXPERIMENTAL PROCEDURES

The chapter on experimental procedures will be divided into four separate sections. The first section (**3.1**) will focus on catalyst preparation and testing. The second section (**3.2**) discusses the procedures followed for determining reaction kinetics. The third section (**3.3**) will focus on Pd composite membrane preparation using a modified electroless plating technique and permeance testing of the membranes with hydrogen and nitrogen. In the last section (**3.4**), the optimised catalyst and a suitable membrane are combined to perform catalytic membrane reactor experiments. The contributions made to the field by performing these experiments were discussed in the introduction (**Chapter 1**).

3.1. OPTIMISING CATALYST COMPOSITION

Catalysis experiments were conducted in two phases. A variety of catalysts were tested at various operating conditions to determine the most suitable ones for ethanol and 2-butanol dehydrogenation. Once the most suitable catalyst was established, an in depth study was performed with that catalyst to determine the reaction kinetics of each reaction. More than 25 catalysts were tested during the screening phase. The variables that were investigated include:

- support type,
- copper loading,
- effect of additives, and
- catalyst particle size.

3.1.1. SUPPORT TYPES

Alumina and silica catalyst supports were supplied by Engelhard. **Table 3.1** tabulates the characteristics of the supports. The surface areas and average pore sizes are not the values from their data sheets, but values determined from laboratory analysis experiments. There was a small difference between the figures supplied on data sheets and the figures determined in the laboratory for the surface area of the alumina support

(< 10%). The difference was more significant for the silica support (about 50%). The 'as received' pellets were crushed and then sieved to obtain different particle size fractions.

A commercial magnesium oxide (MgO) powder (surface area = 27.4 m^2/g) was mixed with a binder and pressed into extrusions. The extrusions were heated to 1200 °C to agglomerate the powder particles. The extrusions were then crushed and sieved into only a 300 to 850 μm fraction. The surface area of the particles was 16.7 m^2/g. Most of the experimental work focussed on the silica and the alumina supports. Only a few experiments were conducted with MgO and thus not much time was spent on trying to prepare a catalyst with a larger surface area.

Table 3.1: Characteristics of alumina and silica supports used

	Alumina	**Silica**
Product code	AL-3996 R	C500-234
Purity	> 99% alumina	99.5% silica max 0.3% alumina
Shape	Extrusions	spheres
Dimensions (mm)	3.5 outer diameter 1.5 inner diameter	3-5
Bulk crush strength (MPa)	0.80	1.40
Bulk density(g/cm^3)	0.50	0.45
BET surface area (m^2/g)	215	446
Average pore size (Å)	132	88

3.1.2. CATALYST PREPARATION

Metals were deposited onto the silica and alumina supports via impregnation. The low porosity of the MgO support made impregnation unsuitable hence adsorption was used for depositing copper.

The MgO support was introduced into a flask containing a copper nitrate solution of a specific concentration. The flask was placed on a magnetic stirrer and the solution stirred

for two hours. Thereafter the Cu-MgO particles were filtered, washed and dried at 90 °C. The catalyst was calcinated at 500 °C and then reduced in hydrogen, in situ, at 350 °C for two hours.

The silica and alumina supports were dried at 200 °C for at least two to three hours and then stored in a desicator. The dried supports were then placed in heated copper solutions of different concentrations. The amount of solution required to impregnate a fixed mass of either silica or alumina was experimentally determined. An excess of about 10% solution was prepared in each case. The copper solution was kept warm on a hotplate while the support was added. The support-solution mixture was stirred throughout while adding the support particles. The hotplate was kept at about 80 °C to evaporate the remaining solution. The paste was stirred every few minutes. When all the water had evaporated, the catalyst was dried in an oven at 120 °C for at least four hours. The catalyst was then calcinated at 500 °C and reduced in situ in hydrogen at 350 °C for two hours. When preparing Cu-Cr, Cu-Co and Cu-Ni-supported catalysts, copper nitrate was mixed with the nitrate of the other metal in the same Cu to other metal ratio as required on the support.

The catalysts used for determining catalyst stability and dehydrogenation kinetics were prepared in a similar manner. The only difference was the reduction temperature. Different reduction temperatures were investigated to determine the effect of sintering during reduction.

3.1.3. SUMMARY OF CATALYSTS INVESTIGATED

Table 3.2 lists pure copper-supported catalysts and **Table 3.3** lists the other catalysts that were prepared and investigated in the screening stage to determine the most suitable catalysts for ethanol and 2-butanol dehydrogenation. For all the catalysts, the Cu percentage is the Cu weight percentage of the total mass of the sample. It is the copper mass divided by the support mass + copper oxide mass (pre-reduced state).

The copper percentage and percentage of the other metal were determined by atomic adsorption (AA). The catalyst (0.100 g) was dissolved in warm aqua regia. When all metal had dissolved, distilled water was added to yield exactly 1000 ml solution. The ppm Cu reading of the solution gave the Cu percentage.

Table 3.2: Different copper loadings investigated for copper-supported catalysts

Silica support (300-850 μm)	Alumina support (850-1180 μm)	MgO support (300-850 μm)
0% Cu	0% Cu	0% Cu
4.2% Cu	8.8% Cu	8.4% Cu
9.2% Cu	13.2% Cu	13.7% Cu
11.7% Cu	18.5% Cu	20.8% Cu
15% Cu	24.0% Cu	
18.6% Cu		
27.7% Cu		
33.5% Cu		

Table 3.3: Other copper-supported catalysts

Silica support (300-850 μm)	Silica support Different fractions	Alumina support (850-1180 μm)
13.5% Cu; 1.5% Co (9:1)	14.1% Cu (150-300 μm)	17.7% Cu; 2.09% Cr (9:1)
13.5% Cu; 1.5% Cr (9:1)	15.0% Cu (300-850 μm)	17.8% Cu; 1.73% Co (10:1)
13.5% Cu; 1.5% Ni (9:1)	13.1% Cu (850-1180 μm)	16.1% Cu; 2.0% Ni (8:1)
14.25% Cu; 0.75% Co (19:1)	14.5% (3000 μm)	
14.25% Cu; 0.75% Cr (19:1)		
14.25% Cu; 0.75% Ni (19:1)		

3.1.4. CATALYST TESTING FOR DETERMINING THE OPTIMUM CATALYST COMPOSITION

The experimental set-up used for catalyst testing was similar to that used for kinetic experiments (see **Figure 3.1**). Heated entry and exit lines were used to vaporise the feed

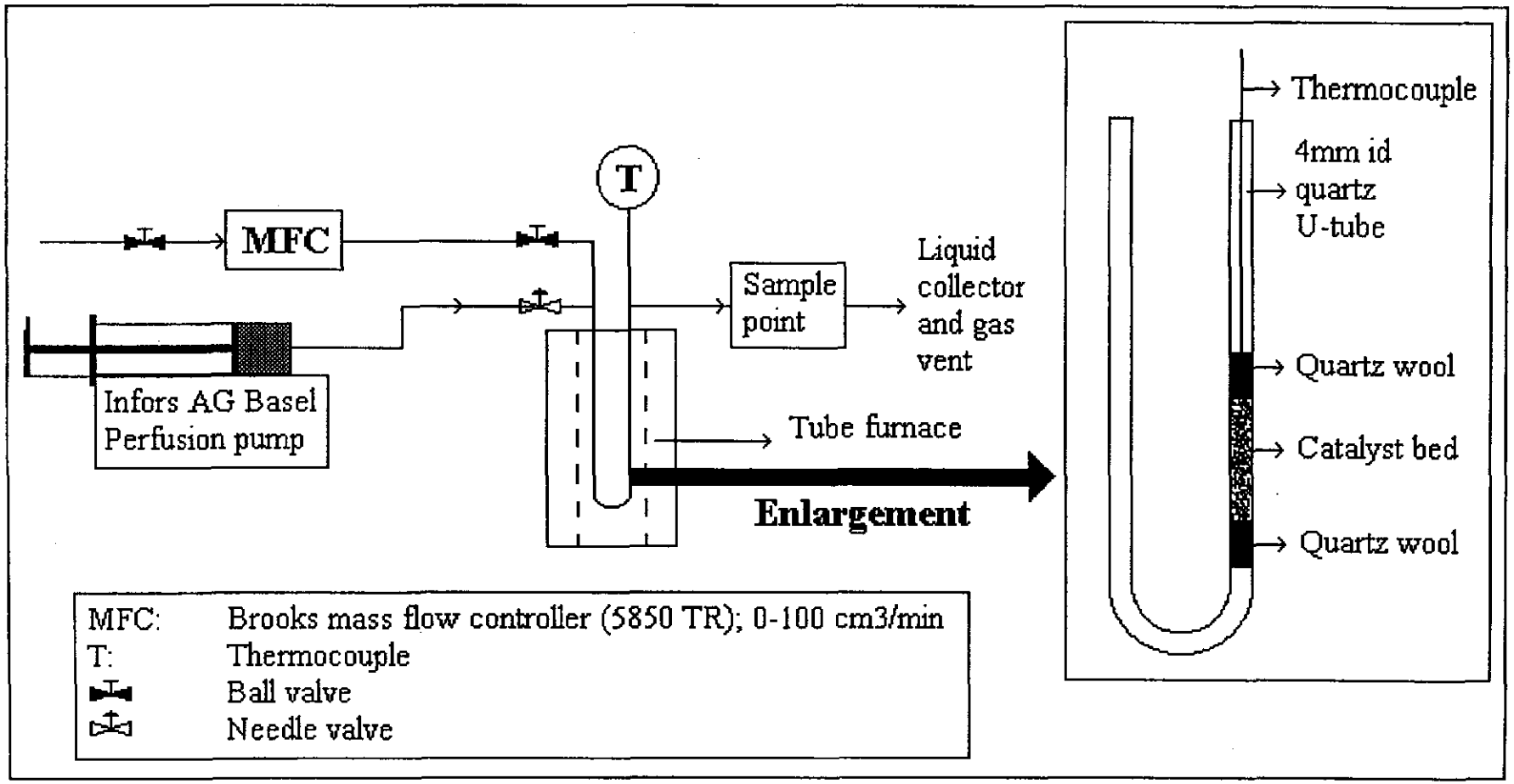

Figure 3.1: Set-up used for testing the kinetics of the catalyst at the CNRS, France

and keep the products in the gas phase. A gas sample was extracted at the sample point with a heated syringe. The syringe was kept inside a stainless steel tube and the temperature of the syringe was controlled at about 100 °C. The first set of experimental tests was performed to determine the optimal catalyst composition and was conducted at the laboratories of the University of Stellenbosch (Stellenbosch, South Africa). The kinetic testing was conducted at the laboratories of the IRC-CNRS (Institut de Recherches sur la Catalyse, Centre National de la Recherche Scientifique) in Lyon, France. **Figure 3.1** is the set-up used at the CNRS. The set-up at Stellenbosch University differed in the following way: Hastings flow controllers (HFC 202C) were used in stead of Brooks, the inner diameter of the quartz tube was 8mm (10mm outer diameter) and a Braun perfusion pump was used.

3.1.4.1. Ethanol reaction

The use of Al_2O_3, SiO_2 and MgO supports were investigated for the ethanol reaction. All the catalysts listed in **Tables 3.2 and 3.3** were tested. **Tables 3.4** and **3.5** list the matrix of flow rates and temperatures used to test for SiO_2 and MgO (**Table 3.4**) and for Al_2O_3 (**Table 3.5**) supported catalysts. The flow rates indicated in the tables are the liquid feed flow rates of only the ethanol. In both cases the ethanol was diluted with nitrogen in the molar ratio ethanol:N_2 = 1:4 and then passed over the catalyst bed in the quartz tube. For SiO_2 and MgO catalysts, 1 g of catalyst was used for each set of runs (6 temperatures at 4 flow rates = 24 runs). For Al_2O_3 catalysts, 3 g of catalyst was used for each set of runs (6 temperatures at 3 flow rates = 18 runs).

Table 3.4: Reactor conditions used to test Cu on SiO_2 and MgO supports in the ethanol dehydrogenation reaction

0.6 ml/h; 240 °C	1.6 ml/h; 240 °C	3.2 ml/h; 240 °C	6.4 ml/h; 240 °C
0.6 ml/h; 280 °C	1.6 ml/h; 280 °C	3.2 ml/h; 280 °C	6.4 ml/h; 280 °C
0.6 ml/h; 320 °C	1.6 ml/h; 320 °C	3.2 ml/h; 320 °C	6.4 ml/h; 320 °C
0.6 ml/h; 360 °C	1.6 ml/h; 360 °C	3.2 ml/h; 360 °C	6.4 ml/h; 360 °C
0.6 ml/h; 400 °C	1.6 ml/h; 400 °C	3.2 ml/h; 400 °C	6.4 ml/h; 400 °C
0.6 ml/h; 440 °C	1.6 ml/h; 440 °C	3.2 ml/h; 440 °C	6.4 ml/h; 440 °C

Table 3.5: Reactor conditions used to test Cu on Al_2O_3 supports in the ethanol dehydrogenation reaction

1.6 ml/h; 180 °C	3.2 ml/h; 180 °C	6.4 ml/h; 180 °C
1.6 ml/h; 220 °C	3.2 ml/h; 220 °C	6.4 ml/h; 220 °C
1.6 ml/h; 260 °C	3.2 ml/h; 260 °C	6.4 ml/h; 260 °C
1.6 ml/h; 300 °C	3.2 ml/h; 300 °C	6.4 ml/h; 300 °C
1.6 ml/h; 340 °C	3.2 ml/h; 340 °C	6.4 ml/h; 340 °C
1.6 ml/h; 380 °C	3.2 ml/h; 380 °C	6.4 ml/h; 380 °C

3.1.4.2. 2-Butanol reaction

The 2-butanol reaction was tested using only SiO_2 and MgO supports. In both cases 1 g of catalyst was used for each set of runs and the 2-butanol to nitrogen molar feed ratio was 1 to 4. The reaction conditions are summarised in **Table 3.6.** . The flow rates indicated in the table are the liquid feed flow rates of only the 2-butanol.

Table 3.6: Reactor conditions used to test Cu on SiO_2 and MgO supports in the ethanol dehydrogenation reaction

1.6 ml/h; 240 °C	3.2 ml/h; 240 °C	6.4 ml/h; 240 °C
1.6 ml/h; 270 °C	3.2 ml/h; 270 °C	6.4 ml/h; 270 °C
1.6 ml/h; 300 °C	3.2 ml/h; 300 °C	6.4 ml/h; 300 °C
1.6 ml/h; 330 °C	3.2 ml/h; 330 °C	6.4 ml/h; 330 °C
1.6 ml/h; 360 °C	3.2 ml/h; 360 °C	6.4 ml/h; 360 °C
1.6 ml/h; 390 °C	3.2 ml/h; 390 °C	6.4 ml/h; 390 °C

3.1.5. PRODUCT ANALYSIS

The ethanol and 2-butanol reaction products were analysed with a HP G1800A gas chromatograph, equipped with a mass spectrometer (for experiments conducted at Stellenbosch University) and flame ionisation detector. A 50 m capillary column (50QGI.5/BPI PONA from SGE) was used. Very good product separation was obtained with an inlet temperature of 250 °C, detector temperature of 300 °C and helium as carrier

gas. Response factors of the main products were calculated after injecting numerous liquid mixtures and constructing response factor curves. Response factors were not taken as linear functions, but were determined by fitting data of many (at least 6) different compositions of each binary mixtures. The ethanol and 2-butanol response factors are listed in **Appendix B1** and **B2**. A short description is also given in **Appendix B1** on how the response factors were determined experimentally.

The following system was used for determining reaction rate kinetics at the CNRS in Lyon, France. Carbon-containing products were analysed on a HP 5850 gas chromatograph equipped with a FID detector. Two capillary columns, a 30 m HP Innowax column and a 30 m HP Plot/Al_2O_3 column, were used in series. Hydrogen analysis was done on a similar GC with a TCD detector. A Porapak Q column and a molecular sieve column were operated in series.

3.1.6. CATALYST CHARACTERISATION

BET (Brunauer-Emmett-Teller) and chemisorption experiments were performed on all catalysts listed in **Tables 3.2 and 3.3**. No chemisorption was performed on Cu/MgO catalysts, because of the low catalyst surface area. A Micromeritics ASAP 2010 was used to determine both total catalyst surface area as well as copper surface area. Determining BET surface areas presented no problems. Samples were dried at 300 °C in situ overnight (14 to 16 hours). Determining copper surface areas was more difficult and resulted in several problems. Prior to analysis, the copper was reduced, in situ, in hydrogen for 2 hours at 260 °C. Both CO and H_2 were used as analysis gasses, but H_2 gave more reliable and reproducible chemisorption results. The copper and catalyst surface areas are listed and discussed in **Chapter 4**. Further catalyst characterisation was performed only on the catalyst used for kinetic testing. This included transmission electron microscopy (TEM), X-ray diffraction analysis (XRD) and total organic carbon analysis (TOC) of samples used.

3.2. KINETIC TESTING

The kinetics of the dehydrogenation of ethanol and the dehydrogenation of 2-butanol were studied using a 14.4 wt % copper on silica catalyst. This was found to be the optimal catalyst from experiments conducted in the catalyst screening phase. All catalyst testing was performed with the set-up shown in **Figure 3.1**.

To determine accurate kinetic data, interphase and intraparticle mass transfer resistance needed to be eliminated or minimised. The data must preferably be gathered in the flow regime, free of interphase mass transfer resistance. Intraparticle mass transfer resistance was minimised by using small catalyst particles. A 300-425 μm particle size was used for all experiments.

Several other important factors had to be taken into account when designing an experiment for determining the kinetic parameters of a reaction. They were:

- The reactor had to be operated as a differential reactor (see **Chapter 5**) to be able to accurately calculate reaction rates. A differential reactor is similar to a plug flow reactor, but the overall conversion is kept low (typically less than 10%) by using very small amounts of catalyst or very high feed flow rates.
- The catalyst bed had to be at a constant temperature.
- If the reaction rate is independent of the feed flow rate, but the conversion is still high, then the catalyst mass can be changed. The amount of catalyst can be reduced, while maintaining the same flow rate, thus lowering the conversion.

3.2.1. ETHANOL DEHYDROGENATION

Catalyst stability tests were performed to determine the temperature range free of significant catalyst deactivation, and to determine the deactivation mechanism.

3.2.1.1. Catalyst deactivation testing

An unused 14.4 wt % copper on silica catalyst was reduced at three different temperatures to determine the effect of reduction temperature on catalyst stability. For deactivation testing, the reaction was continued for 24 hours at the setpoint temperature

and the conversion documented with time increase. An undiluted 99.8% ethanol (from Prolabo) feed was used.

Table 3.7 indicates the different reduction temperatures evaluated. After these initial experiments, all further catalyst reductions were performed at 255 °C for two hours in hydrogen (25 cm^3/min). The catalysts were heated up at 8 °C/min in 50 cm^3/min of nitrogen before being reduced at the reduction temperature.

Table 3.7: Different combinations of reduction and reaction temperatures studied

Reduction T (°C)	400	400	340	340
Reaction T (°C)	400	255	340	255

Table 3.8 summarises all the stability tests performed on the dehydrogenation of ethanol. Catalyst (a) is the standard 14.4 wt % Cu on silica catalyst, while catalyst (b) is a 13.5 wt % Cu, 1.0 wt % Cr and 0.5 wt % Co on silica catalyst. Cr and Co are often added to copper to reduce sintering at a high temperature. Both catalysts were prepared in South Africa from copper nitrate as source. The support used was a silica support from Engelhard. Co and Cr were obtained from their nitrate salts.

Table 3.8: Summary of catalyst deactivation tests for ethanol dehydrogenation

Catalyst (a)				
Reduction T (°C)	400	340	280	220
Reaction T (°C)	255	255	255	255
Catalyst (b)				
Reduction T (°C)	400	340	280	-
Reaction T (°C)	255	255	255	-

The 14.4 wt % Cu on silica catalyst (catalyst (a)) was reactivated after 24 hours and

48 hours of operation at 400 °C. This was done to determine whether coking, sintering or both were the dominating deactivation mechanism. Reactivation consisted of the following:

- Oxidising the catalyst at 400 °C in oxygen for 4 hours,
- Cooling the catalyst down to 255 °C in oxygen,
- Reduction for 2 hours in hydrogen, and
- Heating up to 400 °C in nitrogen.

The reaction was then continued at 400 °C for the next 24 hours.

3.2.1.2. Characterising deactivated catalysts

Catalysts were well dried in nitrogen for 4 hours at the reaction temperature after the 24 hour stability tests. The following techniques were then employed to determine whether sintering and/or coking was the major catalyst deactivation process for copper on silica catalysts:

- XRD analysis with a Bruker AXS D5005 X-Ray Diffractometer.
- TEM analysis with a JEOL 2010 using a LaB_6 source and 200 kV ultra high resolution (c_s = 0.5 mm). EDS was performed with an Isis Link Oxford. Samples were prepared by ultrasonic dispersion in ethanol, followed by deposition on an Al grid (200 mesh) and covering with carbon.
- Total organic carbon (TOC) determination with a Shimadzu SSM 5000A.

3.2.1.3. Determining the mass transfer limited regime

The ethanol reaction rate was studied from 200 °C to 300 °C, at intervals of 25 °C. At each temperature a series of experiments was performed to try and achieve a constant reaction rate as a function of flow rate. This was achieved for temperatures up to 250 °C, but for higher temperatures some difficulty in eliminating interphase mass transfer resistance was experienced. **Table 3.9** summarises the catalyst sample masses and flow rates tested at each temperature.

Table 3.9: Conditions investigated for determining interphase mass transfer limited regime for ethanol dehydrogenation

Reaction T (°C)	Catalyst mass (g)	Min feed flow (ml/h)	Max feed flow (ml/h)
200	0.35	1	14
225	0.35	1	16
250	0.20	2	20
275	0.10	2	20
300	0.10	2	25

3.2.1.4. Determining kinetic parameters

Ethanol was co-fed to the catalyst with nitrogen (an inert gas), hydrogen or acetaldehyde. The nitrogen and hydrogen concentrations were varied by changing the flow rate of the mass flow controller (see **Figure 3.1**). In order to keep the total molar feed rate to the catalyst and the space time constant for all the runs, the ethanol feed was changed accordingly. Mixtures of acetaldehyde and ethanol, with varying acetaldehyde mass percentages, were used to test the reaction at different acetaldehyde feed concentrations.

When co-feeding ethanol with hydrogen or nitrogen, the products were analysed with a FID detector and reaction rates calculated from acetaldehyde production. A TCD detector was used to determine the amount of hydrogen produced when ethanol was co-fed with acetaldehyde. In the latter case, hydrogen production was used to determine reaction rates.

The availability of equipment limited the tests which could be performed at feed rates higher than 14 ml/h, mainly due to the size of the mass flow controller and difficulty with temperature uniformity in the catalyst bed at higher flow rates. All experiments were thus done at feed rates of 14 ml/h and reaction rates had to be adapted, using curves constructed from data in **Table 3.9,** to compensate for mass transfer resistance. For the ethanol dehydrogenation reaction, the reaction rate was determined at 70 different conditions. At least three injections were made into the GC at each condition and the

average value was used for modelling. The conditions for determining the kinetic parameters were as follows:

- T = 200, 225, 250, 275, 300 °C, and
- at each temperature:
  - N_2 molar % in feed = 15, 30, 45, 57 mole %,
  - H_2 molar % in feed = 15, 30, 45, 57 mole %, and
  - Acetaldehyde mass % in feed = 4.4, 11.6, 21.3, 29.8, 50 mass %.

Every day a new catalyst sample was used for experiments. The reaction rates for the catalyst (at the operating temperature) were determined using pure ethanol as feed. All data was determined relative to a set of reference values. Reference values at the same temperature were averaged and each data set normalised, relative to the global average at each temperature. This yielded more accurate and consistent data for modelling.

3.2.2. 2-BUTANOL REACTION

The same equipment and steps used for studying the ethanol reaction were used for studying the 2-butanol reaction. The catalyst was also a 14.4 wt % copper on silica catalyst. Deactivation was determined at 250 °C and 310 °C. Further kinetic experiments were performed at 190, 220, 250 and 280 °C. **Table 3.10** is a summary of reaction conditions investigated to determine the interphase mass transfer limited regime for 2-butanol dehydrogenation.

A feed flow rate of 12 ml/h was used for all further experiments with 2-butanol. The following mixtures were fed to the catalyst at each of the reaction temperatures:

- N_2 molar % in feed = 10, 25, 40, 55, 70 mole %,
- H_2 molar % in feed = 10, 25, 40, 55, 70 mole %, and
  - Methyl ethel ketone mass % in feed = 6.7, 10.6, 20.1, 40.3, 62.8 mass %.

Table 3.10: Conditions investigated for determining interphase mass transfer limited regime for 2-butanol dehydrogenation

Reaction T (°C)	Catalyst mass (g)	Min feed flow (ml/h)	Max feed flow (ml/h)
190	0.15	2	12
220	0.15	2	16
250	0.075	2	16
280	0.075	2	16

Data was gathered in a similar manner to that for ethanol dehydrogenation. Reaction rates were determined relative to a set of reference values, which was then used to calculate more accurate and consistent data for modelling. A GC, with a TCD detector and packed columns, was used for determining hydrogen production rates when MEK was co-fed with 2-butanol. For all other experiments, products were analysed with a FID detector and capillary columns.

3.3. MEMBRANE PREPARATION AND TESTING

This section describes all aspects of pure Pd composite membrane preparation and testing. Preparing and testing Pd alloys will also be discussed.

3.3.1. MEMBRANE SUPPORT

The membranes employed in this study were purchased from SCT (Societé des Céramiques Techniques) and the membranes consisted of three α-alumina layers with decreasing particle sizes. The structure is illustrated in **Figure 3.2**.

The membranes had a length of 250 mm, an outside diameter of 10 mm and an inside diameter of 7 mm. The final layer had a pore size of 200 nm. Further characteristics regarding pore diameter, thickness and porosity of each layer are presented in **Table 3.11**.

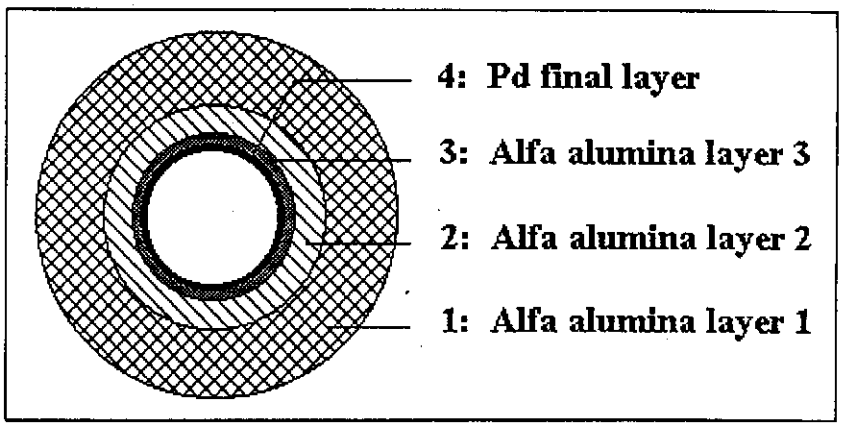

Figure 3.2: SCT membrane structure

Table 3.11: Membrane layer characteristics of a SCT membrane

	Pore diameter (μm)	Layer thickness (μm)	α-alumina particle size (μm)	Porosity (ε)
Layer 1	11	1500	53	0.26
Layer 2	0.64	40	4	0.24
Layer 3	0.2	20	0.9	0.25

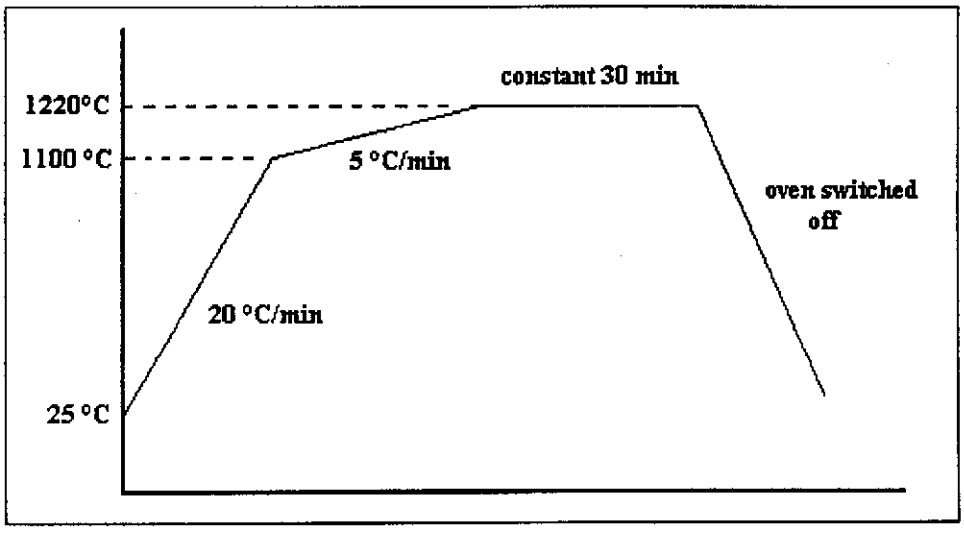

Figure 3.3: Curing process for enamelled membranes

The outside membrane ends had to be sealed with an enamel supplied by SCT prior to plating in order to achieve proper membrane reactor sealing. This process filled the outside membrane pores with a non-porous material, thus preventing gas leaks along the outside membrane surface during the testing stage. Enamel was applied along a length of 10 mm at the membrane ends by dipping the membranes in the enamel slurry. Enamelled membranes were then placed in a high temperature furnace (from Vecstar Furnaces) and cured according to the procedure suggested by SCT and indicated in **Figure 3.3**. Two or three layers of enamel were applied on the membrane ends to obtain good sealing.

3.3.2. COMPOSITE MEMBRANE PREPARATION

A modified electroless plating process was used for preparing composite membranes. Membranes were cleaned and pretreated prior to electroless plating. After plating, the membranes were stirred in ammonia and dried.

3.3.2.1. Electroless plating pre-treatment

Upon completion of the enamelling process, no further cleaning was performed and the masses of the membranes were recorded. Some membranes were supplied with enamelled endings. Those samples were stirred in distilled water for 30 minutes using a RW 11 basic stirrer from IKA Labortechnik. The samples were then placed overnight (14 to 16 hours) in an oven at 200 °C. Their masses were recorded the following morning, after cooling of the membranes in the oven down to 60 °C.

Prior to electroless plating, the membrane surface needed to be activated to provide catalytic centres for the plating process. A two step process using a palladium salt and a tin chloride salt was used. Previously, it was found that the conventional composition of the pre-treatment solutions deposited small amounts of tin. Keuler (1997a) found about 0.2 to 0.4 % Sn (with particle induced X-ray emission) in a 5 micron Pd film prepared with the conventional solutions. For thin Pd films of less than 2 microns this amount would become more significant and might cause a decrease in the hydrogen permeance rate through the film. A higher Pd concentration and a lower Sn concentration were chosen by the author for pre-treatment and are indicated in **Table 3.12**. The conventional

composition of the pre-treatment solution was similar to that of Shu, Grandjean et al. (1993).

Table 3.12: Compositions of pre-treatment solutions

	Conventional composition	This study
Sensitising solution (per litre)		
35 wt % HCl (ml)	1	-
$SnCl_2.2H_2O$ (g)	1	0.45
Activation solution (per litre)		
35 wt % HCl (ml)	1	-
10 wt % $(NH_3)_4Pd(NO_3)_2$ (g)	1.5	-
23 wt % $PdCl_2$	-	1.4
Sn to Pd molar ratio	8.8	1.1

The outside surface of the membrane tubes were wrapped with PTFE tape so that only the insides of the tubes would be catalysed. The set-up for pre-treatment is shown in **Figure 3.4**. The stirrer was a RW 11 basic stirrer from IKA Labortechnik (0 to 2000 rpm) and the stirring speed was set at about 1200 rpm.

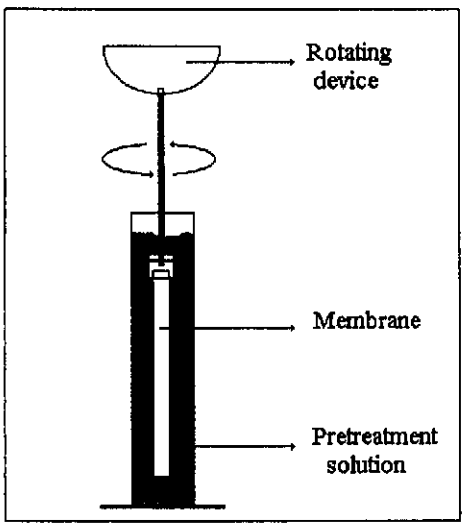

Figure 3.4: Pre-treatment set-up

The procedures and their sequence for pre-treatment are tabulated in **Table 3.13**. Approximately 270 ml of each solution was used. Fresh tin solution was prepared for every membrane, while the Pd solution was changed after every three membranes catalysed.

Table 3.13: Stirring sequence and times used in pre-treatment

	Pd solution	**Distilled water**	**Sn solution**	**Distilled water**
Repeat 3 times	10 minutes	Dip into 10 times	10 minutes	Dip into 10 times
Repeat 3 times	5 minutes	-	5 minutes	Dip into 10 times

After pre-treatment, the teflon tape was removed and the membrane stirred in clean distilled water for an additional half an hour to remove any solution in the membrane pores. The membrane was then placed in an oven at 200 °C overnight and the mass recorded the next morning after cooling: The mass increase varied between 13 and 16 mg for different membranes prepared using a 0.45 g per litre $SnCl_2$ sensitising solution. Some membranes were pre-treated with a 0.25 g per litre $SnCl_2$ sensitising solution, in which case the mass increase was about 8 to 10 mg.

3.3.2.2. Electroless Pd plating

A 2.00 g/litre (2000 ppm) Pd solution was used for electroless plating. The composition of the solution is given in **Table 3.14**. The Pd solution, without the hydrazine in it, was allowed to stand (stabilise) for at least 12 to 16 hours prior to plating. Hydrazine was added just before plating and only to the solution that was used for plating. For some of the initial membranes that were prepared at the laboratories of the CNRS (Lyon, France), a three times higher initial hydrazine concentration was used. The values in **Table 3.14** represent the composition of the plating solution in the latter stages of the project, which produced good quality and reproducible coatings. The hydrazine concentration in **Table 3.14** represents the initial amount that must be added to the palladium solution on a per litre basis. **Table 3.15** lists how the hydrazine was added to the palladium solution.

Table 3.14: Composition of the Pd plating solution per litre (for 2.00 g/litre Pd in solution)

$(NH_3)_4PdCl_2.H_2O$ (g)	4.94
28 wt % Ammonia (ml)	400
EDTA (g)	80
35 wt % hydrazine (ml)	0.65 (hydrazine:Pd = 0.35:1) increased with time
Temperature (°C)	71-73

Three different methods for feeding plating solution to the inside of the membrane tube were tested:

1. Plating solution was pumped continuously through the inside of the tube at flow rates varying between 90 and 120 ml per hour.
2. A membrane was covered on the outside with teflon tape and stirred in the plating solution.
3. A batch process was used in which between 10 and 12 ml plating solution was introduced into the sealed tube at a time and allowed to react for a fixed period of time.

The third process was chosen for preparing all further membranes (see discussion in **Chapter 6**). The plating set-up is shown in **Figure 3.5**. The membrane was sealed in a teflon reactor with O-rings. The reactor had a single shell side outlet allowing for a vacuum to be pulled on the shell side. A defect-plugging technique was developed to produce thin films (< 2 microns). An initial 1 micron Pd base was deposited on the inside of the membrane tube using 35 ml plating solution without any vacuum applied. The membrane was closed off at the bottom with a 10 mm silicon tube which was closed at one side. A silicon tube of about 15 cm was also placed over the membrane at the top. Between 11 and 12 ml plating solution was introduced into the membrane tube fixed in the reactor at a time.

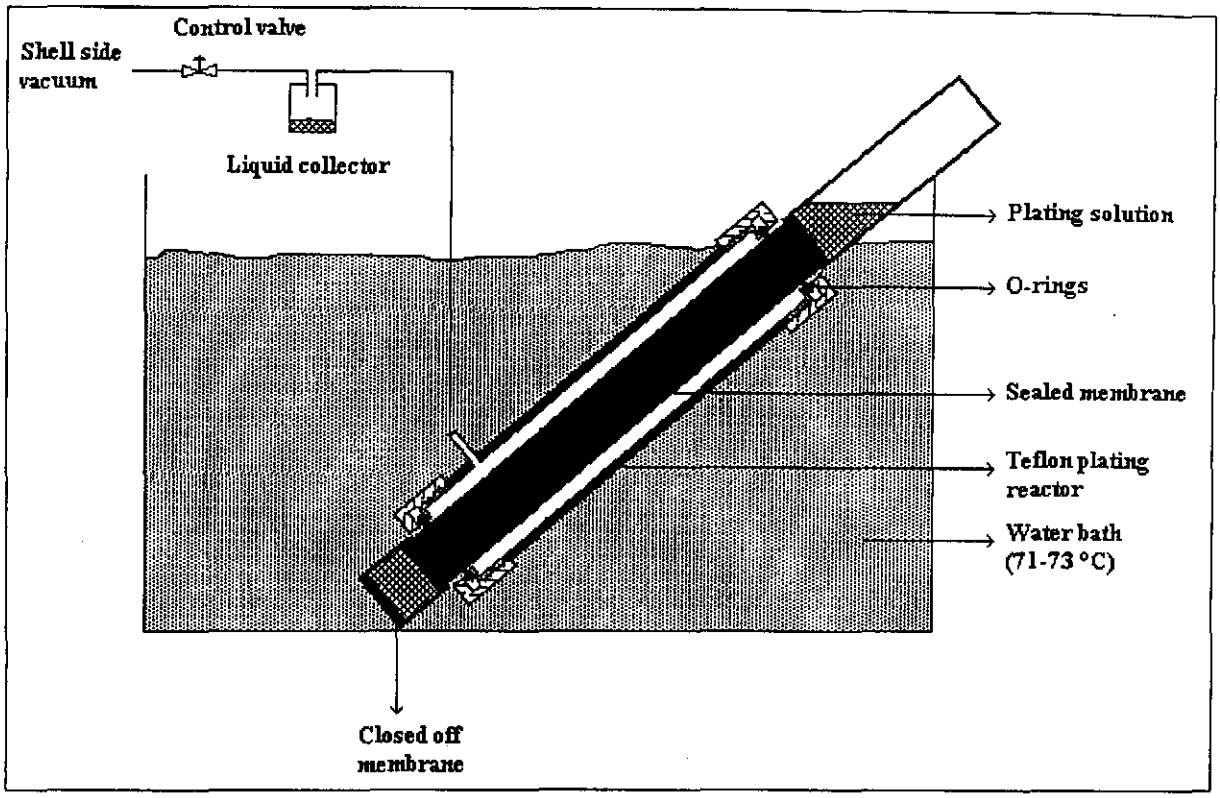

Figure 3.5: Electroless Pd plating set-up

Three to four plating sessions were performed with the same plating solution. Repeated plating sessions ensured that all the Pd in solution was deposited on the membrane. The hydrazine concentration was increased after each plating session to compensate for thermal decomposition of hydrazine. The plating procedure as outlined in **Table 3.15,** is essentially a batch process repeated several times. When preparing a 1 micron film, each session in **Table 3.15** was repeated 3 times (11.5 ml * 3 = 34.5 ml solution). The first 0.15 ml of 1.75 wt % hydrazine that was added to the 11.5 ml plating solution (see **Table 3.15**) is equivalent to 0.65 ml of 35 wt % hydrazine per litre of plating solution, as mentioned in **Table 3.14.**

Membranes were then cleaned and dried overnight before the next layers were applied. The effect of Pd film thickness on hydrogen and nitrogen permeances was investigated. For thicker films (> 2 microns), a thicker initial base was applied, but for membranes of between 1 and 2 microns total thickness, the first layer was always about 0.9 to 1.1 microns. Membrane cleaning or post-treatment will be discussed in the next section.

Table 3.15: Plating procedure used for producing Pd films

Plating session	Reaction time for 11.5 ml plating solution (min)	Vol. 1.75 wt % hydrazine added for 11.5 ml solution (ml)
1	20	0.15
2	20	3 drops
3	20	0.5

After the initial Pd layer was deposited, an additional one, two or three layers were deposited to obtain the final product. The thickness of each layer depended on the required thickness of the final Pd film: for example a film with a final thickness of 1.5 μm required two extra layers of 0.25 μm each. After the second layer, the membrane was once again cleaned and dried overnight before applying the third layer.

For the second and third Pd layers, a vacuum was applied on the shell side of the teflon reactor. Pd solution will concentrate in the more permeable or defected areas in the membrane. More plating will occur in weakly plated (defected) areas, .film defects will be covered with palladium and a film with less defects will result.

Pd membrane preparation focussed on preparing a thin film of thickness less than 2 μm. Some films of between 2 and 5 microns were also prepared to study the effect of film thickness on hydrogen and nitrogen permeance through the film.

3.3.2.3. Membrane cleaning

The same equipment used for pre-treatment, was used for membrane cleaning (**Figure 3.4**). The membrane was removed from the reactor and placed in a cylinder containing 270 ml 15 wt % ammonia solution. The membrane was stirred at a rate of 1200 rpm for one hour. This process was repeated with fresh ammonia solution and finally the membrane was stirred in a similar volume distilled water for half an hour. The membrane was then placed overnight in an oven at 240 °C. In the latter stages of the

work, the membranes were dried at 100 °C and again (two or three times) stirred in ammonia solution and water before drying them at 240 °C. This was an attempt to try and extract more EDTA trapped in the membrane pores.

3.3.2.4. Electroless silver plating

The same equipment and procedures used for palladium plating was also used for silver plating. Two or three silver layers were deposited onto the palladium layer in sequential steps. The mass of silver plated was determined from the membrane mass increase after each plating sessions. After each layer of silver had been deposited, the membrane was washed and dried overnight at 240 °C. If the amount of silver was less than the desired amount (less than 20 wt % Ag in the Pd-Ag film), an additional layer was deposited. The composition of the silver plating bath is given in **Table 3.16**.

Table 3.16: Composition of silver plating bath per litre of plating solution

Ag (ppm)	1000
$AgNO_3$ (g)	1.576
EDTA (g)	40
Ammonia (28%) (ml)	200
Hydrazine (3.5 wt %) (ml)	8.50

The hydrazine concentration (for Ag plating) was increased with time, similar to the procedure for Pd plating (see **Table 3.17**). For every 11 ml fresh plating solution, the procedure in **Table 3.17** was performed. Generally, a maximum of about 75% of silver in solution was deposited on the palladium. An excess of 30% of the required amount of silver that needed to be deposited on the membrane was used in solution for plating. Silver plating was performed and if the deposited silver was not sufficient, a second layer was deposited. For the second layer, the initial silver plating solution was diluted to ensure a volume of 11 ml plating solution. This was necessary because if the silver plating solution (original) was less than 10 ml it would not wet the entire membrane surface and thus not plate over the entire surface.

Table 3.17: Plating procedure used for producing Ag films

Plating session	Reaction time for 11 ml plating solution (min)	Vol. 0.35 wt % hydrazine added for 11.5 ml solution (ml)
1	20	0.4
2	20	0.4
3	20	0.2 ml, 1.75 wt % hydrazine

3.3.3 DETERMINING PALLADIUM FILM THICKNESS

Two methods were used to determine the amount of Pd deposited on the membrane supports. The membranes were weighed after pre-treatment and drying at 200 °C overnight to get the initial mass. The membranes were weighed again, after testing of the membranes were completed, to get the final mass. The difference between the initial mass and final mass was taken as the amount of Pd deposited.

ICP (with a Spectroflame Modula from Analytical Instruments) analysis of the plating solution was performed after plating to determine the amount of palladium deposited. Since the initial mass of the plating solution was known, the mass of the deposited Pd could be calculated. The average of this mass and the measured mass was used to calculate Pd film thickness. The calculated film thickness is an average thickness value.

3.3.4. MEMBRANE TESTING

Membrane permeance testing was performed in the reactor shown in **Figure 3.6**. The reactor was made from stainless steel and graphite rings were used for obtaining an effective membrane to reactor seal. The rings had dimensions of 10.4 by 17.9 mm, a thickness of 5 mm and a density of 1.6 g/cm^3. They were purchased from Coltec Industries (Le Carbone Loraine). Nuts turned into the membrane ends, pushing two fittings onto the graphite rings. Those fittings slid over the membrane ends and were cut with an angle at the bottom edge to be able to wedge into the graphite. When the nuts were tightened, the fittings forced the graphite rings forward and sideways, pushing them

against the enamelled membrane endings. If the nuts were sufficiently tightened, a very good seal was obtained. Over tightening could result in either breaking or cracking of the membrane.

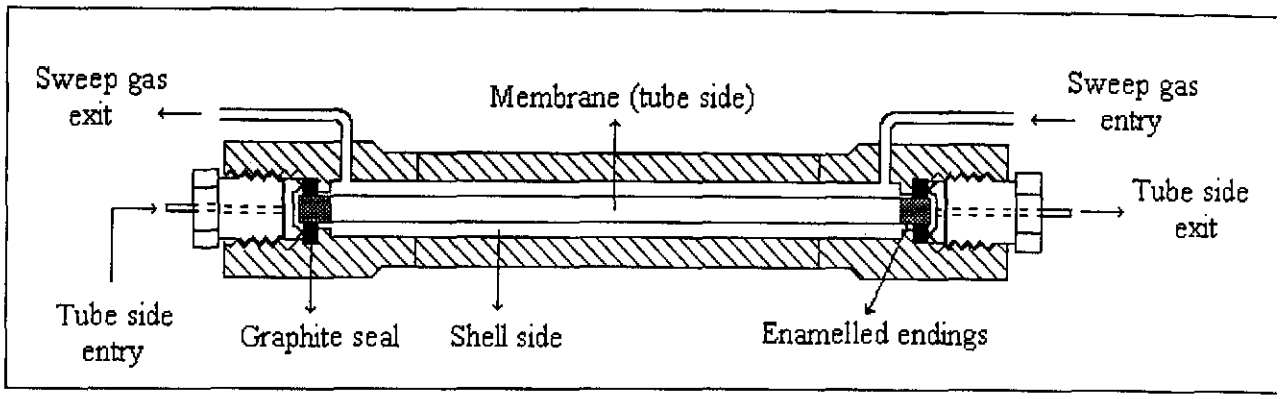

Figure 3.6: Membrane reactor used to test the membrane permeance

Some difficulty was, however, still experienced when trying to obtain good reactor to membrane seals. The main reason was that the enamel on the outside membrane surface was not always of uniform thickness. The equipment shown in **Figure 3.7** was used to minimise the leak resulting from membrane sealing.

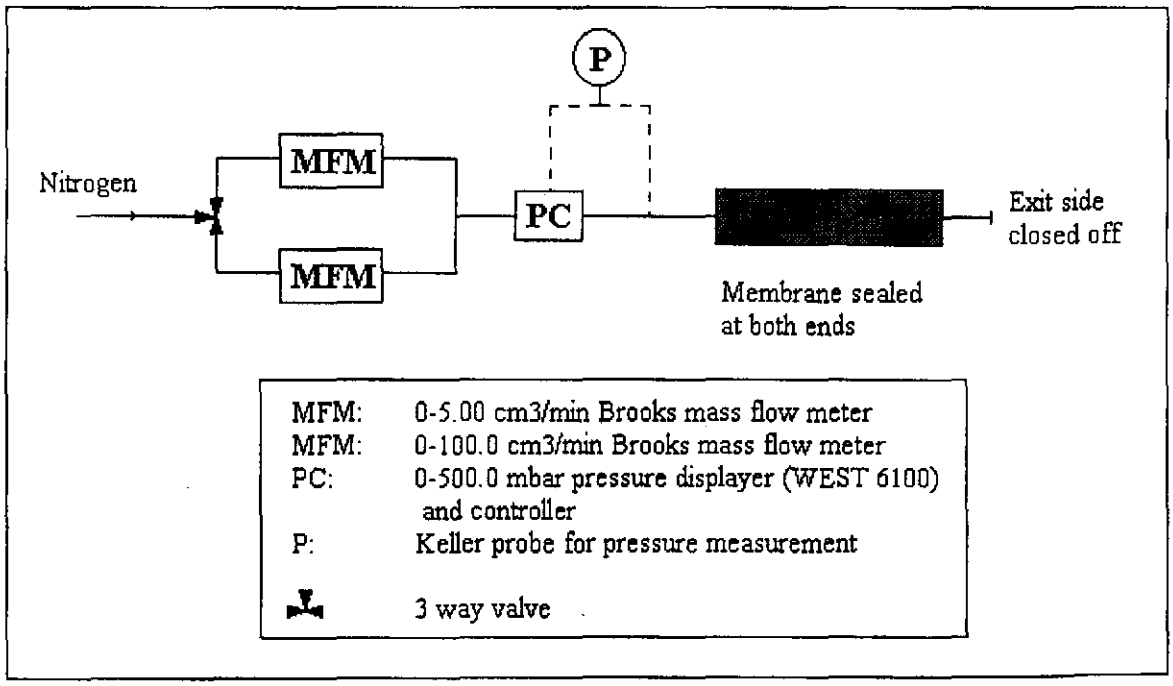

Figure 3.7: Set-up used for membrane testing at room temperature

The membrane was placed inside the reactor, with graphite rings at the edges (see **Figure 3.6**) and the nuts tightened moderately. The reactor (with the exit side closed off) was then connected to a pressure controller and two mass flow meters as indicated in **Figure 3.7**. The pressure controller was set at 400.0 mbar and the value of the mass flow meters monitored while reactor nuts were tightened. Tightening was stopped when, upon further tightening of the nuts, there was no further decline in the reading of the mass flow meters. The nuts on opposing sides were not necessarily turned or tightened equally, to obtain the best seal. Sometimes the reactor had to be re-opened, the membrane shifted slightly and nuts re-tightened to obtain a good seal.

Figures 3.8 and **3.9** show the equipment used for high temperature membrane testing with hydrogen, nitrogen and ethanol as feeds, respectively. In both instances the reactor was wrapped with heating wire and insulated. A thermocouple was placed in the centre of the membrane tube to record the temperature.

For hydrogen and nitrogen testing (**Figure 3.8**), one of the two shell side tubes of the reactor was closed. The reactor was operated in the dead end mode, in other words, the exit tube side was closed and the feed gas forced through the Pd film. The temperature inside the reactor was varied between 330 °C and 450 °C, using a temperature controller. The flow rate of the permeated gas was measured using two bubble flow meters. A 0 to 100 ml flow meter was used for hydrogen measurements and a 0 to 4 ml flow meter for nitrogen. The effect of differential pressure on hydrogen and nitrogen permeance was studied. The mass flow controllers were set on different flow rates and the differential pressure recorded. Initial testing was conducted at the laboratories of the CNRS (Lyon, France). For hydrogen permeance, the maximum differential pressure that could be tested was limited by the mass flow controller (0 to 600 cm^3/min). For films in the order of 1.5 μm, this maximum differential pressure was less than 100 mbar at 450 °C. The pressure probe had a maximum measuring ability of 2000 mbar, which was the limit for testing nitrogen permeance.

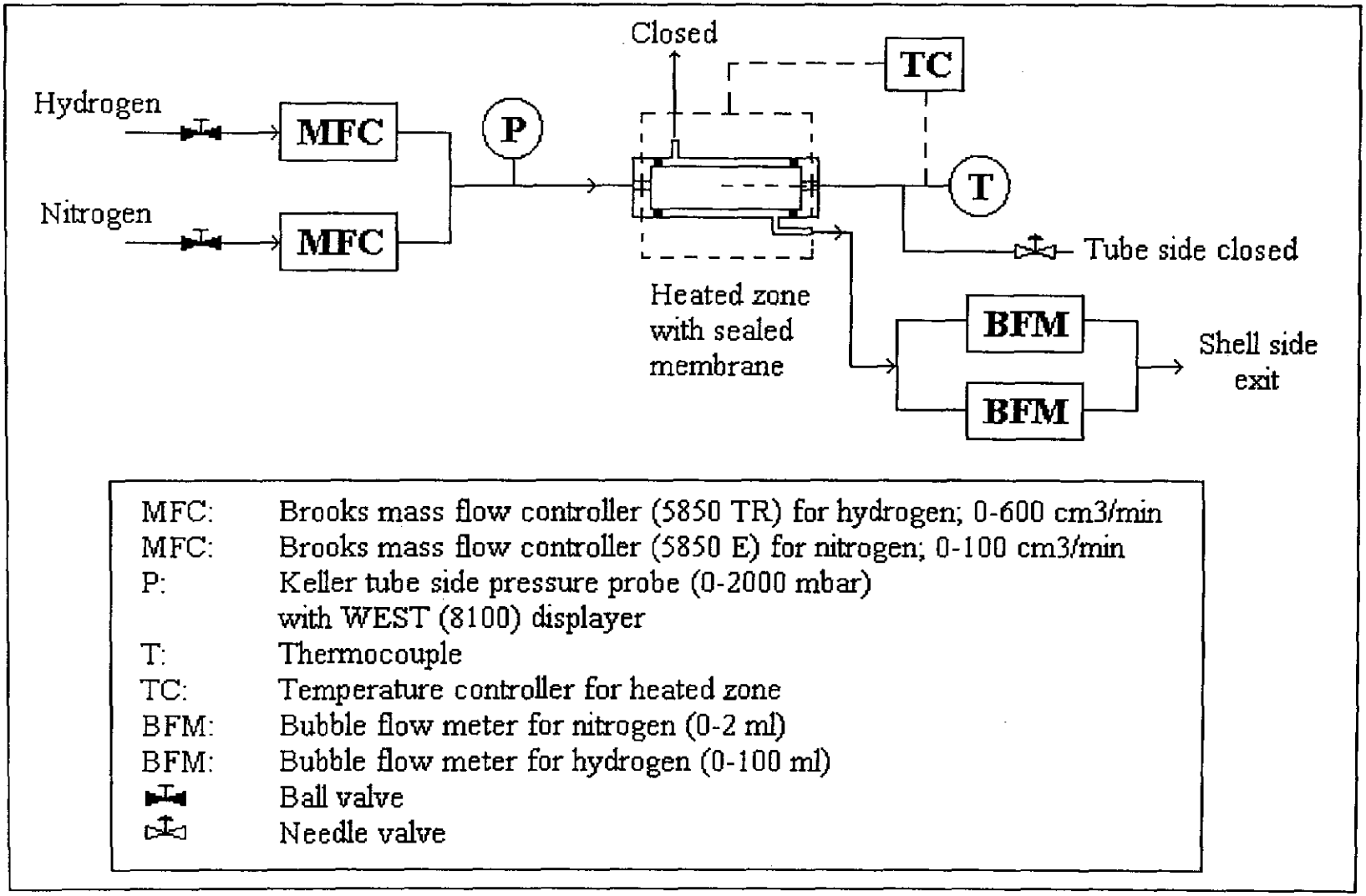

Figure 3.8: Set-up used for high temperature (> 300 °C) hydrogen and nitrogen permeation testing

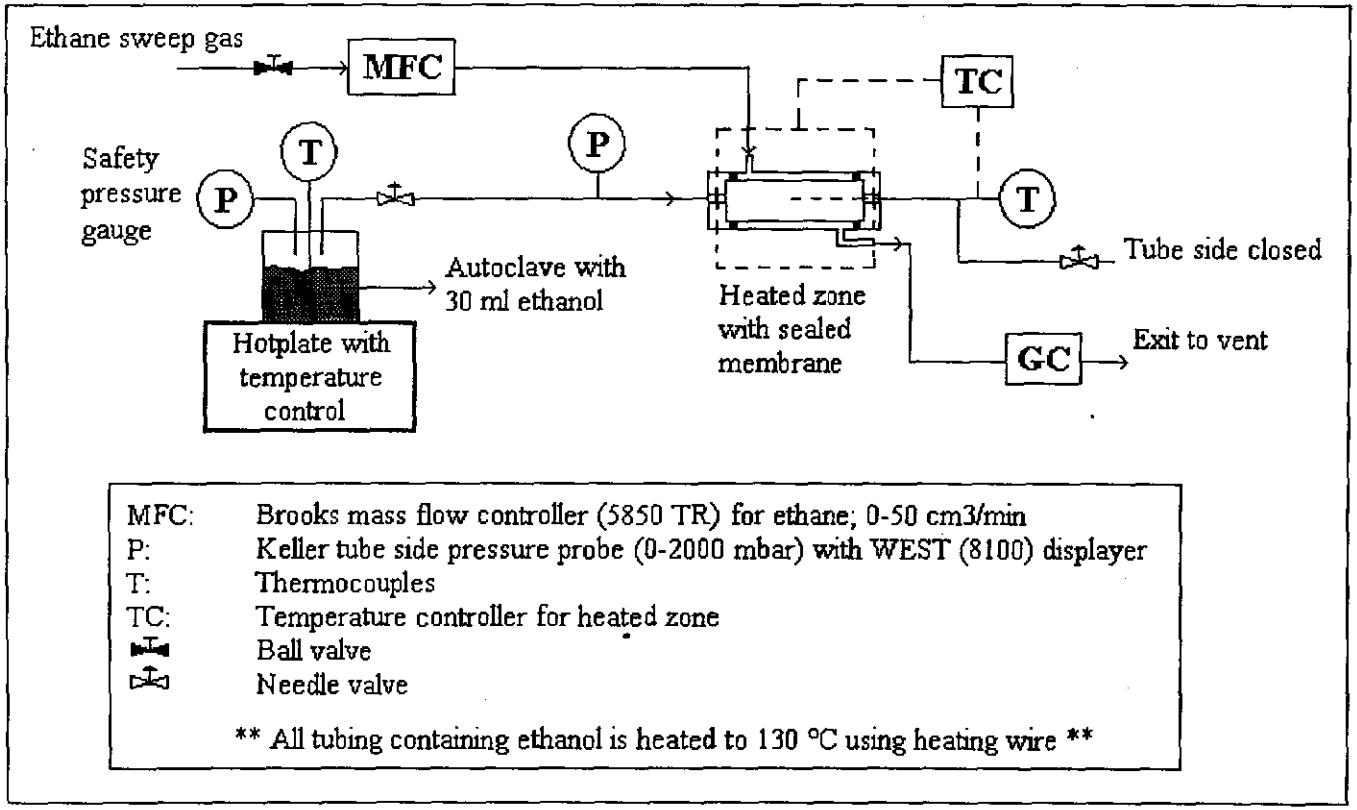

Figure 3.9: Set-up used for testing ethanol permeance

Further testing on both pure palladium films and Pd-Ag alloy films was conducted at the University of Stellenbosch, South Africa. At Stellenbosch, Hastings flow controllers (HFC 202C) were used instead of Brooks and they had a maximum capacity of 1000 cm^3/min. The pressure probe also had a maximum of 2000 mbar.

The apparatus used for ethanol permeance testing is shown in **Figure 3.9**. An ethane sweep gas was used and fed to a gas chromatograph after moving pass the membrane. By measuring the ethanol content in the sweep gas, the ethanol permeance could be calculated. All lines containing ethanol were wrapped with heating wire and insulated. The temperature of the heated lines was kept between 110 °C and 130 °C to prevent any condensation in the lines. An autoclave was used to feed the ethanol to the reactor. The autoclave was well insulated and heated on a temperature controlled hotplate from IKA Labortechnik. The desired tube side pressure could be obtained by correctly setting the temperature of the hotplate.

The autoclave was filled with 30 ml 99.8% ethanol. The testing pressure was stable and fluctuated by less than 1%. The slow ethanol permeance ensured a constant tube side pressure.

After testing, the Pd membrane was kept in nitrogen at 330 °C for 2 hours and then cooled at a rate of 2 °C/min to room temperature (also in nitrogen).

3.3.4.1. Reactor temperature profiles

Temperature profiles across the length of the reactor were determined at various oven temperatures. A constant temperature over the length of the reactor was necessary to assume isothermal conditions for modelling purposes. The heating wire, around the reactor and insulation material, was adjusted until satisfactory profiles were obtained. The final profiles are presented in **Figure 3.10**.

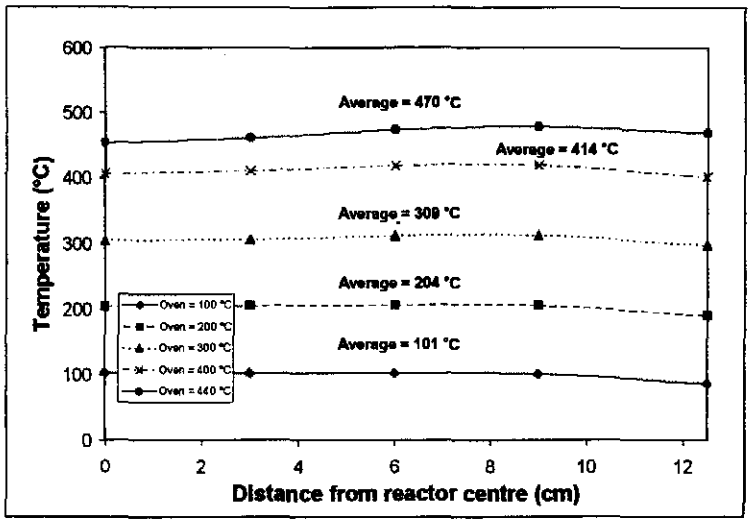

Figure 3.10: Reactor temperature profiles at different oven temperatures

There were two thermocouples for measuring temperature. One was situated inside the membrane tube and one was situated on the outside of the reactor, next to the reactor wall. The temperature controller was connected to the thermocouple on the outside of the reactor wall, since that temperature provided for more stable temperature control than the thermocouple inside the membrane tube. The temperature inside the membrane tube was measured, but not used for control. The temperature difference between the two thermocouples was taken into consideration when setting the reaction temperature. In other words, to control the reaction temperature at for example 300 °C, the oven was adjusted by the difference and set at 291 °C. At 300 °C and below, the temperature profiles were excellent from the centre of the reactor up to a distance of 9 cm from the centre. The variance from the average temperature was less than 5 °C. In the last 3.5 cm, the temperature dropped by between 10 and 13 °C. The total membrane length was 25 cm. Catalytic membrane reactor experiments were performed below 300 °C and the variance in reactor temperature was small enough to assume isothermal conditions. At 400 °C and above, the difference between the oven and reactor temperatures increased. The variance around the average was also larger and increased to between 10 and 15 °C.

3.3.5. MEMBRANE HEAT TREATMENT AND REDUCTION

The membrane reactor was heated from room temperature to 450 °C at 2.5 °C/min in a nitrogen atmosphere. The membrane was then reduced in a hydrogen atmosphere at

450 °C for one and a half hours. A very high EDTA concentration (80 g per litre) was used for plating. The cleaning process and overnight oxidation at 240 °C did not remove all the precursor. It was found that even after reduction not all the carbon in the membrane pores was removed either by oxidation or by thermal decomposition. The heating process was then changed and it produced membranes with higher hydrogen permeances and selectivities. The process was changed as follows:

- Heat the membrane in nitrogen from room temperature to 320 °C, at 2.5 °C/min.
- Switch from using nitrogen to oxygen and force 10 cm^3/min oxygen from the tube side through the membrane pores to the shell side. Cary out oxidation for 2 hours.
- Switch back to nitrogen and heat from 320 °C to 450 °C, at 2.5 °C/min.
- Reduce at 450 °C in hydrogen for 1.5 hours.

3.3.6. PALLADIUM-SILVER ALLOYING

Silver was deposited on the palladium coating to form two separate layers. The hydrogen and nitrogen permeances for pure palladium, palladium-silver without heat treatment and palladium-silver with heat treatment were compared. Different factors were investigated during the alloying procedure to obtain a thorough understanding of what takes place on the membrane surface. Since the number of membranes available for testing was limited, not all the variables could be tested in detail, but a significant amount of data was nonetheless obtained. The variables that were important during alloying included:

- Heating procedure: Membranes can be heated in situ in the reactor (fixed at both ends) or they can be heated in free mode in a tube furnace. In the latter method the membrane is not fixed to a reactor and free to expand along its axis.
- Heating environment: Different heating environments, for example hydrogen, argon or nitrogen, may have different effects.
- Alloying temperature.
- Alloying time.

The alloying experiments were performed on membranes with metal coatings of similar thicknesses. This was important, to be able to compare results of different membranes. Both heating methods were investigated. Membranes were placed either in a constant

temperature tube furnace or in the reactor (**Figure 3.6**) and heated at a rate of 1.5 °C/min to the required temperature. Initial experiments were performed with the membranes in the free mode under the following conditions:

- argon and hydrogen atmospheres,
- alloying temperatures ranging from 520 °C to 600 °C, and
- alloying times up to 150 hours.

The amount of data obtained from membranes heated in the tube furnace, was limited. The oven had to be cooled down (at 1.5 °C/min) to room temperature after each experiment, and the membrane placed in the reactor for testing, before data could be gathered. Not only did the thermal cycling weaken the coating, but the data was also of a discontinuous nature.

Most of the alloying was performed in situ in the reactor. That allowed for continuous monitoring of the process. Permeance and selectivity data could be obtained at any time. The following conditions were tested during alloying in the reactor:

- argon, nitrogen and hydrogen atmospheres,
- alloying temperatures from 500 °C to 600 °C, and
- alloying times from 10 hours to more than 100 hours.

3.3.7. MEMBRANE CHARACTERISATION

Besides permeance testing, the palladium plated SCT membranes were studied using scanning electron microscopy (SEM). SEM was conducted at the Microscope Unit, University of Cape Town, with a Cambridge Stereoscan 440. For top view images, the samples were mounted on aluminum stubs and then gold plated. For cross-section views, the membranes were set in a resin, sanded to expose fresh cross section and then polished with an alumina slurry.

3.4. CATALYTIC MEMBRANE REACTOR EXPERIMENTS

Catalytic membrane reactor experiments were performed in a set-up similar to that shown in **Figure 3.1**. The quartz tube in **Figure 3.1** was replaced by the reactor in **Figure 3.6,** with temperature profiles as in **Figure 3.10**. The alcohol feed passed through a 1 meter coil, which was placed in a pre-heating oven and connected to the reactor inlet. The pre-heating oven ensured that the feed entered the reactor at the reaction temperature. Exit lines were heated with heating wire to keep the products in the gas phase. A heated syringe (120 °C) was used for taking gas samples and injecting them into a GC. The products were analysed with a HP G1800A gas chromatograph, equipped with a mass spectrometer and a flame ionisation detector (for more details see **section 3.1.5**).

For both the ethanol and 2-butanol reactions, the membrane was packed with a 14.4 wt % Cu on silica catalyst. The catalyst particle size fraction was 500 to 850 microns. The catalyst was kept in position with quartz wool at the edges of the membrane (see **Figure 3.11**).

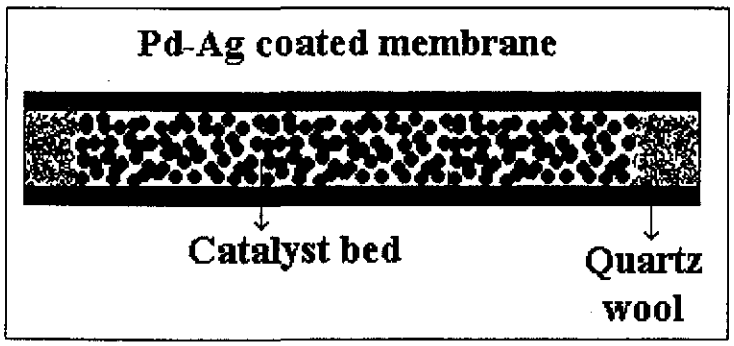

Figure 3.11: Membrane packed with catalyst

During the start-up procedure, the membrane reactor was heated in nitrogen at 2 °C/min from room temperature up to 275 °C. The membrane and the copper catalyst were then reduced in a hydrogen atmosphere (flow of 50 cm^3/min) for 1.5 hours. After 1.5 hours, hydrogen was replaced with nitrogen for a further 10 minutes and then the reactor was either heated or cooled at 2 °C/min to the required reaction temperature. At the required reaction temperature, the alcohol was introduced at 10 ml/h for 1.5 hours before analysis.

3.4.1. ETHANOL DEHYDROGENATION

The ethanol dehydrogenation reaction in the catalytic membrane reactor was investigated from 250 °C to 300 °C. The feed rate depended on the reaction temperature, but varied from 5 ml/h to 30 ml/h. The membrane was packed with 3.00 g catalyst. The following conditions were used for testing ethanol dehydrogenation in a membrane reactor:

- 250 °C: 5, 10 ml/h feed rate,
- 275.°C: 5, 10, 20, 30 ml/h feed rate, and
- 300 °C: 10, 20 ml/h feed rate.

Experiments were first conducted without a sweep gas, to obtain conversions representing a plug flow reactor. An inert sweep gas (nitrogen) was then introduced into the shell side and increased from a sweep gas to feed molar ratio of 1:5 to 4:1. In all experiments co-current flow was used.

3.4.2. 2-BUTANOL DEHYDROGENATION

The dehydrogenation of 2-butanol was conducted in the same manner as the dehydrogenation of ethanol. The membrane was packed with 3.50 g catalyst. The following conditions were used for testing 2-butanol dehydrogenation in a membrane reactor:

- 190 °C: 5, 10, 15 ml/h feed rate,
- 215 °C: 5, 10, 15, 20 ml/h feed rate, and
- 240 °C: 5, 10, 20, 30, 40 ml/h feed rate.

At each feed flow rate, four or five different sweep gas flow rates were tested and the dehydrogenation results compared to results obtained when no sweep gas was used (i.e. a plug flow reator). Nitrogen was used as the sweep gas and the flow was co-current for all experiments.

3.5. SUMMARY

This chapter covered all experimental work performed. There were three basic sections:

- Catalyst optimisation and kinetic testing,
- Membrane optimisation and permeance testing, and
- Catalytic membrane reactor experiments.

The equipment and procedures used in each section were described in detail. The variables that were investigated, were listed. The values at which each variable were tested, were also indicated.

4. OPTIMISING CATALYST COMPOSITION

Both the dehydrogenation of ethanol and 2-butanol were investigated. For each reaction, different catalysts were investigated at a range of operating conditions. The composition of the catalysts and the conditions at which they were tested were discussed in **Chapter 3**. All the data presented in this chapter is for average W/F values at specific temperatures and copper loadings. The W/F ratio is the catalyst mass divided by the feed flow rate. A low W/F value indicates a fast feed rate and a high W/F value indicates a slow feed rate for a constant mass of catalyst. Each experiment was performed at either three or four different feed flow rates. The conversions, yields and selectivities discussed are average values, unless otherwise stated. The following definitions were used:

$$\text{total feed conversion} = \frac{\text{total moles feed reacted}}{\text{total moles feed fed}} \qquad (4.1)$$

$$\text{product yield} = \frac{\text{moles feed converted to product}}{\text{total moles feed fed}} \qquad (4.2)$$

$$\text{product selectivity} = \frac{\text{moles feed converted to product}}{\text{total moles feed reacted}} \qquad (4.3)$$

$$\text{yield} = \text{selectivity} \times \text{total feed conversion} \qquad (4.4)$$

4.1. DEHYDROGENATION OF ETHANOL

The dehydrogenation of ethanol was tested over magnesium oxide, silica and alumina catalysts impregnated with copper. The results for each catalyst will be discussed below. The particle sizes used for each support were listed in **Tables 3.2** and **3.3**.

4.1.1. MgO CATALYSTS

Figures 4.1 to **4.3** show the reaction results for the reaction of ethanol over MgO catalysts. A range of products formed, depending on the reaction temperature and the copper content. The main products were: ethene, propene, butadiene, acetaldehyde, di-ethyl ether, acetone,

1-butanone, 2-butanone and 1-butanol. Below 360 °C there was very little reaction of ethanol (**Figure 4.1**). At low temperatures, acetaldehyde production was low (**Figure 4.2**), but the selectivity towards acetaldehyde was high (**Figure 4.3**). When the temperature increased, both the total ethanol conversion and the conversion to acetaldehyde (this is called the acetaldehyde yield) increased sharply.

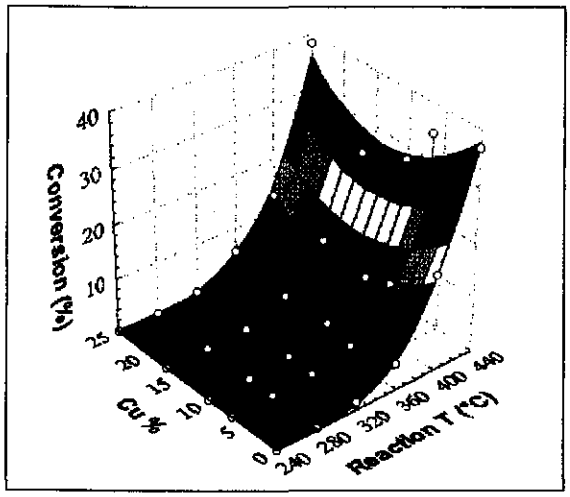

Figure 4.1: Total ethanol conversion for Cu on MgO catalysts

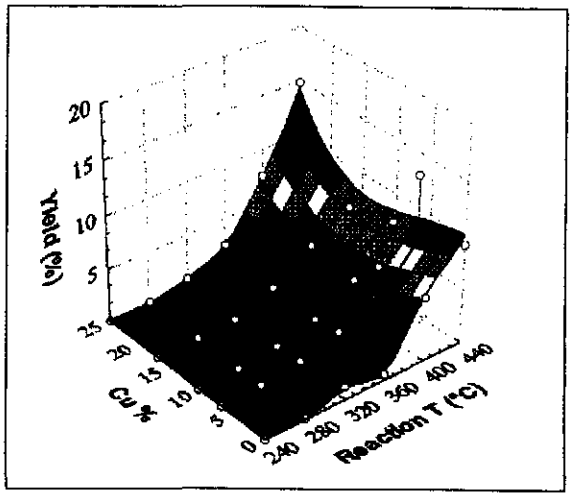

Figure 4.2: Ethanol to acetaldehyde yield (Cu on MgO catalysts)

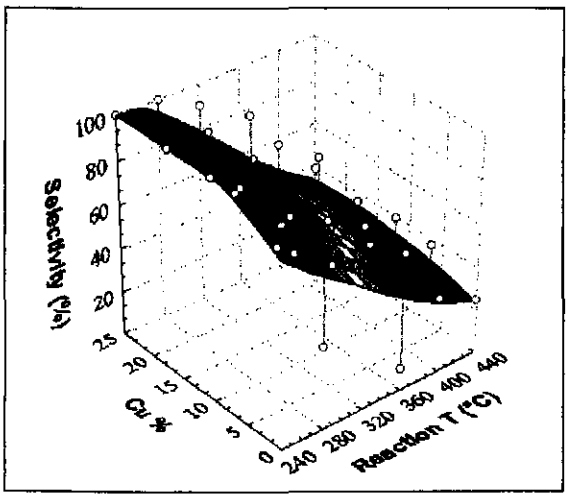

Figure 4.3: Acetaldehyde selectivity for Cu on MgO catalysts

The difference between the values in **Figure 4.1** and **Figure 4.2** is the ethanol converted to other products and this difference is expressed via the selectivity curve. At 440 °C the

selectivity dropped to between 25% and 35% for the various copper percentages. The majority of ethanol was not converted to acetaldehyde, but to 1-butanol. Higher temperatures not only favoured acetaldehyde formation, but also C4 formation.

The Cu content on the catalyst has an effect on the BET surface area of the catalyst. When the Cu content increased, the BET surface area decreased and less support sites were available for reaction (**Table 4.1**). With no copper on the catalyst, the main product was ethene and acetaldehyde was the main by-product. As soon as copper was deposited on the support, ethene production ceased and acetaldehyde production increased. **Figure 4.2** shows an increase in acetaldehyde yield with an increase in Cu content. The selectivity towards acetaldehyde formation (**Figure 4.3**) remained fairly constant with an increase in copper. The ethene that was formed in the absence of copper, was replaced by 1-butanol in the presence of copper. **Table 4.2** gives a summary of the main product and by-product at different conditions.

Table 4.1: BET surface areas for Cu on MgO catalysts in m^2/g

Cu%	**BET (m^2/g) surface area**
0	27.4
6.7	18.5
10.3	15.0
16.9	9.3
24.9	3.6

Using MgO catalysts, both total ethanol conversion and acetaldehyde yield were poor, because of the low BET surface area of the catalysts (see **Table 4.1**). Iwasa and Takezawa (1991) studied ethanol dehydrogenation with a 30 wt % Cu on MgO catalyst at 220 °C. The selectivity towards acetaldehyde production was 74% with ethyl acetate and other C4 species the main by-products. Takezawa et al. (1975) concluded that acetaldehyde was the main product when ethanol reacted over pure MgO between 340 °C and 360 °C. The selectivity under differential conditions was above 90% at those temperatures. A reaction mechanism for

pure MgO catalysts was discussed by Takezawa et al. (1975). Results in this dissertation differ from the results obtained by Takezawa et al. (1975). For a pure MgO catalyst the main product was ethene at 340 °C and the selectivity towards acetaldehyde poor.

Table 4.2: Yield matrix indicating main products and by-products for Cu/MgO

	320/360 °C	440 °C
0% Cu	Ethene (1.6%) Acetaldehyde (0.8%)	Ethene (17.8%) Acetaldehyde (9.1%)
10% Cu	Acetaldehyde (0.8%) 1-Butanol (0.8%)	1-Butanol (9.6%) Acetaldehyde (7.2%)
25% Cu	Acetaldehyde (1.5%) 1-Butanol (1.3%)	Acetaldehyde (14.8%) 1-Butanol (5.0%)

4.1.2. Al_2O_3 CATALYSTS

Alumina is an acidic catalyst, and in theory, the dehydration reaction should be favoured above the dehydrogenation reaction. **Figures 4.4** to **4.6** indicate total ethanol conversion and the formation of reaction products as a function of temperature and copper loading. Both the total ethanol conversion (**Figure 4.4**) and ethene yield (**Figure 4.5**) were very dependant on temperature. An increase in temperature increased the total ethanol conversion and ethene formation became the dominant reaction. For di-ethyl ether formation (**Figure 4.6**), there was an optimum temperature at which a maximum yield was obtained. The optimum temperature was dependent on the copper percentage on the alumina support. The optimum temperature shifted to higher values for higher copper percentages on the support. The highest di-ethyl ether yields were obtained with no copper on the catalysts:

- For 0% Cu: Optimum temperature of 220 °C gave 59% ethanol conversion to ether.
- For 13.2% Cu: Optimum temperature of 260 °C gave 51% ethanol conversion to ether.
- For 24% Cu: Optimum temperature of 260/300 °C gave 42% ethanol conversion to ether.

Figure 4.7 shows the effect of flow rate and temperature on di-ethyl ether yield for a 0% Cu on alumina catalyst. The curves have similar profiles. With a decrease in W/F (due to an increase in F), the optimum ether yield shifts towards the higher temperatures.

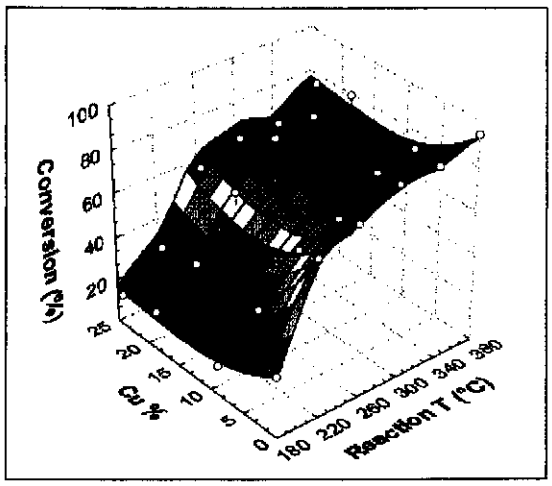

Figure 4.4: Total ethanol conversion (Cu on alumina catalysts)

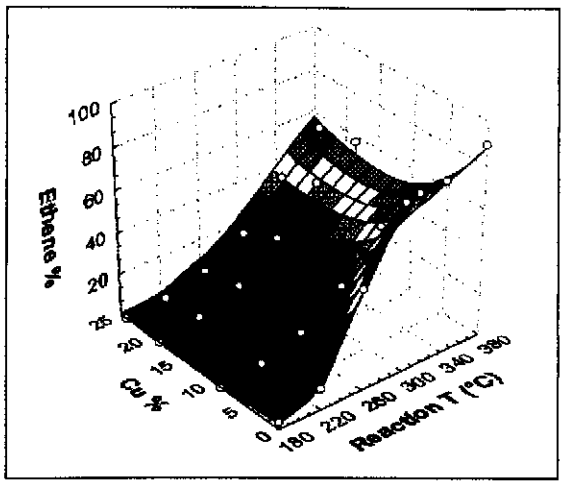

Figure 4.5: Ethanol to ethene yield (Cu on alumina catalysts)

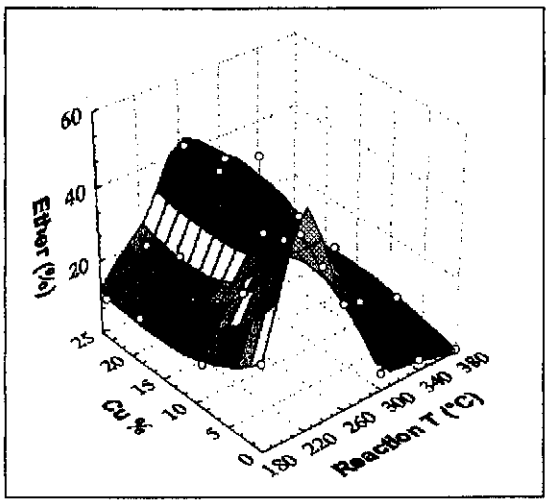

Figure 4.6: Ethanol to di-ethyl ether yield (Cu on alumina catalysts)

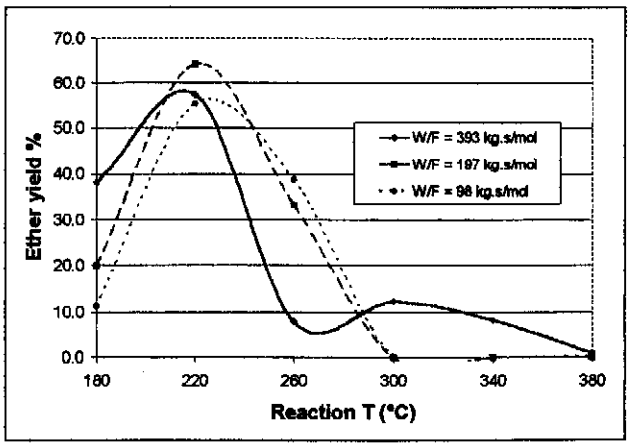

Figure 4.7: Ethanol conversion to di-ethyl ether (0% Cu on alumina) at different W/F ratios

The copper concentration on the support did not have much of an effect on the total ethanol conversion, but had a definite effect on the product distribution. Pure alumina gave the highest ethene and di-ethyl ether yields. The reason was that pure alumina represented the

maximum available acidic sites, resulting in the maximum dehydration products. The ethene and the di-ethyl ether yields dropped when the catalyst was impregnated with copper. For 10% Cu loading and above, the yields remained within a narrow band, with not more than 5% variation from the average.

The main by-products were butenes, acetaldehyde and a small amount of hexenes. **Figures 4.8** and **4.9** show acetaldehyde and butene yields with temperature increasing from left to right. For acetaldehyde production there was an optimum copper loading on the alumina (13.2 wt %), which resulted in the maximum acetaldehyde production. The butene production increased with temperature and was the highest for 8.8 wt % Cu and 13.2 wt % Cu on alumina. Higher and lower Cu loadings caused a decline in butene production.

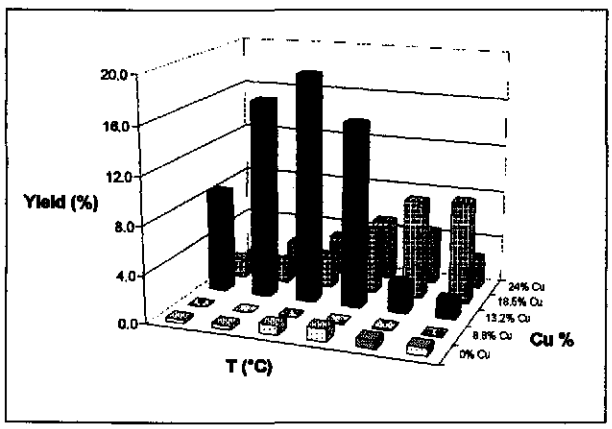

Figure 4.8: Acetaldehyde yields for Cu on alumina catalysts (W/F = 197 kg.s/mol)

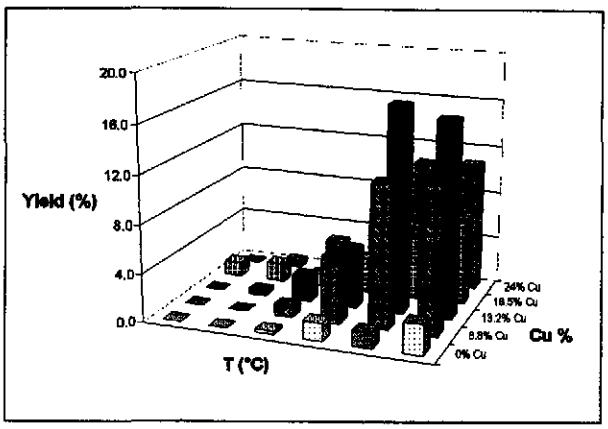

Figure 4.9: Butene yields for Cu on alumina catalysts (average W/F)

De Boer and Visseren (1971) observed a proportionality between the dehydration rate constants and the amount of aluminum on the surface. Iwasa and Takezawa (1991) tested an alumina-based catalyst with a high copper loading (30 wt %) at 220 °C. They reported 54% selectivity towards acetaldehyde production, 19% towards di-etheyl ether and 22% towards C4 production.

Copper alumina catalysts have often been used for cyclohexanol dehydrogenation. The selectivity towards the dehydrogenation reaction was higher for cyclohexanol than for ethanol on alumina-based catalysts. The effects of copper concentration on the selectivity

and activity towards cyclohexanone formation have been investigated (Chang and Saleque, 1993, 1994; Sivaraj et al., 1990).

4.1.2.1. BET and copper surface areas for Cu on Al_2O_3 catalysts

The total catalyst surface area and the copper surface area were determined to investigate their effect on product yield and product distribution. **Figure 4.10** shows total catalyst surface area as a function of copper loading and **Figure 4.11** shows copper surface area as a function of copper loading.

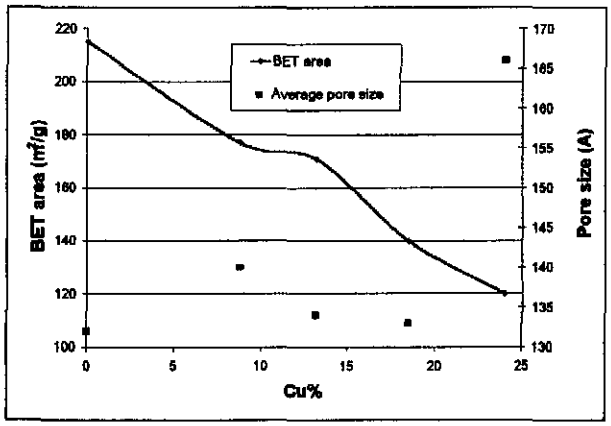

Figure 4.10: Effect of Cu% on catalyst surface area for Cu on alumina catalysts

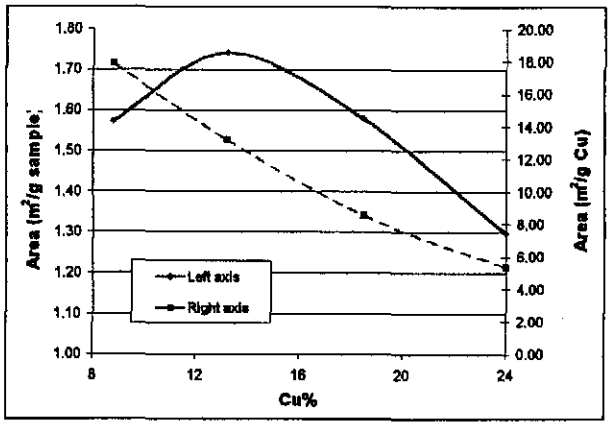

Figure 4.11: Effect of Cu% on Cu surface area for alumina-based catalysts

The total surface area (**Figure 4.10**) declined from 215 m^2/g at 0 wt % Cu to 120 m^2/g at 24 wt % Cu as the deposited copper filled the micro- and mesopores in the support. Ethene and di-ethyl ether formed mainly on the acidic sites, because ethene and di-ethyl ether yields dropped (**Figures 4.5** and **4.6**) when copper was added to alumina, to reduce the number of acidic sites. Even though the catalysts' surface area was almost halved for 0 to 24 wt % Cu loadings, the ethanol converted remained constant. The deposited copper sites provided additional catalytic activity and resulted in more products being formed (mainly butenes and acetaldehyde) to compensate for the loss of dehydration products (ethene and di-ethyl ether). The added copper sites were much more active than the alumina sites, since the small increase in copper surface area (**Figure 4.11**) fully compensated for the large decline in total surface area (**Figure 4.10**).

Copper surfaces areas were determined as described in **Sections 3.1.6** and **4.1.2.2.2**. The copper surface area (in m^2/g sample) had an optimum value at 13.2 wt % Cu on alumina. At that value, the maximum acetaldehyde and butene yields were observed (**Figures 4.8** and **4.9**). From this it could be concluded that copper on alumina catalyses the formation of acetaldehyde and butenes.

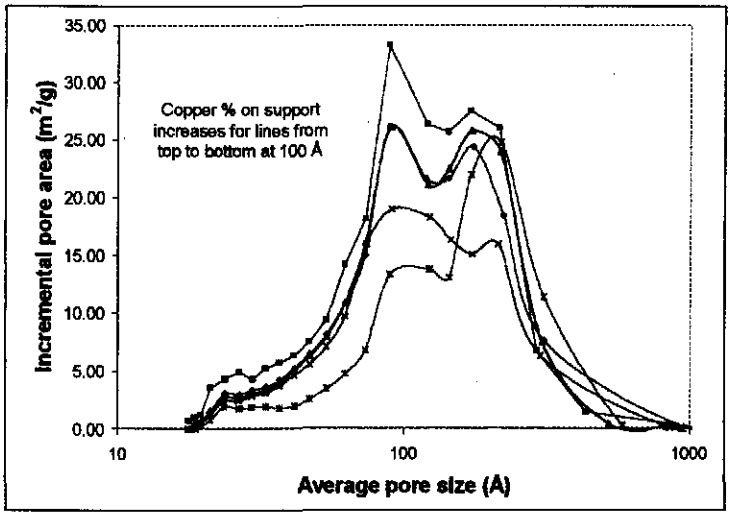

Figure 4.12: Pore size distribution for Cu on alumina catalysts

Figure 4.12 clearly shows how the pore size distribution changed when the copper loading on the support increased. The y-axis is the incremental pore area for every pore fraction from very large to very small pores. The curve with the highest differential area values is the 0% Cu line. As the Cu % increases the differential areas decrease (lines drop on the y-axis for example at 100 Å pore size). The line with the lowest differential area values is the 24 wt % Cu one. **Figure 4.12** shows both a shift in the pore size distribution to higher pore sizes and a decline in the values on the differential area axis with an increase in Cu loading. The average pore size changes from 132 Å for a 0 wt % Cu on alumina catalyst to 166 Å for a 24 wt % Cu on alumina catalyst.

Result were in line with those of other researchers (see **Tables 4.3** and **4.4**) who also obtained a optimum copper percentage (on alumina) giving a maximum copper surface area on their catalysts.

4.1.2.2. Literature data on surface areas of copper catalysts

There are two methods for determining copper surface areas. One method is based on N_2O titration and the other method on either CO chemisorption or H_2 chemisorption. For both methods, the catalyst must be reduced in hydrogen prior to analysis. The catalyst reduction step has been discussed in **Chapter 2** (**2.10.3**). Bonding between copper species and the support sites, interactions between different copper species and the formation of amorphous phases are only a few of the problems encountered when reducing the copper ions to metallic copper. The result is very poor reduction. Better reduction requires higher reduction temperatures, which result in sintering (see **2.10.4.1**) and further deviation from a true copper surface area. Experimentally-determined copper surface areas thus have a significant margin of error.

4.1.2.2.1. N_2O titration

Sivaraj and Kantarao (1988a) described the N_2O titration method. The nitrous oxide decomposes according to the following equation:

$$N_2O\ (gas) + 2Cu_s \rightarrow (Cu_s)_2O + N_2\ (gas) \qquad \textbf{(4.5)}$$

The metallic surface area (S_H) is determined from

$$S_H = n_m X_m / n_s \qquad \textbf{(4.6)}$$

where n_m is the total amount of nitrous oxide molecules that decompose, X_m is the chemisorption stoichiometry and n_s is the amount of copper metal atoms per unit surface area ($1.47*10^{19}$ m^{-2}). The catalyst is first reduced in hydrogen for 5 hours at 250 °C, evacuated (to 10^{-6} Torr) for 2 hours and then reacted with N_2O at 200 Torr and 90 °C. The reaction does not cause a pressure change. After 5 hours of reaction, the remaining N_2O is frozen out in a nitrogen trap and the pressure difference between the initial pressure and final pressure is used to calculate the amount of N_2O that reacted.

4.1.2.2.2. Chemisorption

A detailed discussion on this process can be found in Jeon and Chung (1994). The same apparatus used for measuring BET surface areas is used for chemisorption experiments. The catalyst is first reduced and then either CO or H_2 is used as the analysis gas. The method works on the principle that these two gases adsorb reversibly on Cu^0, but not on Cu^{1+}. Chemisorption is carried out and the first adsorption isotherm constructed. This value represents adsorption onto both $Cu^0$and Cu^{1+}. The catalyst is then evacuated and the gas desorbs from Cu^0, but not from Cu^{1+}. The experiment is repeated, giving a second adsorption isotherm. The second isotherm represents Cu^0, while the difference between the isotherms represents Cu^{1+}.

4.1.2.2.3. Effect of preparation method on catalyst characteristics

Tables 4.3 and **4.4** list BET and copper surface areas for various copper catalysts. The amount of data is not enough to make accurate conclusions regarding copper on silica catalysts.

Table 4.3: Surface areas of unsupported copper catalysts

Catalyst preparation	Analysis method	Reduction conditions	Catalyst Composition	BET (m^2/g)	Copper area m^2/g sample	Reference
Co-precipitation unsupported	N_2O titration	3h in H_2 at 300 °C	Cu	1	1 (1)	Kanoun (1991)
			V_{50}-Cu_{50}	89	10.2 (29)	
			V_{50}-$Cu_{25}Zn_{25}$	146	18.2 (107)	
			Zn_{50}-Cu_{50}	15	2.6 (6.5)	
Co-precipitation unsupported	N_2O titration	3h in H_2 at 300 °C	Cu_{50}-Cr_{50}	163	24 (80)	Kanoun (1993)
			Cu_{50}-Cr_5Al_{45}	188	27 (102)	
			Cu_{50}-Al_{50}	214	8 (14)	
Co-precipitation unsupported	N_2O titration	1h in 10% H_2/Ar at 200 °C	Cu		(9)	Tu (1994a)
			Cr_9Cu_{91}		(18.8)	
			$Cr_{13}Cu_{87}$		(14.5)	

Catalyst composition is in mol percent

Copper surface area: value in brackets is for m^2/g Cu

Many authors have reported either BET or chemisorption data, but not both. In most cases the optimum copper area that was observed, was in accordance with what was discussed in **section 2.10.1.** An exception was Jeon and Chung (1994), who prepared silica-supported catalysts.

Table 4.4: Surface areas of supported copper catalysts

Catalyst preparation	Analysis method	Reduction conditions	Catalyst Composition	BET (m^2/g)	Copper area m^2/g sample	Reference
Urea hydrolysis	N_2O titration	5h in H_2 at 250 °C	Cu_{12}-alumina Cu_{24}-alumina Cu_{31}-alumina		3.9 12.0 7.0	Sivaraj (1990)
Impreg-nation			10 wt % Co on γ-alumina	150		Reddy (1997)
Electroless plating Precipitation Impregnation			Alumina 19.5 wt % Cu 19.5 wt % Cu 12.5 wt % Cu	22.6 23.8 20.5 20.7		Chang (1993)
Urea hydrolysis	N_2O titration	5h in H_2 at 250 °C	Alumina $Cu_{4.2}$-alumina $Cu_{24.4}$-alumina $Cu_{34.2}$-alumina	242 250 103 63	0 13 (308) 41.6 (170) 36.7 (108)	Sivaraj (1988a)
Electroless plating	N_2O titration		γ-alumina $Cu_{10.0}$-γAl_2O_3 $Cu_{18.3}$-γAl_2O_3 $Cu_{24.4}$-γAl_2O_3	138.3 145.4 101.7 82.5	0 4.5 14.2 9.8	Chang (1994)
Precipitation	CO chemi-sorption	4h in H_2 at 250 °C	Cu_{24}-silica Cu_{24}-silica Cu_{24}-silica		2.8 10.3 12.6	Jeon (1994)

Catalyst composition is in mass percent

Copper surface area: value in brackets is for m^2/g Cu.

Chang and Saleque (1993) compared the use of electroless plating, impregnation and precipitation for preparing copper on alumina catalysts. The total BET area declined in that same order, but the BET values showed only a small variance. Similar preparation methods resulted in significant differences in the copper surface areas. Compare values from:

- Kanoun et al (1993) and Tu et al. (1994a),
- Sivaraj and Kantarao (1988a) and Sivaraj et al. (1990), and
- Pure copper values from Kanoun et al. (1991) and Tu et al. (1994a).

The data presented from Jeon and Chung (1994) in **Table 4.4**, show similar Cu percentages on SiO_2. Cu surface areas were obtained for different pH-values of the precipitate.

4.1.2.3. The effect of additives on ethanol conversion and product distribution

Cobalt, chromium or nickel was added to the copper to investigate the effects on product distribution. The effects of these additives on catalyst stability were not investigated at this stage. This was done later (see **Chapter 5**), when conditions were chosen to determine reaction kinetics. **Figure 4.13** shows that at 260 °C and below, Cu-Cr/Al_2O_3 outperformed Cu on alumina catalysts, giving higher total ethanol conversion. For Ni and Co additives, the difference in performance at 260 °C and below compared to pure Cu was small. At 300 °C and above, the pure Cu catalyst performed the best, followed by the Cu-Cr/Al_2O_3 catalyst.

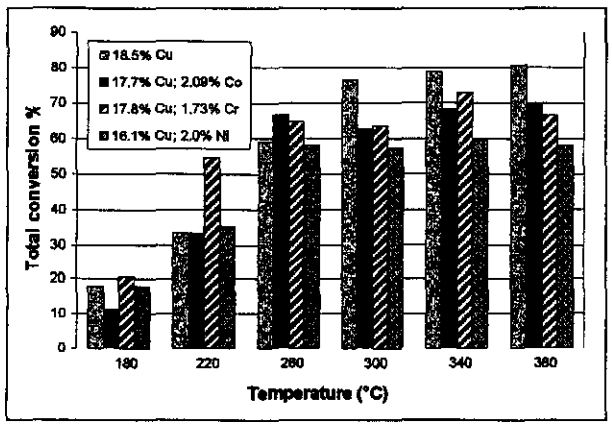

Figure 4.13: Effect of Cr, Ni and Co (on alumina) on total ethanol conversion

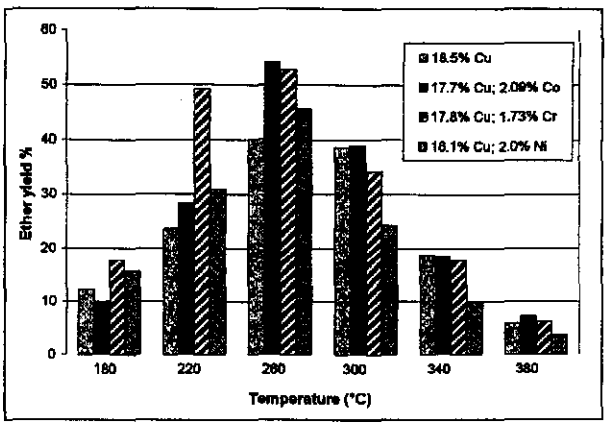

Figure 4.14: Effect of Cr, Ni and Co (on alumina) on ether yield

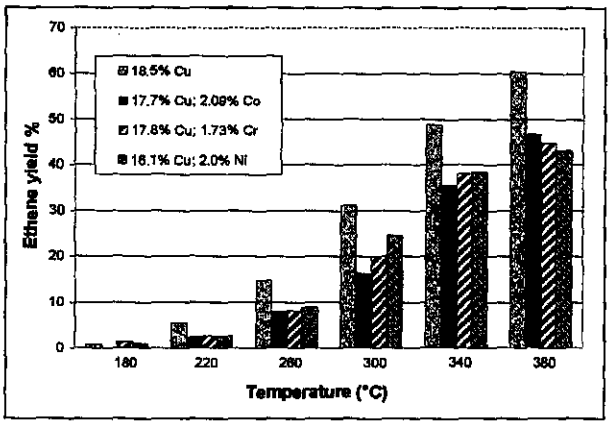

Figure 4.15: Effect of Cr, Ni and Co (on alumina) on ethene yield

Co and especially Cr addition made the catalyst more selective for di-ethyl ether formation (**Figure 4.14**), with significant improvements at 220 °C and 260 °C. For ethene formation (**Figure 4.15**), pure copper on alumina resulted in the best performance at all temperatures, followed by Cu-Ni and Cu-Cr. The addition of additives did not improve the acetaldehyde yields for copper on alumina catalysts. The acetaldehyde yields were below 8% for the different catalysts tested in **Figures 4.13 to 4.15**.

There was little difference in the BET surface areas for the different catalysts as indicated in **Table 4.5**. The larger difference in copper surface areas can only be due to a difference in reduction percentages. Chromium addition makes it more difficult to reduce the Cu^{2+} ions with hydrogen. Some copper will be present as Cu^{2+} and not Cu^{0}. Less Cu^{0} sites will be detected, which results in a lower copper surface area.

Table 4.5: BET and copper surface areas for copper/alumina catalysts with additives

Cu%	Additive	BET area (m^2/g)	Cu area (m^2/g sample)	Cu area (m^2/g Cu)
18.5	-	140	1.58	8.54
17.7	2.09% Co	151	1.67	8.42
17.8	1.73% Cr	157	1.10	5.65
16.0	2.0% Ni	137	1.40	8.72

4.1.2.4. Summary for using Cu on alumina catalysts

This type of catalyst is not suitable for acetaldehyde production via the dehydrogenation reaction. Very good yields of ethene and di-ethyl ether were obtained by suitable choice of the copper loading, addition of the correct additives and performing the reaction at the correct operating conditions. Alumina-based catalysts favoured the dehydration reaction. At higher temperatures (see **Figure 4.9**), butene production became significant for catalysts with the highest copper surface areas.

4.1.3. SILICA CATALYSTS

The variables that were investigated to determine maximum acetaldehyde yield are:

- copper loading,
- temperature,
- feed flow rate,
- effect of additives, and
- effect of catalyst particle size.

The different catalysts investigated were listed in **Tables 3.2** and **3.3**. The operating conditions were listed in **Table 3.4**.

4.1.3.1. The effects of copper loading and temperature on acetaldehyde yield

Figures 4.16 to **4.18** show total ethanol conversion, acetaldehyde yield and acetaldehyde selectivity over the entire range of copper percentages on the silica support and for temperatures ranging from 240 °C to 440 °C. Both total ethanol conversion and acetaldehyde yield increased sharply with temperature. For both the total ethanol conversion and acetaldehyde yield there was an optimum copper concentration that resulted in a maximum ethanol conversion (**Figure 4.16**) and a maximum acetaldehyde yield (**Figure 4.17**). The optimum copper loading on the catalyst was 15 wt %. At 440 °C (with a 15 wt % Cu on silica catalysts) the total ethanol conversion was 89% and the acetaldehyde yield 74% at an average W/F.

The amount of acetaldehyde formed on a pure silica catalyst was negligible. For pure silica, ethene was the main product with no significant amount of by-products. Ethanol conversion to acetaldehyde (acetaldehyde selectivity) was not very dependant on the copper loading **(Figure 4.18)** for copper loadings from 4 to 34 wt %. At 440 °C the selectivity varied between a maximum of 88% (for a 18.6 wt % Cu on silica catalyst) and a minimum of 79% (for a 4.2 wt % Cu on silica catalyst). The selectivity was more dependent on temperature. Up to 320 °C the selectivity remained in the mid 90% level, but it dropped to about 80% at 440 °C. The main by-products were: ethene, di-ethyl ether, etoxy ethane, 1-butanone and ethyl acetate.

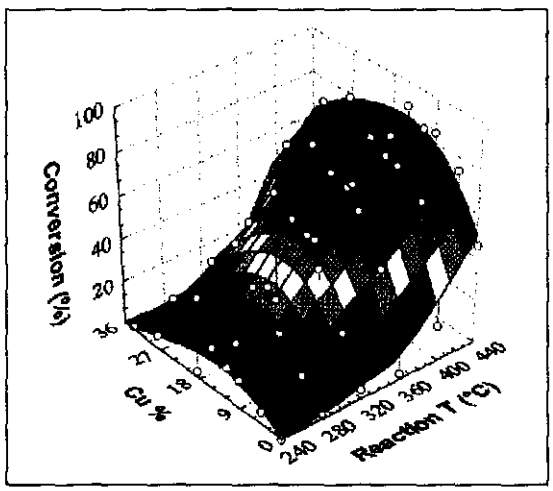

Figure 4.16: Total ethanol conversion (Cu on silica catalysts)

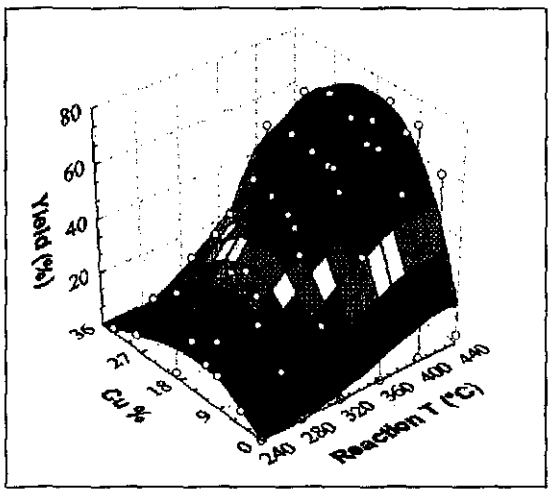

Figure 4.17: Ethanol to acetaldehyde yield (Cu on silica catalysts)

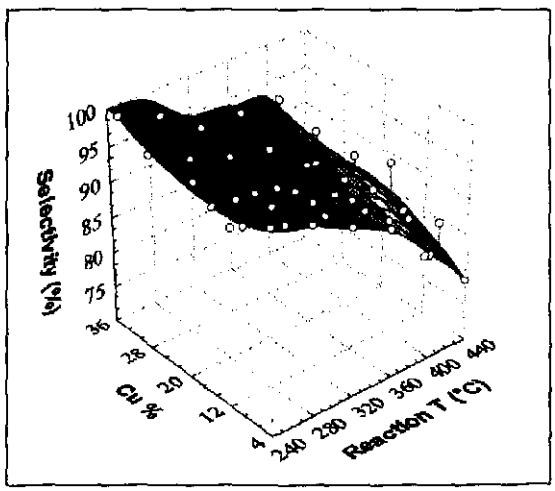

Figure 4.18: Ethanol to acetaldehyde selectivity (Cu on silica catalysts)

Figures 4.19 and **4.20** show the effect of the feed flow rate on total ethanol conversion and acetaldehyde yield for the optimum copper loading. The total ethanol conversion (**Figure 4.19**) remained high, with a decrease in W/F (increase in F) to between 131 kg.s/mol and 66 kg.s/mol. At higher flow rates, i.e. lower W/F values, the total ethanol conversion dropped due to a shorter catalyst contact time. For the shorter contact time, the reaction could not go to completion. There was an optimum W/F ratio for a maximum acetaldehyde yield (**Figure 4.20**). At the highest W/F values (slowest feed rates) the acetaldehyde yield decreased (**Figure 4.20**), due to a very long residence time that increased the formation of propene, di-ethyl ether, 1-butanone and ethyl acetate. For high flow rates (W/F < 66 kg.s/mol) the lower total ethanol conversion caused a lower acetaldehyde yield.

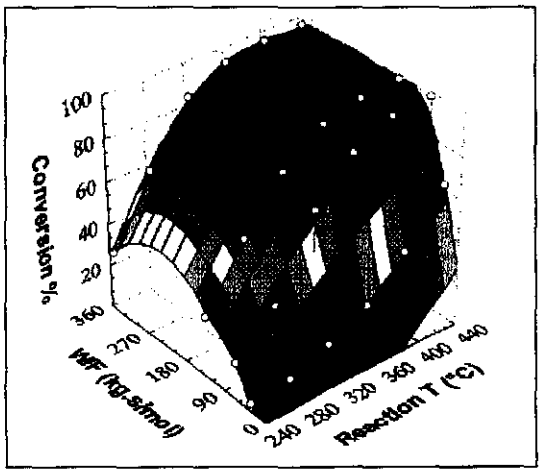

Figure 4.19: Total ethanol conversion (15 wt % Cu on silica catalyst)

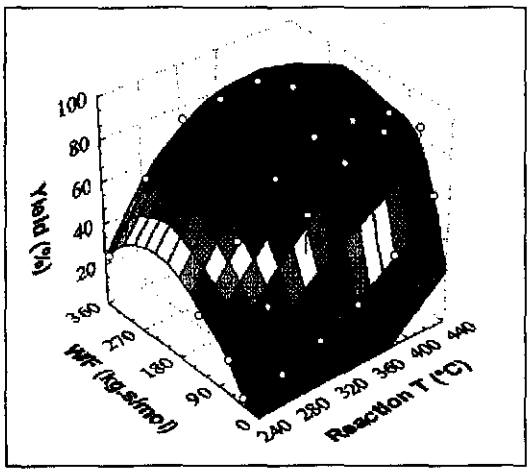

Figure 4.20: Ethanol converted to acetaldehyde (15 wt % Cu on silica)

Iwasa and Takezawa (1991) obtained 78% selectivity towards acetaldehyde formation at 220 °C with a 30 wt % Cu on silica catalyst. The main by-products were C4 species and ethyl acetate.

4.1.3.2. The effect of additives on product distribution and yields

Three additives, Co, Cr or Ni, were added to Cu in 1:9 and 1:19 mass ratios, to determine their effect on catalyst activity and selectivity. The results are shown in **Figures 4.21** to **4.24**. Below 400 °C, the addition of additives inhibited ethanol conversion and the conversion was

lower than for pure copper catalysts (**Figures 4.21** and **4.23**). The addition of Co resulted in the poorest conversions at all temperatures. A higher Ni content (**Figure 4.21**) resulted in better conversions than a lower nickel content (**Figure 4.23**). At both ratios, the Cu-Cr catalysts performed similarly, with Cu:Cr = 9:1 being slightly better. At 400 °C and 440 °C, Cu-Cr catalysts and the one Cu-Ni catalyst (13.5 wt % Cu, 1.5 wt % Ni) gave conversions which differed only marginally from those obtained with a pure copper catalyst.

The addition of additives made the dehydrogenation reaction far less selective. Acetaldehyde yields decreased sharply, even at high temperatures, as indicated in **Figures 4.22** and **4.24**. The by-products formed on each of the three catalyst were:

- Cu-Cr: ethene, propene, butenes, di-ethyl ether, 1-butanone, MEK, ethyl acetate,
- Cu-Ni: ethene, propene, di-ethyl ether, 1-butanone, and
- Cu-Co: ethene, propene, butenes, di-ethyl ether.

Kanoun et al. (1993) calculated catalyst activities and turnover frequencies (TOFs) for Cu-Cr-Al catalysts prepared by precipitation. Variations in the Cr content didn't have a significant effect on the TOFs or activities. Tu et al. (1994a) prepared unsupported Cu-Cr catalysts via precipitation. Their results indicated an optimum ethanol dehydrogenation activity for a Cr:Cu = 4:40 (on mol basis) catalyst. Selectivity data was not included

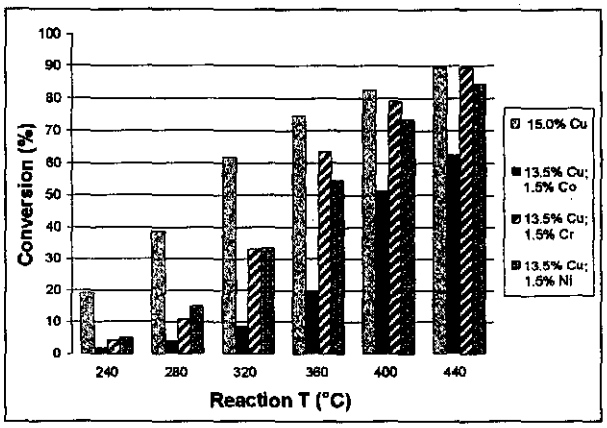

Figure 4.21: Effect of Co, Cr or Ni additives on total ethanol conversion (Cu on silica)

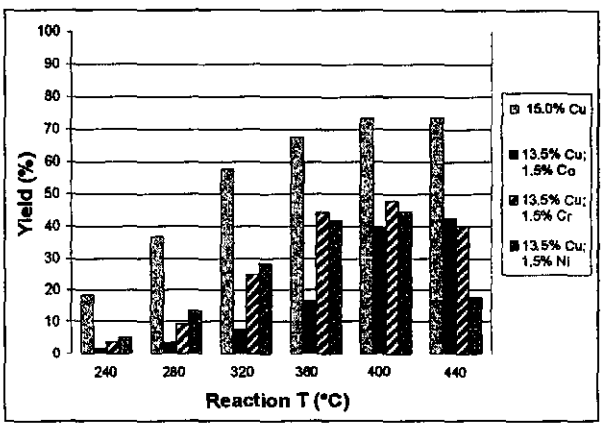

Figure 4.22: Effect of Co, Cr or Ni additives on acetaldehyde yield (Cu on silica)

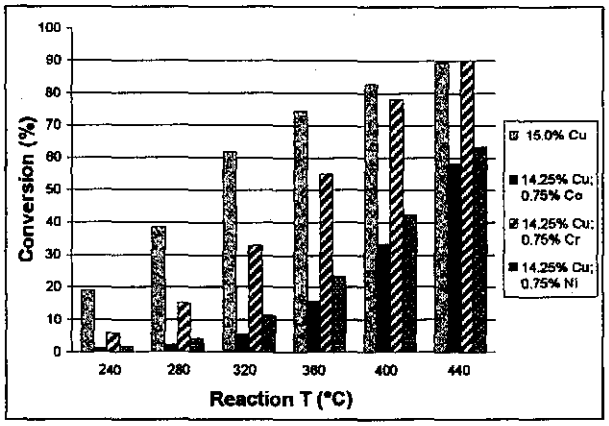

Figure 4.23: Effect of Co, Cr or Ni additives on total ethanol conversion (Cu on silica)

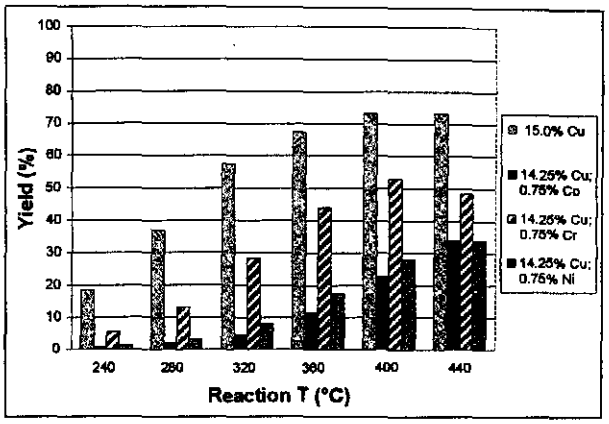

Figure 4.24: Effect of Co, Cr or Ni additives on acetaldehyde yield (Cu on silica)

4.1.3.3 Effect of particle size on acetaldehyde yield

Figures 4.25 and **4.26** show the effect of catalyst particle size on ethanol conversion and acetaldehyde yield. In theory, larger particles cause greater mass transfer resistance from the bulk fluid into the pores and may slow down the reaction rate if the rate is mass transfer limited. Smaller particles reduce mass transfer resistance and improve the reaction kinetics. Experimental results (**Figure 4.25**) were consistent with the theory and the total ethanol conversion declined as the size of the catalyst particles increased.

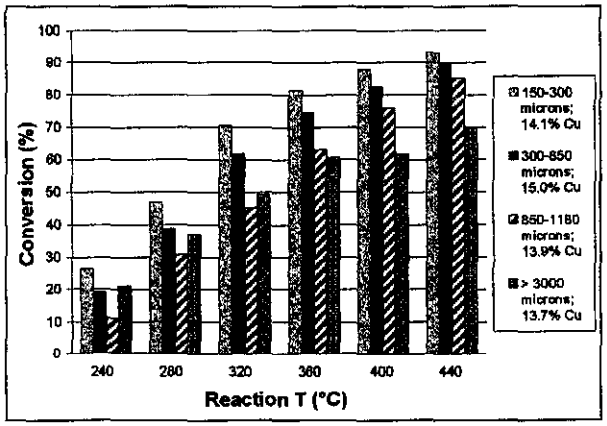

Figure 4.25: Effect of catalyst particle size on total ethanol conversion

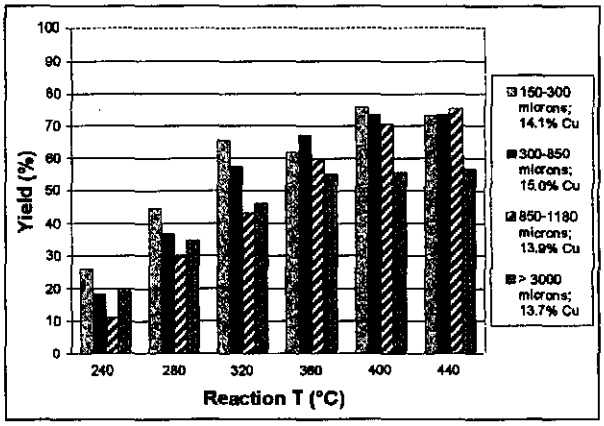

Figure 4.26: Effect of catalyst particle size on acetaldehyde yield percentage

Two effects are responsible for the decrease in ethanol conversion using the larger particles: channelling of the feed gas and intra-particle mass transfer resistance. Channelling usually

starts occurring when the particle diameter is less than one tenth of the reactor diameter. Some channelling occurred for the 3 mm catalyst spheres, because the inside diameter of the quarts tube that housed the catalyst was only 8 mm. For the smaller particles (1.2 mm and less) channelling was less dominant. The decrease in ethanol conversion with the larger catalyst particles confirmed that those two effect were present during the ethanol reactions. **Figure 4.26** indicates that at 360 °C and above, the acetaldehyde yield was similar for all particles up to a size of 1180 μm. The mass transfer limitation for ethanol dehydrogenation to acetaldehyde at 360 °C and above was not significant for particles less than 1180 μm. A further observation that could be made when comparing **Figures 4.25** and **4.26,** was that the selectivity towards acetaldehyde decreased at high temperatures as the catalyst particles became smaller.

4.1.3.4. Surface area data for silica-based catalysts

Figures 4.27 and **4.28** show BET and copper surface areas as a function of copper loading. **Figure 4.29** indicates the change in pore size distribution when the copper content on the catalysts was increased. The BET surface area declined from 446 m^2/g and an average pore size of 87 Å for pure silica, to 201 m^2/g and an average pore size of 94 Å for a 33.5 wt % Cu on silica catalyst. The surface area was about double that of the alumina catalysts (see **Figure 4.10**). The copper surface area increased with increasing copper loading and levelled off above 27 wt % Cu on silica. The values were lower than those for alumina catalysts (**Figure 4.11**) and also much lower than values from literature (**Tables 4.3** and **4.4**). **Figure 4.29** indicates how pores were filled when additional copper was deposited on the catalysts. (The line with the highest differential areas is the one with the no copper.) As the copper percentage on the silica support increases, the values on the differential area axis drop. The line with the lowest differential area at 94 Å is the 33.5 wt % Cu on silica. The change in average pore size is marginal, but the change in BET surface area is significant, moving from 0% Cu to 33.5 wt % Cu.

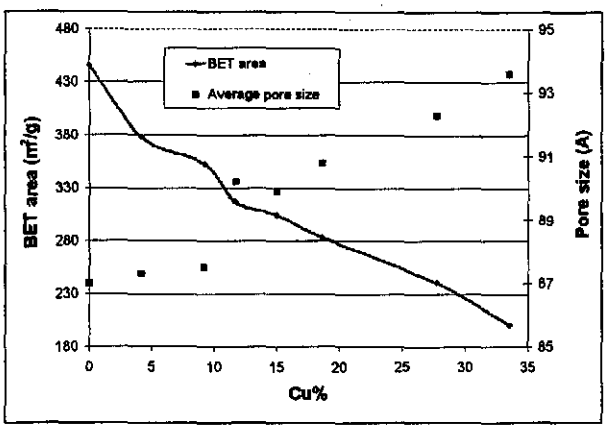

Figure 4.27: Effect of Cu% on catalyst surface area for Cu on silica catalysts

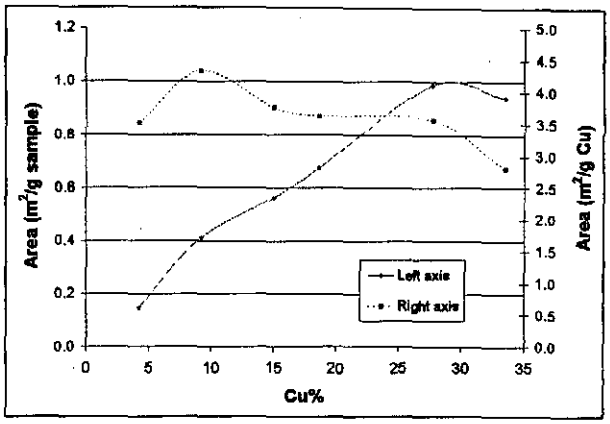

Figure 4.28: Effect of Cu% on Cu surface area for silica-based catalysts

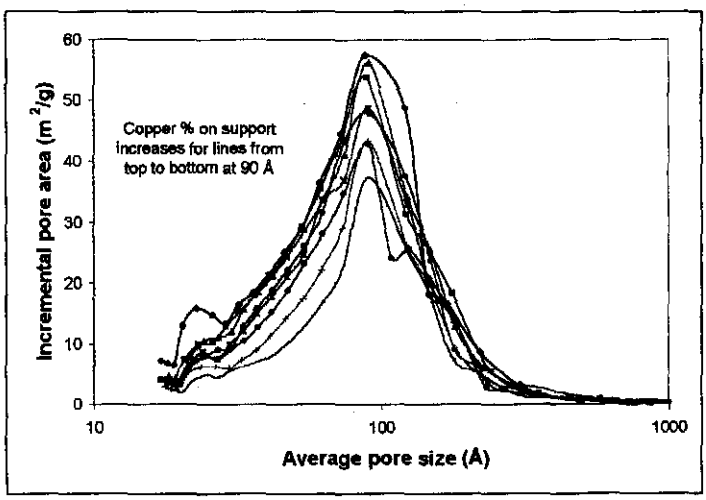

Figure 4.29: Pore size distribution for copper on silica catalysts

The acetaldehyde yield data (**Figure 4.17**) and copper surface area data (**Figure 4.28**) do not correlate well. Many studies have shown that dehydrogenation activity is proportional to the copper surface area (Tu et al., 1994b; Jeon and Chung, 1994), but in the present study there was a difference between the two. The best explanation for this is the unreliability in copper surface area data. Jeon and Chung (1994) did an in depth study on copper on silica catalyst characterisation. They experienced similar problems with determining copper surface areas on silica supports and drew the following general conclusions:

- Copper reduction ranges from 80% in the best cases to as low as 40%, depending on the copper percentage on the silica support. For low copper content catalysts, the strong silica-copper bond makes reduction very difficult.

- Silica solubility increases with solution temperature. An amorphous copper silicate phase forms or can form. This contaminates copper sites, which can inhibit the dehydrogenation reaction and prevent chemisorption.
- Copper surface areas determined by chemisorption, X-ray line broadening and N_2O titration varied by up to a factor of 3, depending on the method employed.
- Copper particles range from small to very large. The catalyst prepared by precipitation is not very homogeneous.

In the present study silica was impregnated with copper solution at about 80 °C, which could lead to the formation of a copper-silicate phase. Since both copper-silica and silica are amorphous, it is difficult to detect the different phases with X-ray diffraction analysis. The existence of a copper-silicate phase and the poor reduction at the lower copper loadings could possibly be responsible for the low copper surface areas and the difference in acetaldehyde yields and copper surface areas. Further TEM and X-ray analyses were performed on a 14.5 wt % Cu on silica catalyst to investigate copper crystallite size and crystallite distribution.

4.1.3.4.1. TEM and XRD data for copper on silica catalysts

Figures 4.30a to **4.30i** show nine TEM images of a 14.5 wt % Cu on silica catalyst reduced at 260 °C in hydrogen for 2 hours. Black spots indicate copper on the support. For the first six images the scale is 20 nm, for the 7^{th} one 50 nm and for the last two 200 nm.

TEM images clearly indicate the non-homogeneity of silica-impregnated copper catalysts. **Figure 4.30a** indicates that some areas of the support had no copper on. Most areas had, however, copper crystallites ranging from as little as a few nm to about 20 nm (**Figures 4.30b** to **4.30d**). **Figures 4.30e** to **4.30g** show areas with copper crystallite agglomerates in the hundreds of nanometer. The last two images (**Figures 4.30h** and **4.30i**) show very large copper clusters, up to the micrometer range. The non-homogeneity of the catalysts makes it very difficult to estimate average crystallite size. X-ray diffraction analysis was performed to obtain a better estimate of copper crystallite size.

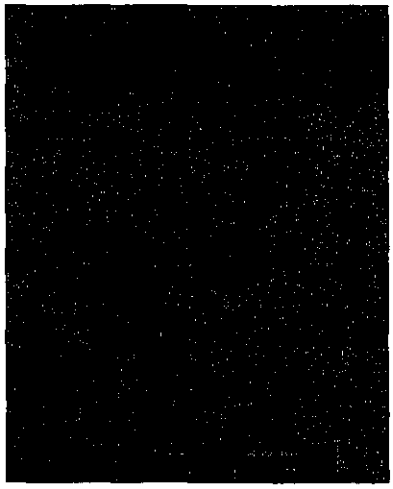

Fig 4.30a: TEM (20 nm)

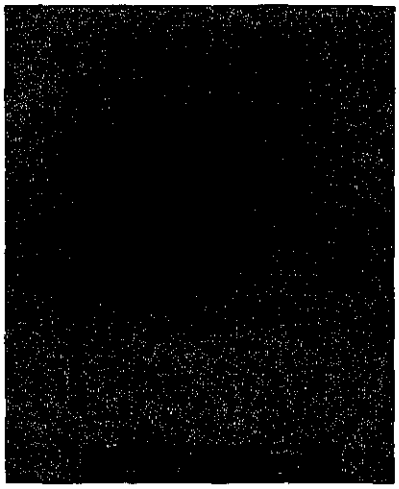

Fig 4.30b: TEM (20 nm)

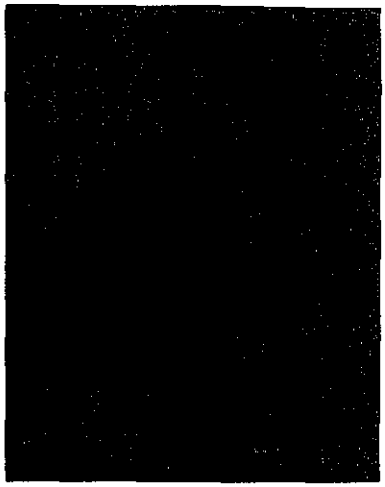

Fig 4.30c: TEM (20 nm)

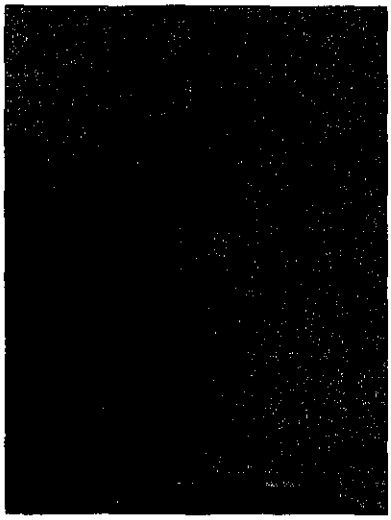

Fig 4.30d: TEM (20 nm)

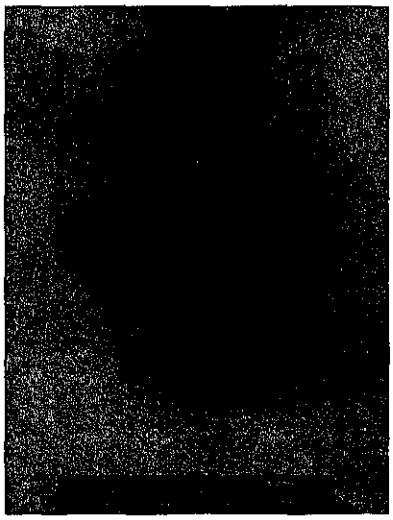

Fig 4.30e: TEM (20 nm)

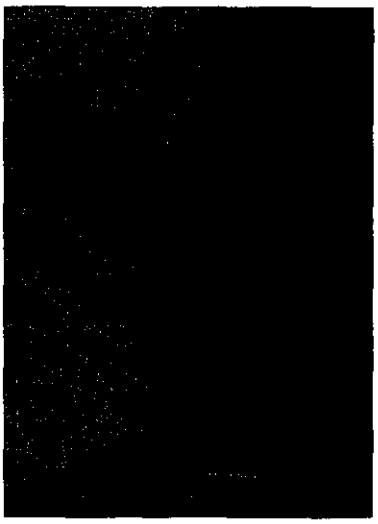

Fig 4.30f: TEM (20 nm)

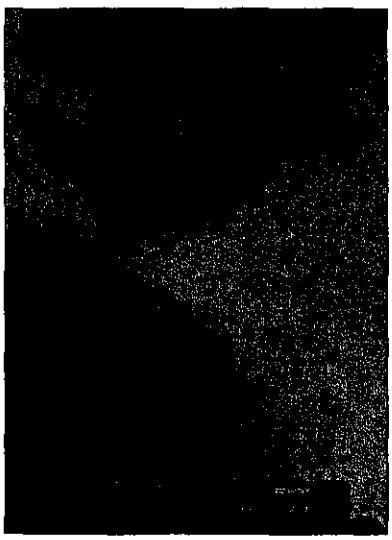

Fig 4.30g: TEM (50 nm)

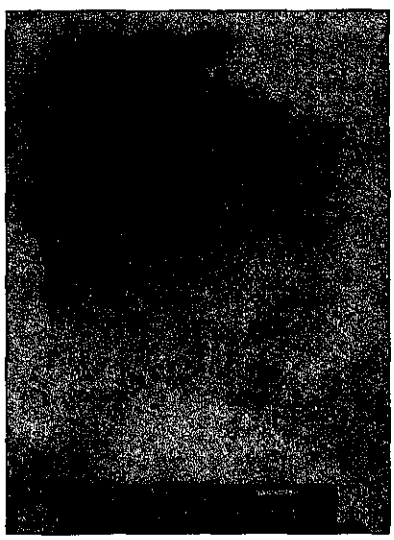

Fig 4.30h: TEM (200 nm)

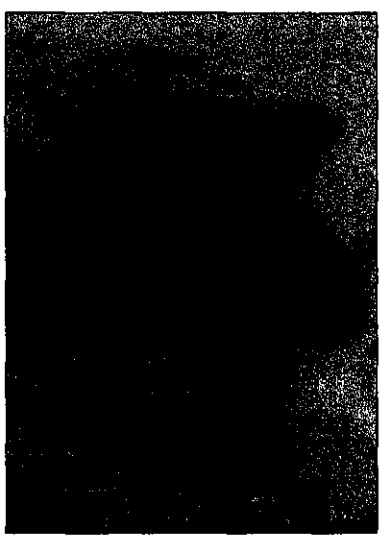

Fig 4.30i: TEM (200 nm)

Figure 4.30: TEM images of the unused 14.4 wt % copper on silica catalyst

X-ray line broadening can be used to calculate average crystallite size, employing Schearer's equation (**equation 4.7**). The crystallite diameter, D in Å, can be expressed as (Tu et al., 1994b):

$$D_{hkl} = \frac{1.542}{x_p \cos(2\theta)} \qquad (4.7)$$

with x the peak width in radians at 2/3 of the peak height and 2θ the angle in degrees at which the peak is recorded. The peak width was 0.20 degrees at a 2θ angle of 43.3 degrees. This yielded an average crystallite size of about 60 nm. For such large crystals the Schearer's equation was not very accurate, but still gave a fair estimate of crystallite size.

4.2. DEHYDROGENATION OF 2-BUTANOL

2-Butanol dehydrogenation was studied using MgO and silica catalysts. The compositions of the catalysts were listed in **Tables 3.2** and **3.3**. The conditions under which the catalysts were tested were listed in **Table 3.6**.

4.2.1. MgO CATALYSTS

When 2-butanol reacted over MgO catalysts, the products were a mixture of butenes and methyl ethyl ketone (MEK). There was less than 1% additional by-products. **Figures 4.31** to **4.33** indicate total 2-butanol conversion and butene and MEK yields as a function of temperature and copper loading. In all three cases the values increased with increasing temperature. The total 2-butanol conversion was the highest for pure MgO, because of the large increase in butene yield in the absence of copper on the catalyst. The addition of copper to the MgO support suppressed butene formation (**Figure 4.32**) at all temperatures. The reaction of 2-butanol to butene took place on the MgO sites. The decline in BET surface areas, when copper was added, was shown in **Table 4.1**. Reaction can take place either on copper sites or MgO sites. The addition of copper sites compensated for the large loss of

MgO sites, with the net result of only a slight decrease in the total 2-butanol reaction rate or conversion (**Figure 4.31**).

The 2-butanol to MEK reaction took place on both the MgO and the copper sites. With no Cu on MgO (**Figure 4.33**), similar amounts of butenes and MEK were formed at all temperatures. MEK formation had to be on the MgO sites. When copper was added to the support, the MEK yield increased to an optimum yield at 16.9 wt % Cu on MgO. For that catalyst, the total surface area was about a third of the value of the pure MgO catalyst (see **Table 4.1**). Further copper addition to the support caused both a decrease in available copper area and available MgO area and resulted in a decline in MEK yield.

The copper sites have much higher catalytic activity for MEK production than the MgO sites do. A simple calculation can verify this:

At 390 °C: 0% Cu on MgO → 35% MEK yield

16.9% Cu on MgO → 47% MEK yield

but MgO surface area is about 1/3 of pure MgO

thus 12% MEK yield from MgO sites

35% MEK yield from Cu sites.

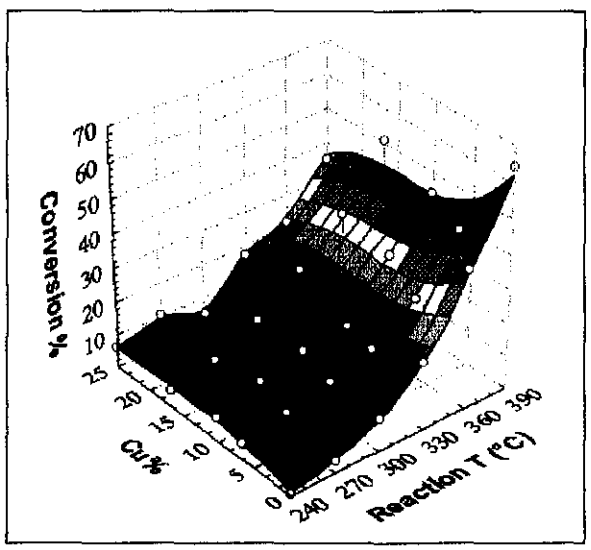

Figure 4.31: Total 2-butanol conversion for Cu on MgO catalysts

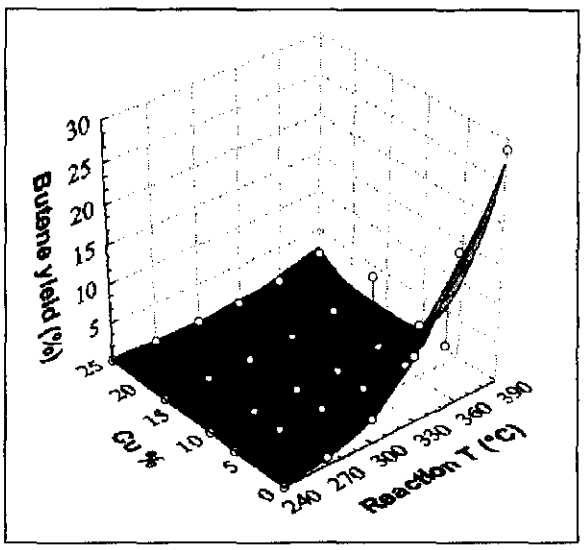

Figure 4.32: Total butene yield for Cu on MgO catalysts

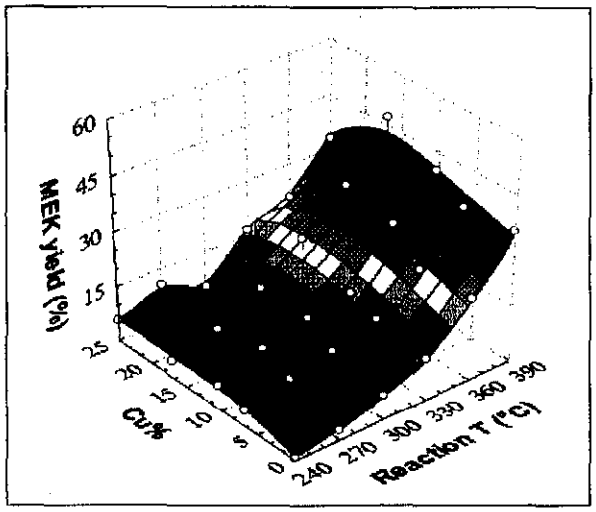

Figure 4.33: MEK yield for Cu on MgO catalysts

Figures 4.34 and **4.35** show the effect of flow rate on MEK yield and selectivity for the best performing catalyst (16.9 wt % Cu on MgO). The selectivity declined with temperature as more butenes were formed. The longer residence time at the low flow rates (high W/F values) improved the MEK yield (**Figure 4.34**), but resulted in a sharp decline in selectivity. The total 2-butanol conversion dropped from 65% to 35% when W/F decreased from 206 to 51 kg.s/mol. The higher flow rates meant that insufficient time was allowed for the 2-butanol to fully react, while the slower rates did. This is also clear in **Figure 4.34** where the MEK yield dropped as W/F decreased.

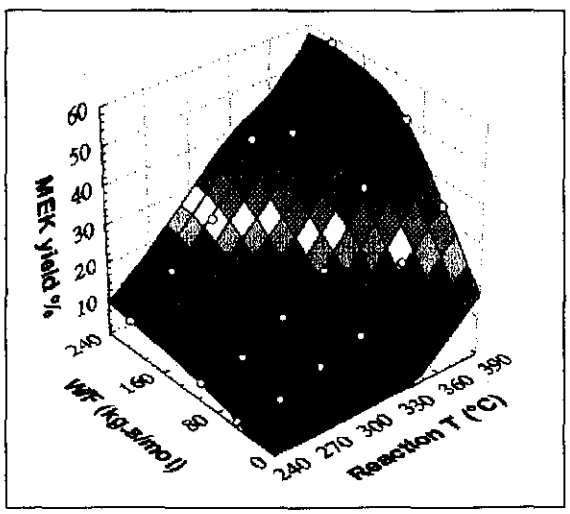

Figure 4.34: MEK yield for a 16.9 wt % Cu on MgO catalyst

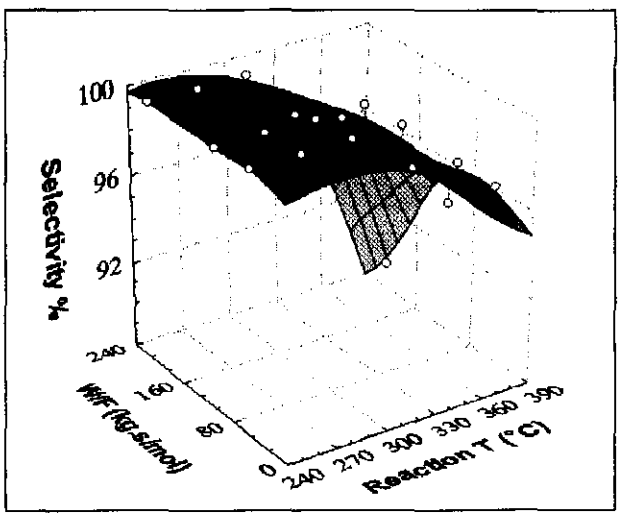

Figure 4.35: MEK selectivity for a 16.9 wt % Cu on MgO catalyst

4.2.2. SILICA CATALYSTS

The silica catalysts that were employed for 2-butanol dehydrogenation were similar to those used for ethanol dehydrogenation. The operating conditions have been listed in **Table 3.6**.

Figure 4.36 shows total 2-butanol conversion as a function of temperature and copper loading. The main product was MEK (**Figure 4.37**) and the only significant by-products were a mixture of butenes (**Figure 4.38**). Total 2-butanol conversion increased sharply with temperature, but started levelling off at about 360 °C. For MEK production, there was an optimum temperature. This temperature was between 300 °C and 360 °C for average W/F values. The optimum temperature did not vary with copper loading. The maximum MEK yield was very dependent on the copper content on the support. At low copper loadings the MEK yield was lower due to butene formation (**Figure 4.38**). As the copper loading increased, butene formation decreased. Butene formation also increased with temperature.

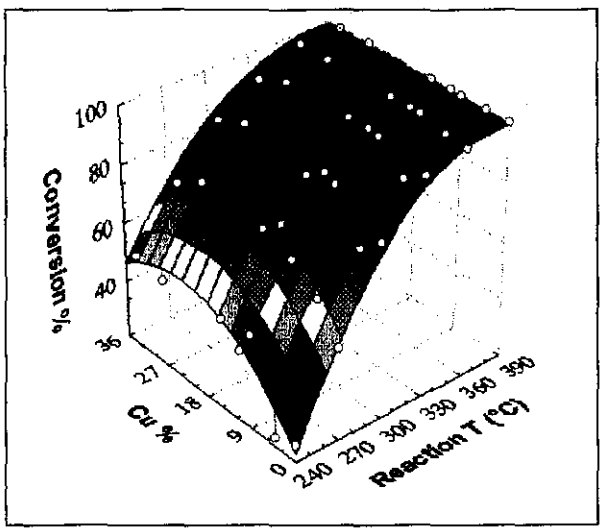

Figure 4.36: Total 2-butanol conversion for Cu on silica catalysts

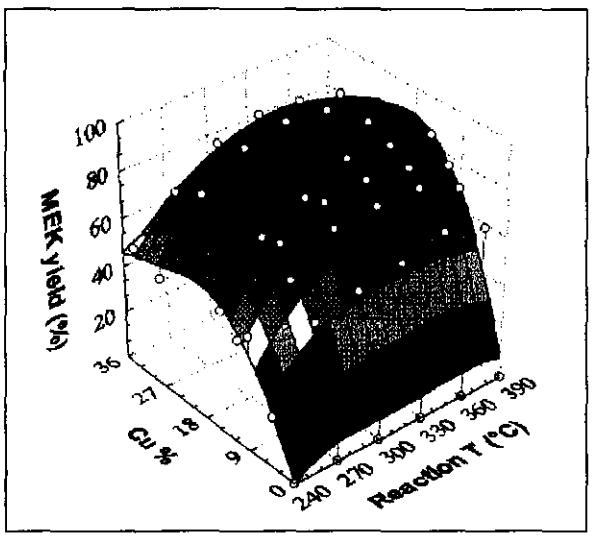

Figure 4.37: MEK yield for Cu on silica catalysts

Butene formation mainly took place on the silica sites, while MEK formation took place on the copper sites. The optimum MEK yield occurred at 15 wt % copper on silica. This was in good agreement with the results obtained for the dehydrogenation of ethanol (see **4.1.3.1**)

MEK yield data (**Figure 4.37**) suggested that the maximum copper surface area should be at 15 wt % Cu on silica.

The optimum catalyst for 2-butanol dehydrogenation was the same as for ethanol dehydrogenation. For a discussion on the characteristics of this catalyst see **4.1.2.4**.

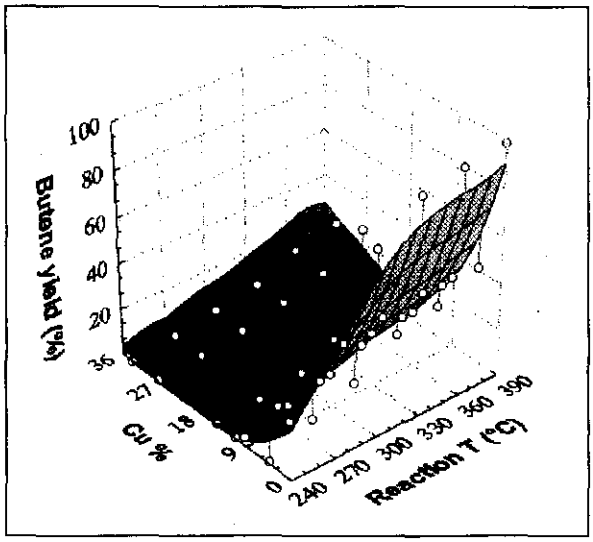

Figure 4.38: Butene yields for Cu on silica catalysts

Figures 4.39 and **4.40** show the MEK yield and selectivity for the best performing catalyst (15 wt % Cu on silica) as a function of temperature and 2-butanol feed flow rate. As mentioned previously the yield increased with temperature. The optimum yield shifted to higher temperatures when the flowrate increased (W/F decreased). For example:

- W/F = 206 kg.s/mol: 93-91% yield at 270-300 °C,
- W/F = 103 kg.s/mol: 93-92% yield at 300-330 °C, and
- W/F = 51 kg.s/mol: 89-87% yield at 330-360 °C.

The selectivity towards MEK production (**Figure 4.40**) decreased with an increase in temperature and decreased very marginally with an increase in W/F. Longer residence times (slower feed rates) stimulated butene formation. At 390 °C the selectivity varied between 83% and 86% for the different feed flow rates.

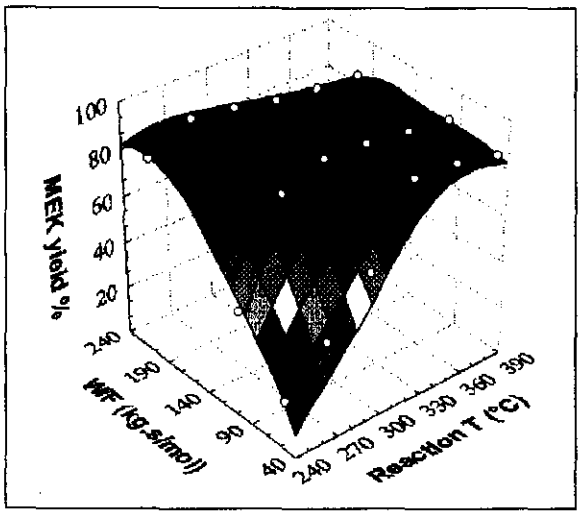

Figure 4.39: MEK yield for a 15 wt % Cu on silica catalyst

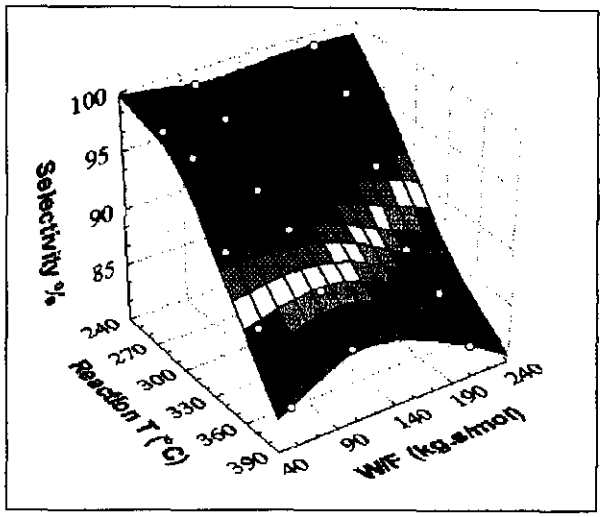

Figure 4.40: MEK selectivity for a 15 wt % Cu on silica catalyst

4.2.2.1. Effect of particle size on 2-butanol conversion

Figures 4.41 and **4.42** show the effects of particle size on total 2-butanol conversion and on MEK yield. At 270 °C and above, catalyst particles up to 1180 μm gave similar values for total 2-butanol conversion. The high conversions indicate very little mass transfer resistance with an increase in particle size. Particles of 3000 μm gave lower 2-butanol conversion due to channelling of the alcohol feed gas (see **Section 4.1.2.3**) and minor mass transfer resistance.

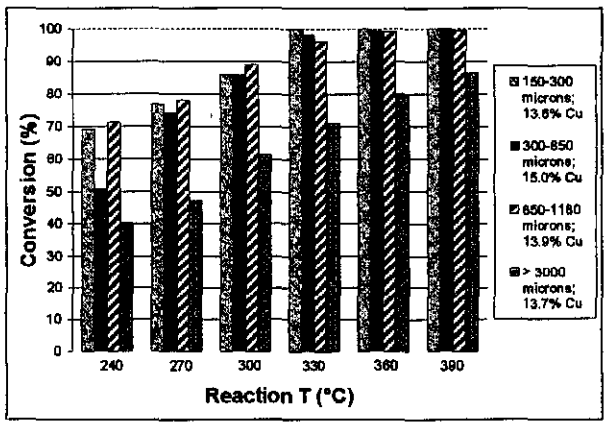

Figure 4.41: Effect of catalyst particle size on total 2-butanol conversion

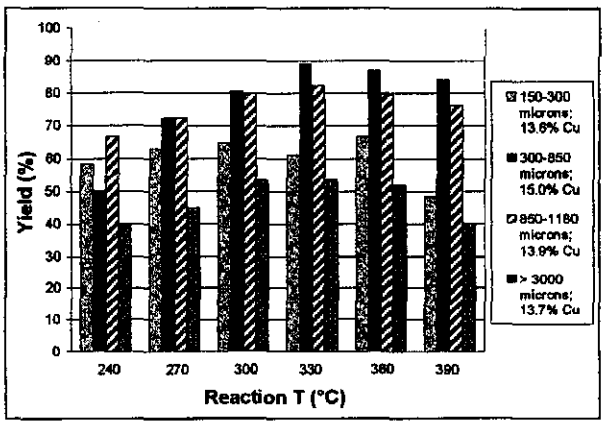

Figure 4.42: Effect of catalyst particle size on MEK yield percentage

The MEK yields (**Figure 4.42**) were the highest for the 300-850 μm fraction. Smaller particles (150-300 μm) and particles ranging from 850-1180 μm gave high butene yields, which decreased the MEK yield.

4.3. SUMMARY

4.3.1. ETHANOL REACTION

The use of alumina supports in the ethanol reaction resulted in the formation of mostly dehydration products (ethene and di-ethyl ether), even at high copper loadings. Some acetaldehyde and butenes were formed with copper on alumina catalysts. The highest acetaldehyde yields were obtained with the catalysts with the highest copper surface area. The use of MgO-based catalysts did lead to the formation of acetaldehyde but, due to the low surface area of MgO supports, the reaction was slow and the conversion low.

Copper-impregnated silica catalysts gave very high acetaldehyde yields. The selectivity towards acetaldehyde formation was high (above 78% in the worst case) for temperatures up to 440 °C. Characterisation of the catalysts indicated that impregnation leads to the formation of a very non-homogeneous catalyst. The copper surface areas for catalysts prepared by impregnation were lower than for catalysts prepared by precipitation or urea hydrolysis. For copper on silica catalysts, the addition of Ni, Co or Cr had a negative effect on acetaldehyde yield. In contrast with this observation, additives to copper on alumina catalysts had a positive effect on di-ethyl ether formation. An increase in particle size of silica-based catalysts caused a decrease in total ethanol conversion. This indicated that mass transfer resistance was important for the reaction of ethanol over Cu-silica. The acetaldehyde yield, however, varied little at 320 °C and above for catalyst particles up to 1180 μm. The mass transfer resistance was more important for other ethanol reactions (for example dehydration and recombination), than for dehydrogenation.

The best dehydrogenation catalyst for ethanol dehydrogenation was a 15 wt % Cu on silica catalyst. **Figure 4.43** compares the equilibrium ethanol conversion for the dehydrogenation reaction with results obtained at different ethanol feed flow rates. For the equilibrium curve the ethanol partial pressure was taken as 0.2 bar, since the feed (1 bar pressure) consisted of nitrogen and ethanol in a molar ratio of 4 to 1 (see section **3.1.4.1**). From 320 °C to 400 °C the acetaldehyde yields were close to the theoretical values for W/F = 131 and 66 kg.s/mol. The difference between the theoretical equilibrium value and the measured values was due to either incomplete conversion of ethanol (for high flow rates, W/F = 33 kg.s/mol) or a drop in acetaldehyde selectivity below 100% (for low flow rates, W/F = 349 kg.s/mol).

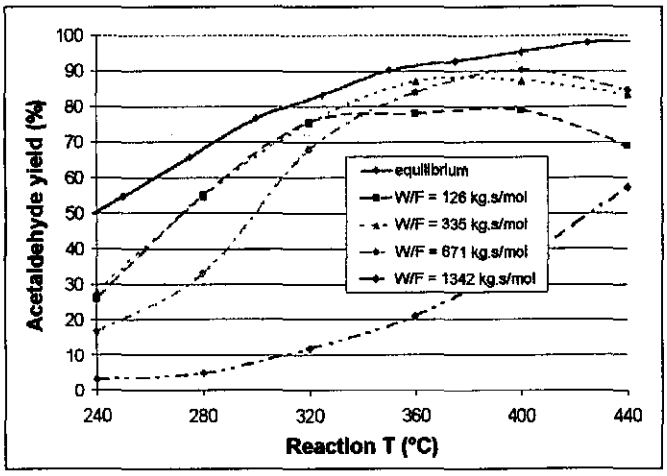

Figure 4.43: Equilibrium ethanol conversion vs. measured values for a 15 wt % Cu on silica catalyst ($P_{ethanol}$ = 0.2 bar for equilibrium curve)

4.3.2. 2-BUTANOL REACTION

The reaction of 2-butanol over MgO and SiO_2 impregnated with copper yielded MEK and butenes. MEK was the main product (except for catalysts without copper), with a mixture of butenes as the by-product. Similar to the ethanol reaction, MgO catalysts gave worse results due to their low surface area.

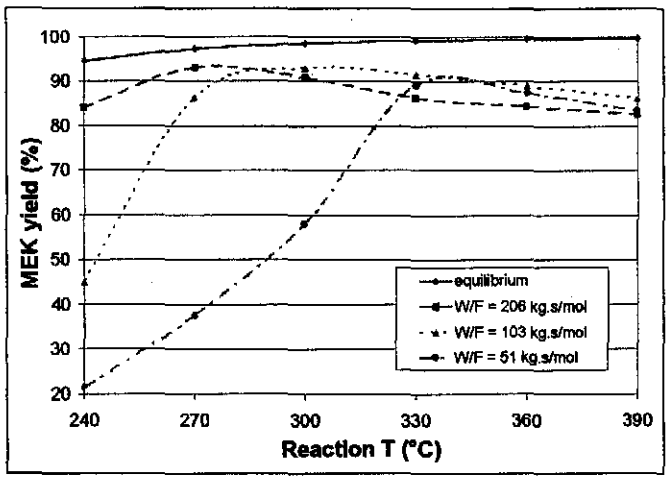

Figure 4.44: Equilibrium 2-butanol conversion vs. measured values for a 15 wt % Cu on silica catalyst ($P_{2\text{-butanol}}$ = 0.2 bar for equilibrium curve)

For silica catalysts there were an optimum copper concentration on the support (15 wt %), which gave the highest MEK yields. Catalyst particles in the range of 300-850 μm gave the highest MEK yields. Smaller or larger particles produced increasing amounts of butenes. For a 15 wt % Cu on silica catalyst the selectivity towards MEK production was close to 100% at 240 °C, but declined to between 83% and 86% at 390 °C for various W/F ratios. **Figure 4.44** compares the equilibrium conversion (theoretical) of 2-butanol to MEK, at a partial pressure of 0.2 bar, with experimental values. For W/F = 51 kg.s/mol, the MEK yield differed considerably from the equilibrium value below 330 °C, while for W/F = 103 kg.s/mol the deviation was below 270 °C. Above these temperatures the experimental values approached the equilibrium values, but were lower due to less than 100% selectivity towards acetaldehyde production. The reaction conversion will be similar to the equilibrium value if the reaction goes to completion at a specific temperature. If the flow rate is too high, however, the reaction will not go to completion, since the reaction time will be too short.

5. REACTION KINETICS

The conditions required for catalyst testing were described in **section 3.2**. The reactions must be performed in the steady state regime. This implies that there should be little or no catalysts deactivation during testing, hence the catalyst deactivation conditions must be determined. The reactor must be isothermal and the catalyst particles free from interphase and intra-particle mass transfer resistance. The reactor must be operated as a differential reactor. For a plug flow reactor, the relationship between the reaction rate and the conversion is given by the following equation.

$$\frac{W}{F} = \int_0^X \frac{dX}{-r_A'} \qquad (5.1)$$

Under differential conditions the conversion is kept low (typically below 10%). **Equation 5.1** can then be simplified to **equation 5.2**.

$$\frac{W}{F_0} = \frac{X}{(-r_A')_{exit}} \qquad (5.2)$$

The difficulty with the integration term is removed, while still maintaining very high accuracy. The following sequence was performed to determine the reaction rate kinetics of both ethanol and 2-butanol dehydrogenation.

1. Determine the temperature range which results in an acceptably low deactivation rate.
2. Determine the flow rate which results in low conversion (below 10%) and which minimises interphase mass transfer resistance.
3. Determine reaction rate kinetics at the above temperatures and flow rates.

Small catalyst particles in the range of 300 to 425 μm were prepared for all experiments to minimise intra-particle mass transfer resistance. The mass of catalyst for testing was varied according to the reaction temperature. At high temperatures, a smaller amount was used to

reduce the total conversion and keep it below 10%. At low temperatures, the catalyst mass was increased to ensure a detectable conversion.

For all the data presented in **Chapter 5**, the following units were used for the reaction rate parameters:

k': mol/kg.cat.h.kPa

K_{eq}: kPa^{-1}

K_i: kPa^{-1}

r': mol/kg.cat.h

Initial kinetic model fitting was performed with the above units and then the final step was to convert the parameters back to the standard units. The standard units were used for process modelling in **Chapters 8** and **9**.

5.1. CATALYST DEACTIVATION TESTING

The effects of reaction temperature and reduction temperature on catalyst deactivation were investigated. For both ethanol and 2-butanol dehydrogenation a 14.4 wt % copper on silica catalyst was employed. Experimental procedures and the testing conditions were discussed in **Section 3.2**.

5.1.1. EFFECT OF REDUCTION TEMPERATURE ON ETHANOL REACTION

Different researchers suggest the use of different reduction temperatures for copper-supported catalysts (see discussion in **4.1.2.2**). Three reduction temperatures were tested and two sets of experiments were performed to determine the effect of reduction temperature on catalyst stability. The results are shown in **Figures 5.1** and **5.2**.

Reduction at 340 °C and 400 °C resulted in low initial reaction rates. Since the initial reaction rates were much lower than the initial reaction rates for catalyst reduced at 255 °C, it was concluded that reduction at 340 °C and 400 °C caused changes in the copper particle size. **Figure 5.1** compares the curves for reduction at 400 °C and 255 °C. The initial activity of the catalyst reduced at the higher temperature was similar to the activity of the catalyst

reduced at the lower temperature after about 12 hours reaction. This was considerably longer than the reduction time (2 hours) of the catalyst reduced at the higher temperature.

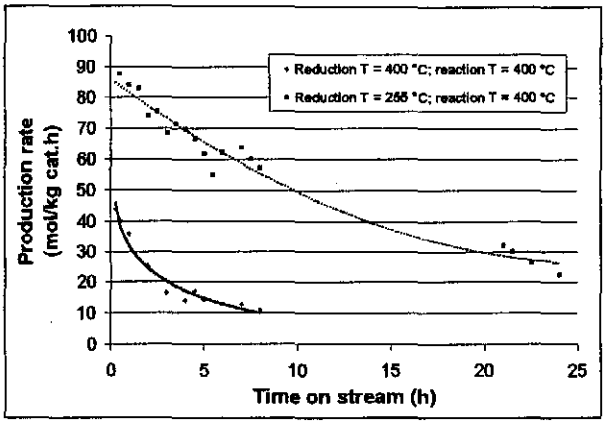

Figure 5.1: Effect of reduction T on acetaldehyde production rate over time (14.4 wt % Cu on silica)

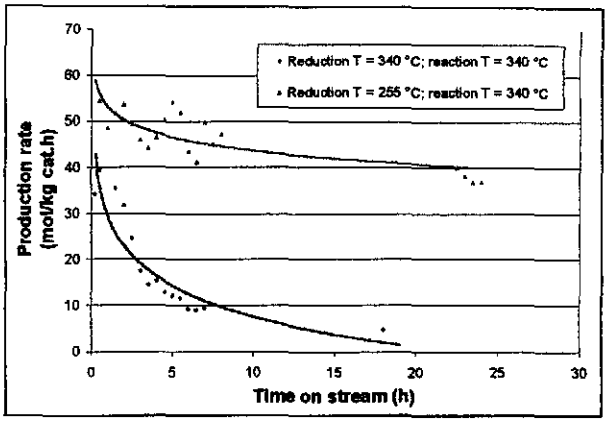

Figure 5.2: Effect of reduction T on acetaldehyde production rate over time (14.4 wt % Cu on silica)

The reducing temperature, the reducing environment and the effect of water formation from the reduction reaction all have an effect on the change of copper particles during reduction. Although there was initially no coking, it did occur over time. From **Figures 5.1** and **5.2** it is clear that sintering of copper occurred at reduction temperatures of 340 °C and 400 °C. To avoid the loss in catalyst activity all further reduction was performed at temperatures between 250 °C and 260 °C.

5.1.2. EFFECT OF REACTION TEMPERATURE AND ADDITIVES ON CATALYST STABILITY

Tests to determine the stability of the catalysts were conducted at 400, 340, 280 and 220 °C. Results are presented in **Figure 5.3**. At 400 °C, the main by-product was ethylene and the selectivity towards acetaldehyde remained high (> 90%) over the tested 24 hour time period. At 340 °C, the main by-products were MEK and butyraldehyde and the selectivity towards acetaldehyde was greater than 90%. At 280 °C, the selectivity was on average about 95% and at 220 °C, the selectivity was 100%. **Table 5.1** summarises the reaction rates as a function of time.

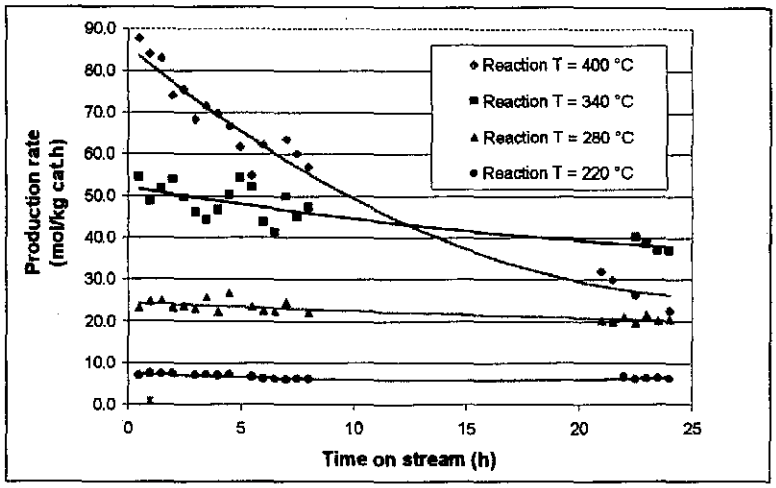

Figure 5.3: Acetaldehyde production rate as a function of time and temperature (14.4 wt % Cu on silica)

Table 5.1: Summary of catalyst deactivation at different reaction temperatures

Reaction T (°C)	Reaction rate (0.5h) mol/kg cat. h	Reaction rate (24h) mol/kg cat. h	% decline
400	87.7	22.6	74
340	54.5	37.0	32
280	23.3	20.5	12
220	7.0	6.3	10

At 220 °C and 280 °C, the catalyst remained stable throughout the 24 hour testing period. In absolute terms there was very little change in reaction rate.

Chromium and cobalt were added to copper to try and improve catalyst stability. Stability tests were repeated with a 13.5 wt % Cu, 1.0 wt % Cr and 0.5 wt % Co on silica catalyst. The results are shown in **Figures 5.4** and **5.5**. Similar stabilities to that of a pure copper catalyst were achieved. The catalysts with additives did, however, show poorer activity towards the dehydrogenation of ethanol. At each temperature tested, the acetaldehyde production rate was lower over time, on average, as indicated in **Table 5.2**. The Cu/Cr/Co on silica catalyst was also less selective towards acetaldehyde production. At 400 °C, the main by-products

were ethylene, MEK and butyraldehyde (similarly at 340 °C and 280 °C). Selectivities are indicated in **Table 5.2**.

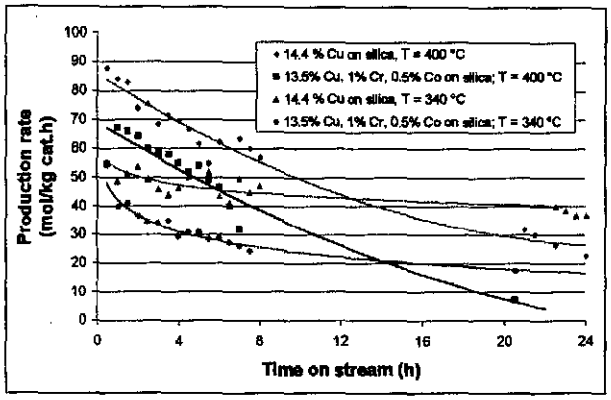

Figure 5.4: Effect of additives (Cr and Co) on acetaldehyde production rate

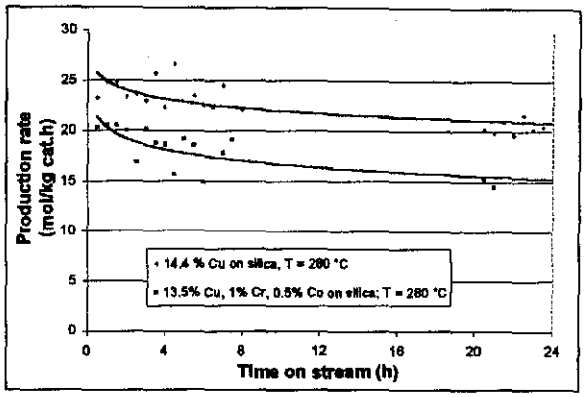

Figure 5.5: Effect of additives (Cr and Co) on acetaldehyde production rate at 280 °C

Table 5.2: Performance of Cu/Cr/Co on silica catalyst

Temperature (°C)	Average decline in reaction rate over time (%)	Selectivity (%) towards acetaldehyde
400	22	70-80
340	35	> 88
280	23	70-90

5.1.3. FURTHER DEACTIVATION TESTING

Further deactivation studies were conducted using XRD, TEM and TOC measurements. The results from XRD measurements were used to calculate crystallite size before and after reaction. **Table 5.3** lists the results obtained. Crystallite size was calculated using Schearer's relation. The peak widths were less than 0.2°, which made XRD not very suitable for detecting sintering. The broader the peaks, the smaller the crystallite sizes. In general, sintering is indicated by peak narrowing for tested samples, compared to a freshly reduced sample. In this study, crystallite sizes measured by XRD were too large to be able to draw accurate conclusions from XRD data.

Table 5.3: XRD and TOC results of tested catalysts

Temperature (°C)	Peak width from XRD (degrees)	Crystallite size (nm)	Carbon wt %
Reduced, but unused	0.20°	60	0.065
220	0.15°	80	3.213
280	0.15°	80	3.386
340	0.14°	80	3.693
400	0.15°	80	3.737

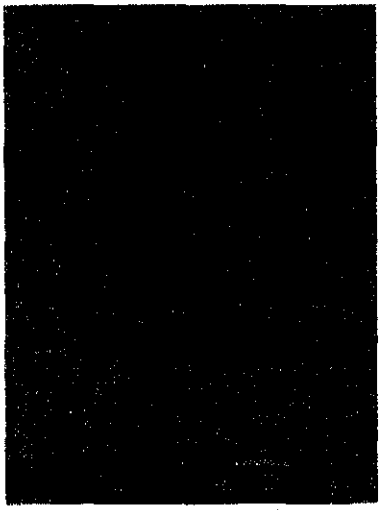

Figure 5.6a: TEM (20 nm)

Figure 5.6b: TEM (20 nm)

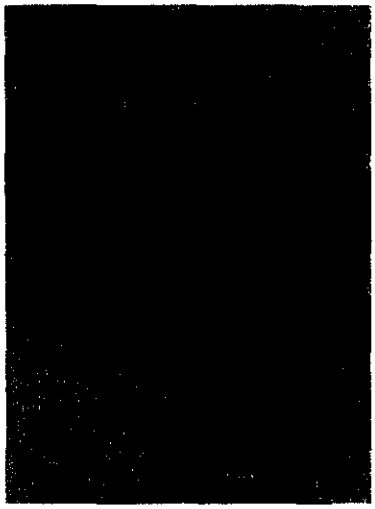

Figure 5.6c: TEM (50 nm)

Figure 5.6d: TEM (50 nm)

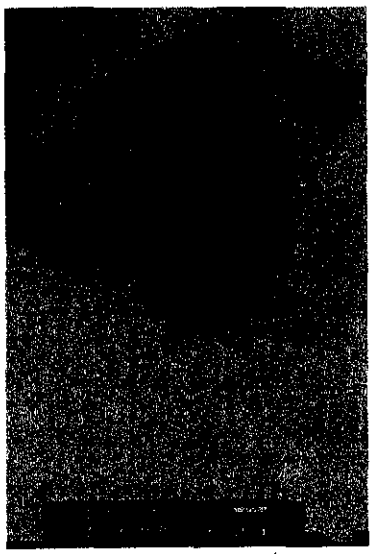

Figure 5.6e: TEM (100 nm)

Figure 5.6f: TEM (100 nm)

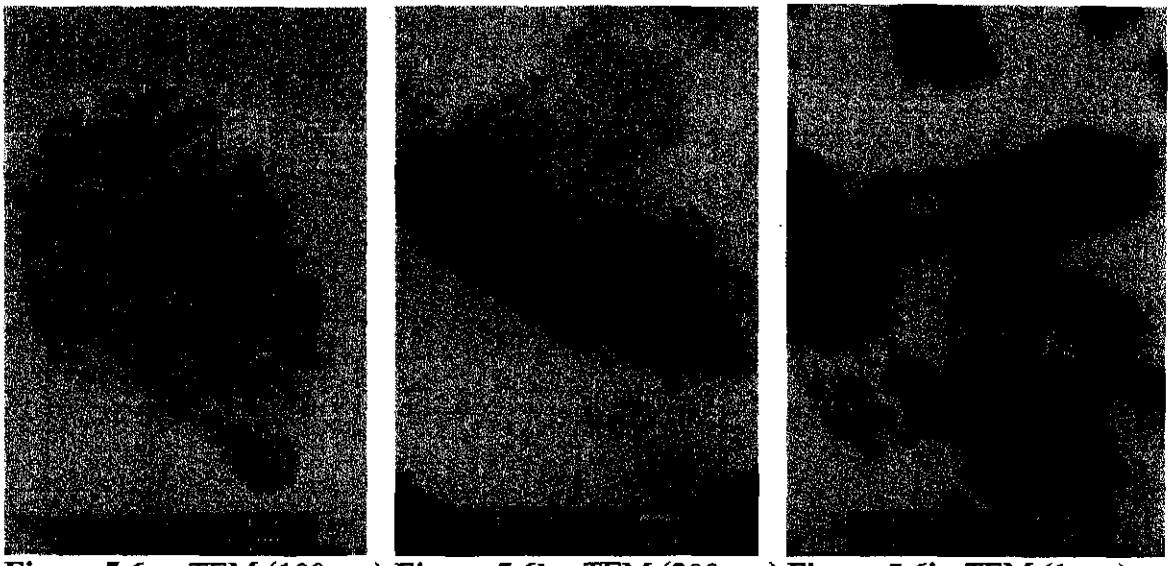

Figure 5.6g: TEM (100 nm) **Figure 5.6h:** TEM (200 nm) **Figure 5.6i:** TEM (1 μm)

Figure 5.6: TEM images of 14.4 wt % copper on silica catalyst after being in use at 400 °C

TEM studies showed a very wide size distribution of copper particles in the unused catalyst. Some areas had copper agglomerates in the 1 micron range, down to 40 to 50 nm. Other areas had small copper crystallites of 4 to 5 nm, evenly distributed over the support (see **Figures 4.30a** to **4.30i**). After reaction at 400 °C, there was definite agglomeration of small crystals (4 to 5nm) to yield bigger polycrystalline particles (**Figures 5.6a** to **5.6i**).

Some areas had no copper (**Figure 5.6a**), similar to observations made of the catalyst before reaction. The small crystallites, in the order of 4 to 5 nm (**Figures 4.30b** to **4.30d**), agglomerated to form particles in the 20 nm range (**Figures 5.6b** to **5.6d**). Larger agglomerates were more frequently observed after reaction than before reaction (see **Figures 5.6f**, **5.6h** and **5.6i**). This confirmed that some sintering occurred during reaction at 400 °C.

Chemisorption results are shown in **Table 5.4**. In each case the surface area was the value after 24 hours at the reaction temperature. The values indicated a decline in copper surface area with an increase in reaction temperature, confirming TEM results. Sintering occurred even at the low temperatures.

Table 5.4: Copper surface areas for 14.4 wt % Cu on silica catalysts

Reaction T (°C)	Copper area (m^2/g sample)	Copper area (m^2/g Cu)	% Decrease
Fresh catalyst	0.56	3.76	
220	0.47	3.15	16
340	0.44	2.96	21
400	0.37	2.49	34

Catalyst reactivation studies were performed to obtain more information regarding the deactivation mechanism. The 14.4 wt % Cu on silica catalyst was reactivated after 24 hours and 48 hours of operation at 400 °C. This was done to determine whether coking, sintering, or both, were the dominating deactivation mechanism. **Figure 5.7** indicates a decline in initial acetaldehyde production rate (about 25% to 30%) after the first re-oxidation step, compared to the first run. This is in good agreement with results in **Table 5.4**. After the second re-oxidation step, the same initial activity as after the first re-oxidation step was obtained. From this experiment it could be concluded that some irreversible sintering occurred during the first 24 hour reaction period. Deactivation that occurred in the second 24 hour period could be recovered by oxidation and hydrogen reduction.

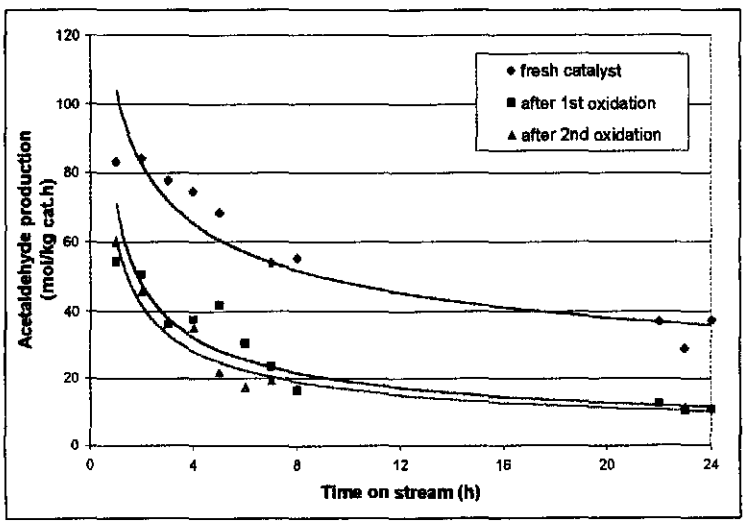

Figure 5.7: Catalyst activity (14.4 wt % Cu on silica) after re-oxidation

5.1.3.1. Deactivation mechanism

The following mechanism for catalyst deactivation is proposed: At all temperatures above 220 °C there is some initial sintering within the first 24 hours of use and the sintering rate increases with temperature. At 400 °C, the reduction in copper surface area after 24 hours of use is twice the amount of the catalyst used at 220 °C for 24 hours. Results of re-oxidation experiments indicate that most of the sintering occurs within the first 24 hours of use.

Sintering and carbon deposition on the catalyst takes place simultaneously. At the higher temperatures, mainly coke-like carbon is deposited, which reduces catalyst activity and prevents ethanol molecules from reaching the active copper sites. At the lower temperatures (280 °C and lower) carbon is present in molecular form, probably as oligomers and polymers that do not prevent ethanol from reaching the active sites.

Coking contributes more to catalyst deactivation than sintering. **Figure 5.7** indicates a decrease in acetaldehyde production rate of 80% for the second 24 hour run at 400 °C after the first re-oxidation step. This value is considerably higher than the decrease in acetaldehyde production due to sintering.

5.1.4. CATALYST STABILITY FOR DEHYDROGENATION OF 2-BUTANOL

A 14.4 wt % copper on silica catalyst was employed for the dehydrogenation of 2-butanol. Stability was tested at 250 °C and 310 °C. Selectivity towards MEK production was very high (> 99%) at both temperatures. At 250 °C, the catalyst was very stable over a 24 hour period, but deactivation took place when the temperature was increased to 310 °C. Further deactivation testing was not conducted. The same sintering effects that were present for the ethanol catalyst are also valid for this reaction, as the same catalyst was used. Deactivation due to coking will differ, because different organic species are present in this reaction, giving rise to different coking kinetics.

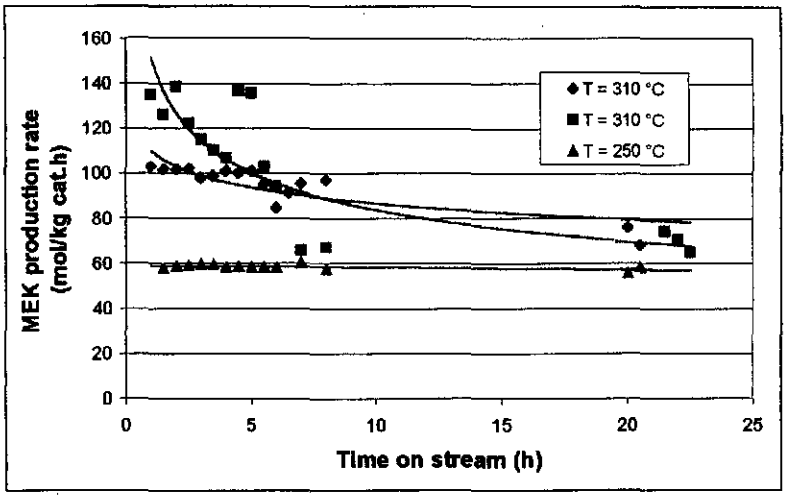

Figure 5.8: MEK production rate as a function of time for a 14.4 wt % Cu on silica catalyst

5.2. REACTION MASS TRANSFER RESISTANCE

To obtain accurate kinetic data, the reaction must be operated in the region free from mass transfer resistance. Mass transfer resistance is dependent on the particle Reynolds number, which in turn is a function of the linear gas velocity past the catalyst particles. The linear gas velocity can be increased to eliminate mass transfer resistance by increasing the feed flow rate and/or decreasing the inside diameter of the quartz tube housing the catalyst. A quartz U-tube with small inside diameter (4 mm) was used for all experiments.

5.2.1. DETERMINING THE MASS TRANSFER LIMITING REGIME FOR ETHANOL DEHYDROGENATION

The liquid feed flow rates were increased from 2 ml/h to 25 ml/h using a perfusion pump. The experimental procedures used for determining the mass transfer limiting regime were described in **section 3.2.1.3** and the mass of catalyst used at each temperature was listed in **Table 3.9**. The results are presented in **Figure 5.9**.

There was significant interphase mass transfer resistance for ethanol dehydrogenation at the higher temperatures. At higher temperatures, the difference between the reaction rate limitations and the mass transfer limitations increased, because the reaction rate became faster (less resistance). A small increase in the feed flow rate (which determines interphase

mass transfer resistance), would thus result in a larger increase in acetaldehyde production rate at high temperatures as compared to lower temperatures.

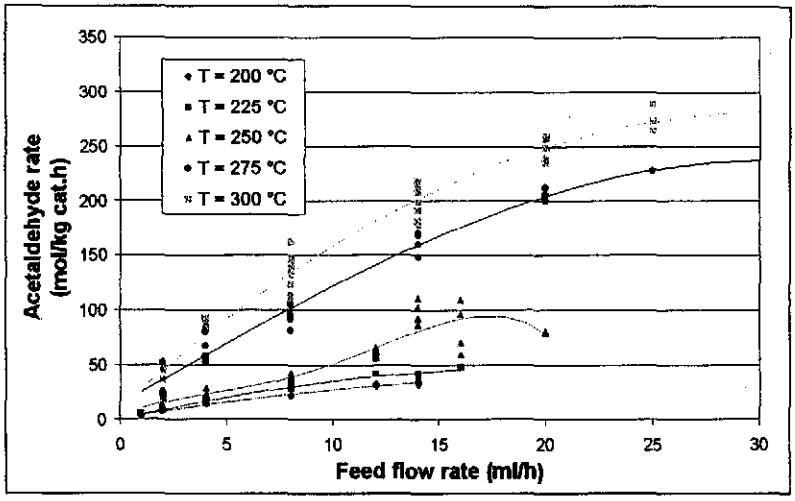

Figure 5.9: The effect of feed flow rate on acetaldehyde production rate

At temperatures of 250 °C and below, the reaction rate was fairly constant above a feed flow rate of 14 ml/h. At 275 °C and 300 °C it appeared, from the data, that the region free of mass transfer resistance commenced at a feed flow rate of 30 ml/h. Due to limitations of the feed pump, it was not possible to do full kinetic studies at such high flow rates. All data for determining kinetic parameters was obtained at a feed rate of 14 ml/h. In the modelling calculations the final rate data at the higher temperatures was to be fitted to the curves in **Figure 5.9,** to compensate for rate reduction from mass transfer resistance.

5.2.2. DETERMINING THE MASS TRANSFER LIMITING REGIME FOR 2-BUTANOL DEHYDROGENATION

Flow rates of 2 to 16 ml/h were tested (see **Table 3.10**). For the 2-butanol dehydrogenation reaction, there was no significant interphase mass transfer resistance (**Figure 5.10**). The MEK production rate remained fairly constant with an increase in 2-butanol feed flow rate at all temperatures tested. There were some fluctuations in the MEK production rates, with a slight downward trend in production rates at the lower temperatures. For modelling purposes, rates at different feed flows were averaged at each temperature. Raizada, Tripathi et al. (1993) reported similar results on interphase mass transfer resistance for the

dehydrogenation of n-butanol over zinc oxide. They concluded that bulk diffusion was not significant.

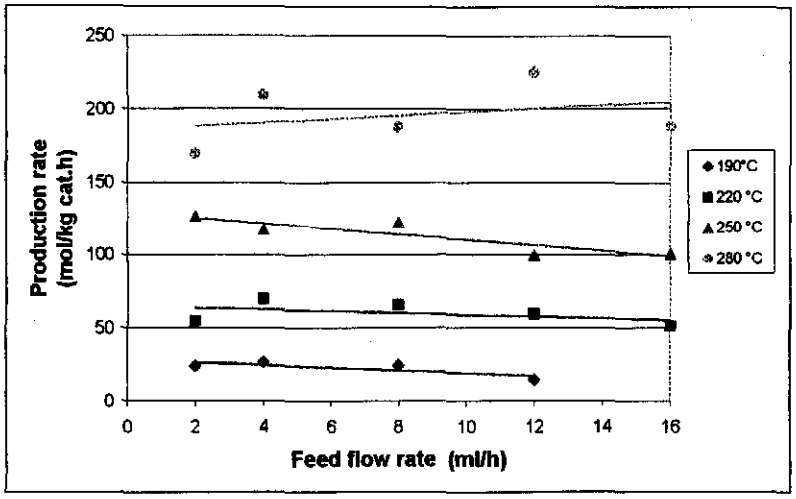

Figure 5.10: The effect of 2-butanol feed flow rate on the MEK production rate

5.3. KINETICS FOR ALCOHOL DEHYDROGENATION

Kinetic data for ethanol dehydrogenation was fitted to the dual site reaction equation (**equation 2.18**). Previous researchers had found this equation to best fit kinetic data for ethanol dehydrogenation over supported copper catalysts (see **Section 2.12.5.3**). The validity of this equation for the reaction conditions ranging from 200 °C to 300 °C was also tested. The reaction equation for the duel site surface reaction mechanism is:

$$r_A' = \frac{k'\left(P_A - P_R P_S / K_{eq}\right)}{\left(1 + K_A P_A + K_R P_R + K_S P_S\right)^2} \qquad (5.3)$$

with A, R, S = ethanol, acetaldehyde, hydrogen

Numerical values for the rate and adsorption coefficients could be calculated using least square analysis. Equation (**5.3**) must be linearised in the unknown coefficients. Rearranging equation (**5.3**) yielded:

$$\sqrt{\frac{P_A - P_R P_S / K_{eq}}{r_A'}} = \frac{1}{\sqrt{k'}}\left[1 + K_A P_A + K_R P_R + K_S P_S\right] \quad \text{or} \tag{5.4}$$

$$y = a + bP_A + cP_R + dP_S \qquad \text{with} \tag{5.5}$$

$$y = \sqrt{\frac{P_A - P_R P_S / K_{eq}}{r_A'}} \qquad \text{and} \tag{5.6}$$

$$a = \frac{1}{\sqrt{k'}};\ b = \frac{K_A}{\sqrt{k'}} = aK_A;\ c = \frac{K_R}{\sqrt{k'}} = aK_R;\ d = \frac{K_S}{\sqrt{k'}} = aK_S \tag{5.7}$$

The constants k' and K_A were expressed by:

$$k' = \frac{1}{a^2} \qquad \text{and} \tag{5.8}$$

$$K_A = \frac{b}{a} \tag{5.9}$$

The constants a and b were determined first (using a pure ethanol feed at different pressures) from the y-axis intercept and the gradient of the best linear fit to the data. The ethanol partial pressure was varied by feeding it with an inert gas (nitrogen). Thereafter the ethanol was fed with hydrogen and acetaldehyde separately, while keeping the total pressure constant at one atmosphere. Different molar feed ratios were used. Equation (**5.5**) can be expressed as:

$$y = a + bP_A + d(101 - P_A) = (a + 101d) + (b-d)P_A \tag{5.10}$$

where d and c are used depending on whether acetaldehyde or hydrogen is used. From the y-axis intercept and the gradient of the best linear fit at each temperature the remaining constants could be determined (in **5.7**). The process was repeated at each temperature, to determine the Arrhenius dependence of each adsorption constant. The Arrhenius equation is:

$$k'(T) = A' e^{-E/R_0 T} \qquad (5.11)$$

Linearising equation (**5.11**) allows for A and E to be determined.

$$Ln(k') = \ln(A') - E/R_0 T \qquad (5.12)$$

5.3.1. ETHANOL DEHYDROGENATION

The parameters in equation (**5.4**) were determined at temperatures of 200 °C to 300 °C with the dual-site reaction mechanism. The linear fits to the data, which were used to determine the parameters, are given in **Appendix C1**. **Figures 5.11** and **5.12** show typical linear fits at 225 °C and 300 °C, respectively.

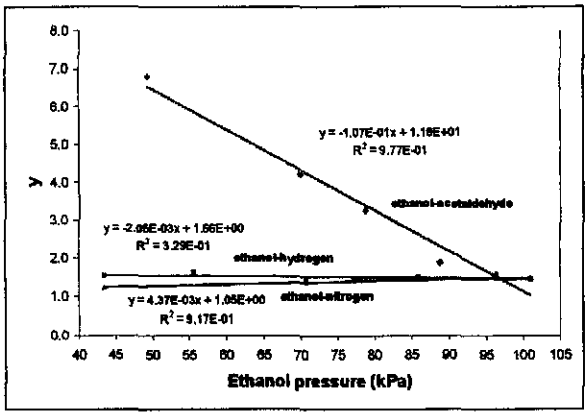

Figure 5.11: Linear fits of reaction rate data at 1 atm. total pressure and 225 °C

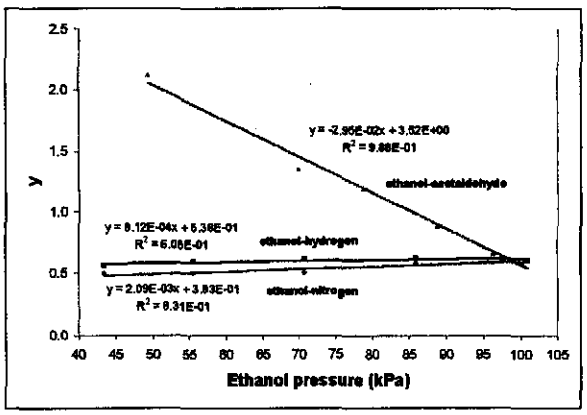

Figure 5.12: Linear fits of reaction rate data at 1 atm. total pressure and 300 °C

The y-value was proportional to the inverse square root of the reaction rate (**equation 5.6**). A decrease in the reaction rate would thus cause an increase in the y-values. For the ethanol-acetaldehyde feed there was a sharp increase in the y-values (decrease in reaction rate) with an increase in acetaldehyde concentration. This indicated that the reaction rate was most sensitive to the acetaldehyde concentration. Acetaldehyde adsorbed strongly on the catalytic sites and reduced the dehydrogenation reaction rate. Hydrogen adsorption on the surface was not very strong and ha only a small effect on the reaction rate.

Good linear fits for the acetaldehyde-ethanol feed in **Figures 5.11** and **5.12** indicated that the reaction rate was not dependant on the acetaldehyde pressure, but on the square of the acetaldehyde pressure. **Table 2.5** listed other possible reaction rate mechanisms. Only equations **(2.18)** and **(2.19)** had the acetaldehyde pressure square term. Furthermore, equation **(2.19)** did not have adsorption coefficients for ethanol, hydrogen and acetaldehyde, but only for either ethanol and hydrogen or ethanol and acetaldehyde. The data confirms that equation **(2.18)** is most suitable for describing the rate mechanism.

The value of each parameter at the different temperatures is given in **Table 5.5**.

Table 5.5: Reaction rate parameters for ethanol dehydrogenation

T (°C)	k mol/kg cat.h.kPa	K_A kPa^{-1}	K_S kPa^{-1}	K_R kPa^{-1}
200	0.9615	0.00707	0.00752	0.1197
225	0.9086	0.00417	0.00593	0.1038
250	1.8699	0.00514	0.00324	0.0694
275	4.5697	0.00432	0.00291	0.0657
300	6.8212	0.00546	0.00368	0.0818

(A = ethanol, S = hydrogen, R = acetaldehyde)

The adsorption coefficients (K_R and K_S) decreased with an increase in temperature from 200 °C to 275 °C. The value of K_A should theoretically also decrease and the calculated values were in reasonable agreement with the theory, excluding the value at 300 °C. The reaction rate coefficient (k') increased with temperature (as expected). This was typical for a reaction which follows the dual site, surface reaction mechanism (Peloso et al., 1979). At 300 °C, the adsorption coefficients deviated from the downward trend. The values were higher than at 275 °C. To comply with the dual site, surface reaction controlling mechanism, the adsorption coefficients must decrease with temperature, and they must be positive (Peloso et al., 1979). The increase in the calculated adsorption coefficients at 300 °C, compared to the values at 275 °C, is illustrated in **Figure 5.13**.

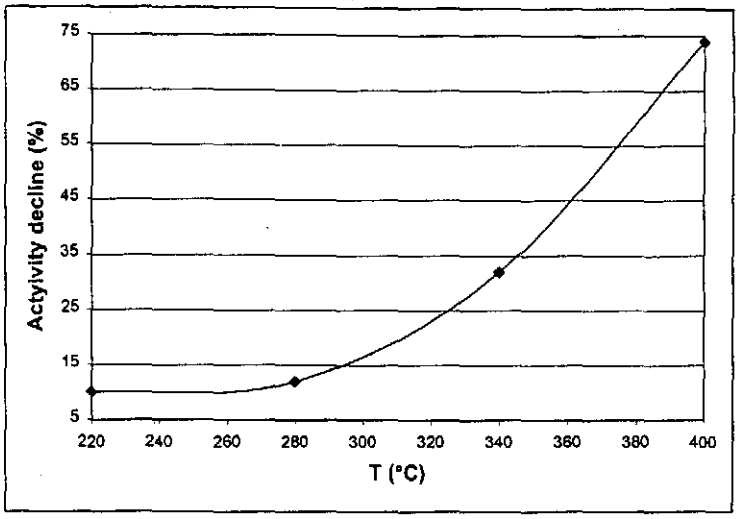

Figure 5.13: % Catalyst deactivation after 24 hours of operation

There was little change in the deactivation rate of the catalyst at temperatures from 200 °C to 275 °C (from 10 % to about 11.2 % over a 24 hour period). At 300 °C, the deactivation rate dropped to 16.5 % after 24 hours of operation. During the testing period at 300 °C (about two days), some deactivation would thus have taken place. This would result in the reaction rate values being lower than the true values, due to catalyst deactivation. These lower 'falsified' reaction rate values are reflected in the rate mechanism as higher adsorption coefficients. Stronger adsorption or higher adsorption coefficients lead to slower rates. Nonetheless, the model still holds at higher temperatures, even though the changes in catalyst activity gave rise to conflicting parameter values.

The Arrhenius parameters for k', K_A, K_R and K_S were determined only at temperatures from 200 °C to 275 °C (thus excluding values at 300 °C) using equation **(5.12)**. All adsorption coefficients (K_A, K_R and K_S) are given in kPa^{-1}. The following expressions were obtained (with T in K):

For T = 473 K to 548 K:

$Ln(k') = 11.291-5491.1/T$ $(R^2 = 0.825)$ **(5.13)**

$Ln(K_A) = 1351.1/T - 7.941$ $(R^2 = 0.487)$ **(5.14)**

$Ln(K_S) = 3586.6/T- 12.444$ $(R^2 = 0.939)$ **(5.15)**

$Ln(K_R) = 2288/T - 6.940$ $(R^2 = 0.927)$ **(5.16)**

The data is shown in **Figure 5.14**.

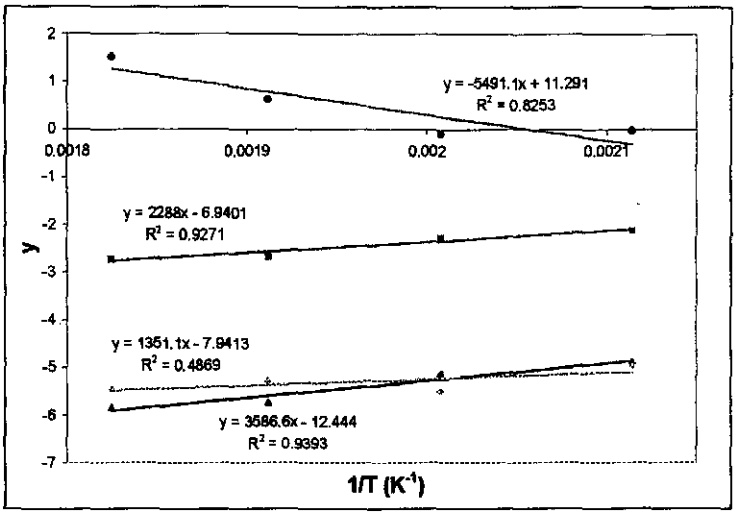

Figure 5.14: Parameters for ethanol reaction equation as a function of temperature

K_{eq} is a constant and could be found in the literature as an empirical correlation (Peloso et al., 1979) or calculated using firsts principles via the Van't Hoff's equation (Fogler, 1992). Many of the correlations were very old and their accuracy doubtful, with the result that an expression was reduced from first principles.

$$\Delta G^0_{Rxn} = G^0_{H_2} + G^0_{Aset} - G^0_{Et} \qquad (5.17)$$

$$\Delta G = \Delta H - T\Delta S \qquad (5.18)$$

$$K_p = \exp\left[\frac{-\Delta G^0_{Rxn}(T)}{R_0 T}\right] \qquad (5.19)$$

K_p in equation (**5.19**) is defined in atmospheres. Using thermodynamic data for ethanol and acetaldehyde, K_p (in atmospheres) could be calculated at different temperatures. K_p values were changed to K_{eq} values in kPa (to standardise all K-values) and then the Arrhenius equation could be fitted through the different K_{eq}-values to obtain the necessary Arrhenius parameters (similar to **5.11** and **5.12**). The equilibrium constant is then:

$$Ln(K_{eq}) = 19.014 - 8503.3/T \quad (5.20)$$

The reaction rate from 473 K to 548 K and at 1 atmosphere feed pressure could now be expressed as:

$$-r_A = \frac{8.014\times10^{4}\times e^{-5491.1/T}\left(P_A - P_R P_S/(1.810\times10^{8}\times e^{-8503.3/T})\right)}{\left(1+3.557\times10^{-4}\times e^{1351.1/T}\times P_A + 3.941\times10^{-6}\times e^{3586.6/T}\times P_S + 9.683\times10^{-4}\times e^{2288/T}\times P_R\right)^2} \quad (5.21)$$

with pressures in kPa and temperatures in K. The accuracy of equation (**5.21**) was tested for all the data from 200 °C to 275 °C (**Figures 5.15** and **5.17**).

5.3.1.1. Equation optimisation

Equation (**5.21**) represents the parameters obtained using multiple linear regression analysis. This will be called model 1. A second model was developed to minimise the error between actual measured reaction rates and the calculated reaction rates.

The structure of the error function was of great importance. Either the model percentage deviation could be used or the actual model value difference. In mathematical format:

- 100*(model value – measured value)/measured value or
- model value – measured value.

The reaction rate increased from 33 (mol/kg cat.h) at 200 °C to 227 (mol/kg cat.h) at 275 °C. At high temperatures, a percentage deviation of 20 %, for example, would result in a large difference in measured reaction rates, while the difference in measured reaction rates at low temperatures and at the same percentage deviation, would be small. It was more important to correctly predict reaction rates at the higher temperatures than at the lower temperatures, thus the actual deviation and not the percentage deviation was used in the error function. Since the deviations in actual rates at the higher temperatures were so much larger than at the lower temperatures, different weights were applied at each temperature to the error function. The error function is as follows:

$$EF = \sum_{1}^{n}(CV - MV)^2_{T=472K} + \left(\frac{(CV - MV)}{1.125}\right)^2_{T=498K} + \left(\frac{(CV - MV)}{1.25}\right)^2_{T=523K} + \left(\frac{(CV - MV)}{2}\right)^2_{T=548K} \quad (5.22)$$

with EF = error function, CV = calculated values, MV = measured values and n the number of experimental points.

The model deviation (MD) from the measured data is simply the following:

$$MD = \sum_{1}^{n}(CV - MV)^2 \quad (5.23)$$

There were 62 experimental reaction rate values. The values in equation (**5.21**) were used as the starting values for further optimisation. The parameters were varied using an 8 dimensional matrix (varying each one of the eight parameters in equations **5.13** to **5.16**). The smaller the error function, the closer the calculated values were to the measured values and the better the fit. As the error function approached the minimum value, the step size for each parameter was decreased to obtain more accurate values. The final step size employed was 0.2 % steps for each of the 8 parameters. A Turbo Pascal program was compiled to determine the error function and calculate the parameter values. The best fit was called model 2. Both model 1 and model 2 were only for data obtained from 200 °C to 275 °C. The parameter values are listed in **Table 5.6** and the models are compared in **Figures 5.15** to **5.20**.

There was a significant improvement in the model deviation and correlation coefficient (R^2-value) of model 2 compared to model 1. When comparing **Figures 5.15** and **5.16**, it could be seen that model 2 gave a much better prediction of values at 548 K (275 °C) than model 1. For model 1, the model values at 548 K were much lower than the measured values. At 523 K, both models gave similar results. At 498 K, model 2 was slightly better, while at 473 K (200 °C) model 1 gave better predictions that model 2. The error function

was structured in such a way as to minimise the difference between the model values and the measured values. The main reason for the improvement obtained by model 2 over model 1, was due to better fitting of measured data at the higher temperatures.

Table 5.6: Kinetic model parameters for ethanol dehydrogenation

Parameters	Model 1	Model 2
A'	$8.014*10^{4}$	$4.6841*10^{5}$
A'_A	$3.557*10^{-4}$	$1.0078*10^{-5}$
A'_R	$3.941*10^{-6}$	$6.2135*10^{-6}$
A'_S	$9.683*10^{-4}$	$6.1854*10^{-4}$
$-E/R_0$	-5491.1	-6424.6
$-E_A/R_0$	1351.1	3187.4
$-E_R/R_0$	3586.6	3390.0
$-E_S/R_0$	2288.0	2245.5
MD	8606.49	4914.21
R^2	0.928	0.966

A' is in [mol/kg cat.h.kPa]; $-E/R_0$ is in K

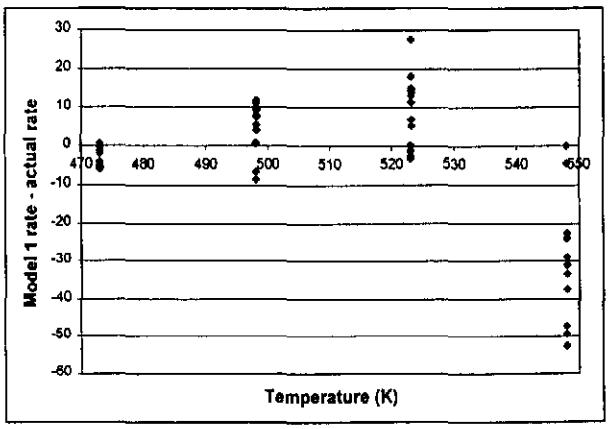

Figure 5.15: Difference between model 1 rates and actual rates at different temperatures

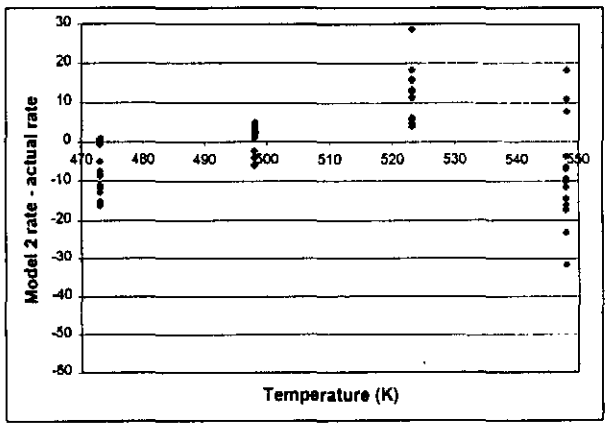

Figure 5.16: Difference between model 2 rates and actual rates at different temperatures

In **Figures 5.17** and **5.18**, the percentage deviation between model values and actual values are shown. For model 2 there are a few points at 498 K and above with very large percentage deviations (greater than 50%). Those are reaction rates at very high acetaldehyde concentrations. The reactions rates at high acetaldehyde concentrations are very low and a small difference between the predicted and measured values cause huge percentage deviations.

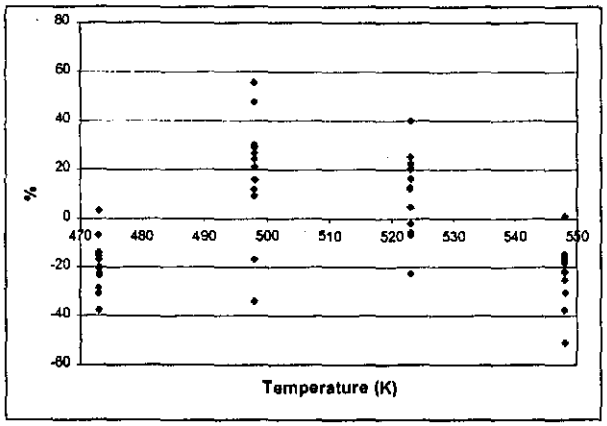

Figure 5.17: Percentage deviation between model 1 rates and measured rates

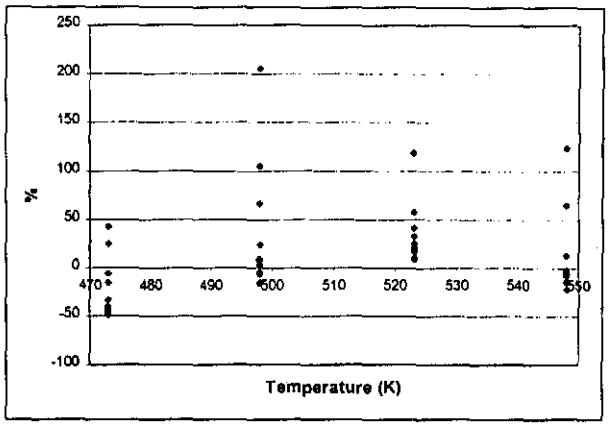

Figure 5.18: Percentage deviation between model 2 rates and measured rates

Figures 5.19 and **5.20** compare the measured reaction rates with the modelled reaction rates. The solid diagonal line on both graphs indicates a perfect fit.

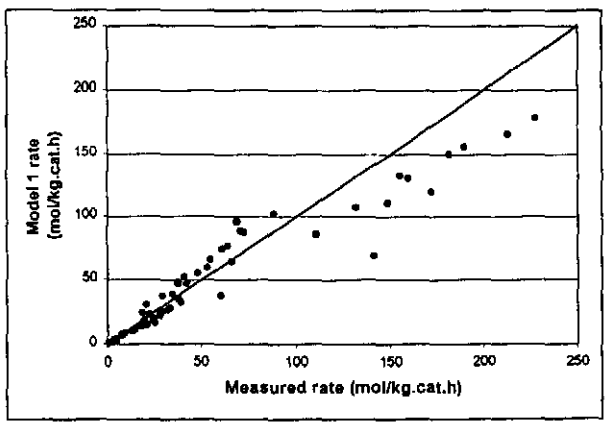

Figure 5.19: Model 1 rates vs. actual rates at different rate values

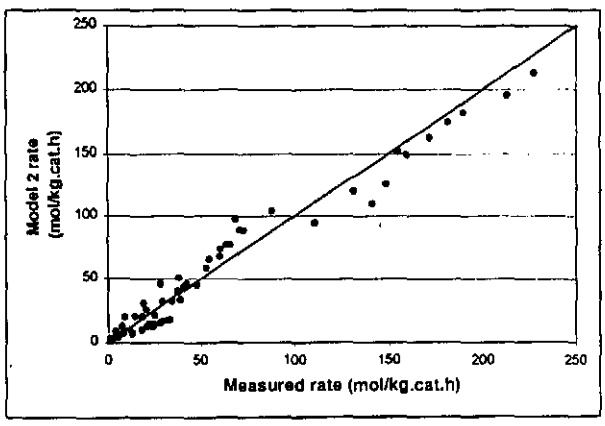

Figure 5.20: Model 2 rates vs. actual rates at different rate values

Figure 5.19 indicates that model 1 fits data well when the reaction rate is below about 50 (mol/kg cat.h), which is the reaction rate at the lower temperatures. At high reaction rates (high temperatures), the model values are significantly lower than the measured values. For model 2, the calculated values show more variance (compared to model 1) for reaction rates below 50 (mol/kg cat.h). For reaction rates above 50 (mol/kg cat.h), the model values are, however, much closer to the measured values than for model 1.

It must be stressed that the models were formulated for data from 200 °C to 275 °C (473 K to 548 K). Measured reaction rates at 300 °C (573 K) were compared to predictions from both model 1 and model 2. The difference between model values and measured values are summarised in **Figure 5.21**. For both models, the model values were generally higher than the measured values (see **Figure 5.13** and the discussion thereof). Model 1 predicted measured reaction rates at 573 K far better than model 2 did. The correlation coefficients are:

- Model 1: $R^2 = 0.953$ and
- Model 2: $R^2 = 0.918$.

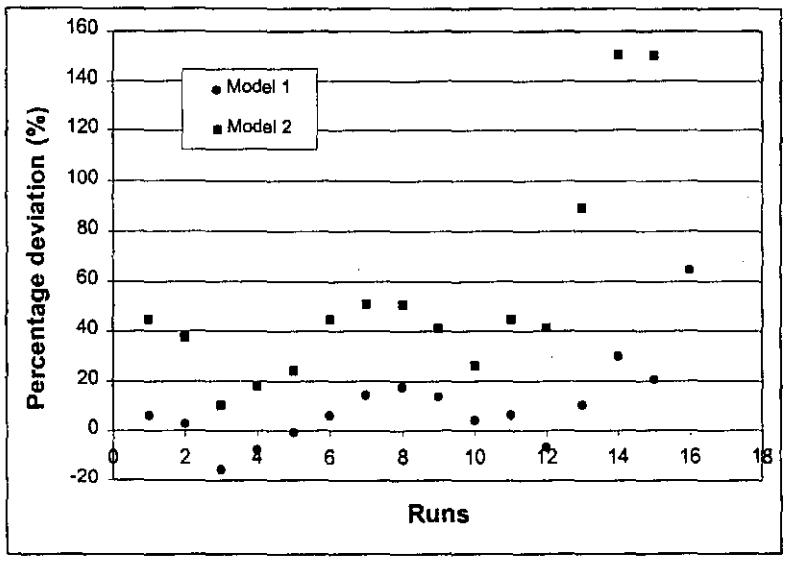

Figure 5.21: Percentage deviation between model values and measured values at 573 K

The reason why model 1 predicted reaction rates at 300 °C better than model 2 did, was due to the fact that catalyst deactivation occurred at 300 °C. The measured reaction rates were much lower than the true reaction rates at 300 °C. Since model 1 generally under predicted

reaction rates, it thus gave a better prediction of the 'lower' reaction rates at 300 °C that resulted due to catalyst deactivation.

5.3.2. 2-BUTANOL DEHYDROGENATION

Table 2.5 listed possible rate equations for reversible reactions. Of equations **2.17** to **2.21**, only **2.18** and **2.19** show an inverse quadratic relationship towards the MEK partial pressure (or concentration). Reaction rate data in this study indicated a strong inverse quadratic relationship between the observed reaction rate and the MEK partial pressure. Perona and Thodos (1957) determined reaction kinetics for the dehydrogenation of 2-butanol between 343 °C and 399 °C over solid brass spheres (65% copper and 35% zinc). Under those conditions, they found the desorption of hydrogen from a single site (equation **2.21**) to be rate limiting. Ford and Perlmutter (1964) used a brass tube (60% copper and 40% zinc) as catalyst and carried out the dehydrogenation reaction at temperatures between 316 °C and 427 °C. From 350 °C to 400 °C alcohol adsorption was rate limiting, while at both higher and lower temperatures the single site surface reaction was rate limiting. Thaller and Thodos (1960) performed experiments with smaller brass catalyst particles (50 to 60 mesh; 65% copper and 35% zinc) with a larger surface area. Below 300 °C the reaction was dual site, surface reaction controlling (equation **2.18**), while at higher temperatures the reaction was dual site, hydrogen desorption controlling.

For equation **2.19** to be applicable, the initial reaction rates for different hydrogen-2-butanol feeds had to be independent of 2-butanol pressure (Thaller and Thodos, 1960). That was not true and equation **2.19** could not be used. Equation **2.18** provided a reasonable fit to the data obtained in this study. The parameters in equation (**5.4**) were determined at temperatures from 190 °C to 280 °C for the dual site, surface reaction controlling mechanism. The linear fits to the data, which were used to determine the reaction rate parameters, are given in **Appendix C2**. **Figures 5.22** and **5.23** show typical linear fits at 220 °C and 280 °C, respectively.

The reaction rate was most sensitive to the MEK concentration. The large negative slope indicates strong MEK adsorption. The adsorption coefficients at the different temperatures are listed in **Table 5.7**.

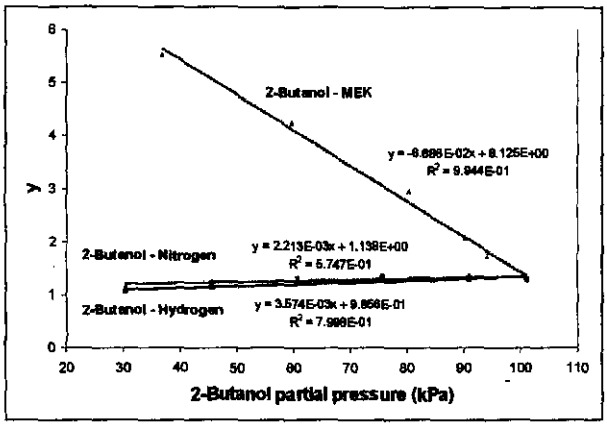

Figure 5.22: Linear fits of reaction rate data at 1 atm. total pressure and 220 °C

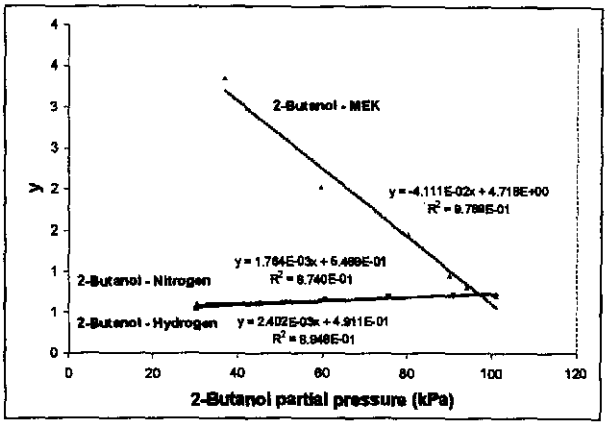

Figure 5.23: Linear fits of reaction rate data at 1 atm. total pressure and 280 °C

Table 5.7: Reaction rate parameters for 2-butanol dehydrogenation

T (°C)	k' mol/kg cat.h.kPa	K_A kPa^{-1}	K_S kPa^{-1}	K_R kPa^{-1}
190	0.339	0.001433	-0.00129	0.11735
220	0.772	0.001195	-0.00126	0.06075
250	1.713	0.002987	-0.00225	0.05232
280	3.342	0.003225	-0.00109	0.06432

(A = 2-butanol, S = hydrogen, R = MEK)

The trends in the k' and K_R values were in line with the theory (Peloso et al., 1979), except at 280 °C where K_R showed an increase instead of a decrease. From initial experiments, the same conclusion could be drawn for this reaction as for the ethanol dehydrogenation reaction (see **5.3.1**). Very little catalyst deactivation took place at 250 °C and below (see **Figure 5.8**), but at 310 °C (**Figure 5.8**) significant deactivation took place. Both sintering and coking played an important role in catalyst deactivation at the higher temperatures. The observed

reaction rate would be lower due to changes in catalyst activity and not due to stronger MEK adsorption.

Both K_A and K_S (the adsorption coefficients for 2-butanol and hydrogen) were negligible compared to the adsorption coefficient of MEK (K_R). When adsorption took place, the reaction rate slowed down. This was because diffusion resistance of the feed molecules to the active sites increased. Negative adsorption coefficients indicated an increase in reaction rates. The negative hydrogen adsorption coefficients (K_S-values) contradicted the theory of the dual site, surface reaction controlling mechanism, but the values were so small that the equation still fitted the data very well.

The reasons for the increase in reaction rate with hydrogen in the feed have been documented for other dehydrogenation reactions and was not unexpected where coking tended to deactivate the catalysts. Sheintuch and Dessau (1996) cited many references where hydrogen was co-fed with either an alcohol or an alkane and where improved dehydrogenation activity was reported. Hydrogen in the feedstream reduced coking (Sheintuch and Dessau, 1996) and it reduces the partial pressure of the alkane or the alcohol, which is favourable for higher conversions (Ertl et al., 1997).

K_A and K_S were taken as zero for a first approximation. The following Arrhenius expressions were formulated for data obtained at temperatures from 190 °C to 250 °C (463 K to 523 K) by using equation (**5.12**), (temperature is in K). **Figure 5.24** represents the data graphically.

For T = 463 K to 523 K:

$Ln(k') = 13.628-6903/T$ $(R^2 = 0.944)$ **(5.23)**

$Ln(K_R) = 3298/T - 9.3377$ $(R^2 = 0.905)$ **(5.24)**

The equilibrium constant for 2-butanol dehydrogenation could be expressed by the following equation (Kolb and Burwell, 1945):

$$Log(K_p) = -2790/T + 1.51*logT + 1.865 \quad \textbf{(5.25)}$$

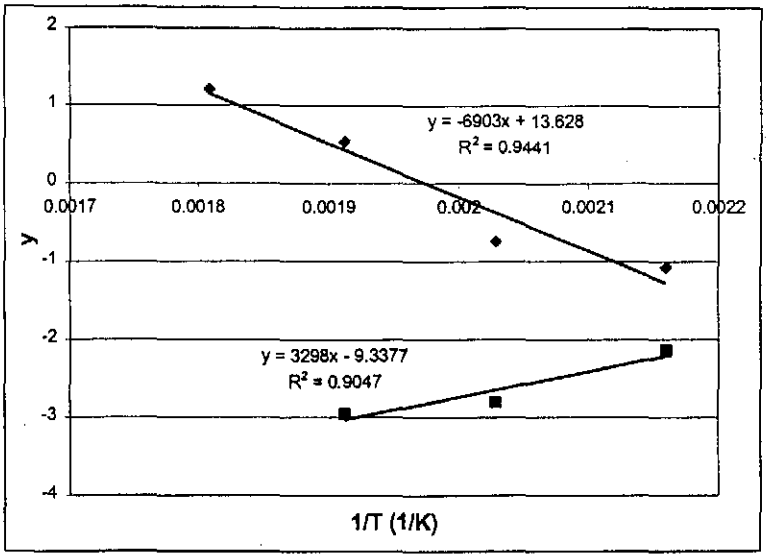

Figure 5.24: Parameters for 2-butanol reaction equation as a function of temperature

K_p, in atmospheres, was solved as a function of temperature and changed to K_{eq} in kPa. The function was then expressed in the exponential form (see equation **5.11**) and substituted into the rate equation (**5.3**) to yield equation (**5.26**).

The reaction equation from 190 °C (463 K) to 250 °C (523 K) could now be expressed as:

$$-r_A' = \frac{8.290\times10^{5}\times e^{-6903/T}\left(P_A - P_R P_S/(3.538\times10^{8}\times e^{-7100/T})\right)}{\left(1+8.804\times10^{-5}\times e^{3298/T}\times P_R\right)^2} \qquad (5.26)$$

with pressures in kPa and temperatures in K.

5.3.2.1. Equation optimisation

The reaction rate parameters for the dehydrogenation of 2-butanol were optimised in the same manner as those of the dehydrogenation of ethanol reaction. A detailed explanation of the steps was discussed in section **5.3.1.1**. For the 2-butanol reaction the error function was taken as:

$$EF = \sum_{1}^{n}(CV - MV)^2_{T=463K} + \left(\frac{(CV - MV)}{1.125}\right)^2_{T=493K} + \left(\frac{(CV - MV)}{1.25}\right)^2_{T=523K} \quad (5.27)$$

The different model parameters are listed in **Table 5.8**, where model 1 is the values determined with multiple linear regression and model 2 is the optimised values. Both models were only valid from 190 °C to 250 °C and at a 2-butanol feed pressure of 1 atmosphere.

Table 5.8: Kinetic model parameters for 2-butanol dehydrogenation

Parameters	Model 1	Model 2
A	$8.290*10^5$	$1.240*10^5$
A_R	$8.804*10^{-5}$	$8.924*10^{-5}$
$-E/R_0$	-6903	-6042
$-E_A/R_0$	3298	3165
MD	12724	3162
R^2	0.9478	0.9430

A is in [mol/kg cat.h.kPa], and

$-E/R_0$ is in K

The most important indicator of model performance, relative to measured data was the model deviation (MD value). The lower the deviation, the better the model. The optimised values of model 2, compare to model 1, gave a more accurate prediction of reaction rates. The exclusion of adsorption coefficients for 2-butanol and hydrogen in the reaction rate equation was an acceptable simplification. Predictions remained accurate without these parameters in the rate equation. **Figure 5.25** compares the performances of model 2 and model 1. Model 2 is more accurate at the higher reaction rate values.

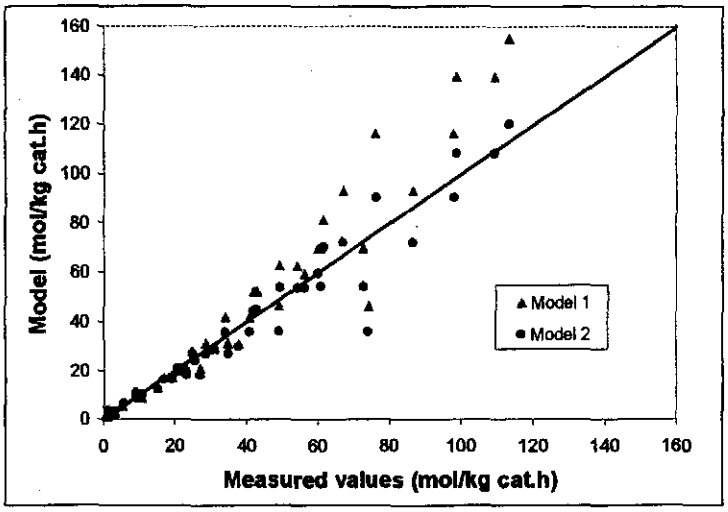

Figure 5.25: Comparison between measured reaction rates and model reaction rates

5.4. SUMMARY

Catalysts reduced at 340 °C and 400 °C showed a sharp decline in activity after reduction compared to catalysts reduced at 255 °C, mainly due to sintering. At 280 °C and below, a 14.4 wt % copper on silica catalyst remained stable over a 24 hour period. At 340 °C and higher, the catalyst deactivated by more than 30% over a 24 hour period. The addition of Cr and Co to Cu did not improve the stability of the 14.4 wt % copper on silica catalyst. The activity of the Cu/Cr/Co on silica catalyst was similar to that of pure copper on silica, but the selectivity towards acetaldehyde production was significantly lower at all temperatures tested. Further deactivation testing indicated that during the first 24 hour period, both sintering and coking occurred during the dehydrogenation of ethanol. Thereafter, coking was the main deactivation mechanism.

For the dehydrogenation of ethanol, there was strong interphase mass transfer resistance, while for 2-butanol dehydrogenation there was no clear indications of interphase mass transfer resistance.

The controlling reaction mechanisms and reaction rate parameters for both the dehydrogenation of ethanol and 2-butanol were determined. Ethanol dehydrogenation was studied from 200 °C to 300 °C and 2-butanol dehydrogenation from 190 ° to 280 °C. Both

reactions could be well described by the dual site, surface reaction controlling mechanism. The reaction rate coefficients and the adsoption parameters for each reaction were determined. In both reactions the organic product (either acetaldehyde or MEK) had a dominant adsorption coefficient.

6. Pd MEMBRANE PREPARATION AND CHARACTERISATION

This chapter will present results on electroless Pd plating. Comments will be made on the various plating steps and the composition of the plating solution. Membrane characterisation results will be presented and discussed. This will include surface characterisation with SEM and permeance testing with both hydrogen and nitrogen. For permeance testing, a positive feed pressure or a sweep gas was employed alternatively.

Permeance results were compared to literature data and the effect of film thickness on permeance parameters will be discussed. Arrhenius parameters were determined by performing experiments at different temperatures.

6.1. MEMBRANE STRUCTURE

A cross section view of the SCT membrane was shown in **Figure 3.2** (as reported here). **Figures 6.1** to **6.3** show the scanning electron microscope images of the same membrane structure obtained from a

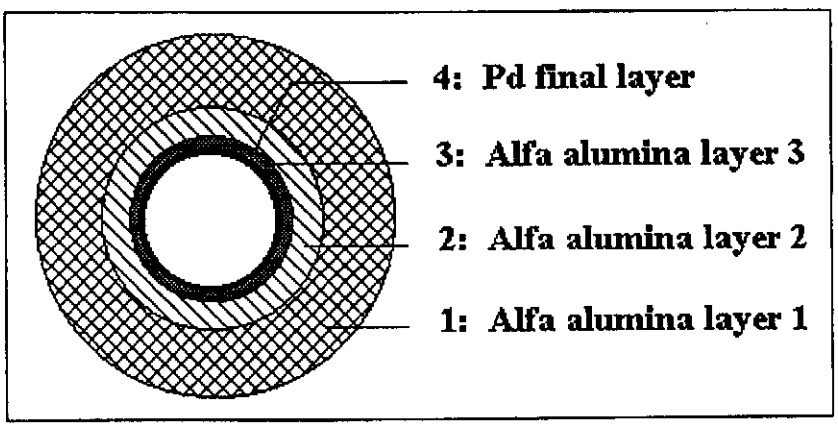

Figure 3.2: SCT membrane structure

Figure 6.1: Cross section view of a three layer SCT membrane

In the cross section view there were the three, clearly visible, layers (**Figure 6.1**). **Figures 6.2** and **6.3** show that the surface had a smooth structure, with plenty of pores. The latter were very suitable for electroless plating.

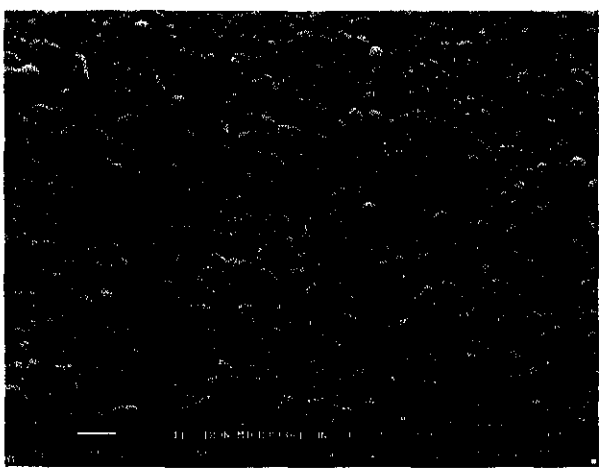

Figure 6.2: Top view (20 000x) of a three layer SCT membrane

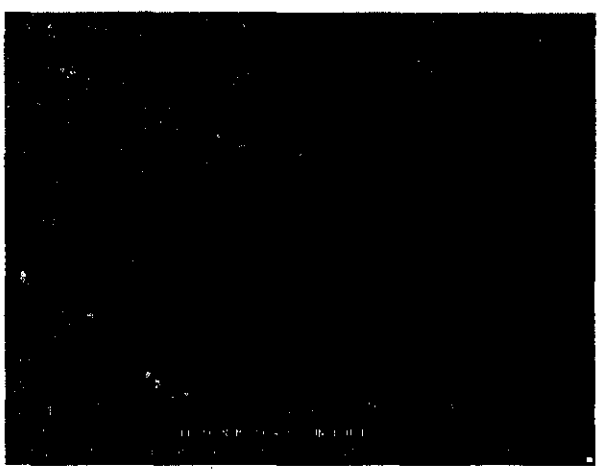

Figure 6.3: Top view (5 000x) of a three layer SCT membrane

6.2. SURFACE PRETREATMENT

Experimental details of the pretreatment process were discussed in section **3.3.2.1**. A few remarks warrant re-emphasised here. The conventional pretreatment solution (as proposed by

Shu et al., 1993) deposited a small amount of tin. Keuler (1997a) found, by PIXE analysis, between 0 and 1% tin in Pd films of 5 microns. Such low tin percentages would increase by about 3 times when the film thickness is reduced to 1.5 microns, since the pretreatment procedure remained the same. The result is that in this study a tin to palladium molar ratio that was about eight times less than the conventional ratio was employed. This was done by both increasing the palladium concentration and reducing the tin concentration in the pretreatment procedure.

The tin in the film should not have a significant effect on the hydrogen permeance parameters. The main reason for reducing the tin was to try and improve its high temperature membrane stability. In the time of this study, another research group had similar ideas to improve the membrane stability. Paglieri et al. (1999) started experimenting with pretreatment procedures without tin. They speculated that tin, with its low melting point (505 K), could enhance metallic diffusion at the grain boundaries and lead to an increase in defects. They concluded that the presence of tin at the alumina-palladium interface contributed to selectivity decline.

6.3. THE ELECTROLESS Pd PLATING PROCESS

The composition of the plating solution and the plating kinetics for the plating of the inside of a membrane tube vary from plating on the outside of a tube. **Table 6.1** indicates the differences between the plating solution composition for plating the inside and the outside surfaces of a membrane. The optimised plating solution composition for plating outside surfaces was taken from Keuler et al. (1997b).

Keuler (1997a) used 27.5 g of 10 wt % solution $(NH_3)_4Pd(NO_3)_2$ per litre of plating solution for plating the outside of membrane tubes (selective layer on the outside). In the present study, 4.96 g of $(NH_3)_4PdCl_2.H_2O$ per litre of solution was used for plating the inside surface of membrane tubes (selective layer on the inside). When plating the inside of tubes, a much higher Pd concentration in the plating solution can be used as compared to plating on the outside. Initially the hydrazine:Pd molar ratio was 1 to 1 at the start for plating the inside of

tubes. Later it was reduced to the value given in **Table 6.1** to slow down the plating rate. In no experiment did decomposition of the plating solution occur while plating the inside of the membrane tube, even though a higher Pd concentration was used, in addition to a much higher hydrazine concentration, initially (hydrazine:Pd of 1:1). The reasons are that the catalysed membrane surface is the only one available for plating and the volume to available plating area ratio is much smaller for tubes on the inside. When plating on the outside of the membrane, plating solution is also in contact with the plating reactor, thus increasing the available area for Pd deposition.

Table 6.1: Composition (per litre) of plating solutions for membrane plating

Components	Outside of tube	Inside of tube
Pd (g)	1.47	2.00
Ammonia (28 wt %) (ml)	200	400
EDTA (g)	100	80
Buffer pH = 10 (ml)	100	-
Hydrazine:Pd molar ratio	about 0.7	0.35 at start
Temperature (°C)	72	72

6.3.1. SOLUTION FEEDING TO MEMBRANE TUBE

Stirring the tubular membrane, covered with teflon tape on the outside, in the plating solution at 72 °C resulted in very poor plating on the inside of the tube. There was insufficient circulation of solution through the tube and the large volume to active surface area also promoted solution decomposition.

The second solution feeding method tested was continuous pumping of solution through the tube fixed in the reactor and placed in the water bath. A flow rate of 120 ml/h was used and the same solution was pumped through the tube several times, increasing the hydrazine concentration after each run. The sharp decline in Pd concentration with time, made this method unsuitable. At a flow rate of 120 ml/h, it took the solution 5 minutes to pass from end to end in the membrane tube. During the first run the Pd concentration dropped by about 30% during that time, resulting in a film of non-uniform thickness over the length of the

membrane. The film was thicker at the entry point than at the exit point, because of the declining Pd concentration and decreasing reaction rate. For this method to be successful, much higher feed flow rates have to be used and the feed direction reversed every few minutes. It was decided to use a batch process to produce coatings of even thickness along the full length of the tube.

Figure 6.4 indicates the decrease in Pd concentration in solution as a function of the number of plating session. Values were obtained using ICP analysis. Hydrazine was added after each plating session. The initial hydrazine:Pd molar ratio was 1 to 1. Half the initial volume of hydrazine was added after 10 minutes of plating. After a further 15 minutes of plating (25 minutes total plating), the original volume of hydrazine was added and then after a further 20 minutes (45 minutes total plating), a few drops of 35 wt % hydrazine was added. Reaction continued for an additional 30 minutes (75 minutes in total). The results are presented in **Figure 6.4**.

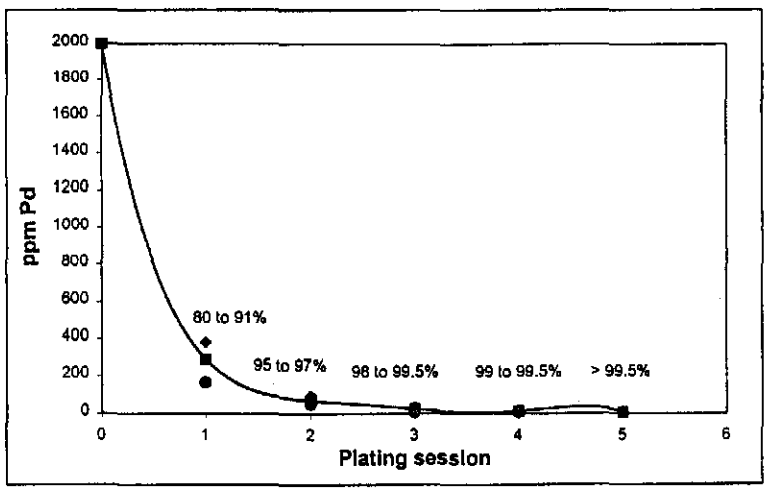

Figure 6.4: Pd concentration in solution after repeated plating sessions

The amount of Pd deposited after the first 10 minute session varied between 80 and 91% of the available amount in the 11.5 ml solution. Four different membranes were tested this way. After 4 plating sessions, 99% of the available Pd was extracted from solution and deposited on the membrane. Poor plating was observed in two cases and the hydrazine concentration reduced to the values listed in **Table 3.14**. The plating procedure was changed to that

tabulated in **Table 3.15**. After the first 20 minute session, between 50 and 60% of the Pd was deposited on the membrane. After three 20 minute sessions, more than 98% of the palladium was deposited.

6.3.2. EFFECT OF PLATING RATE ON MEMBRANE PERFORMANCE

The quality of the Pd coating is very dependent on the plating rate. If the plating rate is too fast, then the coating shows poor selectivity characteristics. The plating rate will become too fast when the hydrazine concentration is too high, the temperature is too high and/or the EDTA concentration is too low. The only variable that was changed, was the hydrazine concentration. Initially, at the start of plating experiments, the hydrazine:Pd molar ratio was 1 to 1, with plating characteristics as in **Figure 6.4**. Ten coatings were prepared in this way on 200 nm α-alumina membranes. Two were defective, because Pd bubbles formed on the membrane surface, causing leaks. After reducing the hydrazine concentration this problem was solved. **Figures 6.5** to **6.11** show SEM images of the two poorly performing membranes. The calculated Pd thickness of membranes (a) and (b) were about 1.5 microns. SEM images (**Figures 6.5** and **6.8**) show similar thicknesses. **Appendix D1** lists all the membranes on which extensive permeance testing was performed. Extensive permeance testing was not performed on membranes (a) and (b) due to their poor selectivity, and therefor they are not listed in **Appendix D1**.

Figure 6.5: Cross section of membrane (a) (10 000x)

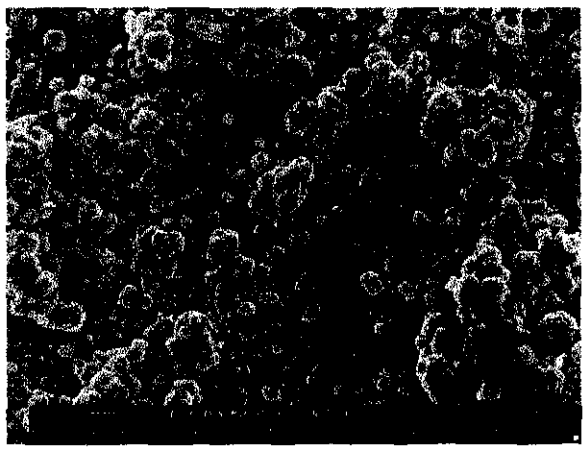

Figure 6.6: Top view of membrane (a) (25 000x)

Membranes (a) and (b) in **Figures 6.5** to **6.11**, had two different surface structures and in both cases there were clear defects. The cross section view of membrane (a) (**Figure 6.5**) indicates poor adhesion of the metal film to the alumina support. The Pd film is the thin layer on top of the alumina base. The dense layer higher up is part of the resin. The surface is not smooth (**Figure 6.6**), but consists of small metal clusters scattered over the surface area. Under high magnification (**Figure 6.7**), there are tiny pores visible in the metal particles. It is those pores or defects that caused poor selectivity.

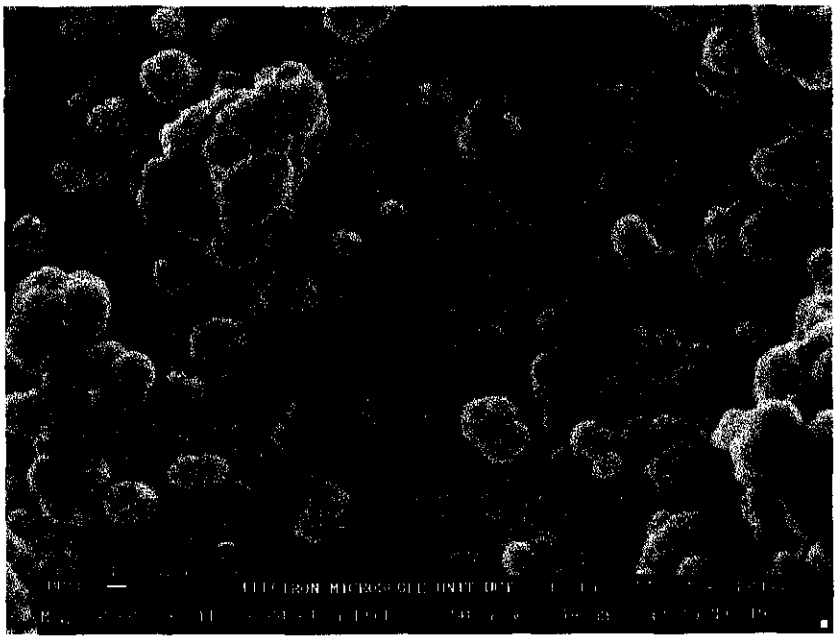

Figure 6.7: Top view of membrane (a) (50 000x)

Figure 6.8: Cross section of membrane (b) (10 000x)

Figure 6.9: Top view of membrane (b) (25 000x)

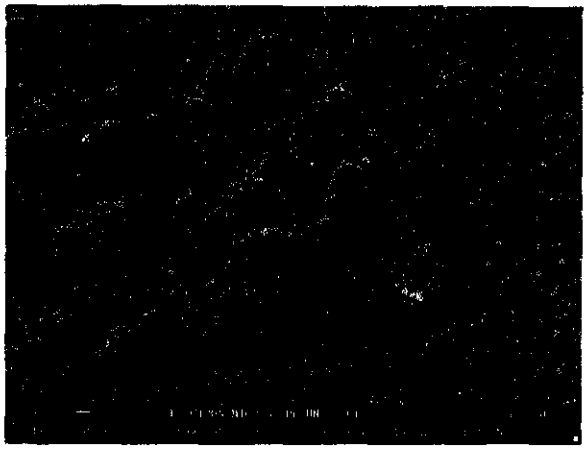

Figure 6.10: Top view of membrane (b) (5000x)

Figure 6.11: Top view of membrane (b) (25000x)

The surface of membrane (b) seems dense both on the cross section view (**Figure 6.8**) and on the top view (**Figure 6.9**) images. There were no continuous defects in the structure. Upon further investigation some areas in the coating were identified where the coating was clearly porous (**Figure 6.10**). These defected areas were spread out over the surface. Furthermore, the defects did not seem to be inside metal clusters as in the case of membrane (a), but between metal particles (**Figure 6.11**).

6.3.3. Pd MEMBRANE THICKNESS MEASUREMENT

Membranes were tested as discussed in **Chapter 3**. The thicknesses of the deposited layers were calculated from the mass increase (mass after testing minus mass before electroless plating). The mass before plating was taken as the mass of the clean membrane plus the mass after pretreatment, divided by two. By doing that, it was assumed that half of the metal deposited during the pretreatment stage penetrated into the membrane's pores and the other half deposited on the outer surface. The samples that were used for testing as well as all their characteristics are listed in **Appendix D1**. Two sets of experiments were performed: Those in which a positive feed pressure was used and those in which a sweep gas was used.

6.3.4. MEMBRANE POST PLATING TREATMENT

After plating, the membranes were stirred in ammonia to dissolve EDTA in the membrane pores. Stirring in ammonia and heating overnight at 240 °C was not sufficient to remove all

carbon from the membrane pores. Brown spots were visible in some areas on the outside membrane surface, indicating the presence of carbon. Two possibilities exist: either 240 °C was too low a temperature for full oxidation to take place or the oxygen to carbon contact in the pores behind the dense palladium layer was very poor.

Hydrogen and nitrogen permeance tests were performed on a membrane without and with additional oxidation treatment. The results are shown in **Figures 6.12** and **6.13**.

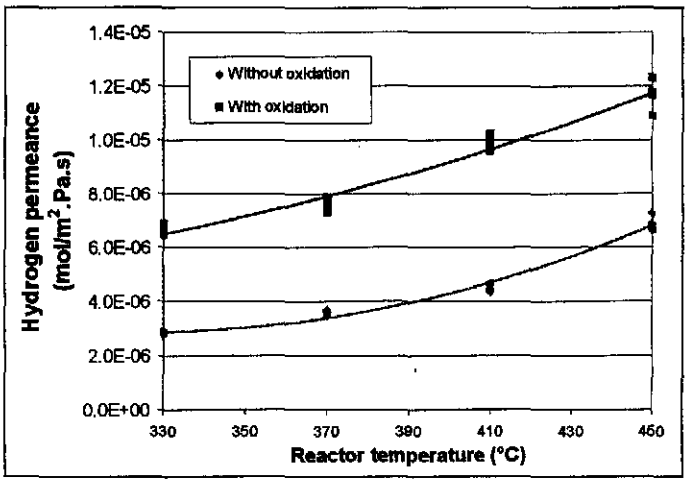

Figure 6.12: Effect of oxidation post treatment on H_2 permeance (membrane 2a, 1.43 μm Pd)

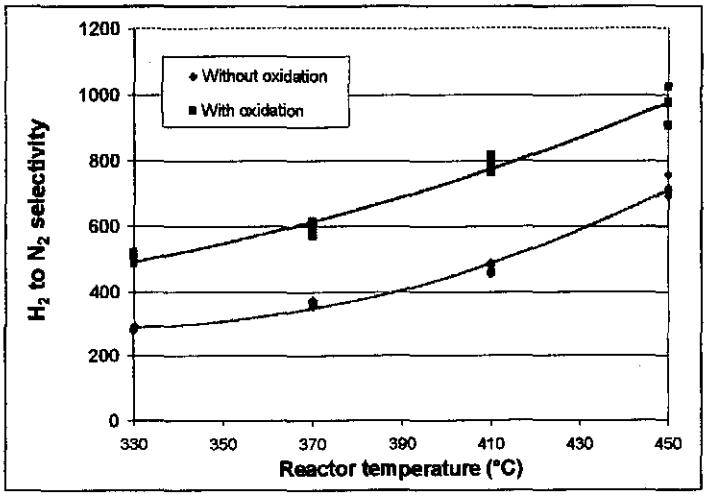

Figure 6.13: Effect of oxidation post treatment on selectivity (membrane 2b, 1.43 μm Pd)

The characteristics of membranes (2a) and (2b) are listed in **Appendix D1**. There was a significant increase in hydrogen permeance after oxidation at 320 °C. These results confirmed the presence of either an EDTA or carbon layer in the pores behind the Pd film. Reduction in hydrogen at up to 500 °C did not thermally decompose the layer. When oxygen was forced through the defects in the Pd film and the membrane support pores under pressure (between 1.0 and 2.5 bar, depending on the membrane selectivity) at 320 °C, most of the remaining precursor was removed. That resulted in higher hydrogen permeances through the Pd membrane and improved selectivity (see **Figures 6.12** and **6.13**).

In certain cases (membrane N7 and N8, see **Appendix D1**), even after oxidation there was some carbon present in the film. A good indicator of the presence of carbon in the film was the rate at which steady state was obtained after the membrane was reduced and switching from nitrogen to hydrogen during analysis. If steady state was obtained quickly (in less than 3 to 5 minutes) it indicated a pure film. When carbon was present in the film it could take 10 to 15 minutes (or even longer) for the hydrogen flux to stabilise (especially at the lower hydrogen feed pressures).

When carbon was present in the film it could be expected that the film would show poorer stability over time at high temperatures compared to pure films. This assumption was, however, not further investigated.

6.4. THE EFFECT OF SUPPORT STRUCTURE ON Pd FILMS

Several Pd plating experiments were performed on SCT membranes with a final 5 nm pore size layer of γ-alumina, to produce Pd films of less than 1 micron. The plating steps were successful and thin films could be synthesised. Upon heating, even at the drying stage (240 °C), bubbles and cracks formed in the film. All selectivity was lost. The loss of selectivity was a combination of poor metal to ceramic adhesion and a difference between thermal expansion coefficients for Pd and γ-alumina.

For those experiments, the higher hydrazine concentration was used (a hydrazine:Pd molar ratio of 1:1). Electroless plating with a lower hydrazine concentrations was not tested on the γ-alumina membranes. A lower hydrazine concentration (a hydrazine:Pd molar ratio = 0.35:1) should yield better results.

6.5. STRUCTURAL CHARACTERISATION OF Pd MEMBRANES

The structure of Pd membranes was investigated with a scanning electron microscope. Membrane (3b) and membrane (11) were studied. Their theoretical thicknesses were:

- 3b: two layers totalling 4.4 microns, and
- 11: 1 layer of 1.5 microns.

Data for all tested (permeances) Pd membranes are listed in **Appendix D1**. Membrane (11) broke in the reactor before permeance testing was performed and there is therefor no permeance data in **Appendix D1** for membrane (11).

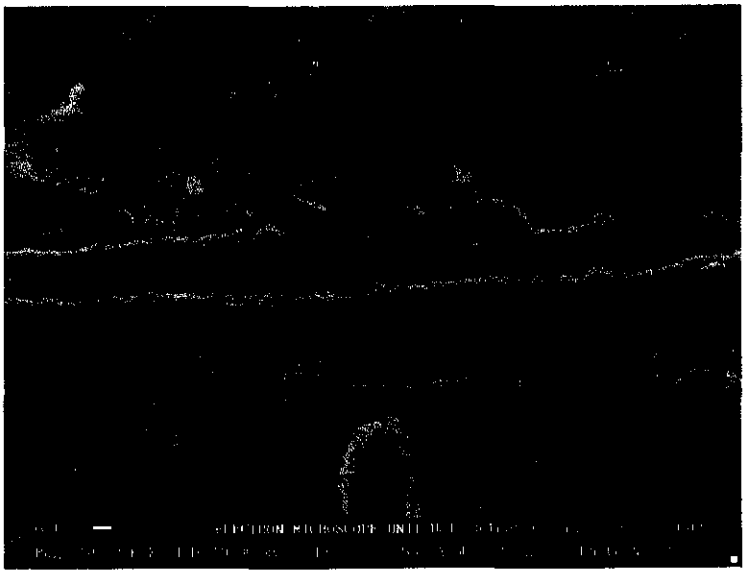

Figure 6.14: Cross section of membrane (3b) (10 000x)

The side view image of (3b) (**Figure 6.14**) clearly shows two Pd layers on the alumina support. Since no alloying was performed after the second coating, a single layer did not form at that stage. After application of the first layer (membrane 3a), the membrane was

tested. A second layer was applied and the membrane (membrane 3b) tested again. The combined thickness of the two layers should be about 4.4 microns. **Figure 6.14** shows, however, a total thickness of closer to 7 microns. This was the only membrane that showed deviation between the calculated Pd thickness and the SEM determined Pd thickness. For other membranes tested by SEM (a, b, c, d and 11), the results of the calculated thicknesses and the SEM determined thicknesses, were a good agreement. Top view images of (3b) (**Figures 6.15** and **6.16**) show a dense structure without any pores or defects. Selectivity data on (3b) confirmed a dense and compact film with very little defects (see **Appendix D1**).

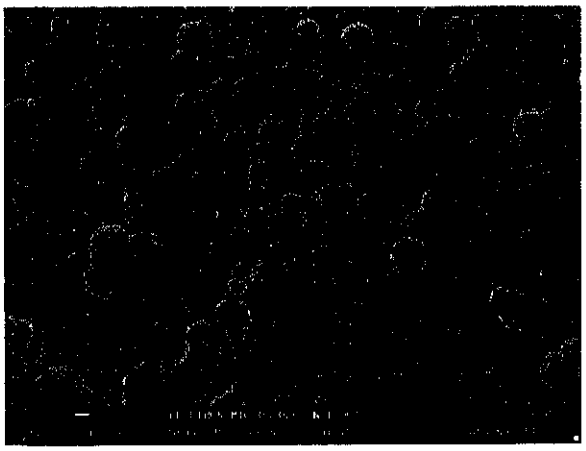

Figure 6.15: Top view of membrane (3b) (5000 x)

Figure 6.16: Top view of membrane (3b) (25 000x)

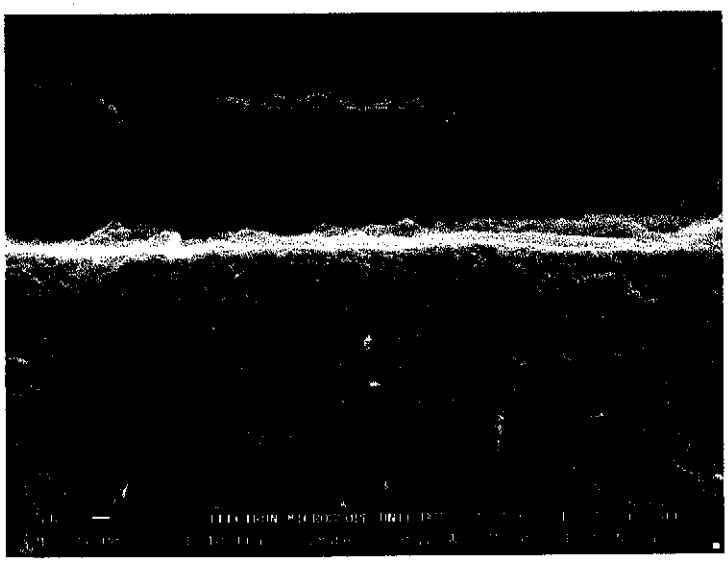

Figure 6.17: Cross section of membrane (11) (10 000x)

The calculated thickness of membrane (11) (1.45 microns) was in good agreement with the SEM determined thickness (from 1.0 and 1.7 microns). **Figure 6.17** shows a very dense layer on top of the 200 nm α-alumina support. Top view images (**Figures 6.18** and **6.19**) confirmed this. Under high magnification (**Figure 6.19**) it appears as if there are more grain boundaries for this thinner film compared to the thicker film of (3b) (**Figure 6.16**).

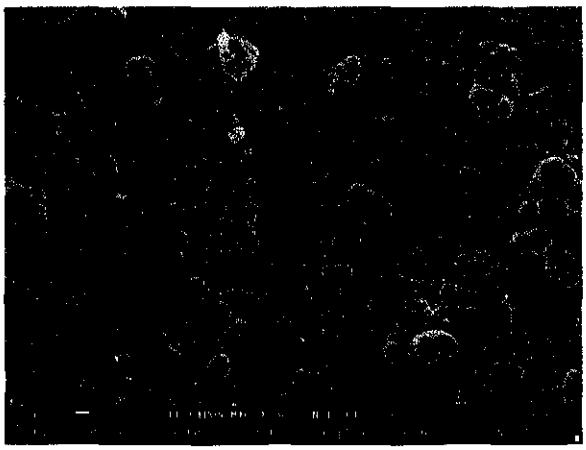

Figure 6.18: Top view of membrane (11) (5000 x)

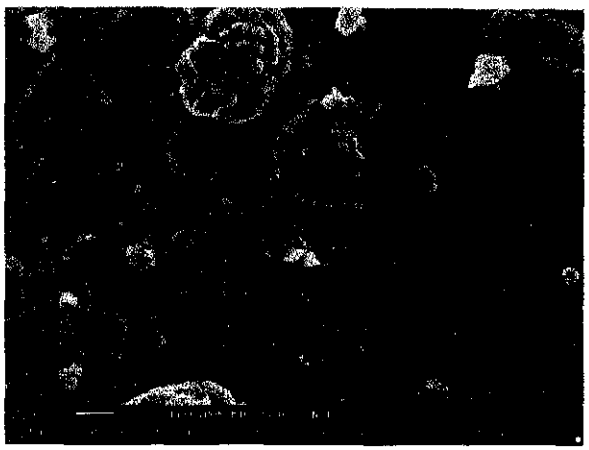

Figure 6.19: Top view of membrane (11) (25 000x)

6.6. PERMEANCE TESTING OF Pd MEMBRANES

Membranes were tested under positive feed pressure conditions and with a sweep gas. Under positive feed pressure conditions, the effects of temperature, pressure difference and film thickness were studied. When a sweep gas was employed, the effects of temperature, space time and sweep gas ratios were tested. All the data is listed in **Appendix D1**.

The hydrogen permeance process was described mathematically in **Chapter 2**. The main equations were:

$$P_{er} = S_c D_0 e^{-E_D/R_0T} = P_0 e^{-E_D/R_0T} \qquad \textbf{(2.7)}$$

$$J = \frac{S_c D_0 e^{-E_D/R_0T}}{l}\left(P^n_{H_{2x}} - P^n_{H_{2y}}\right) = \frac{P_{er}}{l}\left(P^n_{H_{2x}} - P^n_{H_{2y}}\right) \qquad \textbf{(2.8)}$$

Pressure data is necessary to calculate the value of n, which is an indication of the flow process through the film. Temperature data is necessary to calculate the Arrhenius parameters (P_0 and E_D) in equation (**2.7**).

The parameters of each tested membrane were calculated and are listed in **Appendix D1**. The values will be discussed in the followings sections.

6.6.1. THE EFFECT OF ΔP ON H_2 AND N_2 PERMEANCE

Membrane selectivity was determined using hydrogen and nitrogen as testing gases. Nitrogen permeance is an indication of membrane defects or leaking. There are three factors that contribute towards the measured nitrogen permeance. They are:

- Leaking through defects in the electroless plated film,
- Leaking at the membrane reactor, graphite ring, enamel interfaces, and
- Leaking at the porous membrane, non-porous enamel and Pd film interfaces.

The contribution of the final two factors cannot be quantified, but from experience it is known that there is at least some leakage between the membrane and the reactor seal. The measured nitrogen permeance represents the worst case scenario or the maximum value.

6.6.1.1. Nitrogen experiments

Figures 6.20 to **6.23** show nitrogen permeances as a function of pressure and temperature at different Pd thicknesses (1.47 μm to 4.43 μm). The average pressure between the tube and shell side was used, it being the sum of the absolute pressures on the shell and tube sides divided by two. Theoretically, the average pressure should not have any effect on the nitrogen permeance (in mol/m².Pa.s) if it is Knudsen flow. For nitrogen, the permeance is proportional to the amount of defects. The more the defects, the higher the rate. Thinner films thus have a higher nitrogen permeance than thicker films. The effect of film thickness on membrane performance will be discussed in more detail later (**section 6.6.3**). **Figures 6.20** and **6.23** indicate that the nitrogen permeance varied little with an increase in average pressure, confirming that the flow through the membrane was Knudsen flow.

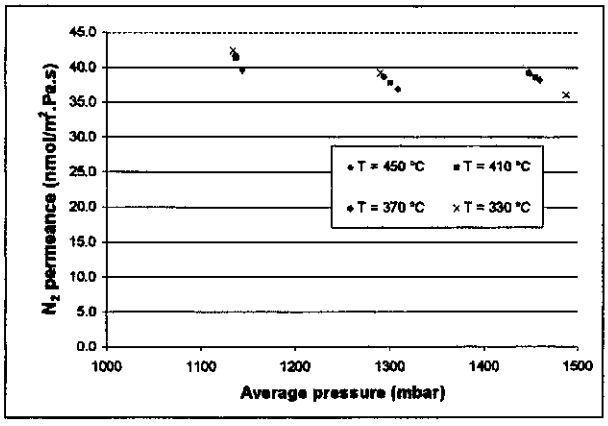

Figure 6.20: Effect of pressure on N_2 permeance for a 1.47 micron Pd film (6)

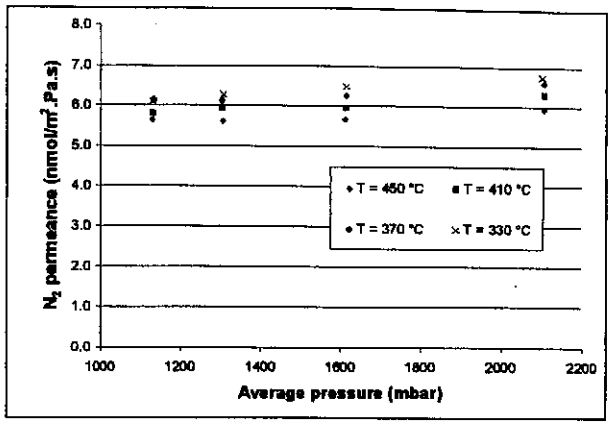

Figure 6.21: Effect of pressure on N_2 permeance for a 2.4 micron Pd film (3a)

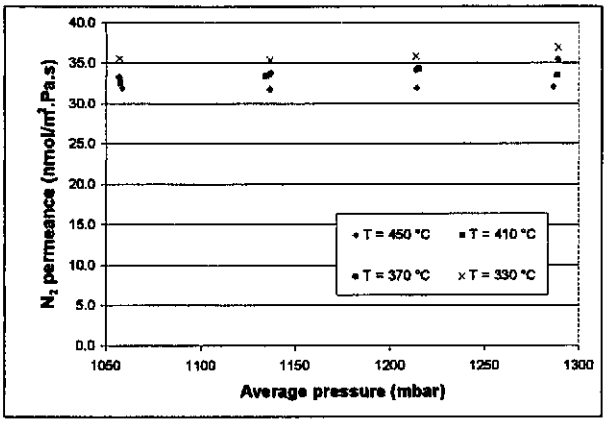

Figure 6.22: Effect of pressure on N_2 permeance for a 3.08 micron Pd film (1a)

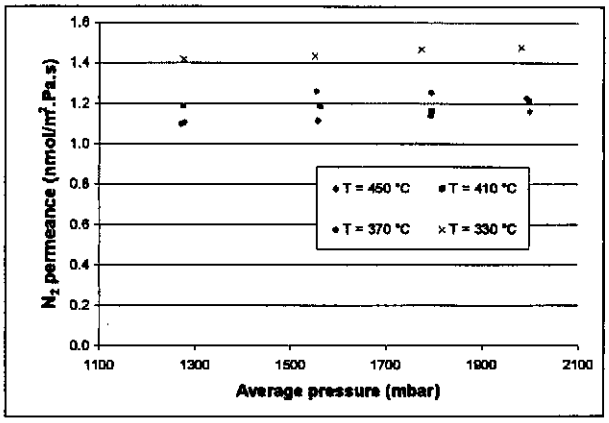

Figure 6.23: Effect of pressure on N_2 permeance for a 4.43 micron Pd film (3b)

6.6.1.2. Hydrogen experiments

The value of n in the flux equation (**2.8**) was calculated for every membrane and results are listed in **Appendix D1**. The R^2-value is an indication of the fit between the measured and calculated data. A value close to 1 indicates a very good fit. The value of n was assumed to be 1 and then the calculated values were compared to the measured values. The R^2-values were also found to be close to 1, indicating that the calculated and measured values were indeed similar. A n-value of 1 indicates a permeance which stays constant at different differential pressures. It must, however, be mentioned that the differential pressures at which the hydrogen permeances were determined were small (typically less than 150 mbar). When

the differential pressures are small, changes in the value of n have little effect on the quality of the fit.

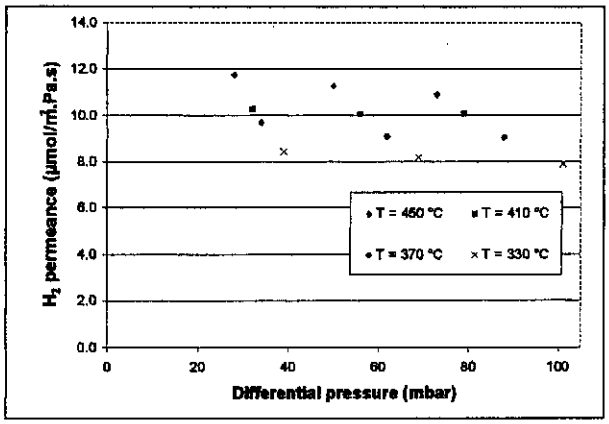

Figure 6.24: Effect of pressure on H_2 permeance for a 1.47 micron Pd film (6)

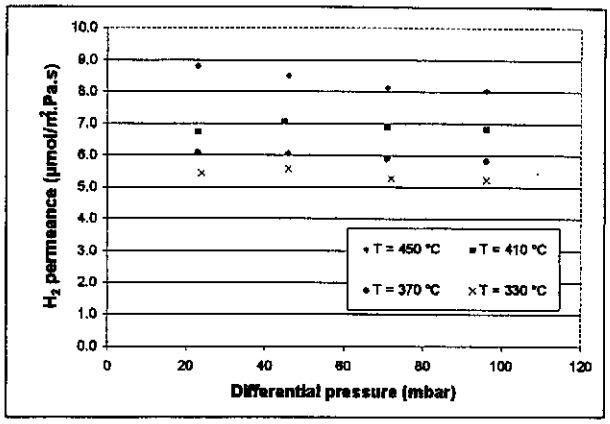

Figure 6.25: Effect of pressure on H_2 permeance for a 2.4 micron Pd film (3a)

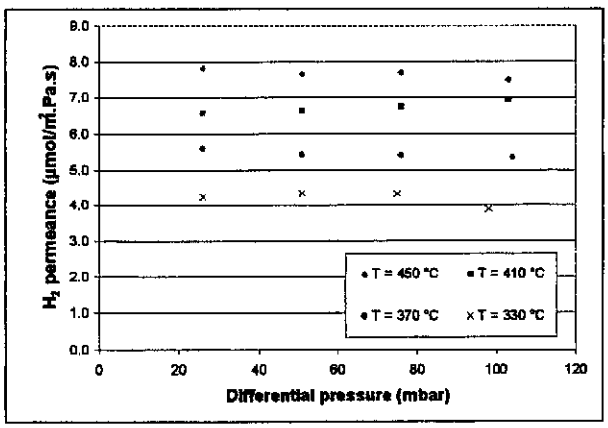

Figure 6.26: Effect of pressure on H_2 permeance for a 3.08 micron Pd film (1a)

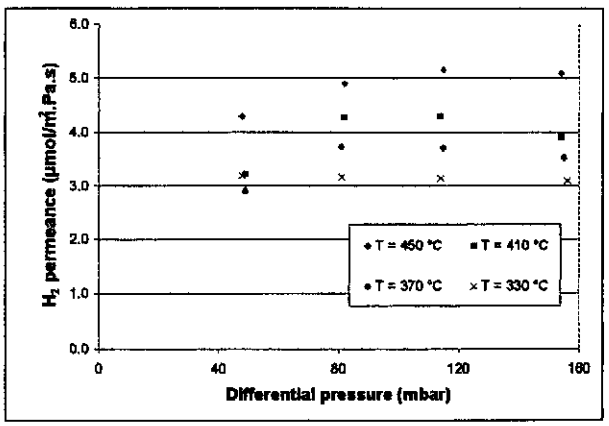

Figure 6.27: Effect of pressure on H_2 permeance for a 4.43 micron Pd film (3b)

The hydrogen permeance (**Figure 6.24** to **6.27**) did not vary considerably with pressure. Differential pressures below 40 mbar caused a slight deviation (see **Figures 6.25** and **6.27**) from the trend. The reason for this was that the error of the pressure probe was between 2 and 4 mbar and thus, at low pressures, there was some error in the measured values. A n-value of 1 indicates that hydrogen chemisorption on the palladium surface is the rate limiting step (Nam et al., 1999; Yan et al., 1994). Sievert's law, where n = ½, is not applicable to the thin films synthesised in this study. Diffusion is not the rate limiting step.

The film thickness and the permeance temperature have a very significant effect on the hydrogen permeance as will be discussed in the next sections.

6.6.2. THE EFFECT OF TEMPERATURE ON H_2 AND N_2 PERMEANCE

If the flow through a membrane is Knudsen flow, the flux through the membrane must decline when the temperature increases (see equation **2.2**).

$$J_i = \frac{G_f S_o}{\sqrt{2\pi M_i R_0 T}} \frac{\Delta P_i}{l} \qquad \textbf{(2.2)}$$

In section **6.6.1.1** pressure data for nitrogen permeance suggested that Knudsen flow might have been the mechanism of nitrogen transport through the defects in the Pd film. This indicated that the defects were in the lower nanometer range. For each of the fifteen Pd films tested, the nitrogen permeance was plotted as a function of temperature (see **Appendix D1**). For ten of the films, the nitrogen permeance declined with an increase in temperature (see **Figure 6.28** for a typical example). In four cases there were no clear permeance trend with temperature change (**Figure 6.29**) and in one case the permeance increased with increasing temperature (**Figure 6.30**).

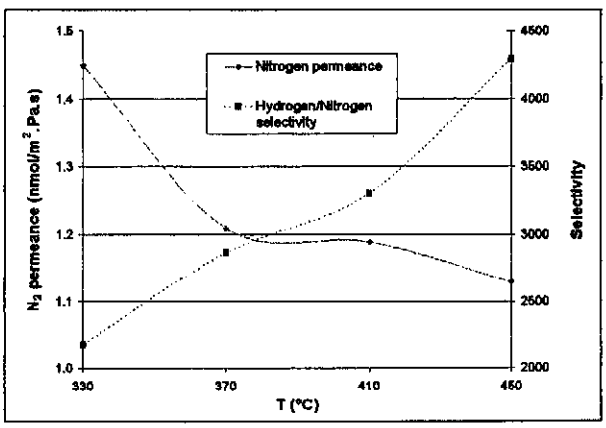

Figure 6.28: Selectivity data for membrane (3a)

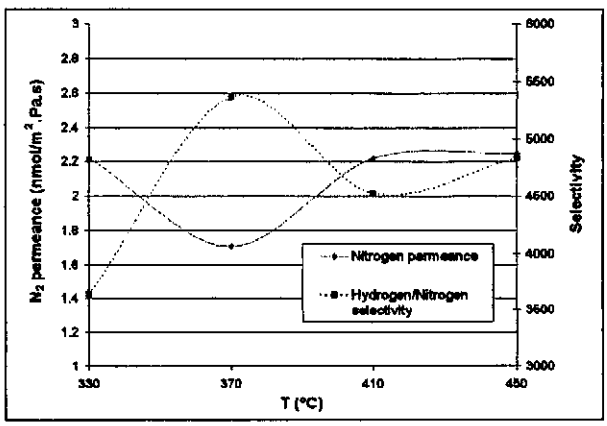

Figure 6.29: Selectivity data for membrane (N8)

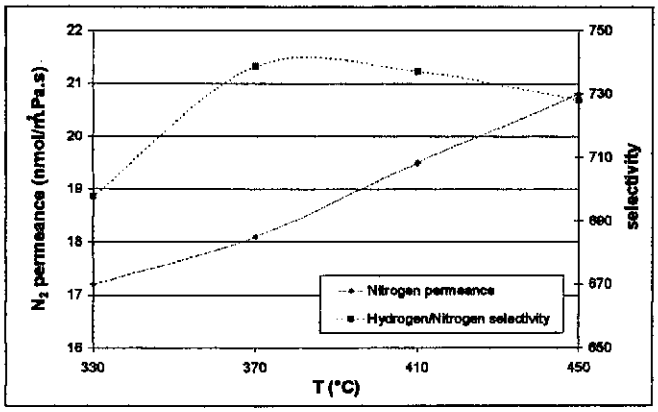

Figure 6.30: Selectivity data for membrane (N2)

The temperature data confirmed that some kind of Knudsen flow dominated when nitrogen passed through the palladium film defects. The reason for the decline in permeance was that the greater vibrational energy of the N_2 molecules at the higher temperature resulted in more resistance to flow through tiny pores and thus a decrease in permeance.

Hydrogen temperature data was fitted to the Arrhenius equation (**2.7**). Arrhenius parameters for each film are listed in **Appendix D1**. The high R^2-values of the Arrhenius fits indicate that the data fitted the equation well. The hydrogen permeance increased with temperature, as predicted by equation (**2.7**). **Figures 6.31** and **6.32** show typical increases in hydrogen permeance with an increase in temperature.

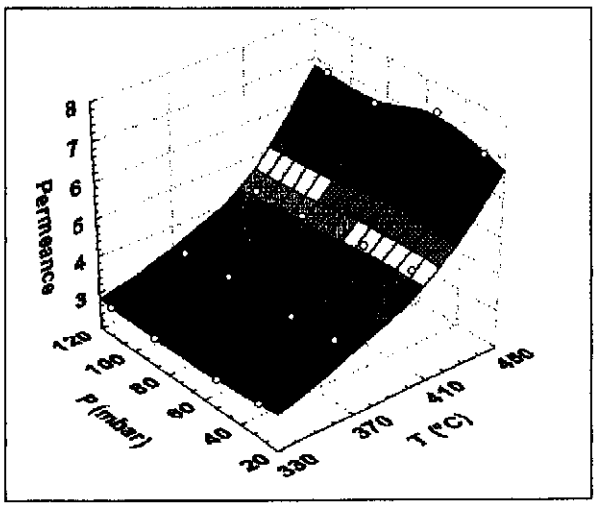

Figure 6.31: Hydrogen permeance in μmol/m^2.Pa.s (membrane 2a)

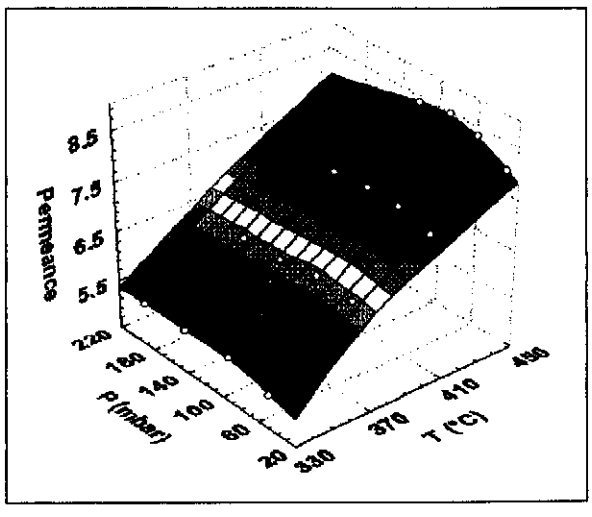

Figure 6.32: Hydrogen permeance in μmol/m^2.Pa.s (membrane N7)

6.6.3. THE EFFECT OF FILM THICKNESS ON PERMEANCE

The effect of film thickness on hydrogen permeance, nitrogen permeance, membrane selectivity and Arrhenius parameters are depicted in **Figures 6.33** to **6.40**. The hydrogen permeance should be inversely proportional to the Pd film thickness (equation **2.9**).

$$P_m = \frac{P_{er}}{l} \qquad (2.9)$$

6.6.3.1. Hydrogen permeance

Data in **Figure 6.33** shows a decrease in hydrogen permeance with an increase in film thickness up to a thickness of about 4.5 microns. Thereafter, the permeance started to level off. The permeance increased with temperature, as mentioned previously (see **6.6.2**). The decrease in permeance was not directly proportional to the inverse thickness. For example; taking values from the quadratic fit at 450 °C at thicknesses of 1.0 and 3.0 microns, yielded permeances of about 7.0 and 13.0 μmol/m^2.Pa.s, respectively. This ratio (almost 1:2) is different from the theoretical prediction (1:3). The reason for this is that the model equations (**2.8** and **2.9**) were formulated for thick foils in the tens and hundreds of microns range. When films become very thin, surface structure and morphology effects come into play, which cause deviation from the model equations. **Figure 6.34** depicts permeances of Pd films from 1.0 to 1.5 micron thickness. The values ranged between 15 and 6 μmol/m^2.Pa.s for temperatures from 330 °C to 450 °C.

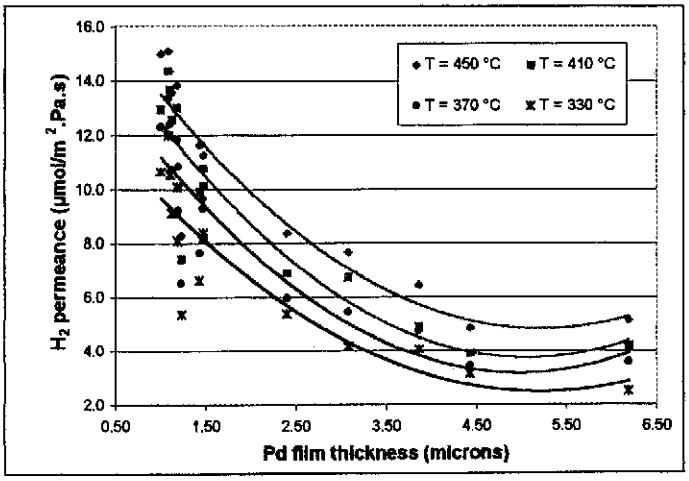

Figure 6.33: Hydrogen permeance for Pd films from 1 to 6.5 micron thickness

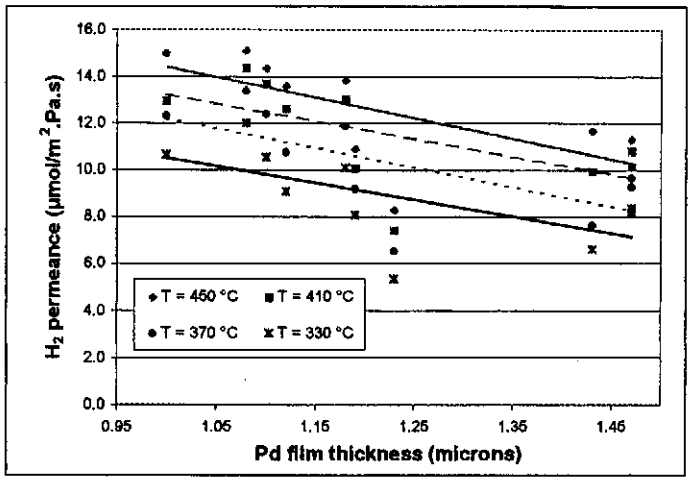

Figure 6.34: Hydrogen permeance for Pd films from 1 to 1.5 micron thickness

6.6.3.2. Nitrogen permeance

Nitrogen permeance generally decreases with an increase in Pd film thickness. Nitrogen permeance as a function of film thickness is given in **Figures 6.35** and **6.36**.

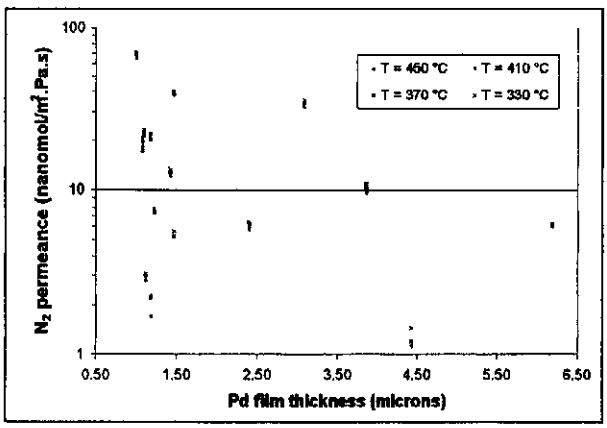

Figure 6.35: Nitrogen permeance for Pd films from 1 to 6.5 micron thickness

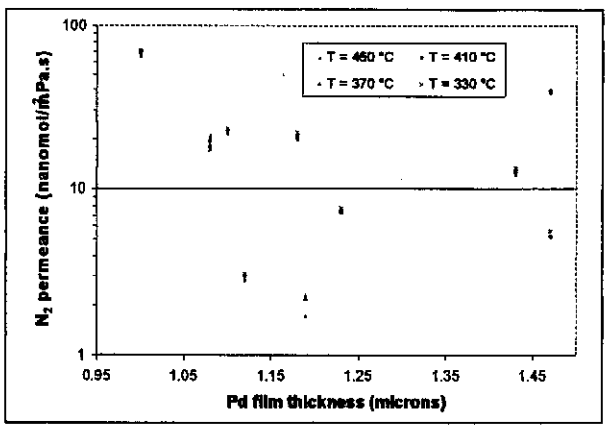

Figure 6.36: Nitrogen permeance for Pd films from 1 to 1.5 micron thickness

For the first membranes that were prepared (membranes 1a, 1b and 1c), the plating process was not well refined and the selectivity was poor as shown in **Figure 6.35** at thicknesses of 3.1, 3.9 and 6.2 microns. If those values were excluded then the decline in nitrogen permeance with an increase in film thickness would be clear. The worst membrane (1.0 µm) had a nitrogen leak rate of 70 nmol/m^2.Pa.s, while the best ones had values close to

1 nmol/m^2.Pa.s. **Figure 6.36** indicates that the majority of the Pd films with thicknesses ranging from 1.0 to 1.5 μm had a nitrogen leak rate of between 20 and 2 nmol/m^2.Pa.s.

6.6.3.3. Membrane selectivity

The selectivity data, which is the hydrogen permeance divided by the nitrogen permeance, is presented in **Figures 6.37** and **6.38**. At all the temperatures tested the selectivity remained above 100, which is an indication of very good membranes. All films of thickness ranging from 1.0 to 1.5 μm had a selectivity of at least 400, except the 1.0 μm film and a 1.47 μm film (see **Figure 6.38**).

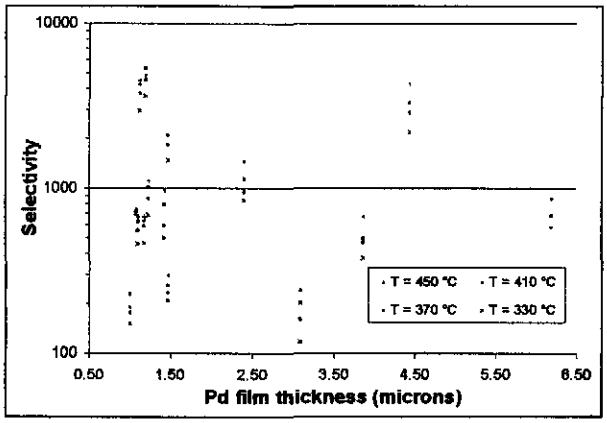

Figure 6.37: H_2 to N_2 selectivity for Pd films from 1 to 6.5 micron thickness

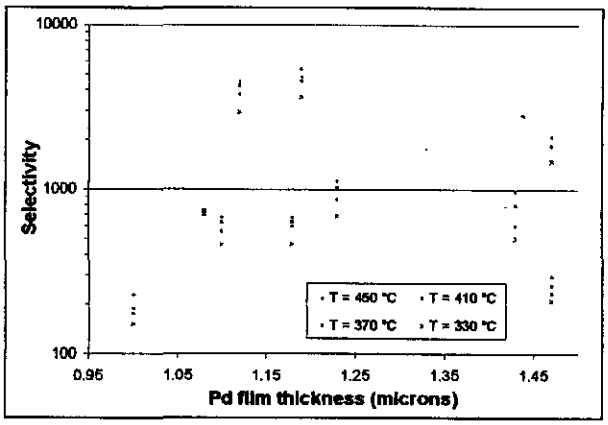

Figure 6.38: H_2 to N_2 selectivity for Pd films from 1 to 1.5 micron thickness

6.6.3.4. Arrhenius parameters for hydrogen permeance

There was significant variance in the Arrhenius parameters for hydrogen permeance. **Figures 6.39** and **6.40** were constructed to illustrate this. The permeance ($P_m = P_{er}/l$) and not the permeability ($P_{er} = P_m * l$), was plotted on the right-hand side axis, to be able to compare values for different Pd thicknesses. A decrease in P_0/l and/or an increase in E_D indicate slower permeance. Both **Figures 6.39** and **6.40** show an increase in activation energy and a very slight decline in P_0/l as expected. The permeance decreased with increasing film thickness.

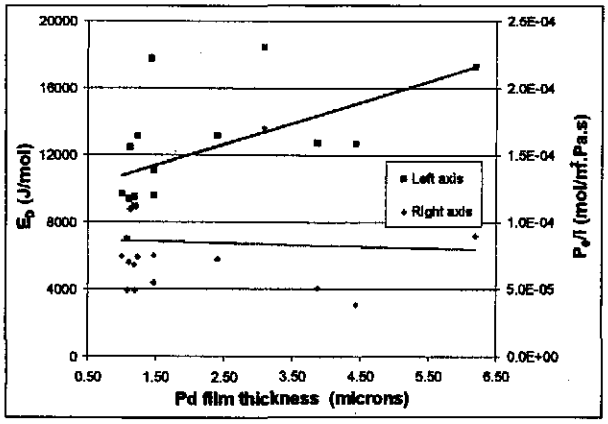

Figure 6.39: Arrhenius parameters for H_2 permeance (1 to 6.5 micron Pd films)

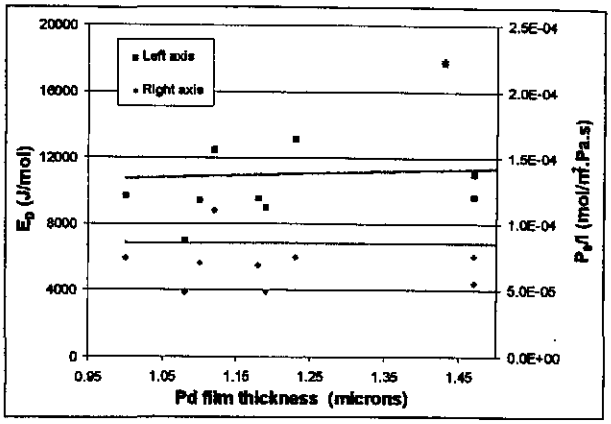

Figure 6.40: Arrhenius parameters for H_2 permeance (1 to 1.5 micron Pd films)

6.6.4. COMPARISON WITH LITERATURE DATA

During the course of this project an extensive database on hydrogen permeance data through palladium films was accumulated. This data was divided into different categories, for example:

- Pure Pd or Pd alloys,
- Substrate type (alumina, porous glass, porous stainless steel or refractory metal),
- Deposition method (electroless plating, CVD, wet impregnation, electroplating etc.), and
- Deposition position (inside tube, outside tube or on flat disk).

The following general remarks summarised in **Appendix E** can be made regarding hydrogen permeance through Pd films:

1. Unsupported Pd films or foils are thick (typically 24 μm and thicker) and hydrogen permeance poor. The best permeance value from literature was 1.2 μmol/m^2.Pa.s at 350 °C (Hurlbert and Konecny, 1961), but usually the values were lower than 1 μmol/m^2.Pa.s even at much higher temperatures.
2. Pd-Ta-Pd (15 μm) foils had permeance values of up to 1.76 μmol/m^2.Pa.s at 340 °C (Peachey et al., 1996).
3. CVD and wet impregnation were successfully used to produce Pd films of less than 1 μm.
4. The surface structure of Pd films prepared by CVD appeared to be unsuitable for high hydrogen permeance. Typically, films had a hydrogen permeance of less than

1 μmol/m^2.Pa.s, except for those prepared by Yan et al. (1994) which had values of up to 4 μmol/m^2.Pa.s.

5. The best values for hydrogen permeance were obtained with alumina substrates. Most hydrogen permeances of films on porous glass were less than 1 μmol/m^2.Pa.s. For films on porous stainless steel permeances were less than 1 μmol/m^2.Pa.s and for films on refractory metals permeances were less than 2 μmol/m^2.Pa.s.
6. The best values obtained with alumina supports and electroless plating were:
   - 9.75 μmol/m^2.Pa.s at 450 °C for plating on a disc by Zhao et al. (1998), but the H_2 to N_2 selectivity of the film was only 23.
   - 2.86 μmol/m^2.Pa.s at 400 °C for plating on the outside of a tube by Kikuchi (1995). The selectivity was not mentioned.
   - 5.27 μmol/m^2.Pa.s at 500 °C for plating on the inside of a tube by Shu et al. (1997b). The selectivity was not mentioned.

The best overall hydrogen permeance values that have been published were for Pd films on modified porous stainless steel discs, prepared by wet impregnation. Film thickness varied from 0.5 to 0.8 μm. The hydrogen permeance was 15.8 μmol/m^2.Pa.s at 450 °C (Jun and Lee, 1999) and 17.8 μmol/m^2.Pa.s at 550 °C (Nam et al., 1999). In both cases the H_2 to N_2 selectivity was above 1000.

6.6.4.1. Hydrogen permeances in the present study

The geometry of membrane tubes is preferable to that of membrane discs for practical installation. Whether the selective layers and the Pd film should be on the inside of the tube or the outside of the tube is debatable. If the Pd film is on the inside of the tube, it is more protected against scratching and damage during installation. From past experience it was found to be easier to coat tubes on the inside than on the outside, because of greater solution stability. Pd films on the outside of tubes have the advantage of a larger surface area per membrane length, compared to coatings on the inside. ECN produces membrane with selective layers on the outside, while SCT produces membranes with selective layers on the inside of the tube.

During the present study some important advances have been made in the preparation of Pd membranes. Pd film thickness on the inside of alumina tubes has been reduced to between 1.0 and 1.5 μm, while maintaining H_2 to N_2 selectivities exceeding 400 for the majority of the films. An important cost advantage is that the cheaper 200 nm α-alumina support was used successfully. The more expensive γ-α-alumina support was not necessary. The thinnest Pd films prepared previously by electroless plating on the inside of membrane tubes were:

- a 2.0 μm film on the inside of an assymetric α/γ-alumina membrane with a 5 nm pore size (from SCT) by Shu et al. (1996b), and
- a 2.1 μm film on the inside of an assymetric α/γ-alumina membrane with a 3-4 nm pore size (from SCT) by Shu et al. (1997b).

The highest permeance obtained for a Pd film on the inside of a tube (see section **6.6.4**), excluding the results from Zhoa et al. (1998), due to poor selectivity, and results from Shu et al. (1997b) and others, where selectivity was not mentioned, is 2.68 μmol/m^2.Pa.s at 467 °C (Li A et al., 1999). In the present study, hydrogen permeances of Pd films from 1.0 to 1.5 μm varied between about 8 and 15 μmol/m^2.Pa.s for temperatures from 330 °C to 450 °C and (**Figures 6.33** and **6.34**). These values are a significant improvement over other published results.

Only the results of Jun and Lee (1999): 15.8 μmol/m^2.Pa.s at 450 °C, and Nam et al. (1999): 17.8 μmol/m^2.Pa.s at 550 °C, are comparable to values in this study, but they used the unfavourable disc membranes.

6.6.5. H_2 PERMEANCE EMPLOYING A SWEEP GAS

Hydrogen permeance through palladium films were also tested using an atmospheric hydrogen feed on the tube side of the membrane and an inert sweep gas (nitrogen) on the shell side of the membrane. Equation (**2.8**) cannot be used in that format. The membrane was treated as a plug flow reactor without chemical reaction, but with permeance, to derive the model equation (**6.1**). Equations were derived from the basic plug flow reactor equations (Fogler, 1992).

$$\frac{dF}{d\left(\frac{L}{L_0}\right)} = J(2\pi r) \tag{6.1}$$

where L is the axial position along the membrane. The axial position is made dimensionless by dividing both sides of **(6.1)** by the reactor length, L_0. Substituting parameters yields:

$$\frac{dF}{d\left(\frac{L}{L_0}\right)} = 2\pi.R_m P_m L_0 (P_{high} - P_{low}) \tag{6.2}$$

For hydrogen, the flow was from the tube side (high H_2 pressure) to the sweep side (low H_2 pressure), while for nitrogen the flow was from the sweep side (high N_2 pressure) to the tube side (low N_2 pressure). Partial pressures was expressed in terms of flow rates. Substituting molar flow rates in **(6.2)** yielded two coupled differential equations:

$$\frac{dF_H}{d\left(\frac{L}{L_0}\right)} = 2\pi.R_m P_{m,H} L_0 100000\left[\frac{F_H}{F_H + F_{N(0)} - F_N} - \frac{F_{H(0)} - F_H}{F_{H(0)} - F_H + F_N}\right] \tag{6.3}$$

$$\frac{dF_N}{d\left(\frac{L}{L_0}\right)} = 2\pi.R_m P_{m,N} L_0 100000\left[\frac{F_N}{F_N + F_{H(0)} - F_H} - \frac{F_{N(0)} - F_N}{F_{N(0)} - F_N + F_H}\right] \tag{6.4}$$

$F_{H(0)}$ is the hydrogen molar feed rate on the tube side and $F_{N(0)}$ is the nitrogen molar feed rate on the shell side. The atmospheric pressure was taken as 100 000 Pa. The boundary conditions for **(6.3)** and **(6.4)** were:

At $(L/L_0) = 0$, $F_H = F_{H(0)}$ and $F_N = F_{N(0)}$ **(6.5)**

Equations (**6.3**) and (**6.4**) were solved using average hydrogen and nitrogen permeances (found in **Appendix D1**) and employing Euler's method (Fogler, 1992) for first order differential equations. A very small step length of 0.001 was chosen.

The amounts of hydrogen that permeated through the Pd films at different sweep gas ratios, hydrogen space times and different temperatures are given in graphical format in **Appendix D1**. Hydrogen flow profiles along the axis of the membrane were calculated for membranes (N4) and (N7), to compare the experimental data with the calculated data. To solve equations (**6.3**) and (**6.4**) the following assumptions were made:

- The reactor was isothermal, and
- Hydrogen and nitrogen permeances were independent of pressure, even at low pressures.

Table 6.2 shows that the error between the experimental values and calculated values was typically less than 1.5%, indicating very high accuracy. It was concluded that the model assumptions were valid and that the model predicted hydrogen permeance very well.

Table 6.2: Experimental H_2 permeances vs. calculated values for membrane (N7)

Space time = 2.37 seconds (200 cm^3/min H_2 feed)				
	Temperature (°C)			
Sweep gas mol % of H_2 feed	**450 °C**	**410 °C**	**370 °C**	**330 °C**
	% H_2 permeated			
5	96.8 (98.2)	96.7 (98.0)	96.3 (97.6)	96.0 (97.0)
10	97.7 (99.0)	97.5 (98.9)	97.2 (98.7)	96.9 (98.4)
20	98.5 (99.5)	98.2 (99.4)	98.1 (99.3)	97.8 (99.1)

Space time = 1.19 seconds (400 cm^3/min H_2 feed)				
	Temperature (°C)			
Sweep gas mol % of H_2 feed	450 °C	410 °C	370 °C	330 °C
	% H_2 permeated			
5	96.7 (98.1)	95.9 (97.6)	93.3 (93.9)	87.9 (85.7)
10	98.3 (99.0)	98.1 (98.9)	97.9 (98.7)	97.6 (98.4)
20	98.9 (99.5)	98.7 (99.4)	98.6 (99.3)	98.6 (99.1)

Values in brackets are the model values or calculated values

Table 6.3 tabulates a similar set of data for membrane (N4). Only at the very low sweep gas flow rates (2.5% of H_2 feed) did the experimental and calculated values deviate by more than 2%.

Table 6.3: Experimental H_2 permeances vs. calculated values for membrane (N4)

Space time = 2.37 seconds (200 cm^3/min H_2 feed)				
	Temperature (°C)			
Sweep gas mol % of H_2 feed	450 °C	410 °C	370 °C	330 °C
	% H_2 permeated			
5	97.8 (97.0)	97.5 (96.8)	97.7 (96.6)	97.4 (95.7)
10	98.6 (98.4)	98.4 (98.3)	98.6 (98.2)	98.3 (97.7)
20	99.2 (99.1)	99.0 (99.1)	99.1 (99.0)	99.0 (98.7)

Space time = 1.19 seconds (400 cm^3/min H_2 feed)				
	Temperature (°C)			
Sweep gas mol % of H_2 feed	450 °C	410 °C	370 °C	330 °C
	% H_2 permeated			
2.5	94.7 (92.0)	92.8 (90.3)	91.4 (87.4)	87.2 (81.2)
5	98.0 (97.0)	97.7 (96.8)	97.6 (96.6)	96.8 (95.6)
10	98.9 (98.4)	98.8 (98.3)	98.8 (98.2)	98.6 (97.7)

Values in brackets are the model values or calculated values

Figures 6.41 and **6.42** show the effects of temperature and sweep gas flow rates on hydrogen permeance through the Pd film of membrane (N7). Both an increase in temperature and sweep gas flow caused an increase in hydrogen permeance. The increase was more sensitive to the sweep gas flow rate (see **Figure 6.42**).

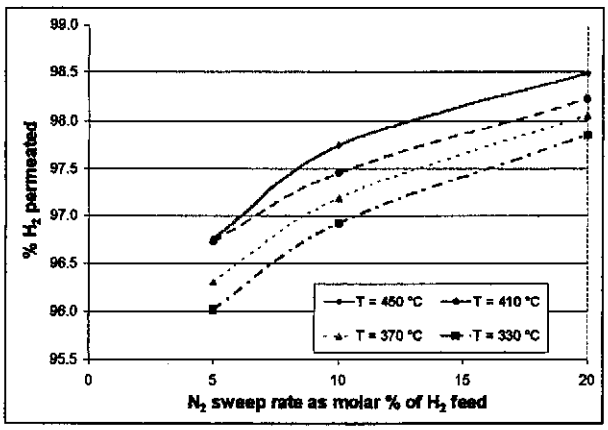

Figure 6.41: % H_2 permeated with N_2 sweep gas and space time = 2.37 s

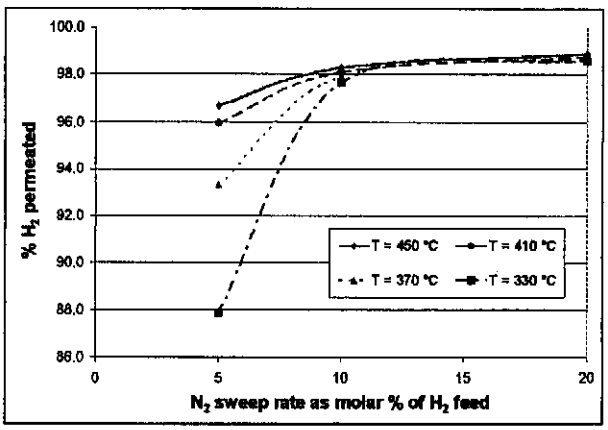

Figure 6.42: % H_2 permeated with N_2 sweep gas and space time = 1.19 s

The effects of space time, temperature and sweep gas flow rate are clearer in **Figures 6.43** to **6.46**, where hydrogen flow along the membrane axis is plotted. By comparing **Figures 6.43** and **6.44** it can be seen that increasing the sweep gas rate was more effective for removing

hydrogen than increasing the temperature was. For all experiments with a hydrogen feed rate of 200 cm^3/min (space time = 2.37 s), equilibrium was achieved at some point along the membrane axis. For a feed flow rate of 400 cm^3/min (**Figures 6.45** and **6.46**), the permeance rate at low temperatures and low sweep gas flow rates was too slow to allow all the hydrogen too permeate through the Pd film. The large effect of sweep gas flow rate on hydrogen permeance can be seen in **Figure 6.46**. Hydrogen permeance was incomplete at a sweep gas flow rate of 20 cm^3/min, but increased to full completion at four tenths of the membrane length for a sweep gas flow rate of 80 cm^3/min.

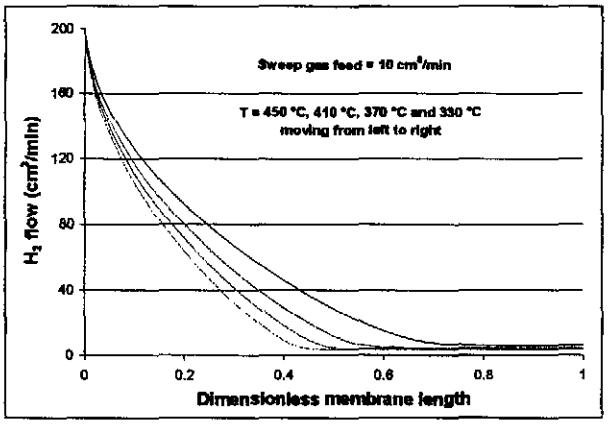

Figure 6.43: H_2 flow in tube (cm^3/min) as predicted by model for N7 (τ = 2.37 s)

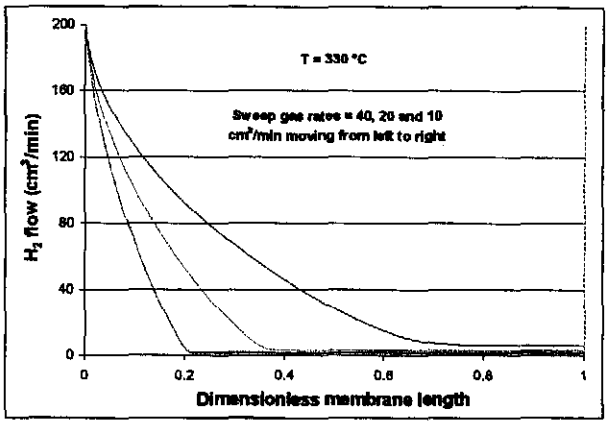

Figure 6.44: H_2 flow in tube (cm^3/min) as predicted by model for N7 (τ = 2.37 s)

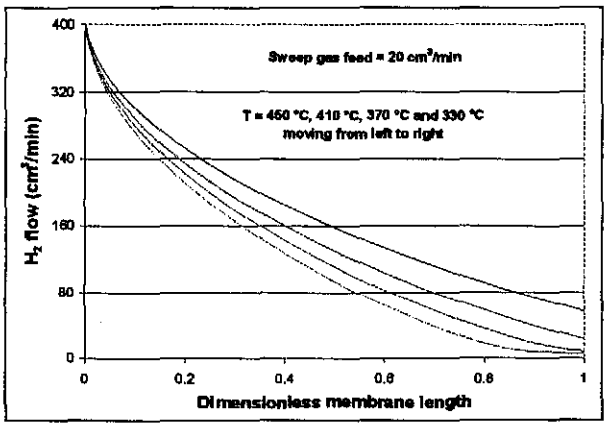

Figure 6.45: H_2 flow in tube (cm^3/min) as predicted by model for N7 (τ = 1.19 s)

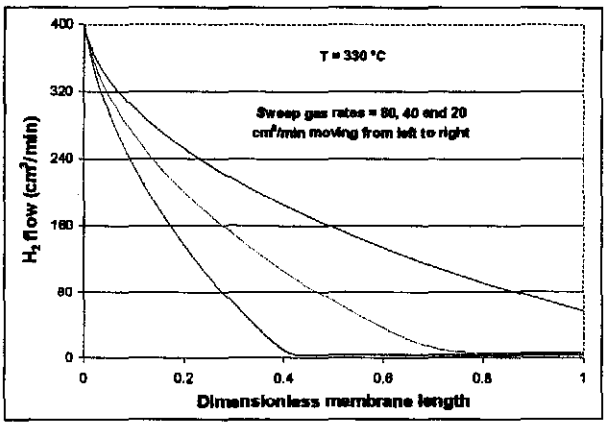

Figure 6.46: H_2 flow in tube (cm^3/min) as predicted by model for N7 (τ = 1.19 s)

Figures 6.47 to **6.52** are a repetition of **Figures 6.41** to **6.46**, but for membrane (N4). Membrane (N4) had significantly higher hydrogen permeance values than (N7) (see **Appendix D1**).

From **Figures 6.49** to **6.52** it can be seen how, when compared to data of (N7), all the curves were shifted to the left. Complete hydrogen permeance for membrane (N4) was achieved much quicker along the membrane axis i.e. at lower dimensionless reactor lengths, than for membrane (N7).

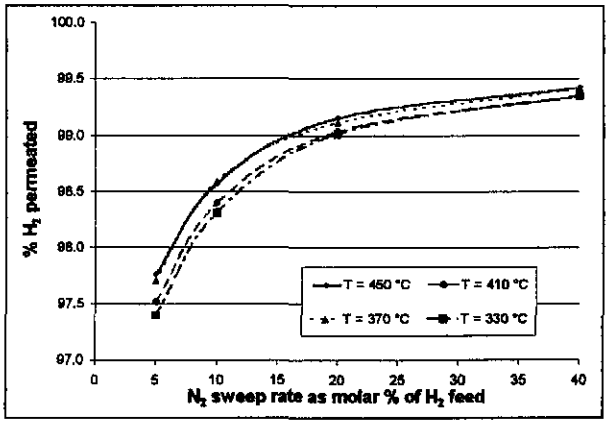

Figure 6.47: % H_2 permeated with N_2 sweep gas and space time = 2.37 s

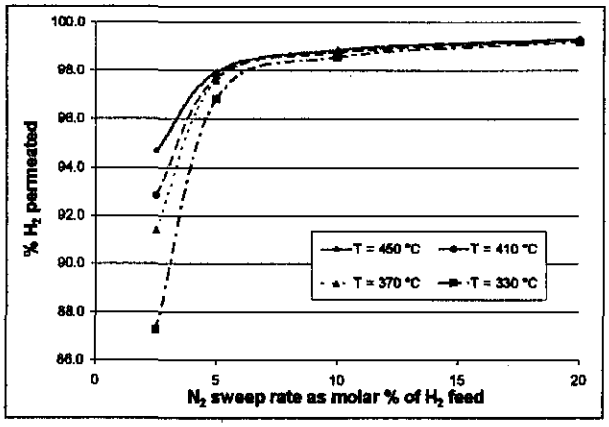

Figure 6.48: % H_2 permeated with N_2 sweep gas and space time = 1.19 s

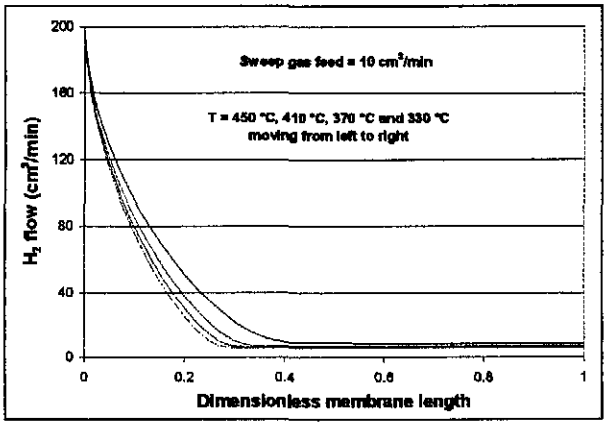

Figure 6.49: H_2 flow in tube (cm^3/min) as predicted by model for N4 (τ = 2.37 s)

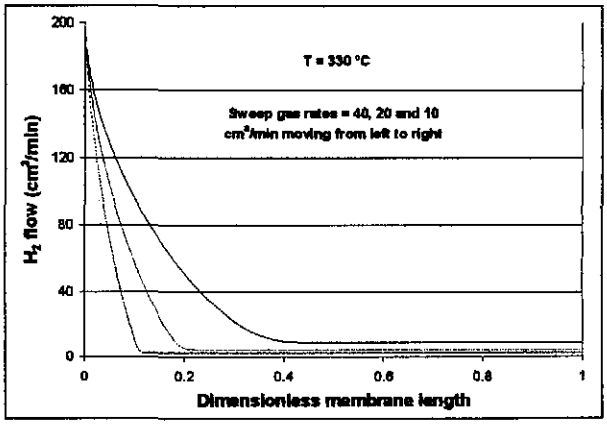

Figure 6.50: H_2 flow in tube (cm^3/min) as predicted by model for N4 (τ = 2.37 s)

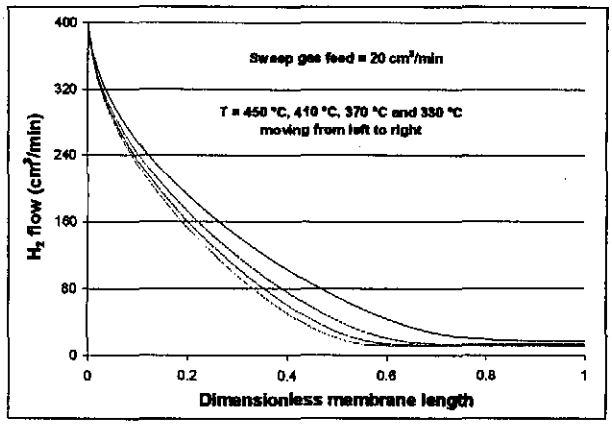

Figure 6.51: H_2 flow in tube (cm^3/min) as predicted by model for N4 (τ = 1.19 s)

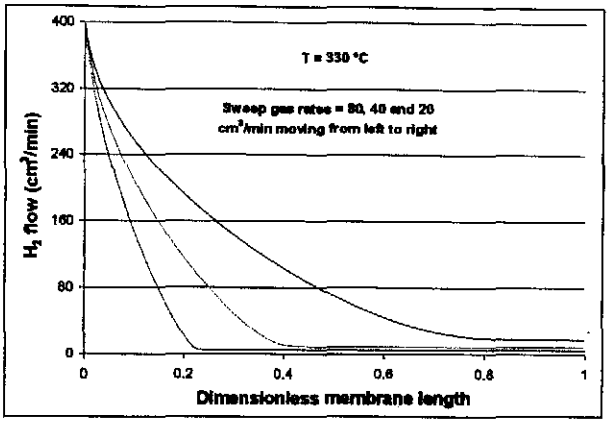

Figure 6.52: H_2 flow in tube (cm^3/min) as predicted by model for N4 (τ = 1.19 s)

6.7. SUMMARY

Each step in the electroless plating process must be carefully optimised to produce thin, highly selective, Pd films. For pretreatment, a low Sn to Pd ratio was employed to limit Sn deposition and increase thermal stability of the film. The quality of the Pd film was very dependent on the plating rate. A high plating rate, due to: a high hydrazine concentration, a low EDTA concentration and/or a high plating temperature, must be avoided to produce selective thin films. In some cases the Pd films had defects due to high plating rates. The last critical step in the membrane production process was the post plating cleaning. After plating, membranes were stirred in ammonia solution for several hours, dried and then further oxidised at 320 °C in pure oxygen before reduction.

Pd films, of thicknesses down to 1 μm, were deposited on the inside of asymmetric SCT α-alumina membranes (200 nm pore size). Hydrogen permeances of Pd films from 1.0 to 1.5 μm, varied between about 8 and 15 $\mu mol/m^2.Pa.s$ for temperatures from 330 °C to 450 °C. Hydrogen to nitrogen selectivity was > 100 for all membranes tested and > 400 for all but two membranes (thickness 1.0 to 1.5 μm) tested. These values are a significant improvement over other published results.

Hydrogen permeance fitted the flux equation well, with the permeance constant at different differential pressures. This implied a n-value of 1 in the flux equation. Temperature data fitted the Arrhenius equation with high accuracy. For the majority of the membranes, nitrogen flow through defects in the films showed signs of Knudsen flow. Finally, hydrogen permeance was tested using an inert sweep gas. Two coupled differential equations were formulated for modelling the membrane as a plug flow reactor with permeance, but without reaction. The equations provided very good fits for the experimental data.

7. Pd-Ag MEMBRANE ALLOYING AND STABILITY TESTING

Pd membranes can only be used above 300 °C. Pd-Ag membranes can, however, be used at lower temperatures since to the α to β phase transition in the Pd crystals is suppressed by the silver addition. This α to β phase transition in the Pd crystals is what causes defects and loss of selectivity in Pd films below 300 °C.

In **Chapter 7** the preparation and testing of Pd-Ag membranes will be described. They will also be compared to pure Pd membranes. The membranes were heat treated at high temperatures in an effort to form a homogeneous alloy between the Pd and Ag. The stability of the membranes was monitored while the alloying process was in progress. The Pd-Ag membranes were also tested at temperatures below 300 °C.

7.1. Pd-Ag MEMBRANE PREPARATION

For supported films, the Pd and Ag deposition processes have an effect on alloying conditions. Pd and Ag can either be deposited as separate successive layers or by a co-deposition process. Different methods for preparing Pd-Ag membranes are listed in **Appendix E**. Co-deposition processes include:

- Sputtering (dc or magnetron) on flat discs and sometimes on the outside of tubes,
- Spray pyrolysis on discs or on the outside of tubes, and
- Electroless plating on any surface.

The main advantage of sputtering is that complex alloys can be prepared. Metals can be deposited in any ratio and with high accuracy. The disadvantage is that the technique is not suitable for depositing metal on the inside of a membrane tube. Even depositing metal on the outside of tubes may cause problems with thickness control and composition uniformity.

Only electroless plating can be used for co-depositing Pd and Ag on the inside of a membrane tube, but the process control is poor. It is very difficult to obtain the desired Pd to Ag ratio on the membrane surface (Shu et al., 1993; Cheng and Yeung, 1999).

The plating kinetics for Pd and Ag in solution differs. Their stabilities also differ, with Pd being more stable in solution than Ag. This resulted in very diluted concentrations having to be used for co-deposition. The Pd to Ag ratio in the starting solution differs considerable from the deposited composition on the membrane. Co-deposition is discussed in more detail in Keuler (1997a), Cheng and Yeung (1999) and Shu et al. (1993).

In the present study, Pd-Ag membranes were prepared by successive Pd and Ag plating. The Pd layer was deposited first, followed by the Ag layer. The plating procedure was discussed earlier in **section 3.3.2.4**. The composition of the plating solution was given in **Table 3.16** and the plating procedure given in **Table 3.17**.

Before the silver layer was deposited, the membrane, covered with teflon tape on the outside, was dipped twice in both the pretreatment solutions. Post plating cleaning was similar to that after Pd deposition.

7.2. UNALLOYED Pd-Ag MEMBRANES

Firstly, unalloyed Pd-Ag membranes were compared to pure Pd membranes and then the effects of alloying studied. **Table 7.1** was taken from **Appendix D2** and summarises the alloying conditions.

In the table, when two temperatures and two times are given in a row, the first heating time is for the first temperature and the second heating time is for the second temperature.

Table 7.1: Alloying procedures used for Pd-Ag membranes

Name	Elements	Alloying	Heating system	Gas	Temp (°C)	Time (h)
8	Pd	No				
8b	Pd+Ag	No				
8c	Pd+Ag	Yes	Tube oven	Ar	550, 600	15, 25
N1	Pd	No				
N1b	Pd+Ag	No				
N1x	New Pd+Ag	Yes	Reactor	H_2	590	10
N3	Pd	No				
N3b	Pd+Ag	No				
N3c	Pd+Ag	Yes	Tube oven	Ar	545	50
N3d	Pd+Ag	Yes	Tube oven	Ar	545	100 (total)
N3e	Pd+Ag	Yes	Tube oven	Ar	545	150 (total)
N4	Pd	No				
N4b	Pd+Ag	No				
N4c	Pd+Ag	Yes	Tube oven	Ar	530	30
N4x	New Pd+Ag	Yes	Reactor	H_2	540	30
N6	Pd+Ag	Yes	Tube oven	Ar	550, 600	15, 25
N2x	New Pd+Ag	Yes	Reactor	Ar, N_2	500, 550	50, 25
N8x	New Pd+Ag	Yes	Reactor	Ar	550	10

7.2.1. CHARACTERISING UNALLOYED Pd-Ag MEMBRANES

Four Pd-Ag membranes were tested prior to alloying. They were: 8b, N1b, N3b and N4b (see **Table 7.1**). The metal layer, at that stage, consisted of a Pd film and a second Ag film. The hydrogen permeances of the membranes are depicted in **Figures 7.1** and **7.2**. The addition of silver resulted in a sharp decline in hydrogen permeance at all temperatures. This confirmed that silver has a very poor hydrogen permeance and that separated Pd and Ag layers in the film should be avoided.

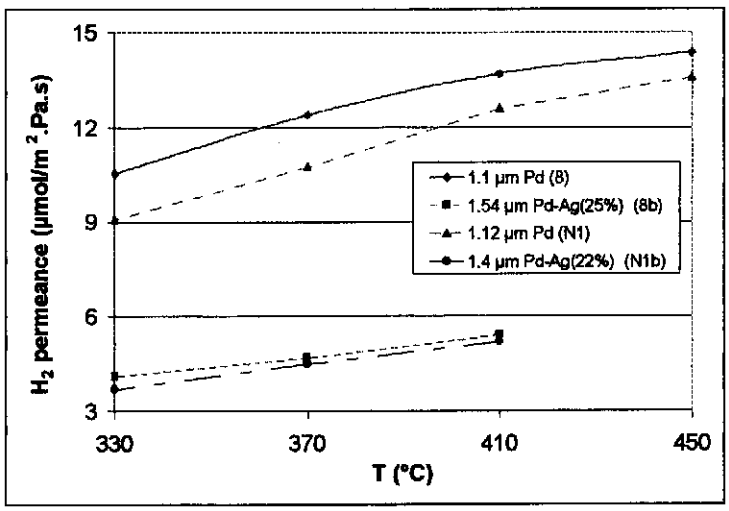

Figure 7.1: Hydrogen permeances for Pd and Pd-Ag membranes (8, N1, 8b, N1b)

Figure 7.2 provides a good example of how silver influences the hydrogen permeance. Metal films of membranes (N3) and (N4b) were of similar thickness. Membrane (N3) consisted of pure Pd, while N4b had a Pd layer of 1.18 µm and a silver layer of approximately 0.25 µm. The hydrogen permeance for membrane (N4b) was more than three times lower than that of (N3), even though this silver layer was very thin.

Pd and Ag can be considered as two resistances in series. The purpose of alloying was to obtain a homogeneous alloy. The two resistances in series would change to two resistances in parallel and the hydrogen permeance would increase.

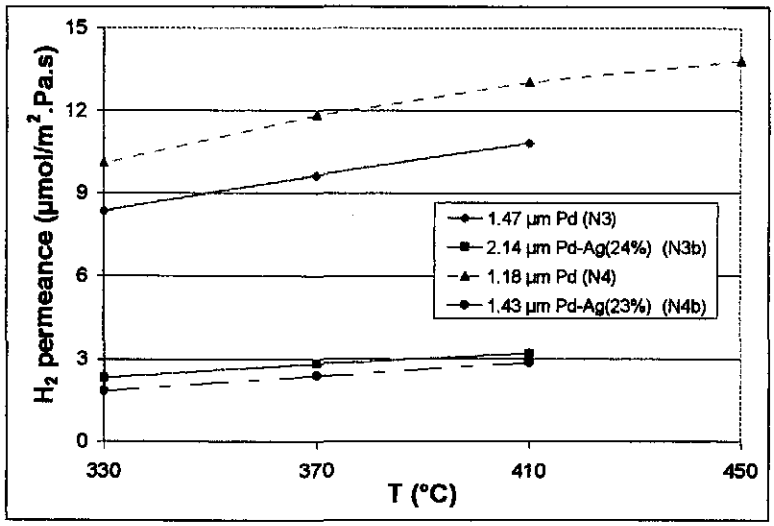

Figure 7.2: Hydrogen permeances for Pd and Pd-Ag membranes (N3, N4, N3b, N4b)

Table 7.2 lists nitrogen permeance and selectivity data for membranes 8b, N1b, N3b and N4b. For all the membranes except (N1b), the nitrogen permeance decreased after the silver layer was deposited. That was expected, since silver plugged defects that were present in the Pd layer. Thicker films tend to have less defects, as discussed in **Chapter 6**. Membrane (N1) had a very low nitrogen permeance and high selectivity. After silver deposition, the film showed poor characteristics. That was the only silver plating experiment that resulted in this behaviour. Other unalloyed Pd-Ag membranes in **Appendix D2** (8b, N3b and N4b) showed good selectivity after silver deposition. Two possible explanations are offered for this behaviour:

- Some kind of physical damaged to the film might have taken place.
- There might have been hydrogen left in the system during cooling after testing (N1). The hydrogen would then have caused some embrittlement of the pure Pd film on which the silver was deposited.

The selectivities of the Pd-Ag films were lower than those of pure Pd films. The loss of hydrogen permeance was far greater than the gain in reducing defects or the decline in nitrogen permeance. The net result was a decline in the H_2 to N_2 ratio.

Table 7.2: N_2 permeance and selectivity data for 8b, N1b, N3b and N4b

Temp. (°C)	N_2 permeance (nmol/m^2.Pa.s)	Selectivity		N_2 permeance (nmol/m^2.Pa.s)	Selectivity
	Membrane 8			**Membrane 8b**	
450	21.42	671			
410	21.85	627		11.48	472
370	22.42	553		11.90	394
330	23.07	457		12.24	336
	Membrane N1			**Membrane N1b**	
450	3	4533			
410	2.97	4251		57.09	91
370	2.84	3784		45.27	99
330	3.08	2953		48.03	77
	Membrane N3			**Membrane N3b**	
410	5.17	2090		3.22	999
370	5.22	1851		3.72	758
330	5.65	1479		3.66	632
	Membrane N4			**Membrane N4b**	
450	20.64	671			
410	20.64	631		11.98	239
370	20.06	591		10.57	226
330	21.83	462		10.19	180

7.2.1.1. Unalloyed Pd-Ag membranes tested with a sweep gas

The equations derived in **section 6.6.5** were used for calculating the hydrogen permeances of membranes 8b, N1b, N3b and N4b. The calculated vs. the measured values of each membrane are compared in **Figures 7.3** to **7.6**.

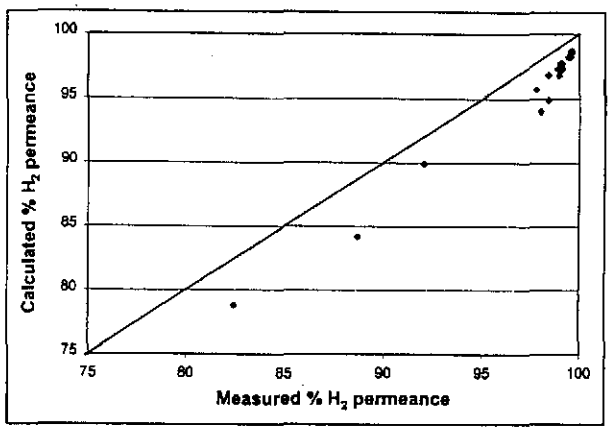

Figure 7.3: Measured vs. calculated % H_2 permeance for 8b

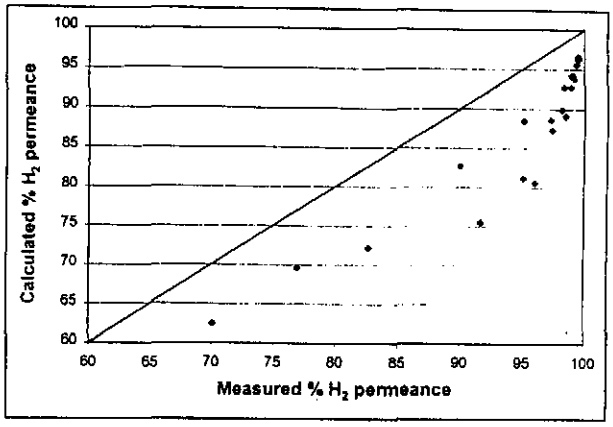

Figure 7.4: Measured vs. calculated % H_2 permeance for N1b

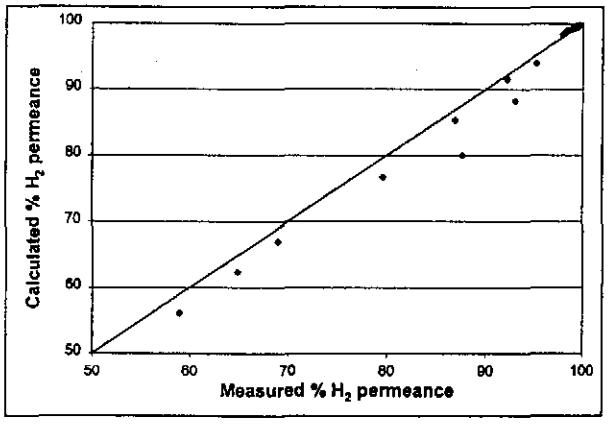

Figure 7.5: Measured vs. calculated % H_2 permeance for N3b

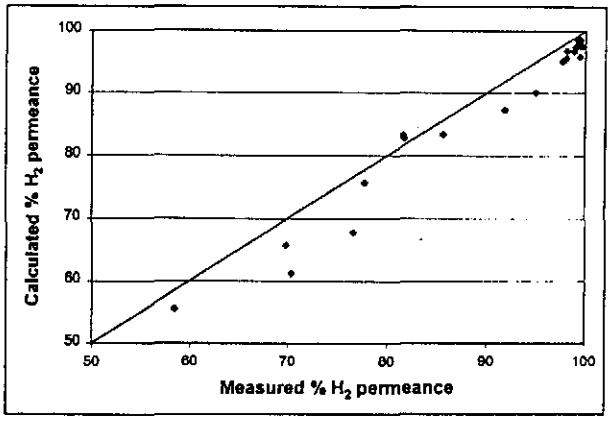

Figure 7.6: Measured vs. calculated % H_2 permeance for N4b

The model equations (listed in **section 6.6.5**) predicted H_2 permeances well, as long as the nitrogen permeances were low (less than 20 nmol/m^2.Pa.s). For membrane (N1b), the error between measured values and calculated values was large due to very poor selectivity of the membrane (high nitrogen permeances). For the other membranes (N3b, N4b and to a lesser extent 8b), the error between the actual and measured values was small. Most of the time the calculated percentage of hydrogen permeated was less than the measured percentage.

Figures 7.7 and **7.8** show the measured hydrogen permeances as a function of temperature and sweep gas flow rate for membrane (N3b). **Figures 7.9** to **7.12** show hydrogen flow profiles along the axis of the membrane for (N3b).

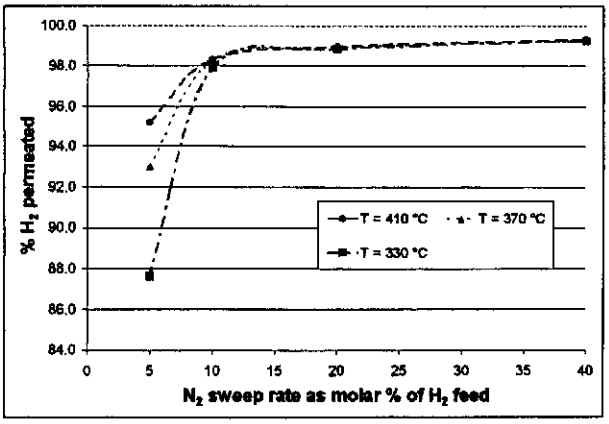

Figure 7.7: % H_2 permeated with N_2 sweep gas and space time = 2.37 s

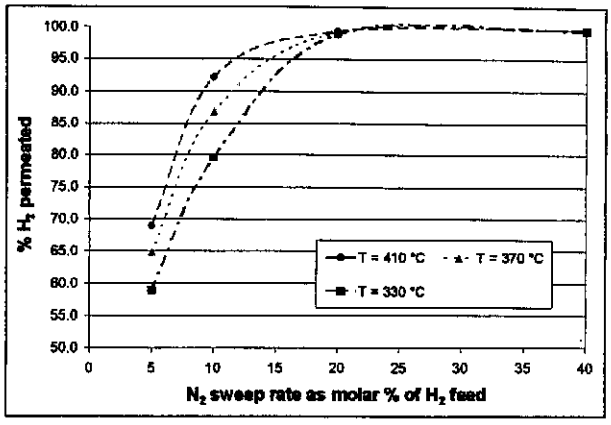

Figure 7.8: % H_2 permeated with N_2 sweep gas and space time = 1.19 s

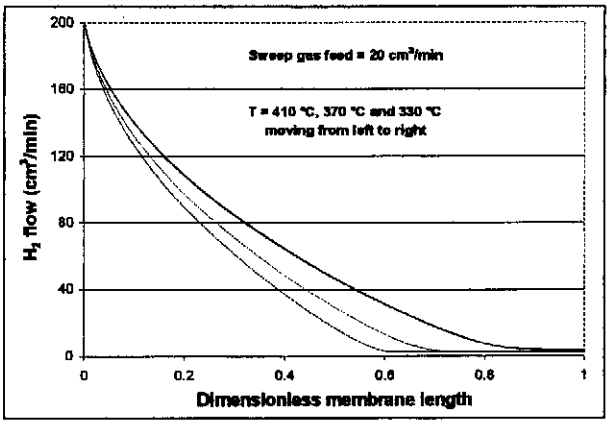

Figure 7.9: H_2 flow in tube (cm^3/min) as predicted by model for N3b (τ = 2.37 s)

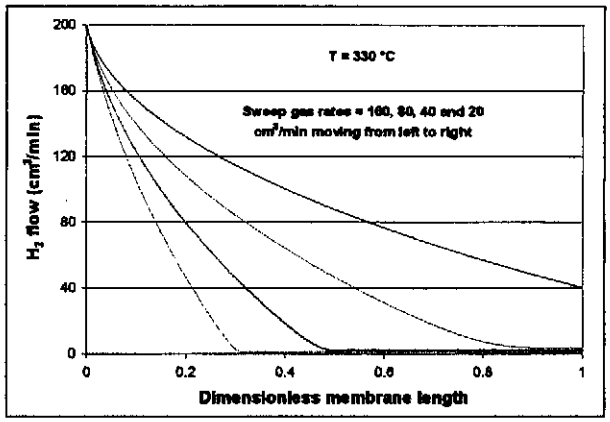

Figure 7.10: H_2 flow in tube (cm^3/min) as predicted by model for N3b (τ = 2.37 s)

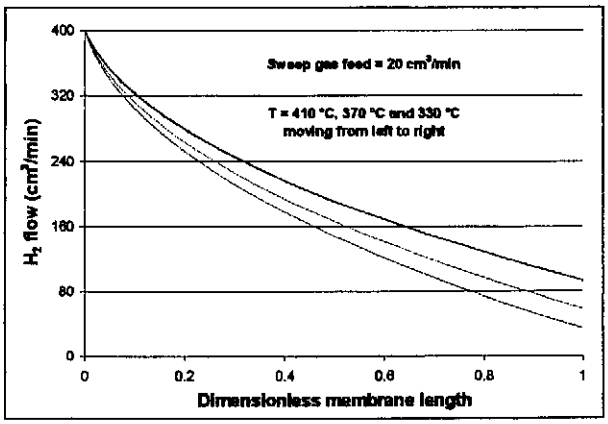

Figure 7.11: H_2 flow in tube (cm^3/min) as predicted by model for N3b (τ = 1.19 s)

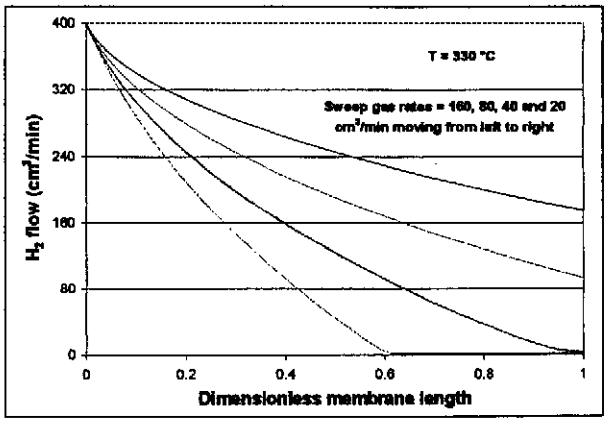

Figure 7.12: H_2 flow in tube (cm^3/min) as predicted by model for N3b (τ = 1.19 s)

Figures 7.7 to **7.12** show that, in most cases, at 330 °C the hydrogen permeance did not go to completion along the length of the membrane tube. When **Figures 7.9** to **7.12** are compared with **Figures 6.43** to **6.46** and **Figures 6.49** to **6.52** (pure Pd films), it can be seen how far the curves shift to the right when silver was added. Much higher sweep gas feed rates were needed to extract a high percentage of hydrogen through the Pd-Ag films.

7.3. LITERATURE DATA ON ALLOYING Pd-Ag MEMBRANES

In **section 7.1** it was mentioned that there are two procedures available for preparing Pd-Ag membranes: either co-deposition or successive deposition. The thickness of the supported film is important when choosing the most appropriate alloying conditions. There is not much literature available on alloying Pd-Ag films; what there is, is mentioned in the next section.

7.3.1. ALLOYING CO-DEPOSITED Pd-Ag FILMS

Cheng and Yeung (1999) co-deposited a 1.2 μm Pd_{88}-Ag_{12} film on the outside of a tubular 5 nm porous Vycor glass membrane with electroless plating. They annealed the membrane in hydrogen at 400 °C and 500 °C, respectively, for a total of 8 hours. After annealing, they found a single phase (obtained from XRD data). They obtained, for the alloyed Pd-Ag membrane, an increase of 1.4 to 1.7 times in hydrogen permeance compared to a pure Pd membrane. The values for both were, however, very low:

- 0.10 μmol/m^2.Pa.s for the Pd_{88}-Ag_{12} film at 500 °C, and
- 0.06 μmol/m^2.Pa.s for the Pd film at 500 °C.

Other references in **Appendix E** do not specifically state if and how they annealed their Pd-Ag membranes.

7.3.2. ALLOYING SUCCESSIVE Pd-Ag FILMS

Uemiya et al. (1991a) deposited successive Pd and Ag layers by electroless plating on the outside of a membrane tube. The support was an asymmetric alumina tube with a 200 nm pore size. Total film thickness ranged from 4.5 to 6.4 μm, with the Ag percentage ranging

from 11 to 30.5 wt %. Membranes were heat treated at 500 °C, but the double layer structure was not changed to a single alloy layer. Membranes were then treated in argon for 12 hours at 800 °C to 900 °C to yield a miscible palladium-silver alloy. They claimed to have 100% selective membranes with a hydrogen permeance varying between 1.45 and 2.24 $\mu mol/m^2.Pa.s$ at 400 °C. The highest value was obtained for a 23 wt % silver film. The reactor they used had a 150 °C temperature difference between the inlet and the centre.

Shu et al. (1996a) prepared Pd-Ag membranes on porous stainless steel disks (200 nm pore size) with successive electroless plating steps. The film consisted of a 2.8 μm Pd-Ag layer. The Pd_{80}-Ag_{20} film was annealed in hydrogen at 500 °C for 5 hours. The Tamman temperatures were 630 °C for Pd and 344 °C for Ag. They claimed that annealing at 500 °C would cause significant vibration and migration of silver atoms into the palladium lattice, resulting in interdiffusion. Silver penetrated into the Pd layer to 1, 1.3 and 1.46 μm after annealing 5 hours at 400 °C, 500 °C and 600 °C, respectively. Results were obtained by Auger electron depth profiling. No hydrogen permeance or selectivity data was provided.

7.3.3. DIFFUSION KINETICS

Diffusion kinetics of thin films has been discussed in Brandes and Brook (1992). Shu et al. (1996a) also summarised the relevant equations. Little data is available on diffusion coefficients of Ag into a Pd matrix. **Table 7.3** lists some diffusion coefficients for the Ag-Pd system.

Table 7.3: Ag-Pd diffusion coefficients

Diffusion process	T range (K)	D_0 (m^2/s)	E_D (kJ/mol)	Reference
Bulk diffusion in $Ag_{78.2}Pd$	988-1215	$4.52*10^{-6}$	183	Brandes [1] (1992)
Chemical diffusion; 50% Ag in Pd	873-1173	$7.4*10^{-10}$	103	Brandes [2] (1992)
Interdiffusion in layered Pd-Ag	773-1073	$2.5*10^{-13}$	72	Shu [3] (1996a)

The Arrhenius equation is applicable for diffusion data:

$$D = D_0 \exp\left(-\frac{E_D}{R_0 T}\right) \qquad (7.1)$$

Figure 7.13 was constructed to compare diffusion rates (of **Table 7.3)** at different temperatures by applying equation (**7.1**). The figure must be interpreted in the following way: The times on the y-axis are indications of the time required to obtain the same amounts of diffusion as after 100h at 500 °C, but at different temperatures. There is a significant difference in the values from the three different sets of diffusion coefficients.

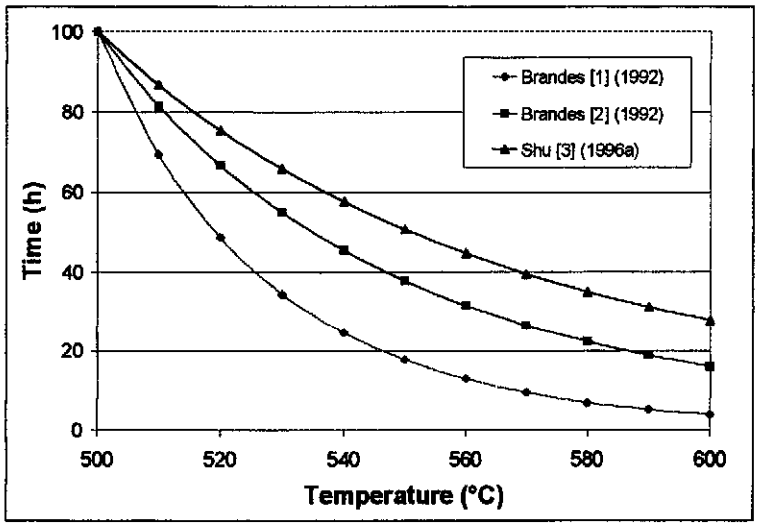

Figure 7.13: Heating times required to obtain similar Pd-Ag diffusion at different temperatures

7.4. ALLOYING RESULTS FOR Pd-Ag MEMBRANES

There seems to be significant differences in diffusion procedures described in **section 7.3**. Uemiya et al. (1991a) only observed alloying after 12 hours at temperatures above 800 °C for films exceeding 5 microns. Shu et al. (1996a), on the other hand, measured significant interdiffusion of Ag into Pd after 5 hours at temperatures as low as 500 °C. Their film had a thickness of 2.8 microns.

In the present study the temperature range used for alloying was from 500 °C to 600 °C. Different alloying times and gas environments were employed. No literature data could be found on alloying films on the inside of a membrane tube. A major problem associated with online diffusion analysis is that the membrane has to be broken to reach the inner surface for determining alloying (XRD analysis) and performing a depth analysis (Auger depth profiling, PIXE analysis or EDX). Once a membrane is broken, it cannot be used again. A different approach was taken in the present study. The permeance and the selectivity of the Pd-Ag films were monitored to determine the effect of annealing on the membrane performance. From the changes in hydrogen permeance and membrane selectivity, certain conclusions could then be drawn.

Two alloying setups were used:

1. A constant temperature tube furnace with the membrane not fixed at either end, and
2. A reactor with the membrane fixed at both ends.

Section 3.3.6 described the advantages of both methods and the different variables investigated.

7.4.1. ALLOYING IN A TUBE FURNACE

Membranes that were heat treated in the tube furnace (8c, N3b-N3e, N4c and N6) are indicated in **Table 7.1**. Permeance and selectivity data are listed in **Appendix D2.** Most membranes were tested with positive feed pressures and with a sweep gas.

7.4.1.1. Alloying at a temperature of 545 °C

The first set of experiments was performed at 545 °C in argon. The oven had to be cooled down after the alloying time to remove the membrane and place it in the reactor. The membrane was tested after 50h, 100h and 150 hours and the results compared to those of both a pure Pd film and an unalloyed Pd-Ag film. Results are presented in **Figure 7.14**.

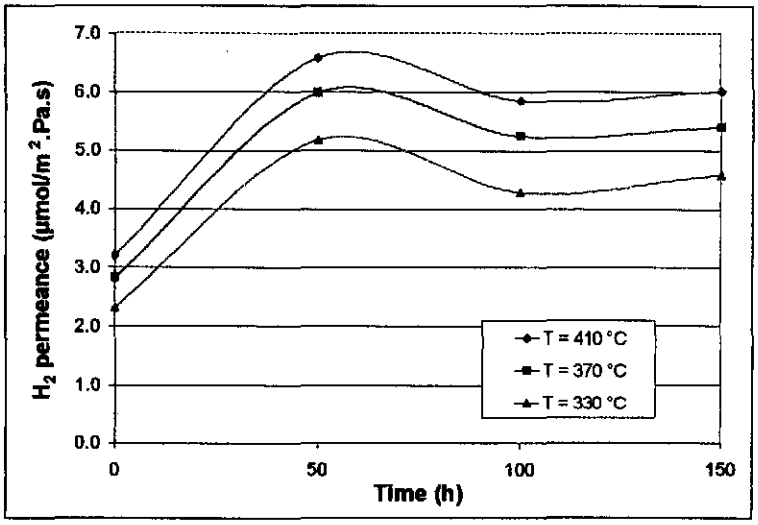

Figure 7.14: Effect of heating time in argon on hydrogen permeance through Pd-Ag (membranes N3b to N3e)

Figure 7.14 indicates a sharp increase in hydrogen permeance after the first 50 hours of heat treatment. The values were more that double those for the unalloyed Pd-Ag film. After 100 hours, the hydrogen permeance showed a slight decline, but values changed little from 100 hours to 150 hours. The increase in hydrogen permeance confirmed that silver diffused into the palladium matrix to yield a structure with less resistance than the separate silver and palladium layers. The decline in hydrogen permeance at 100 hours and 150 hours might be due to one of two reasons:

- The surface structure and morphology of the film changed after prolonged heating, causing a decline in hydrogen permeance, and/or
- Silver diffused through the Pd layer and started accumulating next to the alumina interphase. The structure then started approaching separate layers again, but with a high silver concentration next to the membrane support.

Table 7.4 compares hydrogen permeabilities for the pure Pd film with those of the Pd-Ag films. Permeability (P_m*l) was used rather than permeance to compare values, since permeance did not allow direct comparison of films with different thicknesses. The Pd film had a thickness of 1.47 µm and the Pd-Ag films a thickness of 2.14 µm. The silver content of the film was 24%.

Table 7.4: Effect of heating on hydrogen permeances for membrane N3

Membrane	Heating time (h)	T = 410 °C	T = 370 °C	T = 330 °C
		Permeability (μmol.μm/m^2.Pa.s)		
N3	0	15.89	14.19	12.27
N3b	0	6.87	6.03	4.96
N3c	50	14.10	12.82	11.09
N3d	100	12.54	11.24	9.18
N3e	150	12.90	11.58	9.82

Values in **Table 7.4** indicate that after silver was added to palladium, the hydrogen permeance did not return to the values obtained from the pure palladium. At all heating times (from 0-150 hours), the hydrogen permeances were lower than for the pure palladium. This contradicted results obtained by Cheng and Yeung (1999) and Uemiya et al. (1991a). They recorded improvements for Pd-Ag films compared to Pd films.

Reasons for this contradiction could not be obtained from permeance and selectivity data alone and could not be fully explained without further investigation. It must be noted, however, that the Pd-Ag film produced on membrane (N3) had a hydrogen permeance that was three times higher than that of Uemiya et al. (1991a) and more than 60 times higher than that of Cheng and Yeung (1999). From this initial experiments, it could be concluded that the surface structure and morphology of the metal film had a greater impact on hydrogen permeance than the film composition when the hydrogen permeance was very high and the film very thin (less than 2.5 microns).

7.4.1.1. Alloying at a temperature of 530 °C

Membrane (N4b) was a 1.43 μm $Pd_{77}Ag_{23}$ membrane. The effect of heating it in argon for 30 hours at 530 °C is shown in **Figure 7.15**. There was no real improvement in hydrogen permeance after heat treating the Pd-Ag film in argon for 30 hours at 530 °C.

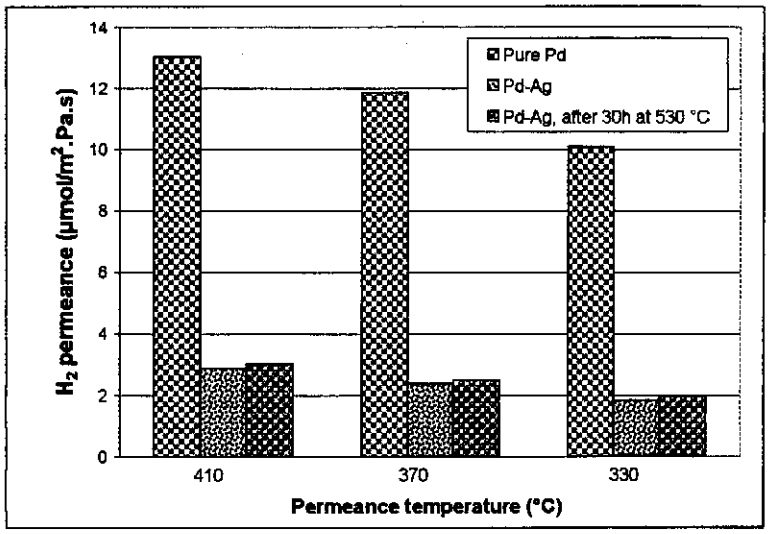

Figure 7.15: Effect of heating in argon on H_2 permeance for N4

7.4.1.3. Alloying at a temperature of 590 °C

Membranes (8b) and (N6) were heat treated in argon for 15 hours at 550 °C, whereafter the temperature was increased to 600 °C for a further 25 hours. Hydrogen permeance testing was not performed on these membranes, because their selectivity became too poor. The effect of temperature on membrane selectivity will be discussed in the following section.

7.4.2. TEMPERATURE STABILITY OF Pd-Ag MEMBRANES

Membrane stability can be expressed in terms of both nitrogen and hydrogen permeances. If both the hydrogen permeance and the nitrogen permeance remain constant over time, the metal film is concidered stable. If the hydrogen permeance decreases and/or the nitrogen permeance increases, then the film quality is deteriorating.

7.4.2.1. Literature data on Pd membrane stability

Depending on the support structure, different mechanisms are responsible for membrane deterioration. Some work has been performed on the stability of Pd deposited on metal substrates (porous stainless steel or a refractory metal). Interdiffusion between Pd and the support metal (see Shu et al., 1996a) resulted in a decline in hydrogen permeance over time (Buxbaum and Kinney, 1996). The effect on nitrogen permeance was not explicitly stated. No interdiffusion occurs when Pd is deposited on an alumina support. Differences in thermal expansion coefficients and changes in film morphology at high temperature could result in

film cracking and pore formation, leading to an increase in the amount of defects in the film and an increase in the nitrogen permeance. Paglieri et al. (1999) performed the first comprehensive study on the effects of film temperature on the film stability of pure Pd film deposited on the inside of alumina membrane tubes. The majority of the films had thicknesses between 8 and 27 micron.

Paglieri et al. (1999) tested membranes from 400 °C to 600 °C, and some even up to temperatures of 800 °C. They showed that the same deactivation occured in films of all thicknesses. The thicker the film, the longer it took for the selectivity to fall at 550 °C. Initial hydrogen to nitrogen selectivities were only about 30 to 80 for most membranes. After several days at 550 °C, selectivity declined to a Knudsen value of about 4. They obtained significant improvements in stability by omitting tin from the pretreatment process and replacing it with Pd acetate. They concluded that the stability of the film was influenced by:

- Tin deposition during pretreatment,
- Components of the electroless plating solution (mainly EDTA) trapped between the alumina surface and the Pd film, causing pore formation upon heating, and/or
- A difference in the thermal expansion coefficients of alumina and Pd.

After plating, the membranes were soaked overnight in water at 70 °C. There was a very good probability that there was EDTA trapped in the 200 nm pores of their membranes. In the present study, plated membranes were rotated at high speed in an ammonia solution for several hours. (EDTA has a high solubility in an ammonia solution, but a very low solubility in water.) Thereafter, membranes were dried and oxidised at 320 °C in pure oxygen. Even then, carbon was still present in some samples.

7.4.2.2. Pd-Ag membrane stability

No data exists on Pd-Ag membrane stability, for films of less than 2.5 microns, deposited on the inside of alumina membrane supports. A Sn to Pd molar ratio, which was about 8 times less than the conventional concentration for pretreatment (Shu et al., 1993), was used for pretreatment. The ratio in the present study was about 12 times lower than that for the full

strength sensitiser tested by Paglieri et al. (1999). Furthermore, a lot of attention was given to post plating cleaning (see **sections 3.3.2.3** and **3.3.5**).

Figure 7.16 shows the increase in N_2 permeance (at the permeance temperatures) of membrane (N4) after 30 hours of alloying in argon at 530 °C. The permeance remained below that of pure Pd, because of the extra thickness of the film. The decrease in permeance was about 50%. The membrane retained good selectivity at 530 °C.

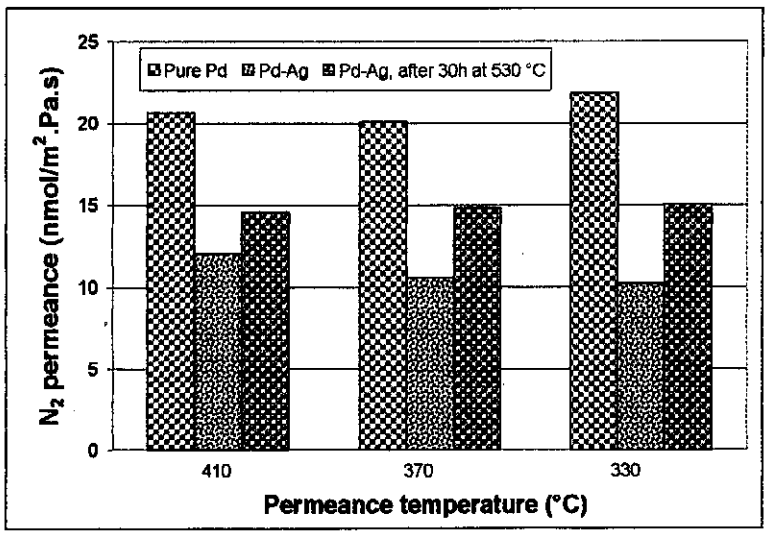

Figure 7.16: Effect of heating in argon on N_2 permeance for N4

Figures 7.17 and **7.18** show nitrogen permeance and selectivity data for membranes (N3b) to (N3e). The heating temperature was 545 °C in argon. **Figure 7.17** shows a steady increase in nitrogen permeance as the amount of defects in the film increased. Nitrogen flow increased with decreasing temperature, indicating that the defects that formed in the film were of Knudsen dimension (5 to 30 nm range). The selectivity of the membrane decreased to values between 110 and 75 for temperatures from 410 °C to 330 °C. A disadvantage of the heating system was that it required cooling before the membrane could be tested. After each set of tests, the membrane had to be reheated to 545 °C to be alloyed further. This repeated temperature cycling, between room temperature and 545 °C, could contribute significantly to the decrease in membrane stability. The complete temperature cycling for membrane (N3) was:

- 25 °C to 450 ° to 25 °C for testing the Pd film,

- 25 °C to 410 to 25 °C for testing the Pd-Ag film,
- 25 °C to 545 to 25 °C for alloying the Pd-Ag film (50 hours at 545 °C),
- 25 °C to 410 to 25 °C for testing the Pd-Ag film,
- 25 °C to 545 to 25 °C for alloying the Pd-Ag film (50h; total = 100 hours at 545 °C),
- 25 °C to 410 to 25 °C for testing the Pd-Ag film,
- 25 °C to 545 to 25 °C for alloying the Pd-Ag film (50h; total = 150 hours at 545 °C), and
- 25 °C to 410 ° to 25 °C for testing the Pd-Ag film.

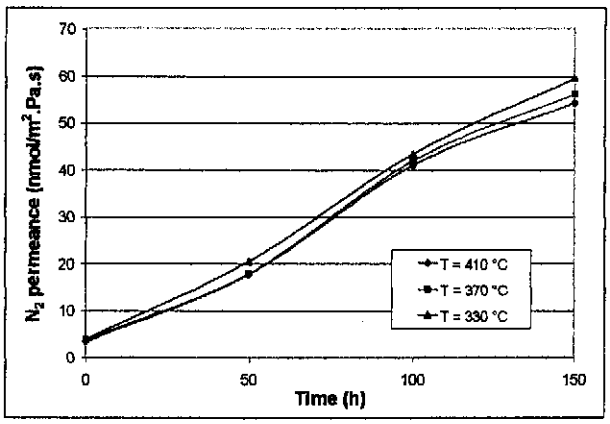

Figure 7.17: Effect of heating in argon on nitrogen permeance (N3)

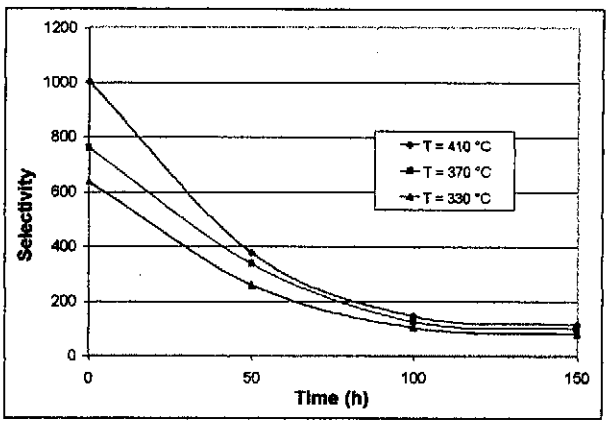

Figure 7.18: Effect of heating in argon on selectivity (N3)

Membranes (8c) (1.54 μm Pd_{75}–Ag_{25}) and (N6) (2.05 μm Pd_{79}–Ag_{21}) were heat treated in argon for 15 hours at 550 °C and then for a further 25 hours at 600 °C. The results are shown in **Table 7.5**. A temperature of 600 °C is too high to tolerate for films of thickness in the order of 2 μm. Selectivity will decrease rapidly, making the membrane unsuitable for separation at those high temperatures.

Table 7.5: Nitrogen permeance of membranes (8c) and (N6) after heating at 600 °C

Sample	N_2 permeance before heating (nmol/m^2.Pa.s)	N_2 permeance after heating (nmol/m^2.Pa.s)
8c	12.2 (330 °C)	114 (room)
N6	8.5 (room)	151.4 (room)

7.4.2.3. Structural changes of Pd-Ag membranes during heating

A scanning electron microscope was used to analyse the surface structure of a Pd-Ag membrane (membrane d) after various heating times. Top view images were taken to detect pore formation and possible clustering with time. Side view images were taken to detect peeling. The film had a theoretical thickness of 1.45 μm, which correlated well with the SEM determined thickness. The silver content was 20%. **Table 7.6** describes the different membrane stages.

Table 7.6: Description of different membrane stages (d1-d3)

Stage	Heat treatment
d1	50h in argon at 545 °C
d2	100h in argon at 545 °C
d3	135h at 545 °C + 25h at 600 °C in argon

Figures 7.19 to **7.30** compare membrane (d) at different heating stages and different magnifications. When comparing **Figures 7.19** to **7.24**, it can be seen that there was an increase in cluster size with an increase in heating time. Small clusters tended to agglomerate to form bigger clusters. Some holes were visible in (d3) (**Figures 7.21** and **7.24**). As agglomeration and segregation took place during prolonged heating at high temperatures, the grain boundaries decreased. To compensate for this decrease, small pores or holes formed.

Figures 7.25 to **7.28** give very clear pictures of membrane changes during heating. After 50 hours of heating, there were no pores visible on the membrane surface. Some pores started to develop after 100 hours of heating. In the middle of the left side of **Figure 7.26** some holes can be seen. Membrane (d3), heated for 135 hours at 545 °C and a further 25 hours at 600 °C, showed two different deterioration mechanisms. There were many pores scattered all over the membrane surface (**Figure 7.27**). Furthermore, some porous clusters started to develop. Two clusters can be seen in the middle left and middle right sides of **Figure 7.28**. What is interesting is that those clusters had a large height dimension, many times the thickness of the film. For the film to have had such an increase in height, the increase in pore area had to be very large.

Figure 7.19: Membrane d1 (25 000x)

Figure 7.20: Membrane d2 (25 000x)

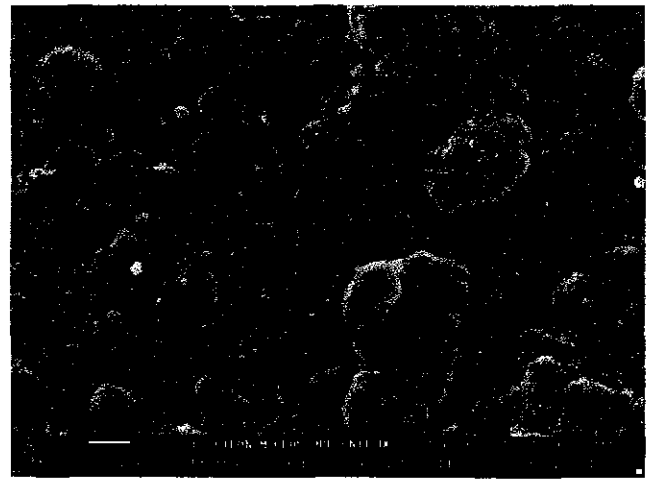

Figure 7.21: Membrane d3 (25 000x)

Figure 7.22: Membrane d1 (50 000x)

Figure 7.23: Membrane d2 (50 000x)

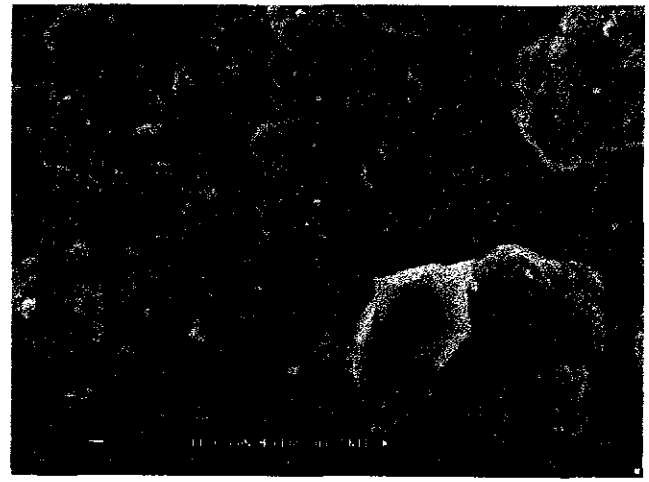

Figure 7.24: Membrane d3 (50 000x)

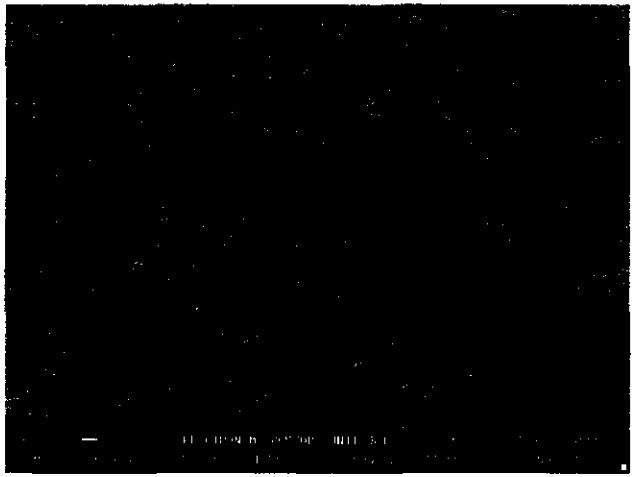

Figure 7.25: Membrane d1 (5 000x)

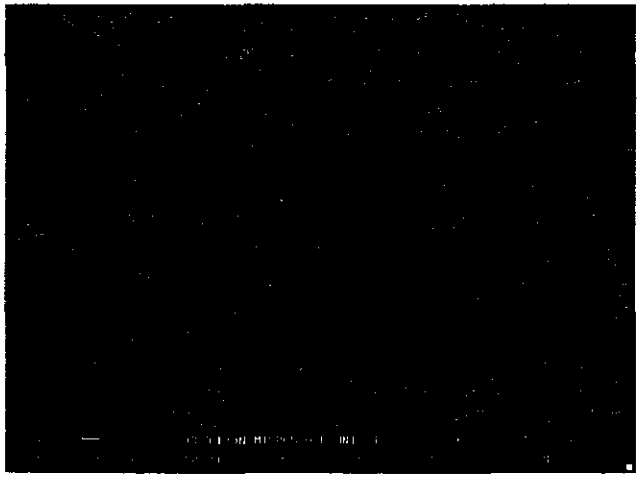

Figure 7.26: Membrane d2 (5 000x)

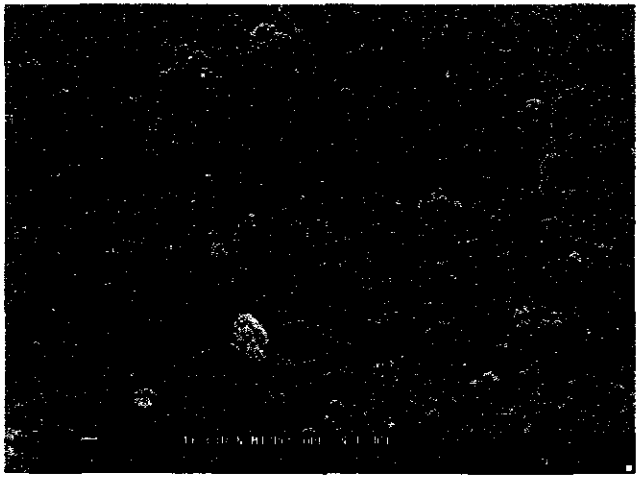

Figure 7.27: Membrane d3 (5 000x)

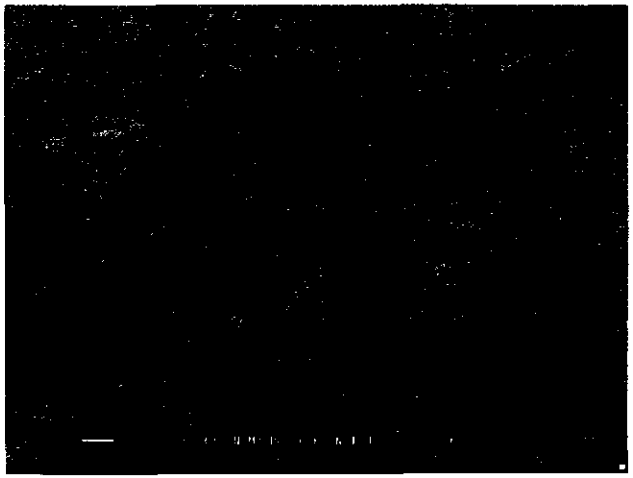

Figure 7.28: Membrane d3 (2000x)

Figure 7.29: Side view of d2

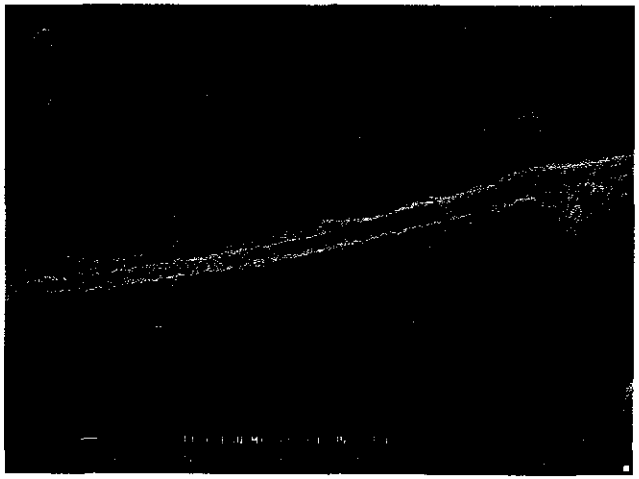

Figure 7.30: Side view of d3

Side view images (**Figure 7.29** and **7.30**) were taken to determine whether thermal expansion caused the film to detach from the support. After 100 hours and after 170 hours, the figures showed that film adhesion to the ceramic support remained strong.

7.4.3. ALLOYING IN SITU IN THE REACTOR

Membranes (N1x), (N2x), (N4x) and (N8x) were heat treated in the reactor. Heat treatment in the reactor had the advantages of continuous analysis and little temperature cycling compared to heating the membranes in the tube furnace. The disadvantage was that each membrane was subjected to high temperature axial stress in the reactor, since both ends of the membrane were fixed to the reactor.

7.4.3.1. Alloying in a hydrogen environment

Experiments were performed in Ar, H_2 or N_2. For membranes (N1x) and (N4x), only hydrogen was employed. Membrane (N4x) had a thickness of 2.13 μm and a silver content of 20 wt % Ag. It was heated in hydrogen at 540 °C for 30 hours. The hydrogen permeance increased with time, from about 4.1 $\mu mol/m^2.Pa.s$ to 5.7 $\mu mol/m^2.Pa.s$ (**Figure 7.31**) during the alloying stage. The nitrogen permeance also increased. The sharp initial increase in N_2 permeance, from 0 to 2.5 hours, was similar to the increase in hydrogen permeance. From 2.5 hours to 30 hours, the increase in nitrogen permeance was much slower than during the first 2.5 hours. This indicates a gradual increase in membrane defects in a hydrogen environment at 540 °C.

Figures 7.32 and **7.33** show hydrogen and nitrogen permeances for membrane (N1x) heated in hydrogen at 590 °C, as a function of time. (N1x) had a thickness of 2.13 μm and a silver content of 22 wt % Ag. Unlike with (N4x), the hydrogen permeance decreased with time at 590 °C (**Figure 7.32**).

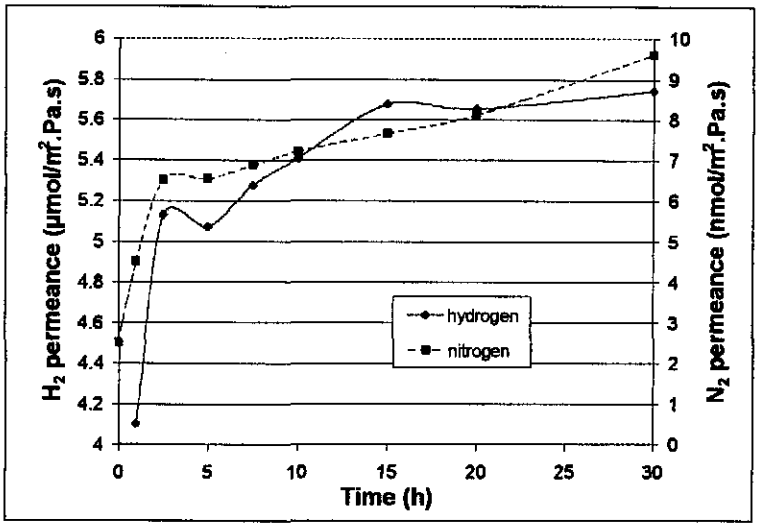

Figure 7.31: Effect of heating time in H_2 on H_2 and N_2 permeance for N4x

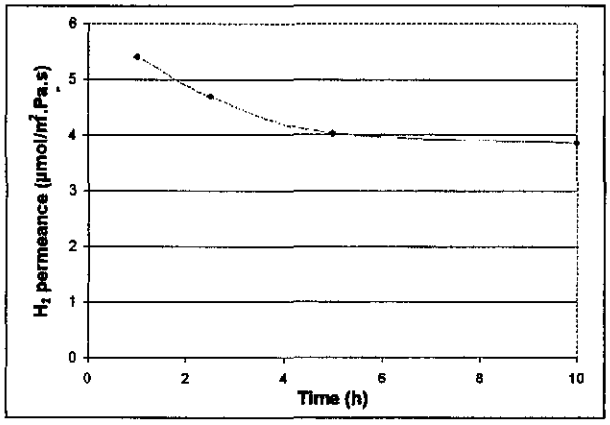

Figure 7.32: Effect of heating time in H_2 at 590 °C on H_2 permeance for N1x

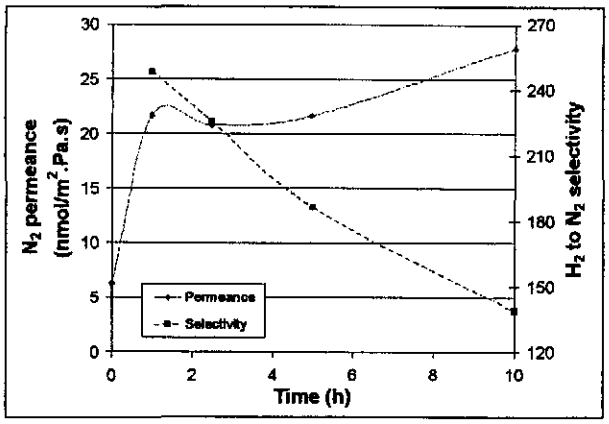

Figure 7.33: Effect of heating time in H_2 at 590 °C on N_2 permeance for N1x

The nitrogen permeance increased sharply (**Figure 7.33**), indicating that defects developed quickly at 590 °C in a hydrogen atmosphere. More defects should favour an increase in hydrogen permeance rather that a decrease in hydrogen permeance. The decrease in hydrogen permeance confirmed that structural and morphological changes took place on the metal alloy surface. There was a decrease in grain boundaries, which resulted in a decrease in hydrogen permeance. **Figure 7.34** shows the effect of temperature on the Pd-Ag film after heat treatment in hydrogen at 590 °C. Both nitrogen and hydrogen permeances were poor compared to the permeances for pure palladium films.

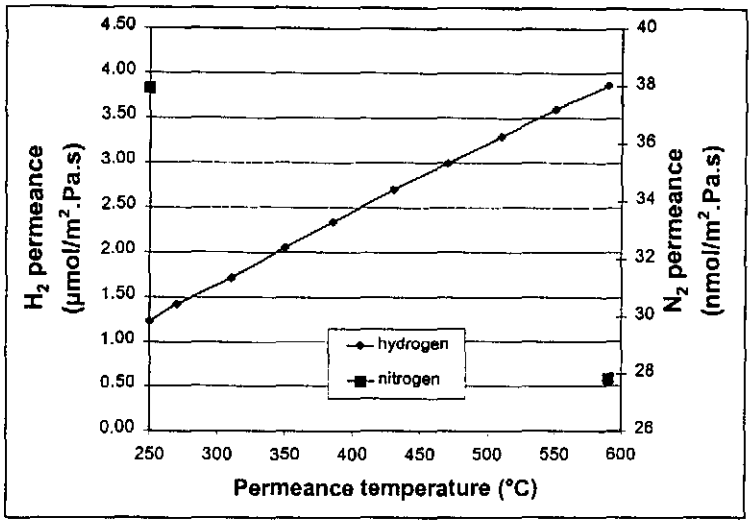

Figure 7.34: Effect of temperature on H_2 and N_2 permeance for N1x

7.4.3.2. Alloying in nitrogen and argon environments

Extensive testing was performed on membrane (N2x). The membrane had a thickness of 2.02 µm and a silver content of 25 wt %. The data is depicted in **Figures 7.35** to **7.38**. For the first 25 hours, the membrane was heated in nitrogen at 500 °C. Hydrogen permeance was determined by switching from nitrogen (or argon) to hydrogen and allowing for one hour in a hydrogen atmosphere before the reading was taken. From hours 25 to 50, the environment was changed to argon at 500 ° C. For hours 50 to 75, the temperature was increased to 550 °C, while maintaining the argon environment.

Experiments in a nitrogen atmosphere (0 to 25h) indicated that nitrogen had a passivating effect on the film. The hydrogen permeance decreased with time (**Figure 7.35**). Apart from the expected increase in nitrogen permeance in the first hour, the nitrogen permeance remained constant at 500 °C for 25 hours. The increase in the first hour was because the surface was activated with the first introduction of hydrogen and any oxides on the surface were reduced.

With the introduction of argon, the hydrogen permeance started increasing at 500 °C. Argon did not cause passivation of the Pd-Ag surface, as was the case with nitrogen. Not many

defects formed in the film at 500 °C from 25 to 50 hours. There was only a very slight increase in argon permeance during this period (**Figure 7.37**).

From 50 to 75 hours, there was a sharp increase in hydrogen permeance at 550 °C in argon (see **Figure 7.35**). Values increased from 3.0 μmol/m^2.Pa.s to 5.3 μmol/m^2.Pa.s. Many defects were introduced into the film during this time (see **Figure 7.37**). The stepwise increase in argon flux indicates that heating in hydrogen was the main reason for the increase in defects. Hydrogen was used for reduction at the following times and the argon permeances were measured before and after hydrogen introduction:

- 50-51 hours,
- 55.5-56.5 hours,
- 63.5-64.5 hours, and
- 73.5-75 hours.

Figure 7.38 shows the effect of temperature on the membrane after 75 hours of heat treatment.

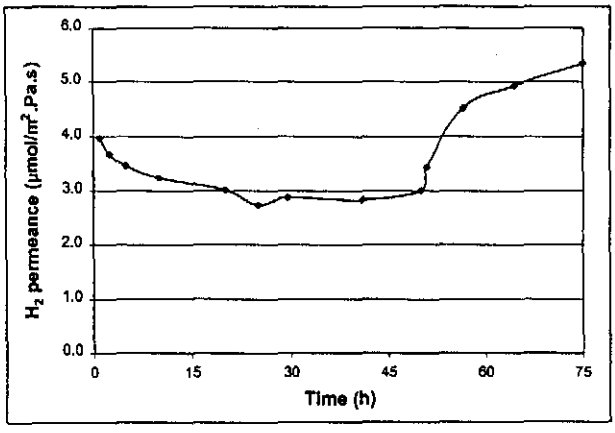

Figure 7.35: Effect of heating time in N_2 and Ar at 500 and 550 °C on H_2 permeance for N2x

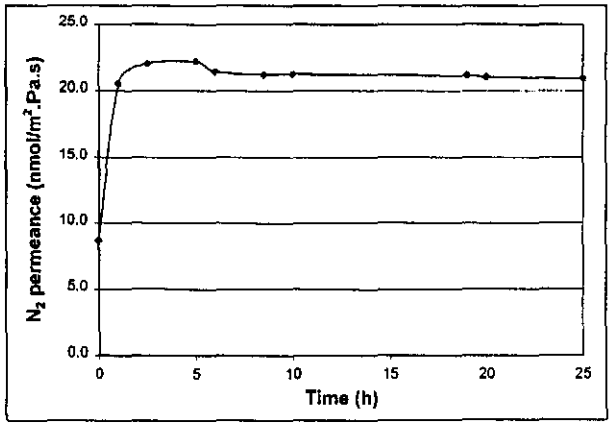

Figure 7.36: Effect of heating time in N_2 at 500 °C on N_2 permeance for N2x

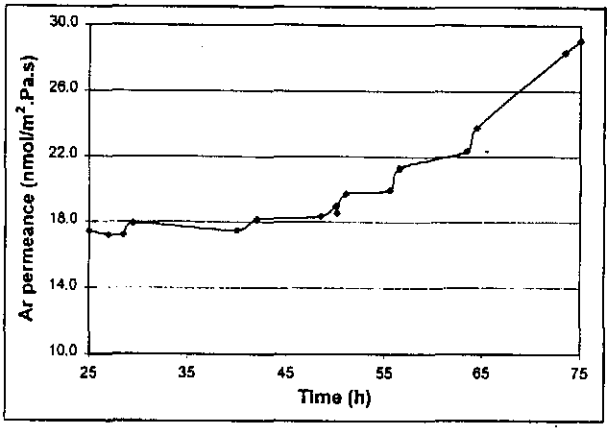

Figure 7.37: Effect of heating time in Ar at 500 and 550 °C on Ar permeance for N2x

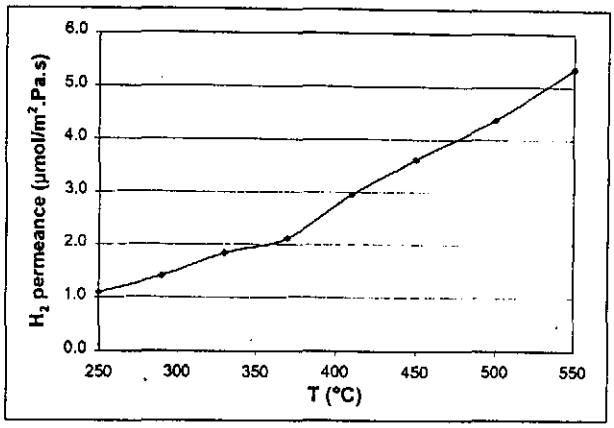

Figure 7.38: Effect of temperature on H_2 permeance for N2x

7.4.3.3. Further treatment of Pd-Ag films

Table 7.7 was compiled to compare the hydrogen permeances of all heat treated Pd-Ag films at 410 °C.

Table 7.7: Hydrogen permeances at 410 °C

Membrane	Thickness (µm)	% Ag	H_2 permeance at 410 °C (µmol/m².Pa.s)
N3c	2.14	24	6.59
N4c	1.43	23	3.02
N1x	2.13	22	2.52
N2x	2.02	25	2.95
N4x	2.13	20	3.16

Values in **Table 7.7** were similar to those of (N3b) and (N4b), where no heat treatment was performed. The exception was (N3c), which had a hydrogen permeance about twice that of the other membranes. The difference between (N3c) and the other membranes was that after 50 hours of heat treatment in argon, (N3c) was oxidised at 320 °C and then reduced. The other membranes were not re-oxidised after heat treatment.

This phenomenon was investigated further. Membrane (N4x) was oxidised after heat treatment (see **7.4.3.1**). (N8x) was prepared, heat treated for 10 hours in argon and then oxidised. The effects of further oxidation on hydrogen permeance for those two membranes are summarised in **Table 7.8**.

After oxidising and reducing the membranes again (after heat treatment), the hydrogen permeances increased. In the case of (N8x), the H_2 permeance more than doubled. On the negative side, additional oxidation weakened the film and created defects. Two different oxidation temperatures and times were tested. Oxidation at 350 °C was too severe. Oxidation for 1 hour at 310 °C yielded much better results. Further oxidation and reduction changed the surface morphology and structure of the film. These changes promoted hydrogen movement through the film.

Table 7.8: Hydrogen and nitrogen permeances at 410 °C after oxidation

Membrane	**Oxidation Temp (°C)**	**Oxidation Time (h)**	**H_2 permeance Before oxidation ($\mu mol/m^2.Pa.s$)**	**H_2 permeance After oxidation ($\mu mol/m^2.Pa.s$)**
N4x	350	3	3.16	4.62
N8x	310	1	2.85	6.03
			N_2 permeance Before oxidation ($nmol/m^2.Pa.s$)	**N_2 permeance After oxidation ($nmol/m^2.Pa.s$)**
N4x	350	3	9.6	24.5
N8x	310	1	13.1	18.2

7.4.3.4. Suggested heat treatment procedure for Pd-Ag films

The following procedure is suggested for heat treating Pd-Ag films of less than 2.5 μm.

- Heat the Pd-Ag membrane in argon up to a temperature of between 540 °C and 550 °C,
- Heat treat in argon for 10 hours at the above temperature,
- Cool down in argon to 310 °C and oxidise in oxygen for 1 hour,

- Heat up to 400 °C in argon, and
- Reduce in hydrogen for 2 hours.

The stability of the Pd-Ag membranes at temperatures from 200 °C to 300 °C were monitored during the catalytic membrane reactor experiments and will be mentioned in Chapter 9.

7.5. FULL CHARACTERISATION OF MEMBRANES N4x AND N8x

Membranes (N8x) and (N4x) were used for catalytic membrane reactor experiments. All H_2 and N_2 permeance data for membranes (N8x) and (N4x) is listed in **Appendix D2**. They were tested at temperatures ranging from 250 °C to 410 °C. **Figures 7.39** and **7.40** plot the hydrogen and nitrogen permeances of membranes (N8x) and (N4x), from 250 °C to 410 °C. **Appendix D2** contains the calculated Arrhenius parameters.

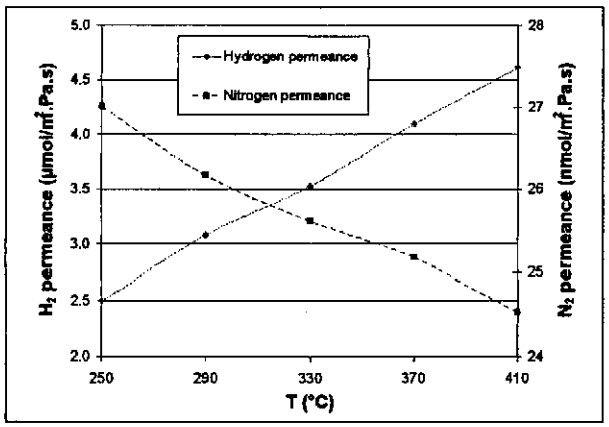

Figure 7.39: H_2 and N_2 permeances for N4x

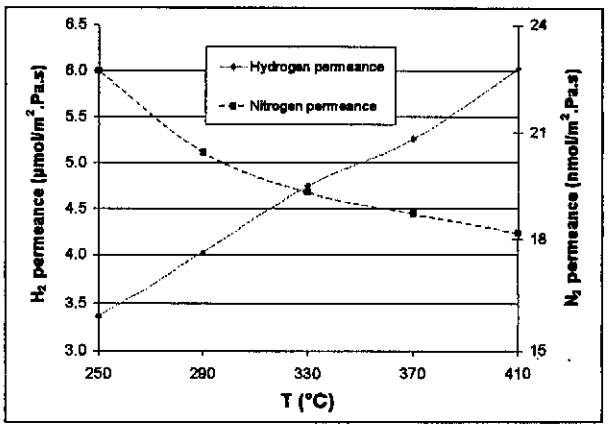

Figure 7.40: H_2 and N_2 permeances for N8x

Calculated values correlated well with measured values when a sweep gas was employed (**Figures 7.41** and **7.42**). For membrane (N8x), the error was typically less than 5%, but for N4x it was sometimes slightly larger. This was due to the higher N_2 permeance of (N4x).

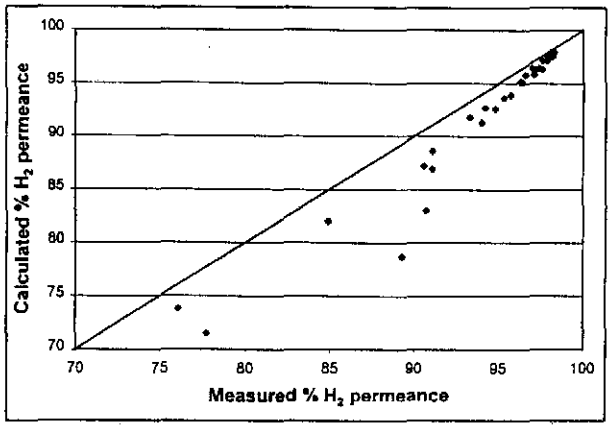

Figure 7.41: Measured vs. calculated % H_2 permeance for N4x

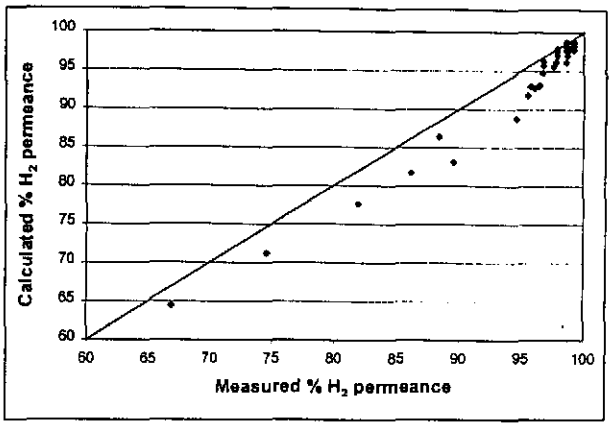

Figure 7.42: Measured vs. calculated % H_2 permeance for N8x

7.6. SUMMARY

Pd-Ag membranes of less than 2.2 μm thickness were prepared by successive electroless plating steps. The permeances of those films at 410 °C ranged from 3.0 to 5.5 μmol/m^2.Pa.s before heat treatment. That was significantly lower than the values for pure Pd films.

Different heat treatment methods were employed to improve the hydrogen permeance of the Pd-Ag film. In all the gas environments tested, the films weakened at and above 590 °C. Hydrogen created defects in the film at a moderate rate at 550 °C and at a fast rate at 590 °C. Furthermore, hydrogen passivated the film at 590 °C but not at 540 °C. Film passivation resulted in a decline in hydrogen permeance. Continuous thermal cycling contributed towards film defection.

Some defects formed in argon at 545 °C after 100 hours of heating, but very few defects formed at 500 °C in either nitrogen and argon. Nitrogen also passivated the film and should not be used for heat treatment. The best conditions for heat treatment were:

- an argon environment,
- at a temperature of 550 °C, and
- a heating time of about 10 to 15 hours.

After heat treatment, the film has to be oxidised at 310 °C for not more than 1 hour and then reduced to obtain the best combination of hydrogen permeance and selectivity. This additional oxidation-reduction step resulted in a great improvement in hydrogen permeance. This phenomenon has not been observed previously by any other research group.

8. CATALYTIC MEMBRANE REACTOR MODELLING

This chapter will focus on the development of a catalytic membrane reactor model. All aspects of the model will be investigated and a complete sensitivity analysis will be performed to determine the effect of each parameter on the performance of the reactor. The effect of the feed rate on reaction conversion is discussed. Experimental data for a plug flow reactor at different feed flow rates are presented.

8.1. REACTANT FEED RATES

Most work performed to date on dehydrogenation in catalytic membrane reactors has been done with very low feed flow rates. This approach exaggerates the theoretical advantages of the membrane reactor and provides very good results. In **Figure 8.1** the region marked by block 1 is the region of very low feed rates. Feed rates increase from left to right and the space times increase from right to left. Data gathered in the region of 1 is of very little practical importance. Such low feed flow rates result in an extremely low product production rate even though the conversion is increased.

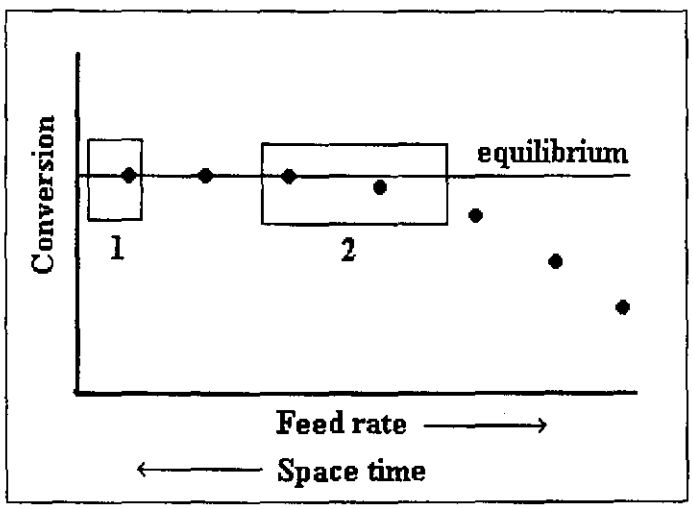

Figure 8.1: Theoretical effect of feed rate on equilibrium conversion

In the present study high feed rates were employed to determine the practical importance of a catalytic membrane reactor. Experiments were performed in the region marked by block 2.

If a catalytic membrane reactor can significantly improve reaction conversion when the feed rate is fast enough not to limit the reaction by the equilibrium conversion, then the reactor becomes of practical importance. **Table 8.1** summarises some experimental conditions employed by other researchers for dehydrogenation reactions with liquid feeds in a membrane reactor. The feed rates used in the present study are included, to illustrate the where the present study 'fits in'.

Table 8.1: Different liquid hourly space volumes (LHSV) used for dehydrogenation reactions in a membrane reactor

Dehydrogenation reaction	Temperature range (° C)	LHSV (h)	Reference
cyclohexane	< 200	48-263	Itoh (1987)
methylcyclohexane	300-400	2-12	Ali (1994)
cyclohexane	185	Approx. 42	Cannon (1992)
ethanol	250-310	5-22*	Deng (1995)
ethanol	175-275	110**	Raich (1998)
ethanol	250-300	0.75-0.25	The present study
2-butanol	190-240	0.4-1.5	The present study

* Assuming a catalyst mass of 3 g and reactor volume of 8 cm^3

** Using an argon feed flow of 6.5 ml/min and a reactor volume of 8 cm^3

8.2. ALCOHOL PERMEATION DATA

The permeance of ethanol through film defects was determined for a pure Pd film and the result compared to the nitrogen permeance of the same film. The experimental set-up and procedure used have been discussed in **section 3.3.4.** **Figures 8.2** and **8.3** show ethanol selectivity as a function of temperature, compared to nitrogen selectivity. Ethanol had a lower permeance through the film than nitrogen, because of the larger molecule size. This resulted in a higher hydrogen to ethanol selectivity compared to the hydrogen to nitrogen selectivity. The nitrogen to ethanol selectivity varied between 3.1 and 4.4, with temperature.

To simplify calculations, an average of 4 was assumed for modelling. This value was different from what would be expected using the Knudsen theory, which suggests a nitrogen to ethanol selectivity of about 1.3. Other transport effects through the defects in the membrane occurred simultaneously with Knudsen flow. Since the measured nitrogen to ethanol selectivity was much larger than the Knudsen value it shows that many defects were smaller than the Knudsen defects. The presence of a large amount of molecular sieving defects would explain the difference between the nitrogen and ethanol permeances. The ethanol molecules were too large to pass through many defects where nitrogen molecules could pass through.

The permeances of other organic species were not measured. The worst case scenario was used for determining permeances for modelling. The selectivities were taken as the ratio between the molecular masses of each species (Knudsen theory) relative to ethanol. This could be expressed as:

$$P_{m,1} = P_{m,2}\sqrt{\frac{M_{r,1}}{M_{r,2}}} \qquad \textbf{(8.1)}$$

The permeance for 2-butanol will thus be 1.27 times lower than that of ethanol.

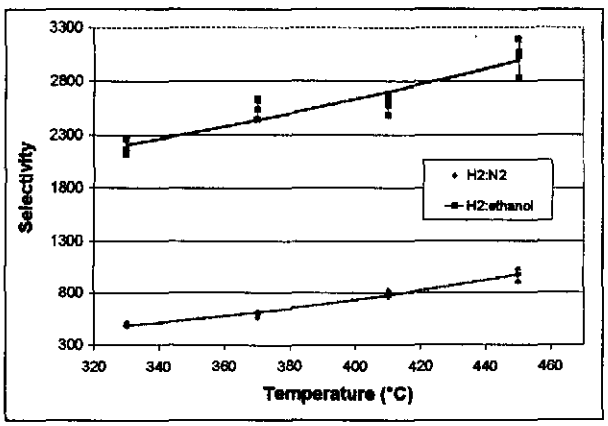

Figure 8.2: Comparison between H_2 to N_2 and H_2 to ethanol selectivities for a 1.5 μm Pd film

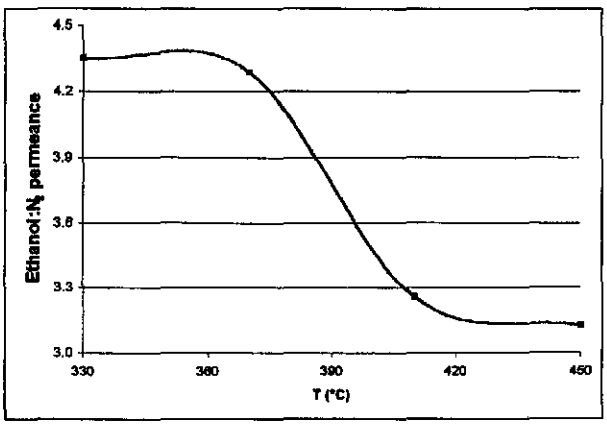

Figure 8.3: Ethanol to nitrogen permeance ratio for a 1.5 μm Pd film

8.3. DEVELOPING A PROCESS MODEL

A preliminary model was constructed to mathematically describe the dehydrogenation of alcohols in a catalytic membrane reactor. The process used a nitrogen sweep gas to create a partial pressure differential across the membrane. The flow of the sweep gas was co-current to that of the feed. A practical sweep gas in industry could be steam, which would supply heat to the endothermic dehydrogenation reaction and create the hydrogen concentration gradient across the membrane. Alternatively, the shell side of the reactor could operate under vacuum conditions.

8.3.1. MODEL ASSUMPTIONS

The following assumptions were made:

- isothermal operation,
- plug flow on both the tube and the shell side,
- isobaric conditions, in other words negligible pressure drop on the shell and tube sides,
- no radial concentration gradients in the catalyst bed, and
- steady state operation.

Both the shell and the tube sides were operated under atmospheric conditions. The pressure drop across the length of the packed membrane tube (length of catalyst bed = 20 cm) was less than 15 mbar. Isobaric conditions along the membrane's axis was therefore a good assumption. To incorporate an axial pressure drop, the Ergun equation (**8.2**) could be used (Fogler, 1992).

$$\frac{dP}{dL} = \frac{G}{\rho g_c D_p}\left(\frac{1-\varepsilon_b}{\varepsilon_b^3}\right)\left[\frac{150(1-\varepsilon_b)\mu}{D_p} + 1.75G\right] \qquad (8.2)$$

where

P	=	pressure	[Pa]
ε_b	=	void fraction of packed bed	

g_c	=	conversion factor (1 for SI units)	
D_p	=	particle diameter	[m]
μ	=	gas mixture viscosity	[kg/ms]
L	=	length down the tube	[m]
U	=	empty column velocity	[m/s]
ρ	=	gas density	[kg/m^3]
G	=	empty column mass velocity = ρU	[kg/m^2s]

For porous membranes (non palladium based) exhibiting Knudsen diffusion, the permeance equation cannot be used and a radial pressure drop model must be employed (Deckman et al., 1995).

Radial concentration models have been studied for a catalytic membrane reactor (Becker et al., 1993; Gobina et al., 1995a-c). Gobina et al. (1995b) found that the radial concentration change was negligible for a membrane with a 7.8 mm inner diameter.

The final assumption of steady state was not very accurate, but was made to simplify calculations. The data was gathered within a 24 hour period to give a better approximation of steady state. Thereafter, both the catalyst and the membrane were re-activated before the next set of tests. Non-steady state is due to both catalyst and membrane deactivation with time, which influences both the kinetics and the separation aspects of the process.

8.3.2. DESIGN EQUATION

A catalytic membrane reactor is a plug flow reactor with separation. The process is illustrated in **Figure 8.4**.

The flow on the tube side can be expressed by:

$$\frac{dF}{dV} = r - \frac{J}{L} \qquad (8.3)$$

or in dimensionless form, with the reaction at bulk conditions

$$\frac{dF_i}{d\frac{L}{L_0}} = \nu_i r_{i,b} \eta V - J_i A_m = L\pi R_m (\nu_i r_{i,b} \eta - \frac{2}{R_m} J_i) = V\left[\nu_i r_{i,b} \eta - \frac{2}{R_m} J_i\right] \qquad (8.4)$$

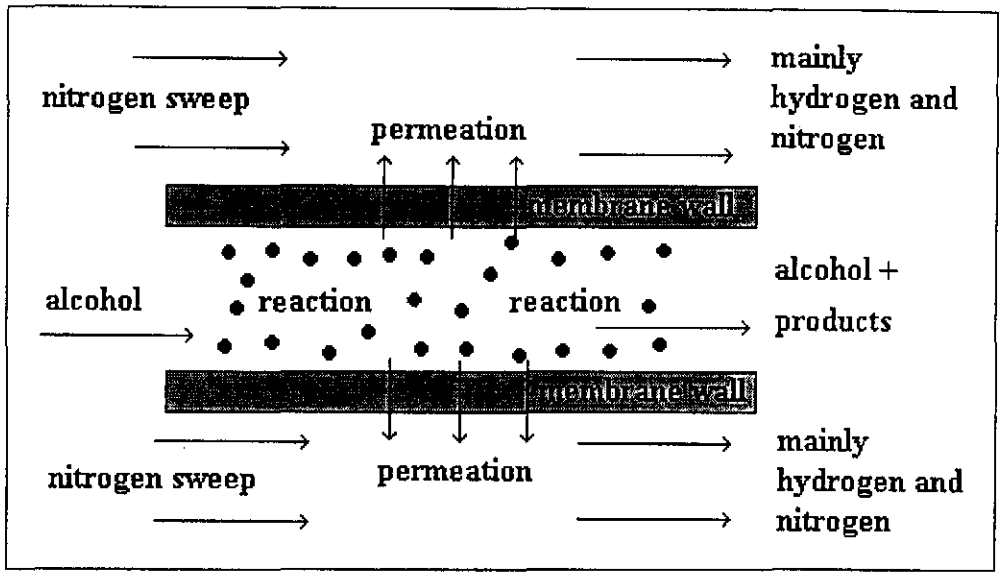

Figure 8.4: Description of catalytic membrane reactor process

Similarly, on the shell side:

$$\frac{dQ_i}{d\frac{L}{L_0}} = V\left[\frac{2}{R_m} J_i\right] \qquad (8.5)$$

In (8.4), i = alcohol feed, reaction products and hydrogen, while in (8.5), i = nitrogen sweep gas. The boundary conditions for co-current flow are:

At $L = 0$, $F_i = F_{i0}$. (8.6)

At $L = 0$, $Q_i = Q_{i0}$. (8.7)

The flux equations were derived in **section 6.6.5**. For equations (6.1) to (6.5), the right hand side of the equations represents the permeance component, expressed in terms of feed flow rates.

A kinetic expression for ethanol dehydrogenation was derived in equation (**5.21**), with optimised parameters in **Table 5.6**. The 2-butanol dehydrogenation expression was given in equation (**5.26**) with optimised parameters in **Table 5.8**. The permeance and kinetic expressions will be summarised in a later section.

8.3.3. MODELLING OF MASS TRANSFER EFFECTS

Interphase and/or intraparticle mass transfer resistance reduce the actual reaction rate, because the reactant concentration within the catalyst particle becomes lower than the bulk concentration. It is important to know whether the process is reaction rate limited or mass transfer limited, or both. Furthermore, it is important to know which mass transfer process is limiting. Sometimes all limitations can be present at once. Mass transfer is dependent on physical mixture properties like diffusion coefficients, density and viscosity. As the reaction takes place, the mixture composition changes continuously along the reactor's axial position. The limiting step in the reaction can change with position.

In most instances, correlations do not exist to predict properties of ternary and higher order mixtures. Furthermore, the available correlations may contain significant errors.

8.3.3.1. Interphase mass transfer resistance modelling

The first step in modelling mass transfer is to calculate the interphase mass transfer coefficient (k_c). Correlations have been formulated to relate this coefficient to various physical properties of the liquid or gas flowing through a packed bed reactor. The most common equation is the Thoenes-Kramers correlation (Fogler, 1992) for flow through a packed bed.

$$\left[\frac{k_c D_p}{D_{A,m}}\left(\frac{\varepsilon_b}{1-\varepsilon_b}\right)\frac{1}{\gamma}\right]=\left[\frac{UD_p\rho_m}{\mu_m(1-\varepsilon_b)\gamma}\right]^{1/2}\left(\frac{\mu_m}{\rho_m D_{A,m}}\right)^{1/3} \qquad (8.8)$$

k_c = mass transfer coefficient [m/s]

D_p = particle diameter (equivalent diameter of sphere of the same volume) [m]

= $[(6/\pi)(\text{volume of pellet})]^{1/3}$ [m]

ε_b	=	void fraction of packed bed	
γ	=	shape factor (external area divided by πD_p^2)	
μ	=	viscosity	[kg/m.s]
ρ	=	fluid density	[kg/m^3]
υ	=	μ/ρ = kinematic viscosity	[m^2/s]
$D_{A,m}$	=	gas phase diffusivity of A in bulk fluid (mixture)	[m^2/s]
U	=	Empty column velocity	[m/s]

Subscript m refers to mixture properties.

The equation is valid for: $0.25 < \varepsilon_b < 0.5$; $40 < Re' < 4000$ and $1 < Sc < 4000$, with

$$Re = \frac{D_p U}{\nu} \tag{8.9}$$

$$Sc = \frac{\nu}{D_{A,m}} \tag{8.10}$$

$$Re' = \frac{Re}{(1-\varepsilon_b)\gamma} \tag{8.11}$$

$$Sh' = (Re')^{1/2}(Sc)^{1/3} \tag{8.12}$$

$$Sh' = \frac{Sh\varepsilon_b}{(1-\varepsilon_b)\gamma} \tag{8.13}$$

For equations (**8.9**) to (**8.13**), mixture properties also apply.

Accurate correlations exist for determining physical properties of mixtures at various temperatures and pressures. Empirical estimation methods have been discussed in Millat et al. (1996).

Diffusion coefficients in multi-component gas mixtures are difficult to calculate. Many accurate correlations exist for determining binary diffusion coefficients (Perry and Chilton, 1973), but not for higher order mixtures. Some studies on diffusion in three component gas

mixtures (Toor, 1957; Duncan and Toor, 1962) and multi-component gas mixtures (Curtiss and Hirschfelder, 1949; Wilke, 1950; Fairbanks and Wilke, 1950) have been performed. In the simplest form, the diffusion coefficient can be estimated by the following:

$$D_{A,m} = \frac{1 - Y_A}{\frac{Y_B}{D_{AB}} + \frac{Y_C}{D_{AC}} + \frac{Y_D}{D_{AD}} + \ldots} \tag{8.14}$$

For laboratory reactors with low flow rates and thus low Reynolds numbers, the Thoenes – Kramers equation is invalid. Satterfield (1980) listed some alternative correlations for determining the mass transfer coefficient.

$$k_c = \frac{0.357}{\varepsilon_b D_p} Re^{0.641} Sc^{0.33} D_{A,m} \tag{8.15}$$

If $3 < Re < 2000$ and $1.8 \text{ mm} < D_p < 9.4 \text{ mm}$

$$k_c = C_1 \frac{D_{A,m}}{D_p} Re \tag{8.16}$$

For: $0.1 < Re < 10$

The value of the constant, C_1, differs depending on the literature source. Satterfield (1980) suggested a value of 0.07, while Collins (1993b) used a value of 0.015, determined from experimental data.

With k_c known, the Mears' criterion can be used to determine whether external diffusion is rate limiting (Fogler, 1992). When

$$\frac{-r'_{A(obs)} \rho_b D_p n}{k_c C_{A,b}} < 0.3 \tag{8.17}$$

where

n	=	reaction order	
D_p	=	particle diameter	[m]
ρ_b	=	bulk density of catalyst bed	[kg/m^3]
$C_{A,b}$	=	bulk concentration of A	[kmol/m^3]
k_c	=	mass transfer coefficient	[m/s]

then external mass transfer effects can be neglected. It is clear from (**8.17**) that external mass transfer will become more important as the feed concentration drops along the membrane axis and $C_{A,b}$ decreases.

To link the reaction rate coefficient and the mass transfer coefficient, a mass balance can be performed around the outside of the catalyst surface.

$$k_c A_p(C_{A,b} - C_{A,surf}) = \eta m r'_{A,surf} \text{ or} \qquad (8.18)$$

$$k_c A_p(P_{A,b} - P_{A,surf})/8.314T = \eta m r'_{A,surf} \qquad (8.19)$$

where

A_p	=	external surface area of the catalyst	
	=	$6m(1-\varepsilon_b)/\rho_b D_p$	[m^2]
m	=	mass of catalyst	[kg]
$r'_{A,surf}$	=	the surface reaction rate	[mol/kg.catalyst.s)
	=	the reaction rate in the absence of any mass transfer limitations	
η	=	effectiveness factor	

The bulk concentration of the reactant is known, but not the surface concentration or the surface rate. Equation (**8.18**) or (**8.19**) must be used to determine the surface concentration or surface pressure in terms of the bulk concentration or bulk pressure. The difference between

the two is due to the external mass transfer resistance. When no external mass transfer resistance is present, the surface concentration is equal to the bulk concentration. It is thus very important to obtain kinetic data free from mass transfer limitations, because if mass transfer limitations are present, the measured rate will be different from the surface rate and calculations will be faulty.

In the cases of ethanol and 2-butanol dehydrogenation, the reaction rate on the right hand side of (**8.18**) or (**8.19**) must be replaced by either equation (**5.21**) or (**5.26**). The surface concentration or pressure of the alcohol must then be determined in terms of the overall effectiveness factor and the bulk concentrations or bulk pressures of all species. The dehydrogenation rate equations include surface partial pressures for the feed as well as for the products. As a first approximation, it can be assumed that the interphase mass transfer resistance of all the species to reach the surface is the same, and then the following simplification can be made:

$$P_{i,surf} = \frac{P_{A,surf}}{P_{A,b}} P_{i,b} \qquad (8.20)$$

Equation (**8.20**) is substituted into the rate equations (**5.21** or **5.26**) and the rate equation is then substituted into (**8.19**). The result is an equation with three unknowns: k_c, η and $P_{A,surf}$. Mathematically $P_{A,surf}$ can be expressed by:

$$P_{A,surf} = f(\eta, k', k_c, P_{i,b}) \qquad (8.21)$$

To solve equation (**8.21**), k, k_c and η must first be determined. All the parameters can be obtained from experimental data by performing experiments in the absence of intraparticle mass transfer resistance (see **8.3.4**).

8.3.3.1.1. The effectiveness factor

The definition and application of the effectiveness factor can cause great confusion. In the present study the effectiveness factor is taken as the difference between the measured

reaction rate and the rate that exists on the catalyst surface. Both the effects of interphase and intraparticle mass transfer resistance are incorporated into η.

$$-r'_{A,b} = \eta(-r'_{A,surf}) \qquad (8.22)$$

The best approach is to determine η experimentally. Very small catalysts particles (< 0.6 mm) must be used to limit internal mass transfer resistance and prevent channelling of the feed gas through the reactor (see **4.1.3.3**). The reaction rate should then be measured in the region where the reaction rate does not change with feed flow rate (Reynolds number). The ratio between reaction rates at low feed flow rates and very high feed flow rates gives an experimental value for η. The value of η is dependent on the feed flow rate or Reynolds number. The effectiveness factor can also be estimated theoretically, as will be discussed in **section 8.3.3.2**.

8.3.3.2. Intraparticle mass transfer resistance modelling

In **section 4.1.3.3** the effect of particle size on ethanol conversion was discussed. **Figures 4.25** and **4.26** show that for particles smaller than 850 μm, the ethanol dehydrogenation results did not vary too much and thus, it is acceptable to ignore intraparticle mass transfer resistance for the experiments in the present study. The theory of intraparticle mass transfer resistance modelling will only be discussed briefly.

The catalyst particle is modelled as a sphere. The concentration of the reactant declines from the outside surface into the pores of the particle. The following expression can be used to describe the radial concentration profile in the particle (Fogler, 1992).

$$\frac{d\left[-D_e \frac{dC_A}{dr'}(r')^2\right]}{dr'} - (r')^2 mr'_A = 0 \qquad (8.23)$$

For non-reversible n^{th} order reactions, the equation can be written in dimensionless form and solved algebraically (Fogler, 1992). For complex reactions, the problem must be solved

numerically. Collins (1993b) formulated equations for solving a reversible reaction. In dimensionless form the following equation was obtained:

$$\frac{1}{r^2}\frac{d}{dr}\left(r^2\frac{dX_{f,A}(r)}{dr}\right)=\frac{k'\rho_b R_p^2}{C_t Y_{A,b} De_A(1-\varepsilon_b)}Z(r) \qquad (8.24)$$

$$\text{where } X_{f,A}=\frac{\text{mole fraction of A in catalyst}}{\text{mole fraction of A in bulk}} \qquad (8.25)$$

and

$$Z(r)=\frac{\left(P_A X_{f,A}(r)-P_R X_{f,R}(r)P_S X_{f,S}(r)/K_{eq}\right)}{\left(1+K_A P_A X_{f,A}(r)+K_R P_R X_{f,R}(r)+K_S P_S X_{f,S}(r)\right)^2} \qquad (8.26)$$

Equations **(8.24)** to **(8.26)** apply for both the dehydrogenation of ethanol and 2-butanol.

Boundary conditions and material balances for each species in the reaction have been summarised by Collins (1993b). The effectiveness factor, η, is the actual overall rate of reaction divided by the rate of reaction at bulk conditions ($C_{A,b}$). Some authors define η as the actual reaction rate divided by the rate that would result if the entire interior surface was exposed to the surface conditions (Fogler, 1992, calls it an internal effectiveness factor). This definition was, however, not used by Collins (1993b). He defined η as an overall effectiveness factor. The effectiveness factor at a specific axial position along the membrane's axis can be expressed by:

$$\eta=\frac{\int_0^1 Z(r)r^2dr}{\frac{r_A'}{k'}\int_0^1 r^2dr} \qquad (8.27)$$

Equation (**8.27**) must be evaluated numerically. Bulk conditions are used for solving equation (**8.27**). With the value of η known, the surface concentrations or partial pressures can be calculated with equation **8.21**. With the surface properties known, the surface reaction rate can be calculated by using equation (**8.18**) or (**8.19**). Finally the reaction rate at bulk conditions can be calculated:

$$-r'_{A,b} = \eta(-r'_{A,surf}) \qquad (8.22)$$

The main goal of the modelling exercise was to calculate the value of η. The surface reaction rate could be measured under special conditions and once η was known, the reaction rate at any bulk conditions could be calculated.

The Weisz-Prater criterion (Fogler, 1992) for internal diffusion can be used to determine whether there are significant internal diffusion limitations. The Weisz-Prater parameter is define by:

$$C_{WP} = \frac{-r'_{A,b}\rho_p R_p^2}{D_e C_{A,surf}} \qquad (8.28)$$

If $C_{WP} << 1$ then there are no internal diffusion limitations.

8.3.3.2.1. Effective diffusion coefficient (De_i)

In equations (**8.23**) and (**8.24**) a new coefficient, the effective diffusion coefficient, was introduced. This coefficient describes the movement of molecules inside a catalyst's pores. Movement can be either through bulk diffusion inside the pores or by Knudsen diffusion. Both these mechanisms are incorporated into the effective diffusion coefficient. Empirical correlations for determining De_i are listed in Satterfield (1980).

8.3.3.3. Summary of modelling mass transfer

Incorporating mass transfer limitations into the reaction rate equation can be summarised by the following steps.

1. Determine the dimensionless parameters, Re and Sc.
2. Calculate the mass transfer coefficient, k_c, using one of the equations (**8.8**), (**8.15**) or (**8.16**). In the case of (**8.16**), C_I will have to be determined experimentally.
3. Determine whether the external mass transfer is rate limiting by testing Mears' criterion (equation **8.17**).
4. Calculate the effective diffusion coefficient defined by Satterfield (1980).
5. If external mass transfer is not rate limiting, then surface conditions can be taken as bulk conditions and the Weisz-Prater criterion can be tested to determine if internal mass transfer is limiting. If both the interphase and itraparticle mass transfer resistances are negligible, then the effectiveness factor equals one.
6. If external mass transfer is rate limiting then the Weisz-Prater criterion cannot be tested since the surface concentrations are not known. The reactant surface concentration or pressure must be calculated in terms of η by using equation (**8.18**) or (**8.19**).
7. The effectiveness factor must be determined from equation (**8.27**).
8. With k_c (after point 3), $P_{A,surf}$ (from point 6) and η (from point 7) known, the surface reaction in equation (**8.19**) can be calculated.
9. The reaction rate using the bulk conditions can now be determine from equation (**8.22**), since both the effectiveness factor and the surface reaction rate are known.

8.3.4. MASS TRANSFER COEFFICIENTS FROM EXPERIMENTAL DATA

Mass transfer coefficients for the dehydrogenation of ethanol and 2-butanol were determined experimentally. As mentioned previously, small catalyst particles were employed to limit internal mass transfer resistance and prevent channelling of the feed gas through the reactor. Only external mass transfer resistance was considered as a first approximation.

8.3.4.1. Ethanol dehydrogenation

The first step in determining the mass transfer coefficient was to determine the Reynolds number and thus the viscosity of the gas mixture. The viscosity is dependant on the mixture composition and the temperature at low pressures. The method of Reichenberg (Millat et al., 1996) was used to determine pure gas viscosities and the method of Davidson to determine the viscosity of the gas mixture (Millat et al., 1996). Binary diffusion coefficients were

determined by Wilke-Lee's (Millat et al., 1996) method and the ethanol diffusion coefficient in the mixture was determined by Wilke's method (Fairbanks and Wilke, 1950). A simplification was made for determining mixture properties. The mixture was assumed to only consist of the three main components, ethanol, acetaldehyde and hydrogen. The ethanol selectivity towards acetaldehyde production was close to 100% for kinetic experiments (**Chapter 5**) and thus the assumption was very good. **Figure 5.9** was taken from **Chapter 5** to show the effects of interphase mass transfer resistance. **Figure 8.5** converts data from **Figure 5.9** to a plot of the effectiveness factor vs. Reynolds number. The surface reaction rates ($r'_{A,s}$) used for calculating the effectiveness factors (see **Figure 5.9**) are listed in **Table 8.2**.

Table 8.2: Surface reaction rates at different temperatures

Temperature (°C)	Surface reaction rate (mol/kg cat.h)
200	33.5
225	47.8
250	88
275	227.3
300	275.8

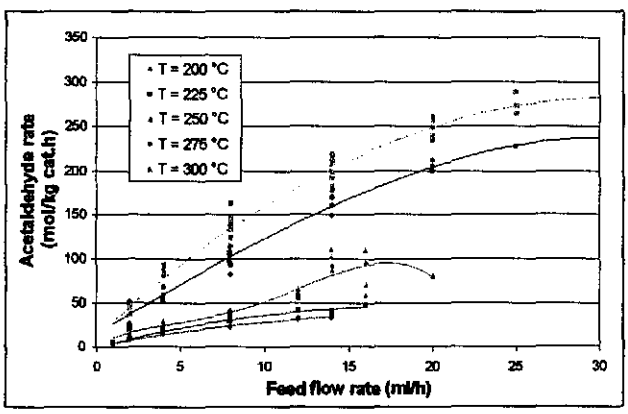

Figure 5.9: The effect of feed flow rate on acetaldehyde production rate

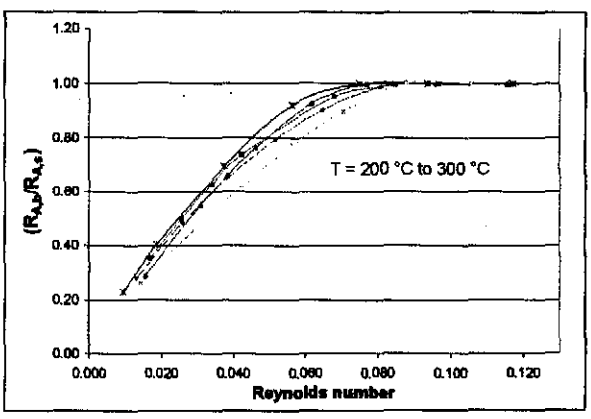

Figure 8.5: Effect of Reynolds number on effectiveness factor

For the low Reynolds numbers in **Figure 8.5**, the format of equation **(8.16)** is best suited to determine the mass transfer coefficient as a function of feed rate, but C_1 is unknown. Equation **(8.19)** is also valid, but in this case C_s is unknown and k_c cannot be determined.

$$k_c = C_1 \frac{D_{A,m}}{D_p} Re \qquad \textbf{(8.16)}$$

$$k_c A_p (C_{A,b} - C_{A,surf}) = \eta m r'_{A,surf} \qquad \textbf{(8.19)}$$

$$A_c/m = 6(1-\varepsilon_b)/\rho_b D_p \qquad [m^2/kg] \qquad \textbf{(8.29)}$$

ε_b was taken as 0.4

ρ_b was taken as 600 kg/m^3

In the region of strong interphase mass transfer resistance, $C_{A,surf} <<< C_{A,b}$. As the Reynolds number increases, the surface concentration will start increasing. An assumption was made that $C_{A,surf} <<< C_{A,b}$ in the region where $\eta < 0.8$. Equation **(8.19)** could be solved at different temperatures and different Reynolds numbers. In **Figure 8.6**, the constant in equation **(8.16)** is plotted against inverse Reynolds number at different temperatures.

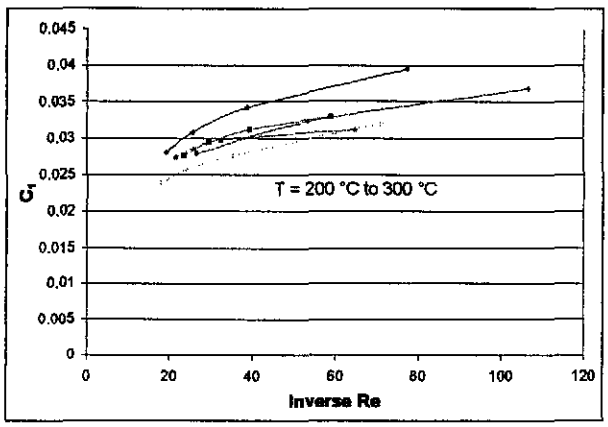

Figure 8.6: C_1 vs. inverse Re at different temperatures

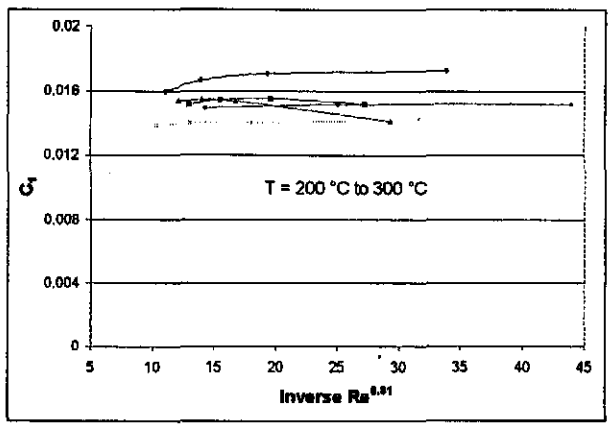

Figure 8.7: C_1 vs. inverse $Re^{0.81}$ at different temperatures

The value of C_1 is not supposed to change when the temperature and/or the feed flow changes (C_1 is a constant). **Figure 8.6** indicates that C_1 was not constant at different inverse Reynolds numbers. A much better correlation was obtained when C_1 was plotted against the inverse of the Reynolds number to the power of 0.81 (**Figure 8.7**). Equation (**8.16**) reduces to:

$$k_c = 0.015 \frac{D_{A,m}}{D_p} Re^{0.81} \qquad (8.30)$$

8.3.4.2. 2-Butanol dehydrogenation

For the dehydrogenation of 2-butanol, the reaction rate did not increase with an increase in feed flow rate (see **Figure 5.10**). Therefore, it could be concluded that the interphase mass transfer resistance was small compared to the reaction rate. The effectiveness factor for 2-butanol dehydrogenation could be taken as 1 with the reaction rate at bulk conditions equalling the surface reaction rate.

8.4. EXPERIMENTAL DATA FOR A PLUG FLOW REACTOR

Both the ethanol and 2-butanol dehydrogenation reactions were studied at different temperatures and different feed rates. Plug flow reactor data is listed in **Appendix F1** and **F2**.

8.4.1. ETHANOL DEHYDROGENATION IN A PLUG FLOW REACTOR

Figures 8.8 to **8.10** compare equilibrium ethanol conversion to acetaldehyde at different temperatures with results obtained when the reactor was operated as a plug flow reactor. Data was taken from **Appendix F1**. Equilibrium values were calculated as described in **section 5.3.1**. At all temperatures the ethanol conversion to acetaldehyde declined with an increase in the feed flow rate. This was consistent with the theory discussed in **Figure 8.1**. The conversion of ethanol to acetaldehyde was lower than the equilibrium conversion. At low feed rates the total ethanol conversion was higher than the equilibrium conversion, because the selectivity towards acetaldehyde production was less than 100%. Some of the ethanol was converted to other products, which increased overall ethanol conversion.

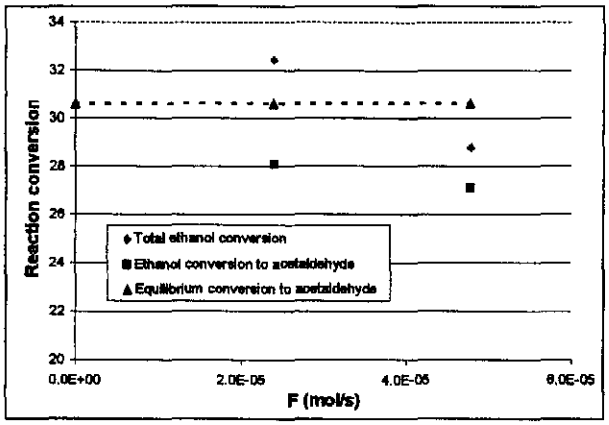

Figure 8.8: Plug flow reactor data for ethanol dehydrogenation at 250 °C

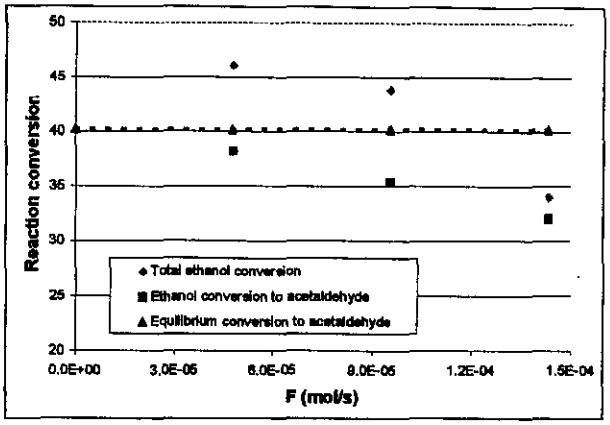

Figure 8.9: Plug flow reactor data for ethanol dehydrogenation at 275 °C

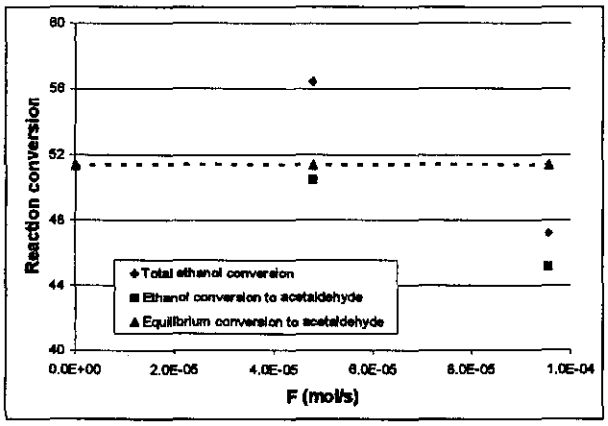

Figure 8.10: Plug flow reactor data for ethanol dehydrogenation at 300 °C

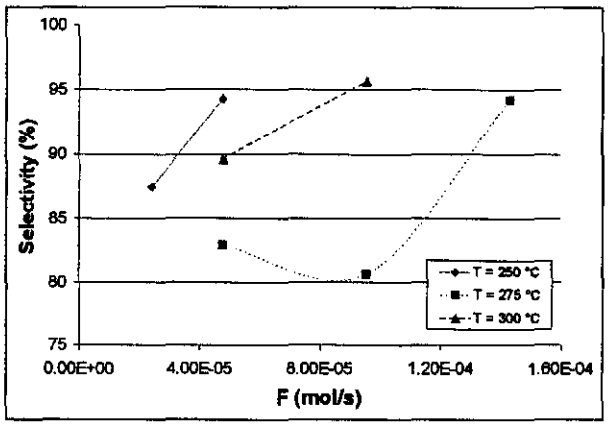

Figure 8.11: Selectivity towards acetaldehyde production for a plug flow reactor

Figure 8.11 shows selectivity towards acetaldehyde production at different temperatures and feed rates. The selectivity dropped at the lower feed rates as more unwanted products were formed. Selectivity was less dependent on temperatures than on reaction time. Side products were formed due to the reaction between acetaldehyde and ethanol. Acetic acid ethyl ester was one of the main by products. Further products that formed were due to acetal and hemiacetal formation (Streitwieser et al., 1992). The acetal, 1,1'-diethoxyethane and the dehydrated acetal, ethoxyethene were present in small quantities in most experiments. Butanals were also present in low concentrations. These products were similar to those observed by Raich and Foley (1998).

At higher feed rates or shorter catalyst contact times, the reaction time was too short for the C4 by products to form and the selectivity towards acetaldehyde increased. Under differential conditions, the selectivity of ethanol dehydrogenation towards acetaldehyde was close to 100% (**Chapter 5**).

Reynolds numbers were determined at each temperature to determine whether the experiments were in the mass transfer limited regime. The Reynolds number is dependent on the reaction conversion and was calculated at different conversions to obtain the boundaries of the Reynolds number. The data for temperatures from 200 °C to 300 °C is shown in **Figures 8.12** to **8.14**.

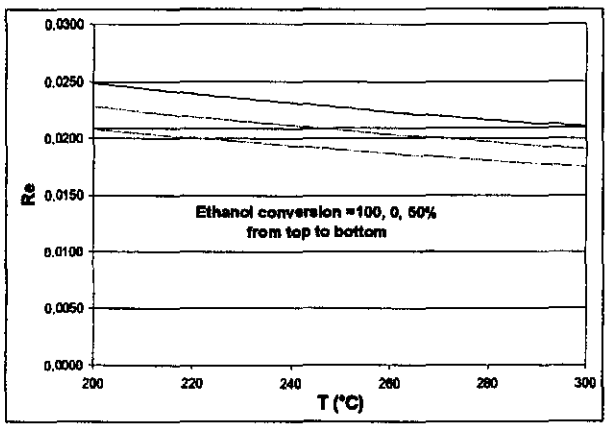

Figure 8.12: Re as a function of temperature and conversion (feed rate = $4.77*10^{-5}$ mol/s)

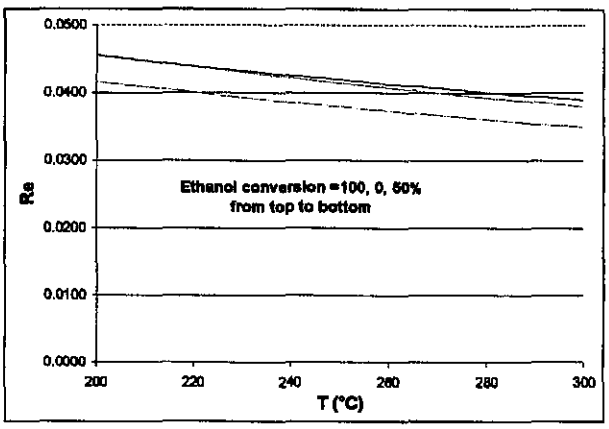

Figure 8.13: Re as a function of temperature and conversion (feed rate = $9.54*10^{-5}$ mol/s)

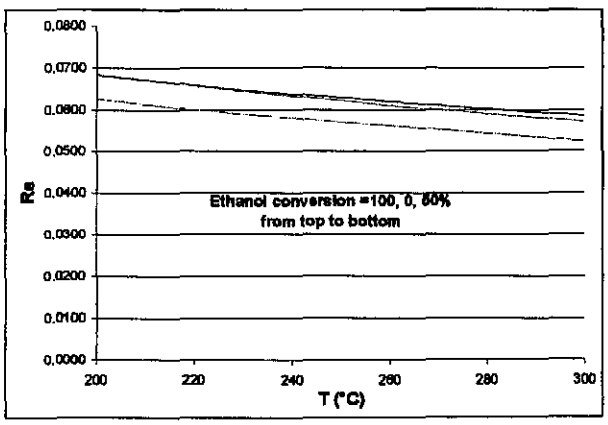

Figure 8.14: Re as a function of temperature and conversion (feed rate = $1.43*10^{-4}$ mol/s)

At all tested feed flow rates, the Reynolds numbers were less than 0.07 and thus in the region of strong interphase mass transfer resistance according to **Figure 8.5**.

8.4.2. 2-BUTANOL DEHYDROGENATION IN A PLUG FLOW REACTOR

In **Figures 8.15** to **8.17** the equilibrium 2-butanol conversion data is compared to measured data for a plug flow reactor. Data was taken from **Appendix F2**.

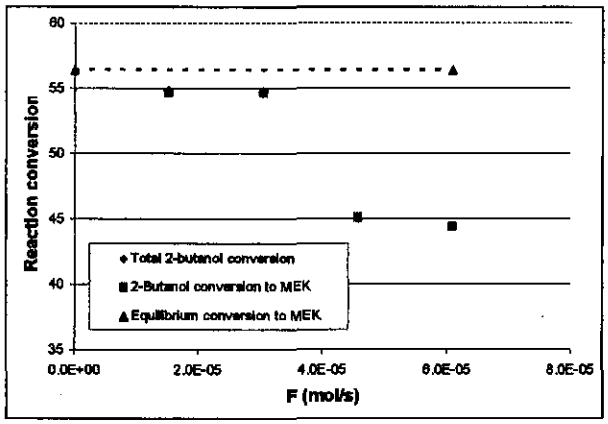

Figure 8.15: Plug flow reactor data for 2-butanol dehydrogenation at 190 °C

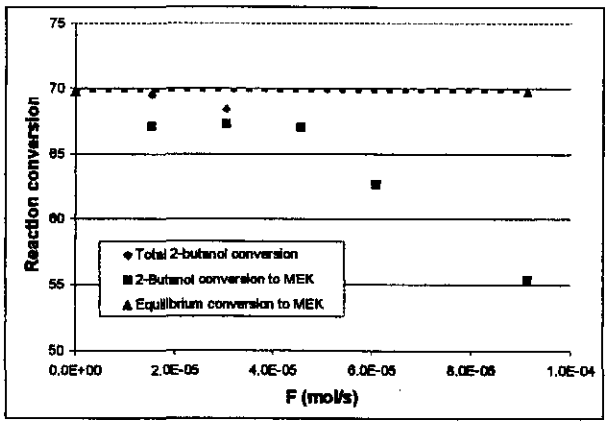

Figure 8.16: Plug flow reactor data for 2-butanol dehydrogenation at 215 °C

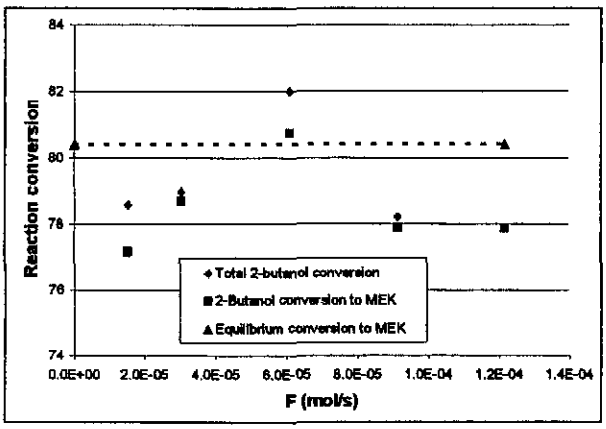

Figure 8.17: Plug flow reactor data for 2-butanol dehydrogenation at 240 °C

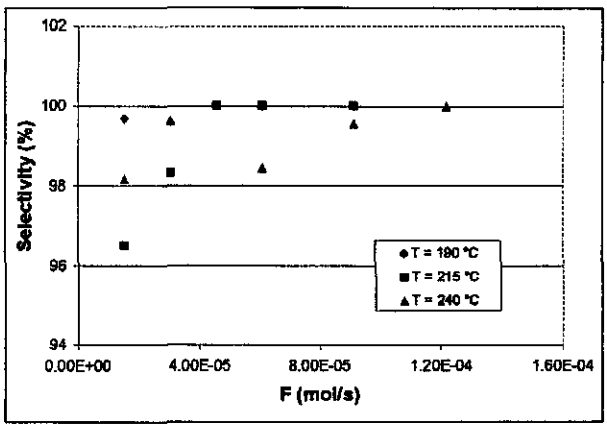

Figure 8.18: Selectivity towards MEK production for a plug flow reactor

The measured conversions at 190 °C (**Figure 8.15**) and at 215 °C (**Figure 8.16**) declined with an increase in the feed flow rate. The reaction time became too short at the higher flow rates

for full conversion to take place. At 240 °C, the reaction rate was very fast compared to the rate at the lower temperatures. Even at the maximum feed flow rates tested, the 2-butanol conversion was still close to that of the equilibrium value and did not decline significantly. Selectivity for this reaction was very high. **Figure 8.18** indicates that the selectivity was more than 96% for all experiments conducted. The main by-product was 3-octanol.

8.4.3. SUMMARY OF MODEL FOR ETHANOL DEHYDROGENATION

Physical properties of the ethanol-acetaldehyde-hydrogen mixture were determined as described in **section 8.3.4.1**. The viscosity of the mixture is dependent on both the temperature and the composition of the mixture. The pressure was kept constant at one atmosphere. The effectiveness factor (**Figure 8.5**) was expressed as a function of Reynolds number at different temperatures. The following equations were obtained:

At 300 °C:

$$\eta = -224.00*Re^3 - 69.20*Re^2 + 18.60*Re + 0.053 \quad \text{for } 0.01 < Re \leq 0.08 \qquad (8.31)$$

$$\eta = 1 \quad \text{for } Re > 0.08$$

At 275 °C:

$$\eta = -241.18*Re^3 - 36.65*Re^2 + 15.89*Re + 0.039 \quad \text{for } 0.01 < Re \leq 0.085 \qquad (8.32)$$

$$\eta = 1 \quad \text{for } Re > 0.085$$

At 250 °C:

$$\eta = 363.16*Re^3 - 189.62*Re^2 + 26.34*Re - 0.080 \quad \text{for } 0.01 < Re \leq 0.08 \qquad (8.33)$$

$$\eta = 1 \quad \text{for } Re > 0.08$$

It should be emphasised that these effectiveness factors will only be true for small particles without intraparticle mass transfer resistance. For larger particles, equation (**8.27**) must be solved using the k_c value determined in equation (**8.30**). The Reynolds number is:

$$Re = \frac{\rho_m U D_p}{\mu} \qquad (8.34)$$

$$U = \frac{8.314T(F_{Et,t} + F_{H_2,t} + F_{Ac,t} + F_{N_2,t})}{P_t(\pi R_m^2)} \tag{8.35}$$

$$\rho_m = \frac{46P_{Et,t} + 44P_{Ac,t} + 2P_{H_2,t} + 28P_{N_2,t}}{1000*(8.314)T} \tag{8.36}$$

with

P_t	=	total pressure	[Pa]
T	=	reaction temperature	[K]

On the tube side:

For ethanol

$$\frac{dF_{Et,t}}{d\left(\frac{L}{L_0}\right)} = V\left[-\rho_b r'_{Et,b}\eta - \frac{2}{R_m}J_{Et}\right] \quad \text{with} \tag{8.37}$$

$$J_{Et} = P_{m,Et}\left(P_{Et,t} - P_{Et,s}\right) \text{ and} \tag{8.38}$$

$$r'_{Et,b} = \frac{k'_{Et}\left(P_{Et,b} - P_{Ac}P_{H_2}/K_{Et,eq}\right)}{\left(1 + K_{Et} \times P_{Et,b} + K_{H_2} \times P_{H_2} + K_{Ac} \times P_{Ac}\right)^2} \tag{8.39}$$

For hydrogen:

$$\frac{dF_{H_2,t}}{d\left(\frac{L}{L_0}\right)} = V\left[\rho_b r'_{Et,b}\eta - \frac{2}{R_m}J_{H_2}\right] \quad \text{with} \tag{8.40}$$

$$J_{H_2} = P_{m,H_2}\left(P_{H_2,t} - P_{H_2,s}\right) \tag{8.41}$$

For acetaldehyde:

$$\frac{dF_{Ac,t}}{d\left(\frac{L}{L_0}\right)} = V\left[\rho_b r'_{Et,b}\eta - \frac{2}{R_m}J_{Ac}\right] \qquad \text{with} \tag{8.42}$$

$$J_{Ac} = P_{m,Ac}\left(P_{Ac,t} - P_{Ac,s}\right) \tag{8.43}$$

For nitrogen:

$$F_{N_2,t} = F_{N_2,s(0)} - F_{N_2,s} \tag{8.44}$$

On the shell side:

For nitrogen sweep gas:

$$\frac{dF_{N_2,s}}{d\left(\frac{L}{L_0}\right)} = 2\pi R_m L_0 P_{m,N_2}\left[P_{N_2,s} - P_{N_2,t}\right. \tag{8.45}$$

For ethanol:

$$\frac{dF_{Et,s}}{d\left(\frac{L}{L_0}\right)} = 2\pi R_m L_0 P_{m,Et}\left[P_{Et,t} - P_{Et,s}\right] \tag{8.46}$$

For hydrogen:

$$\frac{dF_{H_2,s}}{d\left(\frac{L}{L_0}\right)} = 2\pi R_m L_0 P_{m,H_2}\left[P_{H_2,t} - P_{H_2,s}\right] \tag{8.47}$$

For acetaldehyde:

$$\frac{dF_{Ac,s}}{d\left(\frac{L}{L_0}\right)} = 2\pi R_m L_0 P_{m,Ac}\left[P_{Ac,t} - P_{Ac,s}\right] \tag{8.48}$$

The initial conditions were:

At L = 0: $F_{Et,t} = F_{Et,t(0)}$ $F_{Et,s} = 0$

$F_{H_2,t} = 0$ $F_{H_2,s} = 0$

$F_{Ac,t} = 0$ $F_{Ac,t} = 0$

$F_{N_2,t} = 0$ $F_{N_2,s} = F_{N_2,s(0)}$

Finally, the partial pressures need to be expressed in terms of flow rates:

On the tube side:

$$P_{Et,t} = P_t\left[\frac{F_{Et,t}}{(F_{Et,t} + F_{Ac,t} + F_{H_2,t}) + (F_{N_2,s(0)} - F_{N_2,s})}\right] \quad (8.49)$$

$$P_{H_2,t} = P_t\left[\frac{F_{H_2,t}}{(F_{Et,t} + F_{Ac,t} + F_{H_2,t}) + (F_{N_2,s(0)} - F_{N_2,s})}\right] \quad (8.50)$$

$$P_{Ac,t} = P_t\left[\frac{F_{Ac,t}}{(F_{Et,t} + F_{Ac,t} + F_{H_2,t}) + (F_{N_2,s(0)} - F_{N_2,s})}\right] \quad (8.51)$$

$$P_{N_2,t} = P_t\left[\frac{F_{N_2,t}}{(F_{Et,t} + F_{Ac,t} + F_{H_2,t}) + (F_{N_2,s(0)} - F_{N_2,s})}\right] \quad (8.52)$$

On the shell side:

$$P_{Et,s} = P_{t,s}\left[\frac{F_{Et,s}}{F_{Et,s} + F_{Ac,s} + F_{H_2,s} + F_{N_2,s}}\right] \quad (8.53)$$

$$P_{Ac,s} = P_{t,s}\left[\frac{F_{Ac,s}}{F_{Et,s} + F_{Ac,s} + F_{H_2,s} + F_{N_2,s}}\right] \quad (8.54)$$

$$P_{H_2,s} = P_{t,s}\left[\frac{F_{H_2,s}}{F_{Et,s} + F_{Ac,s} + F_{H_2,s} + F_{N_2,s}}\right] \quad (8.55)$$

$$P_{N_2,s} = P_{t,s}\left[\frac{F_{N_2,s}}{F_{Et,s} + F_{Ac,s} + F_{H_2,s} + F_{N_2,s}}\right] \quad (8.56)$$

To solve the model, kinetic coefficients and gas permeances must be known. Membrane (N8x) was used for catalytic membrane reactor experiments. Permeance properties of the membrane are listed in **Appendix D2**. Measured reaction rate coefficients will be used instead of fitted values (from **Chapter 5**) at 250 °C, 275 °C and 300 °C, respectively. **Table 8.3** lists reaction rate coefficients. Reaction rate coefficients were taken from **Table 5.5** and changed to standard units i.e. [Pa], [Pa^{-1}] and [mol/kg.cat.s.Pa]. The permeance data is listed in **Table 8.4** and further data necessary to solve the model is given in **Table 8.5**.

Table 8.3: Ethanol reaction rate parameters

T (°C)	K_{eq} Pa	k mol/kg cat.s.Pa	K_{Et} Pa^{-1}	$K_{Hydrogen}$ Pa^{-1}	K_{Ac} Pa^{-1}
250	10918	5.19E-07	5.14E-06	3.24E-06	6.94E-05
275	24083	1.27E-06	4.32E-06	2.91E-06	6.57E-05
300	56478	1.89E-06	5.46E-06	3.68E-06	8.18E-05

Table 8.4: Permeance data for N8x at 250, 275 and 300 °C

T (°C)	H_2 permeance ($\mu mol/m^2.Pa.s$)	N_2 permeance ($nmol/m^2.Pa.s$)	Ethanol permeance ($nmol/m^2.Pa.s$)	Acetaldehyde permeance ($nmol/m^2.Pa.s$)
250	3.37	22.71	5.68	5.68
275	3.78	21.29	5.32	5.32
300	4.21	20.15	5.04	5.04

Table 8.5: Parameters for solving ethanol dehydrogenation model

R_m [m]	$3.5*10^{-3}$
L_0 [m]	0.18
V [m]	6.93E-06
ρ_b [kg/m^3]	430
ε_b	0.4
m [kg]	0.003

8.4.4. SUMMARY OF MODEL FOR 2-BUTANOL DEHYDROGENATION

The model for 2-butanol dehydrogenation is similar to that of the ethanol dehydrogenation model. **Figure 5.10** shows that the dehydrogenation rate changes very little with feed flow rate, indicating that the interphase mass transfer resistance is small compared to the reaction rate. The effectiveness factor can be taken as 1 and Reynolds numbers do not have to be calculated. The model can be expressed as:

On the tube side:

For 2-butanol

$$\frac{dF_{2But,t}}{d\left(\frac{L}{L_0}\right)} = V\left[-\rho_b r'_{2But,b}\eta - \frac{2}{R_m}J_{2But}\right] \quad \text{with} \tag{8.57}$$

$$J_{2But} = P_{m,2But}\left(P_{2But,t} - P_{2But,s}\right) \quad \text{and} \tag{8.58}$$

$$r'_{2but,b} = \frac{k'_{2but}\left(P_{2but} - P_{MEK}P_{H_2}/K_{2but,eq}\right)}{\left(1 + K_{MEK} \times P_{MEK}\right)^2} \tag{8.59}$$

For hydrogen:

$$\frac{dF_{H_2,t}}{d\left(\frac{L}{L_0}\right)} = V\left[\rho_b r'_{2But,b}\eta - \frac{2}{R_m}J_{H_2}\right] \quad \text{with} \tag{8.60}$$

$$J_{H_2} = P_{m,H_2}\left(P_{H_2,t} - P_{H_2,s}\right) \tag{8.61}$$

For MEK:

$$\frac{dF_{MEK,t}}{d\left(\frac{L}{L_0}\right)} = V\left[\rho_b r'_{2But,b}\eta - \frac{2}{R_m}J_{MEK}\right] \quad \text{with} \tag{8.62}$$

$$J_{MEK} = P_{m,MEK}\left(P_{MEK,t} - P_{MEK,s}\right) \tag{8.63}$$

For nitrogen:

$$F_{N_2,t} = F_{N_2,s(0)} - F_{N_2,s} \tag{8.64}$$

On the shell side:

For nitrogen sweep gas:

$$\frac{dF_{N_2,s}}{d\left(\frac{L}{L_0}\right)} = 2\pi R_m L_0 P_{m,N_2}\left[P_{N_2,s} - P_{N_2,t}\right. \tag{8.65}$$

For 2-butanol:

$$\frac{dF_{2But,s}}{d\left(\frac{L}{L_0}\right)} = 2\pi R_m L_0 P_{m,2But}\left[P_{2But,t} - P_{2But,s}\right] \tag{8.66}$$

For hydrogen:

$$\frac{dF_{H_2,s}}{d\left(\frac{L}{L_0}\right)} = 2\pi R_m L_0 P_{m,H_2}\left[P_{H_2,t} - P_{H_2,s}\right] \tag{8.67}$$

For MEK:

$$\frac{dF_{MEK,s}}{d\left(\frac{L}{L_0}\right)} = 2\pi R_m L_0 P_{m,MEK}\left[P_{MEK,t} - P_{MEK,s}\right] \tag{8.68}$$

The initial conditions were:

At L = 0: $F_{2But,t} = F_{2But,t(0)}$ $F_{But,s} = 0$

$F_{H_2,t} = 0$ $F_{H_2,s} = 0$

$$F_{MEK,t} = 0 \qquad F_{MEK,t} = 0$$

$$F_{N_2,t} = 0 \qquad F_{N_2,s} = F_{N_2,s(0)}$$

Finally, the partial pressures needed to be expressed in terms of flow rates:

On the tube side:

$$P_{2But,t} = P_t\left[\frac{F_{2But,t}}{(F_{2But,t} + F_{MEK,t} + F_{H_2,t}) + (F_{N_2,s(0)} - F_{N_2,s})}\right] \tag{8.69}$$

$$P_{H_2,t} = P_t\left[\frac{F_{H_2,t}}{(F_{2But,t} + F_{MEK,t} + F_{H_2,t}) + (F_{N_2,s(0)} - F_{N_2,s})}\right] \tag{8.70}$$

$$P_{MEK,t} = P_t\left[\frac{F_{MEK,t}}{(F_{2But,t} + F_{MEK,t} + F_{H_2,t}) + (F_{N_2,s(0)} - F_{N_2,s})}\right] \tag{8.71}$$

$$P_{N_2,t} = P_t\left[\frac{F_{N_2,t}}{(F_{2But,t} + F_{MEK,t} + F_{H_2,t}) + (F_{N_2,s(0)} - F_{N_2,s})}\right] \tag{8.72}$$

On the shell side:

$$P_{2But,s} = P_{t,s}\left[\frac{F_{2But,s}}{F_{2But,s} + F_{MEK,s} + F_{H_2,s} + F_{N_2,s}}\right] \tag{8.73}$$

$$P_{MEK,s} = P_{t,s}\left[\frac{F_{MEK,s}}{F_{2But,s} + F_{MEK,s} + F_{H_2,s} + F_{N_2,s}}\right] \tag{8.74}$$

$$P_{H_2,s} = P_{t,s}\left[\frac{F_{H_2,s}}{F_{2But,s} + F_{MEK,s} + F_{H_2,s} + F_{N_2,s}}\right] \tag{8.75}$$

$$P_{N_2,s} = P_{t,s}\left[\frac{F_{N_2,s}}{F_{2But,s} + F_{MEK,s} + F_{H_2,s} + F_{N_2,s}}\right] \tag{8.76}$$

Table 8.6 lists reaction rate coefficients. Values were taken from **Table 5.7** and changed to standard units i.e. [Pa], [Pa^{-1}] and [mol/kg.cat.s.Pa]. Membrane (N8x) was used for experiments. The permeances were determined from data in **Appendix D2**. Values were

estimated at 190 °C, 215 °C and 240 °C, respectively, by fitting an equation through the hydrogen and nitrogen permeance data for membrane (N8x) .

Table 8.6: Reaction rate coefficients for 2-butanol dehydrogenation

T (°C)	K_{eq} Pa	k mol/kg cat.s.Pa	K_R Pa^{-1}
190	73132	9.42E-08	1.17E-04
220	161176	1.94E-07	7.02E-05
250	330120	3.89E-07	5.51E-05

Table 8.7: Permeance data for N8x at 190, 215 and 240 °C

T (°C)	H_2 permeance ($\mu mol/m^2.Pa.s$)	N_2 permeance ($nmol/m^2.Pa.s$)	2-Butanol permeance ($nmol/m^2.Pa.s$)	MEK permeance ($nmol/m^2.Pa.s$)
190	2.40	26.61	5.25	5.25
215	2.81	24.80	4.89	4.89
240	3.22	23.21	4.57	4.57

The other parameters necessary to solve the model are listed in **Table 8.8**.

Table 8.8: Parameters for solving 2-butanol dehydrogenation model

R_m [m]	$3.5*10^{-3}$
L_0 [m]	0.20
V [m]	6.93E-06
ρ_b [kg/m^3]	430
ε_b	0.4
m [kg]	0.0035

8.5. SELECTIVITY ANALYSIS OF THE PROCESS MODEL

The standard values are the measured reaction rate and membrane parameters for ethanol dehydrogenation at 275 °C (**Table 8.9**).

Table 8.9: Parameters for ethanol dehydrogenation at 275 °C

Reaction T (°C)	275
Ethanol feed flow rate (ml/h) (mol/s)	10 $4.771*10^{-5}$
N_2 sweep to ethanol feed molar ratio	1
Shell pressure [Pa]	100000
Tube pressure [Pa]	100000
Reactor length [m]	0.18
R_m [m]	0.0035
ρ_b [kg/m^3]	430
m [kg]	0.0030
ε_b	0.4
k [mol/kg cat.s.Pa]	$1.27*10^{-6}$
$K_{ethanol}$ [Pa^{-1}]	$4.32*10^{-6}$
$K_{acetaldehyde}$ [Pa^{-1}]	$2.91*10^{-6}$
$K_{hydrogen}$ [Pa^{-1}]	$6.57*10^{-5}$
K_{eq} [Pa]	24080
η	1
$P_{m,hydrogen}$ [μmol/m^2.Pa.s]	3.78
$P_{m,nitrogen}$ [nmol/m^2.Pa.s]	21.29
$P_{m,ethanol}$ [nmol/m^2.Pa.s]	5.32
$P_{m,acetaldehyde}$ [nmol/m^2.Pa.s]	5.32

The performance of the membrane reactor can be judged by several factors. The most important factors are the exit alcohol conversion, the fraction of ethanol feed lost through the membrane, the fraction of produced hydrogen permeated to the shell side and the purity of the hydrogen on the shell side. Process conditions, reaction parameters and membrane parameters that yield high alcohol conversion and pure hydrogen on the shell side, represents optimum conditions. The effect of each parameter on the dehydrogenation of ethanol at 275 °C is presented graphically in **Appendix G**. It should be kept in mind that the equilibrium ethanol conversion for a plug flow reactor is 40% at 275 °C and 1 atmosphere total pressure.

Model equations (**8.37**) to (**8.56**) were solved numerically with Euler's method. A very small step length of 0.001 (L/L_0)was employed to obtain results of high accuracy.

8.5.1. THE EFFECT OF k'-VALUES ON MODEL PERFORMANCE

The reaction rate k'-value is one of the most important parameters for manipulating the overall ethanol conversion. Overall conversion goes from 27% to 54% when the k'-value increases from 0.5 to 8 times the standard value (**Appendix G.1**). This represents a very large increase in conversion. Up to a 2 times increase in k'-value, the conversion increases sharply, but thereafter there is little gain in conversion for higher k'-values. The amount of ethanol permeated to the shell side remains low and drops when the reaction rate increases (larger k'-value). For twice the k'-value and larger, the hydrogen purity on the shell side is above 86% and changes little with larger k'-values. The tube side composition also remains constant at the larger k'-values.

In the very first part of the reactor, the hydrogen production rate is much faster than the permeance rate. The driving force shoots up from zero to a maximum value. The faster the rate (larger the k'-value), the higher the maximum hydrogen driving force. The hydrogen driving force then drops quickly to very low values further down the axis of the membrane. At different k'-values there is almost no change in the percentage of produced hydrogen that permeates to the shell side. The percentage of produced hydrogen that permeates to the shell side, increases sharply in the first part of the reactor and then declines slowly as back

diffusion takes place. The ethanol flow rate on the tube side also drops quicker along the membrane's length as the k'-value increases.

An optimum k'-value would be about four times the standard rate. Higher values will not improve the ethanol conversion significantly.

8.5.1.1. Back diffusion

The term back diffusion will be used to describe the situation where hydrogen no longer permeates from the tube side to the shell side. Permeation is reversed and hydrogen permeates from the shell side to the tube side. It happens when the hydrogen driving force becomes negative. The reason why it happens is as follows.

The sweep gas permeance (nitrogen) is much higher than the permeances for ethanol and acetaldehyde. A fraction of the nitrogen sweep gas will permeate from the shell side to the tube side and this fraction is much larger than the amount of ethanol and acetaldehyde that will permeate from the tube side to the shell side. The nitrogen partial pressure will drop on the shell side and increase on the tube side. Once the produced hydrogen reaches a maximum amount permeated, no more hydrogen goes from the tube side to the shell side and back diffusion of hydrogen will commence. The hydrogen partial pressure on the shell side will increase due to a decline in nitrogen partial pressure, which is larger than the combined increase in ethanol and acetaldehyde partial pressures on the shell side. Similarly, the hydrogen partial pressure on the tube side will decrease due to an increase in nitrogen partial pressure. The hydrogen driving force is reversed and hydrogen will permeate back from the shell side to the tube side.

8.5.2. THE EFFECT OF K_{acet} ON MODEL PERFORMANCE

K_{acet} is the acetaldehyde adsorption coefficient and it affects the reaction rate. The higher the value, the slower the reaction rate. The value of K_{acet} plays a significant role in the overall ethanol conversion (see **Appendix G.2**). A twenty fold decrease in K_{acet} improves ethanol conversion from 44% to 53%. The measured acetaldehyde adsorption coefficient was about twenty times larger than the other adsorption coefficients. The lost ethanol feed declines with

a lower K_{acet}, but remains at acceptable levels for all K_{acet}-values. The variance in ethanol conversion for changes in K_{acet} is much smaller than the variance when k is changed. For K_{acet}-values of less than five times the standard value, the improvement in ethanol conversion becomes very small for a further decline in K_{acet}.

Hydrogen purity on the shell side varies between 85% and 88%. On the tube side the nitrogen content is constant at 10%. The initial hydrogen driving force is larger for small K_{acet}-values. The driving force either goes to very low values or to below zero along the axis of the membrane. The lack of a strong driving force results in a low hydrogen percentage permeated to the shell side. The value is 45% and changes little with changes in the value of K_{acet}. This result is similar to that obtained for changing the k'-value.

An optimum K_{acet}-value would be at least 5 times smaller than the standard value.

8.5.3. THE EFFECT OF THE MEMBRANE SELECTIVITY ON MODEL PERFORMANCE

This situation is where there is a constant hydrogen permeance, but changing permeances for all the other species to obtain a changing selectivity. The selectivity has a negligible effect on reaction conversion at standard conditions (see **Appendix G.3**). Conversion remains between 44% and 45% for a variety of selectivities. At different conditions, this might not be true and will be investigated later. Poor selectivity, however, has a very negative effect on the ethanol feed lost through the membrane and the purity of hydrogen on the shell side. For a hydrogen to nitrogen selectivity of less than 150, the hydrogen purity on the shell side drops sharply from just over 80% (at selectivity = 150) to about 30% (at selectivity = 10).

The nitrogen fraction on the tube side increases from 5% at a selectivity of 320 to over 40% at a selectivity of 10. With such an increase in nitrogen content on the tube side, a significant amount of back diffusion can be expected. This is indeed the case and the hydrogen driving force becomes negative at low dimensionless length values for low selectivities. The low percentage of produced hydrogen that permeates to the shell side, indicates very strong back

diffusion. At a selectivity of 10, only 20% of the produced hydrogen permeates to the shell side and this percentage increases to 47% at a selectivity of 320.

A selectivity of at least 150 must be used to ensure that not more than 3% of the ethanol feed is lost through the defects in the Pd-Ag film.

8.5.4. THE EFFECT OF THE REACTION EFFECTIVENESS FACTOR ON MODEL PERFORMANCE

The effectiveness factor is a measure of the decrease in reaction rate due to interphase and intraparticle mass transfer resistance. The factor varies between 0 and 1, where 1 indicates zero mass transfer resistance. A decrease in the effectiveness factor will cause the same effects as a decrease in the k'-value, since both will reduce the overall reaction rate. Figures in **Appendix G.4** are similar to those for k'-values (**Appendix G.1**) in the region where the k'-values are less than the standard k'-value.

The best results will be obtained with the maximum value of the effectiveness factor, i.e. when the effectiveness factor approaches one.

8.5.5. THE EFFECT OF THE ETHANOL FEED RATE ON MODEL PERFORMANCE

The ethanol conversion decreases with an increase in ethanol feed rate, because the contact time decreases and the reaction cannot go to completion along the length of the membrane. The conversion declines from 50% to 34% for flow rates of 0.5 to 2.5 times the standard value (**Appendix G.5**). The higher the feed rate, the smaller the fraction of feed lost through the membrane and the better the purity of the hydrogen on the shell side.

The ethanol fraction at the tube side exit increases with an increase in feed flow rate due to a decrease in conversion. At the higher flow rates, a small hydrogen driving force remains over the full length of the membrane and a maximum percentage (47%) of produced hydrogen permeates to the shell side. At a low flow rate (0.5 multiple), back diffusion takes

place in the second half of the reactor. The hydrogen driving force shifts along the axis of the membrane when the feed rate increases.

The value of the feed rate should be determined by all other parameters. The quality of the membrane and the speed of the reaction rate will determine which feed rate is best suited for the model. For example, if the reaction rate is very slow, it is of no use to employ a very fast feed rate, since the benefits of the membrane reactor will be cancelled.

8.5.6. THE EFFECT OF THE SWEEP GAS ON MODEL PERFORMANCE

The sweep gas flow rate is a very important parameter for the membrane reactor model (see **Appendix G.6**). At a constant temperature only the sweep gas rate and the feed rate can be changed. Reaction rate parameters and membrane parameters are fixed. The sweep gas is necessary to create the hydrogen driving force. Alternatively, a pressure difference between the tube and the shell side can be used. Modelling calculations in the present study will only focus on sweep gas experiments, since reaction rates were determined at atmospheric pressure and not higher pressures.

Ethanol conversion increases from 42% to almost 50% for sweep gas to feed ratios of 0.25 to 8. The ethanol feed lost through the membrane increases slightly, because of a higher ethanol driving force, but it remains at acceptably low values. A hydrogen purity of above 90% is obtained on the shell side for sweep to feed ratios greater than 4. There is a sharp decline in hydrogen content (from 25% to 5%) on the tube side with an increase in sweep rate. The acetaldehyde fraction increases on the tube side as more ethanol is converted and the nitrogen fraction increases as more nitrogen permeates through the membrane at higher sweep rates.

A higher sweep rate reduces the hydrogen partial pressure on the shell side. The result is a higher hydrogen driving force and a higher percentage of produced hydrogen that permeates the membrane. A high sweep rate is very effective for extracting both pure, and a very high percentage of, produced hydrogen. The percentage of produced hydrogen permeated, increases from less than 15% at a sweep to feed rate of 0.25 to over 85% for a sweep to feed rate of 8.

A sweep to feed ratio of at least 4 should be used, but this depends to a large extent on the feed rate and must be chosen in conjunction with the feed rate.

8.5.7. THE EFFECT OF THE H_2 PERMEANCE AT CONSTANT SELECTIVITY ON MODEL PERFORMANCE

In this scenario the permeances of other species increase with the permeance of hydrogen to maintain a constant selectivity. The effect of hydrogen permeance on ethanol conversion is negligible. The conversion changes by little more than 1% over a wide range of hydrogen permeances (**Appendix G.7**). With an increase in hydrogen permeance, more ethanol is lost through the membrane as the ethanol permeance also increases. The hydrogen fraction on the shell side decreases sharply and the nitrogen fraction on the tube side increases sharply with an increase in hydrogen permeance. The main reason is not so much the increase in hydrogen permeance, but the increase in the permeances of other species to maintain the constant selectivity. At a very low hydrogen permeance (0.25 multiple), the hydrogen driving force remains high over the full length of the membrane. In this case, the percentage of hydrogen permeated, increases steadily along the length of the membrane. For higher hydrogen permeances (2 and 4 times the standard rate), back diffusion occurs in the latter part of the membrane.

When comparing the data in **Appendix G.3** and **Appendix G.7**, it is clear that the membrane selectivity plays a more important role in the membrane reactor's performance than the hydrogen permeance does. This statement is true under standard conditions and in the ranges that each parameter was investigated. With the standard selectivity, the hydrogen permeance should not move outside the range of 0.5 to 1.5 times that of the standard permeance.

8.5.8. THE EFFECT OF THE H_2 PERMEANCE AT VARYING SELECTIVITY ON MODEL PERFORMANCE

For this set of modelling conditions the nitrogen, ethanol and acetaldehyde permeances are kept constant at the standard values. The hydrogen permeance is varied and the selectivity changes as the hydrogen permeance changes. The overall conversion remains close to 44%

(**Appendix G.8**). The overall ethanol conversion in **Appendix G.8** is similar to that in **Appendix G.7**, but there is very little change in ethanol feed lost through the membrane. The hydrogen composition on the shell side exit remains constant at just above 88%. The composition of the tube side exit mixture also varies little with changes in the hydrogen permeance. The hydrogen driving forces in **Appendix G.8** are similar to those in **Appendix G.7**, but less back diffusion of hydrogen occurs, since less nitrogen permeates from the shell side to the tube side.

The percentage of produced hydrogen that permeates from the tube side to the shell side starts declining at hydrogen permeances of less than 0.5 times the standard value. At lower hydrogen permeances, the reactor length is too short to reach equilibrium for hydrogen permeance. The result is a decline in hydrogen permeance as compared to when equilibrium is reached.

At standard selectivity, the hydrogen permeance should be at least one half or more of the standard hydrogen permeance for optimum membrane performance.

8.5.9. MODEL PERFORMANCE UNDER NON-STANDARD CONDITIONS

Two situations are presented, in **Appendix G.9** and **G.10,** where the reaction rate is four times the standard rate and the sweep gas to feed ratio is four times higher than the standard ratio, respectively. In **Appendix G.9** the hydrogen permeance is varried, while permeances for the other species remain constant (varying selectivity). In **Appendix G.10** the hydrogen permeance as well as the permeances for the other species are changed (constant selectivity). The results are very similar for the two scenarios except for the fact that less ethanol feed is lost to the shell side when selectivity increases with increasing hydrogen permeance (**Appendix G.9**). In this case, the hydrogen purity on the shell side is above 93% for hydrogen permeances of more than 0.5 times the standard value. The hydrogen driving force is similar for the two sets of data and in both cases above 70% of produced hydrogen permeates through the membrane for hydrogen permeances of 0.5 times the standard value, and more.

In both cases the ethanol conversion reaches a maximum of 64% when the hydrogen permeance is increased. The gain in ethanol conversion is small for hydrogen permeances larger that 0.5 times the standard value. At smaller values the ethanol conversion will drop sharply towards the equilibrium value or lower in the case of higher feed rates. The equilibrium ethanol conversion at 275 °C is 40%. Hence the membrane reactor offers a significant improvement in ethanol conversion. This improvement is more than 50%.

8.5.10. OPTIMISING MEMBRANE PERFORMANCE ON MODEL PERFORMANCE

Two sets of conditions were compared to optimise the membrane performance. The sets were defined as:

- Standard conditions, as in **Appendix G**, and
- Two times standard k'-value ($k = 2.54*10^{-6}$ mol/kg cat.s.Pa); 0.5 times standard K_{act}-value ($K_{act} = 3.29*10^{-5}$ Pa^{-1}); $\eta = 0.9$; H_2 permeance = 3 $\mu mol/m^2.Pa.s$; H_2:N_2 selectivity = 150. Other conditions are similar to the standard conditions.

The second set of conditions represents a slight improvement in catalyst activity. Membrane parameters are similar to those of the optimised membrane. For the standard conditions, the ethanol conversion is 44.5% and the ethanol feed lost through the membrane is 2.33%. For the second set of conditions, the ethanol conversion is given as a function of sweep gas to feed ratio in **Figure 8.19**. Conversion increases sharply with an increase in sweep gas flow rate. The membrane reactor is very effective if a large hydrogen driving force across the membrane can be maintained along the length of the membrane.

To optimise the membrane reactor's performance, two main conditions must be satisfied.

1. The dehydrogenation rate and the hydrogen permeance through the membrane should be similar.
2. A high hydrogen driving force must be maintained along the full length of the membrane.

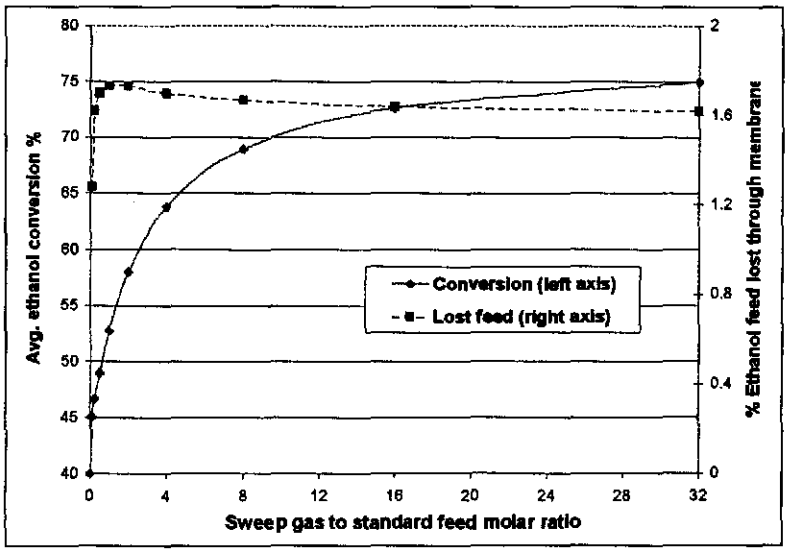

Figure 8.19: Effect of sweep gas to standard feed molar ratio on ethanol conversion and ethanol losses

For the membrane parameters and reaction rate parameters measured in this study, the hydrogen permeance was much faster than the reaction rate for the ethanol dehydrogenation reaction. A more active catalyst will improve the overall ethanol conversion significantly, since the ethanol conversion in the membrane reactor was mainly limited by the reaction rate. The hydrogen driving force may be improved by using a vacuum on the shell side or a positive feed pressure on the tube side instead of a sweep gas. The larger the pressure difference between the shell and the tube sides, the better the overall reaction conversion will be if the reaction rate stays constant (**Figure 8.19**). Higher feed pressures will, however, have a negative impact on the reaction rate and cause a decline in the reaction rate.

8.6. SUMMARY

The effects of feed flow rate on reaction conversion were discussed and the low flow rates that have been investigated in membrane reactors by previous authors, mentioned. Membrane permeance data for ethanol was presented. It was found that the nitrogen to ethanol selectivity of the Pd film membrane was about four to one.

A process model was developed for the catalytic membrane reactor. All model conditions were covered, including the effects of pressure drop along the packed membrane and

interphase and intraparticle mass transfer resistance. The reaction temperature was assumed to be constant and there were no radial concentration profiles in the catalysts bed. Equations were formulated to calculate the mass transfer coefficient for ethanol dehydrogenation at different Reynolds numbers. Experimental plug flow reactor data was compared to equilibrium data at different feed flow rates. At low flow rates, the alcohol conversion was similar to the equilibrium conversion at the tested temperatures. Flow rates were determined where the conversion started decreasing to below the equilibrium values. For the catalytic membrane reactor to be applicable, an improvement in reaction conversion must be obtained in the higher flow rate region.

A thorough sensitivity analysis on catalyst parameters, membrane parameters and process conditions was conducted. The main findings were:

- The reaction rate parameters (k'-value; K_{acet} and η) have a very significant effect on the overall ethanol conversion. A high k-value, a low K_{acet}-value and/or a high effectiveness factor will increase the reaction rate and improve the reaction conversion. The reaction rate parameters have no effect on the percentage of produced hydrogen that exits the shell side. The percentage of produced hydrogen that permeates to the shell side remains similar for different values of each parameter. The hydrogen driving forces have similar profiles and the maximum value increases with reaction rate. The reaction rate parameters have a small effect on the amount of ethanol feed that is lost through the membrane and the purity of hydrogen on the shell side. When the reaction rate is slow, the ethanol driving force will be larger, resulting in more ethanol permeance through the membrane and a decline in hydrogen purity on the shell side.
- Membrane selectivity (H_2:N_2) should be at least 150 to prevent large losses of ethanol feed through the membrane and a low hydrogen purity on the shell side. At low selectivities, hydrogen back diffusion occurs and the amount of produced hydrogen that permeates to the shell side decreases sharply. It is more important to have a high selectivity than a high hydrogen permeance. Very thin films with higher hydrogen permeance, but poorer selectivity should be avoided. There is a negligible improvement in ethanol conversion with higher membrane selectivity and/or higher hydrogen permeance at low sweep rates and low reaction rates. At higher reaction rates and higher

sweep rates, the membrane parameters play very important roles and can result in large improvements in alcohol conversion.

- The two process parameters, the feed rate and the sweep rate, must be chosen in conjunction with one another. In both a plug flow reactor and a membrane reactor, the alcohol conversion will drop with an increase in feed flow rate, because the reaction time becomes shorter. The feed rate has a effect on the percentage of produced hydrogen that permeates to the shell side. At low feed rate, back diffusion of hydrogen will occur. At high feed rates, the purity of hydrogen on the shell side is high. The sweep to feed molar ratio is very important for extracting hydrogen from the tube side to the shell side. At high sweep rates, most of the produced hydrogen can be extracted from the reaction side (tube side) to the shell side. The reaction equilibrium is shifted and the reaction conversion increases.

9. CATALYTIC MEMBRANE REACTOR DATA

The experimental procedures for catalytic membrane reactor testing were discussed in **section 3.4**. The Pd-Ag membrane (N8x) was packed with the optimised catalyst. The optimised catalyst consisted of 14.4 wt % copper on silica, with a particle fraction ranging from 500 to 800 microns. The performance of the reactor with and without an inert sweep gas was compared. The effect of the sweep gas flow rate on reaction conversion and selectivity was studied at different temperatures. Results are listed in **Appendix F**. Experimental data was compared to model predictions for both the dehydrogenation of ethanol and the dehydrogenation on 2-butanol. All data presented was at the exit conditions of the reactor. Experiments conducted to optimise the catalyst composition (**Chapter 4**) were also performed in a plug flow reactor, but the values in **Chapter 4** were not directly comparable to the plug flow reactor data in **Chapter 9**. In **Chapter 4** a diluted feed (feed to nitrogen molar ratio of 1 to 4) was employed, but in this chapter an undiluted feed was used. Conversions for the plug flow reactor will thus be higher in **Chapter 9** than in **Chapter 4,** due to higher feed concentrations.

For ethanol dehydrogenation, two models were constructed. Model 1 used the measured reaction rate and membrane parameters for the reaction at the specific temperatures. In model 2, the reaction rate parameters were changed to better fit the experimental data. Model 2 does not have significant physical importance, but indicates how the parameters must be altered for the model to better predict the experimental data. For 2-butanol dehydrogenation, only one model was developed at every temperature. The model did not use measured kinetic data, since the model then under predicted the experimental 2-butanol conversion significantly. Instead the model used altered parameters to improve the prediction of experimental values (similar to model 2 for ethanol dehydrogenation).

It should also be emphasised that the reaction rate models developed in **Chapter 5** are independent of the membrane reactor models in this chapter. This implies, for example, that model 2 (ethanol dehydrogenation reaction) in this chapter does not use the reaction rate parameters of model 2 in **Chapter 5**, but the reaction rate parameters defined in this chapter.

9.1. ETHANOL DEHYDROGENATION

The results of ethanol dehydrogenation in a membrane reactor are listed in **Appendix F1**. The results at each temperature will be discussed separately (**sections 9.1.1** to **9.1.3**). The following definitions were mentioned in **Chapter 4** and will also be used in this chapter.

$$\text{total feed conversion} = \frac{\text{total moles feed reacted}}{\text{total moles feed fed}} \qquad (4.1)$$

$$\text{product yield} = \frac{\text{moles feed converted to product}}{\text{total moles feed fed}} \qquad (4.2)$$

$$\text{product selectivity} = \frac{\text{moles feed converted to product}}{\text{total moles feed reacted}} \qquad (4.3)$$

$$\text{yield} = \text{selectivity} \times \text{total feed conversion} \qquad (4.4)$$

Standard parameters (measured reaction rate and membrane parameters) for modelling were listed in **Tables 8.3** to **8.5**. Included in the standard parameters is an effectiveness factor of 1.

9.1.1. MEMBRANE REACTOR EXPERIMENTS AT 250 °C

Figures 9.1 and **9.2** show the effects of sweep gas flow rate on exit ethanol conversion at two different ethanol feed flow rates. At a lower flow rate of 5 ml/h (**Figure 9.1**), the plug flow reactor (where the sweep gas to feed ratio is 0) operated at the equilibrium conversion. The overall ethanol conversion was slightly higher than the equilibrium conversion, because ethanol was also consumed to produce other products besides acetaldehyde. The total ethanol conversion increased with an increase in sweep gas flow rate, which is in line with the model equations. At the higher flow rate of 10 ml/h (**Figure 9.2**), the improvements in total ethanol conversion for the membrane reactor were less than at the lower flow rates. The plug flow reactor in **Figure 9.2** yielded an ethanol conversion below the equilibrium value. The

membrane reactor provided a good increase in ethanol conversion even under the higher feed flow rate conditions.

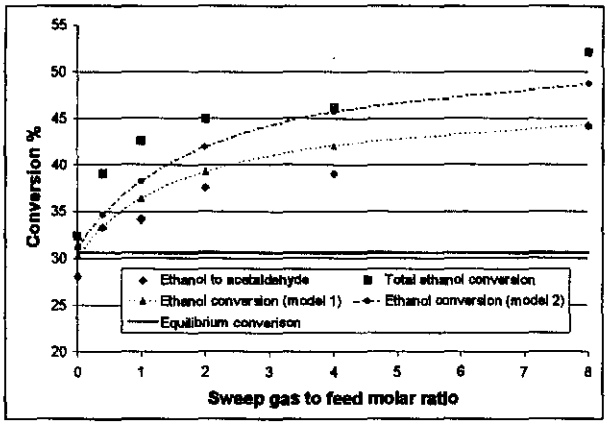

Figure 9.1: Ethanol conversion at 250 °C vs. sweep gas flow rate (F_{et} = 2.39*10^{-5} mol/s)

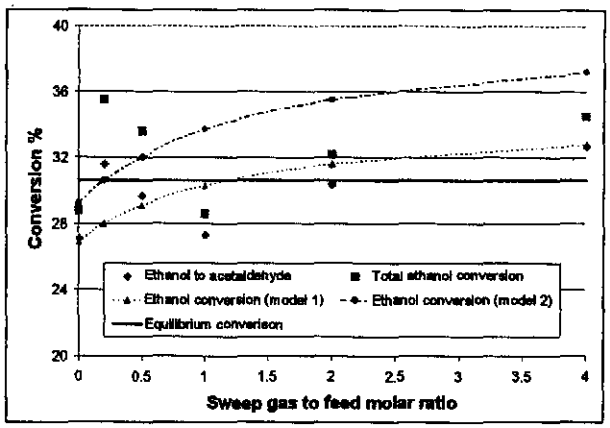

Figure 9.2: Ethanol conversion at 250 °C vs. sweep gas flow rate (F_{et} = 4.77*10^{-5} mol/s)

Two models were formulated to estimate total ethanol conversion for the membrane reactor. Both models only take the dehydrogenation of ethanol into account. They do not account for side reactions. They predict the total amount of ethanol converted and not the acetaldehyde yield. The acetaldehyde yield will be lower than the total ethanol conversion due to the formation of side products.

According to data for a differential reactor (see **8.3.4.1**), the feed flow rates in both these figures (**Figures 9.1** and **9.2**) are in the mass transfer limited regime, resulting in a effectiveness factor of less than one. Modelling calculations with an effectiveness factor of less than 1 and model parameters from **Chapter 8**, totally under predicted the ethanol conversion. The reaction rate for the packed bed, plug flow reactor was much higher than the values obtained from kinetic experiments with a differential reactor. The higher reaction rate could be due to a higher k'-value, lower K_{acet}-value or a higher η-value.

The individual changes in each parameter could not be obtained from plug flow reactor experiments in this study, but the combined effect of the three parameters could be predicted fairly accurately. The hydrogen permeance in the reaction mixture also varied significantly from pure component data. Hydrogen permeance through the Pd-Ag film decreased due to

competitive adsorption on Pd sites. Other components adsorb on Pd and fewer sites are available for hydrogen adsorption. The result was a decrease in hydrogen permeance.

For model 1 in **Figures 9.1** and **9.2**, standard membrane and kinetic parameters were used, but with an effectiveness factor of 1 (see **Tables 8.3** to **8.5**). For model 2, the following values were used for modelling:

- k'-value: 1.5 times the standard value,
- hydrogen permeance: 0.5 times the standard value,
- η: 1,
- other permeances: 0.5 times standard values to maintain standard selectivities, and
- all other data: similar to standard values.

Model 2 gives a much better prediction of the measured data. **Table 9.1** indicates the difference in total ethanol conversion between the model values and the measured values. The average absolute error is defined as the difference between the measured total ethanol conversion and the predicted values, averaged over all the sweep gas flow rates.

Table 9.1: Model differences for ethanol conversion at 250 °C

Feed (mol/s)	Average absolute error in total conversion for model 1 (%)	Average absolute error in total conversion for model 2 (%)
$2.39*10^{-5}$	5.3	2.9
$4.77*10^{-5}$	3.0	3.0

Figure 9.3 shows the selectivity of acetaldehyde as a function of the sweep gas flow rate. At 250 °C, there was no improvement in selectivity with an increase in sweep gas flow rate. Selectivity was between 80% and 95%. The acetaldehyde selectivity was most sensitive to the flow rate and a higher flow rate resulted in a higher acetaldehyde selectivity. By-products (see **section 8.4.1**) required a longer reaction time to form than the acetaldehyde did, and thus decreased with an increase in feed flow rate.

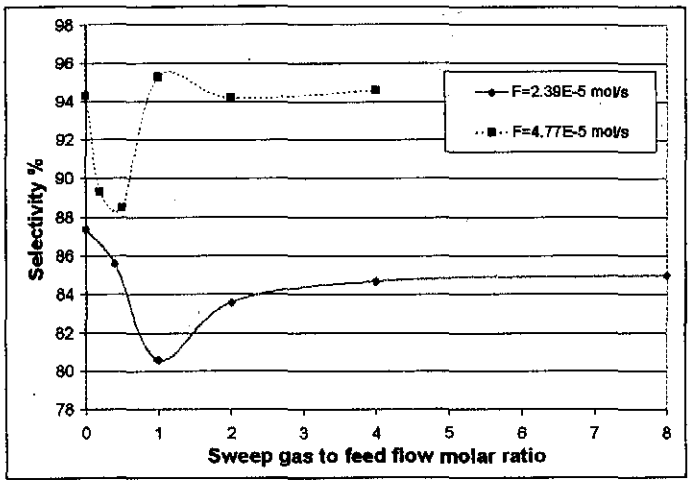

Figure 9.3: Measured acetaldehyde selectivity (250 °C)

The absolute and relative improvements obtained in total ethanol conversions by the membrane reactor are summarised in **Table 9.2**. Absolute and relative improvements are defined by:

$$\text{Absolute improvement} = \text{MRV} - \text{PFRV} \qquad (9.5)$$

$$\text{Relative improvement} = (\text{MRV} - \text{PFRV})/\text{PFRV} \qquad (9.6)$$

With MRV the maximum membrane reactor value and
PFRV the plug flow reactor value.

Table 9.2: Improvements in total X_{et} for the membrane reactor at 250 °C

Flow rate (mol/s)	Sweep to feed molar ratio	Absolute improvement in conversion (%)	Relative improvement in conversion (%)
$2.39*10^{-5}$	8	19.7	60.8
$4.77*10^{-5}$	4	5.7	19.8

9.1.2. MEMBRANE REACTOR EXPERIMENTS AT 275 °C

Figures 9.4 to **9.6** show measured and model data for ethanol dehydrogenation at 275 °C. The feed flow rate in **Figure 9.4** resulted in the equilibrium acetaldehyde yield for the plug flow reactor. The equilibrium ethanol conversion and the measured acetaldehyde yield differed by only about 2%. As the feed flow rate increased, the acetaldehyde yield decreased and the difference between the equilibrium ethanol conversion and the measured acetaldehyde yield increased (see **Figures 9.5** and **9.6**). In **Figure 9.6** the exit ethanol conversion dropped to below the equilibrium value due to the higher feed flow rate. The same principles that were discussed in **section 9.1.1** apply to the experiments performed at 275 °C.

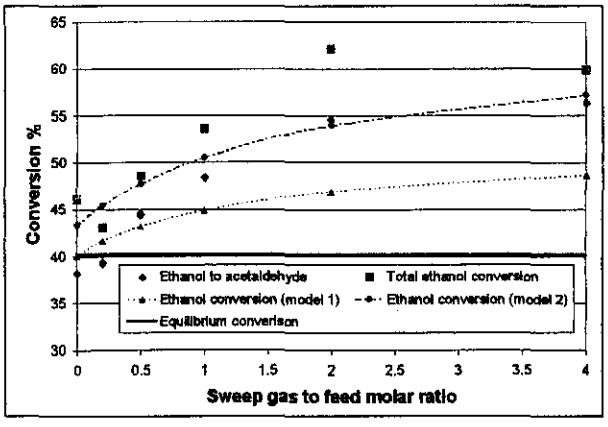

Figure 9.4: Ethanol conversion at 275 °C vs. sweep gas flow rate (F_{et} = 4.77*10^{-5} mol/s)

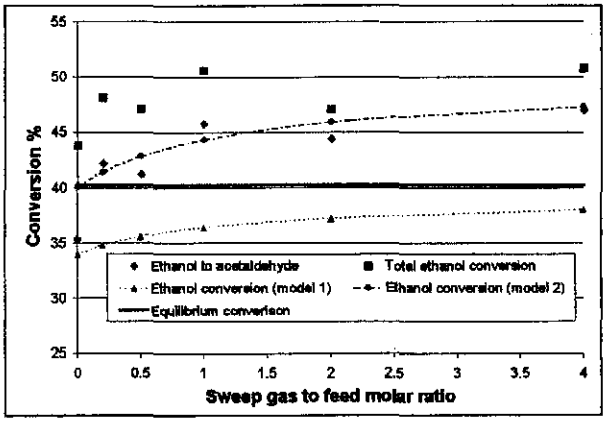

Figure 9.5: Ethanol conversion at 275 °C vs. sweep gas flow rate (F_{et} = 9.54*10^{-5} mol/s)

Model 1 in **Figures 9.4** to **9.6** used the standard parameters with an effectiveness factor of 1. Model 2 had the following parameters:

- k'-value: 2 times the standard value,
- hydrogen permeance: 0.5 times the standard value,
- η: 1,
- other permeances: 0.5 times standard values to maintain standard selectivities, and
- all other data: similar to standard values.

For the highest tested feed flow rate at 275 °C (**Figure 9.6**), model 2 started under predicting values at the higher sweep rates. For lower feed rates (**Figures 9.1**, **9.2**, **9.4** and **9.5**), model 2 was accurate in predicting total ethanol conversion at the higher sweep rates. A very likely explanation for this is the presence of interphase mass transfer resistance. If interphase mass transfer resistance was present, the value of η would increase with an increase in feed flow rate. Since the η-value was fixed at 1 for all calculations, the model would under predict total ethanol conversion at high feed flow rates in the presence of interphase mass transfer resistance. Not enough data was available to determine the k'-value, K_{acet} and η, individually, and therefore values were fixed at each temperature and not treated as variables. The model cannot account for changes in reaction rate parameters with changes in feed flow rate.

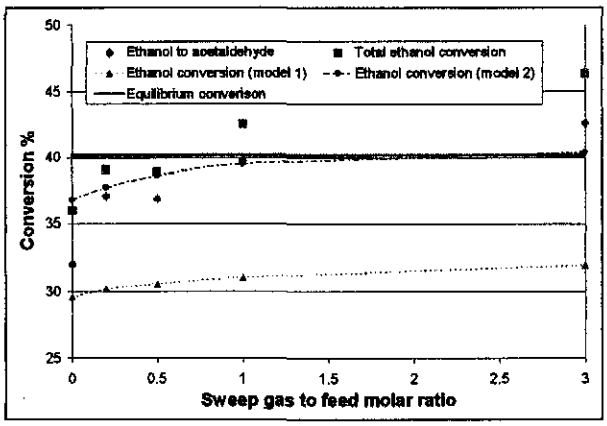

Figure 9.6: Ethanol conversion at 275 °C vs. sweep gas flow rate (F_{et} = 1.43*10^{-4} mol/s)

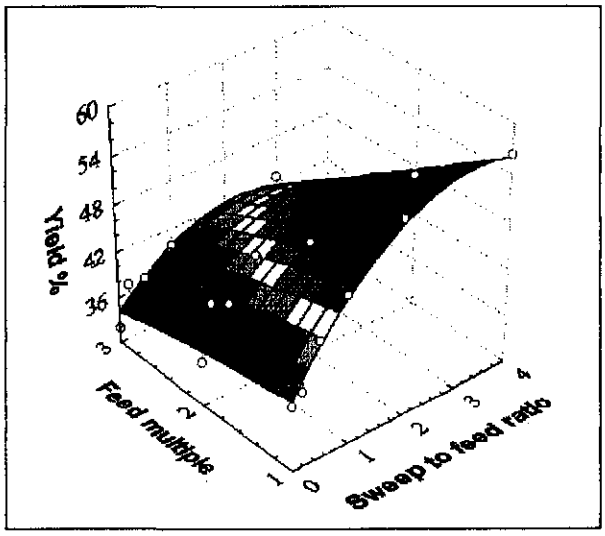

Figure 9.7: Acetaldehyde yield at 275 °C for a membrane reactor

Figure 9.7 shows the combined effect of feed flow rate and sweep gas to feed molar ratio on total ethanol conversion. The feed multiple is the multiple of the standard feed rate (4.77*10^{-5} mol/s). Total ethanol conversion increased more sharply at the lower feed rates with an increase in the sweep gas flow rate. Towards the higher feed rates, the total ethanol conversion for the plug flow reactor (sweep gas to feed molar ratio = 0) dropped slightly.

Model 2 gave accurate predictions of the exit membrane conditions. **Table 9.3** compares the model values with measured values for data at 275 °C.

Table 9.3: Model differences for ethanol conversion at 300 °C

Feed (mol/s)	Average absolute error in total conversion for model 1 (%)	Average absolute error in total conversion for model 2 (%)
$4.77*10^{-5}$	8.0	3.3
$9.54*10^{-5}$	11.9	4.3
$1.43*10^{-4}$	9.9	2.3

Table 9.4 indicates the measured improvements obtained by using the membrane reactor at 275 °C. The higher the equilibrium conversion, the more difficult it becomes to push the reaction's equilibrium further towards the product side. The improvements in total ethanol conversion with a membrane reactor will become smaller at higher temperatures.

Table 9.4: Improvements in total X_{et} for the membrane reactor at 275 °C

Flow rate (mol/s)	Sweep to feed molar ratio	Absolute improvement in conversion (%)	Relative improvement in conversion (%)
$4.77*10^{-5}$	4	13.8	29.9
$9.54*10^{-5}$	4	7.0	16.0
$1.43*10^{-4}$	3	10.4	28.9

Figure 9.8 indicates an improvement in acetaldehyde selectivity at the lower feed rates with an increase in sweep rates. Selectivity ranged between 80% and 95%, with the highest feed rates giving the best selectivities at the lower sweep gas ratios. At the higher sweep gas ratios, selectivity improved to above 90% for all feed rates.

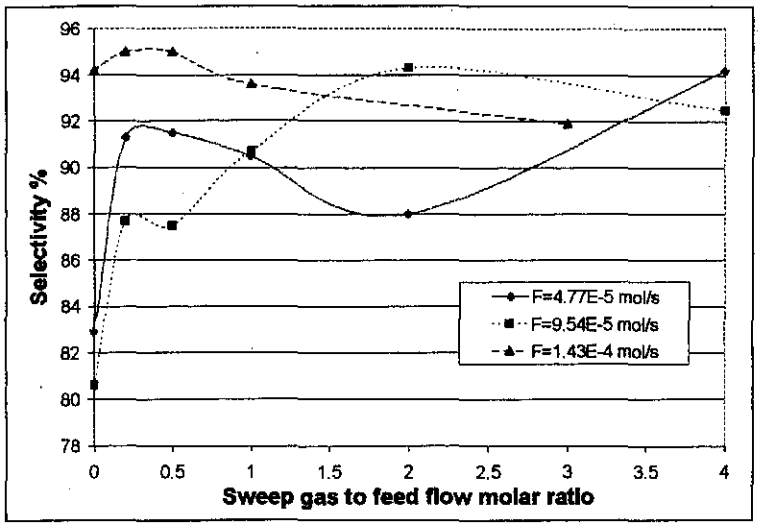

Figure 9.8: Measured acetaldehyde selectivity (275 °C)

9.1.3. MEMBRANE REACTOR EXPERIMENTS AT 300 °C

Measured and model data at 300 °C is presented in **Figures 9.9** and **9.10**. Model 1 predicts total ethanol conversions with the standard parameters at 300 °C and an effectiveness factor of 1. Model 2 used the following parameters:

- k'-value: 2.5 times the standard value,
- hydrogen permeance: 0.5 times the standard value,
- η: 1,
- other permeances: 0.5 times standard values to maintain standard selectivities, and
- all other data: similar to standard values.

At the lower ethanol flow rate (**Figure 9.9**), the exit ethanol conversion was the equilibrium conversion, but at the higher flow rate the exit conversion dropped to below the equilibrium value. At a flow rate of $9.54*10^{-5}$ mol/s and a reaction temperature of 275 °C (**Figure 9.5**), the total ethanol conversion was above the equilibrium value. To be consistent with data at 275 °C, the total ethanol conversion should not have been below the equilibrium value at 300 °C for a plug flow reactor and a feed rate of $9.54*10^{-5}$ mol/s (**Figure 9.10**), due to the higher reaction rate. The conversion was, however, below the equilibrium value. This suggested that the reaction rate was slowed down at 300 °C. This finding is consistent with the catalyst stability data in **Table 5.1**. Between 280 °C and 340 °C there was a sharp decrease in catalyst stability, mainly due to coking. In the membrane reactor at 300 °C,

coking must have occurred during the testing period. Total testing took about 16 hours. After testing at a flow rate of $9.54*10^{-5}$ mol/s (20 ml/h), the feed rate was increased to 30 ml/h, but the plug flow reactor results became very inconsistent.

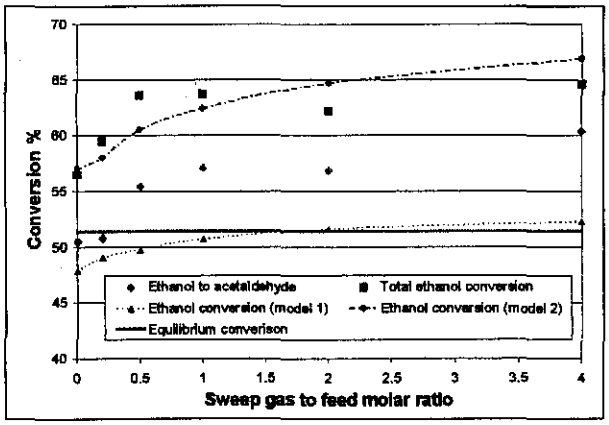

Figure 9.9: Ethanol conversion at 300 °C vs. sweep gas flow rate ($F_{et} = 4.77*10^{-5}$ mol/s)

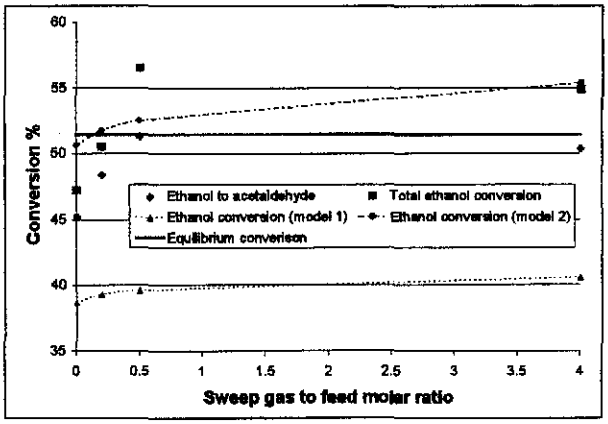

Figure 9.10: Ethanol conversion at 300 °C vs. sweep gas flow rate ($F_{et} = 9.54*10^{-5}$ mol/s)

Table 9.5 tabulates the accuracy of models 1 and 2 at 300 °C. Once again model 2 is very accurate at the tested sweep flow rates, but model 1 under predicts the measured values due to a reaction rate that is too slow in model 1.

Table 9.5: Model differences for ethanol conversion at 300 °C

Feed (mol/s)	Average absolute error in total conversion for model 1 (%)	Average absolute error in total conversion for model 2 (%)
$4.77*10^{-5}$	11.5	1.9
$9.54*10^{-5}$	12.7	2.3

The improvements in total ethanol conversion using a membrane reactor at 300 °C are indicated in **Table 9.6**.

Acetaldehyde selectivity varied between 85% and 96% (**Figure 9.11**). For the plug flow reactor, the selectivity was the highest at the highest feed flow rate. At low sweep rates, the selectivity dropped for both feed flow rates tested and then increased again towards the

higher sweep gas flow rates. In both cases the selectivity was above 90% at the higher sweep gas flow rates.

Table 9.6: Improvements in total X_{et} for the membrane reactor at 300 °C

Flow rate (mol/s)	Sweep to feed molar ratio	Absolute improvement in conversion (%)	Relative improvement in conversion (%)
$4.77*10^{-5}$	4	8.1	14.3
$9.54*10^{-5}$	4	7.7	16.3

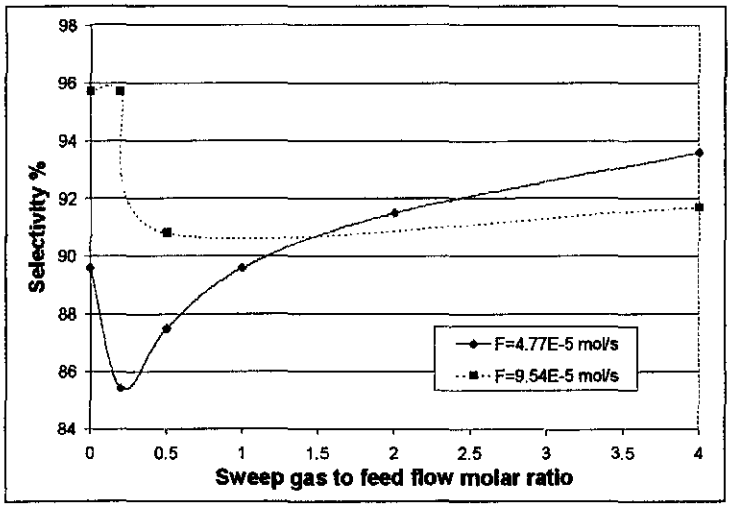

Figure 9.11: Measured acetaldehyde selectivity (300 °C)

9.1.4. FURTHER DISCUSSION OF ETHANOL DEHYDROGENATION

The theory (see **2.9.4.3**) suggests a shift in the reaction equilibrium in a membrane reactor, resulting in higher conversions at the same operating temperature. Catalytic membrane reactor experiments carried out to determine ethanol dehydrogenation confirmed the theory. In **section 8.1**, the effect of feed rate on reaction conversion was discussed. It was said that for the membrane reactor to be of use, the improvements in conversion had to be obtained in region 2 of **Figure 8.1**. For ethanol dehydrogenation in a catalytic membrane reactor, reaction conversion improvements were indeed obtained in this region, and as follows:

- 250 °C: 5.7% absolute or 20% relative improvement, and
- 275 °C: 10.4% absolute or 29% relative improvement.

At 300 °C, coking began to take place and it lead to inaccurate data. From an operating point of view, there seemed to be an optimum working temperature. If the temperature was too low, the reaction kinetics was slow and the conversion poor, even with a membrane reactor. Organic molecules adsorb more strongly onto the Pd-Ag membrane film at low temperatures than at higher temperatures and reduce hydrogen permeance more substantially at lower temperatures. Higher temperatures improve hydrogen permeance in two ways: by increasing the hydrogen permeance kinetics and by reducing the organic molecule adsorption onto the Pd-alloy surface.

On the negative side: at high temperatures, catalyst deactivation occurs quickly, which reduces the activity of the copper based catalyst and leads to poor conversion. Coking will most probably also occur on the membrane surface and thus reduce hydrogen permeance severely. The sensitivity analysis in **Chapter 8** indicated that the performance of the membrane reactor was more sensitive to reaction rate parameters than to membrane parameters. To obtain large improvements in ethanol conversion over the conventional plug flow reactor, the catalyst activity must remain high.

A temperature of 275 °C gave the best ethanol dehydrogenation results. The selectivity towards acetaldehyde formation was above 80% at all times. Selectivity was more dependent on feed flow rate than on temperature or sweep gas flow rate. The selectivity increased with an increase in feed flow rate and also, to a lesser extent, with an increase in sweep gas flow rate. Selectivity was above 90% for all experiments at the highest tested sweep rates, except for the very low feed flow rate of $2.39*10^{-5}$ mol/s. **Figure 9.12** indicates some selectivity profiles at different temperatures. There was a lot of variance in the data at the lower sweep rates, but the final selectivities at the higher sweep rates were not very dependent on temperature.

Total ethanol conversions were modelled with two different models. The first model used standard conditions (as defined in **Tables 8.3** to **8.5**) and an effectiveness factor of 1. In most instances the model under predicted the measured data. This indicated that the reaction rates

determined in kinetic experiments in a differential reactor were much lower than the values in the plug flow reactor. Higher k'-values were employed in the second model, keeping all adsorption coefficients constant. The effectiveness factor was fixed at 1 and the permeances for each component in the reaction was halved. The net result was a model that predicted total ethanol conversion to within 4.5%.

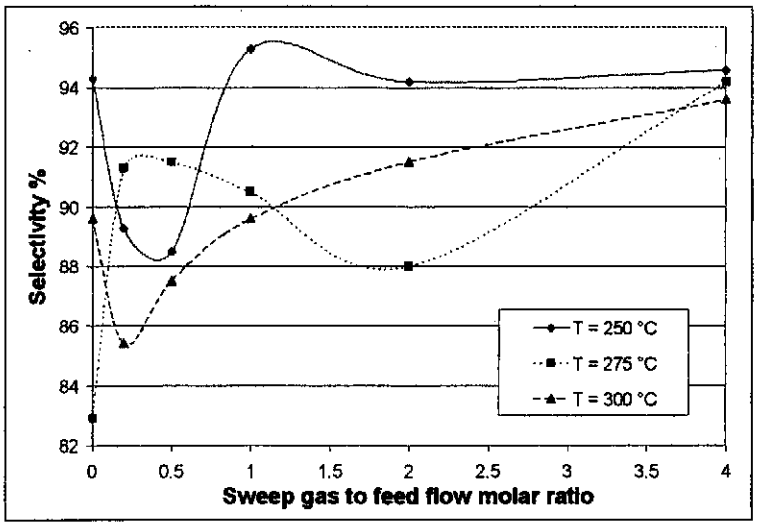

Figure 9.12: Measured acetaldehyde selectivity at a constant feed rate (F_{et} = 9.54*10^{-5} mol/s)

Deng et al. (1995), Liu et al. (1997) and Raich and Foley (1998) studied ethanol dehydrogenation in a membrane reactor, under conditions that differed greatly from those used in the present study. The feed rates that they employed were more than an order of magnitude lower than the feed rates used in this study (see **Table 8.1**). Liu et al. (1997) tested ethanol dehydrogenation as a function of feed rate. At a similar W/F ratio of 1000 g.min/mol to Liu et al. (1997), this study achieved a maximum of 65% conversion at 300 °C compared to their 30%.

Acetaldehyde selectivity in this study was significantly higher than the values obtained by Raich and Foley (1998). This is to be expected at the higher feed rates. They obtained higher conversions because they used a very low feed rate and a very diluted feed. When the partial pressure of ethanol was reduced (by using a diluted feed), the equilibrium conversion for the ethanol dehydrogenation reaction increased.

9.2. 2-BUTANOL DEHYDROGENATION

Results of 2-butanol dehydrogenation in a membrane reactor are listed in **Appendix F2**. Catalytic membrane reactor experiments were performed at temperatures ranging from 190 °C to 240 °C. Standard reaction rate parameters and membrane parameters used for modelling were listed in **Tables 8.6** to **8.8**. Catalytic membrane performance at 190 °C, 215 °C and 240 °C will be discussed separately. For the three dimensional figures shown in this section, the standard feed rate was $3.04*10^{-5}$ mol/s and the feed multiple was the multiple of the standard feed rate.

9.2.1. MEMBRANE REACTOR EXPERIMENTS AT 190 °C

Figures 9.13 to **9.16** show 2-butanol conversion as a function of sweep gas flow rate at different feed rates. The measured exit 2-butanol conversion dropped below the equilibrium value for feed flow rates of $3.04*10^{-5}$ mol/s and higher. The exit conversion was modelled in a manner similar to that for the ethanol dehydrogenation reaction. Initial modelling experiments were performed with reaction rate parameters determined from differential reactor experiments in **Chapter 5**. The reaction rate parameters of **Table 8.6** substituted into equations (**8.57**) to (**8.76**) yielded 2-butanol conversions much lower than the measured values. For further model calculations, the parameters were changed to the following:

- k'-value: 2 times the standard value at 190 °C,
- K_{MEK}: 0.1 times the standard value at 190 °C,
- η: fixed at 1 for all flow rates, and
- permeances: the same as in **Table 8.7** at 190 °C.

Increasing the model's k- value for 2-butanol dehydrogenation alone was insufficient to obtain predicted conversions close to the measured conversions for the plug flow reactor. The MEK adsorption coefficient was also reduced by a factor 10 for modelling. This may seem exaggerated, but it should be noted that the individual adsorption coefficients were determined for pure component data. For example, the MEK adsorption coefficient was determined when only 2-butanol and MEK were passed over the catalyst bed in the differential reactor. The conversion was kept very low and very little hydrogen formed. In

the plug flow reactor, 2-butanol was converted to MEK and hydrogen in equal molar amounts. The MEK was essentially in a MEK-hydrogen environment and not in a MEK-2-butanol environment. The MEK adsorption behaviour could thus be expected to be significantly different from the behaviour in a MEK-2-butanol mixture.

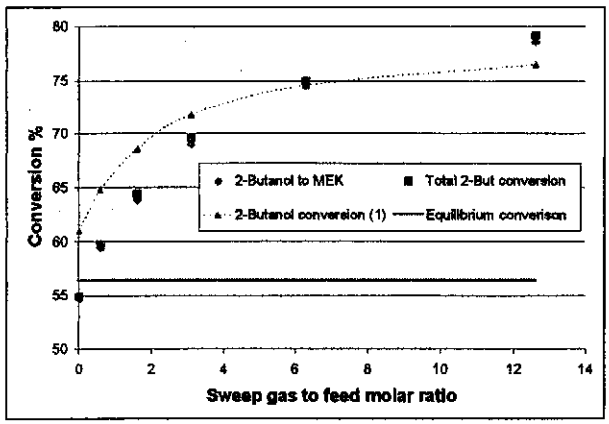

Figure 9.13: 2-Butanol conversion at 190 °C vs. sweep gas flow rate ($F_{2But} = 1.52*10^{-5}$ mol/s)

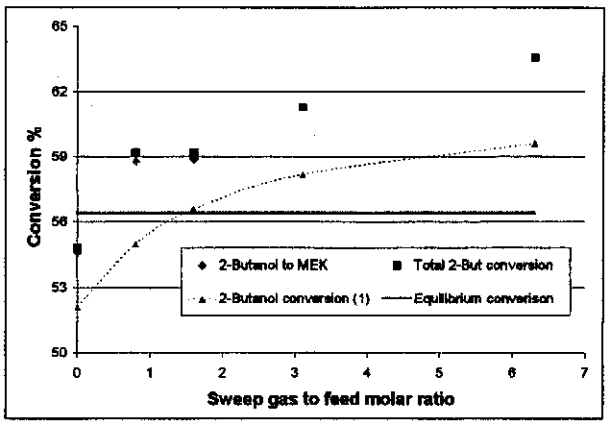

Figure 9.14: 2-Butanol conversion at 190 °C vs. sweep gas flow rate ($F_{2But} = 3.04*10^{-5}$ mol/s)

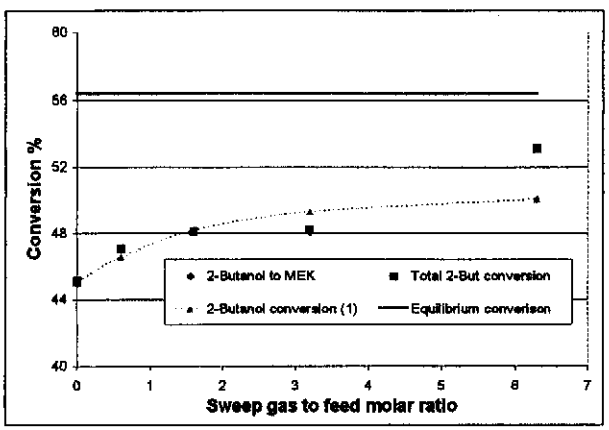

Figure 9.15: 2-Butanol conversion at 190 °C vs. sweep gas flow rate ($F_{2But} = 4.56*10^{-5}$ mol/s)

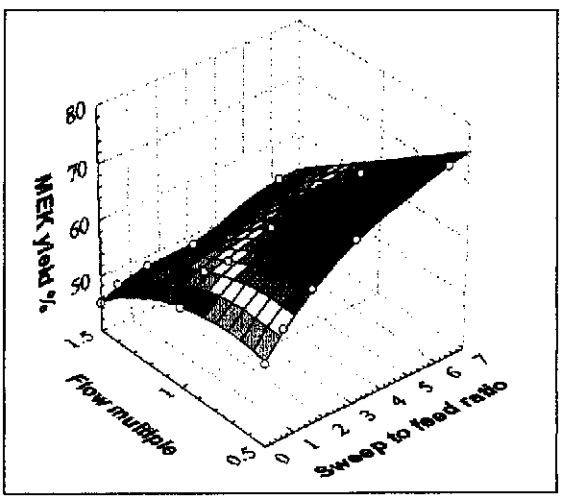

Figure 9.16: MEK yield at 190 °C

The 2-butanol conversion was sensitive towards the feed rate. There was a drop in 2-butanol conversions at 190 °C with an increase in feed rate. **Figure 9.16** illustrates this very clearly.

Optimum conversions were obtained at low flow rates and high sweep ratios as predicted by the membrane reactor model.

At 190 °C, the model predicted the measured values well. There was little difference between the total 2-butanol conversion and the MEK yield, indicating very high selectivity. The best 2-butanol conversion in the membrane reactor at a feed flow rate of $1.52*10^{-5}$ mol/s was 79% and it dropped to 53% at a feed rate of $4.56*10^{-5}$ mol/s.

The improvement in 2-butanol conversion by the membrane reactor is summarised in **Table 9.7**. There was a large improvement in conversion at the lower flow rate. The absolute differences between the model conversions and the measured 2-butanol exit conversions are listed in **Table 9.8**.

Table 9.7: Improvements in total X_{2But} for the membrane reactor at 190 °C

Flow rate (mol/s)	Sweep to feed molar ratio	Absolute improvement in conversion (%)	Relative improvement in conversion (%)
$1.52*10^{-5}$	12.6	24.3	44.3
$3.04*10^{-5}$	6.3	8.8	16.1
$4.56*10^{-5}$	6.3	8.0	17.7

Table 9.8: Model differences for 2-butanol conversion at 190 °C

Feed (mol/s)	Average absolute error in total conversion for model 1 (%)
$1.52*10^{-5}$	3.5
$3.04*10^{-5}$	3.3
$4.56*10^{-5}$	0.9

As mentioned previously (**section 8.4.2**), the selectivity towards MEK production at 190 °C was very high. **Figure 9.17** plots selectivity as a function of feed rate and sweep gas to feed

molar ratio. Selectivity was above 99% for all experiments and increased towards 100% at the higher flow rates. The only by-product observed in some experiments was 3-octanol.

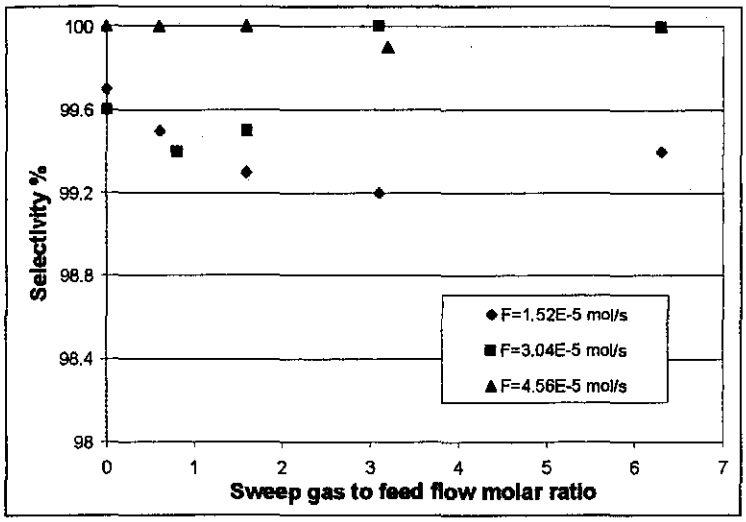

Figure 9.17: Measured MEK selectivity at 190 °C

9.2.2. MEMBRANE REACTOR EXPERIMENTS AT 215 °C

Figures 9.18 to **9.21** summarise 2-butanol conversion at 215 °C in a membrane reactor. **Figures 9.18** to **9.20** show the classic signs of mass transfer resistance for the model values, i.e. an over prediction of conversions at low flow rates and an under prediction of values at high flow rates. The same model parameter ratios employed at 190 °C were employed for modelling calculations at 215 °C. The standard parameter values at 215 °C are listed in **Tables 8.6** and **8.7**.

The model did not take mass transfer resistance into account, since the effectiveness factor was fixed at 1. Kinetic data obtained in the differential reactor indicated a reaction free from interphase mass transfer resistance (see discussion in **section 5.2.2**). The plug flow reactor data contradicted the differential reactor data regarding interphase mass transfer resistance. One possible reason is the difference in the Reynolds numbers of the two situations. For differential reactor experiments, a 4 mm inside diameter tube was used, resulting in much larger gas velocities as compared to the 7 mm inside diameter tube used for plug flow and membrane reactor experiments. By assuming η as a variable dependent on feed flow rate, a better model fit might be obtained, but as a first approximation this was not investigated.

If η decreases with a decrease in feed flow rate, the k'-value must be even higher than the value used for this model. In such a case, the model should be fitted to the measured data at the maximum feed rate with a high η-value to determine the k'-value and K_{MEK}. The η-value must then be reduced at the lower flow rates to yield lower overall reaction rates and lower model conversions at the lower feed rates.

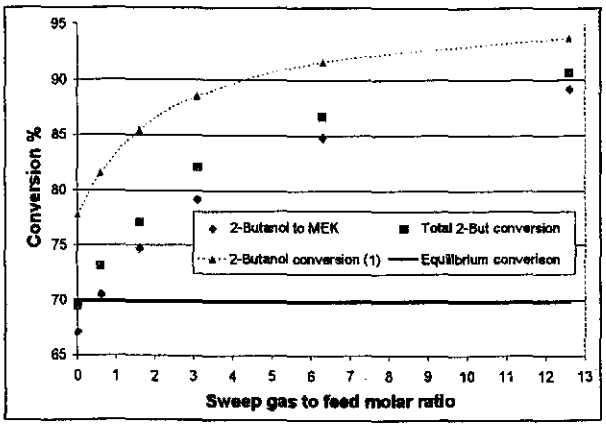

Figure 9.18: 2-Butanol conversion at 215 °C vs. sweep gas flow rate (F_{2But} = 1.52*10^{-5} mol/s)

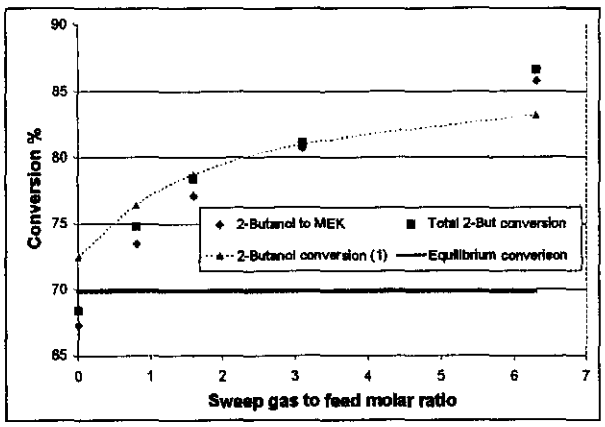

Figure 9.19: 2-Butanol conversion at 215 °C vs. sweep gas flow rate (F_{2But} = 3.04*10^{-5} mol/s)

At a feed rate of 1.52*10^{-5} mol/s and 3.04*10^{-5} mol/s, the exit 2-butanol conversion for the plug flow reactor was similar to the equilibrium conversion. The model values were larger than the equilibrium values. At the highest feed rate tested (6.08*10^{-5} mol/s), the 2-butanol exit conversion in the plug flow reactor dropped below the equilibrium value and the reaction moved into block 2 as described in **Figure 8.1**. **Figure 9.21** indicates the difference in 2-butanol conversion at different feed rates in the plug flow reactor (at zero sweep gas). At high sweep rates, the membrane reactor improved 2-butanol conversion for all feed flow rates tested. The highest conversions were in the region of 90%, with the equilibrium value being 70%.

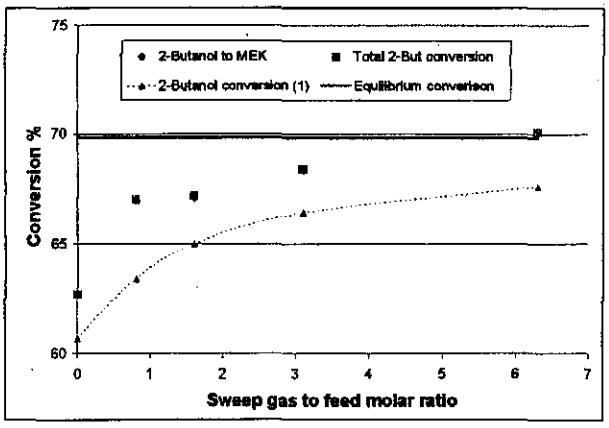

Figure 9.20: 2-Butanol conversion at 215 °C vs. sweep gas flow rate ($F_{2But} = 6.08*10^{-5}$ mol/s)

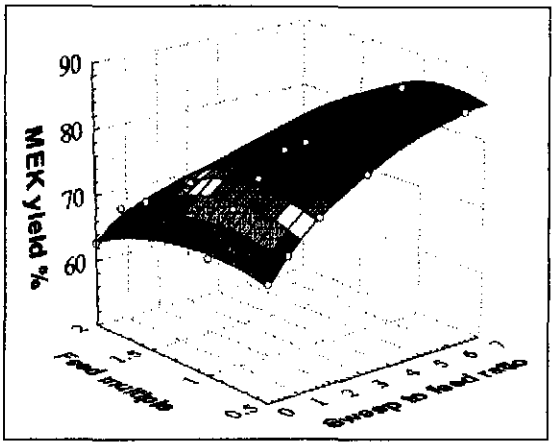

Figure 9.21: MEK yield at 215 °C

The performance of the membrane reactor at 215 °C is listed in **Table 9.9** and the accuracy of the model is summarised in **Table 9.10**.

Table 9.9: Improvements in total X_{2But} for the membrane reactor at 215 °C

Flow rate (mol/s)	Sweep to feed molar ratio	Absolute improvement in conversion (%)	Relative improvement in conversion (%)
$1.52*10^{-5}$	12.6	21.2	30.5
$3.04*10^{-5}$	6.3	18.2	26.6
$6.08*10^{-5}$	6.3	7.4	11.8

Table 9.10: Model differences for 2-butanol conversion at 215 °C

Feed (mol/s)	Average absolute error in total conversion for model 1 (%)
$1.52*10^{-5}$	6.6
$3.04*10^{-5}$	1.9
$6.08*10^{-5}$	2.5

For model differences in **Table 9.10** and in all other tables, the absolute differences are listed. There is no distinction between model values higher or lower than the measured values, only

the difference between them is stated. The model loses accuracy at the lower feed rates, with the difference between measured values and model values increasing to above 6%.

The MEK selectivity at 215 °C **(Figure 9.22)** was high (above 96%), but slightly lower than the values obtained at 190 °C. The selectivity improved with an increase in feed flow rate and at the highest feed flow rate tested, the selectivity reached 100%.

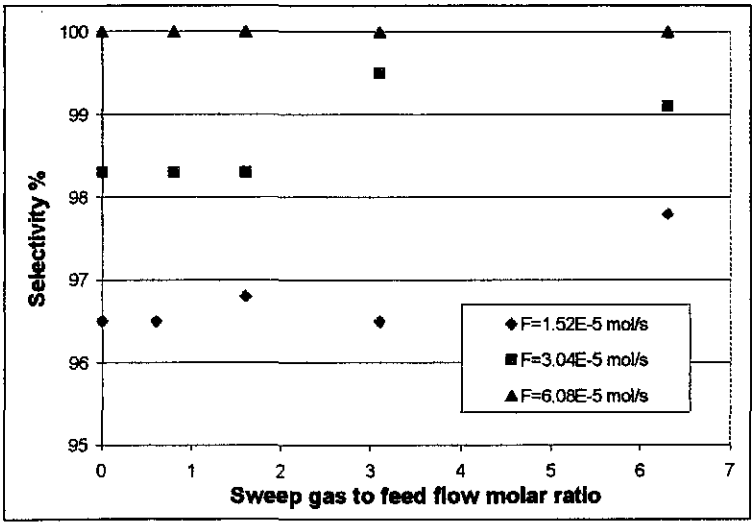

Figure 9.22: Measured MEK selectivity at 215 °C

9.2.3. MEMBRANE REACTOR EXPERIMENTS AT 240 °C

The highest temperature at which 2-butanol dehydrogenation was tested was 240 °C. The results are presented in **Figures 9.23** to **9.26**. Modelling parameters at 240 °C were:

- k'-value: 2 times the standard value at 240 °C,
- K_{MEK}: 0.1 times the standard value at 240 °C,
- η: fixed at 1 for all flow rates, and
- permeances: the same as in **Table 8.7** for 240 °C.

At 240 °C, the exit 2-butanol conversion remained at the equilibrium value for all flow rates tested in the plug flow reactor, up to a feed flow rate of 40 ml/h ($1.22*10^{-4}$ mol/s). Membrane reactor experiments were only performed at feed flow rates of up to 20 ml/h ($6.08*10^{-5}$ mol/s) due to limitations of the sweep gas flow meters. At the low flow rates **(Figure 9.23** and **9.24)** the model over predicts the measured values and at the higher flow

rates, the model under predicts the measured values. The same explanation supplied in **section 9.2.2** is applicable at 240 °C. Initial modelling results indicated the presence of interphase mass transfer resistance at low flow rates for 2-butanol dehydrogenation. The effectiveness factor was not constant with feed flow rate, but declined as the feed flow rate declined. Measured 2-butanol conversions were at or above 90% for all flow rates tested.

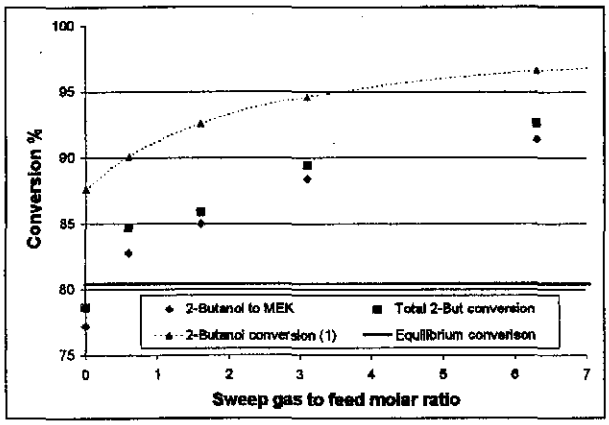

Figure 9.23: 2-Butanol conversion at 240 °C vs. sweep gas flow rate ($F_{2But} = 1.52*10^{-5}$ mol/s)

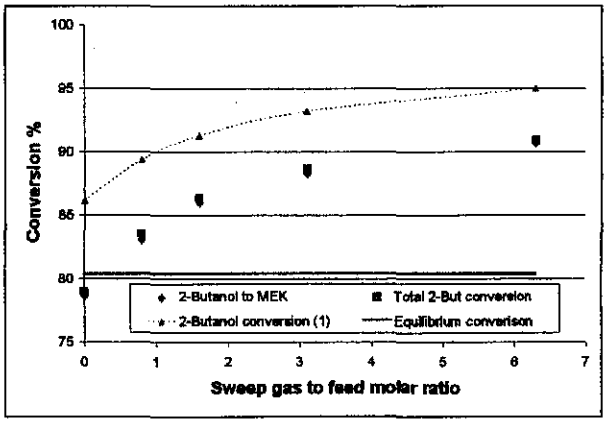

Figure 9.24: 2-Butanol conversion at 240 °C vs. sweep gas flow rate ($F_{2But} = 3.04*10^{-5}$ mol/s)

For the plug flow reactor in **Figure 9.26**, the measured data confirmed, to some extent, the model prediction of interphase mass transfer resistance. At a zero sweep gas to feed molar ratio, the total 2-butanol conversion increased very slightly with an increase in feed flow rate. The improvements in 2-butanol conversion in the membrane reactor for high sweep rates were similar at all feed multiples. If higher feed rates were to be employed, the benefits of the membrane reactor would start declining.

The improvements obtained by the membrane reactor are listed in **Table 9.11**. As mentioned previously, improvements become smaller at the higher temperatures, because the equilibrium conversion becomes very high. The model predicts the measured values at lower feed rates with less accuracy than at the higher feed rates (see **Table 9.12**). The difference between the model predictions and the measured data increases above 5% at the lower feed rates.

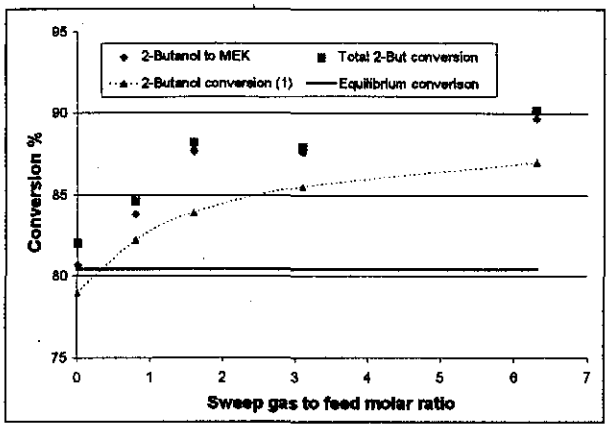

Figure 9.25: 2-Butanol conversion at 240 °C vs. sweep gas flow rate (F_{2But} = 6.08*10^{-5} mol/s)

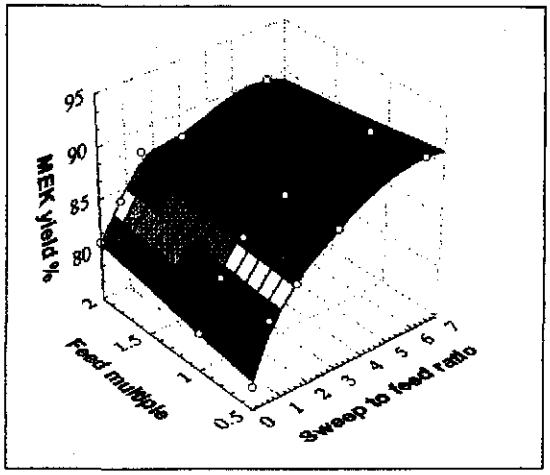

Figure 9.26: MEK yield at 240 °C

Table 9.11: Improvements in total X_{2But} for the membrane reactor at 240 °C

Flow rate (mol/s)	Sweep to feed molar ratio	Absolute improvement in conversion (%)	Relative improvement in conversion (%)
1.52*10^{-5}	12.6	16.8	21.4
3.04*10^{-5}	6.3	11.9	15.1
6.08*10^{-5}	6.3	8.2	10.0

Table 9.12: Model differences for 2-butanol conversion at 240 °C

Feed (mol/s)	Average absolute error in total conversion for model 1 (%)
1.52*10^{-5}	5.5
3.04*10^{-5}	5.3
6.08*10^{-5}	3.1

Selectivity didnot decrease with an increase in temperature up to 240 °C, it remained above 97% (**Figure 9.27**). At higher temperature, butenes will start forming and the selectivity will

drop. **Figure 4.41** shows the MEK selectivity as a function of temperature up to 390 °C. Selectivity at 240 °C was very good but then gradually declined towards the higher temperatures.

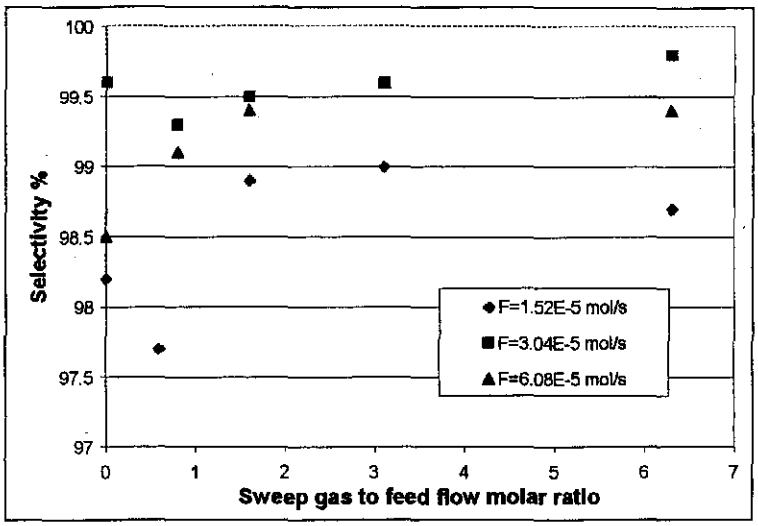

Figure 9.27: Measured MEK selectivity at 240 °C

9.2.4. FURTHER DISCUSSION OF 2-BUTANOL DEHYDROGENATION

For 2-butanol dehydrogenation, the conversion in a plug flow reactor increased sharply with an increase in temperature and decreased with an increase in feed flow rate. The higher the operating temperature and the reaction rate, the higher the feed rates that could be employed before the conversion started decreasing (**Figure 9.28**), due to a decrease in reaction time.

Catalytic membrane reactor experiments were performed with feed flow rates resulting in both equilibrium restricted and non-equilibrium restricted 2-butanol conversion (at 190 °C and 215 °C). For high flow rates resulting in the non-equilibrium restricted conversions, the theoretical benefits of the membrane reactor were confirmed by experimental data. At 240 °C, membrane experiments were only performed for feed flows resulting in the equilibrium restricted conversion.

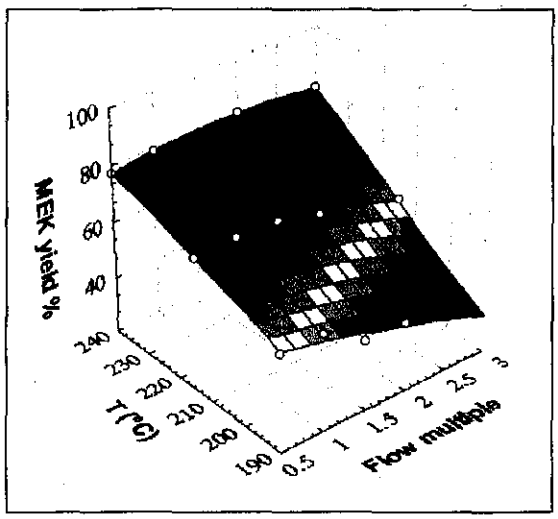

Figure 9.28: MEK yield % vs. flow rate and temperature
(feed multiple of one equals $3.04*10^{-5}$ mol/s (10ml/h))

Figure 9.29 shows the improvements in total 2-butanol conversion obtained from a membrane reactor. **Figure 9.29** illustrates results for a feed rate of $3.04*10^{-5}$ mol/s (10 ml/h). To achieve a high MEK yield, a high operating temperature must be used and the temperature should be kept at or below 250 °C to improve catalyst life. **Figure 5.8** indicates catalyst deactivation over a 24 hour period at different operating temperatures. At 250 °C, the catalyst was stable, but at higher temperatures the activity of the catalyst declined over time. At 240 °C, the membrane reactor gave an increase in MEK yield of about 10%.

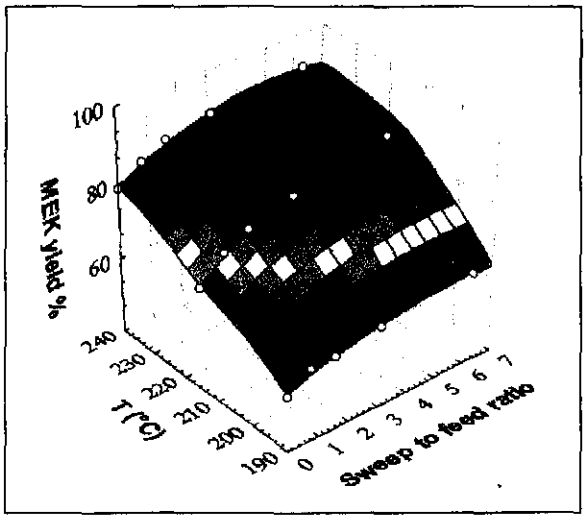

Figure 9.29: Effect of sweep ratio on MEK yield %

No data on 2-butanol dehydrogenation in a membrane reactor could be found in literature. It was not possible to compare results on 2-butanol dehydrogenation with data obtained from other researchers.

9.3. SUMMARY

Theoretical benefits of a catalytic membrane reactor as compared to a plug flow reactor were realised for the dehydrogenation of ethanol and 2-butanol. For ethanol dehydrogenation, catalyst deactivation above 280 °C limits the upper operating temperature of copper based catalysts. For 2-butanol dehydrogenation, the copper based catalyst was stable at 250 °C and lower. Coking at higher temperatures will deactivate the copper on silica catalysts and result in a rapid decrease in catalyst activity.

The optimum working temperature for ethanol dehydrogenation with copper on silica catalysts is between 270 °C to 280 °C. The equilibrium conversion in this temperature range is just over 40% for an undiluted feed at atmospheric pressure. The membrane reactor improved the total ethanol exit conversion from 45% (plug flow reactor) to 60% at low feed flow rates and from 36% to 46% at high feed flow rates. The acetaldehyde selectivity of the reaction was above 80% for all experiments performed. The selectivity was most sensitive to the feed flow rate and the selectivity improved with an increase in feed flow rate. The selectivity also improved with an increase in sweep gas flow rate, but changed little with temperature from 250 °C to 300 °C. At a high sweep gas flow rate, the acetaldehyde selectivity was above 90% for the majority of the experiments.

The membrane reactor is less suited for 2-butanol dehydrogenation, because there are less temperature limitations for this reaction. Improved conversion of 2-butanol can be obtained by increasing the operating temperature up to 250 °C, without any significant deactivation of the catalyst. It is more economical to increase the reaction temperature than to use a membrane reactor at a lower temperature to obtain the same results. The membrane reactor does have some benefits in that it can obtain a near complete conversion at the higher temperatures. Maximum plug flow reactor conversion at 240 °C is 80%. This can be

increased to above 90% at 240 °C by employing a membrane reactor. The exit 2-butanol conversion in the membrane reactor was also modelled with equations developed in **Chapter 8**. A proper model could only be formulated by using a k'-value twice (or more) the value obtained from the differential reactor experiments and a MEK adsorption coefficient one tenth of the value obtained from the differential reactor data. The model predicted the experimental data to within 6.5% of the measured exit 2-butanol conversion. Selectivity towards MEK production was high under all conditions (> 96%) and increased towards 100% at the higher feed flow rates.

The Pd-Ag membrane was stable between 190 °C and 300 °C in both an ethanol and a 2-butanol environment for about 30 working days (450 hours) in total. The same membrane was used for both reactions and the membrane reactor maintained its superior performance as compared to the plug flow reactor for the full duration of testing.

10. CONCLUSIONS

In **Chapter1**, the six main goals of the project were stated. They were:

- To optimise the performance of an alcohol dehydrogenation catalyst,
- To model the kinetics of an alcohol dehydrogenation reaction,
- To optimise the composition and thickness of Pd and Pd-alloy films for hydrogen separation,
- To model the membrane separation process with a sweep gas and a pressure differential,
- To compare the performance of a membrane reactor consisting of the optimised catalyst and optimised membrane with a plug flow reactor, and
- To model the membrane reactor.

The main conclusions to the work performed to reach each goal are summarised in the following few pages.

10.1. CATALYST OPTIMISATION

All catalysts were prepared by impregnating a support with copper. The performances of the catalysts were tested for the dehydrogenation of ethanol and 2-butanol. Three support types were tested and it was found that:

- The alumina support yielded mainly dehydration products and not the required dehydrogenation products,
- The MgO support had a very low surface area and that resulted in very low conversion of ethanol to acetaldehyde, and
- The silica support, impregnated with copper, gave high conversions of both ethanol and 2-butanol towards the desired dehydrogenation products.

For silica based catalysts, there were an optimum copper percentage of 15 wt % on silica to obtain the highest conversion of the alcohol towards the desired product. The addition of cobalt, chromium or nickel stabilisers to copper on silica catalysts had negative effects

on acetaldehyde yield. More by products formed and the yield of acetaldehyde decreased due to a decline in acetaldehyde selectivity. When the same stabilisers were added to copper-alumina catalysts, the effect was positive and the production of di-ethyl ether (the desired product) increased. A catalyst particle size of up to 1180 microns had a very small effect on product yield, indicating that intraparticle mass transfer resistance for both ethanol and 2-butanol dehydrogenation were negligible. The production of methyl ethyl ketone from 2-butanol and acetaldehyde from ethanol, approached the equilibrium conversion at low feed flow rates.

10.2. REACTION MODELLING FOR ETHANOL AND 2-BUTANOL DEHYDROGENATION

A 14.4 wt % copper on silica catalyst was used for all kinetic and stability testing. The stability of the catalyst was determined prior to kinetic testing to determine a stable region for performing kinetic experiments. Copper catalysts was reduced in hydrogen prior to using them. The reduction temperature is critical to prevent sintering of copper particles. Reduction at 400 °C and 340 °C caused severe sintering, but not at 255 °C. For ethanol dehydrogenation, catalyst stability tests were performed from 220 °C to 400 °C and for 2-butanol dehydrogenation, stability tests were performed at 250 °C and 310 °C. For ethanol dehydrogenation, the catalyst was stable up to 280 °C. Higher temperatures caused both sintering and coking of the catalysts even if additives (Co, Cr or Ni) were added to the copper. For 2-butanol dehydrogenation, the copper on silica catalyst was stable at 250 °C.

The ethanol dehydrogenation reaction exhibited strong interphase mass transfer resistance, while for 2-butanol dehydrogenation there was no clear indication of interphase mass transfer resistance. Ethanol dehydrogenation kinetics were determined from 200 °C to 300 °C and 2-butanol dehydrogenation kinetics from 190 °C to 280 °C. Both reactions could be described by the dual site, surface reaction controlling mechanism. The organic products (MEK or acetaldehyde) had dominant adsorption coefficients.

10.3. MEMBRANE OPTIMISATION

A palladium membrane is sensitive towards the operating conditions of the membrane. If the membrane is to be operated above 300 °C, a pure palladium membrane can be used in a hydrogen environment, but if the membrane is to be operated below 300 °C, a palladium alloy must be used. Pure palladium embrittles quickly below 300 °C in hydrogen, and thus becomes unusable.

Palladium films were prepared be electroless plating. To produce a high quality and very thin palladium film, supported on a membrane, each production step must be performed with care. Prior to plating, the asymmetric alumina membrane support must be pretreated with palladium and tin solutions. A high palladium to tin ratio gives a more stable film. Alternatively, new tin free pretreatment solutions can be employed. The initial plating rate should be slow to prevent the formation of defects in the film. The plating rate was controlled by the addition of hydrazine at a constant plating temperature of 71 °C. Thorough cleaning of the membrane after plating is crucial to remove EDTA (from the plating solution) trapped in the membrane pores. Membranes were stirred in ammonia solution, dried at 240 °C and further oxidised at 320 °C to remove organic components in the membrane pores.

Palladium films of thicknesses down to 1 μm were deposited on the inside of asymmetric SCT α-alumina membranes (200 nm pore size). Hydrogen permeances varied between about 8 and 15 $\mu mol/m^2.Pa.s$ for temperatures from 330 °C to 450 °C and palladium films from 1.0 to 1.5 μm. Hydrogen to nitrogen selectivity was above 100 for all membranes tested and above 400 for all but two membranes (thickness 1.0 to 1.5 μm). These values are a significant improvement over other published results.

Silver was deposited on palladium to form palladium-silver films of less than 2.2 μm thick. The separated layers caused a sharp drop in hydrogen permeance through the film. The bi-layer was heat treated to improve hydrogen permeance and form a homogeneous alloy. In a hydrogen atmosphere at 590 °C, defects formed in the Pd-Ag film within

10 hours. The hydrogen also passivated the film at 590 °C. At 550 °C, defects still formed in hydrogen, but at a much slower rate. Some defect formed in an argon atmosphere at 550 °C after more than 100 hours. Few defects formed in both argon and nitrogen at 500 °C. Nitrogen passivated the film and thus argon was chosen for performing alloying experiments.

Alloying should be performed at 550 °C in argon for 10 to 15 hours. Thereafter, the membrane must be cooled down to 310 °C in argon, oxidised in oxygen for 1 hour and then reduced in hydrogen. This additional oxidation reduction step has not been proposed before in literature and a significant improvement in the hydrogen permeance was obtained after this step was performed.

10.4. MEMBRANE MODELLING

For both Pd and Pd-Ag membranes, the hydrogen permeances were accurately described by the flux equation with a value of 1 for the pressure exponent (n-value). Temperature data fitted the Arrhenius equation well and nitrogen flow through defects in the palladium film was Knudsen diffusion. A model was formulated for describing hydrogen permeance in the presence of an inert sweep gas. The model provided a very good fit to the experimental data. Pure Pd membranes were tested at temperatures from 330 °C to 450 °C and Pd-Ag membranes were tested at temperatures from 250 °C to 450 °C with and without a sweep gas.

10.5. MEMBRANE REACTOR VS. PLUG FLOW REACTOR

Flow rates were determined where the plug flow reactor conversion started decreasing to below the equilibrium values. For the catalytic membrane reactor to be applicable, improvement in reaction conversion must be obtained in the higher flow rate region. Theoretical benefits of the catalytic membrane reactor were realised for both ethanol and 2-butanol dehydrogenation in a catalytic membrane reactor, even at the higher flow rates.

For ethanol dehydrogenation in a membrane reactor, the best results were obtained at 275 °C. At 250 °C, the reaction rate was too slow to obtain large improvements in conversion for the membrane reactor compared to the plug flow reactor. At 300 °C, coking of the copper on silica catalyst took place, which deactivated both the membrane and the catalyst and which led to poor results. At 275 °C, the membrane reactor improved the total ethanol exit conversion from 45% (plug flow reactor) to 60% at low feed flow rates and from 36% to 46% at high feed flow rates. Modelling the process with kinetic data obtained from differential reactor experimentss, under predicted the experimental data. By increasing the reaction rate (k'-value and effectiveness factor), a very good fit for the experimental data was obtained.

The dehydrogenation of 2-butanol in a catalytic membrane reactor also resulted in much higher conversions than in the plug flow reactor. The maximum 2-butanol conversion in a plug flow reactor at 240 °C was 80% and that increased to above 90% for the membrane reactor. The process model also under predicted the measured conversions when kinetic data from differential reactor experiments was used for calculating reaction rate parameters. Higher k'-values and lower K_{MEK}-values resulted in a model that fitted the experimental data well.

10.5. MEMBRANE REACTOR MODELLING

A membrane reactor model was developed for constant temperature operation, with no pressure drop across the catalyst bed and no radial concentration profiles in the membrane tube. Small catalyst particles were used to exclude intraparticle mass transfer limitations from the model. Interphase mass transfer limitation was expressed as a function of the Reynolds number.

A sensitivity analysis of the membrane reactor model (for ethanol dehydrogenation) was performed to test the effects of membrane parameters, reaction rate parameters and the operating variables on the overall ethanol conversion. Membrane data from the

optimised membrane and reaction rate data from the optimised catalyst were used as standard inputs for the model.

The reaction rate parameters have a significant effect on the overall conversion, but have no effect on the percentage of produced hydrogen that permeates to the shell side of the reactor. A high k'-value, a low K_{acet}-value and/or a high effectiveness factor will increase the reaction rate and improve the reaction conversion, while a slow reaction will increase the ethanol losses through the Pd-alloy film defects. The membrane selectivity (H_2:N_2) should be at least 150 to prevent large losses of ethanol feed through the film defects, and to prevent severe back diffusion of hydrogen from the shell side to the tube side. The feed flow rate and the sweep gas to feed ratio must be chosen in conjunction with one another. The higher the pressure difference (i.e. the higher the sweep gas flow rate), the better the hydrogen driving force and the higher the overall conversion.

11. FUTURE WORK

Few alcohol dehydrogenation reactions have been studied in a membrane reactor. Of those reactions that have been studied, the feed flow rates have been unrealistically low and/or the hydrogen permeance has been very poor due to thick palladium films. This dissertation concentrated on performing reactions at realistic feed flow rates in a membrane reactor with very high hydrogen permeance and very high selectivity.

The performance of palladium and palladium alloy membranes have been optimised to such an extent that little further work in this area is necessary. Model calculations have shown that little will be gained by further improving membrane selectivity and/or hydrogen permeance. The main challenge now is in improving catalyst activity and stability. Work performed in this dissertation has proved that Pd-based membranes can be used successfully from 190 °C and upwards, without deterioration of the film. From a thermodynamic point of view, higher temperature reactions are more favourable, since a high temperature will improve hydrogen permeance through Pd or its alloy.

The future lies in identifying high value added alkane or alcohol dehydrogenation reactions. Such reactions will typically be found in the pharmaceutical industry and the perfume industry, in the production of pesticides and insecticides and other speciality chemicals. Higher temperatures are beneficial for endothermic reactions to improve conversions and also to improve hydrogen permeance, but result in a decrease of selectivity. Cracking and polymerisation side reactions must be avoided to limit catalyst coking.

After identifying suitable reactions, the catalysts for those reactions should be optimised to maintain high selectivity and high activity over long periods of time. The performance of the membrane, packed with the most suitable catalyst, should then be monitored over a long time period. This step was not part of this dissertation. The final step would then be to scale up the technology.

12. REFERENCES

Abdalla BK, Elnashaie SS, Alkhowaiter S et al., *Applied Catalysis A: General*, **113** (1994a) 89-102

Abdalla BK and Elnashaie SS, *AIChE Journal*, **40** (1994b) 2055-2059

Abdalla BK and Elnashaie SS, *Journal of Membrane Science*, **101** (1995) 31-42

Acharya DR and Hughes R, *Canadian Journal of Chemical Engineering*, **68** (1990) 89-96

Addiego WP, Estrada CA, Goodman DW et al., *Journal of Catalysis*, **146** (1994) 407-414

Agarwalla S and Lund CRF, *Journal of Membrane Science*, **70** (1992) 129-141

Ali JK, Newson EJ and Rippin DWT, *Journal of Membrane Science*, **89** (1994a) 171-184

Ali JK, Newson EJ and Rippin DWT, *Chemical Engineering Science*, **49** (1994b) 2129-2134

Antoniazzi AB, Haasz AA and Strangeby PC, *Journal of Nuclear Materials*, **162-164** (1989) 1065

Aoki K, Yokoyama S, Kusakabe K et al., *Korean Journal of Chemical Engineering*, 13 (1996) 530-537

Aramendía MA, Borau V, Jiménez C et al., *Journal of Catalysis*, **151** (1995) 44-49

Armendáriz H, Aguilar-Ríos G, Salas P et al., *Applied Catalysis A: General*, **92** (1992) 29-38

Armor JN, *Applied Catalysis*, **49** (1989) 1-25

Armor JN, *Catalysis Today*, **25** (1995) 199-207

Armor JN, *Journal of Membrane Science*, **147** (1998) 217-233

Arnold TH, *Chemical Engineering*, (October 30, 1961) 90-92

Athavale SN and Totlani MK, *Metal Finishing*, **87** (1989) 23-27

Athayde AL, Baker RW and Nguyen P, *Journal of Membrane Science*, **94** (1994) 299-311

Bart JCJ and Sneeden RPA, *Catalysis Today*, **2** (1987) 1-124

Basile A, Drioli E, Santella F et al., *Gas Separation and Purification*, **10** (1996) 53-61

Becker YL, Dixon AG, Moser WR et al., *Journal of Membrane Science*, **77** (1993) 233-244

Berteau P and Delmon B, *Applied Catalysis*, **70** (1991) 307-323

Bhattacharyya D, Bej SK and Rao MS, *Applied Catalysis A: General*, **87** (1992) 29-43

Bölt M and Zimmermann H, *AIChE Spring Meeting*, Houston, (1991), Paper 26b

Boot LA, Van der Linde SC, Van Dillen AJ et al., *Studies in Surface Science and Catalysis*, **88** (1994) 491-498

Boot LA, Van Dillen AJ, Geus JW et al., *Journal of Catalysis*, **163** (1996) 195-203

Boudart M and Hwang HS, *Journal of Catalysis*, **39** (1975) 44-52

Bracht M, Alderliesten PT, Kloster R et al., *Energy Conversion Management*, **38** (1997) S159-S164

Brandes EA and Brook GB, *Smithells Metals Reference Book*, 7th Edition, Butterworth-Heinemann Ltd., London (1992), Chapter 13, 1-99

Brinker CJ and Scherer GW, *Sol-gel Science*, Academic Press, New York (1990) 1-40

Brito A, Arvelo R, Villarroel R et al., *React. Kinet. Catal. Lett.*, **54** (1995) 77-83

Brito A, Arvelo R, Villarroel R et al., *Chemical Engineering Science*, **51** (1996) 4385-4391

Bulenkova LF, Shimanskaya MV, Gryaznov VM et al., *Chemical Abstracts*, 92:180393m (1978)

Burggraaf AJ and Cot L, *Fundamentals of Inorganic Membrane Science and Technology*, Elsevier, Amsterdam, The Netherlands (1996) 1-690

Buxbaum RE and Marker TL, *Journal of Membrane Science*, **89** (1993) 29-38

Buxbaum RE and Kinney AB, *Industrial and Engineering Chemistry Research*, **35** (1996) 530-537

Cadus LE, Abello MC, Gomez MF et al., *Industrial and Engineering Chemistry Research*, **35** (1996) 14-18

Cannon KC and Hacskaylo JJ, *Journal of Membrane Science*, **65** (1992) 259-268

Carrizosa I and Munuera G, *Journal of Catalysis*, **49** (1977) 189-200

Casanave D, Giroir-Fendler A, Sanchez J et al., *Catalysis Today*, **25** (1995) 309-314

Chaar MA, Patel D, Kung MC et al., *Journal of Catalysis*, **105** (1987) 483

Chabot J, Lecomte J, Grumet C et al., *Fusion Technology*, **14** (1988) 614

Champagnie AM, Tsotsis TT, Minet RG et al., *Journal of Catalysis*, **134** (1992) 713-730

Chang H and Saleque MA, *Applied Catalysis A: General*, **103** (1993) 233-242

Chang H and Saleque MA, *Journal of Molecular Catalysis*, **88** (1994) 223-238

Chang WS, Chen YZ and Yang BL, *Applied Catalysis A: General*, **124** (1995) 221-243

Cheng S and Shuai X, *AIChE Journal*, **41** (1995) 1598-1601

Cheng YS and Yeung KL, *Journal of Membrane Science*, **158** (1999) 127-141

Chinchen GC, Denny PJ, Jennings JR et al., *Applied Catalysis*, **36** (1988) 1-65

Chung M, Han S, Park K et al., *Journal of Molecular Catalysis*, **79** (1993) 335-345

Church JM and Joshi HK, *Industrial and Engineering Chemistry*, **43** (1951) 1804-1811

Ciavarella P, Moueddeb H and Dalmon J, Workshop: *'Applications and future possibilities of catalytic membrane reactors'*, Turnhout (16-17 Oct 1997) 121-124

Clayson DM and Howard P, *UK Patent*, GB 2,190,397A (1987) 1-4

Cohen RL, D'Amico JF et al., *Journal Electrochemical Society: Electrochemical Science and Technology*, **118** (1971) 2042

Cohen RL and West KW, *Journal Electrochemical Society: Electrochemical Science and Technology*, **120** (1973) 502

Cohen RL and Meek RL, *Plating*, **63** (1976) 47

Collins JP and Way JD, *Industrial and Engineering Chemistry Research*, **32** (1993a) 3006-3013

Collins JP, *Catalytic decomposition of ammonia in a membrane reactor*, PhD Thesis, Oregon State University, USA, (1993b) 1-196

Compagnie des Métaux Précieux, *French Patent* 2,302,273 (1976) 1

Coulter K, Goodman DW and Moore RG, *Catalysis Letters*, **31** (1995) 1-8

Courty P and Chauvel A, *Catalysis Today*, **29** (1996) 3

Craig RG and Dufallo JM, *CEP*, (Feb 1979) 62-65

Craig RG and White EA, *Hydrocarbon Processing*, **59** (1980) 111-114

Cullis CF and Newitt EJ, *Procedures Royal Society A*, **237** (1956) 530-542

Cullity BD, *Elements of X-ray diffraction*, 2nd Edition, Addison-Wesley Publishing Company Inc., Massachusetts, USA (1978) 1-555

Cunningham J, Al-Sayyed GH, Cronin JA et al., *Journal of Catalysis*, **102** (1986) 160-171

Curtiss CF and Hirschfelder JO, *The Journal of Chemical Physics*, 17 (1949) 550-555

De Boer JH and Visseren WJ, *Catalysis Reviews*, **5** (1971) 55-66

Deckman HW, Corcoran EW, McHenry JA et al., *Catalysis Today*, **25** (1995) 357-363

De las Pozas C, Lopez-Cordero R, Gonzalez-Morales JA et al., *Journal of Molecular Catalysis*, **83** (1993) 145-156

Deng J, Cao Z and Zhou B, *Applied Catalysis A: General*, **132** (1995) 9-20

De Ninno A, Violante V and La Barbera A, *Physical Review B*, **56** (1997) 2417-2420

Drago RS and Jurczyk K, *Applied Catalysis A: General*, **112** (1994) 117-124

Duncan JB and Toor HL, *AIChE Journal*, **8** (1962) 38-41

Dunn RO, Schuette GF, Brinkmeyer FM et al., *Procedures De Witt: Petrochemical Review*, Houston (1992) 1

Edlund DJ, *US Patent* 5,259,870 (1993a) 1-10

Edlund DJ and Pledger WA, *Journal of Membrane Science*, 77 (1993b) 255-264

Edlund DJ, *US Patent* 5,393,325 (1995a) 1-14

Edlund DJ and McCarthy J, *Journal of Membrane Science*, **107** (1995b) 147-153

Edlund DJ, *US Patent* 5,498,278 (1996) 1-18

Egloff G and Hulla G, *The Oil and Gas Journal*, **41** (1942) 36-51

Elnashaie SS, Abdalla BK and Hughes R, *Industrial and Engineering Chemistry Research*, **32** (1993) 2537-2541

Ertl G, Knözinger H and Weitkamp J, *Handbook of Heterogeneous Catalysis*, Volume **5**, VCH, Weinheim, Germany (1997) 2140-2165

Fairbanks DF and Wilke CR, *Industrial and Engineering Chemistry*, **42** (1950) 471-475

Faith WL, Keyes DB and Clark RL, *Industrial Chemicals*, 2nd Edition, John Wiley & Sons Inc., New York (1957) 2-3

Feldstein N, *Journal Electrochemical Society: Electrochemical Science and Technology*, **121** (1974) 738-744

Fogler HS, *Elements of Chemical Reaction Engineering*, 2nd Edition, Prentice-Hall, New Jersey (1992) 1-837

Ford FE and Perlmutter DD, *Chemical Engineering Science*, **19** (1964) 371-378

Forster HA, *Hydrocarbon Processing*, **52** (1973) 119-122

Franckaerts J and Froment GF, *Chemical Engineering Science*, **19** (1964) 807-818

Gallaher GR, Gerdes TE and Liu PKT, *Separation Science and Technology*, **28** (1993) 309-326

Gavalas GR, Megiris CE and Nam SW, *Chemical Engineering Science*, **44** (1989) 1829-1835

Gibson MA and Hightower JW, *Journal of Catalysis* **41** (1976) 420-430

Gil A, Ruiz P and Delmon B, *Canadian Journal of Chemical Engineering*, **74** (1996a) 600-605

Gil A, Ruiz P, Delmon B, *Journal of Catalysis*, **159** (1996b) 496-499

Gobina E and Hughes R, *Journal of Membrane Science*, **90** (1994) 11-19

Gobina E, Hou K and Hughes R, *Catalysis Today*, **25** (1995a) 365-370

Gobina E, Hou K and Hughes R, *Chemical Engineering Science*, **50** (1995b) 2311-2319

Gobina E, Hou K and Hughes R, *Journal of Membrane Science*, **105** (1995c) 163-175

Gobina E and Hughes R, *Applied Catalysis A: General*, **137** (1996) 119-127

Grashoff GJ, Pilkington CE and Corti CW, *Platinum Metals Review*, **27** (1983) 157-168

Gryaznov VM, Vedernikov VI and Gul'yanova SG, *Trans. Kinet. Katal.*, **27** (1986a) 142

Gryaznov VM, *Platinum Metals Review*, **30** (1986b) 68-72

Gryaznov VM, Mishchenko AP and Sarylova ME, *French Patent* 2,595,093 (1986c) 1

Gryaznov VM, Serebryannikova OS and Serov YM, *Applied Catalysis A: General*, **96** (1993) 15-23

Haag WO and Tsikoyiannis JG, *US Patent* 5,019,263 (1991) 1

Hakuli A, Kytökivi A, Outi A et al., *Journal of Catalysis*, **161** (1996) 393-400

Hao Y, Tao L and Zheng L, *Applied Catalysis A: General*, **115** (1994) 219-228

Happel J, Blanck H and Hamill TD, *I&EC Fundamentals*, **5** (1966) 289-294

Hara S, Xu W, Sakaki K et al., *Industrial and Engineering Chemistry Research*, **38** (1999) 488-492

Hearle JWS, Sparrow JT et al., *The use of the scanning electron microscope*, Pergamon Press, Oxford, Great Britain, (1974) 1-278

Hino M and Arata K, *Catalysis Letters*, (1990) 1737-1740

Holleck GL, *Journal of Physical Chemistry*, **74** (1970) 503-511

Hongbin Z, Guoxing X, Jinghua G et al., *Catalysis Today*, **25** (1995) 237-240

Horkans J, *Journal Electrochemical Society: Electrochemical Science and Technology*, **130** (1983) 311-317

Hsieh HP, Bhave RR and Fleming HL, *Journal of Membrane Science*, **39** (1988) 221-241

Hsieh HP, *AIChE Symposium Series*, **85** (1989) 53-67

Hsieh HP, Inorganic membranes for separation and reaction, Elsevier Science Publishing Company, New York, USA (1996) 1-591

Hsiung TH, Christman DD, Hunter EJ et al., *AIChE Journal*, **45** (1999) 204-208

Huang L, Chen CS, He ZD et al., *Thin Solid Films*, **302** (1997) 98-101

Hughes R and Koon CL, *Applied Catalysis A: General*, **119** (1994) 153-162

Hunter JB, *US Patent* 2,773,561 (1956) 1

Hunter JB, *Platinum Metals Review*, **4** (1960) 130-131

Hurlbert RC and Konecny JO, *The Journal of Chemical Physics*, **34** (1961) 655-658

Husen PC, Deel KR and Peters WD, *The Oil and Gas Journal*, **69** (Aug 1971) 60-61

Hutson T, Skinner RD and Logan RS, *Hydrocarbon Processing*, **53** (1974) 133-135

Hwang ST and Kammermeyer K, *Canadian Journal of Chemical Engineering*, **44** (1966) 82-89

Ilias S, Su N, Udo-Aka UI et al., *Separation Science and Technology*, **32** (1997) 487-504

Imai T, *US Patent* 4,418,237 (1983), UOP, 1-2

Imai T and Schmidt RJ, *US Patent* 4,886,928 (1989), UOP, 1

Ioannides T and Gavalas GR, *Journal of Membrane Science*, 77 (1993) 207-220

Ishikawa A, Chiang TH and Toda F, *Journal Chemical Society: Chemical Communications*, (1989) 764

Itoh N, *AIChE Journal*, **33**, (1987) 1576-1578

Itoh N and Govind R, *AIChE Symposium Series*, **85** (1989a) 10-17

Itoh N and Govind R, *Industrial Engineering Chemical Research*, **28** (1989b) 1554-1557

Itoh N, *Studies in Surface Science and Catalysis*, **54** (1990) 268-269

Itoh N, *Catalysis Today*, **25** (1995a) 351-356

Itoh N, Machida T, Xu W et al., *Catalysis Today*, **25** (1995b) 241-247

Itoh N and Sathe AM, *Journal of Membrane Science*, **137** (1997) 251-259

Iwasa N and Takezawa N, *Bulletin Chemical Society Japan*, **64** (1991) 2619-2623

James DH and Castor WM, *Ullmann's Encyclopaedia Industrial Chemistry*, 5th Edition, **25** (1994) 329-344

Jansen JC, Koegler JH, Van Bekkum H, et al., *Microporous and Mesoporous Materials*, **21** (1998) 213-226

Jayaraman V, Lin YS, Pakala M et al., *Journal of Membrane Science*, **99** (1995a) 89-100

Jayaraman V and Lin YS, *Journal of Membrane Science*, **104** (1995b) 251-262

Jebarathinam NJ, Eswaramoorthy M and Krishnasamy V, *Applied Catalysis A: General*, **145** (1996) 57-74

Jemaa N, Shu J, Kaliaguine S et al., *Industrial and Engineering Chemistry Research*, **35** (1996) 973-977

Jeon GS and Chung JS, *Applied Catalysis A: General*, **115** (1994) 29-44

Jewett DN and Makrides AC, *Trans Faraday Soc.*, **61** (1965) 932-939

Jia MD, Peinemann KV and Behling RD, *Journal of Membrane Science*, **82** (1993) 15-26

Jiang Z and Wang J, *Separation Science and Technology*, **33** (1998) 1379-1385

Johansson SAE, Campbell JL et al., *PIXE: A novel technique for elemental analysis*, John Wiley and Sons, Great Britain (1988) 1-347

Jorgensen LS, Nielsen PH and Lehrmann P, *Catalysis Today*, **25** (1995) 303

Jorgensen LS, Mogensen G, Lehrmann P et al., 4th Workshop: *'Optimisation of catalytic membrane reactor systems'*, Oslo (30-31 May 1997) 51-57

Julbe A and Guizard C, *Journal of Membrane Science*, **77** (1993) 137-153

Jun C and Lee K, *Journal of Membrane Science*, **157** (1999) 107-115

Jung SH, Kusakabe K, Morooka S et al., *Journal of Membrane Science*, **170** (2000) 53-60

Kameyama T, Dokiya M, Fukuda K et al., *Separation Science and Technology*, **14** (1979) 953

Kameyama T, Dokiya M, Fujishige M et al., *Industrial and Engineering Chemistry Fundamentals*, **20** (1981) 97-99

Kameyama T, Dokiya M, Fujishige M et al., *International Journal Hydrogen Energy*, **8** (1983) 5

Kanoun N, Astier MP and Pajonk GM, *Applied Catalysis*, **70** (1991) 225-236

Kanoun N, Astier MP and Pajonk GM, *Journal of Molecular Catalysis*, **79** (1993) 217-228

Keizer K, Leenaars AFM and Burggraaf AJ, *Eur. Coll. on Ceramics in Adv. Energy Tech.* (1982) 367

Keuler JN, *Preparation and Characterisation of Palladium Composite Membranes*, M.Eng Thesis, University of Stellenbosch, Stellenbosch, South Africa (1997a) 1-203

Keuler JN, Lorenzen L and Sanderson RD, *Plating and Surface Finishing*, **34** (1997b) 34-40

Keuler JN, Lorenzen L, Sanderson RD et al., *Nuclear Instruments and Methods in Physics Research B*, **158** (1999a), 678-682

Kikuchi E, *Japanese Patent* 88,294,925 (1988) 1

Kikuchi E, *Catalysis Today*, **25** (1995) 333-337

Kizling MB, Gustafsson J, Von Krusenstierna O et al., 4th Workshop: *'Optimisation of catalytic membrane reactor systems'*, Oslo (30-31 May 1997) 197-201

Knapton AG, *Platinum Metals Review*, **21** (1977) 44-50

Kolb HJ and Burwell RL, *Journal of the American Chemical Society*, **67** (1945) 1084

Kusakabe K, Yokoyama S, Morooka S et al., *Chemical Engineering Science*, **51** (1996) 3027-3032

Lewis FA, *Platinum Metals Review*, **38** (1994) 112-118

Li A, Liang W and Hughes R, Workshop: *'Applications and future possibilities of catalytic membrane reactors'*, Turnhout (16-17 Oct 1997) 106-109

Li A, Liang W and Hughes R, *Separation and Purification Technology*, **15** (1999) 113-128

Li A, Liang W and Hughes R, *Journal of Membrane Science*, **165** (2000) 135-141

Li ZY, Maeda H, Kusakabe K et al., *Journal of Membrane Science*, **78** (1993) 247-254

Lin Y, Wang I and Yeh C, *Applied Catalysis*, **41** (1988) 53-54

Linkov VM, *Preparation and application of hollow fibre carbon membranes*, PhD Thesis, University of Stellenbosch, Stellenbosch, South Africa (1994) 1-126

Liu B, Cao Y and Deng J, *Separation Science and Technology*, **32** (1997) 1683-1697

Livage J, Henry M et al., *Prog. Solid State Chemistry*, **18** (1988) 259-341

Loc LC, Gaidai NA, Kiperman SL et al., *Kinetics and Catalysis*, **34** (1993) 451-455

Loc LC, Gaidai NA, Kiperman SL et al., *Kinetics and Catalysis*, **36** (1995) 504-510

Loc LC, Gaidai NA, Kiperman SL et al., *Kinetics and Catalysis*, **37** (1996) 790-796

Loweheim FA, *Modern Electroplating*, John Wiley & Sons, New York (1974) 342-357, 739-747

Lu M, Xiong G, Zhao H et al., *Catalysis Today*, **25** (1995) 339

Lundin J, Holmlid L, Menon PG et al., *Industrial and Engineering Chemistry Research*, **32** (1993) 2500-2505

Maestas S and Flanagan TB, *The Journal of Physical Chemistry*, 77 (1973) 850-854

Makarova MA, Paukshtis EA, Thomas JM et al., *Journal of Catalysis*, **149** (1994) 36-51

Makrides AC, *The Journal of Physical Chemistry*, **68** (1964) 2160-2169

Matsubara T, Saito Y, Yamakawa T et al., *Journal of Molecular Catalysis*, **66** (1991) 171-181

Matsuda T, Koike I, Kubo N et al., *Applied Catalysis A: General*, **96** (1993) 3

Matsui J, Sodesawa T and Nozaki F, *Applied Catalysis*, **51** (1989) 203-211

Matsui J, Sodesawa T and Nozaki F, *Applied Catalysis*, **67** (1991) 179-188

Matsumura Y, Hashimoto K and Yoshida S, *Journal of Catalysis*, **117** (1989) 135-143

Matsumura Y, Hashimoto K and Yoshida S, *Journal of Catalysis*, **122** (1990) 352-361

Matsumura Y, Hashimoto K and Yoshida S, *Journal of Molecular Catalysis*, **68** (1991) 73-86

Mendes FMT and Schmal M, *Applied Catalysis A: General*, **151** (1997) 393-408

McBride RB and McKinley DL, *Chemical Engineering Progress*, **61** (1965) 81

McCool B, Xomeritakis G and Lin YS, *Journal of Membrane Science*, 161 (1999) 67-76

McKinley DL, *US Patent* 3,350, 845 (1967) 1

Millat J, Dymond JH and Nieto de Castro CA, *Transport Properties of Fluids*, Cambridge University Press, Cambridge (1996) 296-308

Morooka S, Yan S, Yokoyama S et al., *Separation Science and Technology*, **30** (1995) 2877-2889

Muhler M, Schütze J, Wesemann M et al., *Journal of Catalysis*, **126** (1990) 339-360

Muhler M, Schlögl R and Ertl G, *Journal of Catalysis*, **138** (1992) 413-444

Mulder M, *Basic principles of membrane technology*, 2nd Edition, Kluwer Academic Publishers, The Netherlands (1996) 1-564

Nagamoto H and Inoue H, *Journal Chemical Engineering Japan*, **14** (1981) 377-382

Nagamoto H and Inoue H, *Chemical Engineering Commun.*, **34** (1985) 315-323

Nam S, Lee S and Lee K, *Journal of Membrane Science*, **153** (1999), 163-173

Neely SD, *US Patent* 3,106,581 (1963) 1-10

Newman FC, *Industrial and Engineering Chemistry*, **62** (1970) 42

Noble RD and Stern SA, *Membrane Separations Technology: Principles and Applications*, **2**, Elsevier Science Ltd., (1995) 1-66

Noda S, Hudgins RR and Silveston PL, *Canadian Journal of Chemical Engineering*, **45** (1967) 294-299

Nourbakhsh N, Champagnie A and Tsotsis TT, *AIChE Symposium Series*, **85** (1989) 75-84

Oertel MM, Schmitz J, Weirich VW et al., *Chemical Engineering Technology*, **10** (1987) 248

Ohashi H, Ohya H, Aihara M et al., *Journal of Membrane Science*, **146** (1998) 39-51

Ohno I, Wakabayashi O and Haruyama S, *Journal Electrochemical Society: Electrochemical Science and Technology*, **132** (1985) 2323-2330

Opitz W and Urbanski W, *US Patent* 2,861,106 (1958) 1-6

Osaka T and Takematsu H, *Journal Electrochemical Society: Electrochemical Science and Technology*, **127** (1980) 1021-1029

Paglieri SN, Foo KY, Way JD et al., *Industrial and Engineering Chemistry Research*, **38** (1999) 1925-1936

Parfenova NI, Polyakova VP, Gryaznov VM et al., *Chemical abstracts* 100:11269d (1983)

Peachey NM, Snow RC and Dye RC, *Journal of Membrane Science*, **111** (1996) 123-133

Pearlstein F and Weightman RF, *Plating*, **56** (1969) 1158-1161

Peloso A, Moresi M, Mustachi C et al., *Canadian Journal of Chemical Engineering*, **57** (1979) 159-164

Peña JA, Monzón A and Santamaria J, *Journal of Catalysis*, **142** (1993) 59-69

Perona JJ and Thodos G, *AIChE Journal*, **3** (1957) 230-235

Perry RH and Chilton CH, *Chemical Engineers' Handbook*, 5th Edition, McGraw Hill, Tokyo, Japan, 1973, Chapter 3, 1-250; Chapter 4, 1-75

Pujado PR and Vora BV, *Hydrocarbon Processing*, (1990) 65-70

Purohit MA and Gandhi AN, *Indian Chemical Engineering*, **17** (1975) 26

Quaranta NE, Martino R, Gambaro L et al., *Studies in Surface Science and Catalysis*, **82** (1994) 811-818

Raich BA and Foley HC, *Industrial and Engineering Chemistry Research*, **37** (1998) 3888-3895

Raizada VK, Tripathi VS, Lal D et al., *Journal of Chemical Technology and Biotechnology*, **56** (1993) 265-270

Raman NK and Brinker CJ, *Journal of Membrane Science*, **105** (1995) 273-279

Rao PR, Thangaraj A and Ramaswamy AV, *Journal Chemical Society, Chemical Commun.*, (1991) 1139-1140

Rao UR, Kumar R and Kuloor NR, *Industrial and Engineering Chemistry Proc. Des. Dev.*, **8** (1969) 9

Reddy GK and Rao PK, *Catalysis Letters*, **45** (1997) 93-96

Reidel JC, *The Oil and Gas Journal*, **54** (1957) 166-171

Rezac ME, Koros WJ and Miller SJ, *Journal of Membrane Science*, **93** (1994), 193-201

Rezac ME, Koros WJ and Miller SJ, *Industrial and Engineering Chemistry Research*, **34** (1995) 862-868

Rhoda RN, *Transactions of the Institute of Metal Finishing*, **36** (1959) 82-85

Rodina AA, Gurevich MA and Doronicheva NI, *Russian Journal Physical Chemistry*, **42** (1968) 959-960

Romero E, Rodriguez JC, Pena JA et al., *Canadian Journal of Chemical Engineering*, **74** (1996) 1034-1038

Roshan NR, Mishchenko AP, Polyakova VP et al., *Journal Less-Common Metals*, **89** (1983) 423-428

Ross JRH and Xue E, *Catalysis Today* **25** (1995) 291-301

Rosynek MP, Koprowski RJ and DelliSante GN, *Journal of Catalysis*, **122** (1990) 80-94

Sakamoto Y, Chen FL, Kinari Y et al., *International Journal of Hydrogen Energy*, **210** (1996) 1017-1024

Sanfilippo D, Buonomo F, Fusco G et al., *Chemical Engineering Science*, **47** (1992) 2313-2318

Sano Y, Mizukami F, Yagishita H et al., *Japanese Patent* 06,099,044 (1994) 1

Saracco G, Veldsink JW, Versteeg GF et al., *Chemical Engineering Comm*, **147** (1996) 29-42

Sathe AM, Itoh N and Tominaga M, *Indian Chemical Engineering, Section A*, **36** (1994) 131-135

Satterfield CN, *Heterogeneous Catalysis in Practice*, McGraw-Hill Book Company, New York (1980) 313-369

Sheintuch M and Dessau RM, *Chemical Engineering Science*, **51** (1996) 535-547

Shiau C and Liaw S, *Journal of Chemical Technology and Biotechnology*, **53** (1992) 13-19

Shipley CR, *Plating and Surface Finishing*, **71** (1984) 92-99

Shirai M, Pu Y and Arai M et al., *Applied Surface Science*, **126** (1998) 99-106

Shu J, Grandjean BPA, Van Neste A et al., *Canadian Journal of Chemical Engineering*, **69** (1991) 1036-1060

Shu J, Grandjean BPA, Ghali E et al., *Journal of Membrane Science*, **77** (1993) 181-195

Shu J, Grandjean BPA and Kaliaguine S, *Applied catalysis A: General*, **119** (1994) 305-325

Shu J, Grandjean BPA and Kaliaguine S, *Catalysis Today*, **25** (1995) 327-332

Shu J, Adnot A, Grandjean BPA et al., *Thin Solid Films*, **286** (1996a) 72-79

Shu J, Grandjean BPA, Kaliaguine S et al., *Journal Chem. Society Faraday Trans.*, **92** (1996b) 2745-2751

Shu J, Bongondo BEW, Grandjean BPA et al., *Journal of Materials Science Letters*, **16** (1997a) 294-297

Shu J, Grandjean BPA, Kaliaguine S et al., *Canadian Journal of Chemical Engineering*, **75** (1997b) 712-720

Sivaraj CH and Kantarao P, *Applied Catalysis*, **45** (1988a) 103-114

Sivaraj CH, Reddy BM and Rao PK, *Applied Catalysis*, **45** (1988b) L11

Sivaraj C, Srinivas ST, Rao VN et al., *Journal of Molecular Catalysis*, **60** (1990) L23-L28

Skakunova EV, Ermilova MM and Gryaznov VM, *Izv. Akad. Nauk SSSR. Ser. Khim.*, **5** (1988) 986-991

Smirnov VS, Gryaznov VM, Miropol'skaya MA et al., *Soviet Patent* 437,743 (1978) 1

Sorensen CM and Weber RS, *Journal of Catalysis*, **142** (1993) 1-17

Soria R, *Catalysis Today*, **25** (1995) 285-290

Steitwieser A, Heathcock CH, Kosower EM, *Introduction to Organic Chemistry*, 4th Edition, MacMillan Publishing Company, New York (1992) 379-438

Suzuki H, *US Patent* 4,699,892 (1987) 1

Swift HE, Beuther H and Rennard RJ, *Industrial and Engineering Chemistry Prod. Res. Dev.*, **15** (1976) 131-136

Szabó ZG, Jóvér B and Ohmacht R, *Journal of Catalysis*, **39** (1975) 225-233

Takezawa N, Hanamaki C and Kobayashi H, *Journal of Catalysis*, **38** (1975) 101-109

Thaller LH and Thodos G, *AIChE Journal*, **6** (1960) 369-373

Teo WK and Ti HC, *Applied Biochemistry and Biotechnology*, **24/25** (1990) 521-532

Tiscareno-Lechuga F, Hill CG and Anderson MA, *Applied Catalysis A: General*, **96** (1993) 33-51

Tohji K, Udagawa Y, Mizushima T et al., *Journal Physical Chemistry*, **89** (1985) 5671

Toor HL, *AIChE Journal*, **3** (1957) 198-207

Tsapatsis M, Kim S, Nam SW et al., *Industrial and Engineering Chemistry Research*, **30** (1991) 2152-2159

Tsotsis TT, Champagnie AM, Vasileiadis SP et al., *Chemical Engineering Science*, **47** (1992) 2903-2908

Tu Y, Chen Y and Li C, *Journal of Molecular Catalysis*, **89** (1994a) 179-190

Tu Y, Li C and Chen Y, *Journal of Chemical Technology and Biotechnology*, **59** (1994b) 141-147

Udomsak S and Anthony RG, *Industrial and Engineering Chemistry Research*, **35** (1996) 47-53

Uemichi Y, Shouji K, Sugioka M et al., *Bulletin Chemical Society Japan*, **68** (1995) 385-387

Uemiya S, Matsuda T and Kikuchi E, *Journal of Membrane Science*, **56** (1991a) 315-325

Uemiya S, Sato N, Ando H et al., *Journal of Membrane Science*, **56** (1991b) 303-313

Uemiya S, Sato N, Ando H et al., *Industrial and Engineering Chemistry Research*, **30** (1991c) 585-589

Uemiya S, Sato N, Ando H et al., *Applied Catalysis*, **67** (1991d) 223

Uhlhorn RJR, Keizer K, Burggraaf AJ, *Journal of Membrane Science*, **46** (1989) 225-241

Uhlhorn RJR, Keizer K and Burggraaf AJ, *Presented at the 1990 International Congress on Membranes and Membrane Processes* (ICOM '90), Chicago, 1L, Session 25, 451

Ullmann, *Ullmann's Encyclopaedia of Industrial Chemistry*, **A4,** Fifth Revised Edition, VHC Publishers, Germany (1987) 483-494

Uzio D, Peureux J and Giroir-Fendler A, *Applied Catalysis A: General*, **96** (1993) 83-97

Van den Meerakker JEAM, *Applied Electrochemistry*, **11** (1981) 395

Van den Tillaart JAA, Kuster BFM and Marin GB, *Applied Catalysis A: General*, **120** (1994) 127-145

Van den Tillaart JAA, Kuster BFM and Marin GB, *Catalysis Letters*, **36** (1996) 31-36

Vitulli G, Pitzalis E, Salvadori P et al., *Catalysis Today*, **25** (1995) 249-253

Ward TL and Dao T, *Journal of Membrane Science*, **153** (1999) 211-231

Weaver JA and Metzner AB, *AIChE Journal*, **12** (1966) 655

Welch LM, Groce LJ and Christmann HF, *Hydrocarbon processing*, **57** (1978) 131-136

Weyten H, Prevost I, Duxbury J et al., Workshop: *'Applications and future possibilities of catalytic membrane reactors'*, Turnhout (16-17 Oct 1997) 41-44

Wilke CR, *Chemical Engineering Progress*, **46** (1950) 95-104

Williams C, Makarova MA, Malysheva LV et al., *Journal of Catalysis*, **127** (1991) 377-392

Wu JCS and Liu PKT, *Industrial and Engineering Chemistry Research*, **31** (1992) 322-327

Xomeritakis G and Lin YS, *Journal of Membrane Science*, **120** (1996) 261-272

Xomeritakis G and Lin YS, *Journal of Membrane Science*, **133** (1997) 217-230

Xu W,Yin Y, Li G et al., *Applied Catalysis A: General*, **89** (1992) 131-142

Yan S, Maeda H, Kusakabe K et al., *Industrial and Engineering Chemistry Research*, **33** (1994) 616-622

Yang BL, Kung MC and Kung HH, *Journal of Catalysis*, **89** (1984) 172-176

Yang BL, Cheng DS and Lee SB, *Applied Catalysis*, **70** (1991) 161-173

Yang C, Xu N and Shi J, *Industrial and Engineering Chemistry Research*, **37** (1998) 2601-2610

Yang W, Wu J and Lin L, *Catalysis Today*, **25** (1995) 315-319

Yashima T, Suzuki H and Hara N, *Journal of Catalysis*, **33** (1974) 486-492

Yeung KL, Aravind R, Zawada RJX et al., *Chemical Engineering Science*, **49** (1994) 4823-4838

Yeung KL, Sebastian JM and Varma A, *Catalysis Today*, **25** (1995a) 231-236

Yeung KL and Varma A, *AIChE Journal*, **41** (1995b) 2131-2139

Yoshida H, Konishi S and Naruse Y, *Journal Less-Common Metals*, **89** (1983) 429

Zaspalis VT, Keizer K, Van Praag W et al., *Brit. Ceram. Soc. Proc.*, **43** (1989) 103

Zaspalis VT, Van Praag W, Keizer K et al., *Applied Catalysis*, **74** (1991) 223-234

Zhao HB and Baron GV, Workshop: 'Applications and future possibilities of catalytic membrane reactors', Turnhout (16-17 Oct 1997) 52-58

Zhao HB, Pflanz K, Gü JH et al., Journal of Membrane Science, 142 (1998) 147-157

Zhu Y, Minet RG and Tsotsis TT, Catalysis Letters, 18 (1993) 49-50

Ziaka ZD, Minet RG and Tsotsis TT, Journal of Membrane Science, 77 (1993) 221-232

LIST OF SYMBOLS

A'	=	pre-exponential factor for reaction rate constant	[mol/kg cat.s.Pa]
A_m	=	surface area of metal film	[m^2]
A_p	=	external surface area of the catalyst	[m^2]
C	=	concentration	[mol/m^3]
C_1	=	constant for determining k_c	
C_t	=	total molar density of reaction side gas	[mol/m^3]
C_{WP}	=	Weisz-Prater parameter	
D	=	coefficient for diffusion through a membrane film	[m^2/s]
D_0	=	rre-exponential factor of diffusion coefficient	[m^2/s]
$D_{A,m}$	=	gas phase diffusivity of A in bulk mixture	[m^2/s]
D_{AB}	=	binary diffusion coefficient of A in B	[m^2/s]
D_e	=	effective diffusivity	[m^2/s]
D_{hkl}	=	Schearer's particle diameter	[Angstrom]
D_p	=	catalyst particle diameter	[m]
E	=	activation energy for the rate constant	[J/mol]
E_D	=	diffusion activation energy	[J/mol]
F	=	flow rate on the tube side of reactor	[mol/s]
g_c	=	conversion factor in Ergun equation, 1 for SI units	
G	=	empty column mass velocity	[$kg/m^2.s$]
G^0	=	Gibbs free energy	[J/mol]
G_f	=	geometric factor	
H	=	enthalpy	[J/mol]
J	=	flux	[$mol/m^2.s$]
k	=	reaction rate constant	[$mol/m^3.Pa.s$]
k'	=	reaction rate constant	[mol/kg cat.Pa.s]
k_c	=	mass transfer coefficient	[m/s]
K	=	adsorption coefficient	[Pa^{-1}]
K_{eq}	=	equilibrium constant	[Pa]
K_p	=	equilibrium constant	[bar]

l	=	film thickness	[m]
L	=	distance from reactor inlet	[m]
L_0	=	reactor length	[m]
m	=	catalyst mass	[kg]
M	=	molecular mass	[g/mol]
n	=	pressure exponent or reaction order	
n_m	=	number of N_2O molecules that decomposes	
n_s	=	Cu metal atoms per surface area	[$1.47*10^{-19}$ m^{-2}]
P	=	pressure	[Pa]
P_0	=	pre-exponential factor of permeability coefficient	[mol.m/m^2.Pa.s]
P_{er}	=	permeability coefficient	[mol.m/m^2.Pa.s]
P_m	=	permeance	[mol/m^2.Pa.s]
P_t	=	total pressure	[Pa]
Q	=	flow rate on the shell side of the reactor	[mol/s]
r	=	dimensionless radius (r'/R_p)	
r'	=	radial position in catalyst	[m]
r_A	=	rate of generation for component A in reaction	[mol/m^3.s]
r'_A	=	rate of generation for component A in reaction	[mol/kg cat.s]
R_0	=	Universal constant	[8.314 J/mol.K]
Re	=	Reynolds number	
R_m	=	inner radius of membrane tube	[m]
R_p	=	radius of catalyst particle	[m]
S	=	entropy	[J/mol.K]
S_c	=	Sievert's constant	
Sc	=	Schmidt number	
S_H	=	metallic surface area	[m^2]
Sh	=	Sherwood number	
T	=	temperature	[K]
U	=	empty column velocity	[m/s]
V	=	reactor volume	[m^3]
W	=	catalyst mass	[kg]

x_p	=	peak width	[radians]
X_A	=	conversion of A	
$X_{f,j}(r)$	=	normalised mole fraction of j in catalyst ($Y_j/Y_{j,b}$)	
X_m	=	chemisorption stoichiometry	
Y_j	=	mole fraction of j in catalyst	
$Y_{j,b}$	=	mole fraction of j in bulk fluid	

Greek symbols

α	=	separation factor	
ε_b	=	void fraction of packed bed	
η	=	overall effectiveness factor	
ρ	=	fluid density	[kg/m^3]
ρ_b	=	bulk density of catalyst bed	[kg/m^3]
ρ_p	=	catalyst particle density	[kg/m^3]
τ	=	space time	[s]
μ	=	viscosity	[kg/m.s]
ν_i	=	stoichiometric coefficient for component i in reaction	
υ	=	μ/ρ = kinematic viscosity	[m^2/s]
γ	=	shape factor for Thoenes-Kramers correlation	

Subscripts

0	=	inlet conditions
2But	=	2-butanol
A	=	feed (ethanol or 2-butanol depending on reaction)
Ac	=	acetaldehyde
b	=	at bulk conditions
Et	=	ethanol
H_2	=	hydrogen
i	=	component i

j	=	component j
m	=	mixture properties
MEK	=	methyl ethyl ketone
N_2	=	nitrogen
obs	=	observed
R	=	main products (acetaldehyde or MEK depending on reaction)
s	=	on the shell side of the reactor
surf	=	conditions at the catalyst surface
S	=	hydrogen
t	=	on the tube side of the reactor
W	=	water
x	=	high pressure side
y	=	low pressure side

Note:

- The reaction rates and reaction rate parameters (k, K and r) described in **Chapter 2** were taken from published work in their original format and not transformed to standard units. In each case the published units were stated.
- For kinetic testing in **Chapter 5**, the reaction rates were expressed in (mol/kg.cat.h) and the parameters used kPa instead of Pa for their units. Once the parameters were determined in kPa, it was changed to Pa for modeling in **Chapters 8** and **9**.

LIST OF ABBREVIATIONS

AA	atomic adsorption
BET	Brunauer-Emmett-Teller
CNRS	Centre National de la Recherche Scientifique
CVD	chemical vapour deposition
dc	direct current
ECN	Energy Corporation of the Netherlands
FID	flame ionisation detector
GC	gas chromatograph
HP	Hewlett Packard
ICP	inductively coupled plasma
IRC	Institut de Recherches sur la Catalyse
MEK	methyl ethyl ketone
PIXE	particle induced X-ray emission
SCT	Societé des Céramiques Techniques
SEM	scanning electron microscope
TCD	thermal conductivity detector
TEM	transmission electron microscope
TOC	total organic carbon
XRD	X-ray diffraction

APPENDIX A

List of chemicals used

Name	Purity	Supplier
Ammonia solution	25 wt%	Saarchem
$AgNO_3$	99.9999%	Aldrich
2-Butanol	> 99% (0.1% H_2O)	Riedel-de-Haën
$Co(NO_3)_2.6H_2O$	> 99%	Merck
$Cr(NO_3)_3.10H_2O$	> 97%	Fluka
$Cu(NO_3)_2.3H_2O$	> 99%	ACE
Ethanol	99.8% (0.02 % H_2O)	Merck
Hydrazine	35 wt% solution	Aldrich
MgO	> 97%	Merck
$Na_2EDTA.2H_2O$	> 99%	Saarchem
$(NH_3)_4PdCl_2.H_2O$	99.99%	Aldrich
$Ni(NO_3)_2.H_2O$	98%	Saarchem
$PdCl_2$	59%	Merck
$SnCl_2.2H_2O$	> 98%	Fluka

APPENDIX B1

Ethanol and 2-butanol response factors as determined with a HP G1800A GC

Apparatus: HP G1800A GC and
50 m capillary column (50QGI.5/BPI PONA from SGE)

This apparatus was used for all experiments where the catalyst composition was optimised (**Chapter 4**) and for membrane reactor experiments (**Chapters 8 and 9**). The response factors discussed in **Appendix B1** are only for the work in those two chapters.

The way to interpret the response factors is as follows:
The GC area % of the other component must be calculated relative to the ethanol area %. The response factor is then used to convert the GC area % of the other component to the true mass % of the other component relative to the ethanol mass %. This is done for every component in the mixture and then the true mass percentages are normalised so that they add up to 100%. Mass percentages are then converted to mole percentages to calculate conversions.

Ethanol-acetaldehyde response factors were determined from liquid mixtures kept at about 4°C (in ice water) to keep acetaldehyde in the liquid phase. Ethanol-ethene-mixtures were prepared by filling the reactor in **Figure 3.8** at 200 °C (without the membrane in it) with ethene at atmospheric pressure. The reactor was purged for several minutes to remove air in the reactor and to ensure that there was only ethene in the reactor. Thereafter, all reactor inlets and outlets were closed. The one reactor outlet was modified to allow ethanol injections into and gas extractions from the reactor cavity through a sealed septum. Care was taken to heat and insulate the whole system to prevent any condensation of the ethanol. Ethanol was injected into the ethene cavity to obtain different ethanol-ethene mass ratios and the mixtures were then analysed with the GC to calculate the response factors.

Ethanol response factors:

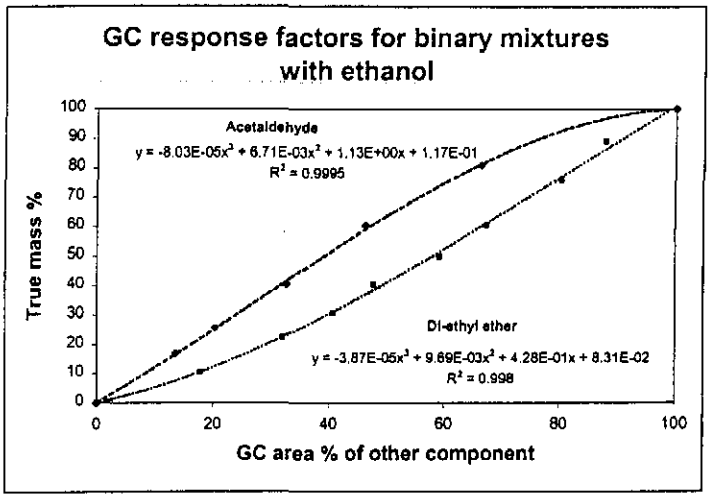

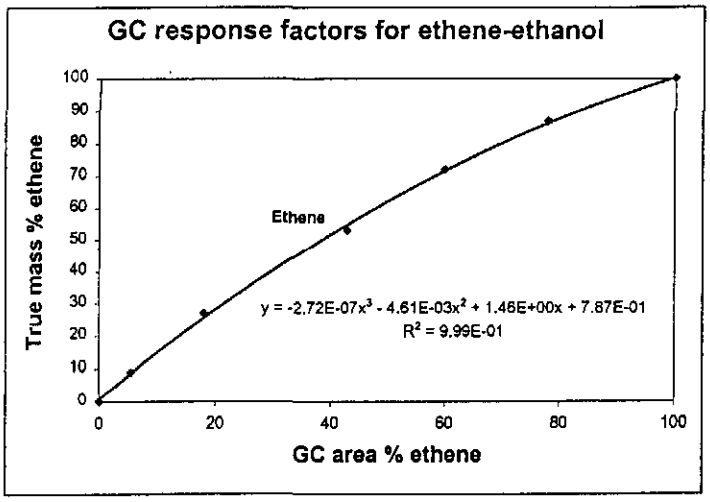

Excluding acetaldehyde, di-ethyl ether and ethene, the majority of other by-products that formed for all ethanol catalyst optimisation experiments (**Chapter 4**) were below 5 GC area %. Exceptions were for MgO catalysts, where the following maximums were detected in different experiments:

propene: max. 10 GC area %

butenes: max. 15 GC area %

1-butanol: max. 16 GC area %

For some Cu on silica optimisation experiments (for ethanol dehydrogenation), up to 12 GC area % propene and 9 GC area % 1-butanone were detected. For SiO_2 and MgO supports, those high percentages were detected at and above 400 °C and at very low ethanol feed flow rates.

For area percentages below 5%, the response factors were determined or estimated. The measured response factors correlated reasonably well with the molecular mass ratio between ethanol and the other component. This observation was used as a very rough approach to estimate the other response factors as indicated.

Correlations for low GC area % (0 to 5% range)

Component	Mr(ethanol)/ Mr(component)	Measured (mass %)/(GC area %)	Factor to convert area % to true mass %
Ethene	1.65	1.65 *	graphic fit
Propene	1.1	?	1.1
Butenes	0.8	?	0.8
Acetaldehyde	1	1.2 *	graphic fit
Acetone	0.8	0.8	0.8
Di-ethyl ether	0.6	0.5 *	graphic fit
Etoxi-ethene	0.6	?	0.6
MEK	0.6	0.6	0.6
1-butanone	0.6	0.6	0.6
1-butanol	0.6	0.55	0.6
Ethyl acetate	0.5	?	0.5
Heavier products	<0.5	?	0.5

* interpolated from measured data presented in the figures

? values were not measured

The error that resulted from this simplification will have little if any effect on the membrane reactor work and model development. The error was restricted to the catalyst optimisation stage, where the same calculation procedures were used for all catalysts tested. Data obtained during the catalyst optimisation stage were not used for fundamental calculations and model development, but only used to compare catalysts. Since the error will be similar for the different catalysts tested, the simplifications in the response factors will not have a significant effect in identifying the optimum catalysts.

For membrane reactor work, the acetaldehyde selectivities were above 80% and no alkanes or heavy products formed. Ethyl acetate was the only component of more than 2 GC area %, which did not have a measured response factor. Even a very large difference between the estimated response factor and the true response factor for ethyl acetate, will have a negligible effect on the total ethanol conversion and the acetaldehyde yield.

2-Butanol response factors:

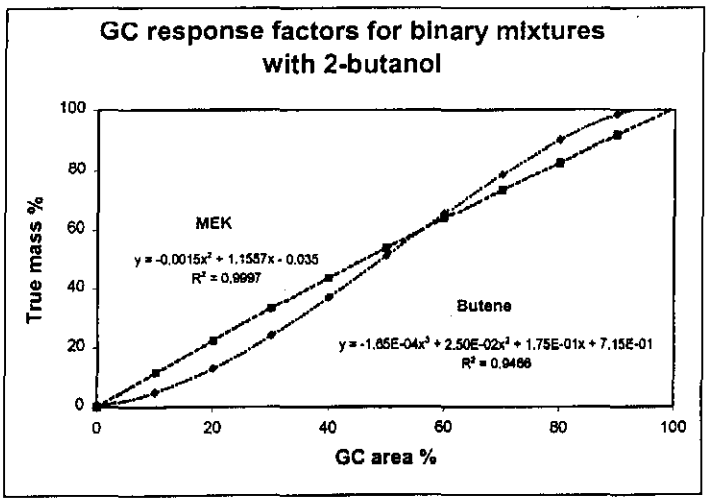

The 2-butanol-butene response factors were determined in the same way as that of the ethanol-ethene response factors. MEK and butenes were the only products that formed in the catalyst optimisation experiments. For membrane experiments, 3-octanol was the only by-product that formed, with a maximum value of up to 3.5 GC area %. The response factor was taken as 0.5.

APPENDIX B2

Ethanol and 2-butanol response factors as determined with a HP 5850 GC

Apparatus: HP 5850 GC equipped with a FID detector and
30m HP Innowax and a 30m HP Plot/Al_2O_3 columns in series

This apparatus was used for al experiment where the kinetics of the optimised catalysts were investigated (**Chapter 5**).

Ethanol response factors:

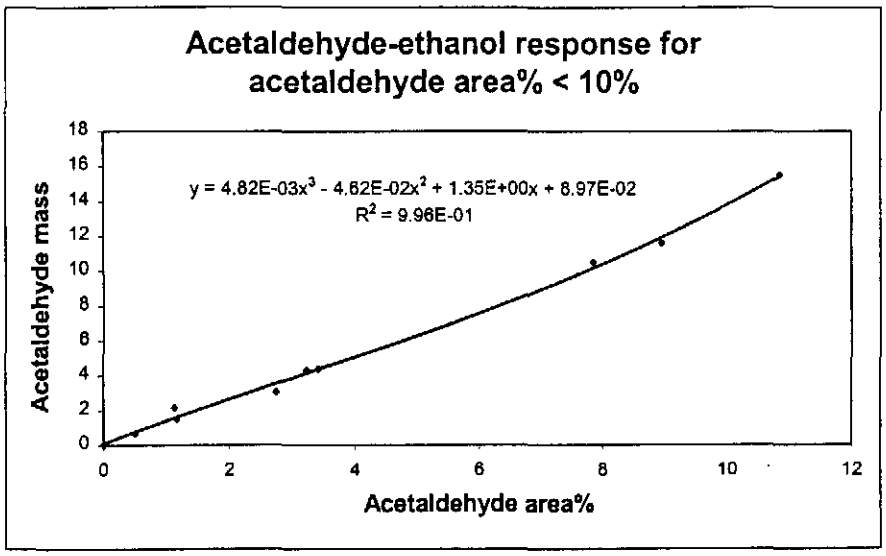

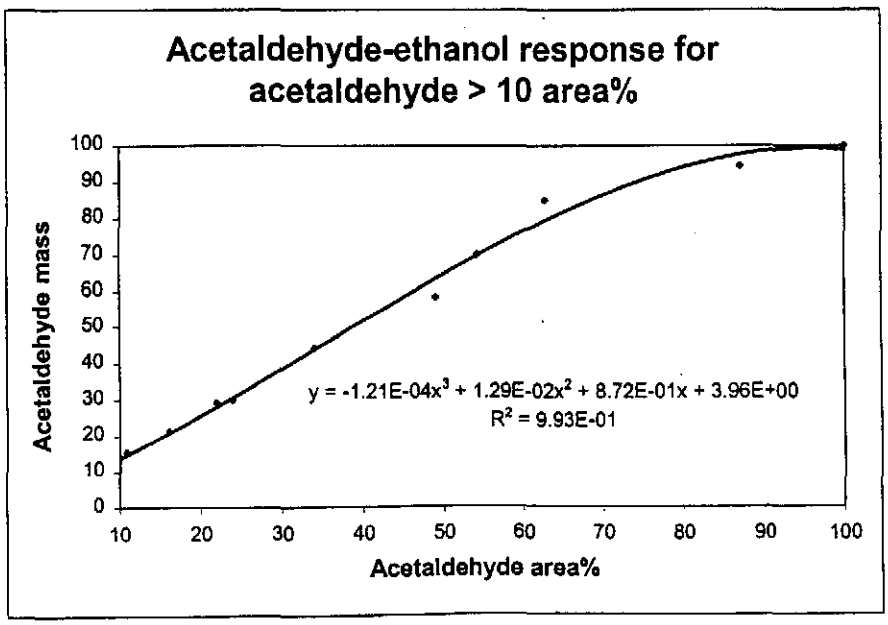

For the kinetic experiments, the selectivity of the reaction towards acetaldehyde formation was above 97%. The ethanol-acetone response factor was measured as 1. All response factors excluding ethanol-acetaldehyde were taken as 1; in other words, the true mass % was taken as the GC area %.

2-Butanol response factors:

The 2-butanol-MEK response factor was equal to 1 over the entire range of MEK GC area percentages. The selectivity of the reaction towards MEK formation was above 98%. All other response factors were taken as 1; in other words, the true mass % was taken as the GC area %.

Note:

For all gas samples, i.e. for determining response factors as well as for all reactor experiments, a heated syringe was used for injections into the GC. A heated syringe was used to prevent condensation of the products in the syringe. A very small tube furnace was made by wrapping heating wire around a ceramic tube and insulating it. The syringe was placed inside the tube prior to taking a gas sample and the temperature inside the tube was controlled at 110 °C. Only the bottom halve of the syringe was heated to still be able to handle it at the top end. A very small gas sample was extracted (about one fifteenth of the syringe volume). This procedure gave very reproducible results when the same gas mixture was injected into the GC. When the syringe was not properly heated, there was significant variation in the results due to condensation of some of the products in the syringe.

For ethanol-acetaldehyde mixtures (liquid), the syringe was not cooled, but used at room temperature when the response factors were determined. At high acetaldehyde concentrations (> 80%) some flashing of acetaldehyde from the syringe might have occurred and the true response factors might differ marginally from the measured values.

APPENDIX C1

Equations for determining ethanol dehydrogenation kinetics

The linear equations determined by least square analysis at each temperature are:

At T = 200 °C:

For an ethanol-N_2 feed:

$y = 7.21*10^{-3}x + 1.02$ $(R^2=0.990)$

For an ethanol-H_2 feed:

$y = 3.70*10^{-5}x + 1.80$ $(R^2=6.77*10^{-5})$

For an ethanol-acetaldehyde feed:

$y = -1.14*10^{-1}x + 13.3$ $(R^2=0.974)$

At T = 225 °C:

For an ethanol-N_2 feed:

$y = 4.37*10^{-3}x + 1.05$ $(R^2=0.988)$

For an ethanol-H_2 feed:

$y = -3.14*10^{-3}x + 1.75$ $(R^2=0.428)$

For an ethanol-acetaldehyde feed:

$y = -1.07*10^{-1}x + 11.8$ $(R^2=0.918)$

At T = 250 °C:

For an ethanol-N_2 feed:

$y = 3.76*10^{-3}x + 0.731$ $(R^2=0.834)$

For an ethanol-H_2 feed:

$y = 1.32*10^{-3}x + 0.963$ $(R^2=0.667)$

For an ethanol-acetaldehyde feed:

$y = -4.76*10^{-2}x + 5.78$ $(R^2=0.977)$

At T = 275 °C:

For an ethanol-N_2 feed:

$y = 2.02*10^{-3}x + 0.468$ $(R^2=0.937)$

For an ethanol-H_2 feed:

$y = -6.95*10^{-4}x + 0.609$ $(R^2=0.620)$

For an ethanol-acetaldehyde feed:

$y = -2.89*10^{-2}x + 3.55$ $(R^2=0.966)$

At T = 300 °C:

For an ethanol-N_2 feed:

$y = 2.09*10^{-3}x + 0.383$ $(R^2=0.831)$

For an ethanol-H_2 feed:

$y = -8.12*10^{-4}x + 0.538$ $(R^2=0.605)$

For an ethanol-acetaldehyde feed:

$y = --2.95*10^{-2}x + 3.52$ $(R^2=0.988)$

K-values

The K-values were determined using both the gradients and the y-axis intercepts of the fitted lines. The values are summarised in **Table C1**.

Table C1: K-values for ethanol dehydrogenation

T (°C)	$K_{S(1)}$ kPa^{-1}	$K_{S(2)}$ kPa^{-1}	K_S kPa^{-1}	$K_{R(1)}$ kPa^{-1}	$K_{R(2)}$ kPa^{-1}	K_R kPa^{-1}
200	0.00772	0.00732	**0.00752**	0.1182	0.1212	**0.1197**
225	0.00660	0.00715	**0.00688**	0.1014	0.1061	**0.1038**
250	0.00314	0.00334	**0.00324**	0.0684	0.0703	**0.0694**
275	0.00298	0.00283	**0.00291**	0.0652	0.0661	**0.0657**
300	0.00401	0.00334	**0.00368**	0.0811	0.0825	**0.0818**

APPENDIX C2

Equations for determining 2-butanol dehydrogenation kinetics

The linear equations determined by least square analysis at each temperature are:

At T = 190°C:

For an 2-butanol-N_2 feed:

$y = 2.461*10^{-3}x + 1.717$ $(R^2 = 0.452)$

For an 2-butanol-H_2 feed:

$y = 4.745*10^{-3}x + 1.501$ $(R^2 = 0.935)$

For an 2-butanol-MEK feed (0-20.5 wt% MEK):

$y = -1.991*10^{-1}x + 22.06$ $(R^2 = 0.993)$

At T = 220°C:

For an 2-butanol-N_2 feed:

$y = 2.213*10^{-3}x + 1.138$ $(R^2 = 0.575)$

For an 2-butanol-H_2 feed:

$y = 3.574*10^{-3}x + 0.986$ $(R^2 = 0.800)$

For an 2-butanol-MEK feed (0-63.5 wt% MEK):

$y = -6.686*10^{-2}x + 8.125$ $(R^2 = 0.994)$

At T = 250°C:

For an 2-butanol-N_2 feed:

$y = 2.282*10^{-3}x + 0.764$ $(R^2 = 0.636)$

For an 2-butanol-H_2 feed:

$y = 3.845*10^{-3}x + 0.575$ $(R^2 = 0.902)$

For an 2-butanol-MEK feed (0-41.0 wt% MEK):

$y = -3.824*10^{-2}x + 4.745$ $(R^2 = 0.955)$

At T = 280°C:

For an 2-butanol-N_2 feed:

$y = 1.764*10^{-3}x + 0.547$ $(R^2 = 0.874)$

For an 2-butanol-H_2 feed:

$y = 2.402*10^{-3}x + 0.491$ $(R^2 = 0.695)$

For an 2-butanol-MEK feed (0-41.0 wt% MEK):

$y = -3.379*10^{-2}x + 4.063$ $(R^2 = 0.980)$

K-values

The K-values were determined using both the gradients and the y-axis intercepts of the fitted lines. The values are summarised in **Table C2**.

Table C2: K-values for 2-butanol dehydrogenation

T (°C)	$K_{S(1)}$ kPa^{-1}	$K_{S(2)}$ kPa^{-1}	K_S kPa^{-1}	$K_{R(1)}$ kPa^{-1}	$K_{R(2)}$ kPa^{-1}	K_R kPa^{-1}
190	-0.00125	-0.00133	-0.00129	0.11730	0.11740	0.11735
220	-0.00132	-0.00120	-0.00126	0.06079	0.06070	0.06075
250	-0.00245	-0.00205	-0.00225	0.05159	0.05304	0.05232
280	-0.00101	-0.00117	-0.00109	0.06364	0.06500	0.06432

APPENDIX D1

Hydrogen and nitrogen permeance data for Pd films

Membrane	Thickness (micron)	T (°C)	Avg. H_2 permeance ($\mu mol/m^2.Pa.s$)	Avg. N_2 permeance ($nmol/m^2.Pa.s$)	Selectivity		Arrhenius parameters for hydrogen permeance		R^2 value for n=1 in permeance equation
1a	3.08	450	7.68	31.95	240		P_0 =	5.243E-10	0.9995
		410	6.73	33.45	201		E_D =	18485	0.9994
		370	5.45	34.13	160		R^2 =	0.9918	1
		330	4.19	35.19	117				0.9853
1b	3.86	450	6.44	9.67	666		P_0 =	1.956E-10	0.9908
		410	4.93	9.99	493		E_D =	12737	0.9994
		370	4.75	10.22	464		R^2 =	0.8981	0.9981
		330	4.06	10.80	376				0.9997
1c	6.19	450	5.14	5.97	860		P_0 =	5.578E-10	0.9993
		410	4.21	6.21	678		E_D =	17282	0.9995
		370	3.59	6.21	578		R^2 =	0.9903	0.9992
2a	1.43	450	6.90	9.61	718		P_0 =	7.127E-10	0.9963
		410	4.53	9.61	472		E_D =	26182	0.9994
		370	3.59	9.87	363		R^2 =	0.9601	0.9994
		330	2.82	9.98	283				0.9994
2b	1.43	450	11.67	12.01	971		P_0 =	3.205E-10	0.9951
		410	9.93	12.50	794		E_D =	17799	0.9976
		370	7.65	12.81	597		R^2 =	0.9832	0.9998
		330	6.60	13.25	498				0.9968
3a	2.40	450	8.37	5.72	1465		P_0 =	1.752E-10	0.9997
		410	6.88	6.00	1147		E_D =	13223	0.9993
		370	5.97	6.28	952		R^2 =	0.9643	0.9997
		330	5.37	6.40	839				0.9987

Membrane	Thickness (micron)	T (°C)	Avg. H_2 permeance ($\mu mol/m^2.Pa.s$)	Avg. N_2 permeance ($nmol/m^2.Pa.s$)	Selectivity		Arrhenius parameters for hydrogen permeance		R^2 value for n=1 in permeance equation
3b	4.43	450	4.86	1.13	4297		P_0 =	1.697E-10	0.9984
		410	3.93	1.19	3306		E_D =	12673	0.9748
		370	3.47	1.21	2869		R^2 =	0.9424	0.9866
		330	3.16	1.45	2179				0.9998
5	1.00	450	15.00	65.67	228		P_0 =	7.504E-11	0.9983
		410	12.96	68.62	189		E_D =	9778	0.9986
		370	12.32	70.54	175		R^2 =	0.9676	0.9969
		330	10.64	70.44	151				0.9997
6	1.47	450	11.30	38.26	295		P_0 =	8.178E-11	0.9987
		410	10.13	39.36	257		E_D =	9654	0.9999
		370	9.27	39.88	232		R^2 =	0.9969	0.9991
		330	8.16	39.25	208				0.9988
8	1.10	450	14.37	21.40	671		P_0 =	7.779E-11	0.9992
		410	13.70	21.90	627		E_D =	9435	0.9989
		370	12.40	22.40	553		R^2 =	0.9642	0.9996
		330	10.54	23.10	457				0.9997
N1	1.12	450	13.59	3.00	4533		P_0 =	1.238E-10	0.9999
		410	12.61	3.00	4251		E_D =	12483	0.999
		370	10.75	2.80	3784		R^2 =	0.9872	0.9995
		330	9.08	3.10	2953				0.9995

Membrane	Thickness (micron)	T (°C)	Avg. H_2 permeance ($\mu mol/m^2.Pa.s$)	Avg. N_2 permeance ($nmol/m^2.Pa.s$)	Selectivity		Arrhenius parameters for hydrogen permeance		R^2 value for n=1 in permeance equation
N2	1.08	450	15.11	20.80	728		P_0 =	5.267E-11	0.998
		410	14.37	19.50	737		E_D =	6984	0.9994
		370	13.38	18.10	738		R^2 =	0.9857	1
		330	11.99	17.20	698				0.9999
N3	1.47	410	10.81	5.20	2090		P_0 =	1.118E-10	0.9992
		370	9.65	5.20	1851		E_D =	11065	0.9999
		330	8.35	5.60	1479		R^2 =	0.9989	0.9998
N4	1.18	450	13.84	20.60	671		P_0 =	8.137E-11	0.9996
		410	13.03	20.60	631		E_D =	9541	0.9986
		370	11.85	20.10	591		R^2 =	0.9745	0.9992
		330	10.09	21.80	462				1
N7	1.23	450	8.28	7.40	1119		P_0 =	9.211E-11	0.9996
		410	7.41	7.30	1021		E_D =	13164	0.9997
		370	6.51	7.50	865		R^2 =	0.9926	0.9998
		330	5.34	7.80	683				0.9998
N8	1.19	450	10.89	2.30	4830		P_0 =	5.815E-11	0.9999
		410	10.05	2.20	4529		E_D =	8993	0.9989
		370	9.19	1.70	5364		R^2 =	0.9958	0.9999
		330	8.07	2.20	3638				0.9997

Name: **1a** **(3.08 µm)**

	Mass (g)
Clean	29.6650
After pretreatment	-
After Pd	29.8607

	(mm)
Plated length	240
Permeable length	230
Inside diameter	7

H_2 permeance parameters	
P_0 (mol.m/m^2.Pa.s)	5.243E-10
E_D (J/mol)	18485
R^2 for Arrhenius fit	0.9918

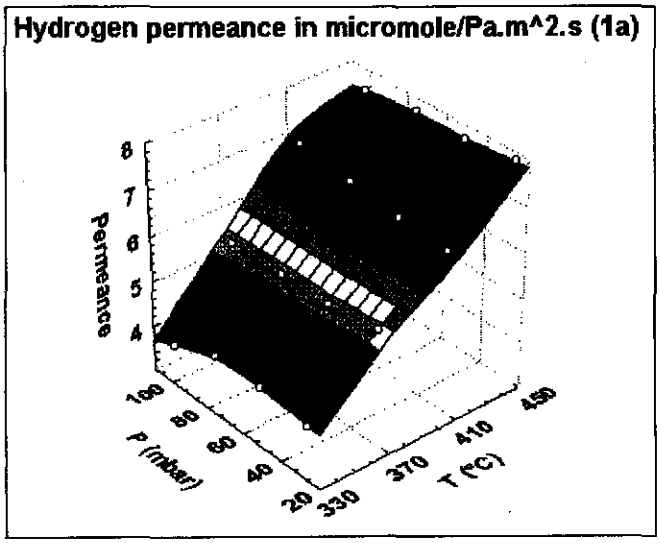

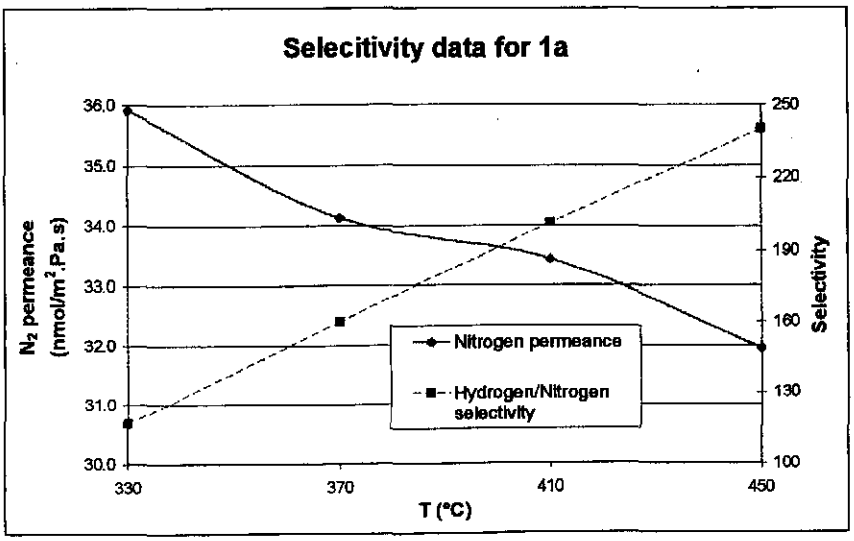

Name: **1b** **(3.86 µm)**

	Mass (g)
Clean	29.6650
After pretreatment	-
After Pd	29.9100

	(mm)
Plated length	230
Permeable length	230
Inside diameter	7

H_2 permeance parameters	
P_0 (mol.m/m^2.Pa.s)	1.956E-10
E_D (J/mol)	12737
R^2 for Arrhenius fit	0.8981

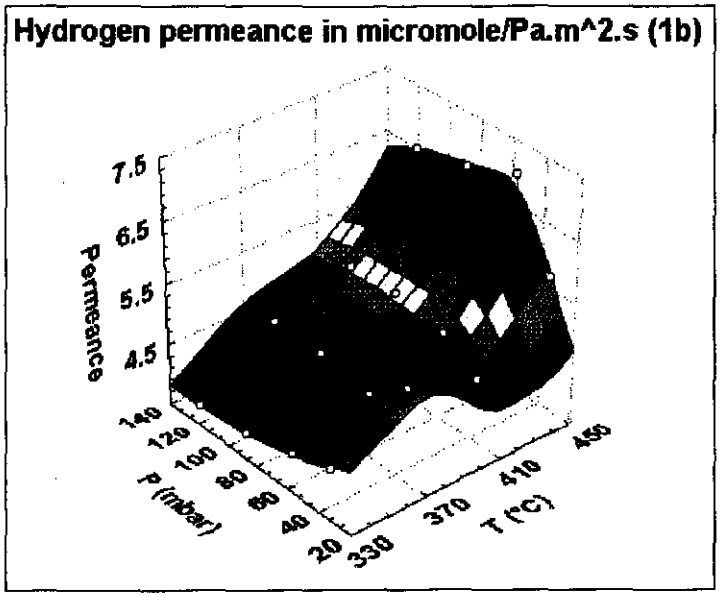

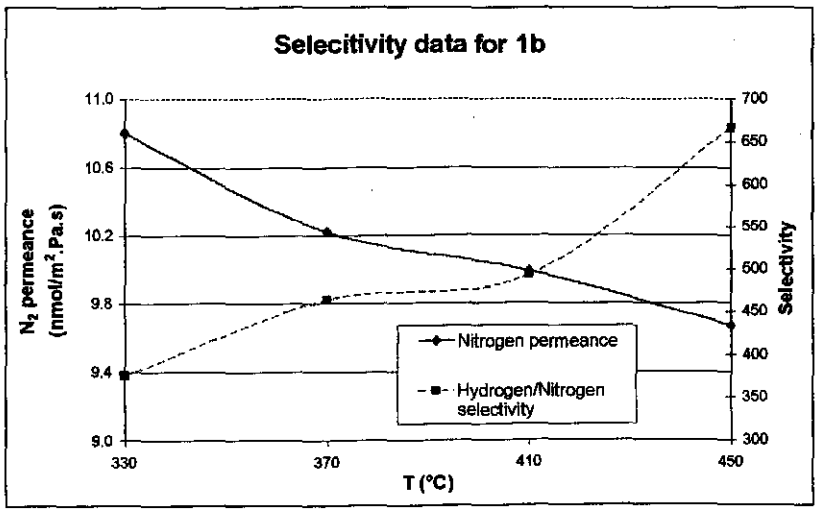

Name: 1c (6.19 µm)

	Mass (g)
Clean	29.6650
After pretreatment	-
After Pd	30.0577

	(mm)
Plated length	230
Permeable length	230
Inside diameter	7

H_2 permeance parameters	
P_0 (mol.m/m^2.Pa.s)	5.578E-10
E_D (J/mol)	17282
R^2 for Arrhenius fit	0.9903

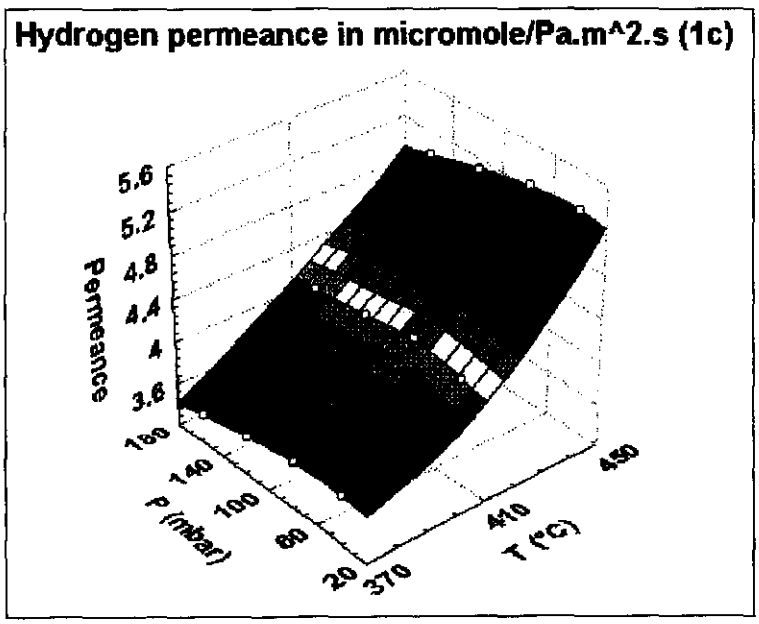

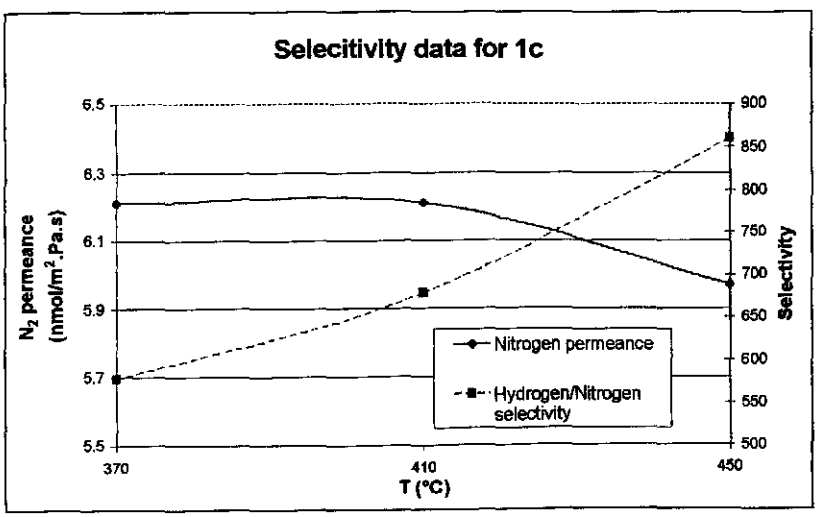

Name: **2a** **(1.43 μm)**

	Mass (g)
Clean	29.2217
After pretreatment	-
After Pd	29.3085

	(mm)
Plated length	250
Permeable length	230
Inside diameter	7

H_2 permeance parameters	
P_0 (mol.m/m^2.Pa.s)	7.127E-10
E_D (J/mol)	26182
R^2 for Arrhenius fit	0.9601

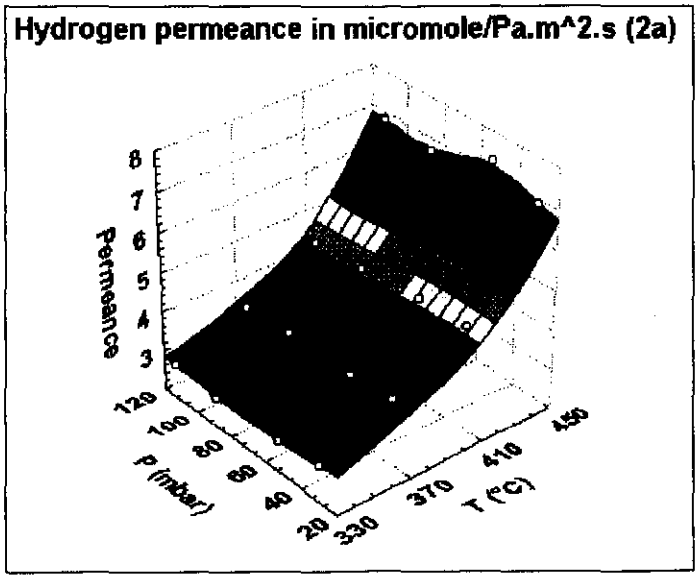

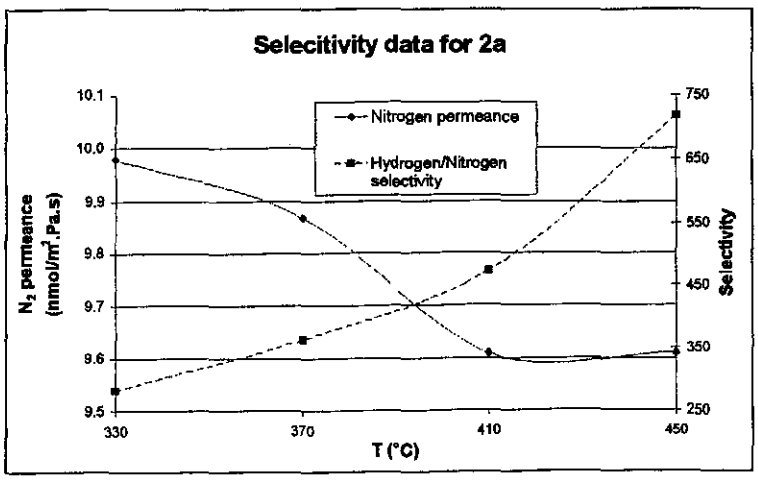

Name: **2b** **(1.43 μm)**

	Mass (g)
Clean	29.2217
After pretreatment	-
After Pd	29.3085

	(mm)
Plated length	250
Permeable length	230
Inside diameter	7

H_2 permeance parameters	
P_0 (mol.m/m^2.Pa.s)	3.205E-10
E_D (J/mol)	17799
R^2 for Arrhenius fit	0.9832

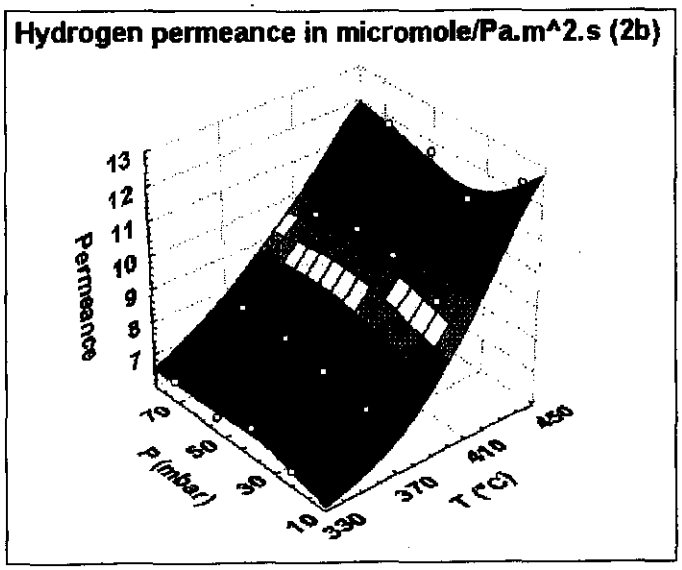

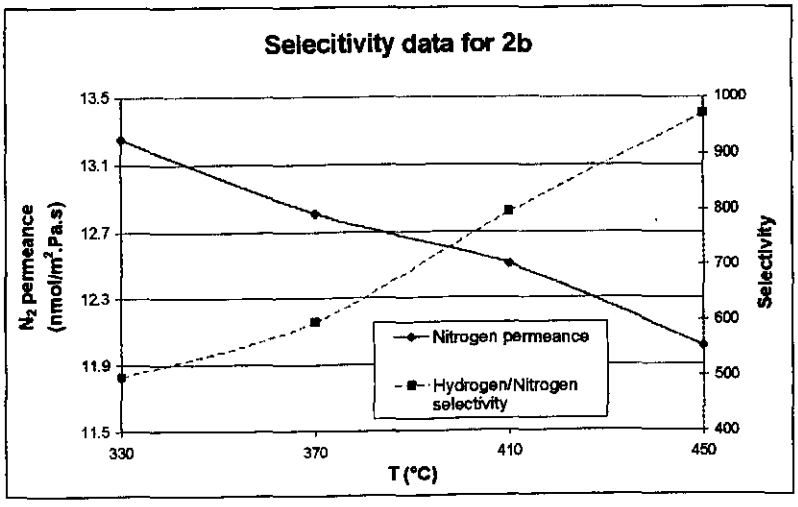

Name: **3a** (2.40 μm)

	Mass (g)
Clean	29.2900
After pretreatment	-
After Pd	29.4486

	(mm)
Plated length	250
Permeable length	230
Inside diameter	7

H_2 permeance parameters	
P_0 (mol.m/m^2.Pa.s)	1.752E-10
E_D (J/mol)	13223
R^2 for Arrhenius fit	0.9643

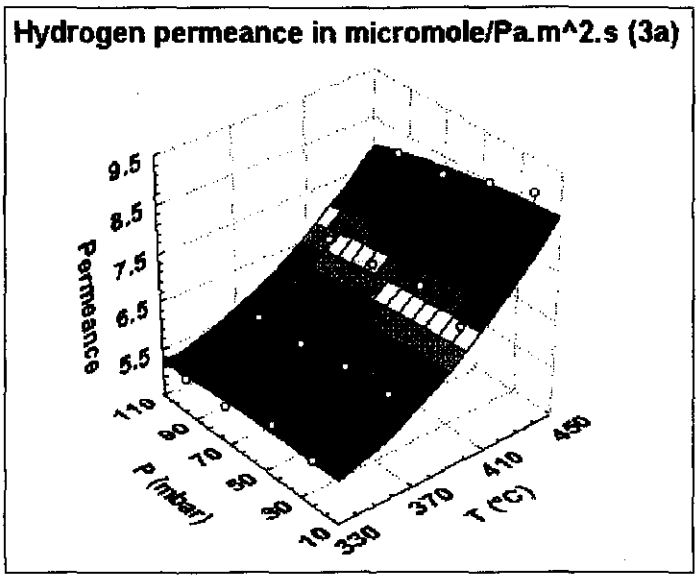

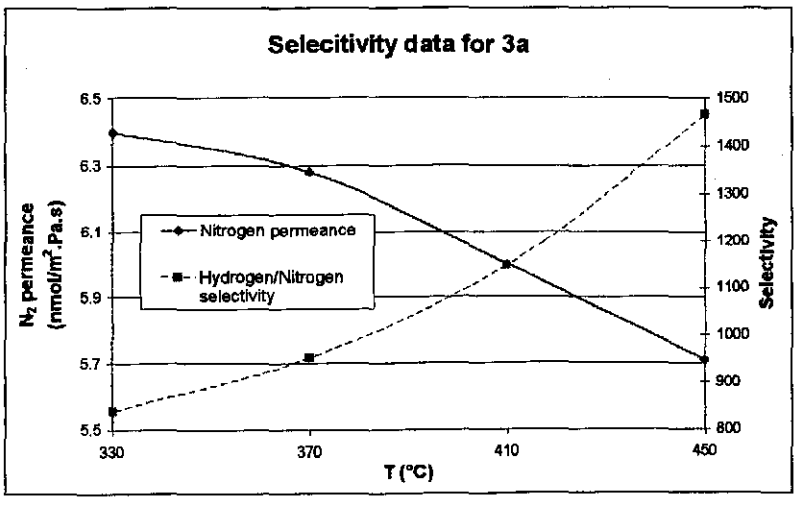

Name: 3b (4.43 µm)

	Mass (g)
Clean	29.2900
After pretreatment	-
After Pd	29.5830

	(mm)
Plated length	250
Permeable length	230
Inside diameter	7

H_2 permeance parameters	
P_0 (mol.m/m^2.Pa.s)	1.697E-10
E_D (J/mol)	12673
R^2 for Arrhenius fit	0.9424

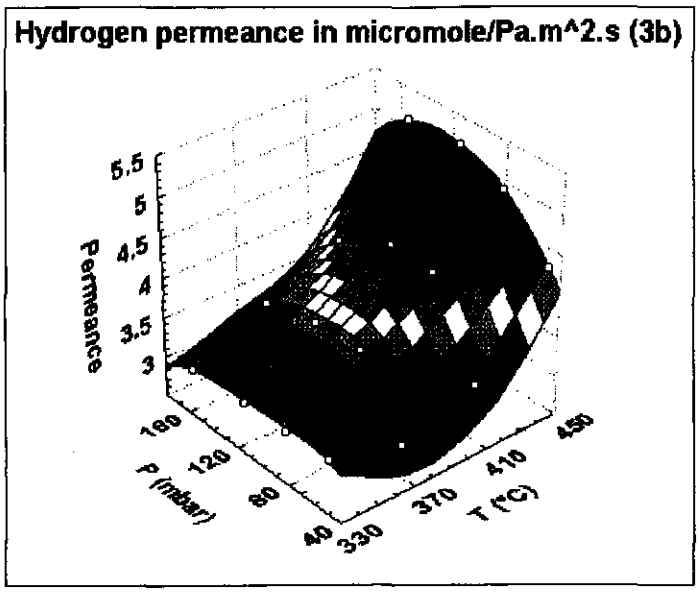

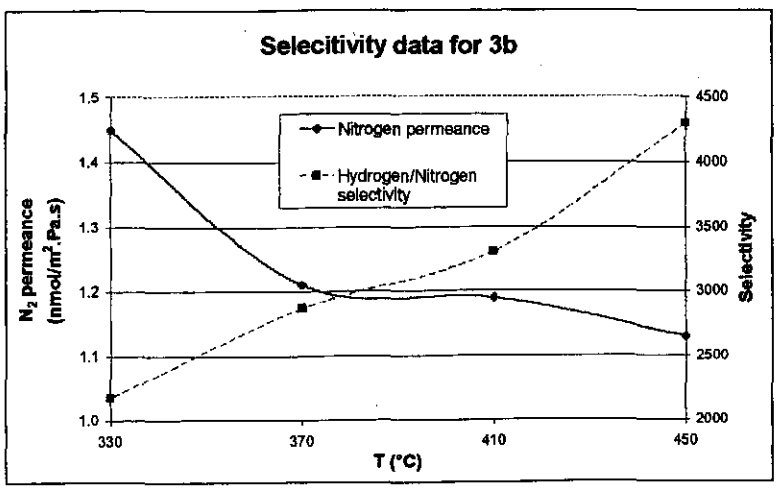

Name: 5 **(1.00 μm)**

	Mass (g)
Clean	28.9540
After pretreatment	-
After Pd	29.0173

	(mm)
Plated length	240
Permeable length	230
Inside diameter	7

H_2 permeance parameters	
P_0 (mol.m/m^2.Pa.s)	7.504E-11
E_D (J/mol)	9778
R^2 for Arrhenius fit	0.9676

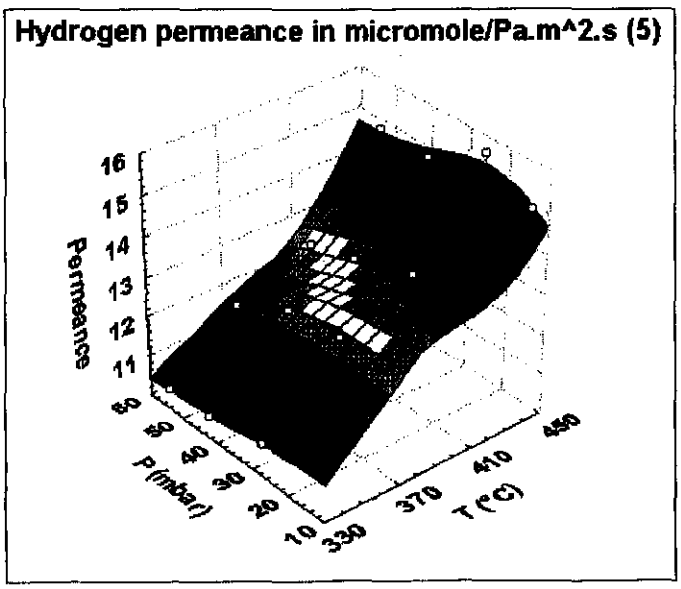

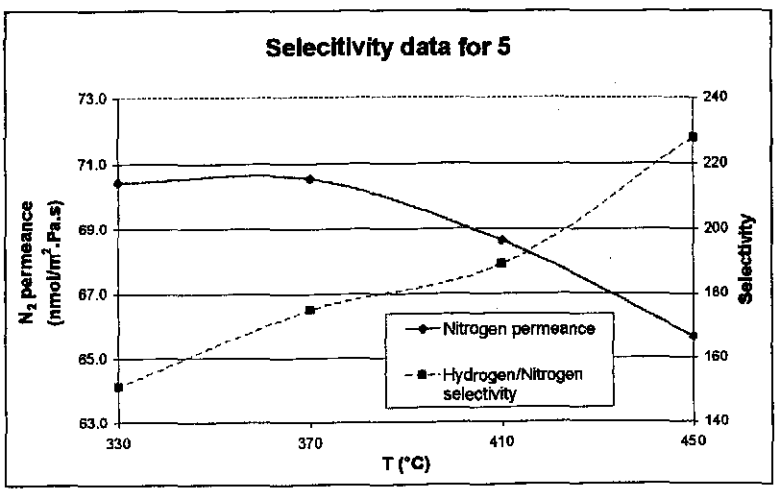

Name: 6 **(1.47 µm)**

	Mass (g)
Clean	28.9106
After pretreatment	-
After Pd	28.9961

	(mm)
Plated length	220
Permeable length	220
Inside diameter	7

H_2 permeance parameters	
P_0 (mol.m/m^2.Pa.s)	8.178E-11
E_D (J/mol)	9654
R^2 for Arrhenius fit	0.9969

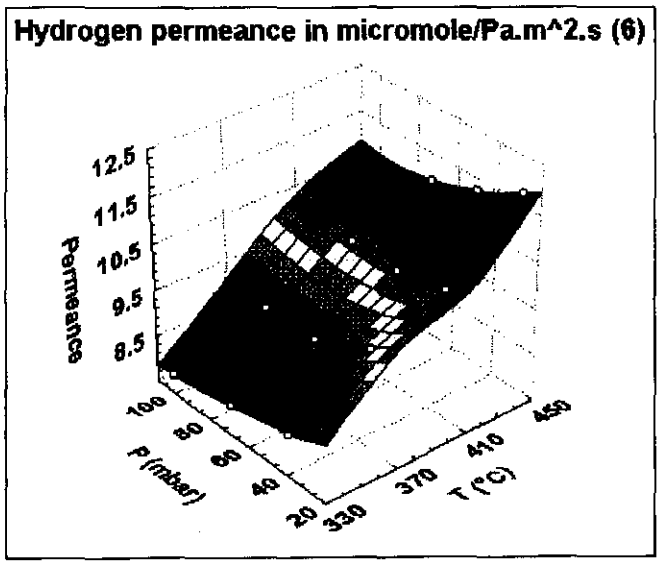

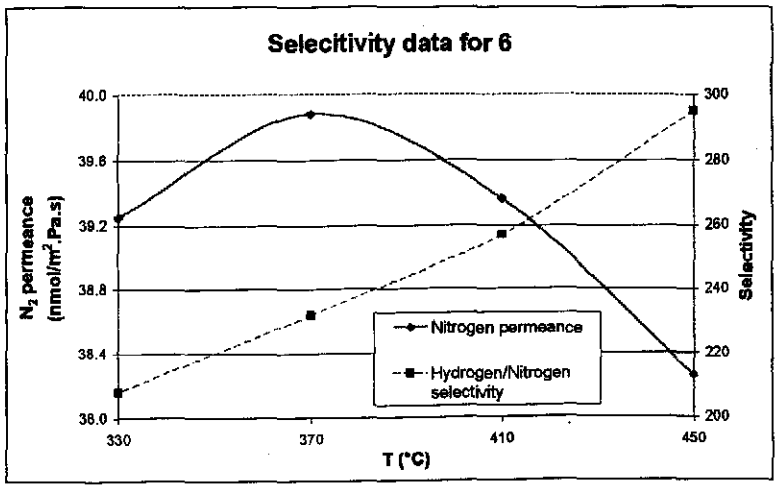

Name: 8 **(1.10 μm)**

	Mass (g)
Clean	28.1700
After pretreatment	28.1730
After Pd	28.2445

	(mm)
Plated length	250
Permeable length	230
Inside diameter	7

H_2 permeance parameters	
P_0 (mol.m/m^2.Pa.s)	7.779E-11
E_D (J/mol)	9435
R^2 for Arrhenius fit	0.9642

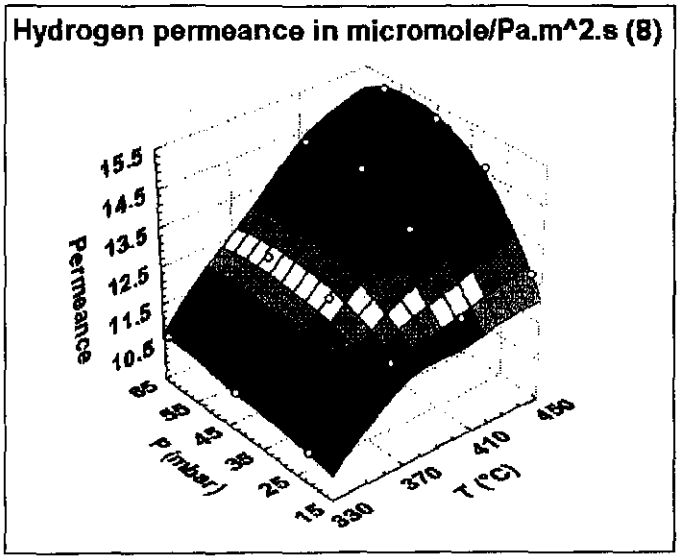

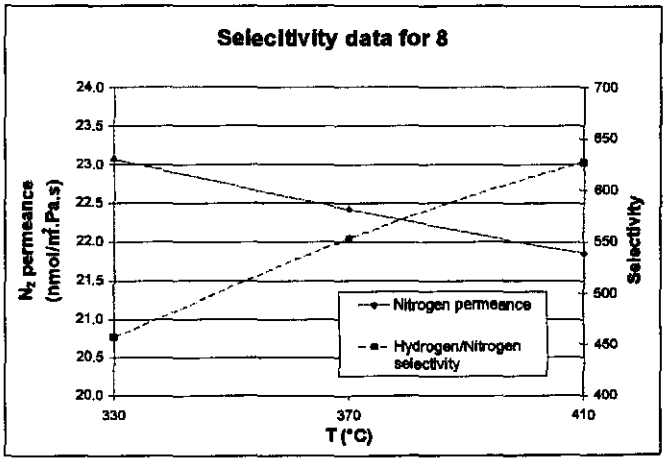

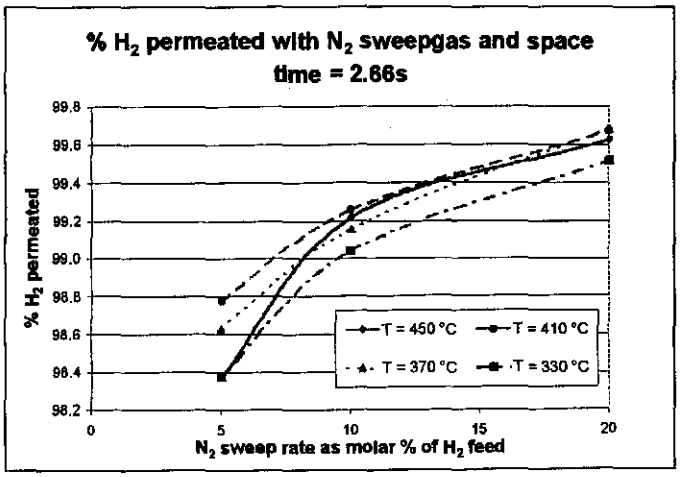

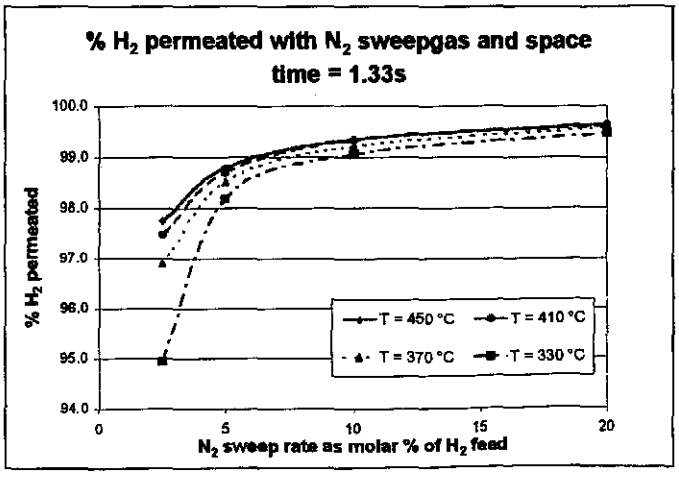

Name: **N1** **(1.12 μm)**

	Mass (g)
Clean	29.3000
After pretreatment	29.3140
After Pd	29.3750

	(mm)
Plated length	230
Permeable length	205
Inside diameter	7

H_2 permeance parameters	
P_0 (mol.m/m^2.Pa.s)	1.238E-10
E_D (J/mol)	12483
R^2 for Arrhenius fit	0.9872

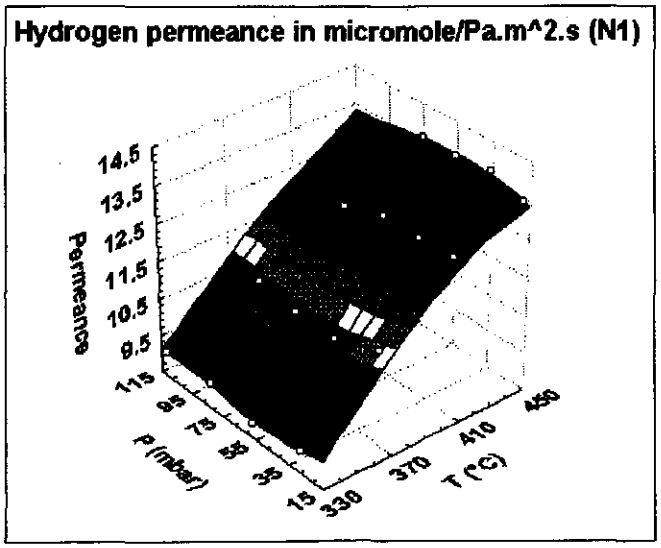

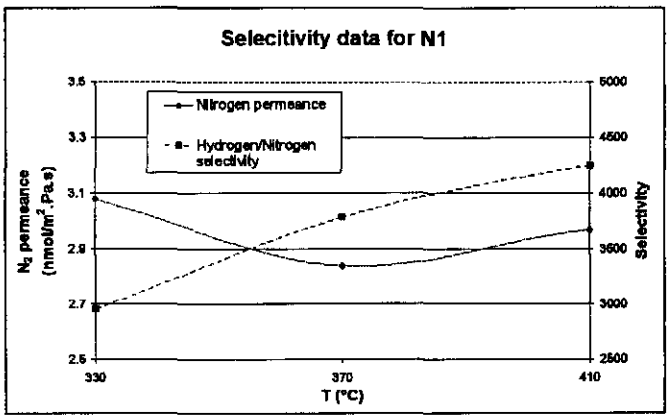

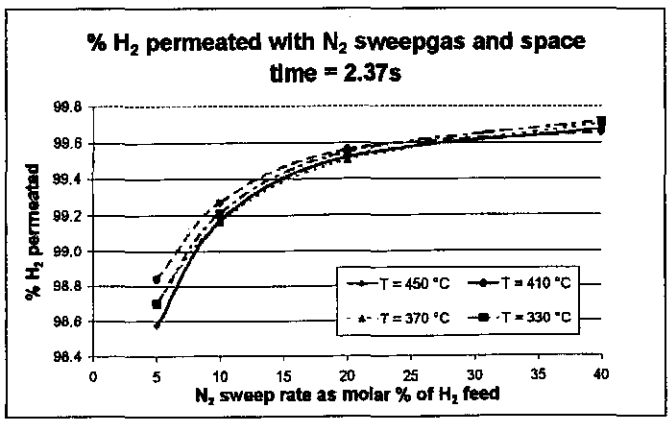

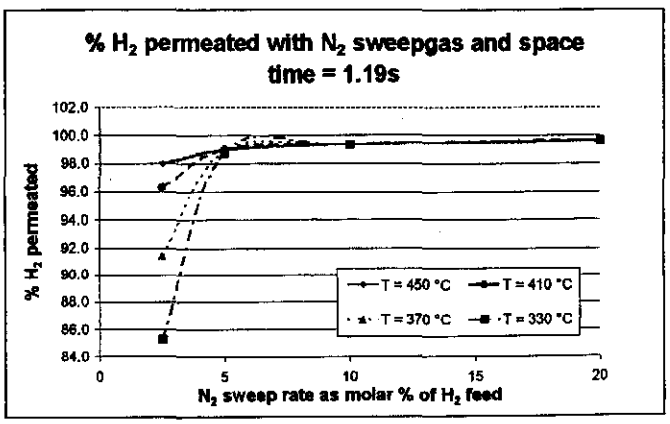

Name: N2 **(1.08 µm)**

	Mass (g)
Clean	28.5746
After pretreatment	28.5905
After Pd	28.6412

	(mm)
Plated length	205
Permeable length	205
Inside diameter	7

H_2 permeance parameters	
P_0 (mol.m/m^2.Pa.s)	5.267E-11
E_D (J/mol)	6984
R^2 for Arrhenius fit	0.9857

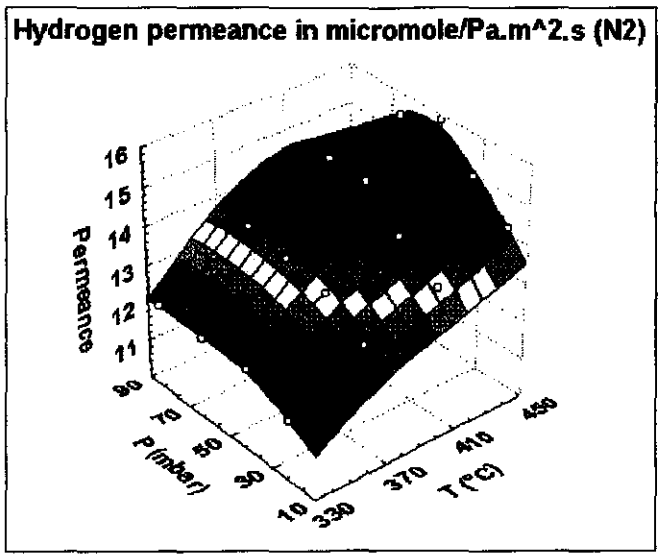

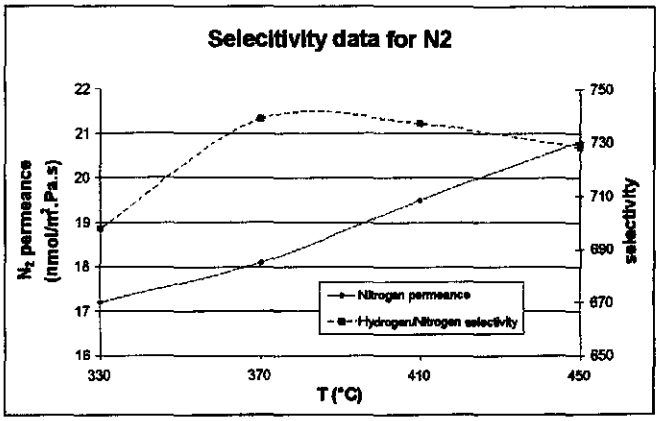

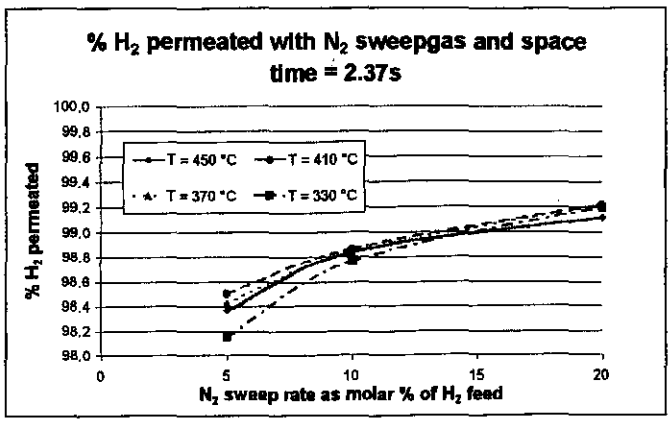

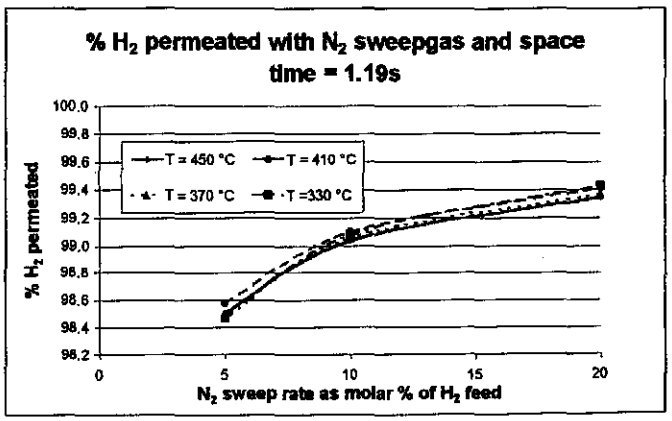

Name: N3 **(1.47 µm)**

	Mass (g)
Clean	28.6470
After pretreatment	28.6575
After Pd	28.7497

	(mm)
Plated length	250
Permeable length	205
Inside diameter	7

H_2 permeance parameters	
P_0 (mol.m/m^2.Pa.s)	1.118E-10
E_D (J/mol)	11065
R^2 for Arrhenius fit	0.9989

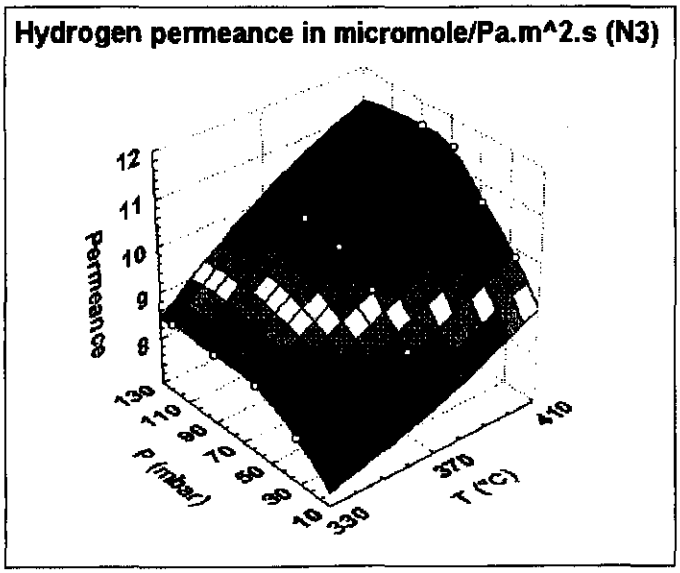

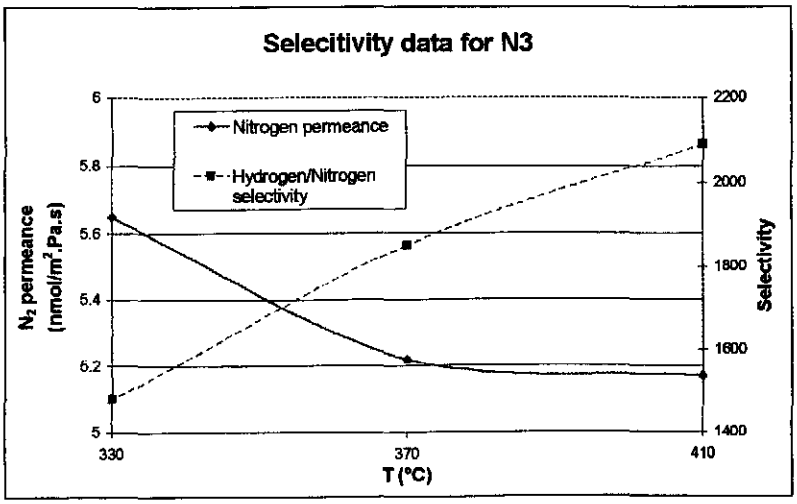

Name: N4 **(1.18 μm)**

	Mass (g)
Clean	28.9363
After pretreatment	28.9540
After Pd	29.0170

	(mm)
Plated length	230
Permeable length	205
Inside diameter	7

H_2 permeance parameters	
P_0 (mol.m/m^2.Pa.s)	8.137E-11
E_D (J/mol)	9541
R^2 for Arrhenius fit	0.9745

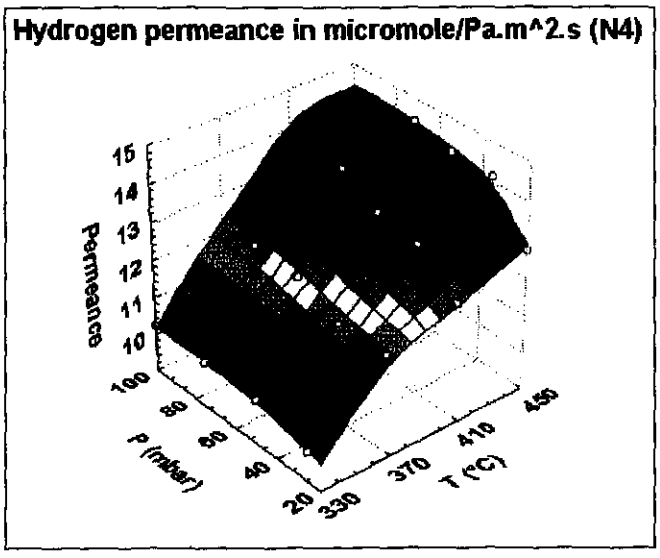

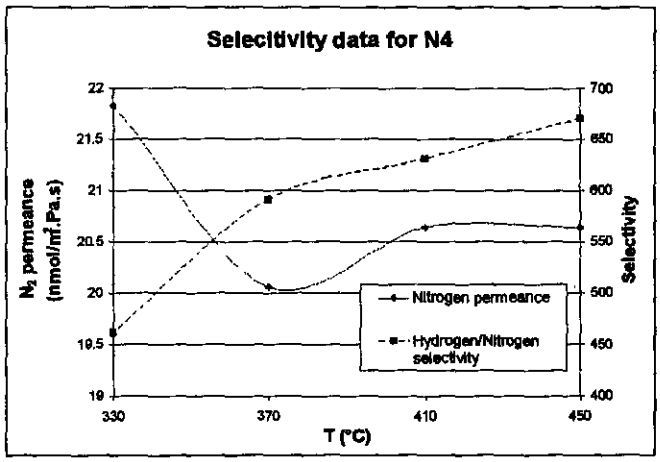

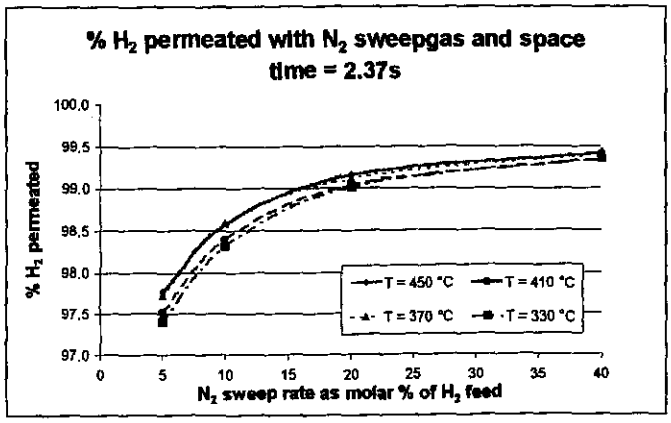

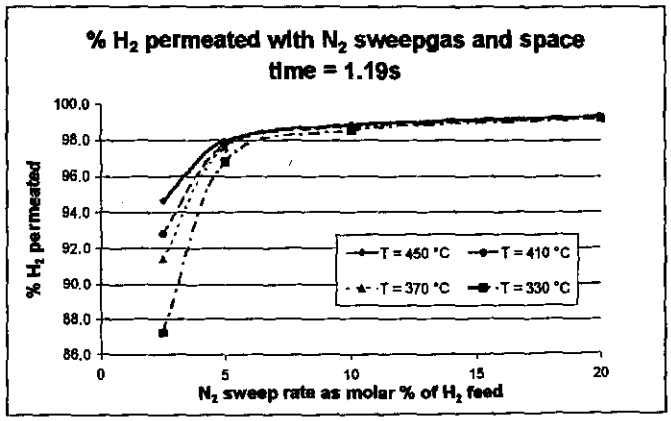

Name: N7 **(1.23 µm)**

	Mass (g)
Clean	29.0120
After pretreatment	29.0275
After Pd	29.0865

	(mm)
Plated length	205
Permeable length	205
Inside diameter	7

H_2 permeance parameters	
P_0 (mol.m/m^2.Pa.s)	9.211E-11
E_D (J/mol)	13164
R^2 for Arrhenius fit	0.9926

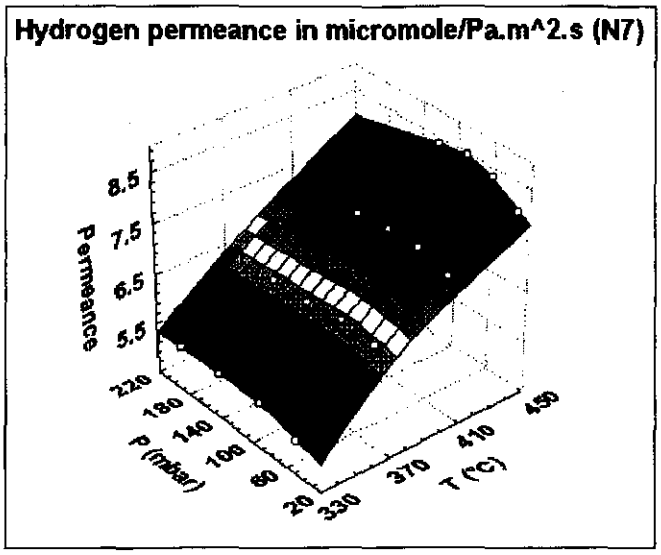

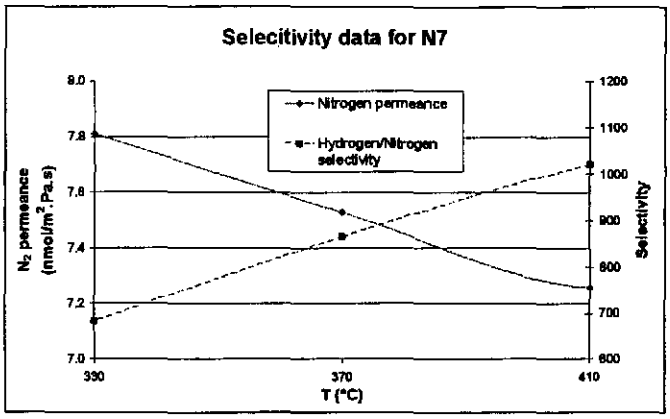

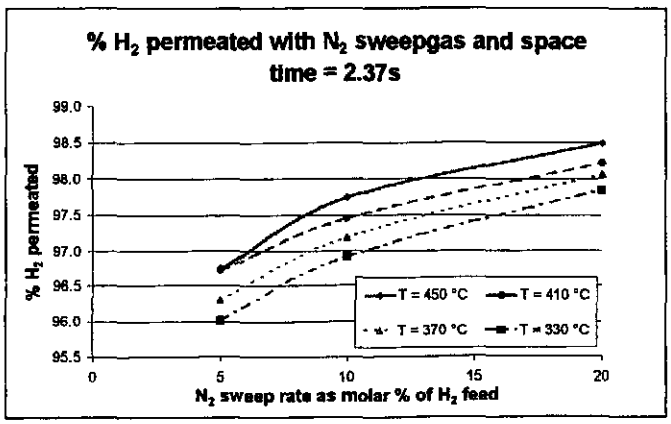

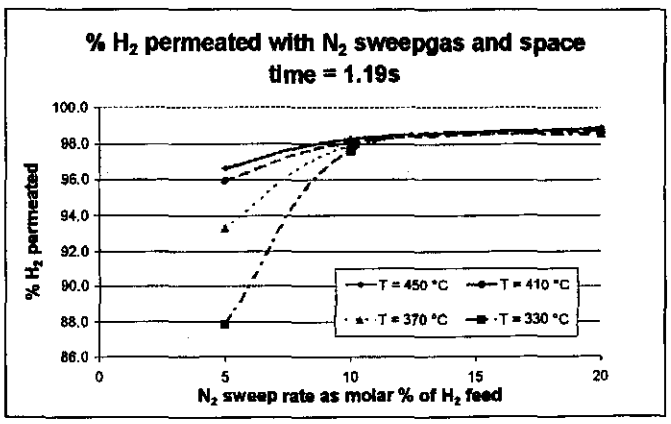

Name: N8 **(1.19μm)**

	Mass (g)
Clean	29.1480
After pretreatment	29.1633
After Pd	29.2200

	(mm)
Plated length	205
Permeable length	205
Inside diameter	7

H_2 permeance parameters	
P_0 (mol.m/m^2.Pa.s)	5.815E-11
E_D (J/mol)	8993
R^2 for Arrhenius fit	0.9958

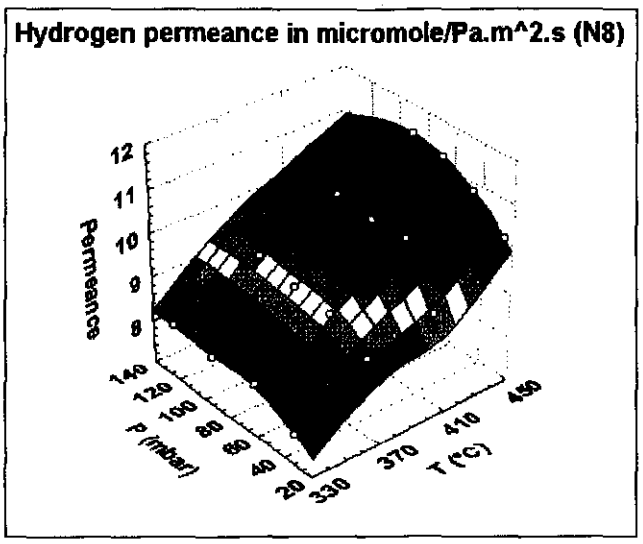

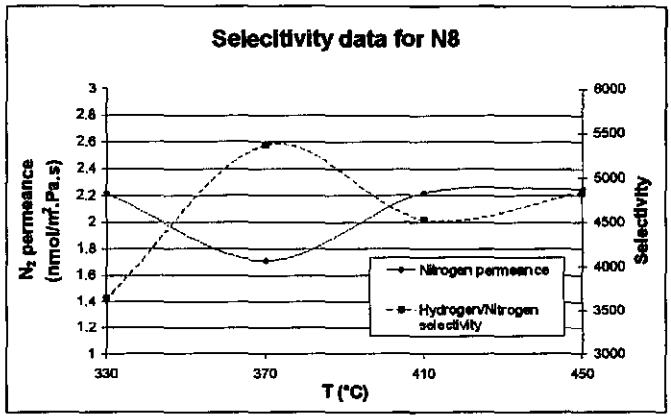

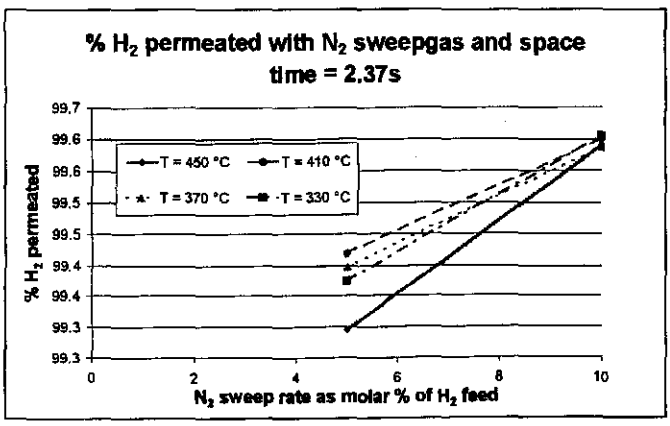

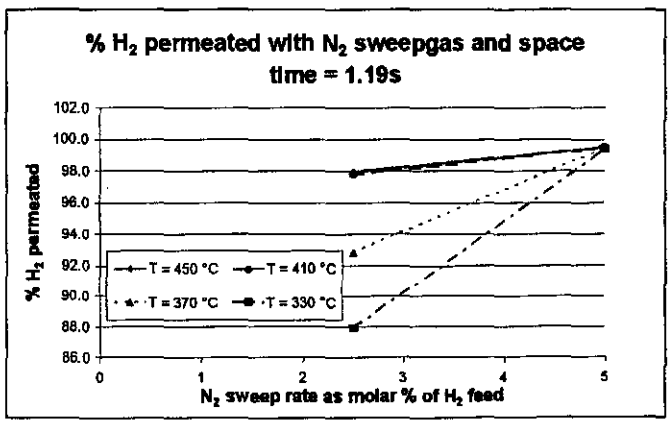

APPENDIX D2

Hydrogen and nitrogen permeance data for Pd-Ag films

Alloying procedures

Name	Elements	Alloying	Heating system	Gas	Temp (°C)	Time (h)
8	Pd	No				
8b	Pd+Ag	No				
8c	Pd+Ag	Yes	Tube oven	Ar	550, 600	15, 25
N1	Pd	No				
N1b	Pd+Ag	No				
N1x	New Pd+Ag	Yes	Reactor	H_2	590	10
N3	Pd	No				
N3b	Pd+Ag	No				
N3c	Pd+Ag	Yes	Tube oven	Ar	545	50
N3d	Pd+Ag	Yes	Tube oven	Ar	545	100 (total)
N3e	Pd+Ag	Yes	Tube oven	Ar	545	150 (total)
N4	Pd	No				
N4b	Pd+Ag	No				
N4c	Pd+Ag	Yes	Tube oven	Ar	530	30
N4x	New Pd+Ag	Yes	Reactor	H_2	540	30
N6	Pd+Ag	Yes	Tube oven	Ar	550, 600	15, 25
N2x	New Pd+Ag	Yes	Reactor	Ar, N_2	500, 550	50, 25
N8x	New Pd+Ag	Yes	Reactor	Ar	550	10

When two temperatures and two times are given in a row, the first heating time is for the first temperature and the second heating time is for the second temperature.

Membrane	Thickness (micron)	T (°C)	Avg. H_2 permeance ($\mu mol/m^2.Pa.s$)	Avg. N_2 permeance ($nmol/m^2.Pa.s$)	Selectivity		Arrhenius parameters for hydrogen permeance		R^2 value for n=1 in permeance equation
8b	1.54	410	5.41	11.50	472		P_0 =	6.550E-11	1
		370	4.69	11.90	394		E_D =	11739	0.9998
		330	4.11	12.20	336		R^2 =	0.9966	0.9996
N1b	1.40	410	5.20	57.10	91		P_0 =	9.752E-11	0.9999
		370	4.49	45.30	99		E_D =	14707	1
		330	3.69	48.00	77		R^2 =	0.9978	1
N3b	2.14	410	3.21	3.20	999		P_0 =	8.064E-11	0.9994
		370	2.82	3.70	758		E_D =	13938	0.9994
		330	2.32	3.70	632		R^2 =	0.9936	0.9991
N3c	2.14	410	6.59	17.60	374		P_0 =	8.762E-11	0.9999
		370	5.99	17.90	335		E_D =	10335	0.9999
		330	5.18	20.30	255		R^2 =	0.9931	0.9998
N3d	2.14	410	5.86	40.80	143		P_0 =	1.348E-10	0.9999
		370	5.25	41.90	125		E_D =	13412	0.9994
		330	4.29	43.10	99		R^2 =	0.9825	0.9997
N3e	2.14	410	6.03	54.10	111		P_0 =	1.022E-07	1
		370	5.41	56.00	97		E_D =	11714	0.9994
		330	4.59	59.30	77		R^2 =	0.9933	0.9999
N4b	1.43	410	2.87	12.00	239		P_0 =	1.236E-10	0.9994
		370	2.37	10.60	226		E_D =	19295	1
		330	1.83	10.20	180		R^2 =	0.9975	0.9996

Membrane	Thickness (micron)	T (°C)	Avg. H_2 permeance ($\mu mol/m^2.Pa.s$)	Avg. N_2 permeance ($nmol/m^2.Pa.s$)	Selectivity		Arrhenius parameters for hydrogen permeance		R^2 value for n=1 in permeance equation
N4c	1.43	410	3.02	14.60	208		P_0 =	2.403E-10	0.9997
		370	2.48	14.80	167		E_D =	20393	0.9995
		330	1.95	15.00	130		R^2 =	0.9985	0.9994
		290	1.49	15.30	95				
		250	1.02	15.50	65				
		210	0.69	15.70	44				
N4x	2.13	410	4.62	24.50	188		P_0 =	7.195E-11	0.9998
		370	4.10	25.20	163		E_D =	11286	0.9997
		330	3.53	25.60	138		R^2 =	0.9983	1
		290	3.08	26.20	118				
		250	2.50	27.00	93				
N8x	2.16	410	6.03	18.18	332		P_0 =	8.469E-11	0.9999
		370	5.26	18.71	289		E_D =	10654	0.9997
		330	4.75	19.31	261		R^2 =	0.9976	0.9996
		290	4.03	20.43	221				
		250	3.37	22.71	185				

Name: **8b** **(1.54 μm)**

	Mass (g)
Clean	28.1700
After pretreatment	28.1730
After Pd	28.2445
After Ag	28.2695
Ag %	25

	(mm)
Plated length	250
Permeable length	230
Inside diameter	7

Oxidation	Yes
Temperature	320 °C
Time	1.5 h

H_2 permeance parameters	
P_0 (mol.m/m^2.Pa.s)	6.550E-11
E_D (J/mol)	11739
R^2 for Arrhenius fit	0.9966

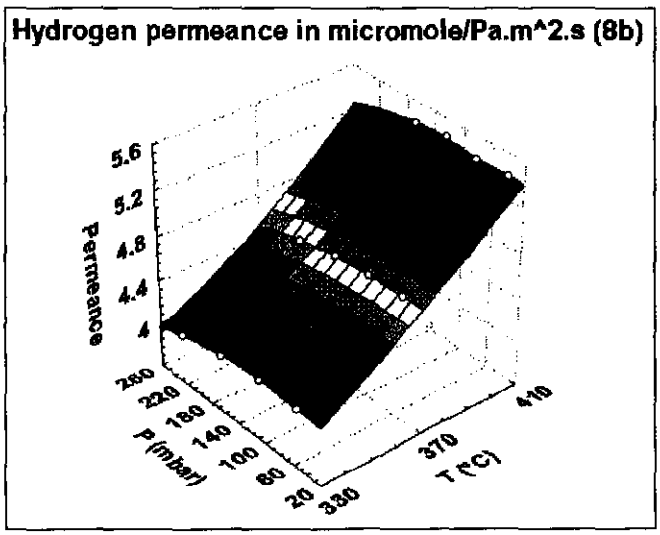

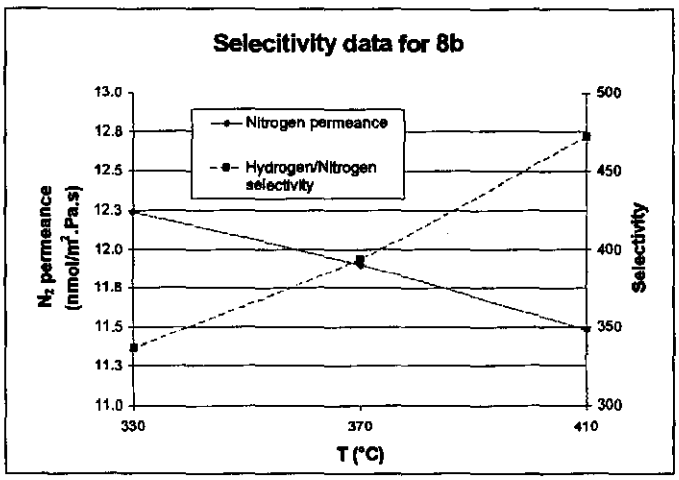

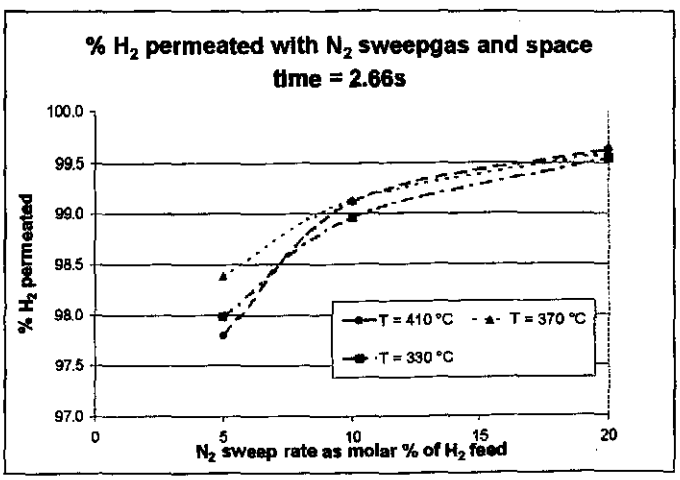

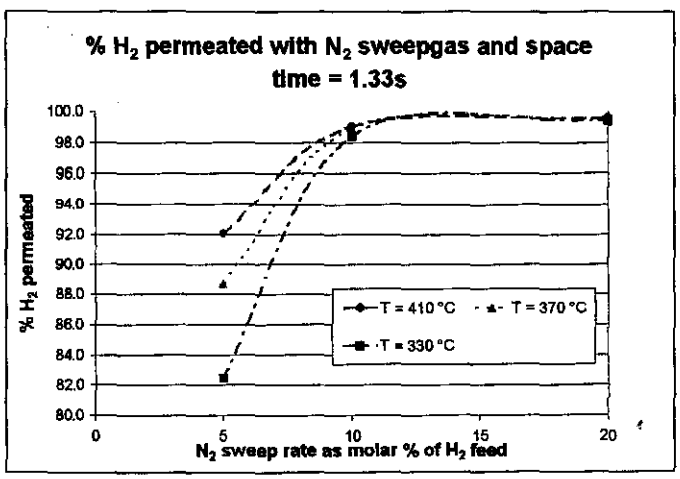

Name: **N1b** **(1.40 µm)**

	Mass (g)
Clean	29.3000
After pretreatment	29.3140
After Pd	29.3750
After Ag	29.3965
Ag %	22

	(mm)
Plated length	250
Permeable length	205
Inside diameter	7

Oxidation	Yes
Temperature	320 °C
Time	1.5 h

H_2 permeance parameters	
P_0 (mol.m/m^2.Pa.s)	9.752E-11
E_D (J/mol)	14707
R^2 for Arrhenius fit	0.9978

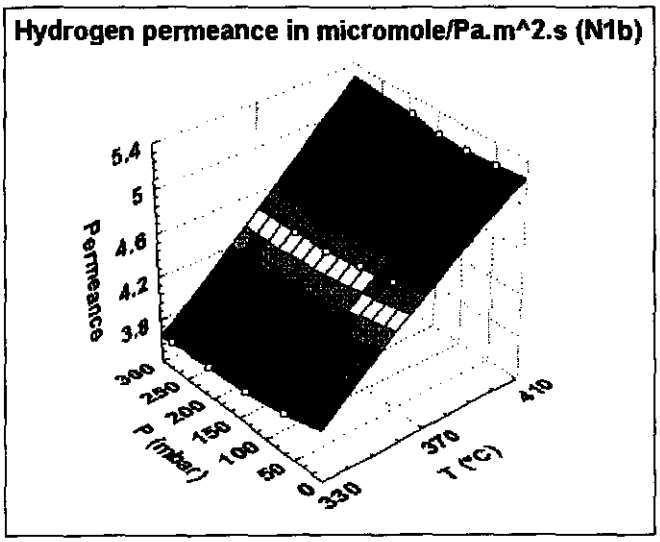

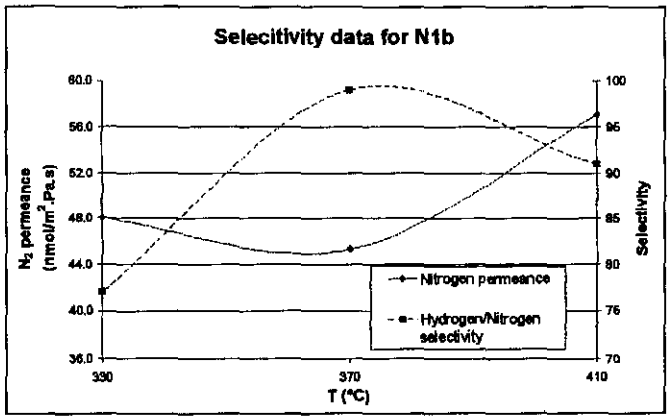

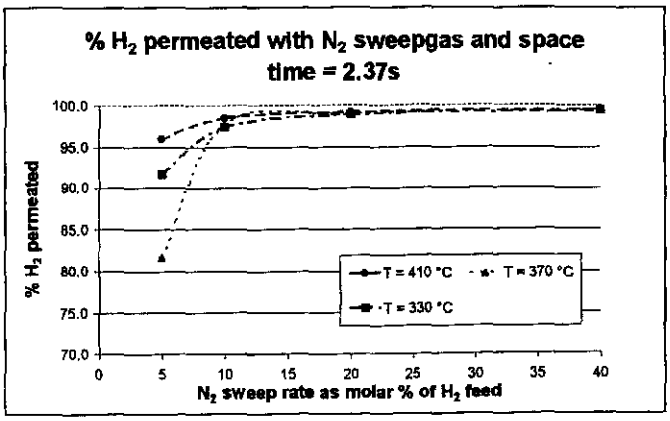

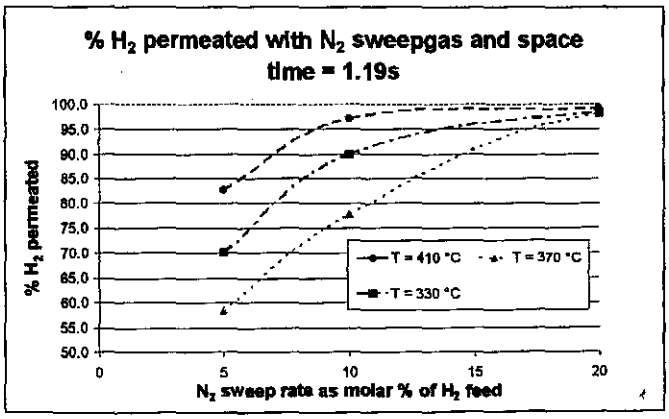

Name: **N3b** **(2.14 µm)**

	Mass (g)
Clean	28.6470
After pretreatment	28.6575
After Pd	28.7355
After Ag	28.7640
Ag %	24

	(mm)
Plated length	205
Permeable length	205
Inside diameter	7

H_2 permeance parameters	
P_0 (mol.m/m^2.Pa.s)	8.064E-11
E_D (J/mol)	13938
R^2 for Arrhenius fit	0.9936

Oxidation	Yes
Temperature	320 °C
Time	1.5 h

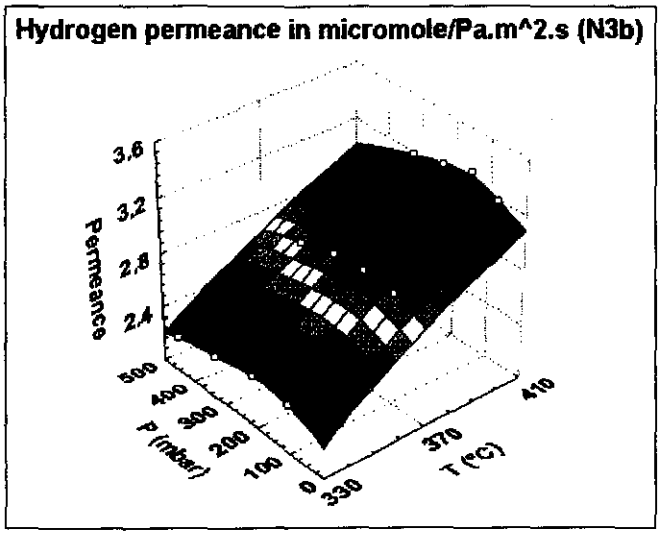

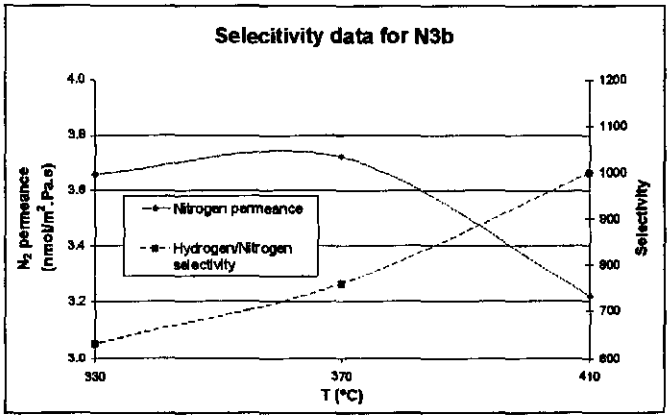

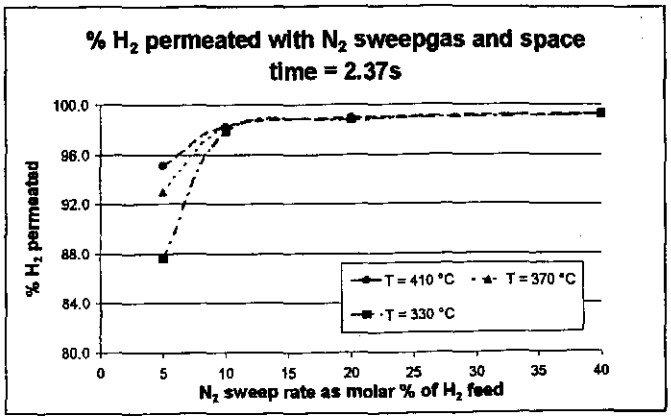

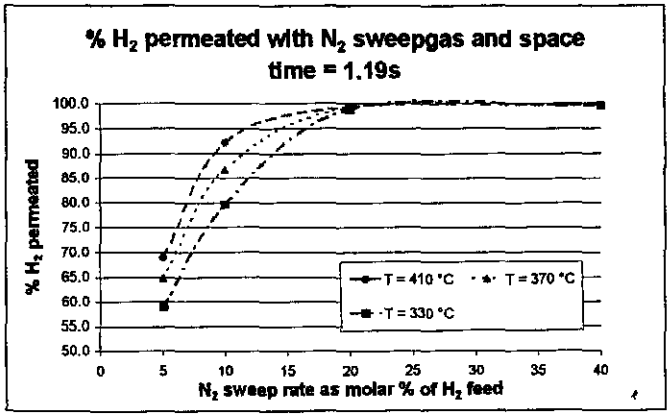

Name: N3c **(2.14 µm)**

	Mass (g)
Clean	28.6470
After pretreatment	28.6575
After Pd	28.7355
After Ag	28.7640
Ag %	24

	(mm)
Plated length	205
Permeable length	205
Inside diameter	7

Oxidation	Yes
Temperature	320 °C
Time	1.5 h

H_2 permeance parameters	
P_0 (mol.m/m^2.Pa.s)	8.762E-11
E_D (J/mol)	10335
R^2 for Arrhenius fit	0.9931

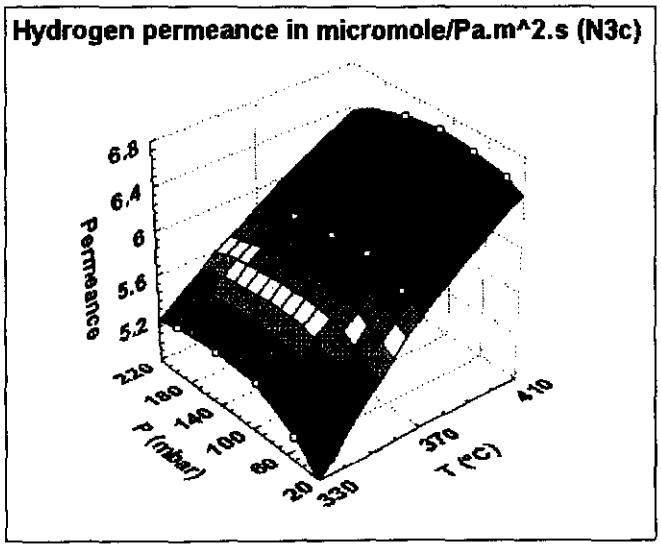

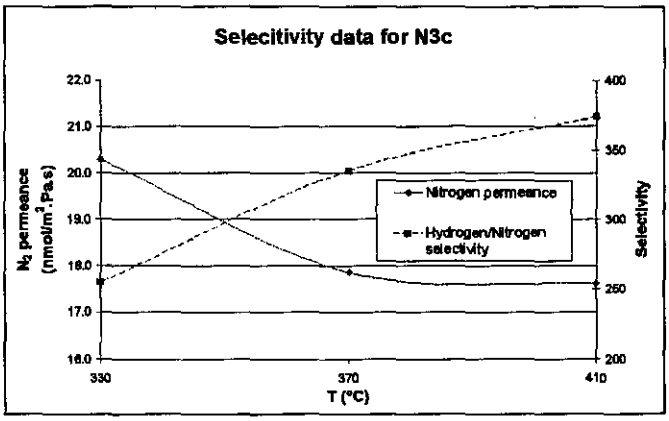

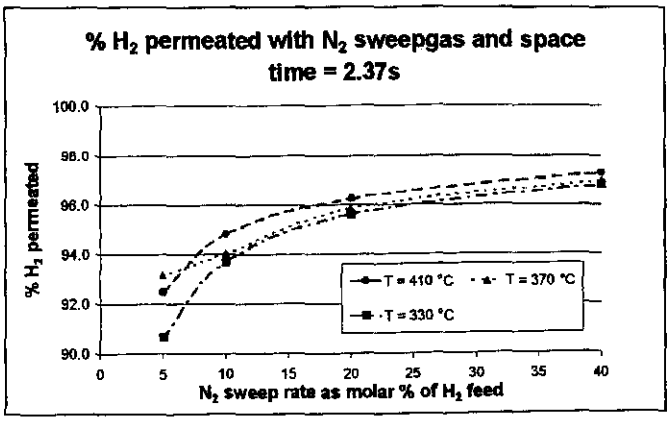

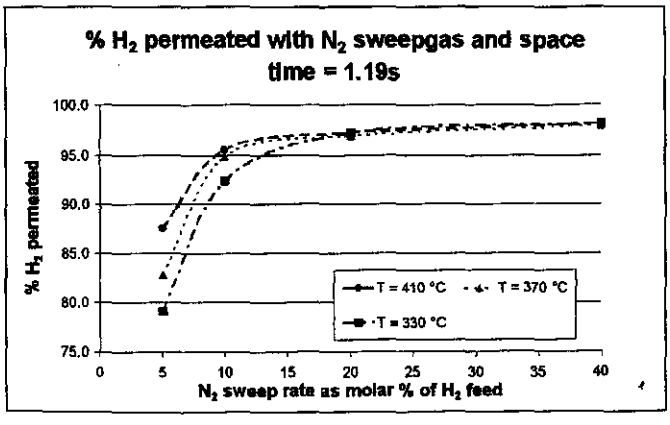

Name: **N3d** **(2.14 µm)**

	Mass (g)
Clean	28.6470
After pretreatment	28.6575
After Pd	28.7355
After Ag	28.7640
Ag %	24

	(mm)
Plated length	205
Permeable length	205
Inside diameter	7

Oxidation	No

H_2 permeance parameters	
P_0 (mol.m/m^2.Pa.s)	1.348E-10
E_D (J/mol)	13412
R^2 for Arrhenius fit	0.9825

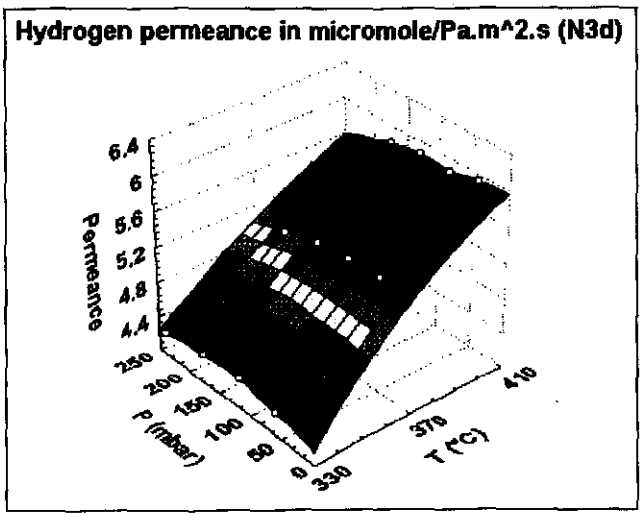

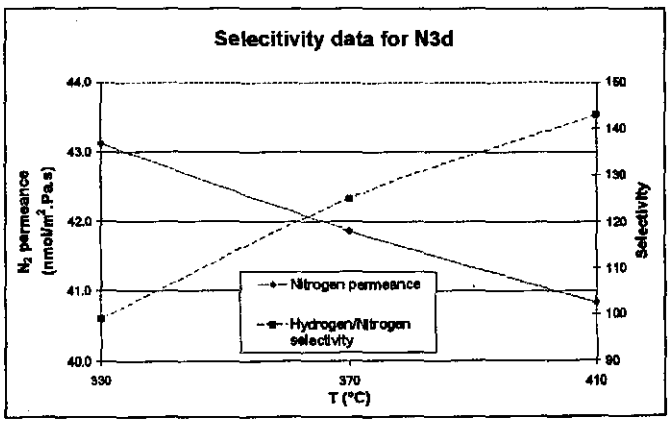

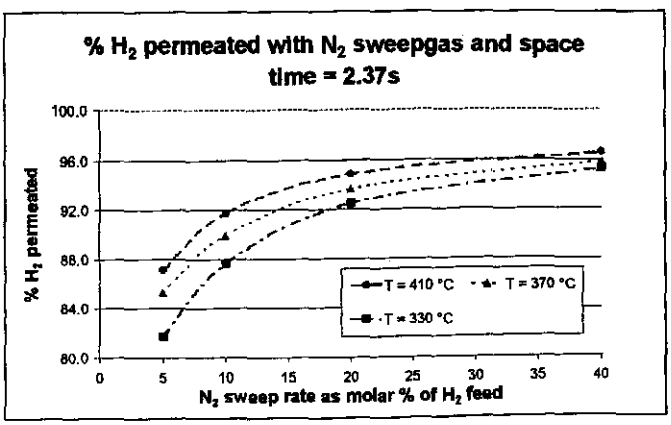

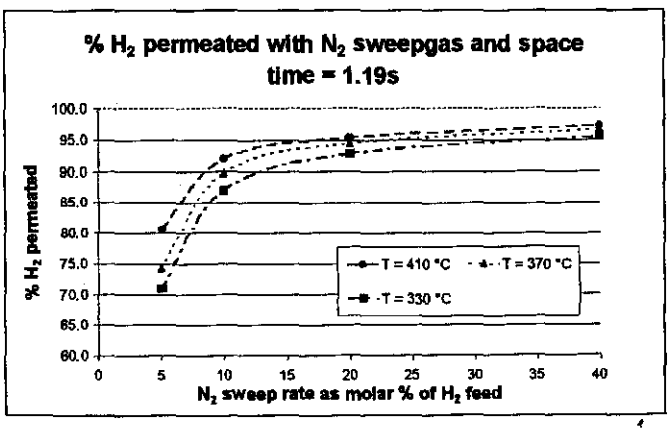

Name: N3e (2.14 µm)

	Mass (g)
Clean	28.6470
After pretreatment	28.6575
After Pd	28.7355
After Ag	28.7640
Ag %	24

	(mm)
Plated length	205
Permeable length	205
Inside diameter	7

Oxidation	No

H_2 permeance parameters	
P_0 (mol.m/m^2.Pa.s)	1.022E-07
E_D (J/mol)	11714
R^2 for Arrhenius fit	0.9933

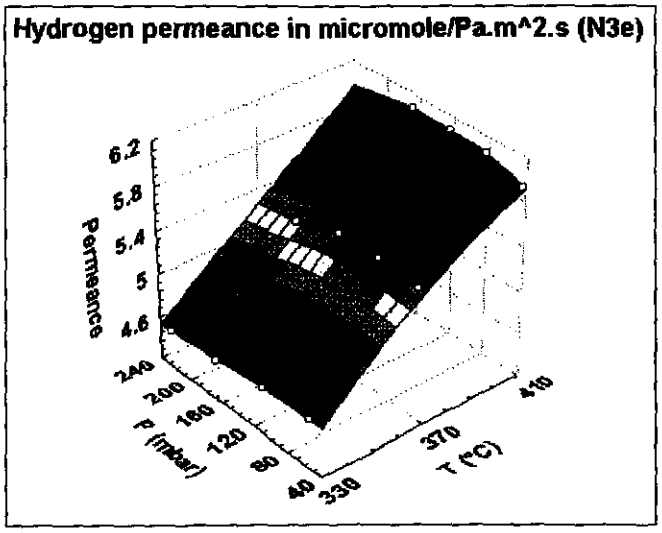

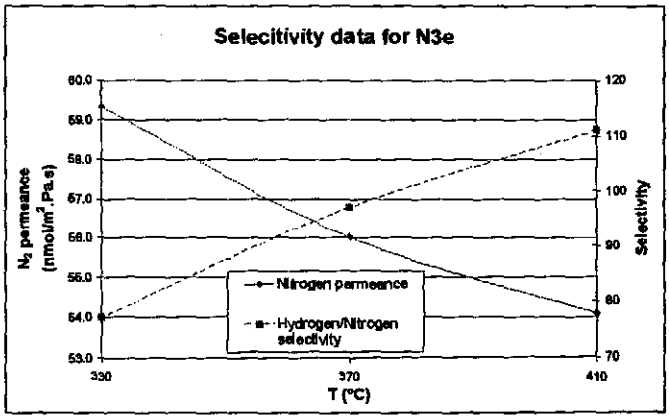

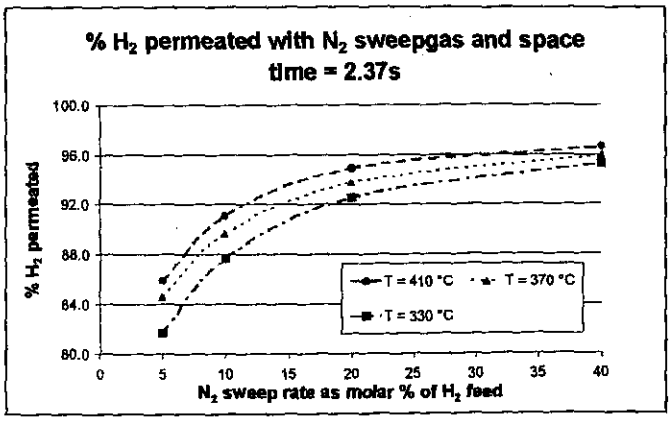

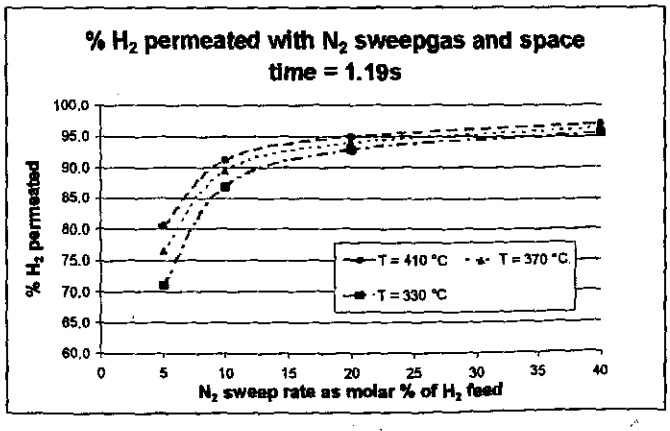

Name: N4b (1.43 µm)

	Mass (g)
Clean	28.9363
After pretreatment	28.9540
After Pd	29.0004
After Ag	29.0197
Ag %	23

	(mm)
Plated length	205
Permeable length	205
Inside diameter	7

Oxidation	Yes
Temperature	320 °C
Time	1.5 h

H_2 permeance parameters	
P_0 (mol.m/m^2.Pa.s)	1.236E-10
E_D (J/mol)	19295
R^2 for Arrhenius fit	0.9975

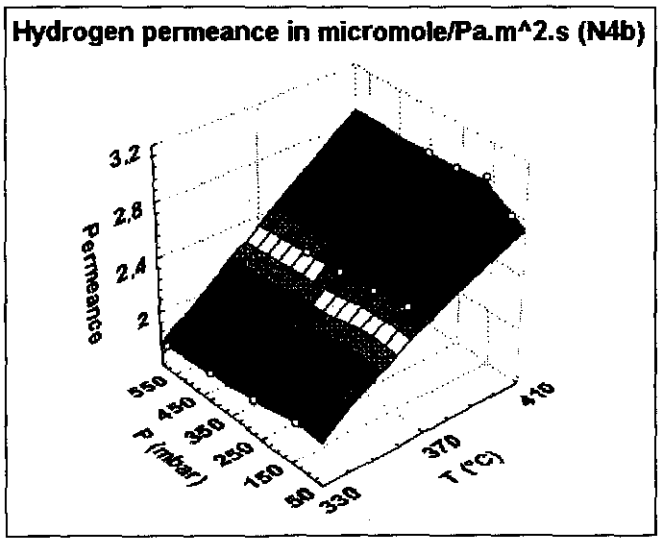

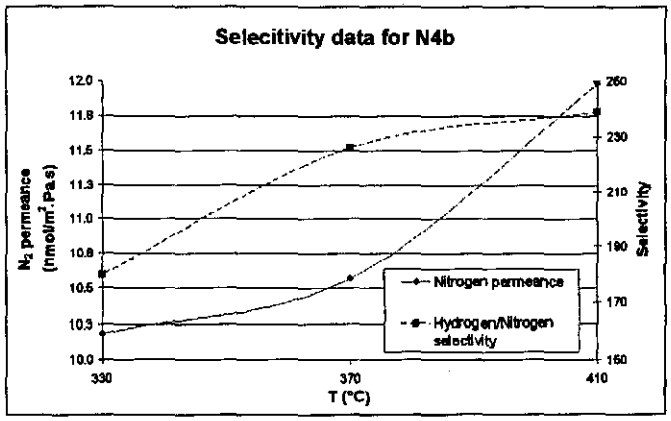

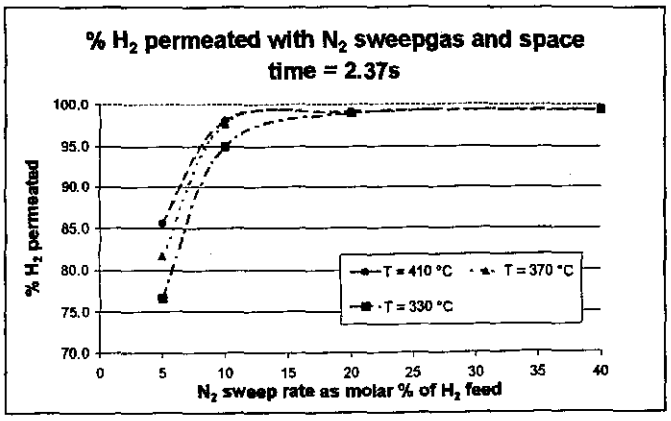

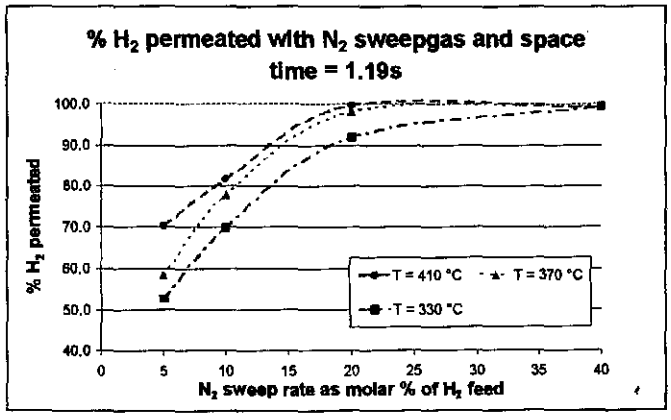

Name: N4c **(1.43 µm)**

	Mass (g)
Clean	28.9363
After pretreatment	28.9540
After Pd	29.0004
After Ag	29.0197
Ag %	23

	(mm)
Plated length	205
Permeable length	205
Inside diameter	7

Oxidation	No

H_2 permeance parameters	
P_0 (mol.m/m^2.Pa.s)	2.403E-10
E_D (J/mol)	20393
R^2 for Arrhenius fit	0.9985

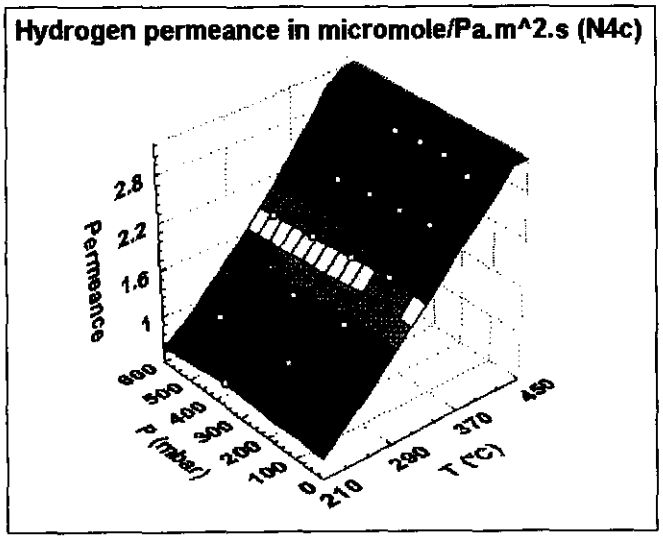

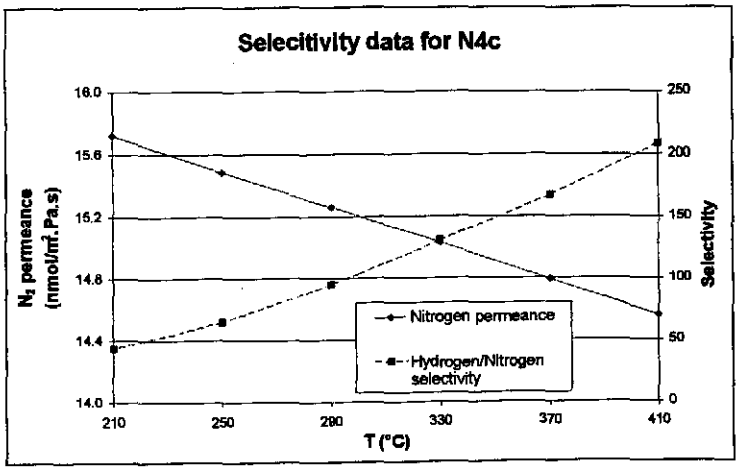

Name: N4x (2.13 µm)

	Mass (g)
Clean	28.9365
After pretreatment	28.9428
After Pd	29.0476
After Ag	29.0760
Ag %	20

	(mm)
Plated length	250
Permeable length	205
Inside diameter	7

Oxidation	Yes
Temperature	350 °C
Time	3 h

H_2 permeance parameters	
P_0 (mol.m/m^2.Pa.s)	7.195E-11
E_D (J/mol)	11286
R^2 for Arrhenius fit	0.9983

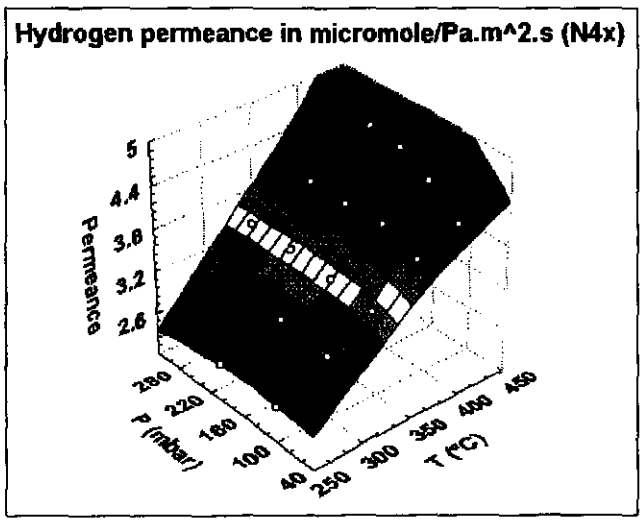

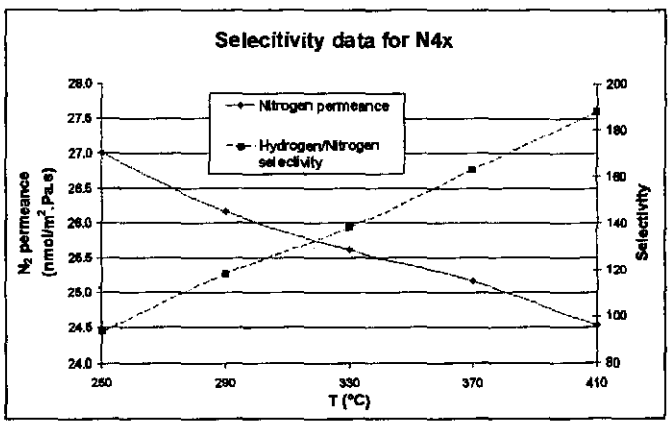

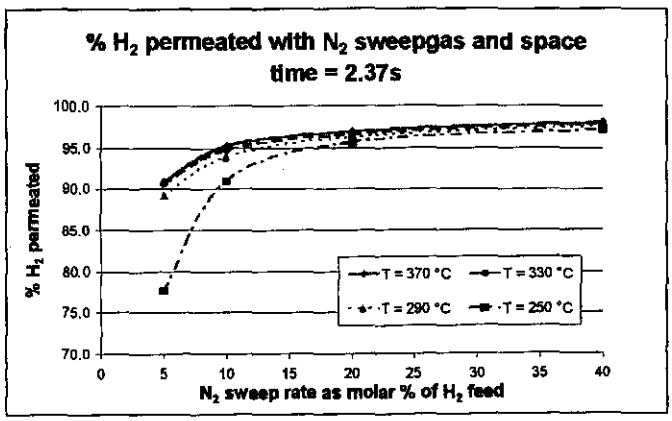

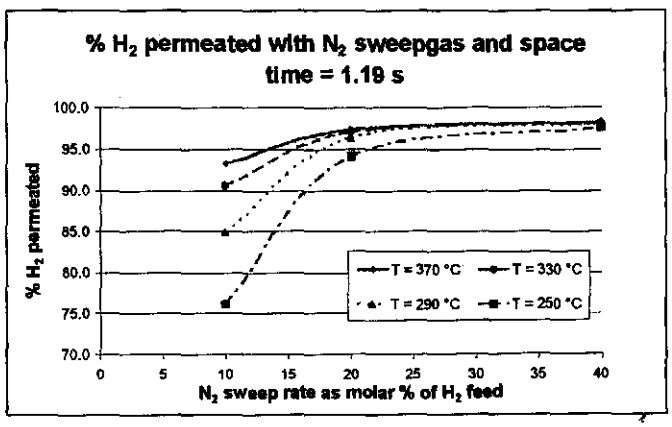

Name: N8x (2.16 µm)

	Mass (g)
Clean	29.1785
After pretreatment	29.1845
After Pd	29.2745
After Ag	29.3030
Ag %	23

	(mm)
Plated length	220
Permeable length	205
Inside diameter	7

Oxidation	Yes
Temperature	310 °C
Time	1 h

H_2 permeance parameters	
P_0 (mol.m/m^2.Pa.s)	8.469E-11
E_D (J/mol)	10654
R^2 for Arrhenius fit	0.9976

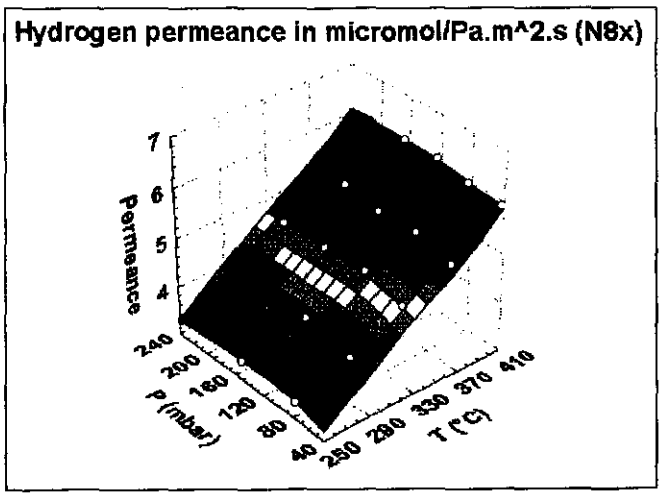

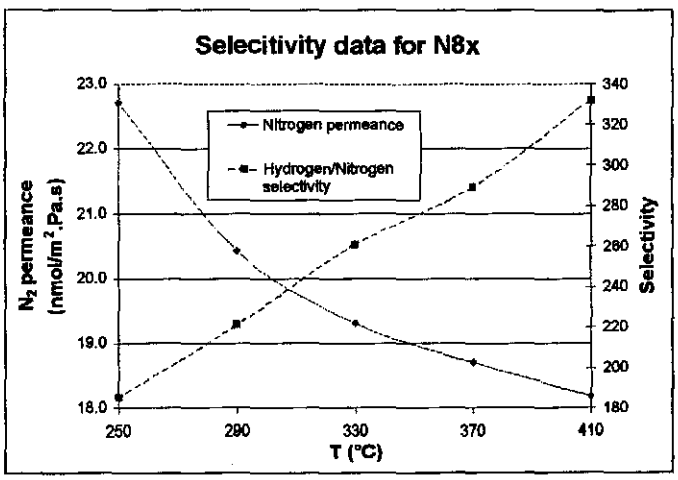

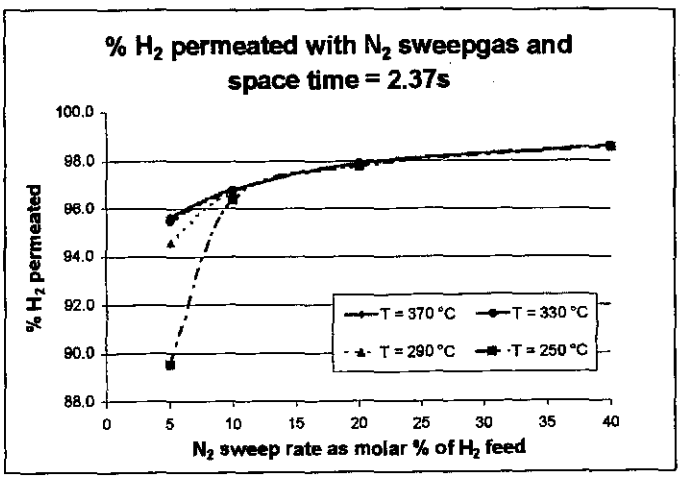

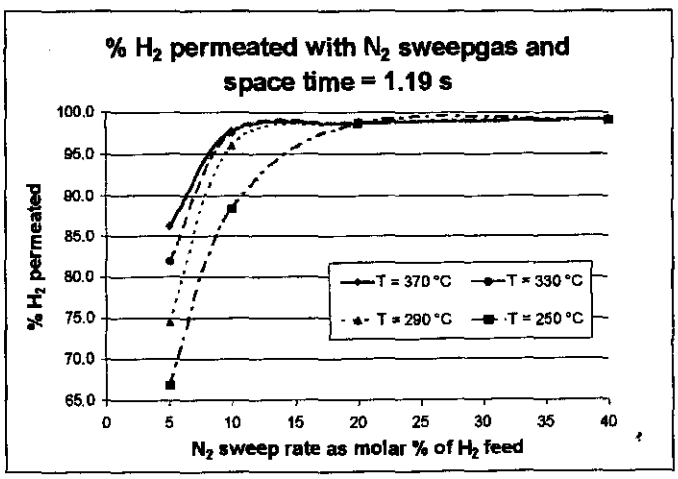

For some membranes a full characterisation was not done:

Name: **8c** **(1.54 µm)**

	Mass (g)			(mm)
Clean	28.1700		Plated length	250
After pretreatment	28.1730		Permeable length	230
After Pd	28.2445		Inside diameter	7
After Ag	28.2695			
Ag %	25		Oxidation	No

Name: **N6** **(2.05 µm)**

	Mass (g)			(mm)
Clean	28.0606		Plated length	250
After pretreatment	28.0702		Permeable length	205
After Pd	28.1680		Inside diameter	7
After Ag	28.1966			
Ag %	21		Oxidation	No

Name: **N1x** **(2.13 µm)**

	Mass (g)			(mm)
Clean	29.3154		Plated length	250
After pretreatment	29.3175		Permeable length	205
After Pd	29.4225		Inside diameter	7
After Ag	29.4527			
Ag %	22		Oxidation	No

Name: **N2x (2.02 µm)**

	Mass (g)			(mm)
Clean	28.5978		Plated length	250
After pretreatment	28.6115		Permeable length	205
After Pd	28.7000		Inside diameter	7
After Ag	28.7335			
Ag %	25		Oxidation	No

APPENDIX E

Literature data on Pd and Pd-alloy thin films

Preparation method	Support description	Coating composition	Thickness (μm)	Temperature (°C); δP (kPa)	Permeance Mol/m^2/s/Pa	Selectivity H_2/gas	Reference
Non Palladium membranes:							
Clean tube	α-alumina 150 nm (NOK)			400	21	3 (N_2)	Kusakabe (1996)
Clean tube	α/γ-alumina (a) 3 nm (SCT)			25	15.8	3.6	Casanave (1995)
Tube	Silica	silica	7.5	440; 300	0.79	56 (CO_2)	Weyten (1997)
Slip casting Tube	α -alumina (a) 200 nm (SCT)	SiO_2	5.0	100	28	3.5 (N_2)	Vitulli (1995)
Tube	α -alumina (a) 200 nm (SCT)	Zeolite 0.6 nm pores			1.15	3.0	Casanave (1995)
CVD in pores of membrane tube	Porous Vycor 4 nm (Corning)	SiO_2 Al_2O_3 B_2O_3 TiO_2		450, 100 450, 100 450, 100 450, 100	0.0191 0.0020 0.0068 0.0041	25 210 20 63	Tsapatsis (1991)
Palladium and palladium alloy foils							
Foil Disc	Foil	Pd	50	350 500	0.30 0.60		Jung (2000)
Foil	Foil	Pd	24	350; 156 350; 444	1.20 0.87		Hurlbert (1961)
Foil	Foil	Pd	20	540; 340	0.23		Grashoff (1983)
Quenching and rolling	Foil	$Pd_{80}Si_{20}$	40	379; 100	0.016	-	Itoh (1995b)
Foil	Foil (TK)	$Pd_{77}Ag_{23}$	150	75; 100	0.029		Itoh (1997)
Foil	Foil	$Pd_{77}Ag_{23}$	100	350; 1950	0.12		Jorgensen (1997)
Foil	Foil	$Pd_{77}Ag_{23}$	100	300; 689 400; 689	0.18 0.20		Ali (1994)

Preparation method	Support description	Coating composition	Thickness (μm)	Temperature (°C); δP (kPa)	Permeance Mol/m^2/s/Pa	Selectivity H_2/gas	Reference
Foil	Ta Foil (GFM)	Pd-Ta-Pd	1-13-1	300; 48 340; 47	1.32 1.76		Peachey (1996)
Foil	Different foil substrates	$Pd_{75}Ag_{25}$	25 on both sides	400; 780	0.66	> 100 (N_2)	Edlund (1996)
Foil	Foil	$Pd_{91}Ru_6In_3$	200	300; 100	0.0000105		Hara (1999)
Foil	Foil	Pd-Al_2O_3-V 25-250-25 (μm)		700; 689	0.43		Edlund (1995b)
Electroless Pd plating on ceramics (discs, inside and ouside of tubes)							
Plating (electr) Disc	Modified α-alumina	Pd	1	450; 101	9.75	23 (N_2)	Zhao (1998)
Plating (electr) disc	α-alumina (s) 150 nm (VCMC)	Pd	8.5 12.0		See comments		Ilias (1997)
Plating (electr) Outside tube	Porous ceramic	Pd	4.5	400	2.86		Kikuchi (1995)
Plating (electr) Outside tube	α-alumina (a) 200 nm (TCC)	Pd	4.5	400; 194	1.54	-	Uemiya (1991a)
Plating (electr) Outside tube	α-alumina (a) 160 nm (ECN)	Pd	10.3	467; 102	2.68	970 (N_2)	Li A (1999)

Preparation method	Support description	Coating composition	Thickness (μm)	Temperature (°C); δP (kPa)	Permeance Mol/m^2/s/Pa	Selectivity H_2/gas	Reference
Plating (electr) Inside tube + pores	α/γ-alumina (a) 5 nm (SCT)	Pd	2.0	300 400 500	0.63 1.39 2.34		Shu (1996b)
Plating (electr) Inside tube	α/γ-alumina (a) 3-4 nm (SCT)	Pd	2.1	450; 2.55 500; 2.55	4.09 5.27		Shu (1997b)
Plating (electr) Inside tube	α-alumina (s) 200 nm (GTC)	Pd	8 16 10	500; 689 450; 689 450; 689	0.19 0.22 0.21	48 (N_2) 200 (N_2) 49 (N_2)	Paglieri (1999)
Plating (electr) Inside tube	α-alumina (a) 200 nm (USF)	Pd	11.4 17	550; 100 550; 100	1.16 0.78	550 (N_2) 63 (N_2)	Collins (1993b)
??	Ceramic tube	Pd	4	350; 1950	2.93	127 (N_2)	Jorgensen (1997)

Electroless Pd plating on porous glass, porous SS and refractory metals

Plating (electr) Outside tube	Porous glass (s) 300 nm (ISI)	Pd	20	400; 196	0.68	-	Uemiya (1991b)
Plating (electr) Outside tube	Porous SS 100 nm (MM)	Pd	??	380; 300	0.42		Li A (2000)
Plating (electr) Disk	Porous SS (s) 500 nm (MM)	Pd	6.0	400; 100	0.53		Jemaa (1996)
Plating (electr) Outside tube	Porous SS 100 nm (MM)	Pd	??	480; 100	0.73	1420 (N_2)	Li A (1997)
Plating (electr) Tube	Niobium 150 μm thick	Pd	2-150-2	??; 100	1.44		Buxbaum (1996)
Plating (electr) Tube	Tantalum 70 μm thick	Pd	2-70-2	420; 100	1.93		Buxbaum (1996)

Preparation method	Support description	Coating composition	Thickness (μm)	Temperature (°C); δP (kPa)	Permeance Mol/m^2/s/Pa	Selectivity H_2/gas	Reference
CVD of Pd on alumina discs and tubes							
CVD (In pores + surface disk)	α/γ-alumina (a) 4 nm	Pd	0.5-1.0	350	0.9	3.6 (N_2)	Xomeritakis (1996)
CVD (In pores + surface disk)	α/γ-alumina (a) 4.5 nm	Pd	1.0-1.5	300	0.21	200 (He)	Xomeritakis (1997)
CVD (In pores + outside tube)	α-alumina 150 nm (NOK)	Pd	4	300; 100 500; 100	4.0 4.0	10000 (N_2) 6700 (N_2)	Yan (1994)
CVD (In pores + outside tube)	α-alumina 150 nm (NOK)	Pd	4.4	400; 200 500; 200	0.38 0.60	3000 (N_2) 1900 (N_2)	Aoki (1996)
CVD (In pores + outside tube)	α-alumina 150 nm (NOK)	Pd	4.4	400	0.80	1330 (N_2)	Kusakabe (1996)
CVD (In pores + outside tube)	α-alumina 150 nm (NOK)	Pd	4.4	400	0.7	1160 (N_2)	Morooka (1995)
Pd membranes prepared by electroplating and wet impregnation							
Wet impregn. Disc	Ni/porous SS 50 nm (MM)	Pd	0.5	450	15.8	1600	Jun (1999)
Electroplating Disc	Ni/porous SS 50 nm (MM)	Pd	0.8	550	17.8	4700	Nam (1999)

Preparation method	Support description	Coating composition	Thickness (μm)	Temperature (°C); δP (kPa)	Permeance Mol/m^2/s/Pa	Selectivity H_2/gas	Reference
Palladium alloys prepared by electroless plating							
Plating (electr) Outside tube	α-alumina (a) 200 nm (TCC)	$Pd_{89}Ag_{11}$ $Pd_{77}Ag_{23}$ $Pd_{69}Ag_{31}$	5.0 5.8 6.4	400; 194 400; 194 400; 194	1.97 2.24 1.45	-	Uemiya (1991a)
Plating (electr) Outside tube	Porous ceramic	$Pd_{77}Ag_{23}$	5.8	400	4.09		Kikuchi (1995)
Plating (chemical)	α/γ-alumina (a)	Pd-Ag	7.5	440; 300	1.60	15000 (CO_2)	Weyten (1997)
Plating (chemical)	α/γ-alumina (a)	Au/Pd-Ag	7.5	440; 300	1.01	4000 (CO_2)	Weyten (1997)
Plating (electr) Outside tube	Porous Vycor 5 nm (Corning)	Pd_{88}-Ag_{12}	1.2	500;170 anneal 400;170	0.10 0.074		Cheng (1999)
Plating (electr) Outside tube	Porous glass (s) 300 nm (ISI)	Pd_{93}-Ag_7	21.6	400; 196	0.32	-	Uemiya (1991b)
Plating (electr) Outside tube	Porous glass (s) 300 nm (ISI)	Pd_{94}-Cu_6	18.9	400; 196	0.21	-	Uemiya (1991b)

Preparation method	Support description	Coating composition	Thickness (μm)	Temperature (°C); δP (kPa)	Permeance Mol/m^2/s/Pa	Selectivity H_2/gas	Reference
Palladium alloys prepared by sputtering							
Sputtering (disc)	α/γ-alumina 3 nm	$Pd_{75}Ag_{25}$	0.35	250	0.28	5.7 (N_2)	Jayaraman (1995b)
Magnetron sputtering (disc)	α/γ-alumina (a) 4.5 nm	$Pd_{75}Ag_{25}$	0.4	300	0.15	80 (He)	Xomeritakis (1997)
Dc sputtering (disc)	α/γ-alumina (a) 4 nm	$Pd_{92}Ag_8$	0.33	300	0.071	63 (He)	McCool (1999)
Spray pyrolysis Outside tube	α/γ-alumina (a) 5 nm (NOK)	$Pd_{76}Ag_{24}$	1.75	500	0.080	24 (N_2)	Li ZY (1993)
Sputtering	MgO_{85}-$Ytria_{15}$ 300 nm (s)	$Pd_{94}Ru_6$	10	700; 1000	1.23		Gryaznov (1993)
Sputtering (disk)	Porous SS (s) (MPV)	$Pd_{94}Ru_6$	10	800, 2000	0.68		Gryaznov (1993)
Sputtering (disk)	Porous SS (s) (MPV)	$Pd_{93.5}In_6Ru_{0.5}$	1.5	372; 100	0.45	-	Gryaznov (1993)
Sputtering (Outside tube)	Porous glass 4 nm	$Pd_{77}Ag_{23}$	6.0	380; 125	0.056		Gobina (1994)
Sputtering	Poly(dimethylsiloxane) coated Membrane (a)	$Pd_{76}Ag_{24}$	0.05	25	0.0031	100 (CO_2)	Athayde (1994)
Sputtering	Polyarilyde (a)	$Pd_{94}Ru_6$	0.4	200; 1000	0.16		Gryaznov (1993)

Comments

1. All permeances were changed from the original units reported to μmol/(m^2.s.Pa)
2. Open cells in the data pages represent data not supplied in the specific reference.
3. Selectivities were only included if permeation data for the other gas was listed as a function of pressure and/or temperature.
4. In one reference (Ilias 1997), the graphs and values mentioned in the paper contradict each other and was thus not included.

Abbreviations

ECN:	Energy Corporation of The Netherlands
GFM:	Goodfellow Metals, Berwyn, PA
GTC:	Golden Technology Company, Colarado
ISI:	Ise Chemical Industry Company
MM:	Mott Metallurgical
MPV:	Metallurgical plant, Vyksa, Russia
NOK:	NOK Corporation, Japan
SCT:	Societé des Céramiques Techniques
SS:	Stainless steel
TCC:	Toshiba Ceramics Co.
TK:	Tanaka Kikinzoku, Japan
USF:	US Filter Corporation, Warrendale, Pennsylvania
VCMC:	Velterop Ceramic Membrane Company of The Netherlands

(a):	asymmetric
(s):	symmetric

APPENDIX F1

Plug flow reactor data and membrane reactor data for ethanol dehydrogenation

Membrane name: N8x **Catalyst:** 3.00 g (14.4 wt% Cu on silica)

Reaction temperature: 250 °C **Catalyst particle size:** 500-800 microns

Feed rate ml/h	Sweep to feed molar ratio		Total ethanol conversion		Ethanol conversion to acetaldehyde			Ethanol conversion to MEK		Ethanol to acetic acid ethyl ester			Reaction selectivity towards acetaldehyde	
				Average		Average			Average		Average			Average
5	0.00		35.7		27.8			0.7		2.8			78.0	
			27.1		26.2			0.5		0.4			96.7	
			34.5	32.4	30.3	28.1		0.7	0.6	1.4	1.5		87.7	87.4
	1:2.5		42.1		34.5			0.8		2.8			81.9	
			31.9		29.0			0.7		0.8			90.9	
			43.4	39.1	36.4	33.3		0.9	0.8	2.4	2.0		84.0	85.6
	1:1		41.9		34.1			0.9		2.4			81.4	
			38.8		32.6			0.8		2.1			84.0	
			47.1	42.6	36.0	34.2		1.2	1.0	3.2	2.5		76.5	80.6
	2:1		43.6		37.3			0.7		2.0			85.4	
			45.4		37.1			0.8		2.3			81.6	
			46.0	45.0	38.5	37.6		0.9	0.8	2.0	2.1		83.7	83.6
	4:1		49.1		41.3			0.7		2.4			84.2	
			50.0		42.3			0.7		2.2			84.7	
			39.4	46.2	33.6	39.1		0.8	0.8	1.4	2.0		85.4	84.7
	8:1		55.3		46.0			0.8		2.5			83.1	
			48.6		41.7			0.9		1.9			85.7	
			52.3	52.1	45.1	44.2		0.7	0.8	1.9	2.1		86.2	85.0

Membrane name: N8x **Catalyst:** 3.00 g (14.4 wt% Cu on silica)

Reaction temperature: 250 °C **Catalyst particle size:** 500-800 microns

Feed rate ml/h	Sweep to feed molar ratio		Total ethanol conversion		Ethanol conversion to acetaldehyde			Ethanol conversion to MEK		Ethanol to acetic acid ethyl ester			Reaction selectivity towards acetaldehyde	
				Average		Average			Average		Average			Average
10	0		27.4		26.4			0.5		0.5			96.3	
			28.5		27.2			0.5		0.5			95.2	
			30.3	28.8	27.7	27.1		0.7	0.6	1.0	0.7		91.4	94.3
	1:5		34.3		31.2			0.9		0.9			90.8	
			36.6	35.5	32.1	31.6		0.8	0.8	1.0	1.0		87.7	89.3
	1:2		35.7		32.4			0.9		0.6			90.6	
			34.8		30.4			0.8		1.4			87.3	
			30.2	33.6	26.5	29.7		0.5	0.7	1.1	1.1		87.6	88.5
	1:1		28.3		27.1			0.6		0.6			95.8	
			28.0		27.1			0.5		0.4			96.7	
			29.9		28.1			0.7		0.6			94.1	
			28.4	28.6	26.9	27.3		0.6	0.6	0.4	0.5		94.6	95.3
	2:1		35.8		33.7			0.8		0.6			94.0	
			31.1		28.9			0.5		0.5			92.9	
			29.8	32.2	28.5	30.4		0.6	0.7	0.4	0.5		95.5	94.2
	4:1		34.6		32.3			0.7		0.5			93.5	
			34.5	34.5	33.0	32.7		0.7	0.7	0.4	0.5		95.7	94.6

Membrane name: N8x **Catalyst:** 3.00 g (14.4 wt% Cu on silica)

Reaction temperature: 275 °C **Catalyst particle size:** 500-800 microns

Feed rate ml/h	Sweep to feed molar ratio		Total ethanol conversion		Ethanol conversion to acetaldehyde			Ethanol conversion to MEK		Ethanol to acetic acid ethyl ester			Reaction selectivity towards acetaldehyde	
				Average		Average			Average		Average			Average
10	no sweep		47.0		38.2			0.9		2.7			81.3	
			45.2	46.1	38.2	38.2		0.9	0.9	2.0	2.4		84.5	82.9
	1:5		43.8		39.4			0.9		1.3			90.0	
			42.4	43.1	39.2	39.3		0.8	0.8	0.8	1.1		92.5	91.3
	1:2		48.2		43.8			0.9		1.1			91.0	
			49.1	48.6	45.1	44.5		0.8	0.9	1.0	1.0		91.9	91.5
	1:1		48.2		43.9			0.9		1.1			91.0	
			58.9	53.6	53.0	48.4		1.1	1.0	1.3	1.2		90.0	90.5
	2:1		62.3		53.7			0.6		1.9			86.2	
			61.8	62.1	55.5	54.6		1.1	0.8	1.8	1.8		89.8	88.0
	4:1		61.8		58.1			1.8		0.6			94.1	
			58.1	59.9	54.7	56.4		1.8	1.8	0.5	0.6		94.2	94.2

Membrane name: N8x **Catalyst:** 3.00 g (14.4 wt% Cu on silica)

Reaction temperature: 275 °C **Catalyst particle size:** 500-800 microns

Feed rate ml/h	Sweep to feed molar ratio		Total ethanol conversion		Ethanol conversion to acetaldehyde			Ethanol conversion to MEK		Ethanol to acetic acid ethyl ester			Reaction selectivity towards acetaldehyde	
				Average		Average			Average		Average			Average
20	0.00		41.8		33.3			0.6		2.5			79.8	
			45.9	43.8	37.4	35.4		0.8	0.7	2.1	2.3		81.5	80.6
	1:5		47.7		40.9			0.8		1.9			85.8	
			48.6	48.1	43.6	42.2		0.8	0.8	1.6	1.7		89.6	87.7
	1:2		43.8		38.9			0.8		1.3			88.8	
			50.4	47.1	43.5	41.2		0.6	0.7	1.7	1.5		86.2	87.5
	1:1		45.9		42.8			0.9		0.8			93.3	
			55.3	50.6	48.7	45.8		0.9	0.9	1.2	1.0		88.1	90.7
	2:1		46.0		44.4			0.7		0.4			96.5	
			48.1	47.1	44.3	44.4		1.0	0.9	0.8	0.6		92.1	94.3
	4:1		55.2		50.8			0.9		1.1			92.0	
			48.4		45.4			0.9		0.7			93.8	
			48.8	50.8	44.8	47.0		0.9	0.9	0.8	0.9		91.9	92.5

Membrane name: N8x **Catalyst:** 3.00 g (14.4 wt% Cu on silica)

Reaction temperature: 275 °C **Catalyst particle size:** 500-800 microns

Feed rate ml/h	Sweep to feed molar ratio		Total ethanol conversion		Ethanol conversion to acetaldehyde			Ethanol conversion to MEK		Ethanol to acetic acid ethyl ester			Reaction selectivity towards acetaldehyde	
				Average		Average			Average		Average			Average
30	0.00		34.3		31.9			0.5		0.7			92.9	
			36.2		34.2			0.6		0.6			94.6	
			31.5	34.0	30.0	32.0		0.4	0.5	0.5	0.6		95.2	94.2
	1:5		40.0		38.0			0.6		0.7			95.1	
			33.6		32.8			0.4		0.3			97.8	
			43.8	39.1	40.4	37.1		1.0	0.7	0.8	0.6		92.2	95.0
	1:2		37.0		34.7			0.6		0.7			93.6	
			36.1		34.8			0.7		0.4			96.3	
			43.6	38.9	41.4	36.9		0.9	0.8	0.5	0.5		95.0	95.0
	1:1		45.3		42.0			1.0		0.7			92.6	
			39.8	42.6	37.6	39.8		0.9	1.0	0.5	0.6		94.6	93.6
	3:1		46.4	46.4	42.7	42.7		1.4	1.4	0.8	0.8		91.9	91.9

Membrane name: N8x **Catalyst:** 3.00 g (14.4 wt% Cu on silica)

Reaction temperature: 300 °C **Catalyst particle size:** 500-800 microns

Feed rate ml/h	Sweep to feed molar ratio		Total ethanol conversion		Ethanol conversion to acetaldehyde			Ethanol conversion to MEK		Ethanol to acetic acid ethyl ester			Reaction selectivity towards acetaldehyde	
				Average		Average			Average		Average			Average
10	no sweep		59.4		50.4			2.9		2.3			84.8	
			58.2		50.3			2.2		2.1			86.4	
			54.5		51.2			1.4		0.3			94.1	
			53.7	56.5	50.0	50.5		1.7	2.1	0.4	1.3		93.2	89.6
	1:5		58.5		52.0			2.2		1.4			88.9	
			60.4	59.5	49.5	50.8		3.7	3.0	1.9	1.6		81.9	85.4
	1:2		67.7		58.6			3.8		1.4			86.6	
			66.9		56.0			3.4		1.6			83.7	
			56.3	63.6	51.9	55.5		2.0	3.1	0.6	1.2		92.2	87.5
	1:1		60.7		54.4			2.1		0.8			89.6	
			66.6	63.7	59.7	57.1		3.0	2.5	1.0	0.9		89.6	89.6
	2:1		62.4		56.3			1.8		1.0			90.3	
			63.5		57.9			2.0		0.6			91.1	
			60.8	62.2	56.6	56.9		1.9	1.9	0.5	0.7		93.0	91.5
	4:1		65.4		60.7			1.8		0.5			92.8	
			63.7	64.5	60.1	60.4		1.5		0.4	0.5		94.4	93.6

Membrane name: N8x **Catalyst:** 3.00 g (14.4 wt% Cu on silica)

Reaction temperature: 300 °C **Catalyst particle size:** 500-800 microns

Feed rate ml/h	Sweep to feed molar ratio		Total ethanol conversion		Ethanol conversion to acetaldehyde			Ethanol conversion to MEK		Ethanol to acetic acid ethyl ester			Reaction selectivity towards acetaldehyde	
				Average		Average			Average		Average			Average
20	0.00		47.8		45.1			1.2		0.3			94.3	
			47.8		45.8			1.3		0.2			95.8	
			46.2	47.2	44.7	45.2		1.2	1.2	0.2	0.2		96.9	95.7
	1:5		48.3		46.4			1.3		0.2			96.2	
			47.7		45.6			1.3		0.2			95.6	
			55.7	50.5	53.0	48.4		1.4	1.3	0.2	0.2		95.3	95.7
	1:2		58.7		52.6			1.3		1.8			89.8	
			57.0		51.9			1.2		1.5			91.1	
			53.8	56.5	49.3	51.3		1.0	1.2	1.5	1.6		91.6	90.8
	4:1		57.4		52.9			1.1		1.3			92.2	
			54.7		49.9			1.0		1.3			91.2	
			52.8	54.9	48.4	50.4		0.9	1.0	1.3	1.3		91.8	91.7

APPENDIX F2

Plug flow reactor data and membrane reactor data for 2-butanol dehydrogenation

Membrane name: N8x

Catalyst: 3.50 g (14.4 wt% Cu on silica)

Reaction temperature: 190 °C

Catalyst particle size: 500-800 microns

Feed ml/h	Sweep:feed molar ratio	Total 2-butanol conversion (%)		2-Butanol to MEK conversion (%)		2-Butanol to 3-octanol conversion (%)		Selectivity towards MEK (%)	
			Avg.		Avg.		Avg.		Avg.
5	0.0	55.3		55.1		0.1		99.7	
		54.3		54.2		0.2		99.7	
		55.0	54.9	54.8	54.7	0.2	0.2	99.6	99.7
	0.6	60.4		60.1		0.3		99.6	
		59.6		59.3		0.3		99.5	
		59.1	59.7	58.7	59.4	0.3	0.3	99.4	99.5
	1.6	64.4		64.0		0.3		99.5	
		64.9		64.5		0.4		99.4	
		63.8	64.4	63.3	63.9	0.6	0.4	99.1	99.3
	3.1	70.5		70.0		0.5		99.3	
		70.9		70.2		0.7		98.9	
		67.3	69.6	66.8	69.0	0.5	0.6	99.3	99.2
	6.3	76.6		76.1		0.6		99.3	
		74.4		73.7		0.7		99.1	
		73.6		73.1		0.5		99.3	
		73.7		73.7		0.0		100.0	
		76.7	75.0	76.2	74.5	0.5	0.4	99.4	99.4
	12.6	81.1		80.5		0.6		99.3	
		78.4		77.8		0.6		99.2	
		78.0	79.2	77.5	78.6	0.5	0.6	99.4	99.3

Membrane name: N8x

Catalyst: 3.50 g (14.4 wt% Cu on silica)

Reaction temperature: 190 °C

Catalyst particle size: 500-800 microns

Feed ml/h	Sweep:feed molar ratio	Total 2-butanol conversion (%)		2-Butanol to MEK conversion (%)		2-Butanol to 3-octanol conversion (%)		Selectivity towards MEK (%)	
			Avg.		Avg.		Avg.		Avg.
10	0.0	55.5		55.3		0.2		99.7	
		55.2		54.9		0.2		99.6	
		53.8	54.8	53.6	54.6	0.2	0.2	99.5	99.6
	0.8	60.3		60.0		0.2		99.6	
		59.7		59.4		0.3		99.5	
		57.6	59.2	57.1	58.8	0.5	0.4	99.1	99.4
	1.6	58.9		58.6		0.4		99.4	
		59.4		59.2		0.2		99.6	
		59.3	59.2	59.1	58.9	0.3	0.3	99.6	99.5
	3.1	61.2		61.2		0.0		100.0	
		59.3		59.3		0.0		100.0	
		63.3	61.3	63.3	61.3	0.0	0.0	100.0	100.0
	6.3	62.7		62.7		0.0		100.0	
		63.6		63.6		0.0		100.0	
		64.6	63.6	64.6	63.6	0.0	0.0	100.0	100.0

Membrane name: N8x

Catalyst: 3.50 g (14.4 wt% Cu on silica)

Reaction temperature: 190 °C

Catalyst particle size: 500-800 microns

Feed ml/h	Sweep:feed molar ratio	Total 2-butanol conversion (%)		2-Butanol to MEK conversion (%)		2-Butanol to 3-octanol conversion (%)		Selectivity towards MEK (%)	
			Avg.		Avg.		Avg.		Avg.
15	0.0	45.3		45.3		0.0		100.0	
		45.9		45.9		0.0		100.0	
		44.0	45.1	44.0	45.1	0.0	0.0	100.0	100.0
	0.6	45.2		45.2		0.0		100.0	
		46.5		46.5		0.0		100.0	
		49.5	47.1	49.5	47.1	0.0	0.0	100.0	100.0
	1.6	46.1		46.1		0.0		100.0	
		51.1		51.1		0.0		100.0	
		47.0	48.1	47.0	48.1	0.0	0.0	100.0	100.0
	3.2	49.7		49.5		0.0		99.6	
		46.9		46.9		0.0		100.0	
		47.6		47.6		0.0		100.0	
		48.6	48.2	48.6	48.1	0.0	0.0	100.0	99.9
	6.3	52.7		52.7		0.0		100.0	
		52.5		52.5		0.0		100.0	
		54.0	53.1	54.0	53.1	0.0	0.0	100.0	100.0
20	0.0	44.8		44.8		0.0		100.0	
		44.1		44.1		0.0		100.0	
		44.4	44.4	44.4	44.4	0.0	0.0	100.0	100.0
	0.8	47.5		47.5		0.0		100.0	
		46.5		46.5		0.0		100.0	
		48.8	47.6	48.8	47.6	0.0	0.0	100.0	100.0

Membrane name: N8x

Catalyst: 3.50 g (14.4 wt% Cu on silica)

Reaction temperature: 215 °C

Catalyst particle size: 500-800 microns

Feed ml/h	Sweep:feed molar ratio	Total 2-butanol conversion (%)		2-Butanol to MEK conversion (%)		2-Butanol to 3-octanol conversion (%)		Selectivity towards MEK (%)	
			Avg.		Avg.		Avg.		Avg.
5	0.0	68.4		65.6		1.9		95.8	
		70.3		67.9		1.7		96.6	
		68.8		66.4		1.7		96.6	
		70.7	69.5	68.6	67.1	1.5	1.7	97.0	96.5
	0.6	73.5		70.8		1.9		96.3	
		72.7		70.3		1.8		96.7	
		73.1	73.1	70.5	70.5	2.0	1.9	96.4	96.5
	1.6	77.8		75.0		2.2		96.4	
		76.5	77.1	74.4	74.7	1.7	1.9	97.2	96.8
	3.1	82.8		79.5		2.8		96.1	
		81.3	82.1	78.9	79.2	2.1	2.5	97.0	96.5
	6.3	85.9		83.6		2.3		97.4	
		86.1		84.5		1.6		98.2	
		88.0	86.7	86.3	84.8	1.8	1.9	98.0	97.8
	12.6	90.4		88.4		2.0		97.8	
		92.3		91.0		1.3		98.6	
		89.5	90.7	88.3	89.2	1.2	1.5	98.7	98.4

Membrane name: N8x

Catalyst: 3.50 g (14.4 wt% Cu on silica)

Reaction temperature: 215 °C

Catalyst particle size: 500-800 microns

Feed ml/h	Sweep:feed molar ratio	Total 2-butanol conversion (%)		2-Butanol to MEK conversion (%)		2-Butanol to 3-octanol conversion (%)		Selectivity towards MEK (%)	
			Avg.		Avg.		Avg.		Avg.
10	0.0	67.9		66.9		0.9		98.5	
		68.8		67.6		1.0		98.3	
		68.6	68.4	67.3	67.3	1.0	0.9	98.2	98.3
	0.8	74.2		72.7		1.3		98.0	
		74.7		73.5		1.0		98.4	
		75.6	74.8	74.4	73.5	1.1	1.1	98.4	98.3
	1.6	78.8		77.1		1.5		97.9	
		77.6		76.6		1.1		98.6	
		78.7	78.4	77.5	77.1	1.2	1.3	98.5	98.3
	3.1	79.7		79.5		0.2		99.7	
		81.9		81.5		0.4		99.5	
		81.7	81.1	81.1	80.7	0.6	0.4	99.3	99.5
	6.3	86.5		85.9		0.6		99.3	
		86.4		85.7		0.7		99.2	
		86.8	86.6	85.9	85.8	1.0	0.8	98.9	99.1

Membrane name: N8x

Catalyst: 3.50 g (14.4 wt% Cu on silica)

Reaction temperature: 215 °C

Catalyst particle size: 500-800 microns

Feed ml/h	Sweep:feed molar ratio	Total 2-butanol conversion (%)		2-Butanol to MEK conversion (%)		2-Butanol to 3-octanol conversion (%)		Selectivity towards MEK (%)	
			Avg.		Avg.		Avg.		Avg.
20	0.0	62.4		62.4		0.0		100.0	
		63.0		63.0		0.0		100.0	
		62.2		62.2		0.0		100.0	
		63.1	62.7	63.1	62.7	0.0	0.0	100.0	100.0
	0.8	67.1		67.1		0.0		100.0	
		66.7		66.7		0.0		100.0	
		67.3	67.0	67.3	67.0	0.0	0.0	100.0	100.0
	1.6	65.7		65.7		0.0		100.0	
		67.9		67.9		0.0		100.0	
		67.9	67.2	67.8	67.1	0.0	0.0	99.9	100.0
	3.1	68.2		68.2		0.0		100.0	
		68.6	68.4	68.6	68.4	0.0	0.0	100.0	100.0
	6.3	70.7		70.7		0.0		100.0	
		69.5	70.1	69.5	70.1	0.0	0.0	100.0	100.0
15	0.0	67.3		67.3		0.0		100.0	
		67.3		67.3		0.0		100.0	
		66.5	67.0	66.5	67.0	0.0	0.0	100.0	100.0
30	0.0	54.8		54.8		0.0		100.0	
		56.8		56.8		0.0		100.0	
		54.8	55.4	54.8	55.4	0.0	0.0	100.0	100.0

Membrane name: N8x

Catalyst: 3.50 g (14.4 wt% Cu on silica)

Reaction temperature: 240 °C

Catalyst particle size: 500-800 microns

Feed ml/h	Sweep:feed molar ratio	Total 2-butanol conversion (%)		2-Butanol to MEK conversion (%)		2-Butanol to 3-octanol conversion (%)		Selectivity towards MEK (%)	
			Avg.		Avg.		Avg.		Avg.
5.0	0.0	78.3		76.7		1.1		98.0	
		78.3		77.2		1.1		98.6	
		79.2	78.6	77.6	77.2	1.1	1.1	98.0	98.2
	0.6	83.4		81.6		1.3		97.9	
		85.9	84.7	83.9	82.8	1.6	1.4	97.6	97.7
	1.6	85.8		84.8		1.0		98.9	
		86.1	85.9	85.1	85.0	0.9	1.0	98.9	98.9
	3.1	88.8		87.9		0.9		99.0	
		88.8		88.0		0.8		99.1	
		90.4	89.4	89.4	88.4	1.1	0.9	98.8	99.0
	6.3	93.1		91.7		1.4		98.5	
		92.0		90.8		1.2		98.7	
		92.8	92.6	91.7	91.4	1.1	1.2	98.8	98.7
	12.6	95.0		93.5		1.4		98.5	
		95.4		94.4		1.0		98.9	
		95.9	95.4	94.4	94.1	1.5	1.3	98.5	98.6

Membrane name: N8x

Catalyst: 3.50 g (14.4 wt% Cu on silica)

Reaction temperature: 240 °C

Catalyst particle size: 500-800 microns

Feed ml/h	Sweep:feed molar ratio	Total 2-butanol conversion (%)		2-Butanol to MEK conversion (%)		2-Butanol to 3-octanol conversion (%)		Selectivity towards MEK (%)	
			Avg.		Avg.		Avg.		Avg.
10	0.0	79.5		79.3		0.2		99.7	
		77.9		77.6		0.3		99.6	
		79.6	79.0	79.3	78.7	0.3	0.3	99.7	99.6
	0.8	84.4		84.1		0.4		99.6	
		82.8	83.6	82.1	83.1	0.5	0.4	99.1	99.3
	1.6	85.8		85.5		0.4		99.6	
		87.0	86.4	86.6	86.0	0.4	0.4	99.5	99.5
	3.1	89.6		89.2		0.4		99.6	
		88.0		87.6		0.4		99.5	
		88.4	88.7	88.1	88.3	0.3	0.4	99.7	99.6
	6.3	91.3		91.0		0.3		99.6	
		90.9		90.5		0.3		99.6	
		90.5	90.9	90.5	90.7	0.0	0.2	100.1	99.8

Membrane name: N8x

Catalyst: 3.50 g (14.4 wt% Cu on silica)

Reaction temperature: 240 °C

Catalyst particle size: 500-800 microns

Feed ml/h	Sweep:feed molar ratio	Total 2-butanol conversion (%)		2-Butanol to MEK conversion (%)		2-Butanol to 3-octanol conversion (%)		Selectivity towards MEK (%)	
			Avg.		Avg.		Avg.		Avg.
20	0.0	82.4		81.2		1.2		98.5	
		81.8		80.6		1.1		98.6	
		81.8	82.0	80.4	80.7	1.4	1.3	98.3	98.5
	0.8	82.2		81.3		0.9		98.9	
		86.1		85.3		0.7		99.2	
		85.6	84.6	84.8	83.8	0.7	0.8	99.1	99.1
	1.6	88.4		87.9		0.5		99.4	
		87.4		87.0		0.4		99.5	
		88.9	88.2	88.2	87.7	0.7	0.5	99.2	99.4
	3.1	87.9		87.4		0.5		99.5	
		88.8		88.5		0.3		99.6	
		87.1	87.9	86.7	87.6	0.3	0.4	99.6	99.6
	6.3	89.2		88.5		0.7		99.2	
		91.2	90.2	90.9	89.7	0.3	0.5	99.6	99.4
30	0.0	77.4		77.1		0.3		99.6	
		78.2		77.8		0.3		99.6	
		79.1	78.2	78.7	77.9	0.4	0.3	99.5	99.6
40	0.0	78.8		78.7		0.0		100.0	
		77.0	77.9	77.0	77.9	0.0	0.0	100.0	100.0

APPENDIX G

Sensitivity analysis for the catalytic membrane reactor model

The following conditions were studied:

1. **The effect of reaction rate k'-values at standard conditions.**
2. **Effect of acetaldehyde adsorption coefficient at standard conditions.**
3. **Effect of H_2 to N_2 selectivity at standard conditions ($P_{m,hydrogen}$ is constant).**
4. **The effect of the effectiveness factor at standard conditions.**
5. **Effect of ethanol feed flow rate at standard conditions.**
6. **Effect of N_2 sweep gas to ethanol molar feed ratio at standard conditions.**
7. **Effect of hydrogen permeance at constant selectivity and standard conditions.**
8. **Effect of H_2 permeance at constant permeances for N_2, ethanol and acetaldehyde.**
9. **Effect of hydrogen permeance at varying selectivity and non-standard conditions.**
10. **Effect of hydrogen permeance at constant selectivity and non-standard conditions.**

Note:

Each of these ten investigations consists of six different figures. For the first three figures, the conditions at the membrane tube exit are used. For the last three figures, data is plotted along the axis of the membrane.

The ethanol conversion in the first figure on each page is defined as follows:

$$X_{ethanol} = \frac{F_{et(0),t} - F_{et,t} - F_{et,s}}{F_{et(0),t}} \qquad \textbf{(G.1)}$$

Standard conditions for ethanol dehydrogenation

Reaction T (°C)	275
Ethanol feed flow rate (ml/h) (mol/s)	10 $4.771*10^{-5}$
N_2 sweep to ethanol feed molar ratio	1
Shell pressure [Pa]	100000
Tube pressure [Pa]	100000
Reactor length [m]	0.18
R_m [m]	0.0035
ρ_b [kg/m^3]	430
m [kg]	0.0030
ε_b	0.4
k [mol/kg cat.s.Pa]	$1.27*10^{-6}$
$K_{ethanol}$ [Pa^{-1}]	$4.32*10^{-6}$
$K_{acetaldehyde}$ [Pa^{-1}]	$2.91*10^{-6}$
$K_{hydrogen}$ [Pa^{-1}]	$6.57*10^{-5}$
K_{eq} [Pa]	24080
η	1
$P_{m,hydrogen}$ [μmol/m^2.Pa.s]	3.78
$P_{m,nitrogen}$ [nmol/m^2.Pa.s]	21.29
$P_{m,ethanol}$ [nmol/m^2.Pa.s]	5.32
$P_{m,acetaldehyde}$ [nmol/m^2.Pa.s]	5.32

Shell and tube flow profiles for standard conditions

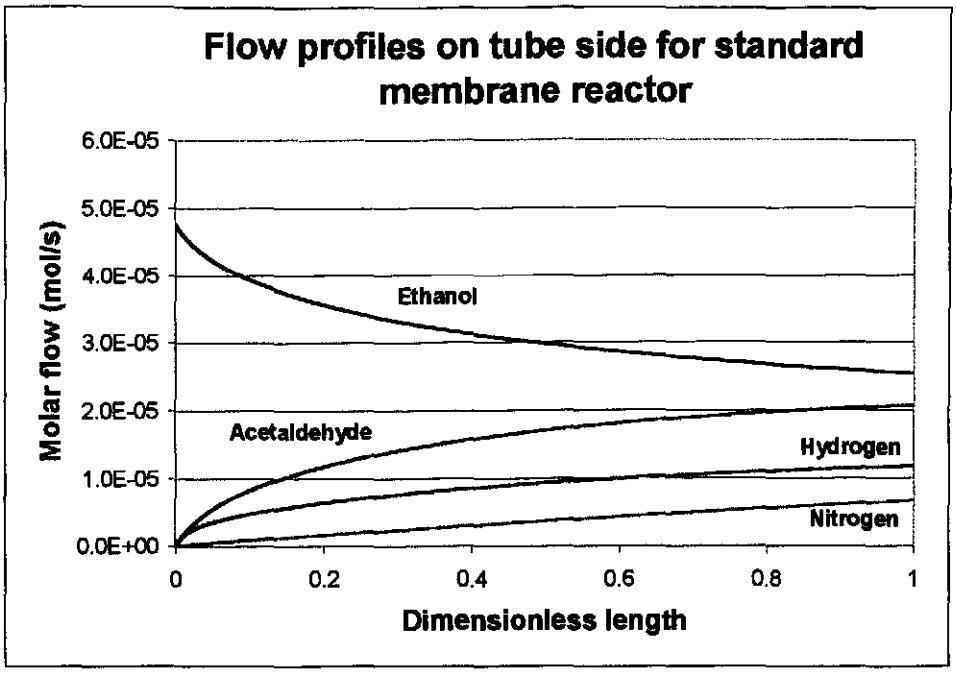

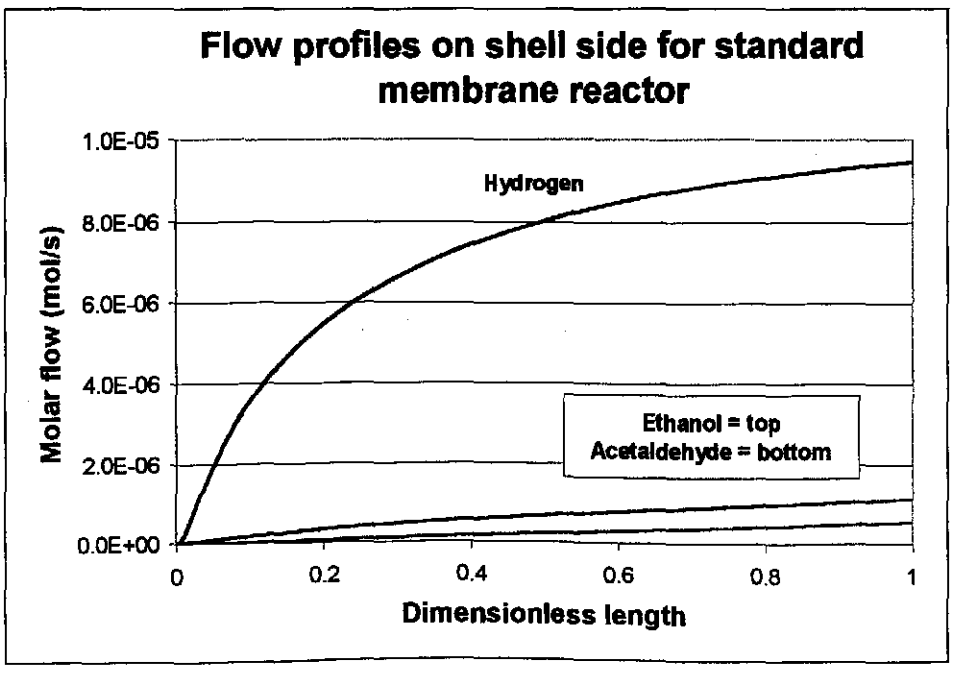

1. The effect of reaction rate k'-values at standard conditions.

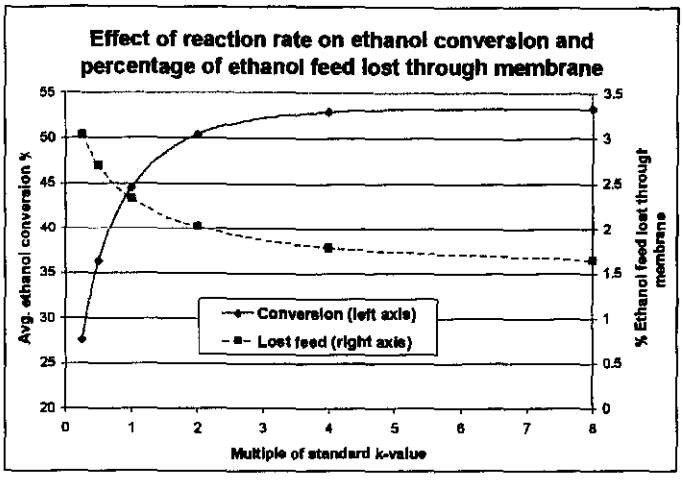

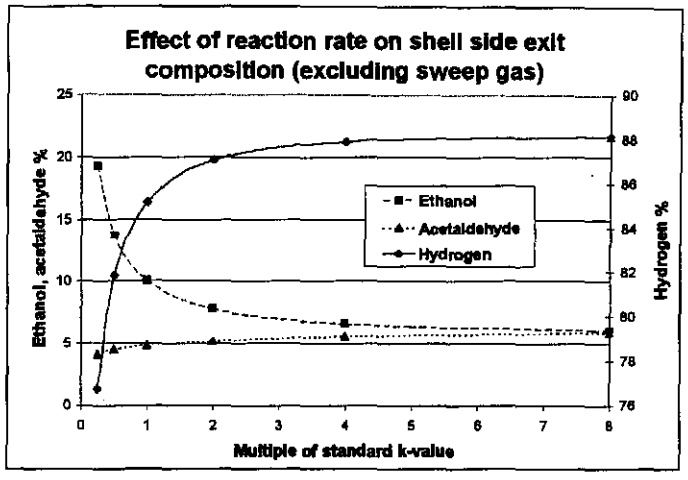

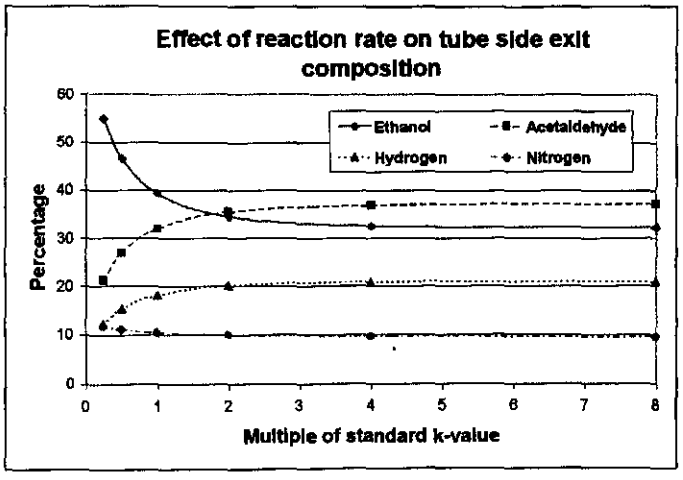

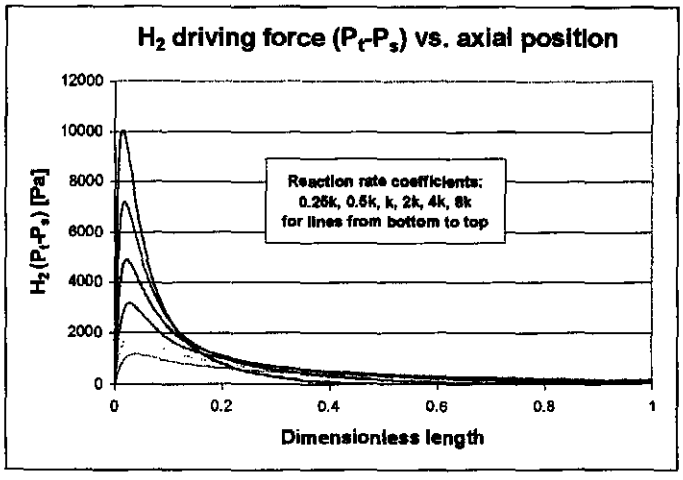

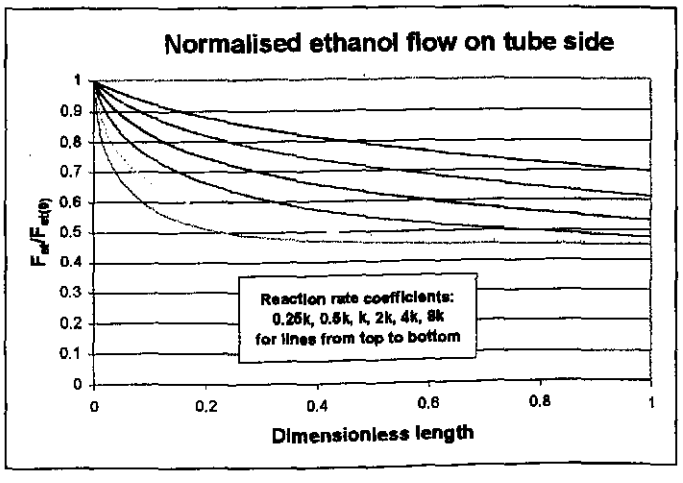

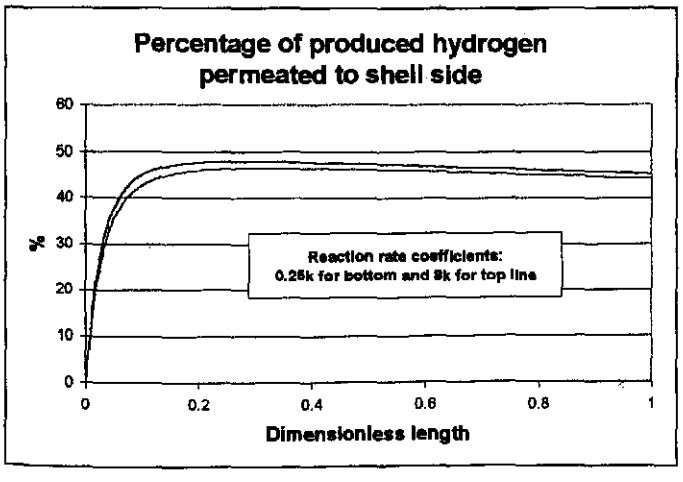

2. Effect of acetaldehyde adsorption coefficient at standard conditions.

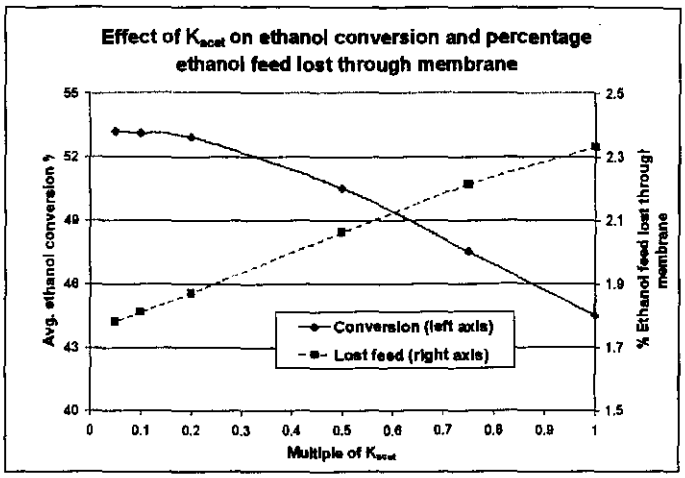

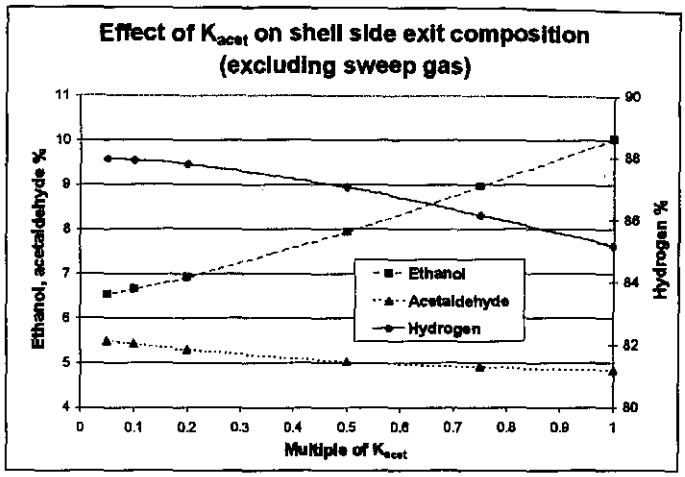

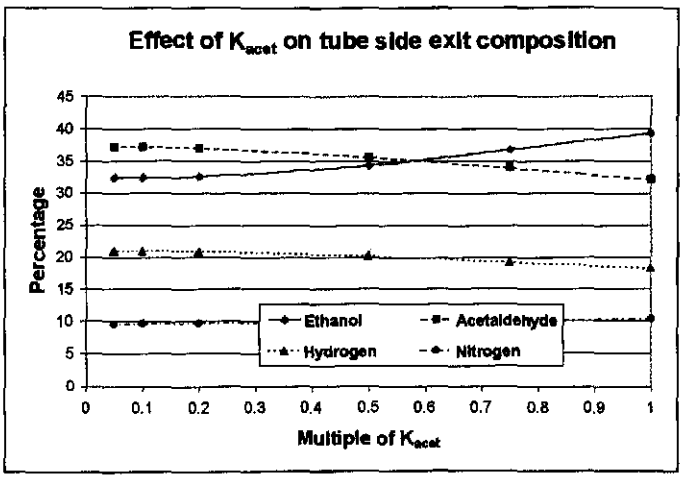

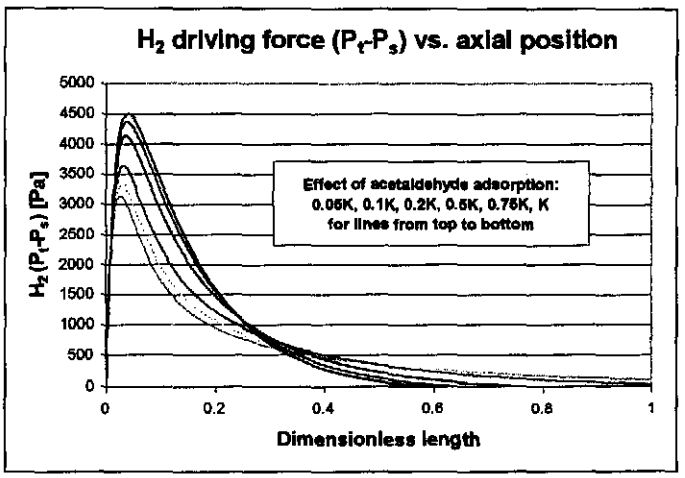

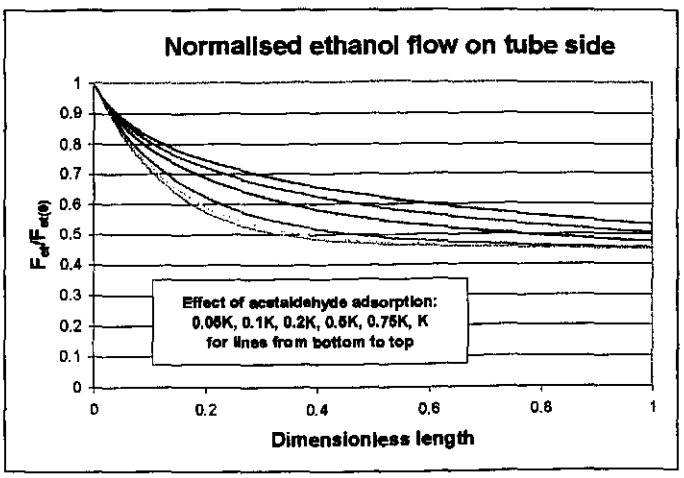

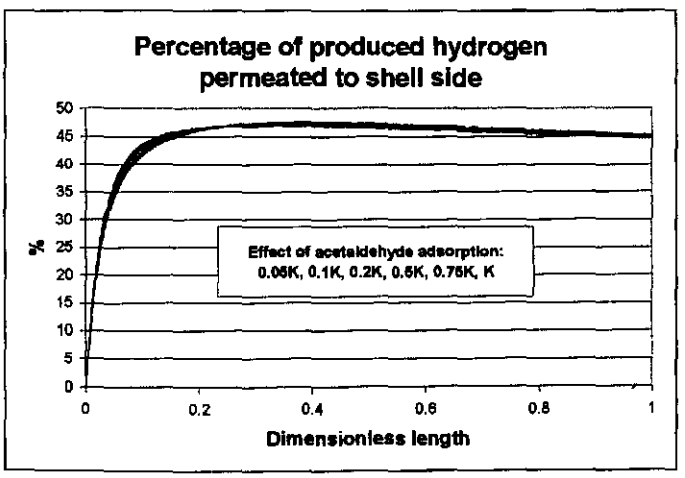

3. Effect of H_2 to N_2 selectivity at standard conditions ($P_{m,hydrogen}$ is constant).

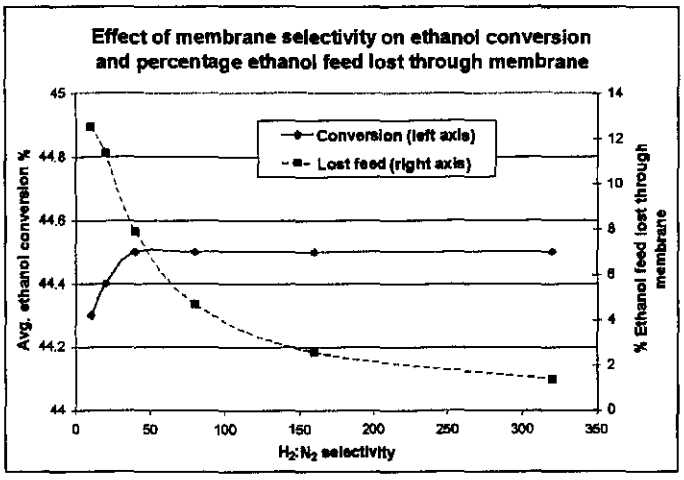

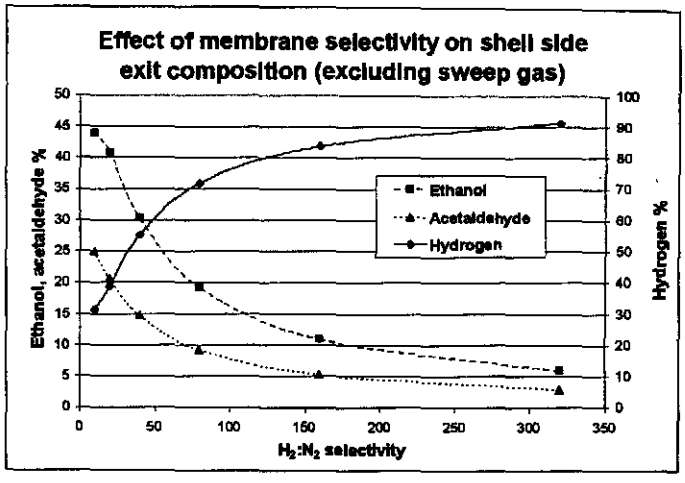

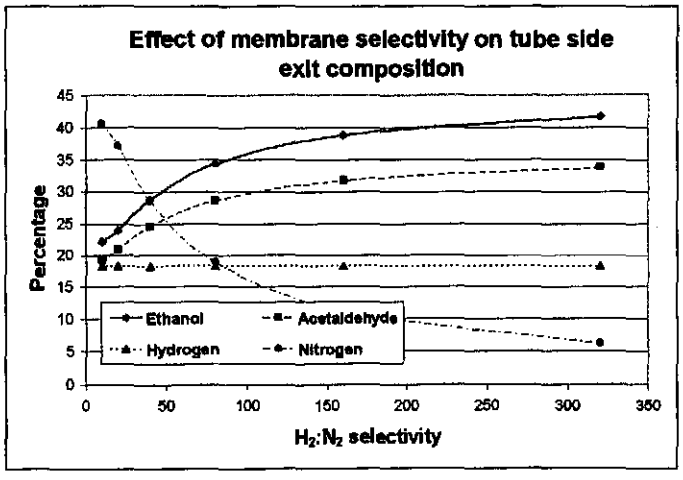

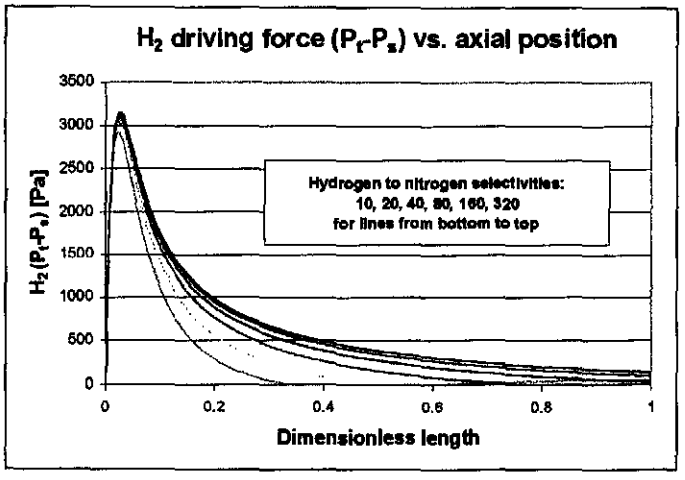

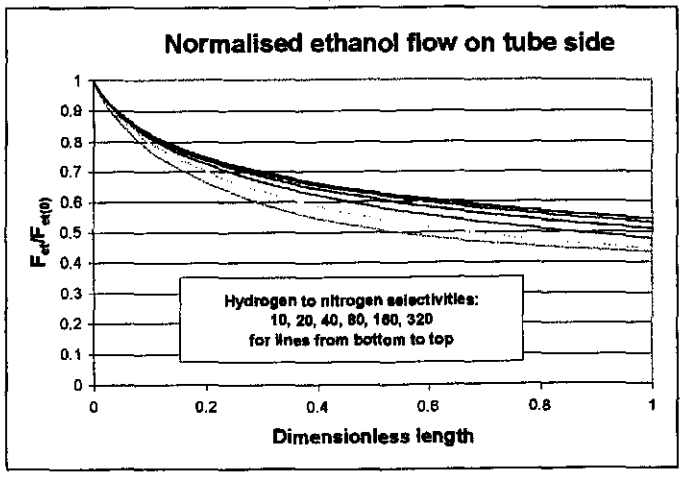

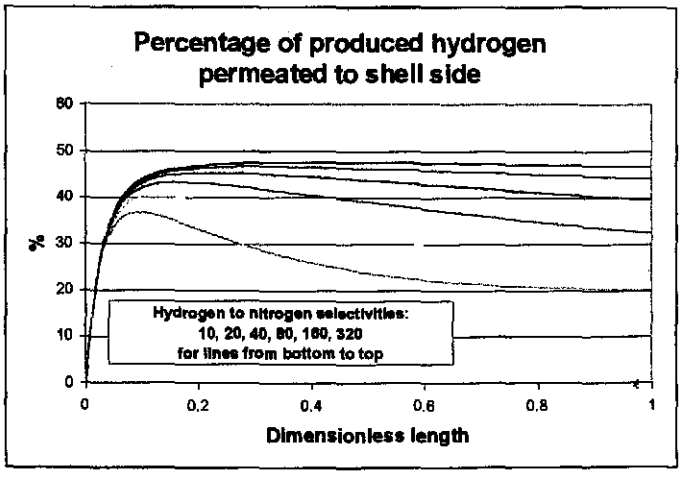

4. The effect of the effectiveness factor at standard conditions.

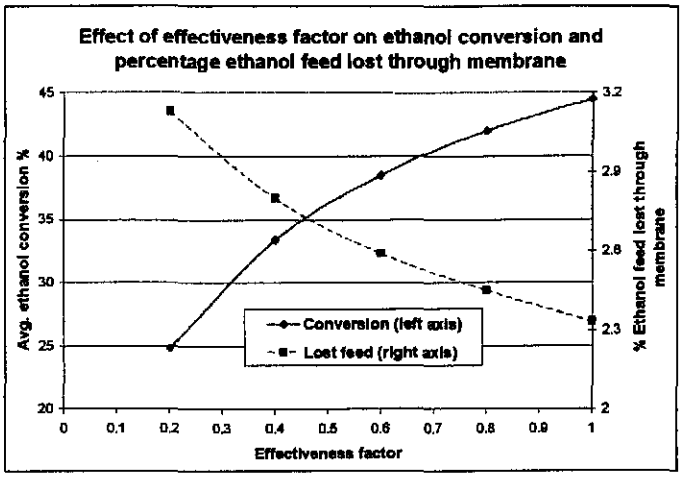

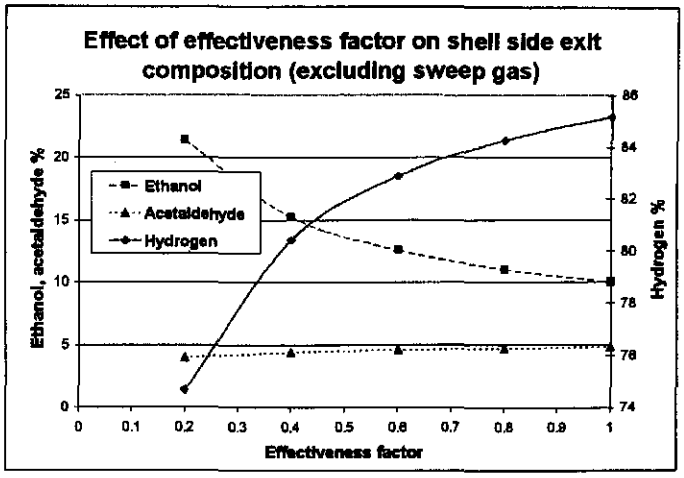

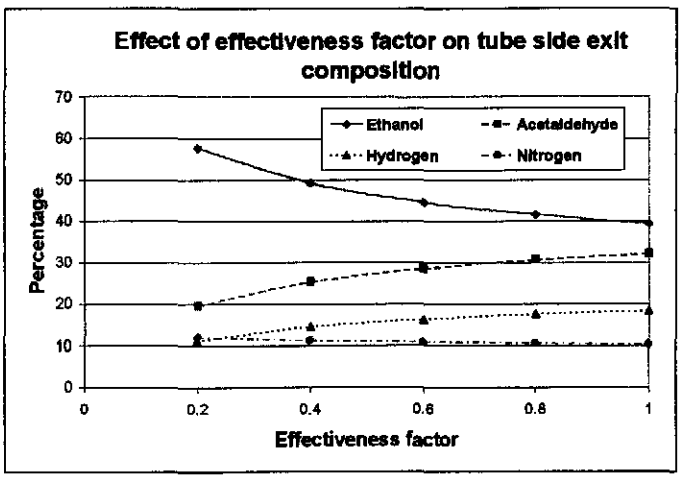

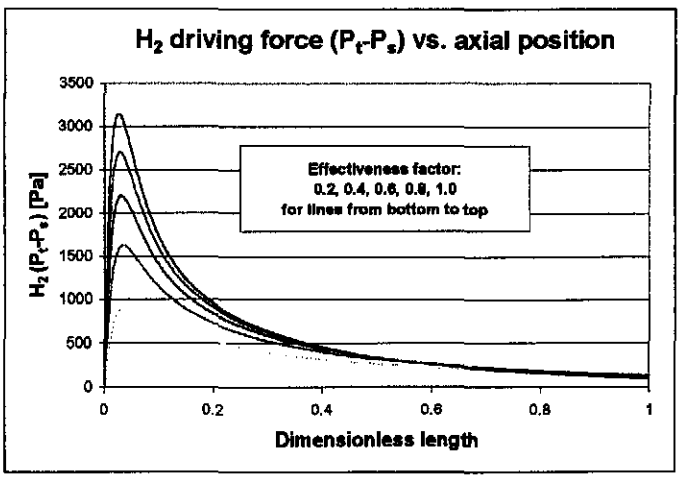

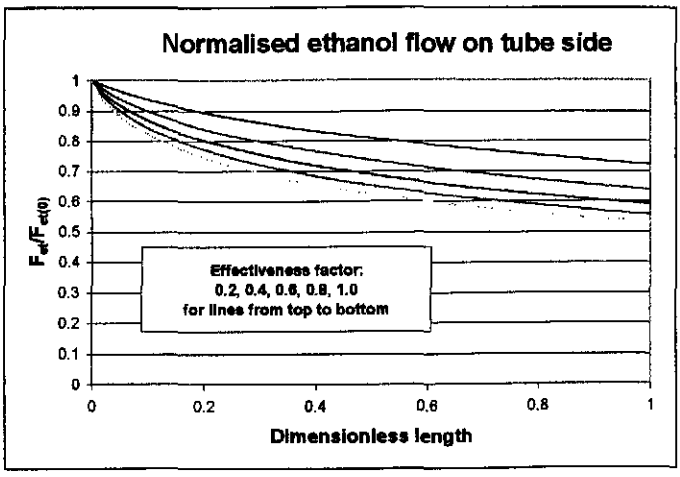

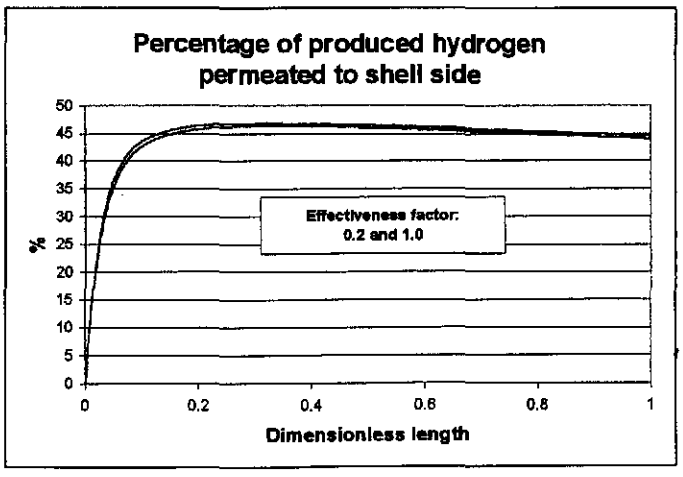

5. Effect of ethanol feed flow rate at standard conditions.

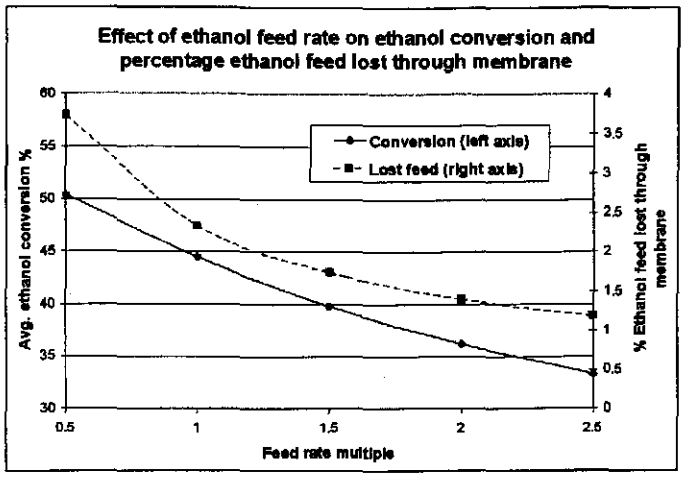

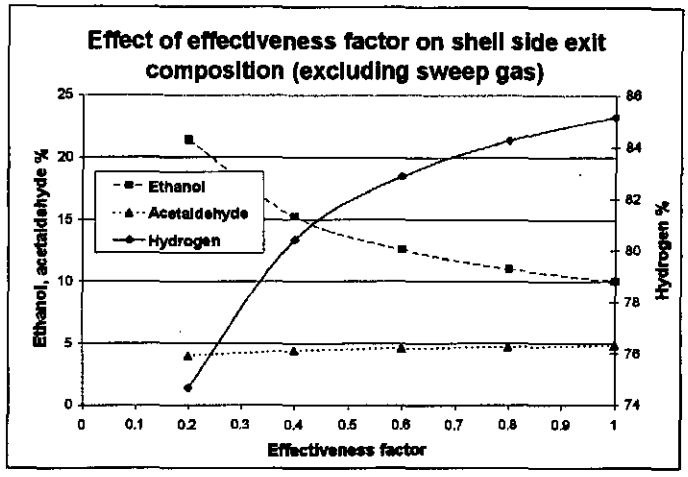

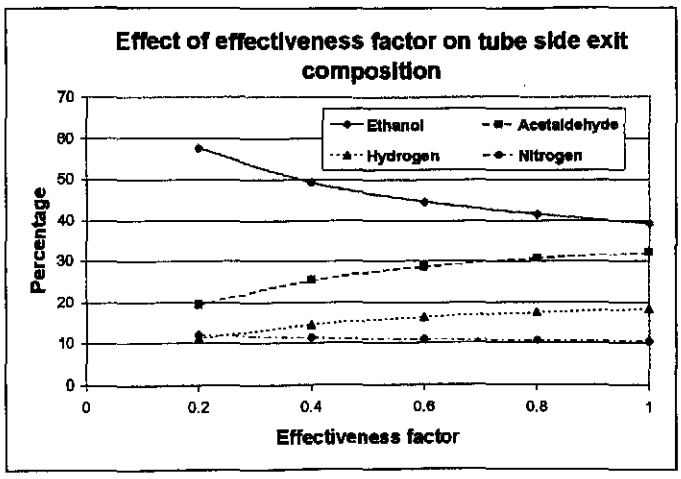

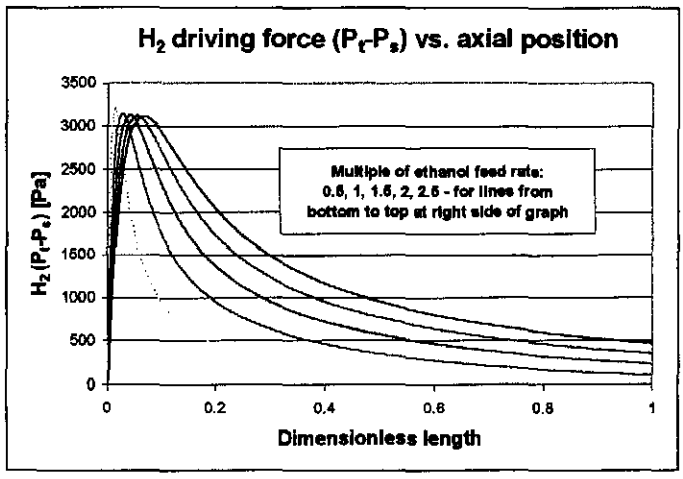

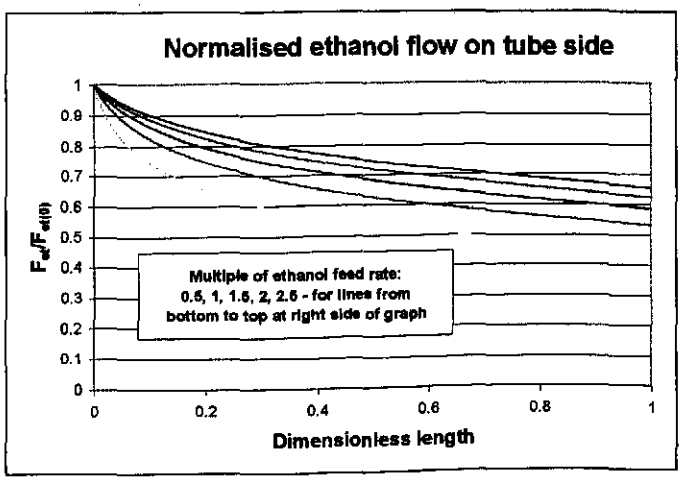

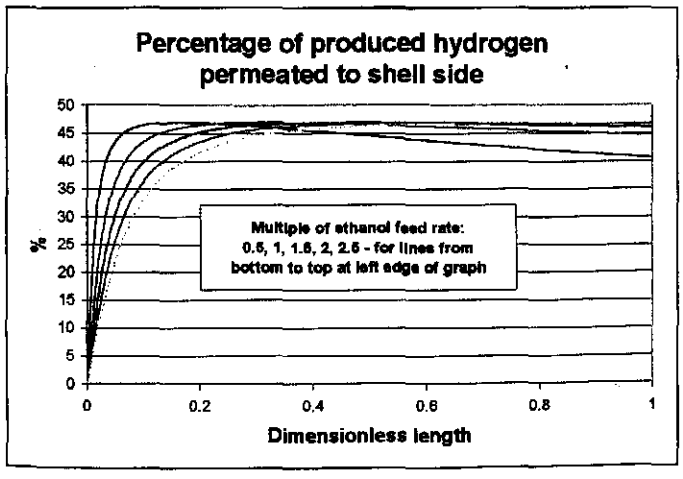

6. Effect of N_2 sweep gas to ethanol molar feed ratio at standard conditions.

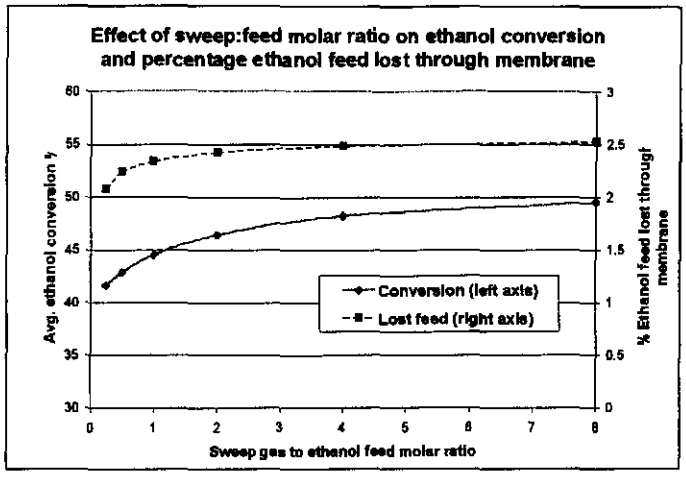

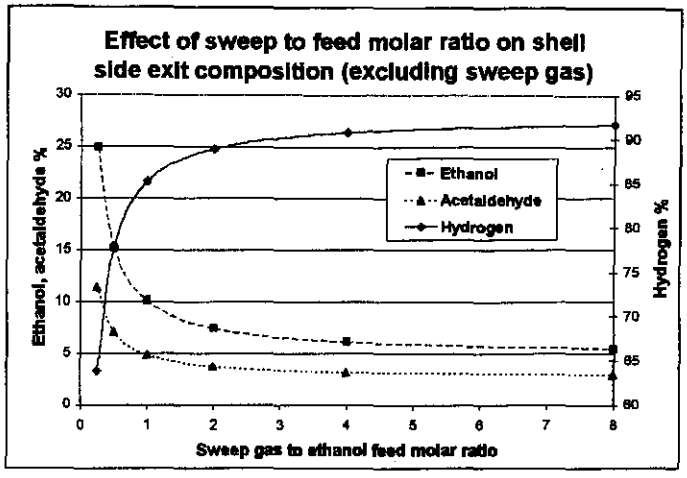

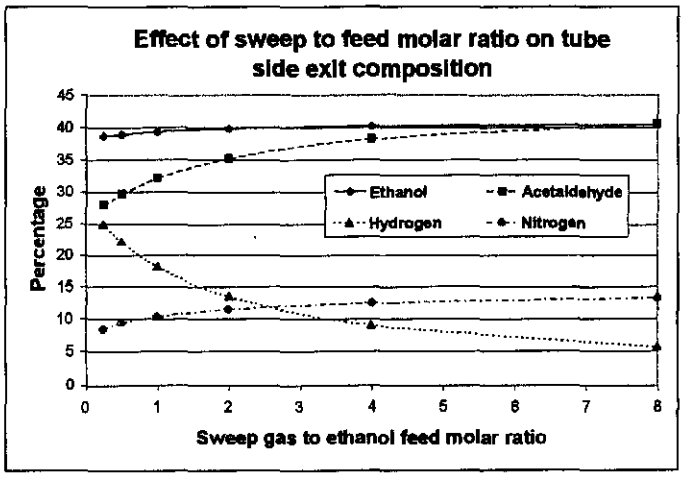

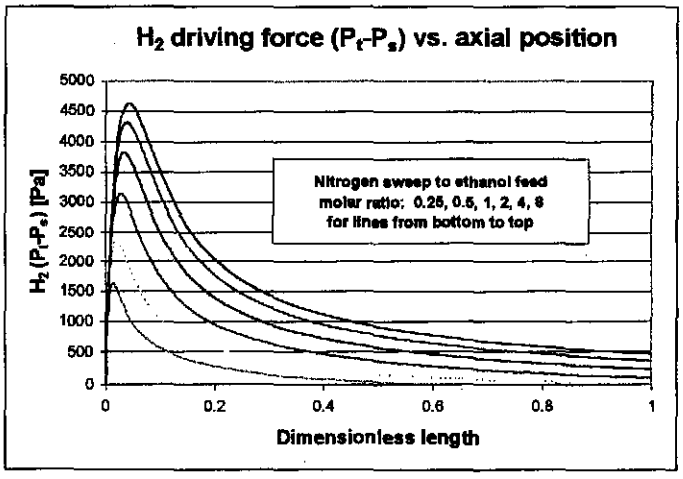

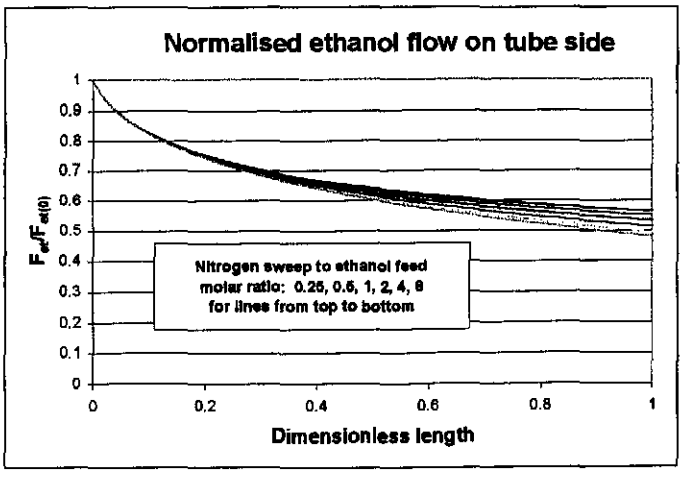

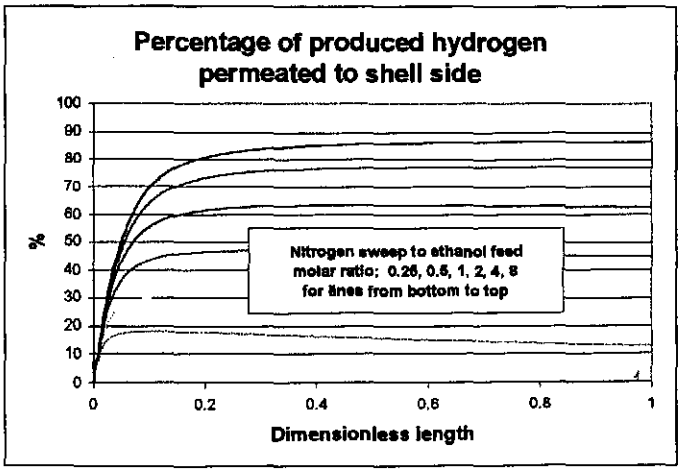

7. Effect of hydrogen permeance at constant selectivity and standard conditions.

For selectivity to be constant; N_2, ethanol and acetaldehyde permeance have to change with H_2 permeance

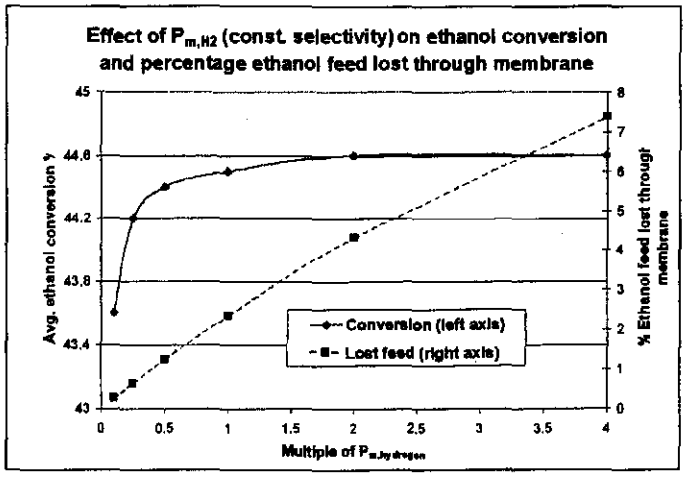

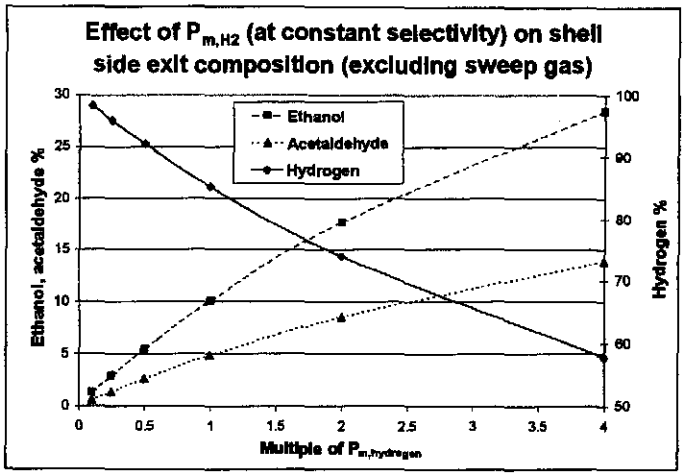

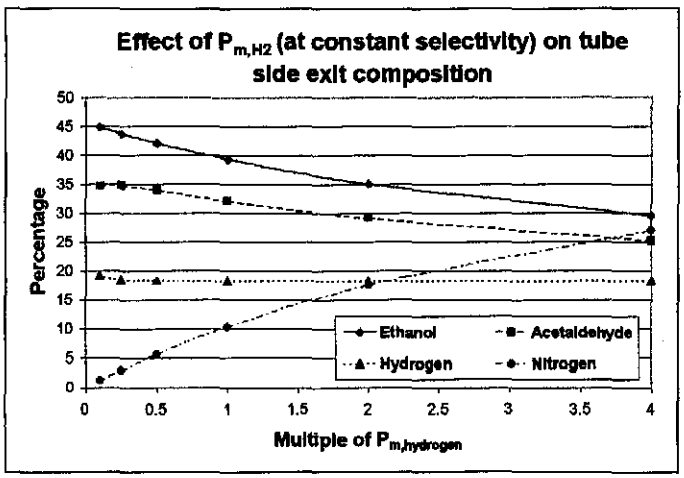

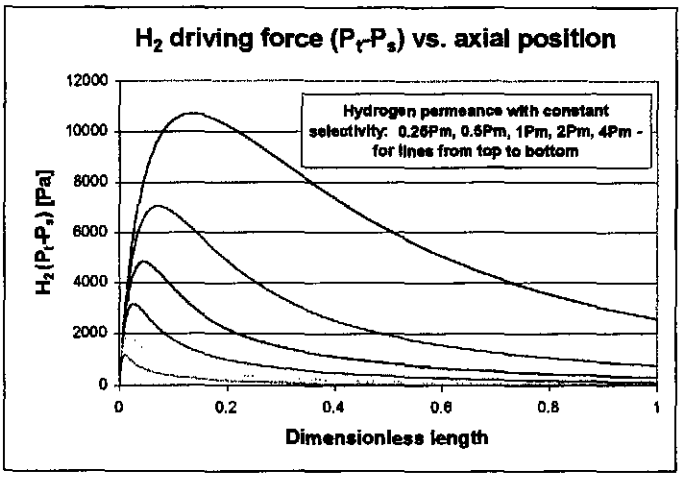

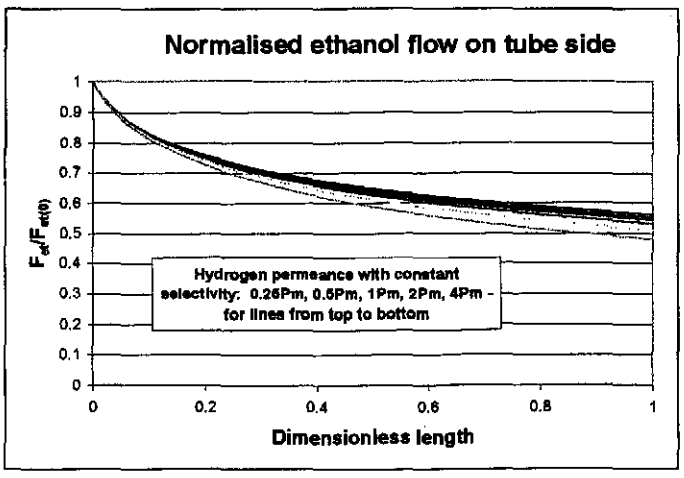

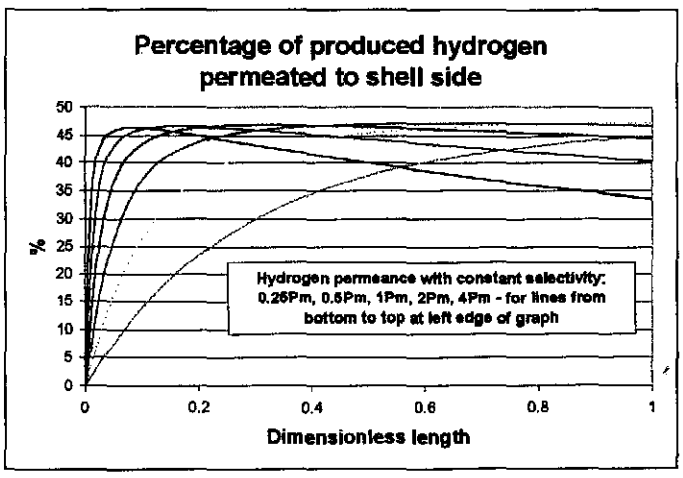

8. Effect of H_2 permeance at constant permeances for N_2, ethanol and acetaldehyde.

This implies that the selectivities will increase with an increase in H_2 permeance

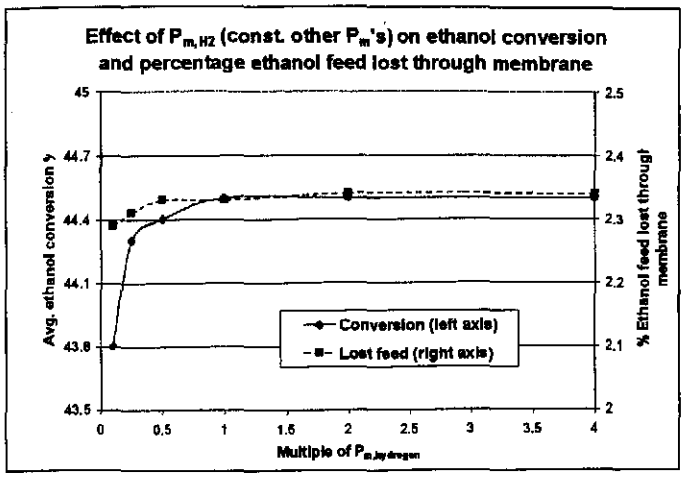

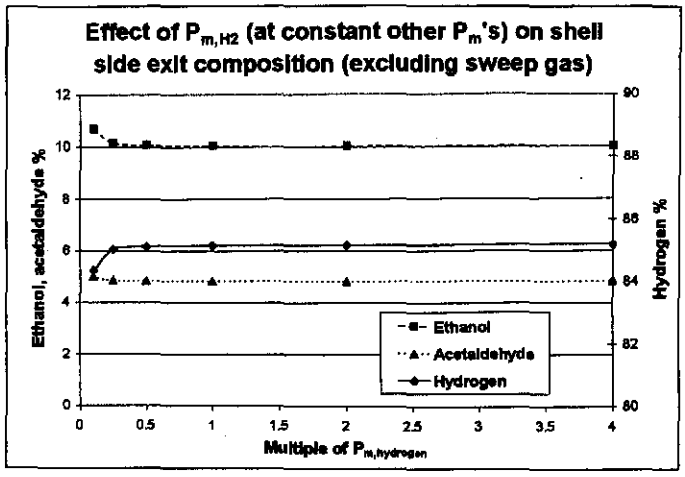

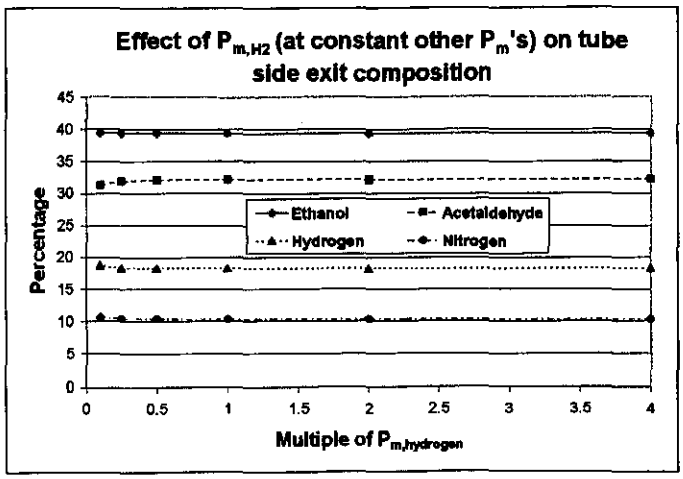

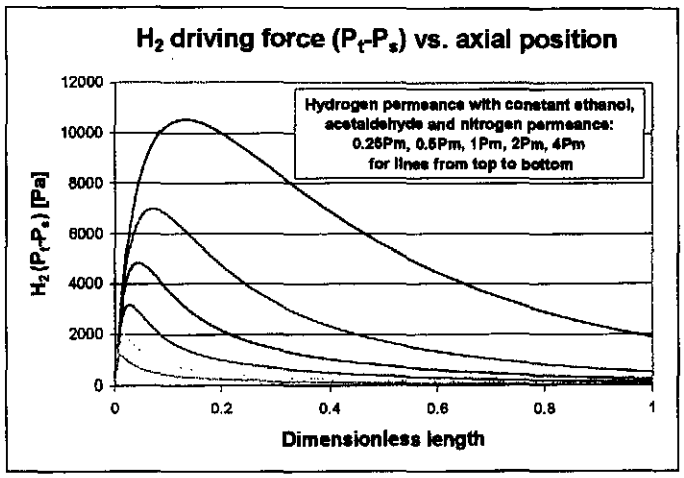

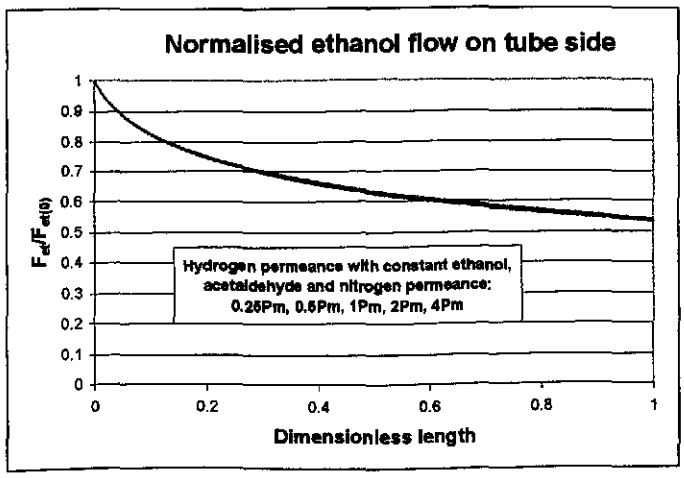

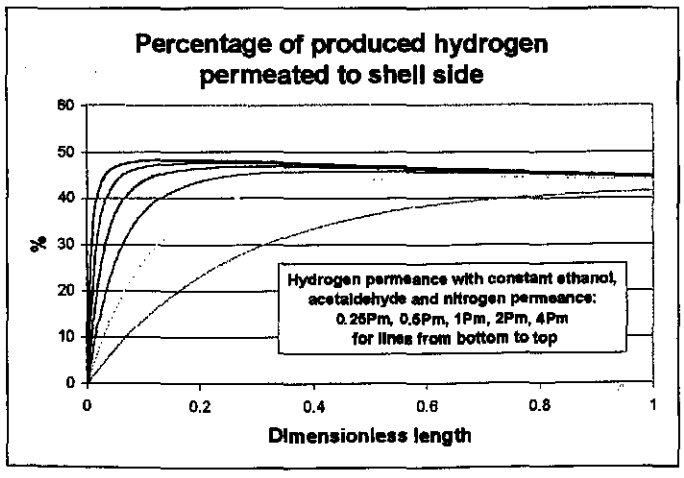

9. Effect of hydrogen permeance at varying selectivity and non-standard conditions.

Four times standard sweep gas flow rate and four times standard k-value

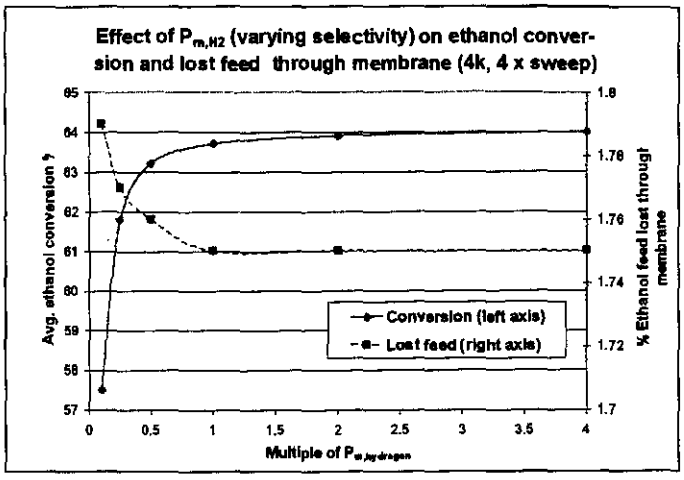

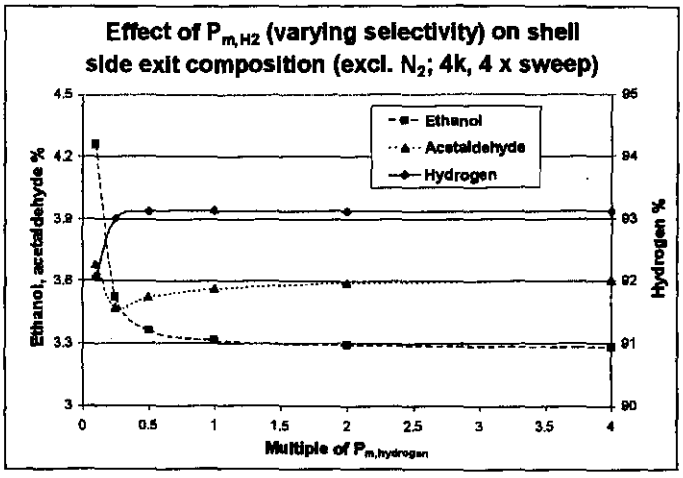

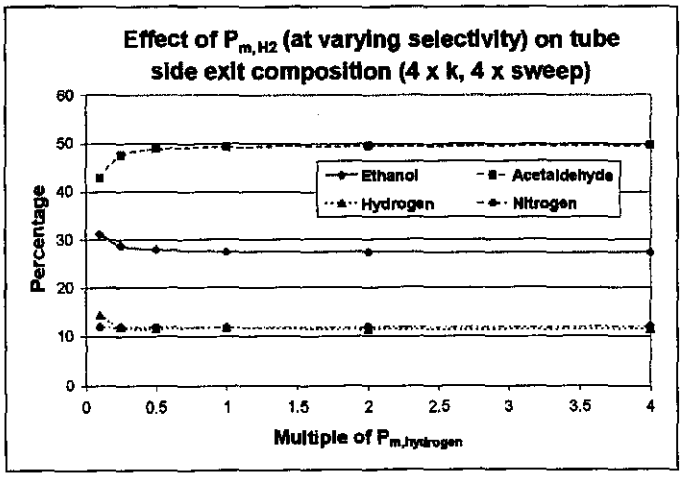

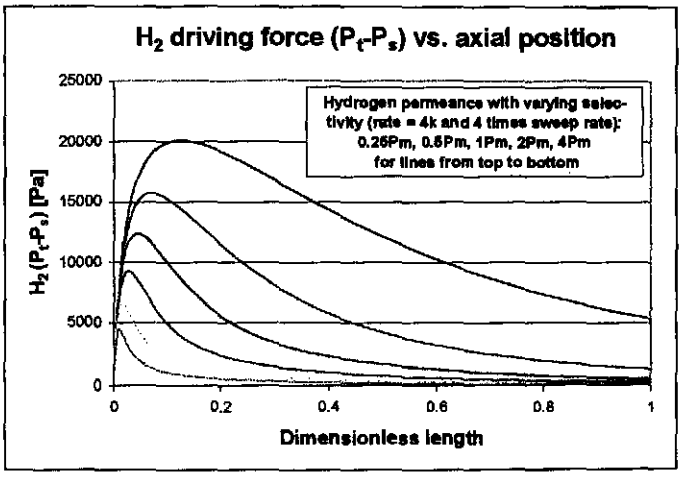

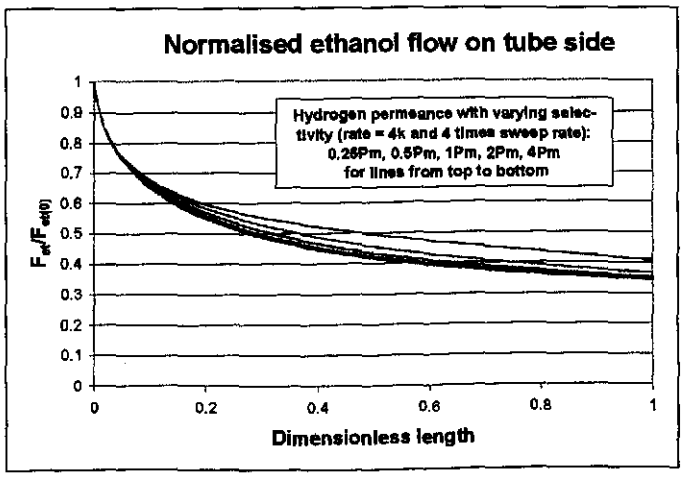

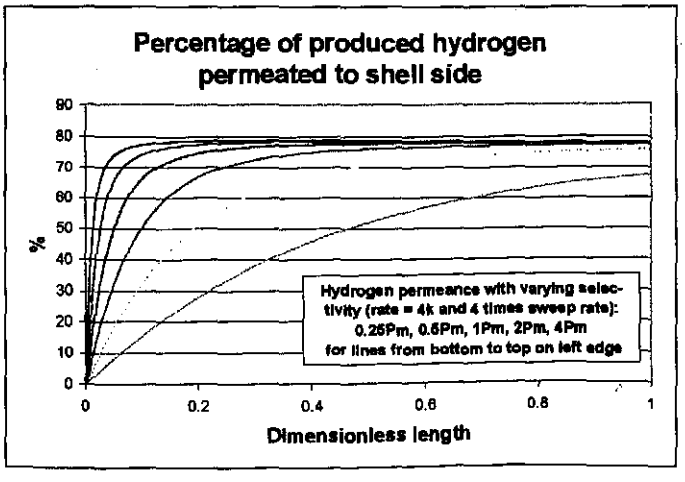

10. Effect of hydrogen permeance at constant selectivity and non-standard conditions.

Four times standard sweep gas flow rate and four times standard k-value